UNIVERSITÉ DE STRASBOURG

ÉCOLE DOCTORALE 414

INSERM U1109 – Tumor Biomechanics

THÈSE présentée par :

Luc MERCIER

soutenue le : **31 octobre 2017**

pour obtenir le grade de : **Docteur de l'université de Strasbourg**

Discipline : Sciences de la Vie et de la Santé

Spécialité : Biologie cellulaire

Disséquer la cascade métastatique par des approches innovantes d'imagerie cellulaire

THÈSE dirigée par :
  Dr. GOETZ Jacky   Université de Strasbourg

RAPPORTEURS :
  Dr. VIGNJEVIC Danijela   Institut Curie
  Dr. MONTAGNAC Guillaume   Institut Gustave Roussy

AUTRES MEMBRES DU JURY :
  Pr. GEORGEL Philippe   Université de Strasbourg

A ma famille, mes parents, Clémence et Judith

Remerciements

Je tiens à remercier mon directeur de thèse, Jacky, qui m'a recruté en tant que premier membre de son équipe de recherche, m'a fait confiance et m'a permis par la suite de réaliser cette thèse. J'ai pendant ces 5 ans de collaboration beaucoup appris à ses côtés.

Je remercie aussi Patricia qui a été ma directrice officielle au début de ma thèse. Merci d'avoir partagé ta grande expérience et de m'avoir apporté ton aide.

Je tiens à remercier aussi mes collègues de travail. Olivier, le chercheur expérimenté. J'ai vraiment apprécié que tu sois mon TC (Task Chief). Vincent le post doc senior devenu CR. Nos longues discussions m'ont beaucoup apporté que ce soit au labo ou en dehors. Sofia ma première collègue de travail dans l'équipe Tumor biomechanics. Guillaume notre super ingénieur en imagerie avec qui j'ai partagé entre autres de longues mais passionnantes journées de segmentation. Seuls ceux qui savent peuvent comprendre… Nina notre « princesse » qui m'a apporté son aide pour la microscopie électronique et qui m'a fait découvrir sa passion pour le lindy hop. Gautier et Naël dits la fine équipe avec qui j'ai partagé mon bureau/labo et de nombreux bons moments. Sébastien notre cher physicien. Merci à Shima et Maria nouvellement arrivé dans notre laboratoire. Merci aussi à Annick pour tes nombreux conseils. Merci également à notre formidable secrétaire, Isabelle, sans qui la vie de labo serait encore plus compliquée.

Je remercie aussi les autres membres de l'équipe MN3T anciens et nouveaux, Thomas et Benoit les post docs, Tristan l'ancien thésard, Sunn le nouveau thésard ainsi que leur cheffe Gertraud.

Je remercie aussi Christiane qui m'a enseigné les techniques de cultures cellulaires mais aussi de microtomie et de cryotomie, un savoir technique irremplaçable.

Merci à Mika et aux animaliers, Michèle, Pierre, Solène, Fanny qui travaillent dans l'ombre mais sans qui rien ne serait possible.

Merci à Jocelyn Laporte et Johan Böhm qui ont permis d'achever ce travail d'imagerie intravitale dans l'oreille de souris.

Merci aussi à Yannick Schwab, grâce à qui je me suis lancé dans cette aventure. Merci aussi à son équipe de l'EMBL et notamment Matthia qui a permis que ce travail de microscopie corrélative soit aussi abouti. C'était un plaisir de travailler ensemble et d'avoir pu apprendre tant de nouvelles techniques.

Je remercie aussi nos différents collaborateurs avec qui j'ai eu l'occasion de travailler. Elodie Henriet de l'équipe de Frédéric Saltel abec qui j'ai travaillé sur les invadopodes. Andrey Klymchenko, Nicolas

2

TABLE DES MATIERES

Liste des abréviations :

AC : Anchor cell
ADN : Acide désoxyribonucléique
AFM : Atomic force microscopy
AMPH2 : Amphiphysin 2
ARN : Acide ribonucléique
ATUM : Automated tape-collecting ultramicrotome
BM : Membrane Basale
BMDC : Bone marrow-derived cells
CAF : Cancer-associated fibroblast
CARS : Coherent Anti-Stokes Raman Scattering
CLEM : Correlative light and electron microscopy
CLSM : Confocal Laser Scanning Microscopy
CNM : Centronuclear myopathy
CTC : Cellules Tumorales Circulantes
DAB : Diaminobenzidine
DNM2 : Dynamin 2
ECM : Matrice Extracellulaire
EGFR : Epidermal growth factor receptor
EMT : Transition épithélio-mésenchymateuse
FGF : Fibroblast growth factor
FRET : Förster resonance energy transfer
FIB/SEM : Focused ion beam / scanning electron microscopy
GFP : Green fluorescent microscopy
HPF : High pressure freezing
MB : Membrane basale
MEB : Microscope électronique à balayage
MEC : Matrice extracellulaire
MET : Microscope électronique à transmission
MTM1 : Myotubularin 1
miniSOG : mini singlet oxygen genrator
NIRB : Near-infrared branding
OPO : Oscillateur Paramétrique Optique
PALM/STORM : Photo-activated localization microscopy / Stochastic optical reconstruction microscopy
PMN : Pre-metastatic niche
SBFSEM : Serial block face scanning electron microscopy
SHG : Second Harmonic Generation
SIM: Structured illumination microscopy
SPIM: Selective Plane Illumination Microscopy
STED: stimulated emission depletion
TGFβ: Transforming growth factor β
THG : Third Harmonic Generation
TMEM: Tumor microEnvironment of metastasis
VEGF: Vascular endothelial growth factor

Liste des figures :

1 Introduction

1.1 Cancer & Métastases

La cancérogénèse est le processus de développement d'une cellule cancéreuse dans lequel plusieurs facteurs entrent en jeu comme les caractéristiques propres de l'individu (hérédité), son mode de vie (alcool, tabagisme) ainsi que les expositions extérieures (infections, facteurs environnementaux). Le cancer est une pathologie à évolution longue qui intervient suite à des mutations génétiques aléatoires de l'ADN qui conduisent à une dérégulation de la division et l'invasion cellulaire. C'est une maladie qui peut se déclarer à tout âge mais néanmoins plus fréquente au-delà de 60 ans. Cette prévalence liée à l'âge s'explique par l'accumulation au cours du temps de mutations et par une probable baisse d'efficacité des mécanismes de réparations de l'ADN. En France, 385 000 nouveaux cas de cancer ont été diagnostiqués en 2015 (INCa).

Une des caractéristiques des cellules cancéreuses est leur pouvoir invasif. Ces cellules peuvent en effet migrer dans la circulation sanguine puis envahir un autre organe à distance de la tumeur primaire. Dans ce nouveau tissu hôte, elles vont continuer à se multiplier pour former une tumeur secondaire qu'on appelle métastase. La formation de métastases est la principale cause de mortalité.

Les cellules cancéreuses n'évoluent pas dans un tissu sain de manière indépendante, elles constituent un lien étroit avec d'autres cellules (Cellules immunitaires, Fibroblastes associés au cancer, Cellules endothéliales) qui vont favoriser la propagation de la maladie, un nouveau type de stroma associé au cancer.

Pour migrer vers un autre organe à distance de la tumeur primaire, la cellule tumorale doit migrer à travers le tissu sain vers la circulation sanguine ou lymphatique. Plusieurs barrières telles que la membrane basale ou la paroi des capillaires sanguins devront être franchies. La cellule tumorale doit ensuite survivre dans le flux sanguin, s'arrêter dans la vasculature de l'organe cible, migrer dans l'organe et enfin se multiplier (Figure 1). Toutes ces étapes rendent le processus de formation de métastases inefficicace avec seulement 0,01% des cellules tumorales circulantes (CTC) qui formeront un foyer cancéreux secondaire (Chiang et al., 2016).
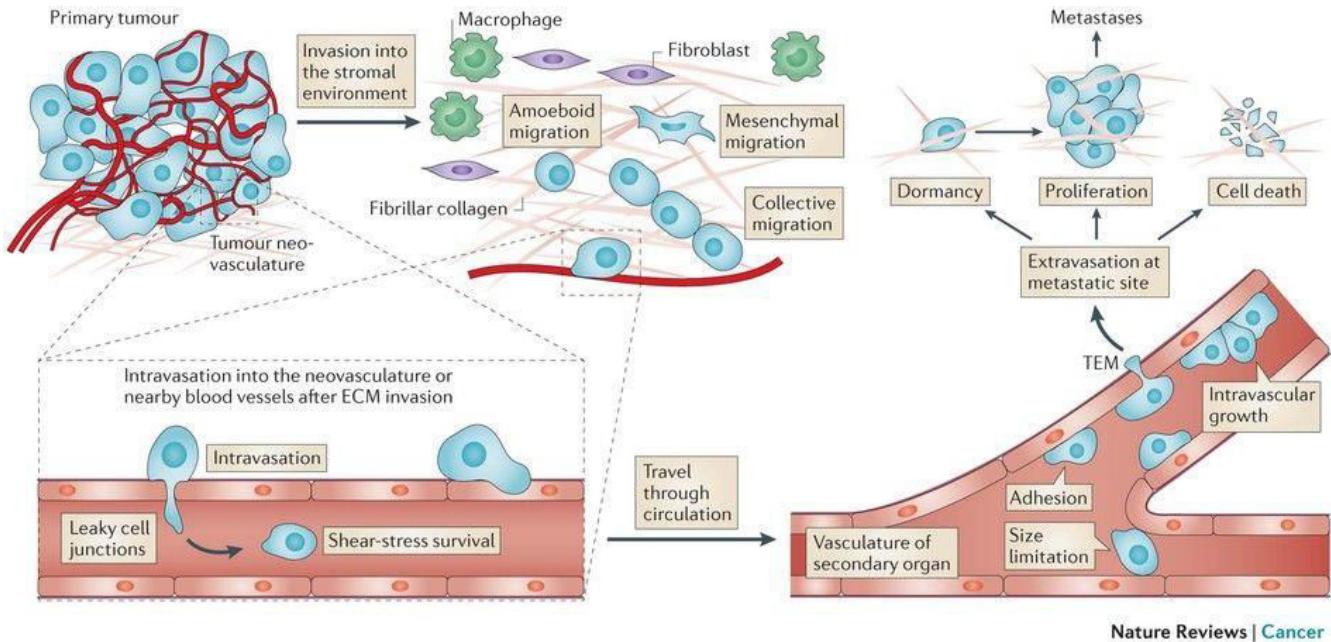
Figure 1 : **Processus de dissémination dans l'organisme des cellules métastatiques.** *Pour envahir l'organisme les cellules cancéreuses provenant de la tumeur primaire doivent acquérir des propriétés invasives et migratoires. Les cellules vont ensuite envahir le stroma et une partie d'entre elles vont se diriger vers un vaisseau sanguin à proximité. Pour ensuite envahir l'organisme entier les cellules peuvent entrer dans la circulation sanguine par un mécanisme appelé intravasation. Les cellules devront alors survivre dans le flux sanguin pour avoir la possibilité de métastaser dans un organe à distance. Les sites spécifiques d'adhésion ou la limitation de taille des capillaires permettent aux cellules tumorales d'adhérer ou de rester bloquées au contact de l'endothélium avant de sortir par extravasation dans un nouvel organe. Enfin, les cellules qui auront métastasé pourront se multiplier dans l'organe, entrer en dormance ou mourir. D'après Reymond et al., 2013*

1.1.1 Passage de la membrane basale

La membrane basale (MB) est une structure dense, formant une couche de 50 à 100 µm d'épaisseur, présente autour d'un épithélium en le séparant du stroma (Figure 2).

Le rôle de la MB est de fournir un support structurel, diviser les tissus en compartiments et de contrôler l'activité cellulaire.
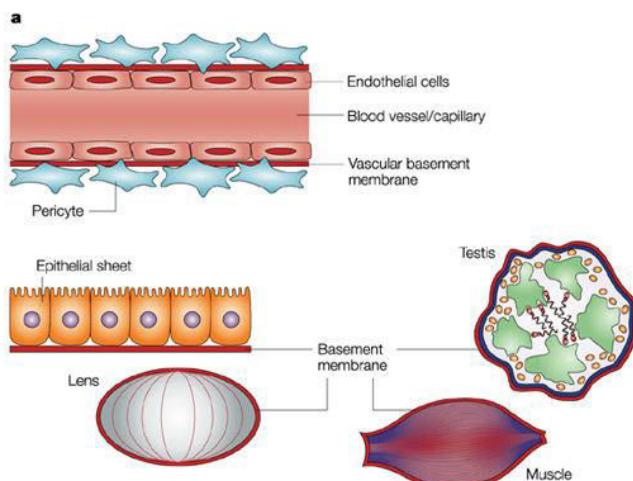
Figure 2 *: **Représentation schématique de la membrane basale dans divers tissus.** Dans la vasculature, la membrane basale est en contact direct avec les péricytes et les cellules endothéliales. La membrane basale se trouve aussi en dessous de cellules épithéliales et au niveau d'autres tissus tels que le cristallin dan l'œil, les testicules ou les fibres musculaires. D'après Kalluri, 2003.*

La MB est constituée principalement de collagène de type IV, de laminine, d'heparan-sulphate proteoglycans et de nidogen/entactin. Ces constituants sont généralement sécrétés par tous les types cellulaires et s'auto assemblent pour former une structure en couches (Kalluri, 2003).

Dans le cas du cancer, les cellules cancéreuses vont se multiplier au niveau de la tumeur primaire pour former un carcinome *in situ* délimité par une MB. Celle-ci ne possédant pas de pores suffisamment larges pour permettre une invasion passive des cellules tumorales, elle forme ainsi la première barrière que devra franchir la cellule tumorale pour envahir l'organisme. Le passage de la MB par les cellules tumorales constitue un des premiers signes du développement de métastases et indique un mauvais pronostic chez le patient.

Trois modalités différentes ont été reportées pour le passage de la MB par les cellules cancéreuses. La dégradation de la MB par une activité protéolytique, le remodelage local de la MB par des forces mécaniques et une synthèse anormale de la MB autour de la tumeur primaire (Glentis et al., 2014)

Plusieurs metalloproteinases, MT1-MMP, MT2-MMP et MT3-MMP sont impliquées dans la dégradation de la MB par des cellules d'adenocarcinum mammaire humain (MDA MB 231) (Hotary et al., 2006). *In vivo* dans un modèle de carcinome, *in situ* chez la souris, il a été démontré que l'expression de MT1-MMP augmente lors de la transition entre carcinome *in situ* vers un carcinome invasif (Lodillinsky et al., 2016).

Les invadopodes, structures riches en actine qui confèrent aux cellules un pouvoir invasif important grâce à des protéases, semblent être impliqués dans la dégradation de la MB (Poincloux et al., 2009; Rowe and Weiss, 2008). L'implication des invadopodes dans le passage de la MB a été prouvée au cours du développement du nématode *C.elegans*. La cellule AC (Anchor cell) dégrade la MB afin de relier les épithéliums utérin et de la vulve entre eux (Hagedorn et al., 2013).

Par ailleurs, les cellules tumorales ont la possibilité de modifier leur forme et d'acquérir la capacité de se frayer un chemin dans une matrice en 3 dimensions sans impliquer la dégradation de la matrice. Elles adoptent pour cela un type de migration appelé amiboïdes se déplaçant grâce à la formation de blebs (Gadea et al., 2007; Sahai and Marshall, 2003).

Plusieurs études ont montré que la synthèse de la BM autour de la tumeur primaire était anormale pouvant ainsi engendrer des zones de moindre résistance par lesquelles les cellules tumorales pouvaient passer pour ensuite envahir la Matrice extracellulaire (MEC).

1.1.2   Migration dans la MEC

Pour envahir la MEC, la cellule cancéreuse d'origine épithéliale doit acquérir dans un premier temps des propriétés migratrices.

Un des principaux phénomènes est la transition épithélio-mésenchymateuse (EMT) où une cellule d'origine épithéliale va perdre ses caractéristiques, polarisation, contact avec la membrane basale, contact cellule-cellule, pour acquérir un phénotype de cellule mésenchimateuse motile (Figure 3). C'est un procédé qui a normalement lieu lors du développement ou des cellules épithéliales peuvent acquérir un phénotype mésenchymateux transitoire.
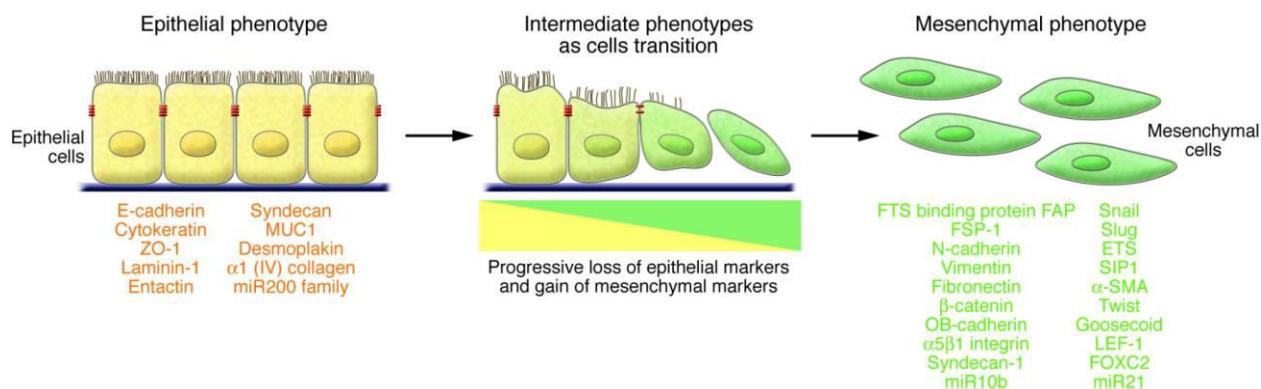
Figure 3 : **Les différentes étapes de la transition épithélio-mésenchymateuse.** Lors de cette transition les cellules épithéliales perdent leur phénotype de cellules jointives pour devenir des cellules avec un phénotype de cellules mésenchymateuse mobiles.

La perte de l'expression de la E-cadhérine est un élément traduisant le fait qu'une cellule a subi l'EMT. En effet cette cadhérine est indispensable à la liaison entre cellules avoisinantes pour la formation d'un épithélium. Certaines cellules vont exprimer des marqueurs mésenchimateux tels que α-SMA, la vimentine, la desmine et la N-cadhérine (Yang and Weinberg, 2008).

In vitro la migration sur des surfaces 2D met en jeu des sites d'adhésion pour permettre aux cellules de s'accrocher à la surface. En effet, à l'échelle cellulaire les effets des mouvements Brownien sont supérieurs aux forces générées par la gravité ne permettant pas à la cellule de maintenir des contacts avec son substrat (Lämmermann and Sixt, 2009).

La migration cellulaire implique que la cellule soit polarisée selon un axe avant-arrière. A l'avant se forment des structures riches en actine comme les filopodes ou les lamellipodes dépendantes des GTPases RAC et CDC42. Cette zone correspond aussi à la zone où vont se former les adhésions focales. A l'arrière le complexe actomyosine attaché aux adhésions focales matures se contracte et entraine l'avancée de la cellule (Mayor and Etienne-Manneville, 2016). La migration cellulaire est un mécanisme en plusieurs étapes comprenant l'extension de la membrane cytoplasmique *via* la

synthèse d'actine, l'adhésion au substrat par des adhésions focales, la contraction du corps cellulaire de l'arrière vers l'avant et enfin le détachement des adhésions à l'arrière de la cellule (Figure 4).
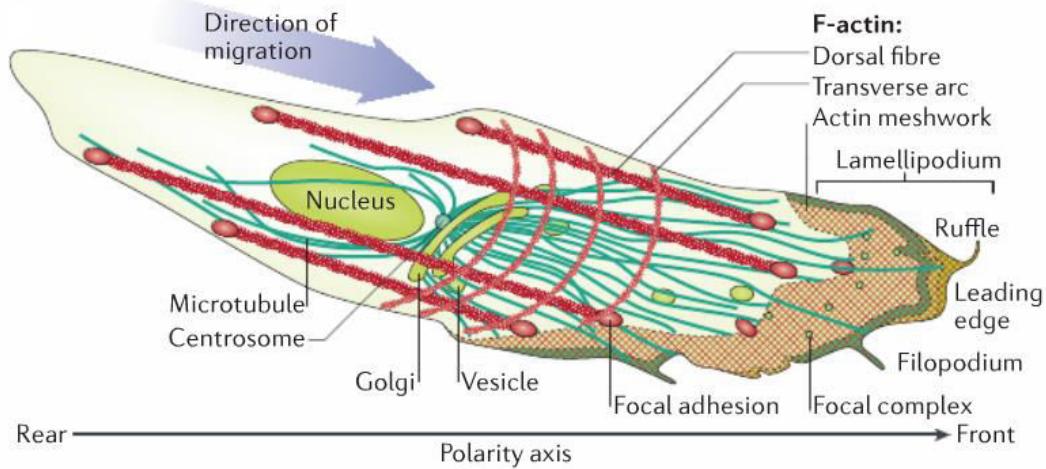
Figure 4 : **Polarisation d'une cellule migratoire**. *Au niveau du front cellulaire des protrusions membranaires actives donnent naissance à des points d'adhésions qui pourront maturer en adhésion focale. Des cables constitués d'actine et de myosine viennent sancrer sur les adhésions focales. Ces cables permettent la rétractation de l'arrière de la cellule entrainant un mouvement de la cellule vers l'avant. Les adhésions focales persisteront jusqu'à ce qu'elles atteignent la zone de rétractation où elles se désassembleront. D'après Mayor et al. 2016.*

Dans une matrice 3D, différents types de migrations cellulaires existent, les cellules peuvent migrer de façon individuelle en adoptant une morphologie mésenchymateuse ou amiboïde, dans ce cas-là les cellules perdent leurs interactions cellules-cellules. Les cellules peuvent aussi migrer de façon collective dans le cas où elles possèdent encore des jonctions intercellulaires.

1.1.2.1 Migration de cellule unique

La migration amiboïde consiste en un déplacement de cellules de formes généralement sphériques ne possédant pas de fibres de stress et ne développant pas avec le MEC de points d'adhésions focaux matures.

Les cellules amiboïdes se déplacent dans la MEC habituellement en absence d'activité de dégradation en se frayant un chemin dans le réseau de collagène (Figure 5). Ces cellules ont la particularité de ne générer que de faibles zones d'adhésions avec la MEC et se déplacent grâce à la formation de petites protrusions ou de blebs. Ces derniers sont des protrusions membranaires sphériques rencontrées dans différents contextes comme la migration cellulaire, l'apoptose, cytokinèse.

14

Les blebs se forment lors du détachement de la membrane plasmique de l'actine corticale sous-jacente grâce au complexe actomyosine. Ce détachement permet aux forces hydrostatiques de pousser la membrane vers l'extérieur (Tinevez et al., 2009). Une fois le bleb formé, l'actine se réassemble à nouveau en actine corticale où d'autres blebs vont se former à partir du premier. Cette déformation et projection active de la membrane plasmique permet aux cellules de se déplacer à travers le maillage constituant la MEC.

Le mécanisme est lié au couple Rho/ROCK qui induit une augmentation de la contractilité du complexe actomyosine.

Dans le cas de la migration mésenchymateuse, les cellules cancéreuses ont développé les mêmes capacités de migration que les cellules constituant le mésenchyme telles que les fibroblastes. Elles adoptent alors un aspect allongé et forment de longues protrusions. Les cellules migrent dans la MEC par des interactions fortes *via* la formation de points focaux d'adhésion comme pour la migration sur un substrat en 2D mais elles sont en plus capables de dégrader la MEC (Figure 5). Ces cellules grâce à leur activité protéolytique notamment *via* la métalloprotéinase MT1-MMP, sont capables de créer des chemins dans la MEC qui seront utilisés par d'autres cellules facilitant ainsi l'invasion tumorale (Friedl and Wolf, 2009; 2008).

1.1.2.2   Migration collective

La migration collective est un mouvement coordonné (même direction et même vitesse) d'un groupe de cellules ayant conservé leurs jonctions cellules-cellules.

Ce phénomène a lieu dans de nombreux processus biologiques comme la formation de tissus et d'organes au cours du développement, la cicatrisation, la régénération tissulaire, l'angiogenèse et enfin l'invasion tumorale (Weijer, 2009; Friedl and Gilmour, 2009; Mayor and Etienne-Manneville, 2016).

Le principe de migration collective est le même que pour la migration de type mesenchymateuse mais se distingue par le fait que les jonctions cellules-cellules soient toujours présentes dans toute la masse cellulaire (Figure 5). Par conséquent la migration collective nécessite une polarisation coordonnée des cellules composant le front de migration mais aussi une coordination des forces de contraction permettant le déplacement de la masse cellulaire (Friedl and Gilmour, 2009).

Dans la plupart des cas une ou plusieurs cellules leader situées à l'avant de la masse cellulaire gardent des caractéristiques de cellules mésenchymateuse leur permettant de générer des tractions vers l'avant et de dégrader la MEC qui les entoure pour favoriser leur avancée (Friedl and Alexander, 2011). La coordination de l'activité du cytosquelette et des intégrines dans la masse cellulaire ne se fait pas uniquement par les jonctions cellules-cellules mais implique aussi les cadhérines ainsi que

les connexines impliquées dans la communication entre cellule à travers les jonctions gap (Friedl and Wolf, 2003).
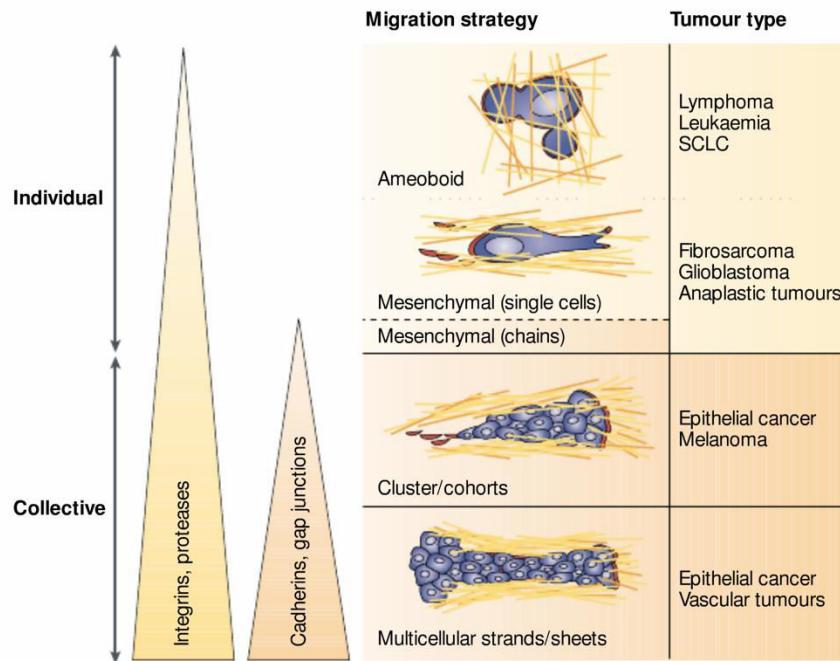
*Figure 5 : **Différents mécanismes d'invasion tumorale.** La migration cellulaire, collective ou individuelle est déterminée par différents programmes moléculaires. La capacité d'interaction avec la MEC via des intégrines et la dégradation grâce à des metalloprotéinases est spécifique aux migrations de type mesenchymateuses et collectives. Les adhésions cellules-cellules et la communication via des jonctions gap est spécifique de la migration collective. Selon le type de tumeur les caractérisitiques migratoires ne sont pas les mêmes. D'après Friedl and Wolf, 2003.*

Pendant la progression tumorale, le stroma se modifie, Il a été démontré que les fibroblastes pouvaient aider les cellules conservant des caractéristiques épithéliales et ainsi migrant collectivement à se déplacer dans la MEC en les guidant à travers des chemins modelés par les fibroblastes (Gaggioli et al., 2007; Labernadie et al., 2017).

1.1.3 L'intravasation

L'intravasation est un phénomène qui ne concerne pas uniquement les cellules cancéreuses. En effet, ce phénomène a lieu au cours du développement mais aussi au cours de la réponse immunitaire. En réplique à des signaux de croissances ou à un foyer infectieux, différents types cellulaires peuvent rejoindre la circulation sanguine en passant à travers les cellules endothéliales puis se disséminer vers d'autres organes.

De la même manière, la cellule cancéreuse doit entrer la circulation lymphatique ou sanguine pour atteindre un organe à distance de la tumeur primaire et former une métastase. Plusieurs facteurs favorisent l'intravasation des cellules cancéreuses dans la circulation sanguine.

Les facteurs angiogéniques sont des facteurs importants pour le développement de la tumeur primaire. En effet, lorsque la tumeur primaire est supérieure à 1mm^3, un phénomène d'hypoxie s'installe en son centre (la limite de diffusion de l'oxygène est comprise entre 100 et 200µm). Pour contrer ce phénomène, les cellules cancéreuses sont capables de sécréter des facteurs de croissance comme le Vascular Endothelial Growth Factor (VEGF), se liant au récepteur VEGFR2 exprimé à la surface des cellules endothéliales (Potente et al., 2011) entrainant la formation de nouveaux vaisseaux sanguins à partir de la vascularisation préexistante, ce processus a pour nom l'angiogenèse tumorale. Elle permet la vascularisation de la masse tumorale, favorisant ainsi sa croissance. Plus la vascularisation est abondante au niveau de la tumeur primaire plus il y a de chances que la cellule tumorale entre dans la circulation sanguine (Tien et al., 2001). Les vaisseaux sanguins nouvellement formés possèdent de nombreuses anormalités comme les jonctions entre les cellules endothéliales non parfaites (Yuan et al., 1995; Baluk et al., 2003) permettant ainsi aux cellules cancéreuses d'entrer dans la vasculature. Le FGF (Fibroblast Growth Factor) est aussi un autre facteur angiogénique impliqué dans la croissance de la vasculature ainsi que dans l'augmentation de la fréquence de cellules tumorales qui entrent la circulation sanguine (Zhang, 1999).

D'autres facteurs favorisent la motilité et l'intravasation des cellules cancéreuses. L'inactivation du TGFβ (Tumor Growth Factor β) réduit le nombre de CTC sans impacter la formation de la tumeur primaire et sa vascularisation dans un modèle de cancer murin (Muraoka et al., 2002). L'EGFR (Epidermal Growth Factor Receptor) est un récepteur à tyrosine kinases exprimé dans différents types de cancer comme le cancer du sein, des poumons, de l'œsophage, et de la tête et du cou. Le récepteur à l'EGF contribue à la croissance, la différenciation, l'adhésion, la migration et la survie des cellules cancéreuses (Seshacharyulu et al., 2012). Il a été démontré que la surexpression de l'EGFR dans des cellules d'adénocarcinomes mammaires MTLn3 entraine un accroissement de la motilité de ces dernières en lien avec une augmentation de l'intravasation (Xue et al., 2006).

Les protéases ont un rôle dans la migration cellulaire mais elles facilitent aussi l'intravasation. L'expression par les cellules cancéreuses de métalloprotéinases tel que MMP-1 permet aux cellules de migrer dans la MEC mais aussi facilite l'intravasation (Juncker-Jensen et al., 2013).

Les cellules cancéreuses peuvent aussi avoir recours aux invadopodes, qui permettent aux cellules cancéreuses de dégrader la MEC par la présence de métalloprotéinases qui favorisent la formation de métastases (Gligorijevic et al., 2012). La formation des invadopodes peut être induite par contact direct entre la cellule tumorales et des macrophages *via* l'activation de RhoA. Les invadopodes

favorisent la migration dans la MEC mais aussi le passage de l'endothélium (Roh-Johnson et al., 2013).

L'intravasation peut aussi se faire par l'intervention d'autres types cellulaires. En situation normale les macrophages ont pour rôle d'éliminer les cellules anormales qu'elles soient endommagées ou mutées. Cependant les macrophages peuvent être impliqués dans la formation de métastases en favorisant le remodelage de la MEC et en favorisant l'intravasation. Ils sont ainsi recrutés par la masse tumorale et perdent leur fonction immune (Condeelis and Pollard, 2006). Récemment il a été démontré que des macrophages périvasculaires tumorigénique exprimant le récepteur Tie2 sont aussi responsables de l'angiogenèse mais aussi de l'intravasation de cellules tumorales dans la vascularisation sanguine par un phénomène de perméabilité transitoire du vaisseau sanguin (Harney et al., 2015; Condeelis and Pollard, 2006).

Une fois dans la circulation sanguine, les CTC doivent survivre dans le flux sanguin. Les plaquettes agissent comme un écran protecteur en s'agrégeant autour des CTC les protégeant ainsi du flux sanguin mais aussi en les camouflant par production de fibrine, les rendant ainsi non détectables par les cellules immunitaires (leucocytes et natural killer) (Nieswandt et al., 1999; Palumbo et al., 2007; 2005).

1.1.4 L'extravasation

Les cellules tumorales devront ensuite quitter la circulation sanguine par extravasation pour proliférer dans un nouvel organe.

D'autres types cellulaires sont aussi capables de sortir de la circulation sanguine tels que les leucocytes. Ces cellules ont la particularité de « rouler » sur les cellules endothéliales et de s'arrêter au niveau du site d'extravasation par des mécanismes d'adhésion via les sélectines et l'interaction des protéines ICAM1/VCAM1 (Vestweber, 2015). Les leucocytes quittent la circulation sanguine par extravasation en passant soit par la jonction entre deux cellules endothéliales (Paracellular diapedesis) soit directement à travers une cellule endothéliale (Transcellular diapedesis).

Deux hypothèses sont apparues pour expliquer comment les cellules tumorales s'arrêtent et sortent du vaisseau sanguin. La première par S. Paget qui formula en 1889 la théorie du Seed & Soil. Cette théorie explique que la graine (Seed), la cellule cancéreuse, ne peut métastaser que dans un organe où l'environnement (Soil) lui est favorable. Une deuxième hypothèse émise par J. Ewing dans les années 1920 explique que l'extravasation de la cellule cancéreuse dans un organe spécifique s'explique uniquement par les caractéristiques physiques du flux sanguin au niveau de l'organe.

Actuellement les deux hypothèses semblent ne pas pouvoir être mutuellement exclusives et ces deux hypothèses sont toujours d'actualité.

En effet des études ont montré qu'un type de cellules tumorales ne métastase pas au hasard mais généralement dans les mêmes organes (Weiss, 1992). Ainsi, les cellules de cancer du sein ont tendance à métastaser préférentiellement dans les os, le cerveau, le foie et les poumons alors que les cellules de cancer de la prostate métastasent préférentiellement dans les os (Nguyen et al., 2009).

Ce comportement peut s'expliquer par le fait que la tumeur primaire est capable d'induire la formation d'un microenvironnement favorable dans un organe à distance. Ce microenvironnement propice à assurer la survie et la croissance des cellules tumorales, serait formé avant même leur arrivée dans l'organe. La première description de ce phénomène a été faite en 2005 (Kaplan et al., 2005). L'équipe a montré que des cellules de moelle osseuse dérivées de la lignée hématopoïétique (BMDC : Bone Marrow-Derived Cell) exprimant VEGFR1 formaient des clusters de cellules au niveau de site pré-métastatiques avant l'arrivée des cellules tumorales. Les cellules tumorales entrainent la prolifération de cellules stromales qui contribueraient au dépôt de fibronectine au niveau des sites prémetastatiques favorisant l'adhérence dans ces zones des BMDC via l'intégrine α4β. L'expression de VEGFR1 par les BMDC favorise l'adhérence et la croissance des cellules tumorales. Enfin, selon le type de tumeur les BMDC vont se localiser au niveau des organes où se forment d'habitude les métastases confirmant que la niche pré-métastatique est spécifique du type de tumeur primaire.

Des études plus récentes ont mis en évidence l'implication d'autres facteurs dans l'établissement de niches pré-métastatiques (PMN). Il existe parmi eux les exosomes qui sont des vésicules à bicouches lipidiques de taille nanométrique comprise entre 50 et 140 nm de diamètre. Ces vésicules se retrouvent dans tous les fluides et servent de cargo pour transporter du matériel génétique (ADN, ARNm et miRNA) (Valadi et al., 2007), des lipides ainsi que des protéines. Les exosomes sécrétés par les cellules tumorales reprogramment ou éduquent les cellules qui les endocytent vers un phénotype pro-métastatique ou pro-inflammatoire créant la PMN (Peinado et al., 2012; 2017; Costa-Silva et al., 2015). Les exosomes dérivés des cellules de mélanome B16-F10 contiennent le récepteur au facteur de croissance hépatique qui a pour effet de renforcer l'expression de plusieurs facteurs de croissance chez les BMDC entrainant leur sortie de la moelle osseuse et la formation d'une PMN dans les poumons (Peinado et al., 2012). Les exosomes issus de différentes lignées tumorales qui ont un tropisme pour le foie, les poumons ou le cerveau vont fusionner avec les cellules constituant ces organes pour préparer la PMN. Le mécanisme est basé sur la différence d'expression des intégrines au niveau des exosomes. Ainsi les exosomes exprimant les intégrines α6β4 et α6β1 sont associés avec une métastase pulmonaire alors que les exosomes exprimant αvβ5 vont favoriser la formation de métastases dans le foie. La fusion des exosomes avec les cellules résidentes favorise l'expression du gène pro-migratoire et pro-inflammatoire S100 rendant la zone permissive pour la croissance de cellules métastatiques (Hoshino et al., 2015).

Les exosomes peuvent aussi préparer la PMN en délivrant aux cellules endothéliales des micro ARN (miRNA) entrainant la déstabilisation des jonctions entre les cellules endothéliales favorisant l'extravasation des cellules tumorales. Les miRNA sont de petites séquences non codantes d'ARN qui se lient à la séquence 3'UTR (Untranslated region) d'ARNm conduisant à la non traduction en protéine de l'ARNm. La dérégulation de la production des miRNA est liée à la formation de cancer (Chen et al., 2008b). Des exosomes issus de cellules d'adénocarcinome mammaire humain MDA-MB-231 contenant le miR-105 injectés dans la circulation sanguine de la souris se retrouvent concentrés dans les organes préférentiellement colonisés (cerveau et poumons) par les cellules d'adénocarcinome. Cette augmentation de miR105 dans le cerveau et les poumons a pour conséquence une baisse d'expression de la protéine des jonctions serrées ZO-1 ainsi qu'une augmentation de la perméabilité vasculaire favorisant la formation de métastases (Zhou et al., 2014).

D'autres facteurs favorisent l'arrêt et l'extravasation dans un organe. La formation de métastases dans le foie est facilitée par un accroissement du dépôt de fibronectine du côté de la lumière du vaisseau chez les souris développant un cancer du côlon. Les CTC adhèrent au réseau de fibronectine via la talin1, protéine impliquée dans les adhésions focales (Barbazán et al., 2017).

Enfin, les CTC peuvent aussi se retrouver bloquées dans un capillaire, de taille similaire ou inférieure à la cellule tumorale, avant de sortir du flux sanguin et envahir un nouveau tissu (Massagué and Obenauf, 2016). Une fois bloquées, les CTC vont former des liaisons avec les cellules endothéliales notamment via les sélectines dont l'expression à la surface des cellules endothéliales peut être induite par la sécrétion de cytokines inflammatoires par les cellules cancéreuses (Auguste et al., 2007). Par la suite, d'autres liaisons mettant en jeu les intégrines vont se mettre en place pour stabiliser la liaison entre CTC et cellules endothéliales (Shibue and Weinberg, 2009).

Les CTC en contact avec le vaisseau sanguin peuvent migrer à travers l'endothélium grâce aux invadopodes et à la production de la métalloprotéinase MT1-MMP (Leong et al., 2014).

1.1.5 Croissance de la métastase

Afin de ne pas mourir une fois la cellule cancéreuse dans le nouvel organe, un processus d'angiogenèse doit se mettre en place pour permettre aux cellules de se multiplier. Les cellules cancéreuses peuvent aussi entrer dans un état de dormance et ne se réactiver qu'au bout de plusieurs années (Figure 6) (Chambers et al., 2002; Massagué and Obenauf, 2016).

La multiplication cellulaire repose sur la capacité des cellules tumorales à recruter les cellules endothéliales pour former un nouveau réseau vasculaire. Sujet encore débattu aujourd'hui, les cellules tumorales seraient ainsi capable en sécrétant du VEGF de recruter des BMDC qui sont impliquées dans la formation d'une nouvelle vascularisation (Gao et al., 2008; Lyden et al., 2001; Quail and Joyce, 2013).

Les macrophages associés aux tumeurs participent aussi à la croissance métastatique dans le poumon (Qian et al., 2009; 2011)
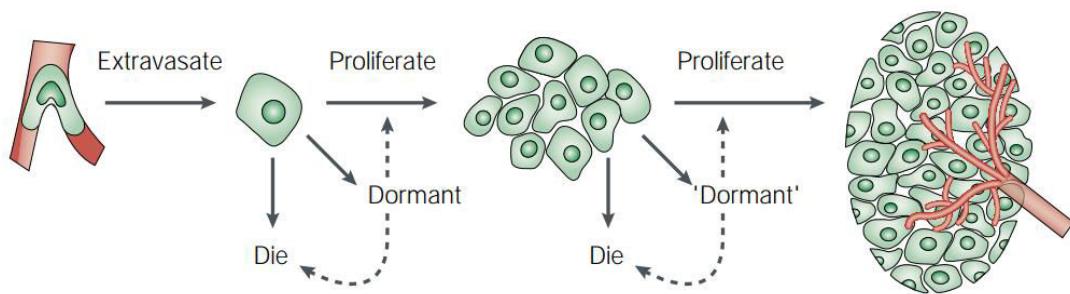
Figure 6 : **Destins possibles d'une cellule cancéreuse dans un organe secondaire.** *Les cellules cancéreuses peuvent exister dans le second organe comme des cellules solitaires, petites métastases pré-angiogéniques ou plus grosses métastases vascularisées. Les cellules dormantes solitaires sont des cellules qui ne prolifèrent pas et qui n'entrent pas en apoptose. Les micro-métastases pré-angiogéniques dormantes connaissent une multiplication et une apoptose égale ayant comme résultante une croissance nulle de la masse tumorale. D'après Chambers et al., 2002.*

Dans ces différentes phases de la cascade métastatique une structure spécialisée de la cellule intervient régulièrement, il s'agit des invadopodes.

1.2   Les invadopodes : structures spécialisées dans l'invasion cellulaire

Les invadopodes sont des structures riches en actine qui confèrent aux cellules cancéreuses un pouvoir invasif plus important en facilitant la dégradation, via des métaloprotéinases, de la matrice extracellulaire, favorisant ainsi l'intravasation et l'extravasation (Paz et al., 2014).

La première description de telles structures, appelées alors podosomes, a été faite sur des cellules fibroblastiques BHK (Baby Hamter Kidbey cells) cultivées sur un substrat de fibronectine et transformées par l'oncovirus du sarcome de Rous, premier oncovirus découvert en 1911. Les podosomes ont d'abord été décrits comme des structures adhésives et protrusives constituées d'actine et de vinculine. La localisation préférentielle de ces structures ponctiformes sous le noyau de la cellule donne l'impression de former des pieds cellulaires d'où le nom podosome (Tarone et al., 1985). Ce n'est que quelques années plus tard qu'une autre équipe a démontré que des fibroblastes transformés par l'oncovirus du sarcome de Rous dégradent la matrice de fibronectine aux niveaux des podosomes grâce à des protéases résidantes. Les podosomes ont alors été renommés en invadopodia traduisant le fait que ces structures permettent aux cellules qui les produisent d'envahir la matrice extracellulaire (Chen, 1989).

Actuellement le terme podosome est réservé aux cellules normales tandis que le terme invadopodia est utilisé pour les cellules cancéreuses. Le terme invadosome est lui utilisé afin de rassembler toutes les structures impliquées dans l'invasion et la dégradation de la MEC (Murphy and Courtneidge, 2011). Les invadopodes et les podosomes partagent la même fonction de dégradation péricellulaire, ces protrusions se différencient ainsi des autres structures impliquées dans la migration et l'adhésion cellulaire (Filopodia, Lamellipodia, Adhésions focales).

Les cellules normales telles que les macrophages, cellules endothéliales, ostéoclastes peuvent former des podosomes. Par exemple les ostécoclastes remodellent la matrice osseuse grâce aux podosomes (Teitelbaum, 2000).

1.2.1 Composition

Les invadosomes sont composés en leur centre d'actine de type filamenteuse (Actine-F), et de protéines liant et régulant l'actine tel que N-WASP (Neuronal Wiskott-Aldrich Syndrome), Cortactine ainsi que le complexe ARP2/3 (Eddy et al., 2017; Paterson and Courtneidge, 2017). Autour se concentrent des protéines, comme les intégrines β1 et β3, la vinculine et la paxiline (Destaing et al., 2010; Badowski et al., 2008), ces protéines sont nécessaires à l'ancrage de l'invadopode dans la MEC.

Les invadopodes se retrouvent distribués sous la cellule de façon individuelle ou groupés et peuvent aussi se regrouper pour former des structures appelées rosettes selon le type cellule et de matrice.

Les invadopodes sont constitutifs de certaines cellules cancéreuses mais absents dans la plupart des lignées cellulaires. Les invadopodes sont cependant inductibles par des cytokines telles que PDGF, VEGF et le TGF-β. La MEC peut aussi stimuler la formation d'invadopodes (Artym et al., 2015) .

Les principales différences entre les podosomes et les invadopodia sont la taille de la structure, la durée de vie et les différentes métaoprotéinases sécrétées.

L'assemblage d'un invadopode se fait en 3 étapes (Eddy et al., 2017) qui sont l'initialisation, la stabilisation et enfin la maturation (Figure 7).

L'initiation se fait par le recrutement autour d'un complexe Actine-cortactine d'un assemble de molécules favorisant la polymérisation de l'actine ainsi que des molécules se liant à l'actine comme la cofiline. Parmi les protéines favorisant la polymérisation de l'actine on retrouve la protéine N-WASP qui contrôle sous la dépendance de plusieurs voies de signalisation la polymérisation de l'actine dans la cellule en liant et en activant le complexe formé par les protéines Arp2/3 (Actin-related protein).

La stabilisation se fait grâce au recrutement de Tks5 qui est une protéine d'échafaudage essentielle à la formation d'un invadopode mature (Seals et al., 2005). Tks5 contient un domaine amino-terminal homologue au domaine Phox (PX). Ce domaine permet d'ancrer la protéine dans la membrane

plasmique via une liaison avec les lipides phosphorylated phosphatidylinositol (Pi(3,4) P2). Tks5 possède aussi un domaine Src homology 3 (SH3) qui est un domaine non catalytique facilitant les interactions protéines-protéines (Courtneidge et al., 2005). La production de Pi(3,4)P2 entraine une meilleur stabilisation par l'intermédiaire de Tks5. L'actine commence ensuite à polymériser via la voie de la cofiline et du complexe Arp2/3. En plus de l'actine, les microtubules et la vimentine sont aussi impliqués dans l'élongation de l'invadopode (Schoumacher et al., 2010).
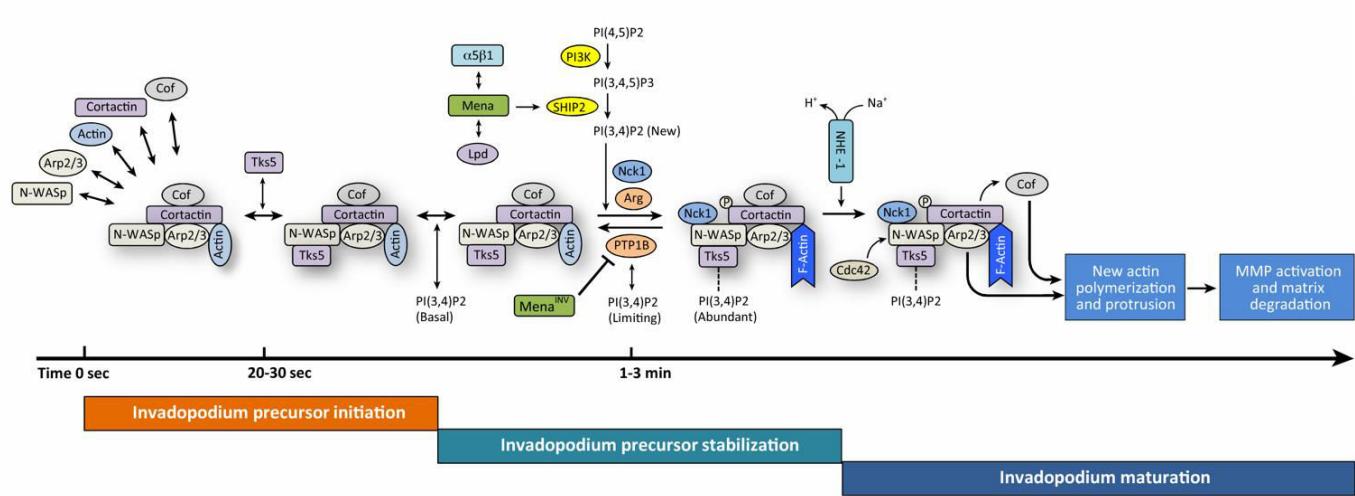
Figure 7 : **Formation d'un invadopode : de son initiation à sa maturation.** *L'arrivée de la cofilin, Arp2/3 et N-WASP sur un complexe actin-cortactin signe l'initiation de la formation d'un invadopode. La protéine d'échafaudage Tks5 arrive 20 s plus tard et stabilise le précédent complexe en faisant la liaison avec PI(3,4)P2 contenu dans la membrane plasmatique. Les minutes suivantes montrent une production d'actine ainsi que la formation de la protrusion. Mena permet la maturation de la strucure en délivrant SHIP2 au niveau du précurseur. SHIP2 entraine une production de PI(3,4)P2 entrainant le recrutement de Mena^{INV}. Le maintien de la phosphorylation de la cortactin a pour conséquence la production d'actine conduisant ainsi à la maturation de l'invadopode et de la dégradation de la matrice. D'après Eddy et al., 2017*

Trois protéases différentes sont retrouvées au niveau des invadopodes (Paterson and Courtneidge, 2017; Murphy and Courtneidge, 2011; Linder, 2007). Les Métaloprotéases de la matrice tels que MMP2, MMP9 et MT-MMP et les ADAM

Les cathepsines cystéines protéases (cathepsin B) et les protéases serine (seprase, urokinase-type plasminogen activator ou uPA

Plusieurs études ont démontré l'implication des invadopodes dans les différentes étapes de la cascade métastatique. La composition et la structure de la MEC (densité des fibres de collagène, diamètre des vaisseaux sanguins, concentration de cellules tumorales, nombres de macrophages) a

un effet sur la motilité cellulaire. Les cellules migrant plus lentement sont celles qui possèdent des invadopodes et la création des invadopodes est dépendante de la taille des vaisseaux sanguins présents (Gligorijevic et al., 2014). La déplétion de N-WASP *in vivo*, protéine essentielle à la formation d'invadopodes (Lorenz et al., 2004), réduit le nombre de cellules tumorales circulantes (CTC) ainsi que le nombre de métastases pulmonaires (Gligorijevic et al., 2012). Dans un modèle de membrane choriollantoic d'embryon de poulet (Kim et al., 2016), les cellules exprimant les invadopodes peuvent extravaser au niveau de la jonction entre les cellules endothéliales ou par remodelage local de l'endothélium (Leong et al., 2014). Il a aussi été prouvé que les invadopodes sont nécessaires à l'extravasation dans le poumon de cellules de cancer de la vessie lorsqu'elles sont injectées dans la circulation sanguine de la souris (Tokui et al., 2014).

Les invadopodes sont aussi une plateforme d'attachement d'endosomes multivésiculaires CD63 et Rab27a positifs entrainant la sécrétion d'exosomes. De plus la formation des invadopodes et la sécrétion des exosomes fonctionnent de façon synergique c'est-à-dire que l'inhibition de la formation des invadopodes a pour conséquence la réduction de la sécrétion des exosomes et inversement (Hoshino et al., 2013).

1.2.2 Les invadopodes linéaires

Récemment, un nouveau type d'invadopode a été décrit *in vitro*. Lorsque les cellules sont en contact avec une matrice constituée de fibres de collagène de type 1 (le type le plus présent dans la MEC) les invadopodes se réorganisent le long de la fibre de collagène leur conférant ainsi un aspect linéaire (Juin et al., 2012). Ce type d'invadopode est appelé invadopode linéaire (LI). Les LI expriment comme les invadopodes ou les podosomes les protéines N-WASP et cortactin ainsi que la protéine d'échaffaudage Tks5. Les LI se différencient par contre des invadopodes classiques par leur indépendance aux intégrines β1/β3 pour leur formation et par l'absence de l'anneau protéique constitué de la taline, vinculine, paxilline.

De nombreux types cellulaires peuvent former des LI telles que les cellules endothéliales, macrophages, fibroblastes et les cellules cancéreuses.

Le récepteur au collagène DDR1 (Discoïdin Domain Receptor) est impliqué dans la formation des LI. DDR1 est un récepteur à tyrosine kinase activé par les collagènes de type I et IV (Rammal et al., 2016). Lorsque DDR1 est activé par le collagène, Cdc42, une RhoGTPase impliquée dans la formation d'invadopodes, se retrouve à son tour activé par Tuba qui est une GEF (Guanine nucléotide Exchange Factor) spécifique de Cdc42 (Juin et al., 2014) entrainant la formation du LI (Figure 8).

Les LI possèdent l'ensemble des marqueurs communs aux invadopodes, la protéine d'échaffaudage Tks5, les protéines se liant à l'actine N-WASP et cortactine, les métaloprotéase tel que MT1-MMP ainsi que la RhoGTPase Cdc42 (Martino et al., 2016).
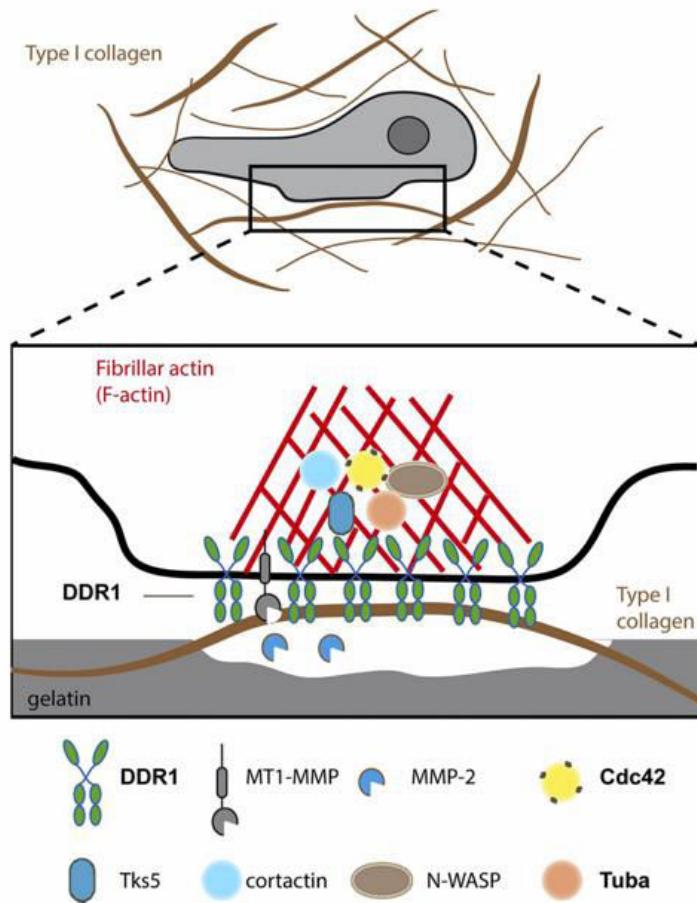
*Figure 8 : **Architecture et principaux constituants d'un invadopode linéaire.** Lorsque les cellules sont déposées sur des fibres de collagènes de type 1, DDR1 est activé le long des fibres induisant l'activation de Cdc42 via Tuba. L'invadopode linéaire se forme ensuite par le recrutement de N-WASP, cortactin et Tks5 les composants classiques d'un invadopode. Le LI est capable de dégrader la MEC via MT1-MMP et MMP2. D'après Juin et al., 2014.*

	Podosome	**Invadopodia**	**Linear invadopodia**
Description	Actin-rich core that is surrounded by a ring of actin-associated and signalling proteins	Actin-rich core that is surrounded by a ring of actin-associated and signalling proteins	Actin-rich bundle not surrounded by ring proteins
Location	Ventral cell surface, often clustered behind the leading edge of the cell	Ventral cell surface, often situated under the nucleus	Ventral cell surface in contact with collagen 1 fibers
Protrusive dimension	Width: 0.5–2 µm; length: 0.5–2 µm	Width: 0.5–2 µm; length: >2 µm	Width: 1–2 µm; length: >4 µm
Actin rearrangement	Branched and unbranched actin filaments	Branched actin filaments at the cell surface and unbranched actin filaments through the tip of the protrusion	Not known
Lipids involved	PtdIns(3,4,5)P$_3$	PtdIns P2, PtdIns P and lipid rafts (caveolin 1)	Not known
Microtubule dependance	Required for elongation and/or formation	Required for elongation but not formation	Not known
Pericellular proteolysis	Yes, through MT1MMP and UPAR13,1	Yes, through MMP2, MMP9, MT1MMP, seprase, UPAR, ADAM12, ADAM15 and ADAM19	Yes, through MT1MMP
Duration of structure	Minutes	Hours	Hours

*Tableau 1 : **Caractéristiques de différents invadosomes**. D'après Juin et al. 2012 et Murphy and Courtneidge 2011.*

Comme les invadosomes partagent des composants communs (Tableau 1), il est actuellement suggéré que ces structures dérivent toutes d'un même précurseur et que les invadosomes sont des structures plastiques qui changent de conformation selon le microenvironnement (Martino et al., 2016). Comme vu précédemment les invadopodes sont impliqués dans les différentes étapes de la cascade métastatique, dégradation de la MB, migration dans la MEC, intravasation et extravasation. Selon les structures que les cellules tumorales rencontrent elles pourraient former un invadopode (Dégradation de la membrane basale) ou un LI (Migration dans la MEC) (Figure 9).
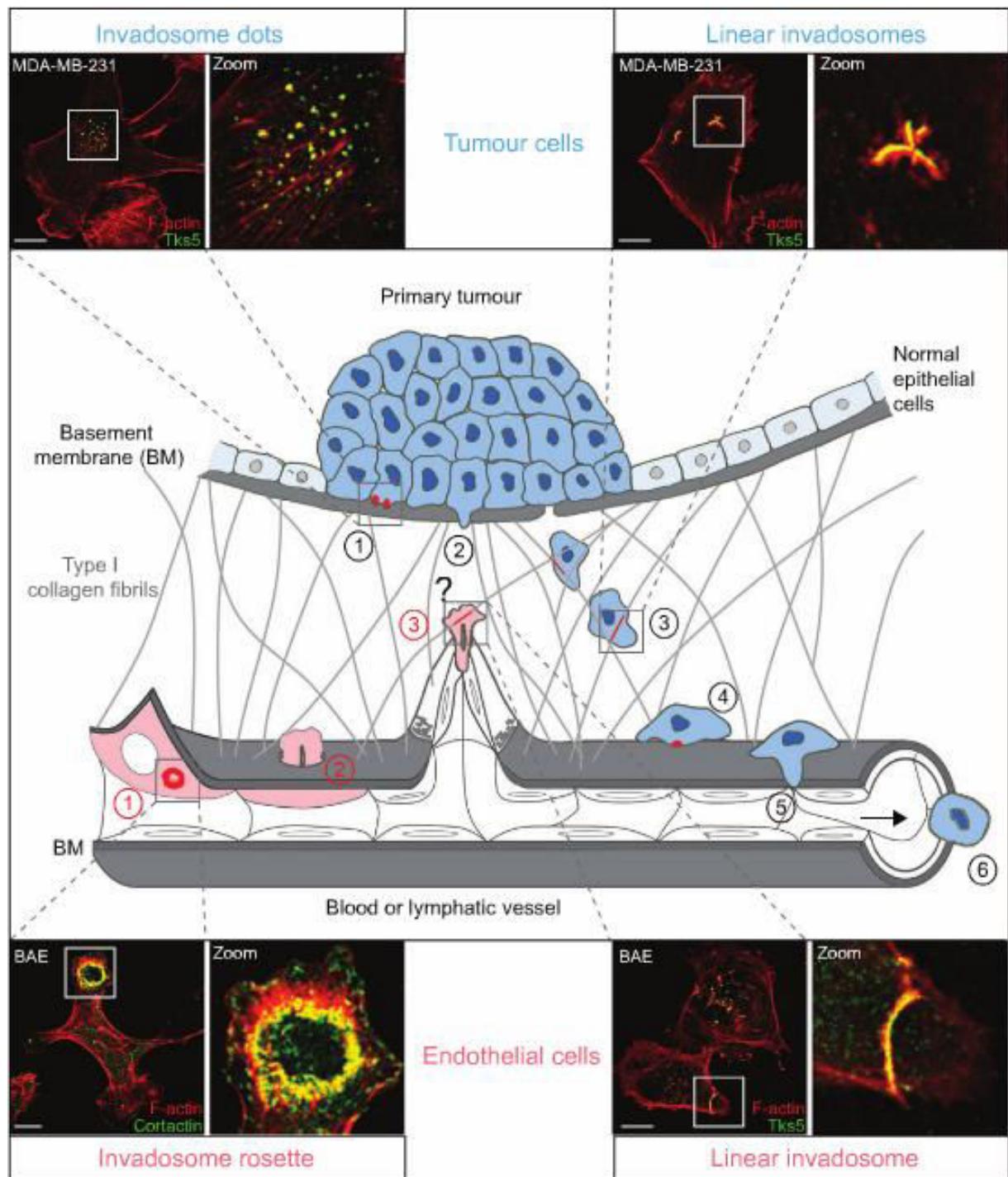
Figure 9 : **Roles possible des invadosomes in vivo.** *1, Dégradation de la BM par les cellules tumorales ; 2, Protrusion à travers la BM ; 3, Les LI se formerait dans le stroma riche en fibres de collagène ; 4, Dégradation de la BM des vaisseaux sanguins ; 5, Intravasation d'une cellule tumorale ; 6, Dissémination de la cellule tumorale par voie sanguine.* **Chiffres rouges :** *1, Dégradation de la membrane basale par une cellule endothéliale ; 2, Protrusion d'une cellule endothéliale ; 3, Formation de LI par les cellules endothéliales engagées dans un processus de neo-angiogénèse. D'après Martino et al., 2016*

Les cellules endothéliales forment aussi deux types de structures, les rosettes et les LI. Lors du processus de neo-angiogénèse les cellules endothéliles pourraient se frayer un chemin en dégradant la MEC grâce à des LI.

Les invadopodes ont été essentiellement étudiés *in vitro* mais leur existence et leur structure n'est pas encore connue *in vivo*.

Plusieurs techniques d'imagerie permettent de suivre la progression métastatique au cours du temps sur l'animal entier. Parmi elles, l'Imagerie par Résonnance Magnétique (IRM), la tomographie aux rayons X ou luminographe permettent d'imager un ou plusieurs animaux simultanément. Toutes ces techniques d'imagerie du petit animal permettent de visualiser le devenir de la tumeur primaire (croissance, vascularisation) ainsi que des cellules tumorales dans l'organisme (sites métastatiques).

Par contre la résolution offerte par ces systèmes, de 1 mm pour le luminographe à 10 µm pour l'IRM, ne permettent pas d'imager les structures cellulaires ou sub-cellulaires mis en jeu lors de l'invasion tumorale (Beerling et al., 2011).

La microscopie intravitale (IVM : Intravital Microscopy) se révèle ainsi comme étant la technique de prédilection pour visualiser la dynamique des cellules tumorales à l'échelle subcellulaire.

1.3   Microscopie intravitale

La microscopie sur cellules en cultures 2D ou sur des matrices 3D aussi bien que sur des explants de tissus permettent d'obtenir des informations fondamentales sur le fonctionnement cellulaire jusqu'aux interactions moléculaires. Cependant ces modèles ne reflètent pas la réelle organisation physiologique des tissus dans lequel ces cellules se trouvent. En effet, dans des conditions physiologiques les cellules évoluent dans un environnement 3D en contact avec d'autres types cellulaires et sont soumis à de multitudes de signaux provenant du système nerveux et du chimiotactisme provenant du milieu extracellulaire. C'est pour ces différentes raisons que les chercheurs tentent d'imager les processus biologiques *in situ*.

Les premières approches de microscopie intravitale se sont développées au cours du 19ème siècle. Rudolph Wagner en 1839 est un des premiers à avoir étudié les interactions des leucocytes avec les vaisseaux sanguins dans la patte de grenouille.

D'abord limité à l'imagerie d'organes chirurgicalement exposés (Irwin and Macdonald, 1953) ou de tissus transparents, la microscopie intravitale s'est considérablement développée grâce à l'introduction de la microscopie confocale. La microscopie confocale permet en effet de réaliser des coupes optiques de l'échantillon observé tout en possédant une meilleure résolution que la microscopie conventionnelle champ plein. Plus récemment d'autres techniques de microscopie

appliquées à l'imagerie de petits organismes se sont développées comme la microscopie à feuille de lumière (Light Sheet Microscopy ou Single Plane Illumination Microscopy).

1.3.1 Microscopie confocale

Le principe de la microscopie confocale a été décrit par M. Minsky en 1961, travaillant sur l'intelligence artificielle ce chercheur voulait comprendre comment les neurones étaient reliés entre eux. Cependant il était impossible avec les microscopes de l'époque d'obtenir une visualisation en 3D d'une coupe de tissu. En effet la diffusion de la lumière dans un tissu empêche d'obtenir une image nette en profondeur. C'est pour cela qu'il eut l'idée d'un microscope imageant un échantillon point par point équipé d'une pièce optique empêchant la lumière hors du plan focal d'atteindre le détecteur (Minsky, 1988).

L'apparition des lasers au début des années 60 a pu donner naissance aux premiers microscopes confocaux. Il aura fallu attendre 1987 pour que les premiers microscopes confocaux à fluorescence appliqués à l'imagerie cellulaire fassent leur apparition (van Meer et al., 1987; White et al., 1987).

La microscopie confocale utilise un laser continu, le flux de photons est constant au cours du temps. L'échantillon est scanné par le laser points par points dans ses 3 dimensions x,y et z. Les photons provenant du cône d'excitation et de la diffusion dans l'échantillon sont éliminés grâce à une pièce situé devant le détecteur, appelé pinhole. Seules les photons provenant du plan focal sont ainsi collectés.

Offrant une meilleure résolution dans les 3 dimensions ainsi que la possibilité de réaliser des coupes optiques d'échantillons épais, la microscopie confocale a été une avancée majeure dans le domaine de la microscopie photonique. Elle a en effet permis de visualiser des échantillons dans des conditions plus proche des conditions physiologiques en évitant la coupe fine de l'échantillon, ouvrant ainsi la voie vers la microscopie intravitale.

Le microscope confocal à balayage laser est cependant limité par sa vitesse d'acquisition. Le développement du microscope confocal équipé d'un spinning disk (SDCM Spinning Disk Confocal Microscope) accélère l'acquisition d'images grâce à l'acquisition simultanée de plusieurs points grâce à l'utilisation d'un disque de Nipkow.

La microscopie confocale est utilisée pour l'imagerie de petits organismes transparents tels que *C. elegans* (Nguyen et al., 2016) ou le poisson zèbre (Kissa and Herbomel, 2010). Elle a aussi été utilisée pour l'imagerie à la surface de différents organes chez le rat, la microcirculation dans le cerveau (Villringer et al., 1994) et l'imagerie d'astrocytes chez la souris (Pérez-Alvarez et al., 2013) ainsi que le recrutement des plaquettes dans divers organes (Jenne et al., 2011).

1.3.2   Single Plane Illumination Microscopy (SPIM)

La technique de SPIM repose sur le principe que l'illumination et la détection se fait par deux objectifs disposés orthogonalement (Huisken and Stainier, 2009). Cette technique permet de diminuer la phototoxicité par rapport à la microscopie confocale car seul le plan d'excitation est illuminé pour l'imagerie. La détection sur l'ensemble du plan d'illumination se faisant part une caméra permet une vitesse d'acquisition supérieure à la microscopie confocale. La combinaison de ces deux facteurs, faible phototoxicité et imagerie rapide autorise l'imagerie sur le long terme (Tomer et al., 2012) ainsi que l'imagerie de phénomènes rapides (Ahrens et al., 2013; Chhetri et al., 2015).

Une des limitations du SPIM pour l'imagerie intravitale est qu'elle ne peut s'appliquer idéalement que sur des organismes ou des embryons de petites tailles (quelques millimètres) (Huisken et al., 2004).
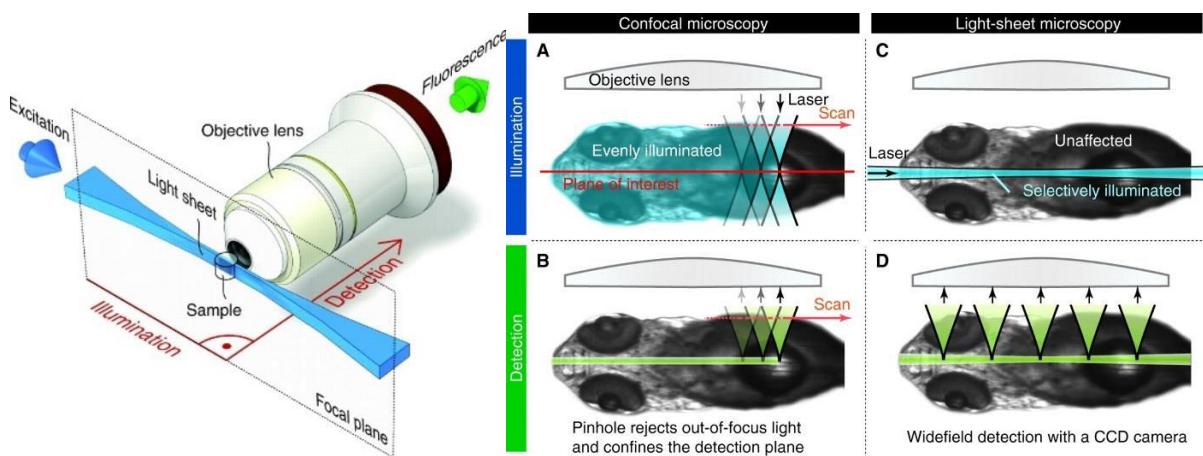
*Figure 10 : **Schéma optique d'un SPIM.** La détection du signal se fait à 90° par rapport à l'excitation, permettant l'acquisition d'images sur tout le plan focal. Comparaison du microscope confocal avec le SPIM. Contrairement au confocal le SPIM illumine uniquement un plan de l'échantillon et la détection se fait sur tout le plan. La microscopie confocale utilise un scanner ce qui rends l'acquisition plus lente de plus à chaque passage du scanner tout l'échantillon est illuminé par le laser, rendant cette technique plus phototoxyque que le SPIM. (Huisken and Stainier, 2009)*

La majorité de la lumière visible entre 400 et 700nm utilisée en microscopie confocale ou SPIM est absorbée par les tissus biologiques (Boulnois, 1986; Phan and Bullen, 2010) car ils sont riches en hémoglobine. De plus la diffusion de la lumière dans les tissus ne rend possible l'imagerie qu'à la surface des organes (moins de 100µm) (Masedunskas et al., 2012). Pour l'imagerie en profondeur dans des tissus diffusant, une autre technique de microscopie est privilégiée, la microscopie multiphotonique. En effet, l'excitation multiphotonique permet de contrer l'effet de la diffusion de la lumière dans les tissus, de plus les longueurs d'ondes utilisées sont généralement supérieures à 800 nm ce qui permet de profiter de la fenêtre optique. La fenêtre optique est l'ensemble des longueurs d'ondes pour lesquelles l'absorption de la lumière par les tissus est moindre (Figure 14).

1.3.3 Microscopie multiphotonique

La théorie d'absorption multiphotonique a été formulé dans les années 1930 par Maria Göppert-Mayer (Göppert-Mayer, 1931). Le principe de l'excitation multiphotonique repose sur le fait qu'une molécule fluorescente, pour qu'elle soit excitée, absorbe plusieurs photons quasi-simultanément (autour de 10^{-16}s) (Zipfel et al., 2003). La molécule retourne ensuite à son état fondamental en émettant un photon d'énergie égale à la somme de l'énergie des photons absorbés moins le décalage de stokes (Figure 11). Ce processus est dit non linéaire car l'interactions de deux photons avec la molécule fluorescente de manière quasi simultanée a pour conséquence la dépendance quadratique de l'absorption par rapport à l'intensité de la lumière d'excitation. En doublant l'intensité lumineuse d'excitation, la fluorescence émise est quadruplée.

De ce fait le signal provenant d'une excitation non linéaire provient essentiellement de la région où les photons sont le plus concentré au niveau du plan focal (Figure 11) (Helmchen and Denk, 2005).
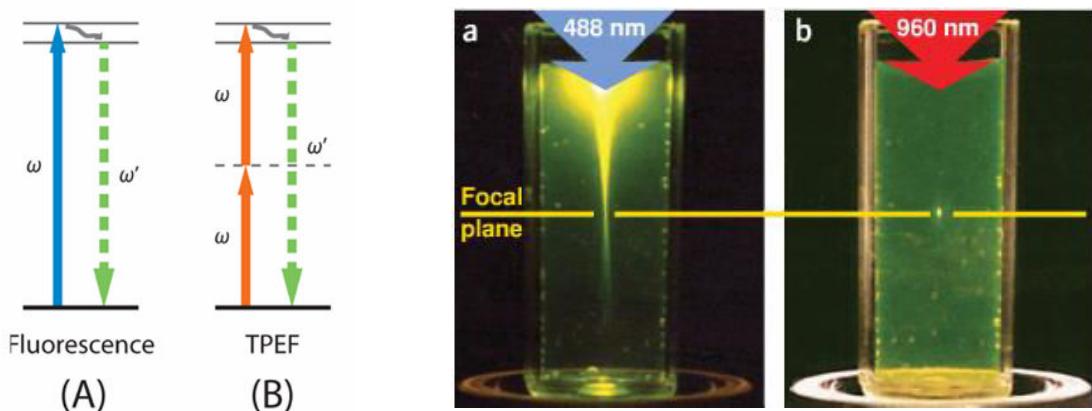
*Figure 11 : **Comparaison de l'excitation linéaire et l'excitation non linéaire.** A gauche, le diagramme de Jablonski représente en **A** l'excitation monophotonique où une molécule absorbe un photon d'énergie ω et émet un photon d'énergie plus faible ω'. En **B**, l'excitation à deux photons où une molécule absorbe deux photons simultanément d'énergies ω et émet un photon de plus haute énergie ω'. A droite, deux cuves de fluoroscéine sont illuminées à gauche par un laser monophoton induisant une excitation monophoton et à droite par un laser femtoseconde induisant une excitation biphotons. L'excitation monophotonique se propage tout le long du cône d'illumination alors que l'excitation biphotonique n'a lieu qu'au niveau du plan focal. D'après Streets et al., 2014; Zipfel et al., 2003.*

La probabilité qu'une molécule exposée aux rayons du soleil absorbe deux photons simultanément est de l'ordre de 10 millions d'années (Denk and Svoboda, 1997). A cause de la très grande intensité lumineuse nécessaire pour générer une excitation à deux photons, il aura fallu attendre les années 60 et l'invention des lasers pour que cette théorie puisse être vérifiée dans des cristaux de $CaF_2:Eu^{2+}$ (Kaiser and CGB, 1961) puis dans des cristaux organiques (Peticolas et al., 1963).

1.3.4 Le microscope multiphotonique

Le premier microscope bi-photonique est apparu dans les années 90 (Denk et al., 1990). Basé sur le même principe que le microscope confocal à balayage laser (CLSM : Confocal Laser Scanning Microscope), l'échantillon est balayé par le laser et l'image est reconstruite point par points. Contrairement à l'excitation continue qui se propage tout au long du cône d'illumination, l'excitation non linéaire est confinée au volume focal. L'utilisation du pinhole qui permet d'éliminer l'excitation hors plan focal pour le CLSM est ainsi inutile pour le microscope biphotonique (Figure 12).
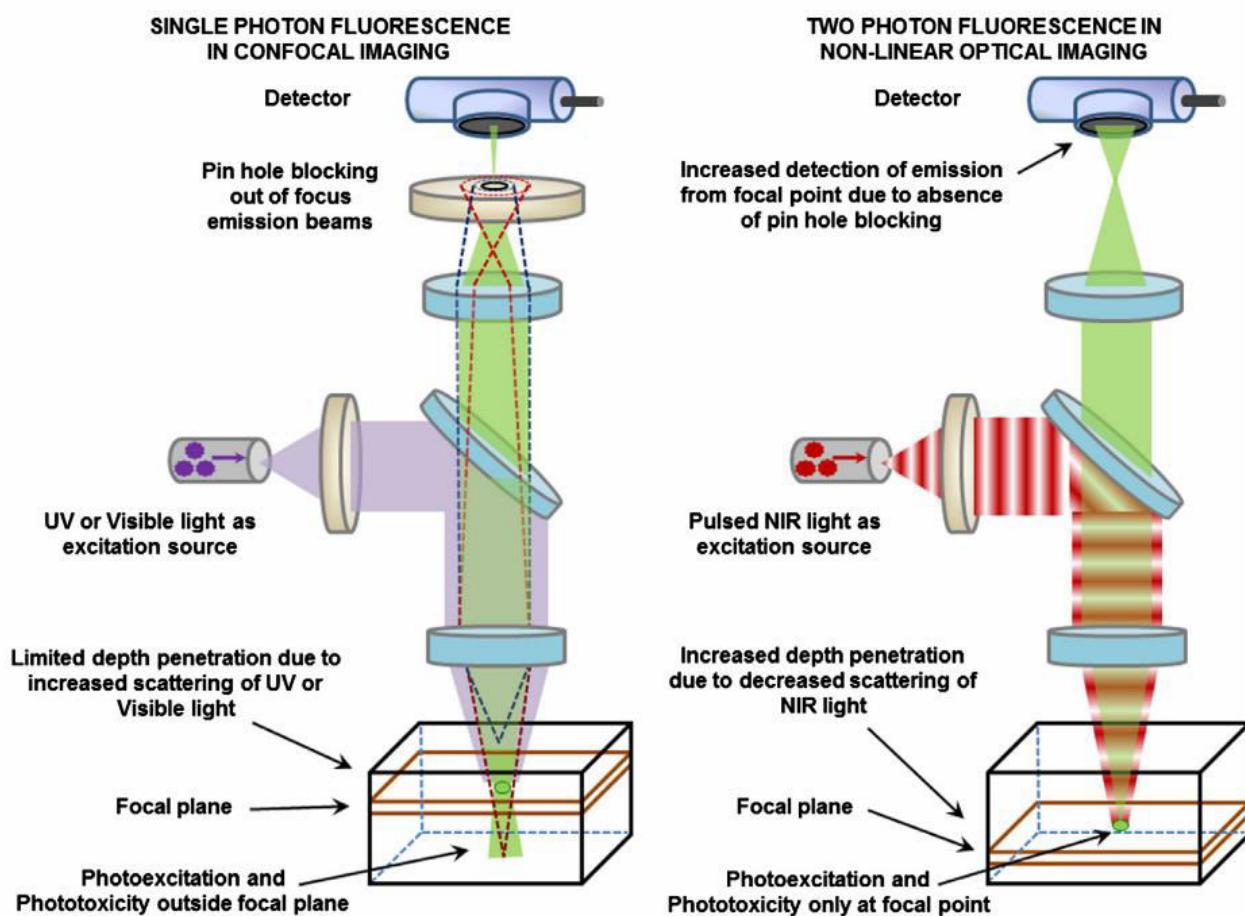
Figure 12 : **Comparaison de l'excitation de fluorescence mono-photon en microscopie confocale et l'excitation à deux photons en microscopie non linéaire** *D'après Thomas et al., 2014.*

Afin d'augmenter la probabilité qu'une molécule fluorescente absorbe deux photons simultanément il faut concentrer les photons dans le temps et l'espace. Pour cela l'utilisation de lasers pulsés ou femtoseconde fournit la grande intensité lumineuse, sous forme de paquets de photons, nécessaire à l'excitation deux-photons (Figure 13). La combinaison de ce type de lasers avec des objectifs de grande ouverture numérique est indispensable (Stutzmann and Parker, 2005).

Au cours de cette thèse le laser femtoseconde utilisé était un Chameleon Ultra II (Coherent) accordable entre 680 et 1080nm et produisant des pulses de 100fs.
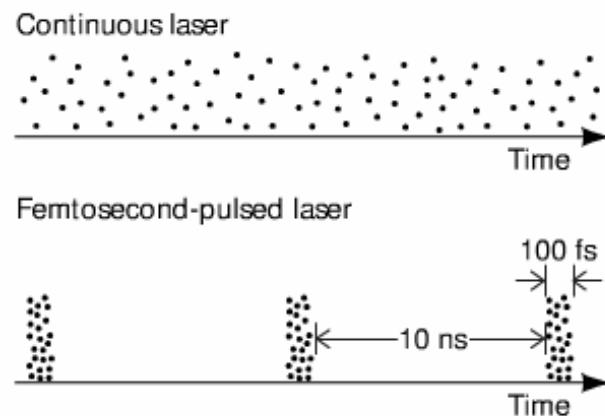
Les propriétés non linéaires de l'absorption multiphotonique confine l'excitation dans un faible volume résultant un rapport signal sur bruit amélioré et une plus faible phototoxicité (Helmchen and Denk, 2005). De plus, le coefficient d'absorption de plusieurs composants tissulaires est au moins dix fois moins important à 800 qu'à 450nm (Figure 14). La diffusion de la lumière est également inférieure à une longueur d'onde supérieur à 800nm. Toutes ces propriétés ont pour effet de pouvoir imager plus profondément dans les tissus comparé à la microscopie confocale monophoton (Figure 15).
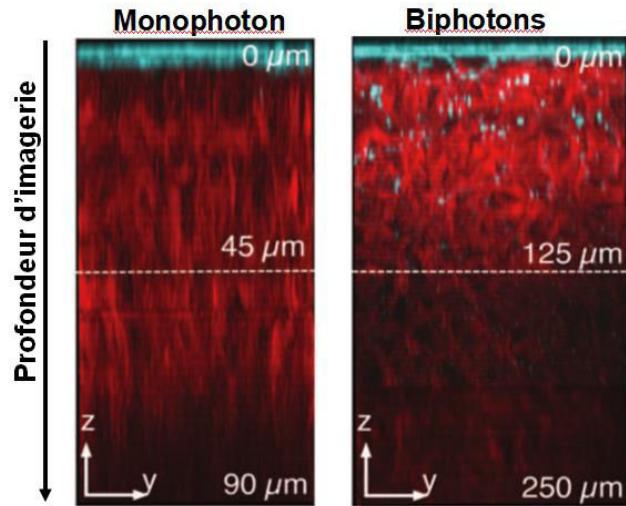
Figure 15 : **Comparaison de la profondeur d'imagerie CLSM vs 2PEM**. *Imagerie réalisée dans le foie de souris. L'imagerie confocale monophoton permet d'imager jusqu'à 90µm de profondeur alors que dans les mêmes conditions le microscope biphotons permet d'atteindre des profondeurs de 250µm. D'après Masedunskas et al., 2012.*

1.3.5   Autres types de microscopie non linéaire

L'absorption multiphotonique offre d'autres possibilités d'interactions non linéaires avec la matière. L'intérêt de ces techniques est de générer des signaux qui sont endogènes à l'échantillon imagé ne nécessitant ainsi aucun marquage spécifique. Une des plus utilisées est la génération d'harmoniques, génération de seconde ou de troisième harmonique (SHG et THG respectivement). La SHG permet d'imager des structures organisées et ne possédant pas de centre de symétrie tel que les fibres de collagènes ou les fibres musculaires. La THG est produit lors de variation de l'indice de réfraction permettant ainsi la visualisation des membranes par exemple. Une autre technique non linéaire utilisée est la diffusion Raman ou CARS (Coherent anti_Stokes Raman Scattering) où l'imagerie est basée sur l'état vibrationnel des molécules (Figure 16).
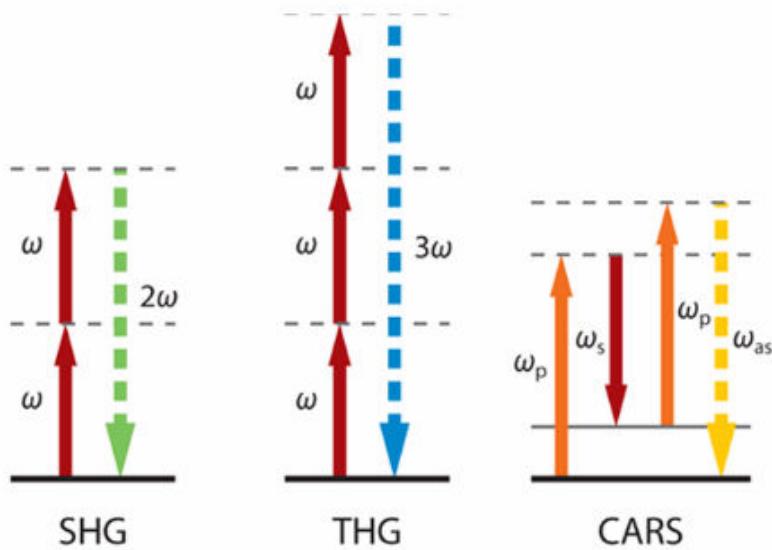
1.3.5.1   Génération de seconde harmonique (SHG)

1.3.5.1.1   La SHG endogène

Le phénomène de génération de seconde harmonique (SHG) a été découvert pour la première fois en 1961 dans des cristaux de quartz (Franken et al., 1961) Plus tard une autre équipe a démontré que des tissus riches en collagène pouvaient générer de la SHG (Fine and Hansen, 1971). Il a fallu ensuite attendre le développement de microscope multiphotonique pour appliquer cette technique à l'imagerie cellulaire et tissulaire (Campagnola et al., 1999).

Ce phénomène nécessite que la lumière interagisse avec une molécule qui ne possède pas de centre de symétrie. La lumière qui est produite par SHG a une longueur d'onde exactement deux fois plus petite que la longueur d'onde d'excitation. Contrairement aux phénomènes de fluorescence, les photons ne sont pas absorbés par la molécule et il n'y a pas de perte non radiative de l'énergie.

Les principales macromolécules qui génèrent un signal SHG endogène sont le collagène et les fibres musculaires striées. La source du signal SHG dans le muscle est formée par les faisceaux épais de myosine (Plotnikov et al., 2006).

Protéine majoritaire de la MEC, le collagène représente la protéine la plus présente dans le règne animal. 16 types de collagène différent existent mais 80 à 90% du collagène que l'on retrouve dans le corps est constitué des collagènes I, II et III (Lodish et al., 2017). Le collagène est une structure non-centrosymétrique arrangée en triple hélice. Seuls les collagènes I,II,III et V forment des fibrilles (Figure 17), le type IV est organisé en feuillet dans la membrane basale.
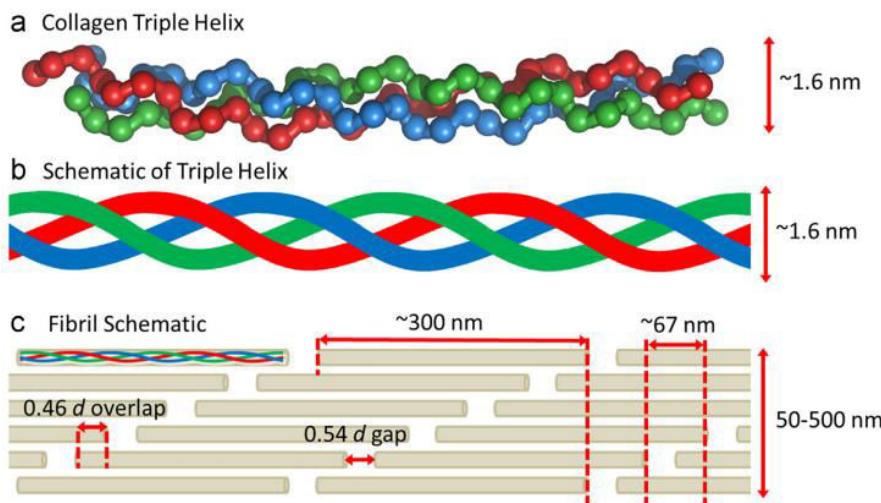
Figure 17 : **Organisation structurale du collagène fibrillaire. a :** Dans la formation du collagène des chaines en hélices de procollagène forment une triple hélice d'environ 300nm de longueur. **b :** Représentation schématique d'une triple hélice formée par 3 chaines de procollagène. **c :** Arrangement des triples hélices en fibrilles. Les triples hélices sont arrangées de façon échelonnées conduisant à la formation de zones de recouvrement et d'écart entre les fibrilles. Cette disposition particulière est à l'origine de l'apparence « en bandes » particulière du collagène. D'après Sherman et al., 2015.

Du fait de son organisation quasi cristalline le collagène de type I est celui qui génère le plus fort signal SHG (Cox and Kable, 2006).

La SHG est devenue une méthode efficace pour étudier l'organisation du collagène dans la peau (Campagnola et al., 2002), les tendons ou les artères. La SHG est aussi utilisée pour l'imagerie des fibres musculaires (Ramspacher et al., 2015). Elle a aussi été utilisée pour évaluer le taux de fibrose dans le foie (Gailhouste et al., 2010)

Dans le cadre du cancer, la SHG a été utiliser pour imager *in vivo* l'invasion tumorale de cellules cancéreuses le long de fibres de collagène (Wang et al., 2002; Alexander et al., 2008), le remodelage du collagène dans le microenvironnement tumorale *in vivo* (Wu et al., 2015) favorisant l'invasion tumorale (Provenzano et al., 2006).

1.3.5.1.2 Des marqueurs exogènes

Des marqueurs membranaires générant un signal SHG sont utilisés pour mesurer des potentiels transmembranaires (Millard et al., 2004)

Ces dernières années des nanoparticules cristallines ont été utilisées comme sondes générant un signal de SHG. Le barium titanate ($BaTiO_3$) a été utilisé comme marqueur couplé à un anticorps sur cellules (Hsieh et al., 2010). Ces sondes ont la particularité de générer un fort signal permettant de

les distinguer de la SHG endogène sans subir de photobleaching. Ces particules sont de plus compatibles avec le vivant du fait de leur faible toxicité (Staedler et al., 2012).

Elles ont été utilisées *in vivo* injectées ou couplées à un anticorps chez le poisson zèbre (Pantazis et al., 2010) ainsi que chez la souris (Grange et al., 2011)

1.3.5.2 Génération de troisième harmonique (THG)

La THG suit le même principe que la SHG, trois photons vont être diffusés pour produire un photon qui aura trois fois l'énergie des photons incidents (Barad et al., 1997). La THG apparait à l'interface de différentes structures, c'est le cas lorsque l'indice de réfraction change (Müller et al., 1998).

Cette technique est utilisée pour l'observation de structures membranaires riches en lipides ou des gouttelettes lipidiques(Débarre et al., 2006). La THG est une technique plus versatile que la SHG car les molécules n'ont pas besoin d'avoir une architecture particulière pour générer la THG. Un des désavantages est le fait de devoir utiliser une longueur d'onde d'excitation très élevée (entre 1180 et 1350nm) pour pouvoir collecter un signal dans le spectre de la lumière bleu (autour de 400nm) (Weigelin et al., 2016). Un Oscillateur Paramétrique Optique (OPO) est alors utilisé permettant d'atteindre ces longueurs d'ondes.

Le spectre d'émission de la SHG et de la THG, contrairement à la fluorescence, est centré autour de la valeur de la longueur d'onde d'excitation divisée par 2 ou 3 selon la nature du processus (Figure 18). Il est alors facile de distinguer et de collecter les différents signaux.
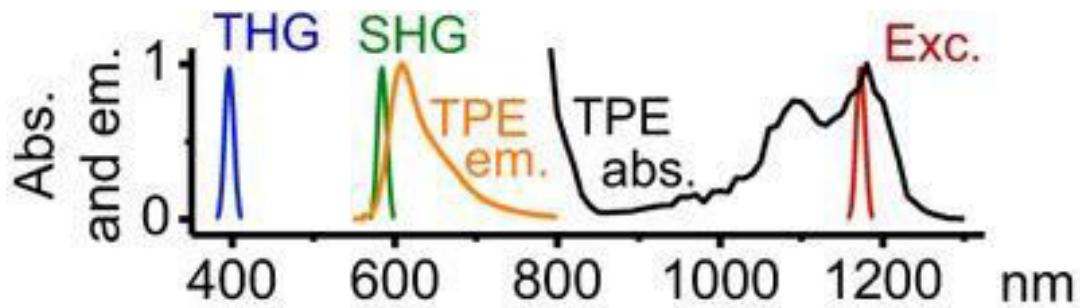
Figure 18 : **Spectre d'émission des types les plus communs de microscopie non linéaire**. *L'utilisation d'une seule longueur d'onde d'excitation à 1180nm permet l'exctiation de la mCherry (TPE abs.) mais aussi la génération de SHG à 590nm et de THG à 390nm (Weigelin et al., 2016)*

L'avantage de la SHG et de la THG est de pouvoir imager un échantillon sans devoir introduire de marqueurs extérieurs, l'observation se fait ainsi sur un échantillon non perturbé. La combinaison de ces différentes techniques d'imagerie non linéaires appliquée permet d'imager à la fois les cellules d'intérêt ainsi que l'environnement dans lequel elles évoluent (Figure 19).

Appliqué au cancer ces techniques ont permis d'imager in vivo l'invasion tumorale le long de fibres de collagène (Wang et al., 2002) et l'angiogenèse tumorale au cours du temps (Alexander et al., 2008).
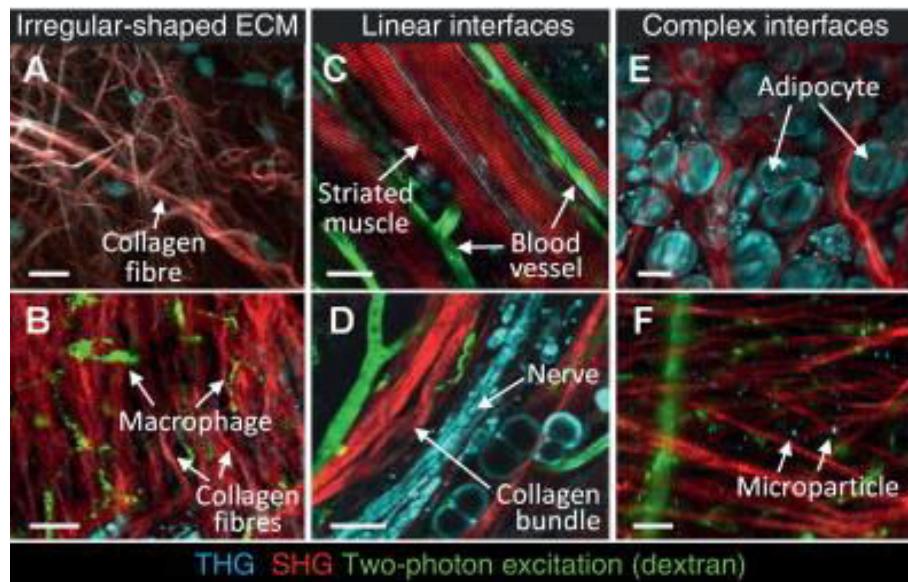
Figure 19 : **La combinaison de différents types de microscopie non linéaire permet d'imager de nombreux constituants de la matrice extracellulaire.** *La SHG permet d'imagers les fibres musculaires ainsi que les fibres de collagènes. La THG permet la visualisation des adipocytes et des nerfs. L'excitation à deux photons permet de visualiser les vaisseaux sanguins par fluorescence. (Alexander et al., 2013)*

1.3.5.3   La microscopie Coherent Anti-Stokes Raman Scattering (CARS)

La microscopie CARS permet d'imager les molécules en mesurant l'état vibrationnel de leur liaison. La réalisation d'images CARS repose sur l'intervention de 4 ondes (Four waves mixing). Deux ondes d'excitation stokes qui interviennent une seule fois, l'onde de pompe qui intervient deux fois et enfin le signal qui est mesuré.

La principale application de la microscopie CARS en biologie et l'imagerie des structures lipidiques qui contiennent de nombreuses liaisons C-H.

Les membranes lipidiques, les gaines de myeline, les goutelettes lipidiques chez *C.elegans*.

1.3.6   Imager les organes en profondeur grâce aux fenêtres implantables

Afin d'imager des organes situés en profondeur les chercheurs au début du 19ème siècle ont déjà commencé à implanter des fenêtres. Ces fenêtres implantées chirurgicalement à l'animal facilitent l'accès à l'organe que l'on veut imager en supprimant la couche de peau ou d'os opaque à la lumière.

Chez la souris de nombreuses fenêtres peuvent être implantées selon l'organe étudié (Figure 20).

Fenêtre cranial : Une craniotomie est pratiquée, ensuite une bague en métal permet de maintenir une lamelle au niveau de l'ouverture du crâne (Goldey et al., 2014). Cette technique a permis d'étudier la circulation cérébrale jusqu'à 1,6mm de profondeur (Kobat et al., 2011) de mettre en évidence le phénomène d'extravasation (Kienast et al., 2010).

Fenêtre dorsale : Ici un pli de peau est maintenu par un système de pince qui peut être en métal ou en plastique. Un des côtés est ouvert circulairement et une lamelle est placée au niveau de l'ouverture (Algire, 1943). C'est une technique qui est utilisé pour suivre l'angiogénèse, l'invasion tumorale (Alexander et al., 2008).

Fenêtre au niveau des glandes mammaires : Ce type de fenêtre a permis pour la première fois d'imager une tumeur se formant spontanément chez la souris exprimant l'oncogène polyomavirus middle T sous le contrôle du mouse mammary tumor virus (MMTV) long terminal repeat upstream MMTV-PyMT (Zomer et al., 2013).

Fenêtre abdominale : Dérivée de la fenêtre mammaire, elle permet l'imagerie des organes internes comme le foie, l'intestin, le pancréas ou les reins. Ce type de fenêtre a notamment permis l'imagerie de la formation de métastase dans le foie de souris.
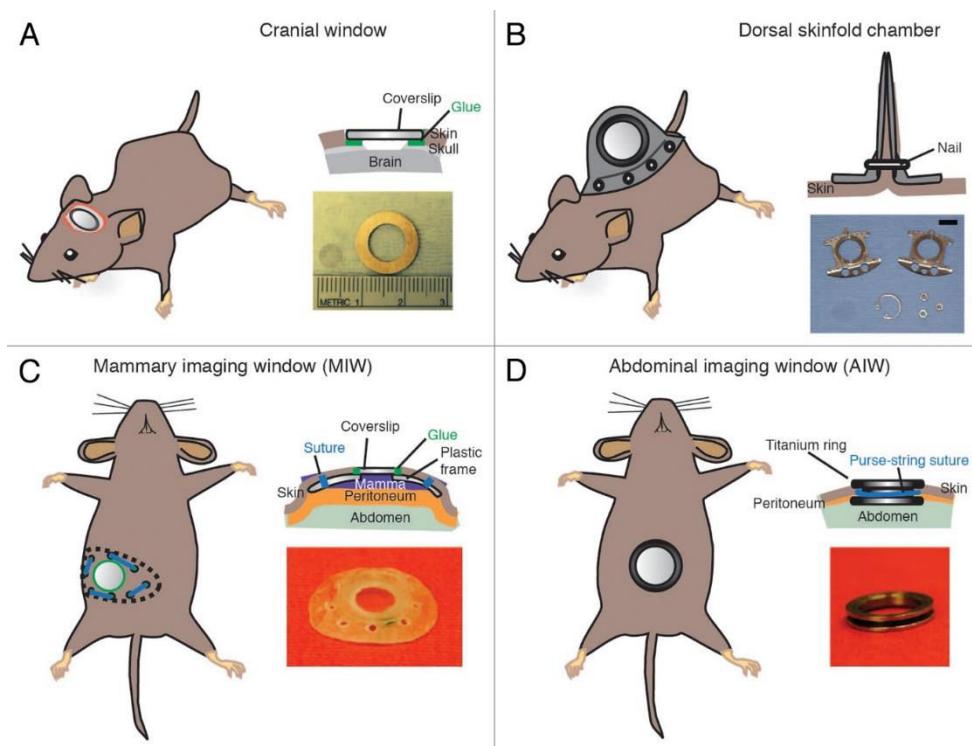
Figure 20 : **Principales fenêtres implantables chez la souris pour l'étude du cancer.** *A : La fenêtre cranienne est colée à l'os du crane. B : Le pli de peu est maintenue entre deux pièces métalliques. C : La fenêtre est maintenue par la peau qui s'insère dans la rigole au niveau de la fenêtre, le tout est ensuite suturé. D : Dérivée de la fenêtre mammaire, la fenêtre abdominale se pose de la même façon. D'après Alieva et al., 2014.*

Ces différentes fenêtres permettent aux chercheurs de pouvoir imager des organes qui dans des conditions physiologiques sont inatteignables pour la microscopie. De nouvelles fenêtres sont développées pour imager d'autres organes comme les ovaires chez la souris (Bochner et al., 2015) ou les poumons (Headley et al., 2016).

1.3.7 Contributions de la microscopie intravitale dans l'étude de la cascade métastatique

La microscopie intravitale et l'apparition de la GFP a été une évolution majeure dans l'étude du cancer *in vivo* (Paris and Sesboüé, 2004). Elle a en effet permis d'observer et de comprendre les étapes clés de la formation de métastases à l'échelle cellulaire.
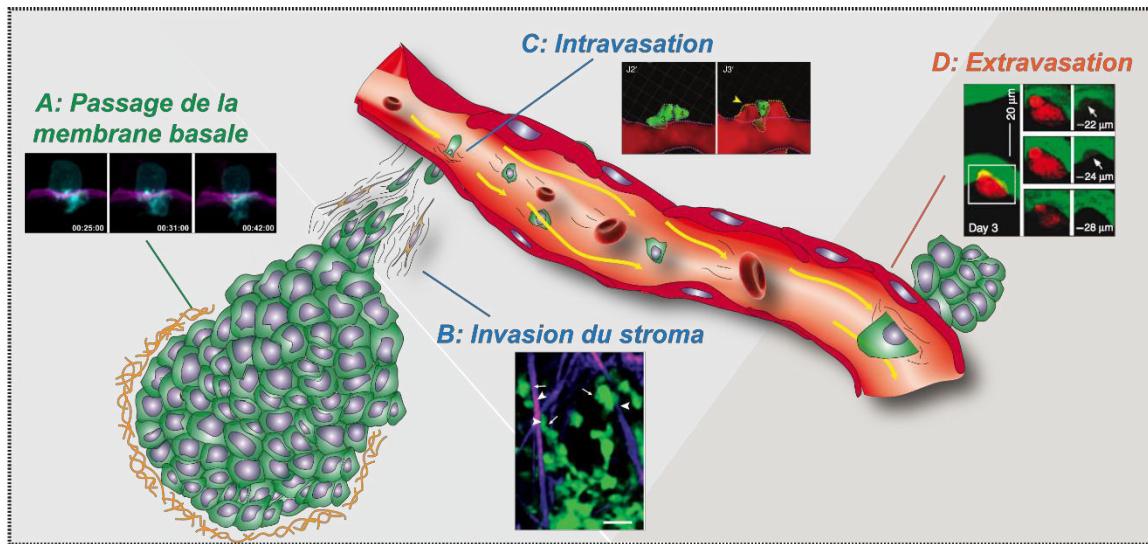
Figure 21 : **La microscopie intravitale a permis d'imager les principales étapes de la cascade métastatique**. **A** : Passage de la membrane basale par une cellule AC chez C.Elegans. **B** : Des cellules tumorales vertes qui migrent le long de fibres de collagène en violet. **C :** Intravasation d'une cellule tumorale (verte) dans la circulation sanguine de la souris. **D**: Extravasation d'une cellule tumorale (rouge) dans le cerveau de souris.

La dégradation de la membrane, première étape dans la formation de métastase, est essentiellement étudiée *in vitro* sur des coupes de tissus (Lodillinsky et al., 2015)ou en culture (Hotary et al., 2006) elle a aussi pu être étudiée *in vivo* chez *C.elegans* (Hagedorn et al., 2013) (Figure 21) et dans le modèle de membrane chorioallantoic de poulet (Ota et al., 2009).

L'apparition de la protéine fluorescente GFP a permis la création de lignées cellulaires fluorescentes. Ces lignées ont permis de suivre par fluorescence la mobilité des cellule tumorales dans la tumeur primaire (Farina, 1998). La greffe de fenêtre optique notamment au niveau des glandes mammaires a ensuite permis d'étudier la migration sur le long terme. L'utilisation d'autres protéines fluorescentes comme Dendra-2 permet de suivre sur plusieurs jours une population de cellules (Gligorijevic et al., 2009; Kedrin et al., 2008). La protéine Dendra est une protéine photoconvertible c'est-à dire qu'elle fluoresce dans son état normal dans le vert mais après illumination à 405 nm cette protéine fluoresce dans le rouge permettant ainsi de distinguer de la masse tumorale verte une population de cellules

rouges. La microscopie multiphotonique a aussi permis de mettre en évidence la migration des cellules tumorales le long des fibres de collagènes, imagées par SHG, pour envahir la MEC dans la glande mammaire de souris (Wang et al., 2002) (Figure 21) mais aussi dans le derme (Alexander et al., 2008) .

Une des premières tentatives de descriptions du phénomène d'intravasation a été réalisé par injection de cellules MTLn3 fluorescentes dans la glande mammaire du rat. Après quelques semaines la tumeur a été exposé par chirurgie et les images ont été réalisées par microscopie confocale. L'étude a montré que les cellule métastatiques MTLn3 s'orientaient vers les vaisseaux sanguins alors que les cellules non métastatiques MTC n'adoptaient pas cette disposition. (Wyckoff et al., 2000). Le phénomène d'intravasation a été imagé quelques années plus tard par microscopie multiphotonique dans la glande mammaire de rats (Wang et al., 2002). Grace aux progrès techniques et de la biologie moléculaire, il a été récemment montré que l'intravasation de cellules tumorales se fait dans un environnement précis appelé TMEM pour Tumor MicroEnvironment of Metastasis. Le TMEM est constitué de trois types cellulaires : un macrophage associé à la tumeur en contact direct avec une cellule tumorale et une cellule endothéliale. Le TMEM favorise l'intravasation de la cellule tumorale par une perméabilité transitoire de l'endothélium (Harney et al., 2015) (Figure 21).

L'extravasation de la cellule tumorale est particulièrement étudiée chez le zebrafish (Stoletov et al., 2010) mais a aussi été mis en évidence par imagerie multiphotonique dans le cerveau et le foie de la souris (Kienast et al., 2010; Ito, 2001) (Figure 21).

Cependant les techniques de microscopie intravitale n'offrent pas la résolution optique nécessaire pour imager la structure de la machinerie cellulaire mis en jeu dans les différentes étapes de la cascade métastatiques. Les microscopes optiques qu'ils soient champ plein, confocaux ou multiphotons ont une résolution axiale limitée supérieur à 200 nm. Cette limite a été étudiée par E. Abbe qui a formulée en 1873 la théorie de la limite de diffraction (Abbe, 1873). Cette limitation est causée par la taille du spot lumineux dans ces dimensions latérales (x et y) qui ne peuvent pas être plus petites que la longueur d'onde d'excitation divisé par deux fois l'ouverture numérique de l'objectif (Sahl et al., 2017). La limite de résolution d'Abbe est définie par la formule suivante : $R_{Abbe} = \frac{\lambda}{2NA}$ où λ est la longueur d'onde d'exciation et NA (Numerical Aperture) est l'ouverture numérique de l'objectif.

Dans les années 90 sont apparus les premiers principes physiques d'imagerie de super-résolution avec le développement des premiers systèmes au début des années 2000. Trois chercheurs (S. Hell, E. Betzig et W. Moerner) se verront récompensés en 2014 par le prix Nobel de chimie pour le développement de ces nouvelles méthodes d'imagerie (Van Noorden, 2014).

Différentes techniques de microscopie dites de super-résolution existent offrant une résolution latérale entre 20 et 80 nm. La technique de PALM (Photoactivated localization microscopy) (Figure

22) offre une résolution de 20 nm essentiellement utilisées sur des cellules fixées (Huang et al., 2008) car c'est une technique qui nécessite une forte intensité d'excitation et nécessite un long temps d'acquisition (York et al., 2012). Le STED (Stimulated emission depletion) (Figure 22) permet d'atteindre une résolution comprise entre 20 et 100 nm. Cette technique nécessite l'utilisation de deux sources lumineuses une pour l'imagerie de fluorescence et l'autre en forme de donut qui permet d'éteindre la fluorescence autour de la zone d'excitation. Le volume d'excitation correspond alors à une soustraction entre le volume d'excitation et le volume de désexcitation autour du point focal. Plus l'intensité lumineuse du donut est importante plus la résolution s'améliore. Enfin la technique SIM (Structured illumination microscopy) (Figure 22) offre une résolution axiale de l'ordre de 100 nm. Le SIM utilise la technique de lumière structurée pour imager l'échantillon. En imageant plusieurs images en faisant varier l'orientation du motif et sa phase, on peut après traitement obtenir des images avec une meilleure résolution.
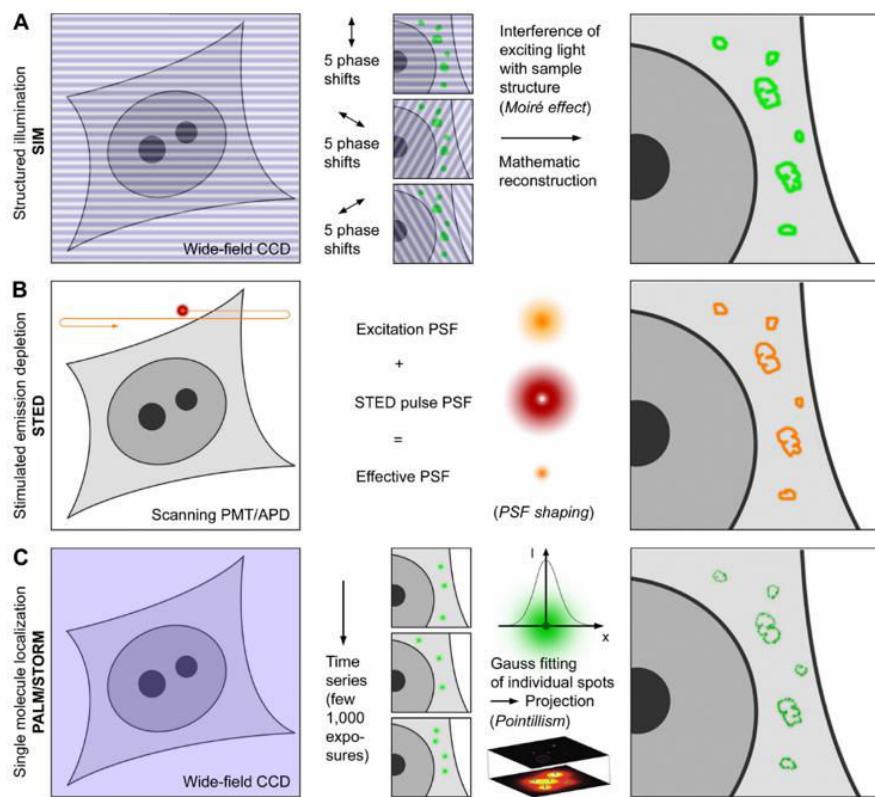
*Figure 22 : **Principes des techniques de microscopie super-résolution. A :** La technique SIM consiste à illuminer l'échantillon de façon non uniforme. Un effet de moiré est généré par l'interférence entre la lumière d'excitation structurée et les informations des structures de l'échantillon en dessous de la limite de diffraction. Une reconstruction mathématique permet la génération d'images d'une résolution deux fois meilleur que la microscopie champ plein. **B :** En microscopie STED le plan focal est scanné par deux faisceaux lasers superposés. Un laser excite les molécules fluorescentes, le second laser en forme de donut et d'une longeur d'onde plus importante force les molécules fluorescentes à retourner à leur état fondamental par un processus d'émission stimulé. **C :** La technique PALM/STORM utilise un nombre limité de fluorophores qui son dans leur état d'émission de photons. Cela est réalisable par photoactivation, photoswitch ou par clignottements. Les molécules sont ensuite détectées par une caméra et leur position est précisément déterminé par une Gaussienne.*

Ces techniques d'abord employées à l'études de cellules fixées commencent à faire leur apparition pour l'imagerie d'organismes multicellulaires *in vivo*. Elles ont ainsi été appliquées à l'imagerie de *C. elegans* (Rankin et al., 2011), de l'embryon de poisson zèbre (Gabor et al., 2015; York et al., 2012) et de l'embryon de drosophile (Schnorrenberg et al., 2016).

Pour l'instant seule la technique de STED a été utilisée pour l'imagerie intravitale appliquée à l'étude de la dynamique des épines dendritiques à la surface du cerveau de souris (Berning et al., 2012).
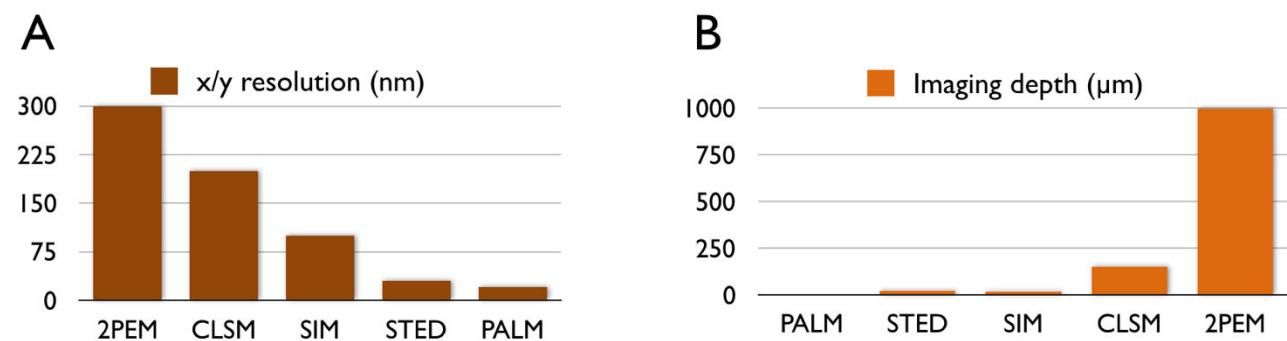
Figure 23 : **Comparaison de résolution et de profondeur d'imagerie entre différentes techniques d'imagerie. A** : La microscopie à deux photons (2PEM) offre la moins bonne résolution latérale. **B** : L'application des techniques de super résolution à l'imagerie intravitale est limitée par la profondeur d'imagerie inférieur à 50µm. CLSM : Confocal Laser Scanning Microscopy, SIM : Structured Illumination Microscopy, STED : Stimulated emission depletion, PALM : Photoactivated localization microscopy. D'après Schermelleh et al., 2010.

Ces techniques de super-résolution offrent une résolution significativement meilleure que les techniques de microscopie confocale ou multiphoton (Figure 23) mais elles sont difficilement utilisables pour l'imagerie intravitale chez la souris. En effet ce sont encore des techniques d'imagerie qui sont moins rapide mais surtout elles n'offrent pas le même pouvoir de pénétration dans les tissus (Figure 23), généralement inférieur à 50 µm, que l'imagerie multiphoton, supérieur à 1000 µm dans le cerveau (Schermelleh et al., 2010).

Une solution pour améliorer la résolution est de coupler imagerie intravitale 2PEM avec la microscopie électronique, cette technique s'appelle CLEM pour Correlative Light and Electron Microscopy.

1.4 La microscopie Corrélative (CLEM)

La microscopie corrélative est une technique qui permet d'étudier un même échantillon avec deux modalités d'imagerie différentes, la microscopie photonique et électronique. La microscopie de fluorescence offre une résolution comprise entre 200 et 20 nm et ne permet que d'imager des structures qui sont préalablement marquées par des sondes fluorescentes. La microscopie électronique offre une résolution d'environ 2 nm et ne repose pas sur un marquage spécifique, toutes

les structures sont distinguables à l'échelle ultrastructurale. Cette technique combines ainsi les avantages des deux techniques d'imagerie permettant de cibler la structure d'intérêt dans l'espace et le temps par microscopie photonique et ensuite imager exactement la même structure d'intérêt à très haute résolution par EM.

Une des principales difficultés est le saut d'échelle entre les deux techniques avec comme principale défit de retrouver la structure d'intérêt par microscopie électronique.

Les premières expériences de CLEM sont apparues à la fin des années 80 (Hayat, 1987). A l'époque les coupes du bloc de résine étaient séquentiellement préparées pour la microscopie optique et pour l'EM. Des coupes semi fines de 300 à 500 nm étaient colorées au bleu de toluidine et ensuite imagées par microscopie optique. Les coupes ultra-fines suivantes de 50 à 70 nm d'épaisseur étaient imagées par EM. L'épaisseur des sections semi-fines rendaient souvent impossible d'examiner l'ultrastructure de l'échantillon car la cellule entière ne pouvait ne plus être présente dans les coupes ultra fines suivantes (MIRONOV and BEZNOUSSENKO, 2009). La CLEM ne se faisait alors pas sur la même structure ou la même cellule mais plutôt dans la même région.

La CLEM connu un nouvel engouement à la fin des années 90 avec la possibilité de combiner microscopie à fluorescence et EM (Svitkina and Borisy, 1998).

Actuellement de nombreuses procédures de CLEM existent et sont applicables aux cellules en culture ou aux petits organismes tels que le poisson zèbre ou le vers *C. elegans*. A l'inverse, au début de ma thèse aucun protocole de CLEM n'était directement applicable sur de petits animaux comme la souris

1.4.1 La microscopie électronique

Un microscope électronique utilise un faisceau d'électrons émis en générale par un filament de tungstène. Ces électrons sont accélérés par une haute tension et focalisés sur l'échantillon par des lentilles électrostatiques.

La résolution étant dépendante de la longueur d'onde, l'utilisation d'électrons qui ont une longueur d'onde inférieur aux ondes lumineuses permet d'obtenir une résolution supérieure à celle offerte par la microscopie photonique. La résolution offerte par la microscopie électronique est de l'ordre de 2nm.

Les microscopes électroniques fonctionnent selon deux principes soit les électrons doivent traverser l'échantillon on parle de microscope électronique à transmission (MET/TEM) ou alors le faisceau d'électrons est balayé sur l'échantillon on parle alors de microscope électronique à balayage (MEB/SEM). Des évolutions récentes d'imagerie en série du bloc permettent d'augmenter le débit de la microscopie électronique en automatisant la coupe et l'imagerie de l'échantillon

1.4.1.1 Le microscope électronique à transmission (MET)

Le premier microscope électronique à transmission commercial est apparu en 1938 (Siemens UM-100) mais il a fallu attendre les années 60 pour que les techniques de préparation des échantillons (fixation, coloration, inclusion résine, couteaux en diamants) soient optimales pour ce type d'imagerie.

L'échantillon à imager doit être extrêmement fin car les électrons, pour pouvoir former une image, doivent traverser l'échantillon. Les échantillons sont ainsi la plupart du temps inclus dans une résine très dure (Epon) permettant de réaliser des coupes ultrafines entre 50 à 250nm d'épaisseur grâce à l'utilisation d'un ultramicrotome équipé d'un couteau en diamant.

L'échantillon est contrasté à l'aide de métaux lourd (tétroxyde d'osmium OsO_4, Acétate d'uranyl). Les électrons plus ou moins absorbés par ces zones denses vont donner le contraste de l'image.

Le MET est la technique de microscopie électronique qui offre la meilleure résolution en x/y. La résolution en z dépend de l'épaisseur de coupe.

1.4.1.2 Le microscope électronique à balayage

Le MEB utilise un faisceau d'électrons qui balaye la surface de l'échantillon. Les électrons qui sont capturés pour former l'image sont de deux types. Les électrons secondaires proviennent de l'échantillon, ils ont été éjectés par interaction inélastique avec le faisceau d'électrons. Ces électrons permettent d'imager la topographie de l'échantillon. Comme les échantillons biologiques sont constitués de matériel non dense, la quantité d'électrons secondaires n'est pas suffisante. Pour augmenter la quantité d'électron secondaires les échantillons sont recouvert d'une fine pellicule de métal (or,palladium) qui produira une grande quantité d'élections secondaires.

Les électrons dit backscattered sont issus de l'interaction élastique entre le faisceau d'électrons et les noyaux constituants l'échantillon.

Cette technique n'est pas limitée par l'épaisseur de l'échantillon elle peut être utilisée pour l'imagerie de cellules en culture mais aussi d'insectes entiers.

1.4.1.3 Microscopie électronique en volume

1.4.1.3.1 Coupes sériées

Le MET peut-être utilisé pour reconstruire un modèle en 3D soit en effectuant des images des coupes ultrafines sériées de l'échantillon soit en réalisant de l'imagerie par tomographie sur coupes plus épaisses.

L'imagerie de coupes sériées est une technique qui ne requiert pas d'équipements particuliers mais repose plutôt sur le savoir-faire de l'expérimentateur (Figure 24). En effet, réaliser de nombreuses

coupes sériées tout en conservant leur orientation, leur ordre et leur intégrité nécessite une vraie expertise.

La tomographie consiste à imager la même zone sous différents angles selon un axe perpendiculaire au faisceau d'électrons. En général l'échantillon est basculé de +70° à -70° avec un incrément de 1 à 2° (Chen et al., 2008). Les différents tomogrames sont ensuite combinés pour obtenir une visualisation en 3D de l'échantillon avec une résolution axiale d'environ 2nm (Peddie and Collinson, 2014).

Le MEB est aussi utilisé avec un système de coupes sériées de l'échantillon appelé ATUM (Automated Tape-collecting Ultramicrotome) (Figure 24). Ce système permet de récolter automatiquement les coupes sériées de 30nm d'épaisseur (Briggman and Bock, 2012) sur un support adhésif. Comme le support adhésif est opaque aux électrons seule le MEB peut être utilisé pour l'imagerie (Hayworth et al., 2006). Ce système a pour avantage de pouvoir réaliser des coupes plus fines de l'ordre de 30nm mais aussi d'éliminer les erreurs engendrées par des coupes sériées réalisées manuellement.

1.4.1.3.2 Image en série du bloc de résine

Le principe de cette technique est d'automatiser la coupe de l'échantillon et l'acquisition d'images. Pour ce faire un MEB et un dispositif de coupes ou d'érosions de l'échantillon sont couplés.

La première technique à avoir été introduite en 2004 est le SBFSEM (Serial Block Face Scanning Electron Microscopy) (Figure 24) par W. Denk, l'inventeur du microscope multiphotonique (Denk and Horstmann, 2004). Un ultramicrotome est ici intégré dans la chambre du microscope électronique à balayage.

Une deuxième technique est le FIB/SEM (Focused Ion Beam / Scanning Electron Microscope) (Figure 24). Cette technique utilise à la place d'un ultramicrotome un canon d'ions Gallium. Le FIB/SEM offre la meilleure résolution en z, d'environ 3 à 5nm (Narayan and Subramaniam, 2015; Briggman and Bock, 2012).
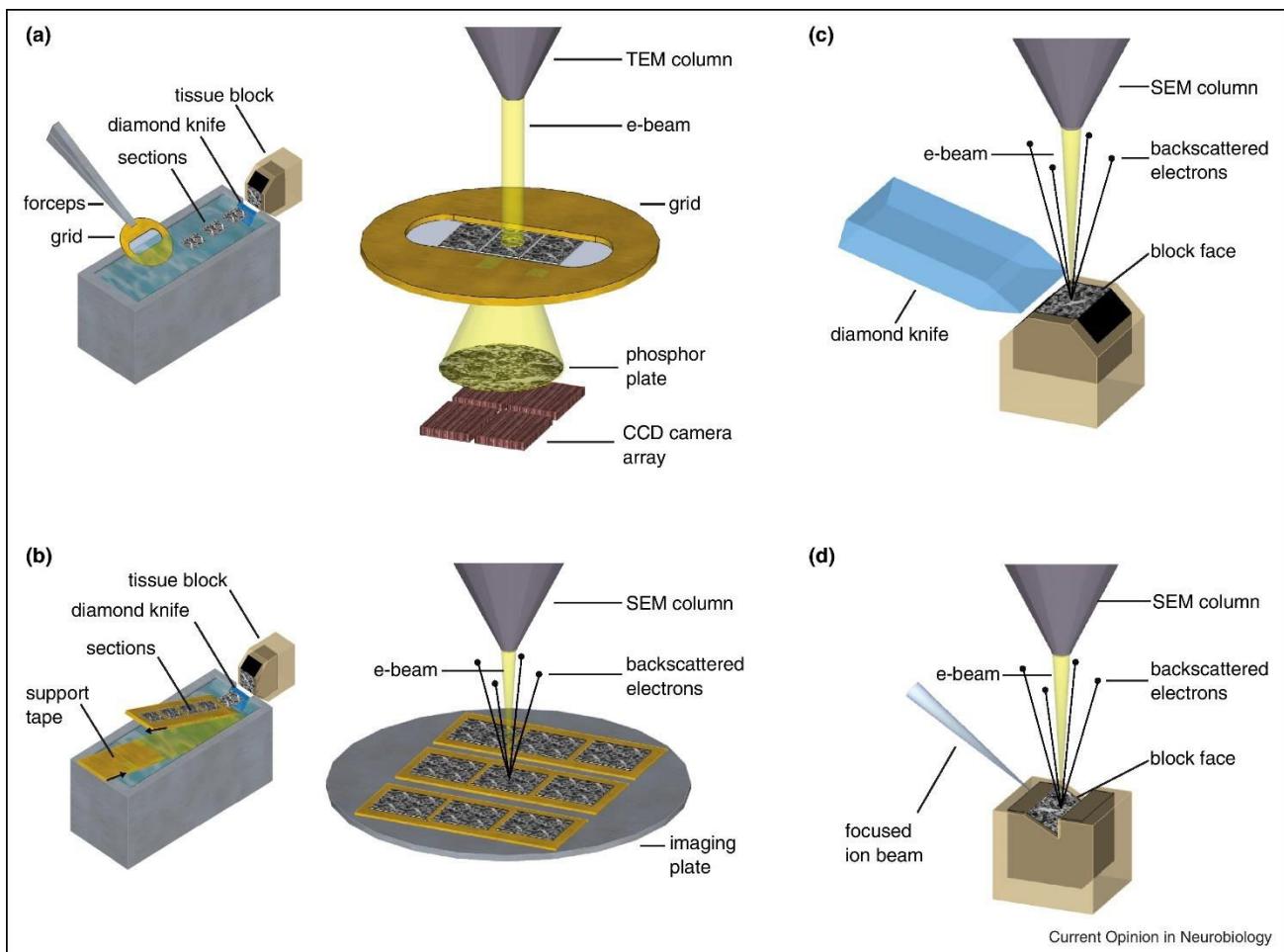
*Figure 24 : **Les différentes techniques permettant la reconstruction 3D d'un échantillon.** a : La technique de coupes sériées requiert le moins de matériel mais est difficile à mettre en œuvre sur de grands échantillons. b : ATUM (Automated Tape-collecting Ultramicrotome) Les coupes sériées sont récoltés sur un ruban adhésif et l'imagerie se fait par MEB. c: Serial Block face Scanning microscopy. Un ultramicrotome est incorporé à MEB, les coupes et l'imagerie se font de manière automatisée. d: FIB-SEM (Focused Ion Beam – Scanning Electron Microscopy) cette technique utilise un canon ionique qui érode la surface de l'échantillon. L'acquisition des images électronique se fait par MEB. D'après Briggman and Bock, 2012.*

1.4.2   CLEM sur cellules

1.4.2.1   Systèmes commerciaux tout en un

De nombreux systèmes commerciaux existent pour la réalisation de CLEM sur cellules *in vitro*. Des systèmes d'imagerie bi-modalitées, photonique et électronique permettent sur un même appareil de réaliser des images de fluorescence et ensuite des images par microscopie électronique. L'échantillon doit être ainsi à la fois compatible pour la microscopie de fluorescence mais aussi pour la microscopie électronique, c'est-à-dire qu'une fois inclus dans la résine la fluorescence doit être préservée. Le système iCorr commercialisé par FEI incorpore un microscope à fluorescence et un microscope électronique à transmission (Agronskaia et al., 2008). La fluorescence est utilisée pour repérer la région d'intérêt sur des coupes, de 70 à 120 nm d'épaisseur, qui devra ensuite être imagée par microscopie électronique.

47

Le système SECOM proposé par Delmic combine un microscope à fluorescence inversé ainsi qu'un microscope électronique à balayage. Basé sur la microscopie à balayage, ce système ne nécessite pas d'inclure et de couper l'échantillon avant observation au microscope électronique (Liv et al., 2013).

Un autre système commercialisé par Jeol (ClairScope) utilise un microscope électronique à balayage dit atmosphérique. Ici, la partie photonique ainsi que l'échantillon sont positionnés en dehors de la cavité dépressurisée. L'échantillon et la partie électronique sont séparés par une membrane de SiN d'environ 100nm d'épaisseur. L'avantage de ce système est de pouvoir conserver les cellules dans leur boite de culture en milieu liquide. Un des désavantages des techniques de balayage est l'imagerie en profondeur qui est inférieur à 3µm.

Ces systèmes tout en un sont utilisables pour l'observation de structures distribués de façon homogène dans l'échantillon à observer ou bien que la caractérisation en 3D ne soit pas nécessaire (absence de reconstruction 3D par microscopie photonique et faible pénétration des techniques de MEB). De plus l'observation d'échantillons préalablement fixés et inclus ne permet pas l'observation de phénomène dynamique. Pour toutes ces raisons il est alors nécessaire de séparer les deux modalités d'imagerie et d'utiliser des points de repères pour retrouver la structure d'intérêt par microscopie électronique.

1.4.2.2 La CLEM en deux étapes

Dans ce cas il est alors nécessaire de cultiver les cellules sur des support comportant des points de repère qui seront visibles sur le bloc de résine. Pour cela il existe des boites à fond de verre microgravées commerciales (Ibidi ou MatTek) une autre solution est de produire ses propre support (Spiegelhalter et al., 2014).

L'avantage de cette méthode est de pouvoir combiner n'importe quelle technique d'imagerie de fluorescence à n'importe quel type de microscopie électronique selon l'objet d'étude.

La préparation la plus courante de l'échantillon pour la microscopie électronique implique de fixer l'échantillon par des agents chimiques. La fixation chimique est un processus lent et susceptible de créer des artefacts alors que la congélation haute pression (HPF : High Pressure Freezing) permet une fixation en quelques millisecondes tout en préservant plus efficacement l'ultrastructure de l'échantillon (Korogod et al., 2015). Cette technique d'HPF permet ainsi d'imager l'ultrastructure d'un événement cellulaire dynamique par microscopie électronique (Spiegelhalter et al., 2010; VERKADE, 2008). L'HPF est aussi utilisée pour conserver la fluorescence sur les coupes pour EM, la corrélation se faisant ainsi directement sur les coupes (Kukulski et al., 2011).

Des systèmes basés sur la photo-oxydation de la diaminobenzidine (DAB) en un produit visualisable par microscopie électronique rend la corrélation plus facile. L'illumination d'un marqueur attaché à la

protéine d'intérêt induit la génération d'oxygène singulet capable d'oxyder la DAB. Dans l'échantillon fixé la DAB oxydée réagit alors avec l'osmium qui la rend ainsi facilement visible par EM (Pagano et al., 1989; Deerinck et al., 1994).

C'est le cas de la flavoprotein protéine fluorescente miniSOG (mini Singlet Oxygen Generator) qui provient de la plante arabidopsis. Cette protéine est à la fois visualisable par fluorescence et par microscopie électronique car elle est capable après illumination en lumière bleue de générer de l'oxygène singulet induisant la photo-oxydation de la DAB (Shu et al., 2011). L'utilisation d'anticorps HRP (Horseradich peroxidase) dirigés contre la protéine fluorescente peuvent aussi être utilisés pour obtenir un résultat semblable (Mironov et al., 2000).

Les techniques de super résolution sont aussi compatibles avec la CLEM (Kopek et al., 2017).

La CLEM *in vitro* a permis de faire des découvertes importantes comme la description de l'échafaudage des sous unités du complexe ESCRT impliquées dans le relargage de particules virales (Engelenburg et al., 2014) ainsi que la description temporelle et spatiale du mécanisme moléculaire mis en place pour l'endocytose chez la levure (Kukulski et al., 2012).

1.4.3   CLEM sur petits organismes

Les modèles *in vitro* offrent de multiples avantages pour la biologie cellulaire mais n'arrivent pas à recréer la complexité des tissus *in vivo*. Ainsi corréler microscopie intravitale et EM permet d'étudier à haute résolution temporelle et spatiale un évènement biologique clé dans son environnement d'origine.

Aucun système commercial n'existe pour la réalisation de CLEM sur les petits organismes tel que le poisson zèbre, le vers *C. elegans* ou l'embryon de drosophile.

La principale difficulté dans ce type d'échantillon est de retrouver la région d'intérêt lors de l'acquisition d'images par microscopie électronique. En effet, malgré le fait que l'échantillon entier peut-être traité pour la microscopie électronique, devoir examiner l'échantillon entier par EM est une tâche fastidieuse. La communauté scientifique a dans ce sens produit de nombreuses procédures de CLEM applicables à de tels organismes permettant de retrouver efficacement par EM la structure d'intérêt.

Une façon de pouvoir réaliser de la CLEM sur ces petits organismes est de conserver ou transférer le signal de fluorescence des protéines d'intérêts en un marqueur aussi visualisable par EM.

La fluorescence peut être conservée dans le bloc de résine par HPF. Une fois l'échantillon coupé pour la microscopie électronique, les sections sont examinées par microscopie de fluorescence pour retrouver la zone d'intérêt. La fixation par HPF conserve aussi les sites antigéniques ce qui rend possible le marquage de la protéine fluorescente avec des anticorps couplés à des billes d'or visibles

per EM (Nixon et al., 2009). Une autre possibilité est de transformer le signal de fluorescence en un composé dense aux électrons essentiellement par l'oxydation de la DAB. Cette méthode peut être réalisé en utilisant des anticorps couplés à une peroxydase, photo-oxydation par un fluorochrome ou l'utilisation peroxydases encodées génétiquement.

Une autre technique de corrélation repose sur des points de repères qui sont soit propres à l'échantillons ou ajoutés pendant la préparation de l'échantillon (Figure 25). Cette approche nécessite la relocalisation précise de la ROI dans l'échantillon préparé pour la microscopie électronique. La technique d'ultramicrotomie ciblée permet de calculer la position exacte de la région d'intérêt par rapport à des repères ajoutés par microgravure du bloc de résine. Ces points de repère sont positionnés grâce à la superposition des images de microscopie intravitale sur une image de l'échantillon inclus dans le bloc de résine. Les marques sont ensuite utilisées pour récolter les coupes correspondant précisément à la ROI. Cette technique a été utilisée sur le vers C. Elegans sur l'embryon de drosophile et sur l'embryon de poisson zèbre (Hyenne et al., 2015; Kolotuev et al., 2010; Goetz et al., 2014; 2015).

Les repères anatomiques sont aussi utilisables pour la corrélation. Par exemple chez le poisson zèbre, des lignées transgéniques permettent d'imager par fluorescence les cellules endothéliales constituant les vaisseaux sanguins (Armer et al., 2009). D'autres éléments peuvent être utilisés pour cibler la ROI comme le système nerveux et la limite entre matière grise et blanche (Ham et al., 2014), les mélanocytes (Durdu et al., 2014)

1.4.4   CLEM sur petits animaux

La réalisation de CLEM sur la souris est un challenge technique lorsqu'on veut imager par IVM et ensuite par EM une petite structure comme une cellule unique ou un organite dans un organisme aussi complexe. A l'inverse des petits organismes, comme le poisson zèbre par exemple, il est impossible de préparer l'animal entier pour la microscopie électronique. Il faut ainsi réduire la taille de l'échantillon à examiner pour le rendre compatible avec la préparation pour la microscopie électronique tout en s'assurant de conserver et ensuite retrouver la ROI par EM.

La neuroscience a été un domaine qui a été productif en termes de protocoles de CLEM appliqués à l'étude de la formation des neurones, des synapses et des épines dendritiques dans le cerveau de la souris.

La méthode principale est appliquée à l'imagerie du cerveau, elle consiste à imager à travers une fenêtre crâniale des neurones marqués par la GFP puis de fixer la souris par injection intracardiaque. Le cerveau est ensuite découpé en coupes de 60 – 100µm par vibratome parallèlement au plan d'imagerie. Le vibratome est un microtome qui utilise une lame de rasoir vibrante pour couper un tissu. Cet appareil à l'avantage de pouvoir couper des tissus dans leur état natif sans avoir recours à

des techniques d'inclusions. Les sections sont ensuite examinées par microscopie conventionnelle pour retrouver la région qui a été précédemment imagée *in vivo*. La protéine GFP est ensuite marquée par des anticorps couplés à une péroxydase générant la polymérisation de la DAB en composé dense aux électrons aussi visible sur les coupes générées par vibratome. Après inclusion en résine la position de la ROI est retrouvée dans les coupes sériées en comparant la vasculature avec les données d'imagerie intravitale. Finalement le neurone marqué par la DAB est retrouvé en examinant la coupe par microscopie électronique. (Knott et al., 2009).

Une autre méthode est de marquer la position de la ROI par Near-infrared branding (NIRB) (Bishop et al., 2011). Après imagerie intravitale et fixation, les sections générées par vibratome sont inspectées par microscopie à fluorescence pour retrouver la ROI. La ROI est ensuite marquée par ablation laser induite par un laser au même plan que la structure. Le marquage est visible ensuite sur la section de vibratome et par microscopie électronique permettant de retrouver facilement la structure à imager par microscopie électronique à transmission ou FIB-SEM (Figure 25).

Aucun de ces protocoles n'est cependant applicable à l'étude du cancer car les structures à observer sont de tailles bien plus importantes que des cellules dendritiques ou des axones ou des synapses ne permettant leur observation dans une seule coupe généré par vibratome (Karreman et al., 2016).
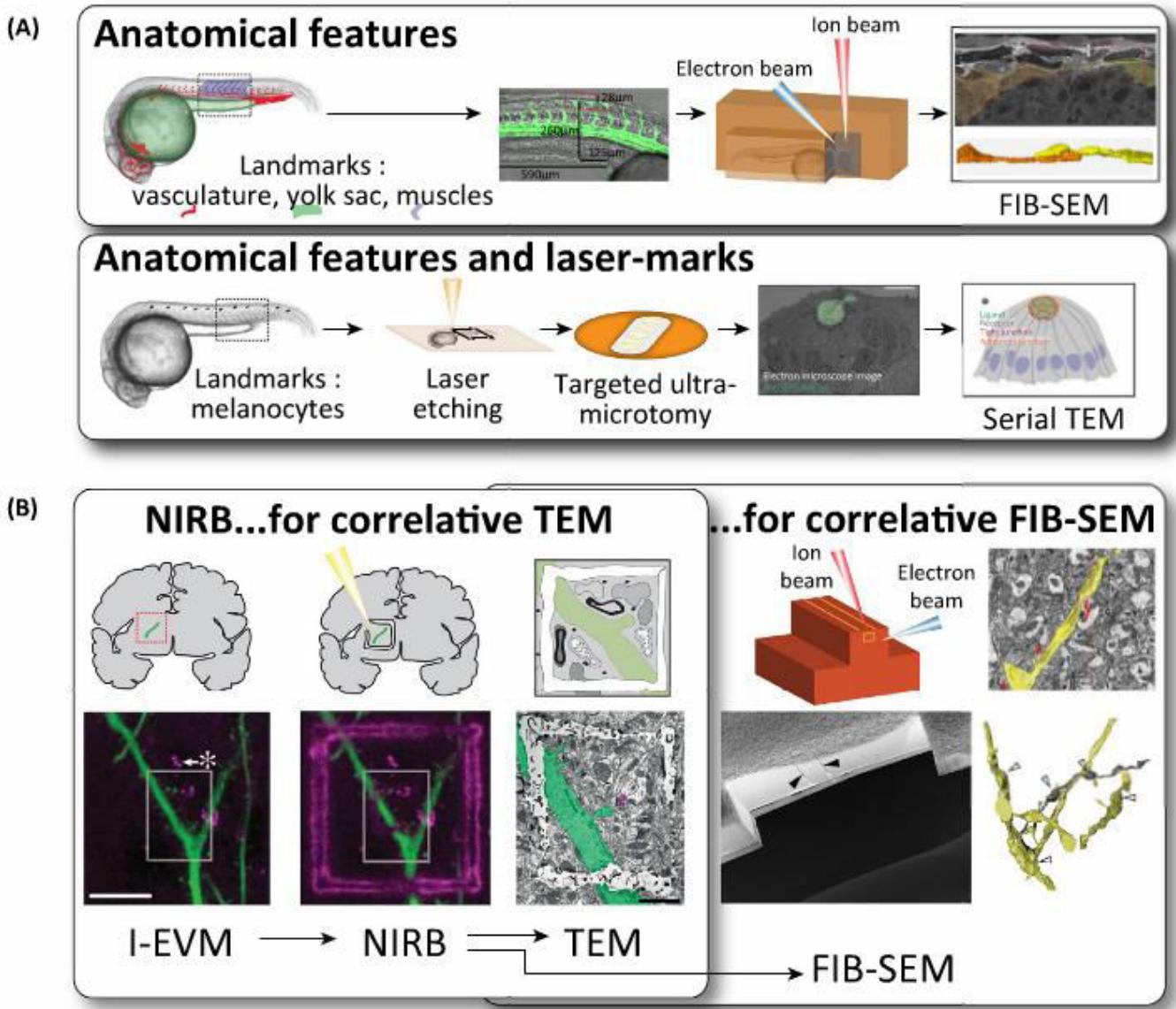
*Figure 25 : **Différentes approches pour retrouver la ROI observée par microscopie intravitale dans le bloc de résine.** A : Les repères anatomiques (mélanocytes, vasculature, yolk, muscles) présent dans le tissu peuvent être utilisés pour retrouver la ROI par FIB-SEM, ou un marquage laser après inclusion en résine permet de cibler la structure pour la microscopie électronique à transmission. B : La ROI peut être délimitée par NIRB sur des coupes de tissu pour ensuite retrouver précisément la ROI par MET ou FIB-SEM. D'après Karreman et al. 2016.*

1.5 Manuscrit n°1 : Revue de techniques d'imagerie.

The Company of
Biologists

COMMENTARY

Seeing is believing: multi-scale spatio-temporal imaging towards *in vivo* cell biology

Gautier Follain[1,2,3,4,*], Luc Mercier[1,2,3,4,*], Naël Osmani[1,2,3,4,*], Sébastien Harlepp[2,5,6,*] and Jacky G. Goetz[1,2,3,4,‡]

ABSTRACT

Life is driven by a set of biological events that are naturally dynamic and tightly orchestrated from the single molecule to entire organisms. Although biochemistry and molecular biology have been essential in deciphering signaling at a cellular and organismal level, biological imaging has been instrumental for unraveling life processes across multiple scales. Imaging methods have considerably improved over the past decades and now allow to grasp the inner workings of proteins, organelles, cells, organs and whole organisms. Not only do they allow us to visualize these events in their most-relevant context but also to accurately quantify underlying biomechanical features and, so, provide essential information for their understanding. In this Commentary, we review a palette of imaging (and biophysical) methods that are available to the scientific community for elucidating a wide array of biological events. We cover the most-recent developments in intravital imaging, light-sheet microscopy, super-resolution imaging, and correlative light and electron microscopy. In addition, we illustrate how these technologies have led to important insights in cell biology, from the molecular to the whole-organism resolution. Altogether, this review offers a snapshot of the current and state-of-the-art imaging methods that will contribute to the understanding of life and disease.

KEY WORDS: Cell biology, Imaging, *In vivo* imaging, 1PEM, 2PEM, CLEM, LSFM, SIM, SPIM, STED microscopy

Introduction

Understanding complex and integrated cellular behaviors can be performed at various levels. The post-genomic era led to the development of numerous 'omics' efforts with the ambitious goal of predicting and, thereby, anticipating the treatment of clinical phenotypes by integrating multi-scale information from the patient. This concept of personalized and precision medicine faces the challenge to integrate the extremely large amount of available 'omics' biomedical data for the development of personalized treatments to cure patients in a routine day-to-day clinical practice. Cell biology is playing a main role in the understanding of clinical phenotype at a cellular scale. Performing *in vivo* cell biology aims to understand a disease at a subcellular scale and to integrate this information into the wider context of a tissue or an organ. Although

multi-omic approaches can grasp snapshots of a disease at multiple scales, they are often restricted to a selected time-point that does not fully represent the dynamics of cells and tissues. Thanks to the recent development of fast and high-resolution imaging approaches, *in vivo* models, gene editing, cell and biomaterial engineering, as well as high-throughput procedures, it is now possible to probe and understand – at multiple scales – the link between subcellular phenomenon and cell phenotype, both in normal or pathophysiological contexts. Because pathologies often emanate from subcellular and dynamic events that are then integrated in tissues, access to the full cellular organization is required, in 3D and in real-time, and within its most relevant context.

In this Commentary, we aim to provide a snapshot of existing as well as recent developments in live-cell imaging, which now makes the concept of *in vivo* cell biology a reachable target. Here, *in vivo* refers to imaging performed in whole living animals. Because animal models are central in understanding cellular phenotypes that are essential to development or disease progression, we start by summarizing the basics of intravital imaging, which aims to visualize an event of interest in its most representative biological context. We particularly emphasize recent developments in nonlinear microscopy, which offers means to image cellular and micro-environmental behaviors in a non-invasive manner. Because phototoxicity is an important criterium in performing live *in vivo* cell biology, we then summarize the recent development and latest improvements in light-sheet microscopy, which offers unprecedented information at the organismal scale for small animals. Cell biology is tightly linked to biomechanics and has led to the emergence of a widespread concept of mechanobiology that aims to unravel the contribution of mechanical forces to biological events and disease. We thus also provide a glimpse of the existing biophysical methods that can be applied to *in vivo* cell biology and highlight some of their applications (see Box 1). We continue by describing the recent developments in super-resolution imaging and illustrate the recent developments with some biological applications that clearly suggest that *in vivo* super-resolution can be reached within the next few years. Finally, because the highest resolution can still not be obtained on living animals, we conclude by discussing the recent progress made in correlative light and electron microscopy (CLEM), including in the area of intravital correlative microscopy, which offers access to high-resolution imaging of cellular events *in vivo*. We also provide a summary table that, for each technology, lists the advantages and limitations, the resolution that can be achieved, the technical difficulties and the key applications in cell biology (Table 1).

Intravital imaging – tracking biological events *in vivo* within higher organisms

Dynamic visualization of biological processes in their natural environment is an important challenge for cell biologists. There is an obvious difference between the thickness of samples that are

[1]Microenvironmental Niche in Tumorigenesis and Targeted Therapy, Inserm U1109, MN3T, Strasbourg F-67200, France. [2]Université de Strasbourg, Strasbourg F-67000, France. [3]LabEx Medalis, Université de Strasbourg, Strasbourg, F-67000, France. [4]Fédération de Médecine Translationnelle de Strasbourg (FMTS), Strasbourg F-67000, France. [5]DON: Optique ultrarapide et nanophotonique, IPCMS UMR7504, Strasbourg 67000, France. [6]LabEx NIE, Université de Strasbourg, Strasbourg F-67000, France.
*These authors contributed equally to this work

‡Author for correspondence (jacky.goetz@inserm.fr)

J.G.G., 0000-0003-2842-8116

Journal of Cell Science • Advance article

1

Box 1. A snapshot of the available biophysical tools for assessing cellular forces

A Manipulating tools
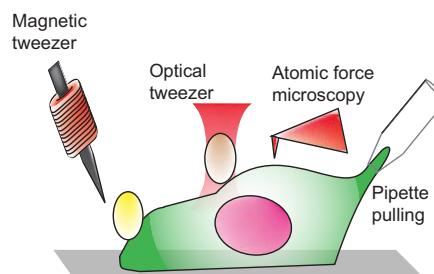
B Micropatterning tools
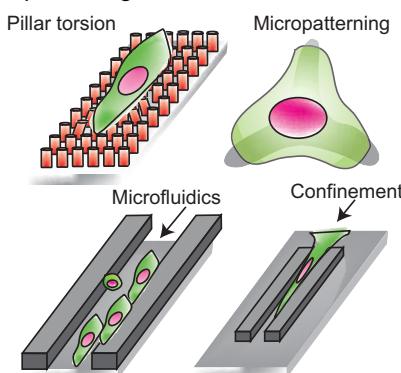
C Optical tweezers *in vivo*
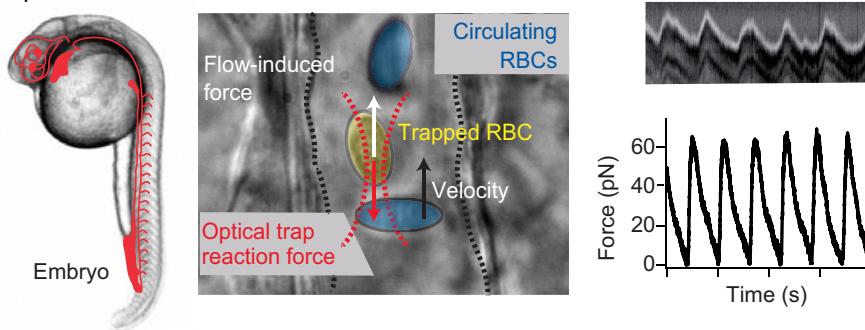
In addition to imaging cell behavior, a wide palette of biophysical tools is available to cell biologists when assessing and quantifying cellular mechanical forces. Whereas these tools are mostly suited for assessing forces *in vitro* (for theoretical background, see e.g. Neuman and Nagy, 2008; Kim et al., 2009; Ahmed et al., 2015) (panels A and B), some can be applied *in vivo* and to offer detailed quantification of forces in living animals (panel C). (A) Magnetic tweezers originate from the interaction of a magnetic bead fixed to the cell membrane with a magnetic field gradient (Tanase et al., 2007; Salerno et al., 2010). Historically used *in vitro* to measure mechanical properties at the single molecule (Graves et al., 2015; Strick et al., 1996) or at the single cell level (Collins et al., 2014; Marjoram et al., 2016), magnetic tweezers have recently shown their efficacy in measuring forces *in vivo* during embryonic development (Brunet et al., 2013; Desprat et al., 2008). Optical tweezers require a strongly focused laser beam that generates a 3D trap, which behaves as a spring (Ashkin, 1997). This optical technique has originally been used for *in vitro* measurement of viscoelastic properties of single molecules (Klajner et al., 2010; Smith et al., 1996) or single cells (Ashkin and Dziedzic, 1987; Ashkin et al., 1987; Dao et al., 2003). Recently, this technique has been applied *in vivo* for quantifying cell junction elasticity (Bambardekar et al., 2015; Sugimura et al., 2016) and proepicardial cell adhesion (Peralta et al., 2013), as well as for trapping circulating blood cells, thereby addressing haemodynamic forces in zebrafish (Anton et al., 2013) and mouse (Zhong et al., 2013). In atomic force microscopy (AFM), a cantilever is transiently brought in contact with the cell surface (Tartibi et al., 2015), cell nuclei (Lanzicher et al., 2015), or biological material such as cell-derived matrices (Tello et al., 2016). The analysis of its deflection over contact is linked to the exerted force and the mechanical response of the cell, which are mostly viscoelastic (Young modulus and viscosity). Even though this contact technique is mostly adapted to *in vitro* samples obtained either through cell culture (Kuznetsova et al., 2007; Ossola et al., 2015) or biopsies (Plodinec et al., 2012), AFM can be also used *in vivo*; for example, in mouse blood vessels (Mao et al., 2009). Micropipette pulling consists in locally aspirating the cell through a microforged pipette and in following the deformation for single cells (Guilak et al., 2000; Hochmuth, 2000; Chivukula et al., 2015) or for clusters of cells (Guevorkian et al., 2010, 2011). Traction force microscopy (Schwarz and Soiné, 2015) and pillar deformation (Khare et al., 2015) use calibrated soft substrates. Upon spreading, cells exert forces, which subsequently deform the substrate; these deformations inform about the localization and the amount of applied forces (Balaban et al., 2001; Gupta et al., 2015). (B) The development of improved micropatterning approaches allows the precise assessment of how surface topography influences the behavior of intracellular organelles or the cytoskeleton (Théry et al., 2006; Versaevel et al., 2012). The fast-evolving field of microfluidics has recently been used to assess how fluid forces (Perrault et al., 2015; Vartanian et al., 2008), mechanical confinement (Liu et al., 2015) or topological constrictions (Raab et al., 2016; Thiam et al., 2016) influence the behavior of cells. Measuring the migration time through confined 3D geometry provides information regarding cellular migration over topological constrictions (Thiam et al., 2016). Thus, when combined with imaging approaches, these biophysical tools offer a quantitative approach to the study of biomechanical events. (C) Optical tweezers can be applied *in vivo* on a zebrafish embryo. Focusing the laser spot in the vasculature allows the trapping of red blood cells (RBC). Pulsatility of the blood flow is visible upon kymographic analysis of the RBC displacement in the trap. This displacement is proportional to the drag force that RBCs are subjected to.

mounted on glass slides *in vitro* and whole living organisms. Here, intravital imaging refers to *in vivo* imaging within higher organisms, such as rats and mice. However, similar technologies can be used for imaging embryos and, thereby, can exploit the advantages provided by nonlinear microscopy (see below). The main drawback of conventional widefield microscopy applied to voluminous samples

is that it is impossible to provide clear and sharp images. Indeed, imaging quality within the focal plane is highly perturbed by out-of-plane scattered light. To circumvent this problem, Marvin Minsky developed – already more than fifty years ago – the first prototype of a confocal scanning microscope (Minsky, 1961). Modern confocal microscopes work on the principle of point scanning, whereby the

Table 1. Pros and cons of current imaging technologies

	1/2PEM	LSFM	Super Resolution	CLEM
Sample type	Fixed and/or live single cells up to higher organisms (mouse, rat)	Fixed and/or live single cells to embryos (ZF, fly, etc.)	Fixed and/or live single cells to embryos (ZF, fly, etc.)	Live to fixed sample Single cells to higher organisms (mouse, rat)
Resolution	200–2 nm			
	Cellular to subcellular	Cellular to subcellular	Subcellular to single molecule	nanometer
Speed	High	High to very high	Low	Very low
Penetration	Very high when using 2PEM	High	Low	Limited by light microscopy
Data volume	Small	Large	Large for PALM/STORM Small for SIM and STED	Large
Technical difficulty	Animal handling under the microscope	Data acquisition and processing	Data processing for PALM/STORM and SIM	Finding the ROI again between imaging modalities, time-consuming
Main advantage	Most-established method, easy, versatile	Best compromise between resolution and speed ratio	Best localization (sub-diffraction limited)	Best overall resolution when combined with electron tomography
Specific feature	**1PEM:** Better resolution compared to widefield microscopy	Long-term 3D imaging with high-speed or high 3D resolution	**STED:** Increased resolution for any 1PEM and 2PEM sample compatible with confocal imaging	Compatible with any *in vivo* model
	2PEM: In-depth long-term imaging of mice, fluorescent imaging and label-free imaging	**SPIM:** Multiview imaging increases 3D acquisition speed	**SIM:** Fast 2D and 3D sub-diffraction imaging	Requires manpower Requires access to sophisticated EM technologies for 3DEM
		DSLM: More suitable for super-resolution technologies	**PALM/STORM:** single-molecule resolution, single-particle tracking	
Biological application	Cancer biology, developmental biology, neurosciences, stem cell biology	Cell biology, developmental biology, neurosciences	Cell biology, developmental biology, neurosciences, biophysics	Cancer biology, developmental biology, neurosciences, stem cell biology
Commerciallly available	Yes	Yes	Yes	No (*in vivo*), Yes (*in vitro*)

1PEM, one-photon excitation microscopy; 2PEM, two-photon excitation microscopy; 3DEM, 3-dimension electron microscopy; CLEM, correlative light and electron microscopy; DSLM, digitally scanned light-sheet microscopy; LSFM, light-sheet fluorescence microscopy; PALM, photo-activated localization microscopy; ROI, region of interest; SIM, structured illumination microscopy; SPIM, single plane illumination microscopy; STED, stimulated emission depletion; STORM, stochastic optical reconstruction microscopy; ZF, zebrafish.

sample is scanned by a laser spot, i.e. confocal laser scanning microscopy (CLSM) (Fig. 1A). The emitted light from the focal plane is selected through a pinhole and optically conjugated with the focal plane before being detected on sensitive photodetectors. Although this technology has provided a tremendous amount of biological insights, it was limited by its acquisition speed, which was not sufficiently fast to capture dynamic subcellular events. Acquisition speed has recently been improved by the coupled development of resonant scanners and sensitive detectors. Accelerated acquisition regimes can also be achieved by using spinning disk confocal microscopy (SDCM). Instead of scanning the sample point-by-point, SDCM is capable of acquiring multiple points at the same time (Fig. 1A), on a charge-coupled device (CCD) camera, thus increasing the data acquisition rate. The main drawback of SDCM is the cross-talk between pinholes; this can be circumvented by increasing the inter-pinhole distance or by decreasing the out-of-focus light by using two-photon excitation

(Shimozawa et al., 2013). Both CLSM and SDCM have been ground-breaking for imaging *in vitro* as well as *in vivo*; for instance, relatively thin model systems (Fig. 1C), such as tissue explants and organoids, or small organisms, such as *Caenoerhabditis elegans* (Nguyen et al., 2016) or zebrafish embryos (Kissa and Herbomel, 2010). Recent advances in CLSM have led to the development of the so-called Airyscan concept (Zeiss), whose detector array allows to efficiently collect the photons from the entire Airy diffraction image with confocal resolution owing to the intrinsic size of each detector. Thus, when coupled to ultra-sensitive detectors, Airyscan exploits an increase in photon yield to improve sensitivity, speed or resolution (http://blogs.zeiss.com/microscopy/news/en/zeiss-lsm-880-airyscan-introducing-fast-acquisition-mode/).

CLSM has been successfully used for imaging microcirculation in the rat brain (Villringer et al., 1994) and astrocytes in the mouse brain (Pérez-Alvarez et al., 2013). SDCM has been used to describe the recruitment of platelets in several mouse organs, including brain,
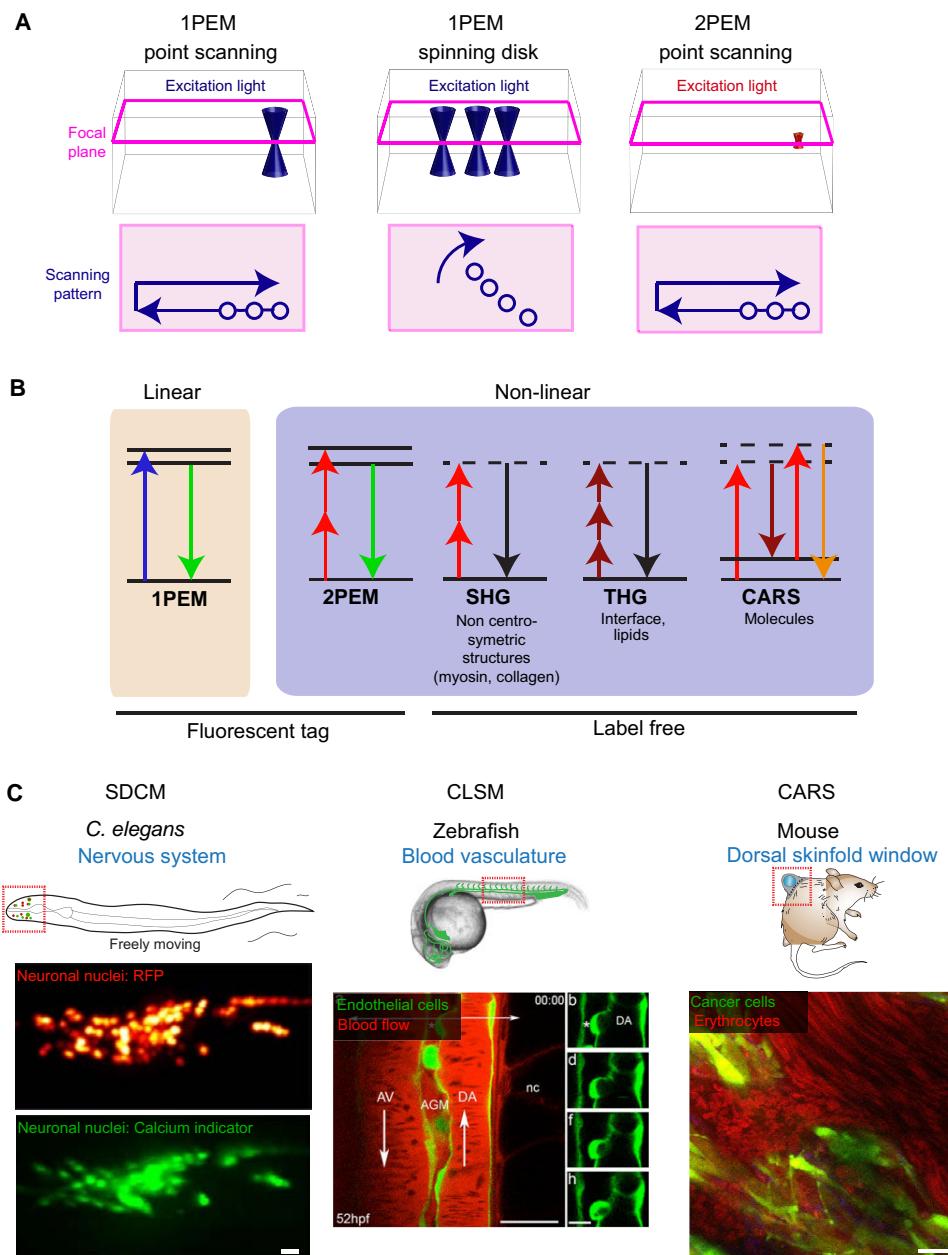
Fig. 1. Technical considerations and biological applications of intravital imaging. (A) Comparison between one-photon excitation microscopy (1PEM) and two-photon excitation microscopy (2PEM). In 1PEM, the excitation light illuminates the focus (pink line) and out-of-focus planes, and a pinhole is needed to eliminate the signal originating from the out-of-focus planes. In 2PEM, excitation occurs only at the focus plane (pink line) and a pinhole is not required because the excitation is already confocal. As shown in the illustrations at the bottom, 1PEM and 2PEM point scanning create the image of the sample by imaging one point at a time, whereas the spinning disk performs multiple acquisitions simultaneously. (B) Jablonski diagram of linear and nonlinear processes. 1PEM: the molecule is excited by absorbing a photon; after internal conversion the molecule returns to its ground state and emits a red-shifted photon. 2PEM: the molecule is excited by absorbing two photons at the same time; it returns to the ground state by emitting one photon of energy that is higher than that of the excitation photons. Second harmonic generation (SHG): two photons are scattered by a molecule and emit one photon of half the excitation wavelength. Third harmonic generation (THG): three photons are scattered by a molecule and produce one photon of a third of the excitation wavelength. Coherent anti-stokes Raman spectrocopy (CARS): a pump photon (first red arrow, pointing up) excites the molecule to a virtual state before a second photon (referred to as Stokes photon; brown arrow pointing down), forces the de-excitation of the molecule to above ground state. A third photon from the pump beam (second red arrow, pointing up) is used to elevate the molecule to a new virtual state, from which it will relax and emit a blue-shifted photon (orange arrow pointing down). (C) Biological applications of linear and nonlinear microscopy processes. Left: spinning disk confocal microscopy (SDCM) is used for ultra-fast neuronal calcium imaging in a freely moving *C. elegans*. (Red: neuronal nuclei; green: the protein calcium sensor GCaMP6s). Scale bar:10 μm. Adapted with permission from Nguyen et al., 2016. Middle: confocal laser scanning microscope (CLSM) used for long-term (>70 h) time-lapse imaging of zebrafish vasculature, highlighting the emergence of a hematopoietic stem cell in the ventral wall of the dorsal aorta (green). Scale bars: 25 μm (left panel), 10 μm (right panel). Adapted with permission from Kissa and Herbomel, 2010. Right: multimodal nonlinear microscopy used to study tumor mass and vascularization within a skinfold dorsal chamber in mouse. Red, erythrocytes imaged by using CARS; green, cancer cells imaged by using 2PEM. Scale bar: 15 μm. Adapted with permission from Lee et al., 2015.

liver and cremaster muscle (Jenne et al., 2011). Nevertheless, most of the visible light is absorbed (Boulnois, 1986) and scattered by tissues, thus limiting depth in intravital confocal microscopy to the organ surface of an animal (<100 µm in thickness) (Masedunskas et al., 2012; see also Fig. 1C). In order to be able to image relevant biological events deeper in tissues, researchers took advantage of the optical transparency of the tissues in the near-infrared or infrared wavelengths (Boulnois, 1986) and of the discovery of pulsed lasers to develop two-photon microscopy (Helmchen and Denk, 2005), thereby making it possible to image deeper into the tissues of living animals.

Multiphoton microscopy for imaging *in vivo*

The principle of two-photon absorption was originally described in 1931 (Göppert-Mayer, 1931) but it took until 1963 for the first pulsed laser to be developed (Peticolas et al., 1963); later on, this turned into the first two-photon laser scanning microscope (Denk et al., 1990). In classic CLSM, the energy carried by a single laser photon allows the excitation of fluorophores, whereas in two-photon excitation microscopy (2PEM), each photon carries half the energy and, thus, the excitation requires the simultaneous absorption of two photons (Fig. 1B). For this purpose, the photon density has to be high, both in time (femtosecond laser pulses) and in space (through the usage of lenses with high numerical aperture). Compared to classic CLSM, 2PEM can achieve non-invasive, deep imaging in voluminous live samples owing to several properties. First, the nonlinear properties of the multiphoton absorption confine the excitation to a small volume (Fig. 1A), resulting in an enhanced signal-to-background-noise ratio and a lesser phototoxicity (Helmchen and Denk, 2005). Second, infrared light is less-well absorbed and scattered by biological tissues, and allows deeper imaging than when regular one-photon excitation (1PE) microscopy (hereafter referred to as 1PEM) is applied. Because the excitation is limited to the focal plane, the photo-toxicity typically induced by 1PEM is drastically reduced. Pinholes are not required in two-photon excitation (2PE) microscopy (hereafter referred to as 2PEM), which makes it possible to use non-descanned detectors that can be placed closer to the sample, thereby enhancing the signal. Together, these advantages allow imaging of biological phenomena that take place deep within a living organism. For example, 2PEM can easily image through the skin of living mice, and has been used for tracking xenografted cancer cells and their immune responses in mouse ear skin (Li et al., 2012), and for tracking features of muscle diseases in neuromuscular junctions (Mercier et al., 2016). Skin pigmentation can be – owing to light absorption – a major barrier in optimized imaging, and imaging windows have been developed for rodents to reach the deeper organs. This technique has been particularly useful in cancer biology for the imaging of subcutaneous tumors (using the dorsal skin-fold chamber), lungs (Headley et al., 2016), brain (Kienast et al., 2010) and abdominal organs, such as the intestine (Ritsma et al., 2014) or the liver (Ritsma et al., 2012), as well as mammary tumors (Zomer et al., 2015). Although regular 2PEM allows penetration of up to 1 mm into tissues (Theer et al., 2003), improved imaging depths through scattering tissues (the heterogeneity of biological tissues leads to photon absorption and re-direction, without any loss in energy, that can create imaging artifacts) can be obtained by increasing the wavelength of excitation to >1000 nm with optical parametric oscillators (Kobat et al., 2011). Furthermore, the use of powerful pulsed femtosecond lasers opened the door to nonlinear microscopy, which has the unique ability to provide endogenous signals from living non-labeled scattering tissues (discussed below).

Label-free intravital imaging

The most-commonly used techniques to perform intravital imaging require the presence of fluorescently labeled molecules and, therefore, do not allow the imaging of endogenous non-labeled structures and their physiological environment. Below, we discuss several nonlinear microcopy methods that exploit the physical and optical properties of molecules, as well as advanced optics, for the imaging of non-labeled material within living tissues.

Second harmonic generation microscopy (SHG) (Fig. 1B) is the most popular nonlinear imaging technique and has first been described in 1963 (Franken et al., 1961). SHG allows to visualize endogenous, non-centrosymmetric molecules, such as collagen and myosin, which upon light scattering produce a photon at half the incident wavelength. SHG has been proven to be a highly useful technology for the non-invasive intravital imaging of the collagen-rich microenvironment during tumor invasion (Wang et al., 2002), of muscle defects in the mouse ear (Mercier et al., 2016) and of zebrafish embryos (Ramspacher et al., 2015). Furthermore, nanoparticles generating second harmonics have been used *in vivo* and represent new imaging tools (Grange et al., 2011; Pantazis et al., 2010).

Third harmonic generation (THG) microscopy (Fig. 1B) is a non-linear scattering process that originates from the polarization properties of the excited volume and from variations of the refraction index in that volume, such as in water–lipid and water–protein interfaces found, for instance, in cellular membranes and extracellular matrix structures (Weigelin et al., 2016). THG is mostly used in tumor biology to visualize ECM structures (Alexander et al., 2013) but has also been used to image lipid bodies in *Drosophila melanogaster* embryos (Débarre et al., 2006). Another label-free imaging approach relies on the Raman effect (also known as Raman scattering), i.e. the inelastic scattering of a photon upon interaction with matter, which has first been described in 1928 by Raman and Krishnan, 1928. Coherent anti-Stokes Raman scattering (CARS) microscopy detects structures by simultaneously illuminating a sample with a pump and a Stokes beam, upon which a pump and a Stokes photon match the energy of the excited vibrational state of a molecule within the sample. A second pump photon is used to elevate the molecule to another virtual state before relaxation of the molecule causes an emission of photons (anti-Stokes emission) that is shifted into the blue spectrum (Fig. 1B). Intravital CARS microscopy has been applied to *C. elegans* to examine the impact of genetic variations in metabolic pathways on lipid storage (Hellerer et al., 2007) (Fig. 1C). One of the great advantages of using nonlinear microscopy *in vivo* is the possibility of combining fluorescent signals with information obtained from endogenous, unlabeled structures. For example, SHG and CARS have been combined with 2PEM in the imaging of tumors within dorsal skin-fold chambers, and have provided access to tissue structures (SHG), cancer cell behavior (2PEM) and blood flow measurement (CARS) *in vivo* (Lee et al., 2015).

Yet, although the field of intravital imaging in higher organisms has expanded tremendously in the past few years, this approach, nevertheless, suffers from drawbacks associated with light absorption and scattering that impair its use for high-resolution imaging of subcellular events of interest. These limitations can be circumvented by using the CLEM approaches we discuss in the last section of this review. However, imaging of less voluminous samples or organisms can be performed with several approaches described in the following sections.

5

Light-sheet fluorescence microscopy (LSFM)

An important concern in modern cell biology is the ability to perform observations over long periods of time to follow, for example, processes during embryonic development. This can now be achieved by using light-sheet fluorescence microscopy (LSFM). LSFM was originally developed to overcome the resolution limitations of conventional fluorescence microscopy, in which the resolution is diffraction limited, with the axial resolution being about twice that of the lateral resolution. LSFM is an optical imaging technique, initially based on a plane excitation that is obtained by focusing a laser beam through a cylindrical lens, while the detection is performed in an orthogonal plane (Reynaud et al., 2008). This optical geometry retains the same diffraction resolution limitation in the detection plane but offers the same resolution in the excitation axis. Nowadays, complementary metal oxide semiconductor (cMOS) cameras are used to ensure a detection of the entire field at high speed and high resolution, way beyond the detection obtained with scanning technologies. Thus, owing to a reduced acquisition time as well as the simultaneous and selective illumination of the detection plane, LSFM significantly decreases the phototoxicity and photobleaching compared to classic confocal microscopy (Keller and Ahrens, 2015; Lim et al., 2014; Pampaloni et al., 2015; Weber and Huisken, 2011); it is therefore highly useful in imaging dynamic events that take place in small and transparent organisms and embryos. In this section, we briefly focus on the two main technological strategies that have been developed to achieve this specific illumination, single plane illumination microscopy (SPIM) and digitally scanned light-sheet microscopy (DSLM). We also provide a snapshot of their current use by describing some of the biological insights that LSFM have made possible.

Single plane illumination microscopy (SPIM)

Single plane illumination microscopy (SPIM) is the first version of LSFM; here, a cylindrical lens focusing light orthogonally to the observation plane creates the light sheet (Fig. 2A). This technology is suitable for imaging of entire animals and was highlighted already in 2004 as a means to image deep inside living zebrafish and *Drosophila* embryos. Indeed, LSFM turned out to be highly efficient in following morphogenetic events for several hours at high resolution, high speed and without photo-damaging the embryos (Huisken et al., 2004). LSFM has since continuously evolved, resulting in the development of optical systems that use several illumination and detection paths, such as multiview (MuVi)-SPIM (Krzic et al., 2012) or SimView SPIM (Tomer et al., 2012). These techniques are based on a dual light-sheet system that can switch between four different light pathways in less than 50 ms. This setup allows the acquisition of four, nearly simultaneous images from different regions in the sample (scanned in one dimension by using a piezo stage), thus making it possible to image a large-volume sample for instance a *Drosophila* embryo in 35 s (Tomer et al., 2012) (Fig. 2B). Alternatively, if the acquisition rate is not limiting, LSFM can be coupled to a sample holder mounted on a rotational stage (Jakob et al., 2016).

The potential of SPIM for high-speed *in vivo* imaging has been elegantly demonstrated for the developing Zebrafish heart – this being a very challenging task owing to its small size (250 μm) and its high beat frequency of 2–4 Hz (Mickoleit et al., 2014). Subsequently, multi-view SPIM strategy (named here 'IsoView') was successfully used to study the development of the *Drosophila* embryo and the brain of Zebrafish larvae, with an unprecedented spatio-temporal resolution (Fig. 2C). Here, the authors compared

their setup with lattice light-sheet microscopy (see below) to emphasize the superior imaging depth and acquisition speed their particular approach can afford (Chhetri et al., 2015). In addition, SPIM has been combined with laser ablation (optical damaging of cells or intracellular region by using a powerful and focused laser) to unravel mechanical coupling of two important morphogenetic events in *Drosophila*: endoderm invagination and axis extension (Lye et al., 2015). In addition, several groups have implemented SPIM to accelerate commonly performed imaging. For example, MuVi-SPIM together with a customized software package can be used to increase acquisition speed and analysis by several orders of magnitude, which allows to – almost instantaneously – record individual cell shapes over an entire embryo (Stegmaier et al., 2016).

Digitally scanned light-sheet microscopy (DSLM)

In DSLM, the illumination plane is obtained by deflecting the beam with a galvanometric mirror through the excitation objective (Fig. 2D). Here, 3D volumes are obtained by 2D scanning methods. This method was pioneered by the Stelzer group in 2008 and has been applied for imaging the early stages of development of zebrafish embryos (Keller et al., 2008). In this study, the authors successfully reconstructed in 3D the collective migration patterns of several cell type precursors during gastrulation with an unprecedented temporal and x/y resolution. When combined with Bessel beams and/or multiphoton illumination, an increase in spatial resolution can be obtained. Bessel beam illumination is an alternative method to the typical Gaussian beam illumination and consists of feeding back the focal plane of the excitation objective with an annular illumination (Planchon et al., 2011). However, Bessel illumination creates side lobes (i.e. lateral intensity peaks) in the illumination plane, which impair reaching the desired resolution. Therefore, in addition to the Bessel illumination, it is currently possible to use diffractive optics that generate a structured illumination convoluted to the Bessel beam (Gustafsson et al., 2008); this allows image acquisition below the diffraction limit (Gao et al., 2012). Moreover, this setup strongly benefits from a two-photon illumination with associated increased penetration and decreased photobleaching and/or phototoxicity (Truong et al., 2011); this drastically reduces the risk of adversely affecting the physiology of the event studied (Ahrens et al., 2013; Wolf et al., 2015). A recent, but main update in this field was provided by the group of Eric Betzig with the demonstration of the lattice light-sheet microscopy (Chen et al., 2014) as an improvement of Bessel beam LSFM. In this setup, a fast-switching, spatial light modulator is used to generate the Bessel beam mask before it enters in the excitation objective. This permits a tremendous gain of speed at a resolution that is equivalent to that obtained with SIM (Chen et al., 2014; see below). More recently, by using the same strategy of coupling super-resolution and LSFM, lattice light-sheet–point accumulation for imaging of nanoscale topography (PAINT) microscopy has been introduced (Fig. 2E). Although image acquisition may take several days, this technique makes it possible to extend the 3D visualization of single-molecule localizations in thicker and more voluminous samples, such as in dividing cells (Legant et al., 2016).

At the moment, there are only few examples for biological applications of the latest versions of DSLM. For example, lattice light-sheet microscopy has been used to study the microtubule organization during HeLa cell division *in vitro* (Yamashita et al., 2015). Owing to the superior temporal and spatial resolution that can be achieved (below the diffraction limit and with a time interval of <1 s), the authors provided new insights into the growth
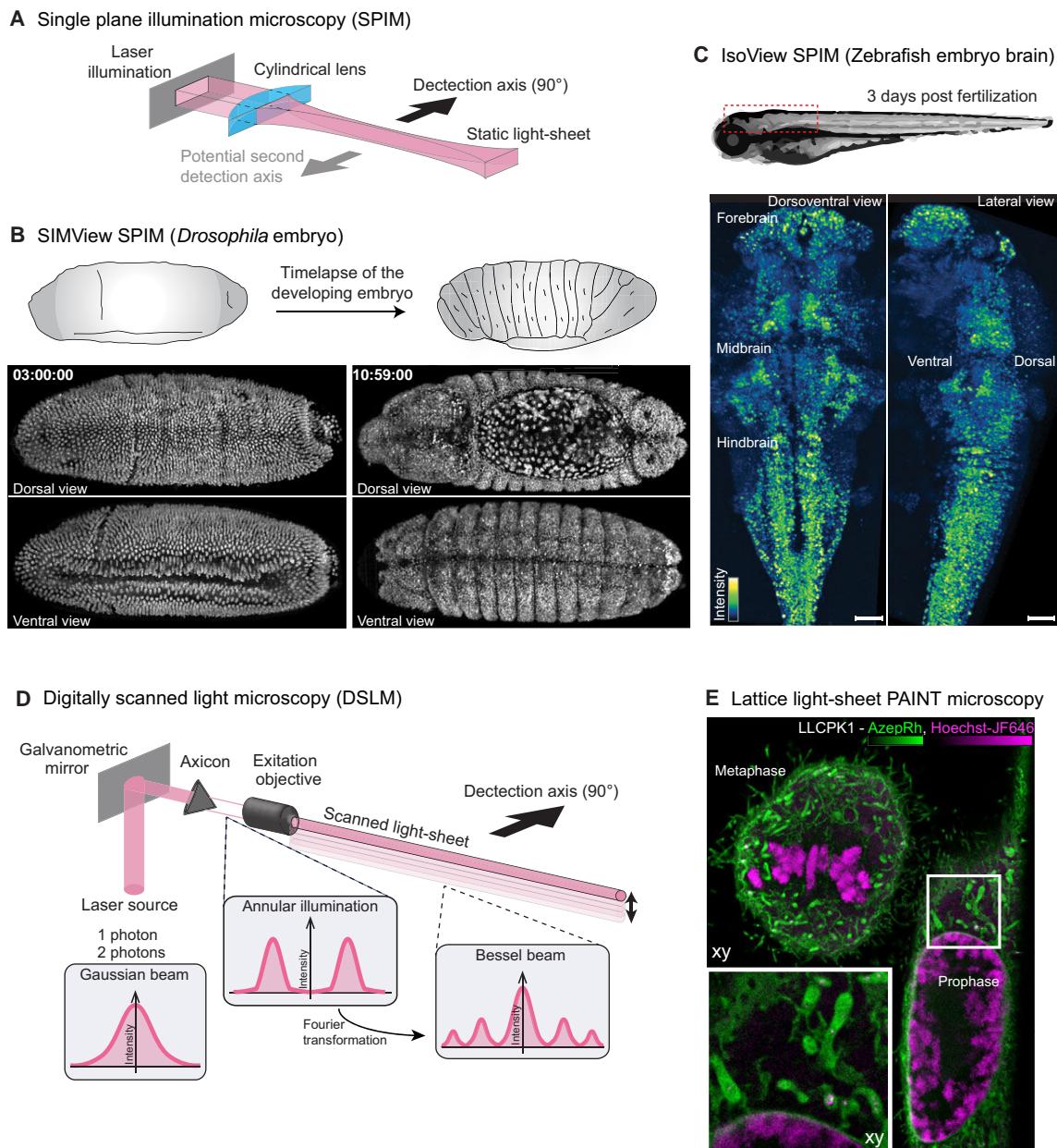
Fig. 2. Light-sheet microscopy and examples of biological applications. (A) Optics setup for SPIM. A cylindrical lens induces the formation of the light-sheet that can be scanned in 1D for volumetric imaging. Arrows indicate the detection axes (black arrow, usual 90° detection axis; gray arrow, potential second objective position for multiview SPIM). (B) SIMView SPIM imaging of nuclei during the development of *Drosophila* embryo, illustrating the possibility to carry out long-term image acquisition without photo-damage or photobleaching; adapted with permission from Tomer et al., 2012. (C) IsoView SPIM of zebrafish embryo brain (using a nuclear GCaMP6 Ca²⁺ probe), illustrating the power of this technique to record volumetric data *in vivo* at high speed and high resolution. Scale bars: 50 μm. Adapted with permission from Chhetri et al., 2015. (D) Illustration of the optical setup for Bessel beam digitally scanned light miscroscopy (DSLM), for which the beam is scanned in 2D for imaging in three dimensions. Laser source can be either one or two photons. The insets show the evolution of the laser intensity profile (Gaussian beam) through the axicon (a type of lens with a conical surface), leading to annular illumination, as well as the beam profile after being focused through the excitation objective. The Bessel profile is created at that step. (E) Imaging of dividing porcine kidney cells by using PAINT DSLM. DNA is labeled with Hoechst-JF₆₄₆, intracellular membranes are labeled with AzepRh. At cost of acquisition speed and a complex post-processing procedure, this technology allows so-far-unprecedented 3D resolution of a wide field of view. Adapted with permission from Legant et al., 2016.

mechanisms of microtubules. In addition, by imaging living zebrafish embryos with LSFM, the interaction between Schwann cells and axons during neuron damage repair was observed *in vivo* (Xiao et al., 2015). More recently, two-photon Bessel beam light-sheet microscopy was optimized to study how cells maintained in a 3D culture mechanically react to changes in their microenvironment, at a subcellular level and without spatial constraint (Welf et al., 2016). Taken together, these recent studies demonstrate that LFSM is a particularly promising tool for studying mechano- and cell biology.

Requirements for LSFM

It is important to emphasize here that LSFM is extremely demanding with regard to computing resources owing to the large datasets that need to be handled. Image acquisition generates hundreds of gigabytes that need to be stored quickly. Thereafter, post-processing and reconstructions in three dimensions require enormous computer resources. These computing demands need to be consciously addressed in the future to ensure LSFM is amenable to cell biologists. In addition, only few commercial systems that are available for the wider scientific community currently exist for LSFM. This is mainly due to the fact that optical setups are typically designed and mounted in order to address a specific biological question of interest.

Taken together, there is, however, no doubt that LSFM will be used more widely in the coming decade. Thanks to its versatility, it offers multiple advances over other imaging approaches, such as increased spatio-temporal resolution with significantly reduced phototoxicity and/or photobleaching at all scales (Fig. 2B,C and E; Table 1), from *in toto* imaging of small animals with SPIM, to studying subcellular compartments in detail with DSLM.

Super-resolution microscopy – digging below the light-diffraction

Fluorescence microscopy has become one of the most useful tools for cell biologists owing to its non-invasive properties and high versatility. The past decades have witnessed significant technological improvements of microscopy setups regarding sensitivity and acquisition speed, as well as the development of brighter and more photostable fluorescent probes. These developments shifted fluorescence microscopy – which was mainly used for descriptive purposes – towards a more quantitative approach, in which the careful analysis of the large datasets allowed the deciphering of complex cellular processes at the biological and physical level. However, conventional fluorescence imaging is limited by light diffraction to a resolution (i.e. the minimal distance at which two physically distinct objects will appear as separated) of ∼200 nm in the x/y plane (lateral resolution) and ∼600 nm along the z axis (axial resolution), which is several orders of magnitude above the size of single proteins. Thus, reaching a resolution of a few tens of nanometers had been a main quest for microscopy optics experts and imaging computer scientists, and ultimately led to the 2014 Nobel Prize being awarded to Eric Betzig, Stefan Hell and William Moerner for their essential contributions in the development of super-resolution microscopy or nanoscopy. Furthermore, since 2007 the introduction of commercially available systems has granted the cell biology community access to these new tools, opening the door to a new era of cellular and sub-cellular imaging. Because subcellular and biomechanical processes are fast, dynamic and reversible in nature, they require fast imaging techniques to be monitored (Eyckmans et al., 2011; Hoffman et al., 2011; Janmey and Miller, 2011). Thus, we will introduce here nanoscopy approaches that can be used to study subcellular and biomechanical mechanisms by describing selected examples.

Stimulated emission depletion (STED) microscopy

An important quest for cell biologists is to have access to live and high-resolution imaging of their favorite fluorescent proteins or molecules. This can now be performed by using stimulated emission depletion (STED), which facilitates, for example, live intracellular vesicular trafficking in multiple situations. STED microscopy works on the basis of a scanning confocal microscope, where resolution is improved by using a doughnut-shaped depletion beam that is shifted into the red-light spectrum, which 'wraps' the excitation beam (Fig. 3A). In this configuration, fluorophores illuminated by the depletion beam are forced to return to ground state and emit at depletion wavelength, which is filtered out, while the 'nondepleted' fluorophores at the center, emit normally. This optical trick result in a smaller emission volume and increases the lateral resolution to 20-70 nm (Klar et al., 2000; Willig et al., 2007). When live imaging is desired, speed acquisition may be reduced by relying on higher laser output. However, increased laser power will ultimately lead to increased phototoxicity. The use of continuous wave (CW) beams and time-gated detection allows the effective use of reduced laser powers and efficient increased resolution, thereby making gated CW STED compatible with live imaging (Willig et al., 2007; Westphal et al., 2008; Vicidomini et al., 2011).

STED was effectively used to monitor vesicular trafficking in real-time in living cultured neurons (Westphal et al., 2008), image GFP-labeled neurons in *Caenorhabditis elegans* (Rankin et al., 2011) and, more recently, follow the trafficking of EGFP-labeled vesicles in living neurons in *Drosophila* larvae with a rate above 100 frames per second (Schneider et al., 2015). These examples suggest that STED microscopy is well suited to image fast and dynamic processes in small transparent organisms, such as *C. elegans*, *Drosophila melanogaster* or zebrafish embryos. However, when considering higher organisms, conventional lasers are not able to perform intravital imaging, and confocal microscopes must be coupled to selective plane illumination microscopy (SPIM) or multiphoton excitation (discussed above). For instance, a combination of STED and SPIM was used to image >100 µm deep into the tissues of entire zebrafish embryos, resulting in a 40–250% improvement of resolution (Friedrich et al., 2011; Scheul et al., 2014; Friedrich and Harms, 2015). Axial resolution, which is often a limiting factor when using light-sheet illumination, has recently been significantly improved with reversible saturable or switchable optical linear fluorescence transitions (RESOLFT) nanoscopy and, thus, offers access to high-speed imaging with lowered laser power (Hoyer et al., 2016). 2PE lasers have a better penetrance into the tissue (<1 mm) and reduced photo-damaging, and the resulting laser spot is spread less along the z axis, thus providing a better axial resolution (Denk et al., 1990; Helmchen and Denk, 2005). 2PE-STED allowed, for example, to monitor, in real-time, the dynamics of neurons within the brain of living mice through a cranial window (Fig. 3D) to a depth of 15–90 µm and with a resolution of ∼40–90 nm (Berning et al., 2012; Takasaki et al., 2013; Willig et al., 2014; Coto Hernández et al., 2016). The major technical challenge is based on the fact that efficient STED requires a perfect alignment of the excitation and depletion beams. However, as tissues are not homogenous, imaging of deeper layers unavoidably decreases resolution (Takasaki et al., 2013).

Structured illumination microscopy (SIM)

Although image reconstruction remains very complex and artifact-prone, structured illumination microscopy (SIM) is the simplest of the super-resolution techniques. It works in the basis of a wide-field microscope into which a grating pattern is inserted into the light path. By generating interferences (i.e. *Moiré* fringes), SIM provides access to spatial information regarding the fluorescence signal. The pattern is rotated at predefined angles, and several images are acquired, usually nine to 15 (Fig. 3B). The spatial information revealed by each frame is then computed to reconstruct a sub-diffraction image, which allows to double the resolution compared
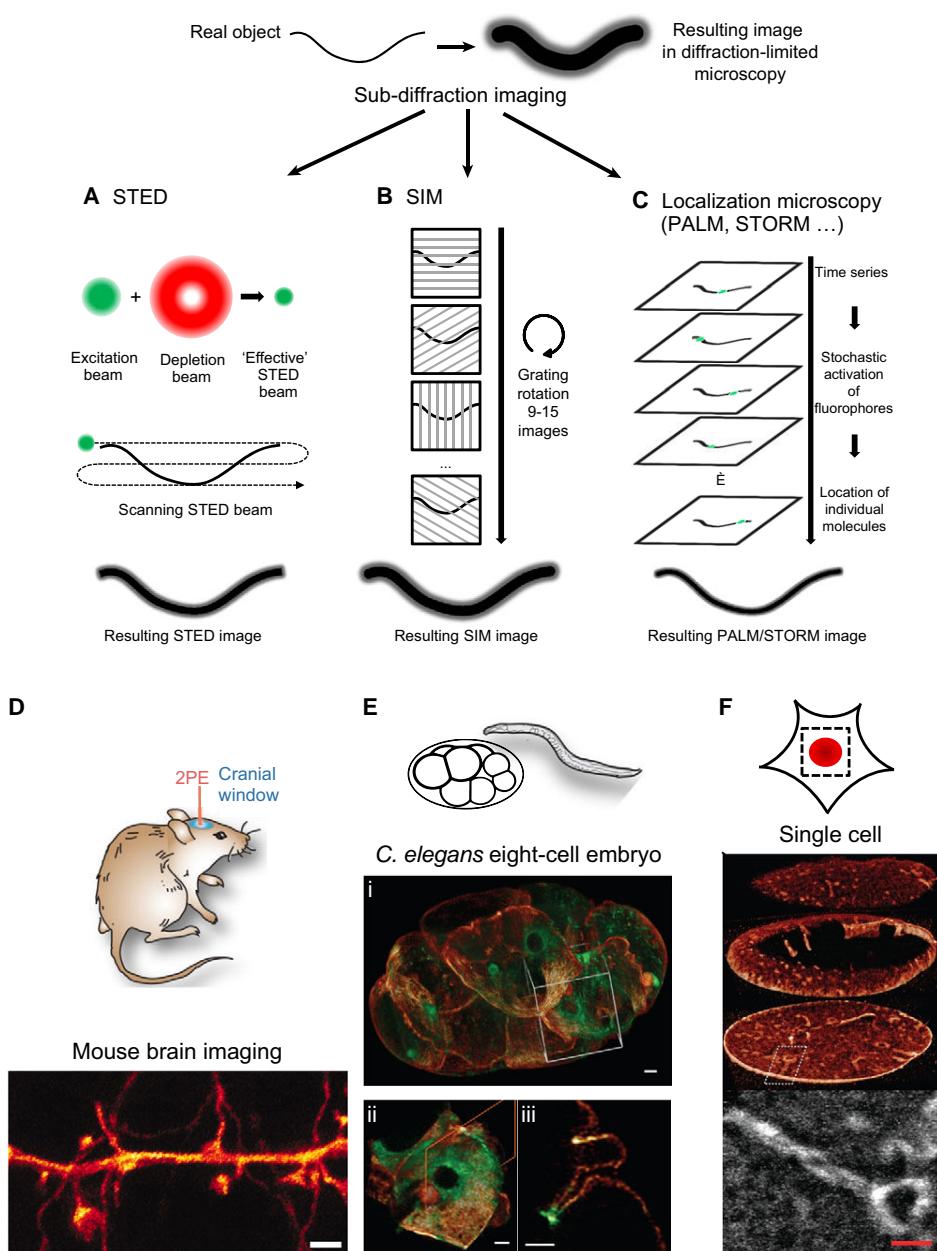
Fig. 3. Super-resolution microscopy and its biological applications. (A) Stimulated emission depletion (STED) microscopy is achieved on the basis of a line-scanning confocal microscope, in which the resolution is increased by using a second red-shifted depletion beam that 'depletes' unwanted activated fluorophores at the edges of the diffracted excitation beam. This results in a detection size in the focal plane reduced to the tens of nanometers. (B) Structured illumination microscopy (SIM) microscopy is a widefield microscopy technique. Here, increased resolution is achieved by introducing a diffraction grating in the optical path. The grating is then turned to selected angles and the sub-diffraction image is reconstructed from all the images acquired (typically 9 to 15). (C) Localization microscopy techniques, such as PALM and STORM, achieve high resolution by excitation of stochastic fluorophores coupled with computer-assisted high-precision localization of individual molecules. (D) Direct STED imaging of live mouse brain through an observation window at a depth of 10–15 μm. 2PE, two-photon excitation. Adapted with permission from Berning et al., 2012. Scale bar: 1 μm. (E) *C. elegans* eight-cell embryo expressing GFP-myosin and mCherry-membrane marker. (i) Live image using SIM combined with Bessel beam illumination. (ii) Cropped view from the 3D section in i. (iii) Single-plane view corresponding to the orange plane in ii, showing a cytokinetic ring. Adapted with permission from Gao et al., 2012. Scale bar: 2 μm. (F) 3D rendering of the nuclear envelope of U2OS cell expressing Dendra2–LaminA excited with dithered lattice light-sheet illumination and acquired with 3D PALM (top). Super-resolution maximum-intensity projection of the boxed area (bottom). Adapted with permission from Chen et al., 2014. Scale bar: 1 μm.

to conventional microscopy (Gustafsson, 2000). Alternatively, to protect living samples from excessive light exposure, the nonlinearity of photo-convertible fluorescent proteins can be used with SIM to achieve a similar resolution (Rego et al., 2012; Li et al., 2015). Furthermore, by engineering the grating to create three coherent beams, which form an illumination pattern varying laterally and axially or by using multifocal illumination patterns, the resolution can also be improved by a factor of two in all directions (Gustafsson et al., 2008; York et al., 2012).

Since SIM works on the basis of wide-field imaging and thus requires only a few planes to reconstruct a sub-diffraction image, it is probably the best-suited live-imaging approach to monitor dynamic events at subcellular level. However, one should keep in mind that resolving structures of <50–100 nm in size remains a difficult task. Nevertheless, SIM was successfully used to monitor

the dynamics of subcellular structures and organelles, such as mitochondria, clathrin-coated vesicles, microtubules and actin cytoskeleton in living cells, both in 2D and 3D at a speed of up to 11 frames per second (Fiolka et al., 2012; Kner et al., 2009; Shao et al., 2011). More recently, up to 200 frames were obtained in <0.5 s by using total internal reflexion fluorescence (TIRF) with a high numerical aperture objective in order to limit out-of-focus excitation and to increase the axial resolution on the basal side of the sample (Li et al., 2015). The use of cMOS cameras, which are faster than regular electron multiplying CCD (EMCCD) cameras, helps to further improve the number of frames acquired per second and allows the 3D recording of the entire volume of a single cell in culture within ~1 s (Fiolka et al., 2012). Recently, 3D-SIM has been combined with lattice light-sheet illumination and achieved a similar rate of acquisition with less invasive light exposure (Li et al.,

2015). Furthermore, the combination of SIM and Bessel beam plane illumination was used to image the development of a *C. elegans* embryo (Fig. 3E), and the chromosomal rearrangement in a *Drosophila* syncytium with a three- to fivefold increase in resolution and an image acquisition speed that captured the total volume of the embryo within 1 s (Gao et al., 2012). Furthermore, multifocal plane illumination SIM was used to image the dynamics of the endoplasmic reticulum in cultured cells at 100 frames per second, or of the blood flow in zebrafish at 37 frames per second (York et al., 2013).

Localization microscopy

Localization microscopy encompasses a family of techniques that allows the precise localization of fluorophores at single-molecule level; here, the precision directly reflects the number of photons emitted by a single source. The sub-diffraction image is then reconstructed from the localizations obtained for the single fluorophores. These techniques rely on the possibility to excite only a few fluorophores within the image plane, rather than all of them; this makes it possible to differentiate between fluorophores, whose distance is below the diffraction limit. This is achieved by photo-manipulation of fluorophores, i.e. by turning them on or off (Fig. 3C). In photo-activated localization microscopy (PALM), photo-manipulation is mediated by using photo-activatable fluorescent proteins (Betzig et al., 2006; Hess et al., 2006), whereas stochastic optical localization microscopy (STORM) uses a pair of organic dyes, of which one - following Förster resonance energy transfer (FRET) - activates the second one, which is imaged until it is switched off (Heinlein et al., 2005; Rust et al., 2006). Furthermore, direct STORM (dSTORM) allows the localization of single molecules by photoswitching an organic dye between its fluorescent and non-fluorescent state (Heilemann et al., 2005, 2008). Altogether, localization microscopy is the most efficient sub-diffraction technique with a lateral resolution <10~20 nm (Betzig et al., 2006; Hess et al., 2006). Localization microscopy has also been implemented for 3D imaging, and several technical approaches have been used to achieve sub-diffraction 3D imaging. For instance, in combination with PALM, simultaneous detection of each imaged focal plane and of a second plane that is 350 nm closer to the objective, improves the axial resolution to 75 nm (Juette et al., 2008). In addition, combination of multifocal excitation and localization microscopy has demonstrated the simultaneous imaging of a 4-µm volume within single cells with a resolution of 20×20×50 nm (Hajj et al., 2014).

The main drawback of localization microscopy is that the sub-diffraction resolution is achieved by localizing single fluorophores over time, which makes it less suitable for imaging fast dynamic processes. However, localization microscopy can be used for high-resolution single-particle tracking (spt) (Manley et al., 2008), which can be very useful for understanding key cell biological events. For example, spt-PALM has recently been applied to track integrins within and outside of focal adhesions, and to quantify their diffusive properties (Rossier et al., 2012). Furthermore, this approach was used to demonstrate that the mechanical properties of the glycocalyx layer promote focal adhesion growth by channeling membrane-associated integrins into clusters (Paszek et al., 2014). In another example, 3D PALM was used in *Drosophila* embryos to analyze the clustering of E-cadherin at cell–cell junctions (Truong Quang et al., 2013). In addition, PALM has been combined with confocal correlation microscopy for high-resolution mapping of glutamate receptors in individual neurons that had been annotated by standard confocal microscopy in *C.*

elegans (Vangindertael et al., 2015). As live imaging also requires imaging at high speeds in order to being able to track dynamic events, faster cMOS cameras have been developed that allow the recording of fast events at high-resolution (Huang et al., 2013). Moreover, 3D PALM has recently been combined with lattice light-sheet illumination to image single cells in culture (Fig. 3F), as well as mouse stem cells spheroids at high speed (Chen et al., 2014). Taken together, although super-resolution imaging offers new possibilities in live and *in vivo* cell biology, there are still some limitations that impede obtaining nanoscale resolution of these events (Table 1).

Correlative light and electron microscopy (CLEM) – moving towards nanoscale resolution of dynamic *in vivo* phenomena

The most interesting biological events usually occur only infrequently and involve single molecules or organelles that are separated by only few nanometers. The perfect imaging approach, thus, would make it possible to obtain macroscopic views of tissues and structures and, at wish, to easily zoom into the most-discrete details or subcellular structures, organelles or proteins. As discussed above, live imaging with light microscopy is extremely useful to characterize the dynamics of cellular events *in vivo* and allows imaging of living samples in 3D, but it only has a limited spatial resolution. Electron microscopy (EM) achieves a much higher resolution but, generally, allows the imaging of fixed specimen with a limited screening ability. This makes it a challenging technique when studying rare objects such as single metastatic cells within a full organ (lung, brain, liver). CLEM combines live confocal microscopy with EM for the characterization of biological samples at high spatial and temporal resolution (de Boer et al., 2015) (Fig. 4A). CLEM can be used for virtually any biological event that can either be imaged (Goetz et al., 2014) or quantified by using biophysical approaches. The main bottleneck of the approach is the challenge to align the region of interest (ROI) that has been identified by light microscopy with the EM image. However, the increasing popularity of CLEM has led to the development of novel procedures and microscopy setups, although these were mainly developed to retrieve the ROI within a small sample, e.g. thin sections of cells or tissue to be imaged with transmission EM. The difficulty to accurately align the ROI within samples that have a complex 3D organization, such as large cells, embryos, small organisms or tissues, is still a major hurdle. Here, we will discuss the recent developments in CLEM by providing a snapshot of available procedures and techniques that help to reliably track biological events of interest at the highest spatial and temporal resolutions. We and others have recently contributed to the significant progress in the field of correlative light- and electron microscopy. by combining intravital imaging of entire organisms with EM, which we here refer to as intravital CLEM (Goetz et al., 2014, 2015; Karreman et al., 2014, 2016; Maco et al., 2013). Intravital CLEM enabled important discoveries in several areas of life science, such as cell biology (Avinoam et al., 2015), neuroscience (Allegra Mascaro et al., 2013; Maco et al., 2013), cancer research (Karreman et al., 2016), virology (Hellström et al., 2015) and developmental biology (Durdu et al., 2014; Goetz et al., 2014), and is highly likely to contribute to future breakthroughs in biological research.

Ground-breaking *in vitro* CLEM

CLEM has primarily and successfully been applied to *in vitro* situations. By preserving the fluorescence signal within a resin-embedded block for its easy correlation with the EM image, the Briggs group has established a ground-breaking technique that

10
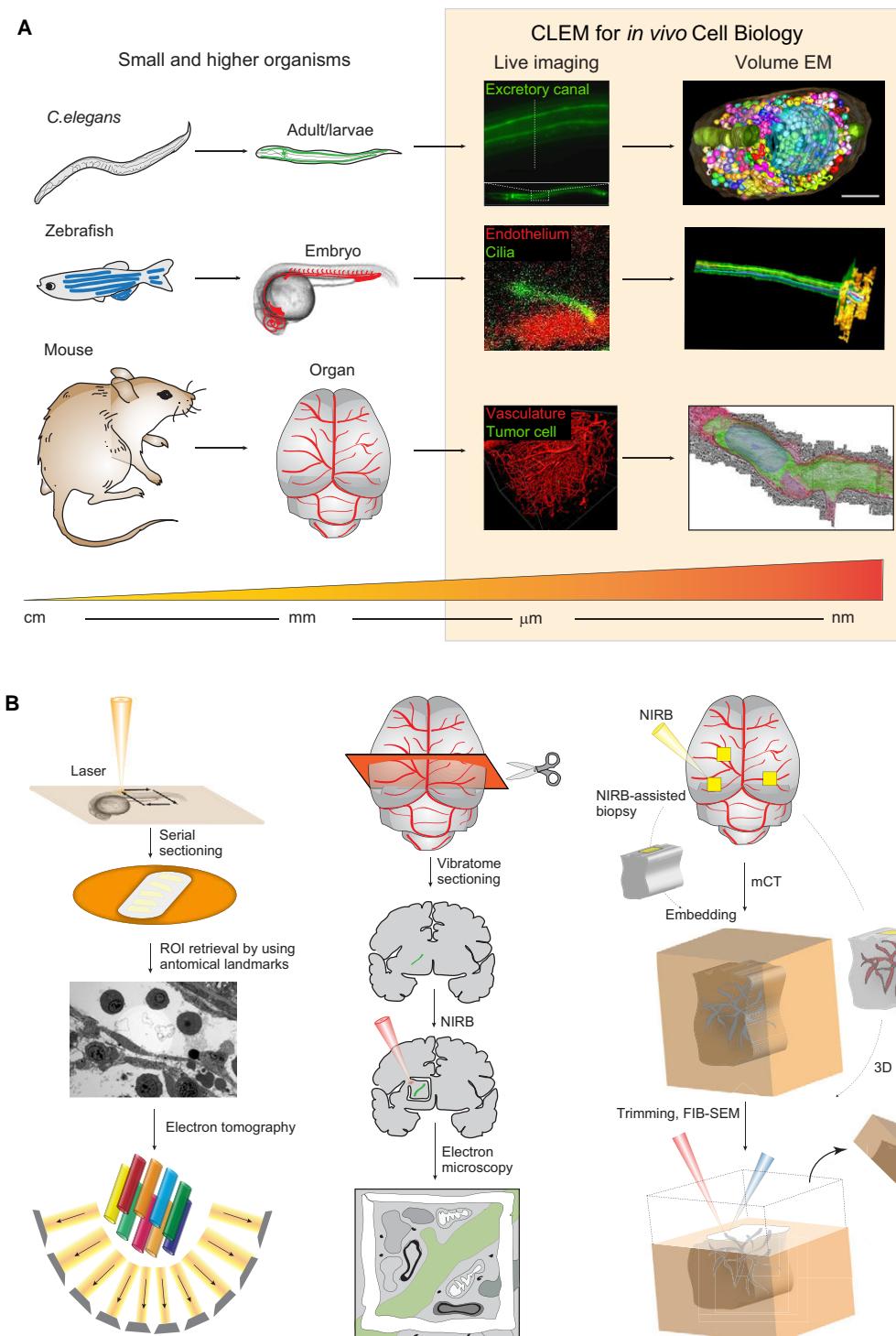
Fig. 4. Intravital CLEM and its biological applications. (A) Examples of intravital CLEM performed on *C. elegans*, zebrafish embryos and mice. In *C. elegans*, intravital CLEM has been used to study the ultrastructure and formation of the excretory canal by using correlative fluorescence and volume EM (serial electron tomography). Adapted with permission from Kolotuev et al., 2013. In the zebrafish embryo, CLEM was used to dissect the ultrastructure of endothelial cilia that sense and transduce blood flow forces. Adapted with permission from Goetz et al., 2014. In mice, we recently developed a mutimodal approach that combines intravital 2PEM imaging, X-ray micro-computed tomography (mCT) and focused ion beam scanning EM (FIB-SEM; see panel B); this made it possible to retrieve single brain metastatic cells for their dissection at high-resolution). Adapted with permission from Karreman et al., 2016. (B) A snapshot of the existing intravital CLEM procedures. Targeted ultramicrotomy, and subsequent volume EM, can be performed upon laser carving in the flat-embedded resin sample (left). Alternatively, near-infrared branding (NIRB)-guided marks can be physically drawn on vibratome sections of the mouse brain for guiding ultramicrotomy and/or volume EM (middle). NIRB can also be used for whole-organ 'tattooing' (e.g. ear, brain) and thereby guide the biopsy of the region of interest (ROI) in voluminous samples, such as the mouse brain. Resin-embedded ROIs are then scanned by using mCT, the volumes are then registered and the position of the ROIs retrieved; this allows 3DEM by using FIB-SEM (right).

allowed them time-lapse recordings of endocytosis gaining ultrastructural information from resin sections imaged by applying electron tomography (Kukulski et al., 2011, 2012). These elegant studies elucidated how proteins that control membrane budding, such as clathrin, actin and amphiphysin, drive invagination, elongation and fission of endocytic vesicles. Further work using CLEM showed that vesicle budding appears to involve the assembly of clathrin adaptors (Skruzny et al., 2015) and the bending of a dynamic preassembled clathrin coat (Avinoam et al., 2015). Similar approaches of preserving the fluorescence signal have been used in CLEM of zebrafish embryos (Nixon et al., 2009), *C. elegans* (Watanabe et al., 2011) and mammalian cells (Paez-Segala et al., 2015; Peddie et al., 2014). CLEM can also be performed thanks to the development of bimodal probes, such as the mini singlet oxygen generator (miniSOG) (Shu et al., 2011) and proteins of the ascorbate peroxidase (APX) family, in particular APEX2 (Lam et al., 2015). MiniSOG is a fluorescent flavoprotein that, when genetically encoded, is used as a versatile tag that emits fluorescence and, in response to illumination, generates singlet oxygen that transforms diaminobenzidine into electron-dense precipitates that can by imaged by using EM. The engineered peroxidase APEX, by contrast, can be used for EM and proximity labeling upon its fusion to a protein of interest, (Mick et al., 2015). Alternatively, events or regions of interest can be tracked over the two imaging modalities, with recording of coordinates imprinted on the culture dish, by using either commercialized (Al Jord et al., 2014) or laser-micropatterned culture substrates (Spiegelhalter et al., 2010). This method allows the fast freezing (e.g. high-pressure freezing) of dynamic events within seconds for their ultrastructural characterization. A similar approach has recently been used to characterize centriole duplication in multi-ciliated ependymal cells, which grow multiple motile cilia that efficiently propel the cerebrospinal fluid in brain ventricles. By combining live super-resolution imaging of ependymal progenitors by using EM, Al Jord and colleagues could show that multiple centrioles derive from the pre-existing progenitor cell centrosome following multiple rounds of procentriole seeding, thereby unraveling an unexpected centriolar asymmetry that differs from the archetypal duplication program found in other ciliated cells (Al Jord et al., 2014). Similarly, *in vitro* CLEM has been combined with the 3D electron microscopy (3DEM) technique focused ion beam scanning electron microscopy (FIB-SEM) to show that invadopodia of cancer cells potentially mature in response to a mechanical interplay with the nucleus (Revach et al., 2015). Their EM data revealed that invadopodia are composed of actin bundles that interact with and indent the nucleus at the apical side. Finally, many of the issues that are encountered when retrieving the ROI in EM after light microscopy and sample transfer can be avoided by using integrated microscopes that are specially designed for CLEM studies; the latter also allow the combination of atomic force microscopy and EM (for a review see de Boer et al., 2015).

CLEM of multicellular and 3D samples – probing biomechanics at high resolution

A major gap in cell biology is to understand cell biological events in a realistic pathophysiological context. This can only be approached by using light microscopy in living animals, i.e. intravital imaging. Although single-photon and light-sheet imaging allow to image small organisms, such as *Drosophila*, *C. elegans* and zebrafish embryos at any depth, the event of interest might be beyond the imaging depth of the fluorescence microscope in higher organisms, such as mice. As discussed above, this can be easily overcome by surgical implantation of imaging windows and the use of multi-photon microscopy (Helmchen and Denk, 2005), which permits to acquire high-quality fluorescent images deep inside animals (see above).

However, most organs are not directly optically accessible and require surgical procedures to expose the tissue of interest, as is employed in neuroscience (Dombeck et al., 2007) and cancer research (Ellenbroek and van Rheenen, 2014). The second, and biggest, challenge resides in the difficulty to retrieve the ROI in voluminous resin-embedded 3D samples (up to a few mm^3). In small organisms and embryos, anatomical landmarks, such as fluorescent or visible structures that have been imaged *in vivo* can be utilized to provide key anchor points for pinpointing the event of interest in the resin-embedded tissue (Durdu et al., 2014; Goetz et al., 2014, 2015; Kolotuev et al., 2010, 2013; Müller-Reichert et al., 2007). This has proven to be very useful in zebrafish embryos for correlating the blood flow that is sensed by endothelial cilia to their inner ultrastructure (Fig. 4A,B). In addition to anatomical landmarks, artificial markers can be carved in the resin, which – upon superimposition with the intravital image – facilitate targeted ultramicrotomy by EM. Of note, laser etching had been originally pioneered on glass coverslips for micropatterning-assisted CLEM of cells (Spiegelhalter et al., 2010). In resin- and flat-embedded small organisms, it facilitates the retrieval of a precise ROI located within the intravital image and, for instance, afforded the characterization of how fibroblast growth factor (FGF) activity controls the frequency at which rosette-like mechanosensory organs, e.g. the zebrafish lateral line primordium, are deposited through the assembly of microluminal structures that constrain FGF signaling (Durdu et al., 2014). Studies performed in *C. elegans* provide additional examples of laser-assisted targeted ultramicrotomy; these have helped to further clarify at high resolution the formation of excretory canals, as well as the contribution of exosomes to alae formation (Hyenne et al., 2015) (Fig. 4A). Laser etching can also be used directly on hydrated tissues to precisely locate the ROI. This technology, called near-infrared branding (NIRB) has been developed a few years ago and enables to highlight the position of the ROI, either owing to laser-induced autofluorescence or upon photooxidation of the NIRB mark (Bishop et al., 2011) (Fig. 4B). In that study, by using NIRB on brain vibratome sections, single cortical dendritic spines that had been previously recorded in a living mouse could be dissected at unprecedented resolution (Bishop et al., 2011). Furthermore, NIRB-guided retrieval of the ROI in vibratome sections allows to combine intravital imaging with 3DEM, such as FIB-SEM, which was shown to provide nanoscale isotropic imaging of axons and dendrites (Maco et al., 2013). Combined with state-of-the-art optogenetic tools, intravital CLEM holds great promises for resolving long-standing questions in brain connectivity. For instance, NIRB has recently been customized to perform tissue surface 'tattooing', which facilitates the retrieval of the ROI before embedding (Karreman et al., 2014) (Fig. 4B). However, although this approach allowes to selectively target the ROI-contained volume in *x* and *y* direction, the *z*-position within the block cannot be estimated from it, and serial sectioning throughout the block is required for ROI retrieval. Combined with anatomical landmarks, NIRB-assisted tattooing of the mouse ear skin was used to precisely correlate intravital imaging of subcutaneous tumors with high-resolution electron tomography (Karreman et al., 2014). However, these techniques do not provide the opportunity to predict where the ROI is within the resin-embedded sample; being able to achieve this would greatly increase throughput and facilitate *en block* imaging, which is of utmost importance when working with

high-volume samples. One way to circumvent this issue is to implement a third imaging modality to map the resin-embedded ROI and thereby predict the position of the ROI by cross-correlating the topology of anatomical landmarks. This opportunity is provided by X-ray micro-computed tomography (microCT), which uses the presence of heavy metals, such as osmium – and which are required for EM – to resolve a number of anatomical structures, such as the vasculature, hair follicles and collagen fibers (Karreman et al., 2016). This approach has been used on brain vibratome sections and allowed to locate photo-oxidized neuronal structures (Bushong et al., 2015). Moreover, microCT can be used on voluminous samples, such as brain biopsies, and allows to accurately resolve the brain capillary architecture. We have recently shown that implementing microCT as an intermediate step between intravital imaging of brain metastasis and FIB-SEM allows the high-resolution imaging of single metastatic cells (Karreman et al., 2016). The combination of state-of-the-art light and intravital microscopy techniques together with the growing approaches for 3DEM will provide scientists with an unprecedented toolbox that can help to resolve – *in vivo* and at very high resolution – many of the current questions surrounding cell biology. We believe that intravital CLEM has the potential to provide the link between cell biology and relevant pathophysiological contexts and, undoubtedly, will become the next-generation microscopy for *in vivo* cell biologists (Table 1).

Conclusions

We have summarized here the imaging approaches that are currently used for studying any cell biological event of interest. Cell biologists are now in the great position to have access to a wide and still-growing palette of fast, non-invasive, high-resolution, label-free technologies that make true '*in vivo* cell biology' a goal that is within reach in the near future. It is of utmost importance to continue to pursue the development of high-resolution and animal-suitable imaging approaches in order to visualize the cell biology of any given disease within an animal model. This giant leap forward will enable us to model, image, quantify and understand the complexity of cell biology within its most relevant contexts, thereby contributing to the wealth of knowledge and to the design of optimal therapeutic strategies to deal with life-threatening pathologies.

References

Ahmed, W. W., Fodor, É. and Betz, T. (2015). Active cell mechanics: measurement and theory. *Biochim. Biophys. Acta Mol. Cell Res.* **1853**, 3083-3094.

Ahrens, M. B., Orger, M. B., Robson, D. N., Li, J. M. and Keller, P. J. (2013). Whole-brain functional imaging at cellular resolution using light-sheet microscopy. *Nat. Methods* **10**, 413-420.

Al Jord, A., Lemaître, A.-I., Delgehyr, N., Faucourt, M., Spassky, N. and Meunier, A. (2014). Centriole amplification by mother and daughter centrioles differs in multiciliated cells. *Nature* **516**, 104-107.

Alexander, S., Weigelin, B., Winkler, F. and Friedl, P. (2013). Preclinical intravital microscopy of the tumour-stroma interface: invasion, metastasis, and therapy response. *Curr. Opin. Cell Biol.* **25**, 659-671.

Allegra Mascaro, A. L., Cesare, P., Sacconi, L., Grasselli, G., Mandolesi, G., Maco, B., Knott, G. W., Huang, L., De Paola, V., Strata, P. et al. (2013). In vivo single branch axotomy induces GAP-43-dependent sprouting and synaptic remodeling in cerebellar cortex. *Proc. Natl. Acad. Sci. USA* **110**, 10824-10829.

Anton, H., Harlepp, S., Ramspacher, C., Wu, D., Monduc, F., Bhat, S., Liebling, M., Paoletti, C., Charvin, G., Freund, J. B. et al. (2013). Pulse propagation by a capacitive mechanism drives embryonic blood flow. *Development* **140**, 4426-4434.

Ashkin, A. (1997). Optical trapping and manipulation of neutral particles using lasers. *Proc. Natl. Acad. Sci. USA* **94**, 4853-4860.

Ashkin, A. and Dziedzic, J. (1987). Optical trapping and manipulation of viruses and bacteria. *Science* **235**, 1517-1520.

Ashkin, A., Dziedzic, J. M. and Yamane, T. (1987). Optical trapping and manipulation of single cells using infrared laser beams. *Nature* **330**, 769-771.

Avinoam, O., Schorb, M., Beese, C. J., Briggs, J. A. G. and Kaksonen, M. (2015). ENDOCYTOSIS. Endocytic sites mature by continuous bending and remodeling of the clathrin coat. *Science* **348**, 1369-1372.

Balaban, N. Q., Schwarz, U. S., Riveline, D., Goichberg, P., Tzur, G., Sabanay, I., Mahalu, D., Safran, S., Bershadsky, A., Addadi, L. et al. (2001). Force and focal adhesion assembly: a close relationship studied using elastic micropatterned substrates. *Nat. Cell Biol.* **3**, 466-472.

Bambardekar, K., Clément, R., Blanc, O., Chardès, C. and Lenne, P.-F. (2015). Direct laser manipulation reveals the mechanics of cell contacts in vivo. *Proc. Natl. Acad. Sci. USA* **112**, 1416-1421.

Berning, S., Willig, K. I., Steffens, H., Dibaj, P. and Hell, S. W. (2012). Nanoscopy in a living mouse brain. *Science* **335**, 551-551.

Betzig, E., Patterson, G. H., Sougrat, R., Lindwasser, O. W., Olenych, S., Bonifacino, J. S., Davidson, M. W., Lippincott-Schwartz, J. and Hess, H. F. (2006). Imaging intracellular fluorescent proteins at nanometer resolution. *Science* **313**, 1642-1645.

Bishop, D., Nikić, I., Brinkoetter, M., Knecht, S., Potz, S., Kerschensteiner, M. and Misgeld, T. (2011). Near-infrared branding efficiently correlates light and electron microscopy. *Nat. Methods* **8**, 568-570.

Boulnois, J.-L. (1986). Photophysical processes in recent medical laser developments: a review. *Lasers Med. Sci.* **1**, 47-66.

Brunet, T., Bouclet, A., Ahmadi, P., Mitrossilis, D., Driquez, B., Brunet, A.-C., Henry, L., Serman, F., Béalle, G., Ménager, C. et al. (2013). Evolutionary conservation of early mesoderm specification by mechanotransduction in Bilateria. *Nat. Commun.* **4**, 2821.

Bushong, E. A., Johnson, D. D., Kim, K.-Y., Terada, M., Hatori, M., Peltier, S. T., Panda, S., Merkle, A. and Ellisman, M. H. (2015). X-ray microscopy as an approach to increasing accuracy and efficiency of serial block-face imaging for correlated light and electron microscopy of biological specimens. *Microsc. Microanal.* **21**, 231-238.

Chen, B.-C., Legant, W. R., Wang, K., Shao, L., Milkie, D. E., Davidson, M. W., Janetopoulos, C., Wu, X. S., Hammer, J. A., Liu, Z. et al. (2014). Lattice light-sheet microscopy: imaging molecules to embryos at high spatiotemporal resolution. *Science* **346**, 1257998.

Chhetri, R. K., Amat, F., Wan, Y., Höckendorf, B., Lemon, W. C. and Keller, P. J. (2015). Whole-animal functional and developmental imaging with isotropic spatial resolution. *Nat. Methods* **12**, 1171-1178.

Chivukula, V. K., Krog, B. L., Nauseef, J. T., Henry, M. D. and Vigmostad, S. C. (2015). Alterations in cancer cell mechanical properties after fluid shear stress exposure: a micropipette aspiration study. *Cell Health Cytoskelet.* **7**, 25-35.

Collins, C., Osborne, L. D., Guilluy, C., Chen, Z., O'Brien, E. T., III, Reader, J. S., Burridge, K., Superfine, R. and Tzima, E. (2014). Haemodynamic and extracellular matrix cues regulate the mechanical phenotype and stiffness of aortic endothelial cells. *Nat. Commun.* **5**, 3984.

Coto Hernández, I., Castello, M., Lanzanò, L., d'Amora, M., Bianchini, P., Diaspro, A. and Vicidomini, G. (2016). Two-photon excitation STED microscopy with time-gated detection. *Sci. Rep.* **6**, 19419.

Dao, M., Lim, C. T. and Suresh, S. (2003). Mechanics of the human red blood cell deformed by optical tweezers. *J. Mech. Phys. Solids* **51**, 2259-2280.

de Boer, P., Hoogenboom, J. P. and Giepmans, B. N. G. (2015). Correlated light and electron microscopy: ultrastructure lights up! *Nat. Methods* **12**, 503-513.

Débarre, D., Supatto, W., Pena, A.-M. M., Fabre, A., Tordjmann, T., Combettes, L., Schanne-Klein, M. -C. and Beaurepaire, E. (2006). Imaging lipid bodies in cells and tissues using third-harmonic generation microscopy. *Nat. Methods* **3**, 47-53.

Denk, W., Strickler, J. H. and Webb, W. W. (1990). Two-photon laser scanning fluorescence microscopy. *Science* **248**, 73-76.

Desprat, N., Supatto, W., Pouille, P.-A., Beaurepaire, E. and Farge, E. (2008). Tissue deformation modulates twist expression to determine anterior midgut differentiation in Drosophila embryos. *Dev. Cell* **15**, 470-477.

Dombeck, D. A., Khabbaz, A. N., Collman, F., Adelman, T. L. and Tank, D. W. (2007). Imaging large-scale neural activity with cellular resolution in awake, mobile mice. *Neuron* **56**, 43-57.

Durdu, S., Iskar, M., Revenu, C., Schieber, N., Kunze, A., Bork, P., Schwab, Y. and Gilmour, D. (2014). Luminal signalling links cell communication to tissue architecture during organogenesis. *Nature* **515**, 120-124.

Ellenbroek, S. I. J. and van Rheenen, J. (2014). Imaging hallmarks of cancer in living mice. *Nat. Rev. Cancer* **14**, 406-418.

Eyckmans, J., Boudou, T., Yu, X. and Chen, C. S. (2011). A Hitchhiker's guide to mechanobiology. *Dev. Cell* **21**, 35-47.

Fiolka, R., Shao, L., Rego, E. H., Davidson, M. W. and Gustafsson, M. G. L. (2012). Time-lapse two-color 3D imaging of live cells with doubled resolution using structured illumination. *Proc. Natl. Acad. Sci. USA* **109**, 5311-5315.

Franken, P. A., Hill, A. E., Peters, C. W. and Weinreich, G. (1963). Generation of optical harmonics. *Phys. Rev. Lett.* **118**.

Friedrich, M. and Harms, G. S. (2015). Axial resolution beyond the diffraction limit of a sheet illumination microscope with stimulated emission depletion. *J. Biomed. Opt.* **20**, 106006-106006.

Friedrich, M., Gan, Q., Ermolayev, V. and Harms, G. S. (2011). STED-SPIM: stimulated emission depletion improves sheet illumination microscopy resolution. *Biophys. J.* **100**, L43-L45.

Gao, L., Shao, L., Higgins, C. D., Poulton, J. S., Peifer, M., Davidson, M. W., Wu, X., Goldstein, B. and Betzig, E. (2012). Noninvasive imaging beyond the diffraction limit of 3D dynamics in thickly fluorescent specimens. *Cell* **151**, 1370-1385.

Goetz, J. G., Steed, E., Ferreira, R. R., Roth, S., Ramspacher, C., Boselli, F., Charvin, G., Liebling, M., Wyart, C., Schwab, Y. et al. (2014). Endothelial cilia mediate low flow sensing during zebrafish vascular development. *Cell Rep.* **6**, 799-808.

Goetz, J. G., Monduc, F., Schwab, Y. and Vermot, J. (2015). Using correlative light and electron microscopy to study zebrafish vascular morphogenesis. *Methods Mol. Biol.* **1189**, 31-46.

Göppert-Mayer, M. (1931). Uber Elementarakte mit zwei Quantensprüngen. *Ann. Phys.* **401**, 273-294.

Grange, R., Lanvin, T., Hsieh, C.-L., Pu, Y. and Psaltis, D. (2011). Imaging with second-harmonic radiation probes in living tissue. *Biomed. Opt. Express* **2**, 2532-2539.

Graves, E. T., Duboc, C., Fan, J., Stransky, F., Leroux-Coyau, M. and Strick, T. R. (2015). A dynamic DNA-repair complex observed by correlative single-molecule nanomanipulation and fluorescence. *Nat. Struct. Mol. Biol.* **22**, 452-457.

Guevorkian, K., Colbert, M.-J., Durth, M., Dufour, S. and Brochard-Wyart, F. (2010). Aspiration of biological viscoelastic drops. *Phys. Rev. Lett.* **104**, 218101.

Guevorkian, K., Gonzalez-Rodriguez, D., Carlier, C., Dufour, S. and Brochard-Wyart, F. (2011). Mechanosensitive shivering of model tissues under controlled aspiration. *Proc. Natl. Acad. Sci. USA* **108**, 13387-13392.

Guilak, F., Tedrow, J. R. and Burgkart, R. (2000). Viscoelastic properties of the cell nucleus. *Biochem. Biophys. Res. Commun.* **269**, 781-786.

Gupta, M., Kocgozlu, L., Sarangi, B. R., Margadant, F., Ashraf, M. and Ladoux, B. (2015). Micropillar substrates: a tool for studying cell mechanobiology. *Methods Cell Biol.* **125**, 289-308.

Gustafsson, M. G. L. (2000). Surpassing the lateral resolution limit by a factor of two using structured illumination microscopy. *J. Microsc.* **198**, 82-87.

Gustafsson, M. G. L., Shao, L., Carlton, P. M., Wang, C. J. R., Golubovskaya, I. N., Cande, W. Z., Agard, D. A. and Sedat, J. W. (2008). Three-dimensional resolution doubling in wide-field fluorescence microscopy by structured illumination. *Biophys. J.* **94**, 4957-4970.

Hajj, B., Wisniewski, J., El Beheiry, M., Chen, J., Revyakin, A., Wu, C. and Dahan, M. (2014). Whole-cell, multicolor superresolution imaging using volumetric multifocus microscopy. *Proc. Natl. Acad. Sci. USA* **111**, 17480-17485.

Headley, M. B., Bins, A., Nip, A., Roberts, E. W., Looney, M. R., Gerard, A. and Krummel, M. F. (2016). Visualization of immediate immune responses to pioneer metastatic cells in the lung. *Nature* **531**, 513-517.

Heilemann, M., Margeat, E., Kasper, R., Sauer, M. and Tinnefeld, P. (2005). Carbocyanine dyes as efficient reversible single-molecule optical switch. *J. Am. Chem. Soc.* **127**, 3801-3806.

Heilemann, M., van de Linde, S., Schüttpelz, M., Kasper, R., Seefeldt, B., Mukherjee, A., Tinnefeld, P. and Sauer, M. (2008). Subdiffraction-resolution fluorescence imaging with conventional fluorescent probes. *Angew. Chem. Int. Ed.* **47**, 6172-6176.

Heinlein, T., Biebricher, A., Schlüter, P., Roth, C. M., Herten, D.-P., Wolfrum, J., Heilemann, M., Müller, C., Tinnefeld, P. and Sauer, M. (2005). High-resolution colocalization of single molecules within the resolution Gap of far-field microscopy. *ChemPhysChem* **6**, 949-955.

Hellerer, T., Axäng, C., Brackmann, C., Hillertz, P., Pilon, M. and Enejder, A. (2007). Monitoring of lipid storage in Caenorhabditis elegans using coherent anti-Stokes Raman scattering (CARS) microscopy. *Proc. Natl. Acad. Sci. USA* **104**, 14658-14663.

Hellström, K., Vihinen, H., Kallio, K., Jokitalo, E. and Ahola, T. (2015). Correlative light and electron microscopy enables viral replication studies at the ultrastructural level. *Methods* **90**, 49-56.

Helmchen, F. and Denk, W. (2005). Deep tissue two-photon microscopy. *Nat. Methods* **2**, 932-940.

Hess, S. T., Girirajan, T. P. K. and Mason, M. D. (2006). Ultra-high resolution imaging by fluorescence photoactivation localization microscopy. *Biophys. J.* **91**, 4258-4272.

Hochmuth, R. M. (2000). Micropipette aspiration of living cells. *J. Biomech.* **33**, 15-22.

Hoffman, B. D., Grashoff, C. and Schwartz, M. A. (2011). Dynamic molecular processes mediate cellular mechanotransduction. *Nature* **475**, 316-323.

Hoyer, P., de Medeiros, G., Balázs, B., Norlin, N., Besir, C., Hanne, J., Kräusslich, H.-G., Engelhardt, J., Sahl, S. J., Hell, S. W. et al. (2016). Breaking the diffraction limit of light-sheet fluorescence microscopy by RESOLFT. *Proc. Natl. Acad. Sci. USA* **113**, 3442-3446.

Huang, F., Hartwich, T. M. P., Rivera-Molina, F. E., Lin, Y., Duim, W. C., Long, J. J., Uchil, P. D., Myers, J. R., Baird, M. A., Mothes, W. et al. (2013). Video-rate nanoscopy using sCMOS camera-specific single-molecule localization algorithms. *Nat. Methods* **10**, 653-658.

Huisken, J., Swoger, J., Bene, F. D., Wittbrodt, J. and Stelzer, E. H. K. (2004). Optical sectioning deep inside live embryos by selective plane illumination microscopy. *Science* **305**, 1007-1009.

Hyenne, V., Apaydin, A., Rodriguez, D., Spiegelhalter, C., Hoff-Yoessle, S., Diem, M., Tak, S., Lefebvre, O., Schwab, Y., Goetz, J. G. et al. (2015). RAL-1 controls multivesicular body biogenesis and exosome secretion. *J. Cell Biol.* **211**, 27-37.

Jakob, P. H., Kehrer, J., Flood, P., Wiegel, C., Haselmann, U., Meissner, M., Stelzer, E. H. K. and Reynaud, E. G. (2016). A 3-D cell culture system to study epithelia functions using microcarriers. *Cytotechnology.* [Epub ahead of print] doi:10.1007/s10616-015-9935-0

Janmey, P. A. and Miller, R. T. (2011). Mechanisms of mechanical signaling in development and disease. *J. Cell Sci.* **124**, 9-18.

Jenne, C. N., Wong, C. H. Y., Petri, B. and Kubes, P. (2011). The use of spinning-disk confocal microscopy for the intravital analysis of platelet dynamics in response to systemic and local inflammation. **6**, e25109.

Juette, M. F., Gould, T. J., Lessard, M. D., Mlodzianoski, M. J., Nagpure, B. S., Bennett, B. T., Hess, S. T. and Bewersdorf, J. (2008). Three-dimensional sub–100 nm resolution fluorescence microscopy of thick samples. *Nat. Methods* **5**, 527-529.

Karreman, M. A., Mercier, L., Schieber, N. L., Shibue, T., Schwab, Y. and Goetz, J. G. (2014). Correlating intravital multi-photon microscopy to 3D electron microscopy of invading tumor cells using anatomical reference points. *PLoS ONE* **9**, e114448.

Karreman, M. A., Mercier, L., Schieber, N. L., Solecki, G., Allio, G., Winkler, F., Ruthensteiner, B., Goetz, J. G. and Schwab, Y. (2016). Fast and precise targeting of single tumor cells in vivo by multimodal correlative microscopy. *J. Cell Sci.* **129**, 444-456.

Keller, P. J. and Ahrens, M. B. (2015). Visualizing whole-brain activity and development at the single-cell level using light-sheet microscopy. *Neuron* **85**, 462-483.

Keller, P. J., Schmidt, A. D., Wittbrodt, J. and Stelzer, E. H. K. (2008). Reconstruction of Zebrafish early embryonic development by scanned light sheet microscopy. *Science* **322**, 1065-1069.

Khare, S. M., Awasthi, A., Venkataraman, V. and Koushika, S. P. (2015). Colored polydimethylsiloxane micropillar arrays for high throughput measurements of forces applied by genetic model organisms. *Biomicrofluidics* **9**, 014111.

Kienast, Y., von Baumgarten, L., Fuhrmann, M., Klinkert, W. E. F., Goldbrunner, R., Herms, J. and Winkler, F. (2010). Real-time imaging reveals the single steps of brain metastasis formation. *Nat. Med.* **16**, 116-122.

Kim, D.-H., Wong, P. K., Park, J., Levchenko, A. and Sun, Y. (2009). Microengineered Platforms for Cell Mechanobiology. *Annu. Rev. Biomed. Eng.* **11**, 203-233.

Kissa, K. and Herbomel, P. (2010). Blood stem cells emerge from aortic endothelium by a novel type of cell transition. *Nature* **464**, 112-115.

Klajner, M., Hebraud, P., Sirlin, C., Gaiddon, C. and Harlepp, S. (2010). DNA binding to an anticancer Organo-Ruthenium complex. *J. Phys. Chem. B* **114**, 14041-14047.

Klar, T. A., Jakobs, S., Dyba, M., Egner, A. and Hell, S. W. (2000). Fluorescence microscopy with diffraction resolution barrier broken by stimulated emission. *Proc. Natl. Acad. Sci.* **97**, 8206-8210.

Kner, P., Chhun, B. B., Griffis, E. R., Winoto, L. and Gustafsson, M. G. L. (2009). Super-resolution video microscopy of live cells by structured illumination. *Nat. Methods* **6**, 339-342.

Kobat, D., Horton, N. G. and Xu, C. (2011). In vivo two-photon microscopy to 1.6-mm depth in mouse cortex. *J. Biomed. Opt.* **16**, 106014.

Kolotuev, I., Schwab, Y. and Labouesse, M. (2010). A precise and rapid mapping protocol for correlative light and electron microscopy of small invertebrate organisms. *Biol. Cell* **102**, 121-132.

Kolotuev, I., Hyenne, V., Schwab, Y., Rodriguez, D. and Labouesse, M. (2013). A pathway for unicellular tube extension depending on the lymphatic vessel determinant Prox1 and on osmoregulation. *Nat. Cell Biol.* **15**, 157-168.

Krzic, U., Gunther, S., Saunders, T. E., Streichan, S. J. and Hufnagel, L. (2012). Multiview light-sheet microscope for rapid in toto imaging. *Nat. Methods* **9**, 730-733.

Kukulski, W., Schorb, M., Welsch, S., Picco, A., Kaksonen, M. and Briggs, J. A. G. (2011). Correlated fluorescence and 3D electron microscopy with high sensitivity and spatial precision. *J. Cell Biol.* **192**, 111-119.

Kukulski, W., Schorb, M., Kaksonen, M. and Briggs, J. A. G. (2012). Plasma membrane reshaping during endocytosis is revealed by time-resolved electron tomography. *Cell* **150**, 508-520.

Kuznetsova, T. G., Starodubtseva, M. N., Yegorenkov, N. I., Chizhik, S. A. and Zhdanov, R. I. (2007). Atomic force microscopy probing of cell elasticity. *Micron* **38**, 824-833.

Lam, S. S., Martell, J. D., Kamer, K. J., Deerinck, T. J., Ellisman, M. H., Mootha, V. K. and Ting, A. Y. (2015). Directed evolution of APEX2 for electron microscopy and proximity labeling. *Nat. Methods* **12**, 51-54.

Lanzicher, T., Martinelli, V., Puzzi, L., Del Favero, G., Codan, B., Long, C. S., Mestroni, L., Taylor, M. R. G. and Sbaizero, O. (2015). The cardiomyopathy lamin A/C D192G mutation disrupts whole-cell biomechanics in cardiomyocytes as measured by atomic force microscopy loading-unloading curve analysis. *Sci. Rep.* **5**, 13388.

Lee, M., Downes, A., Chau, Y.-Y., Serrels, B., Hastie, N., Elfick, A., Brunton, V., Frame, M. and Serrels, A. (2015). In vivo imaging of the tumor and its associated microenvironment using combined CARS/2-photon microscopy. *IntraVital* **4**, e1055430.

Legant, W. R., Shao, L., Grimm, J. B., Brown, T. A., Milkie, D. E., Avants, B. B., Lavis, L. D. and Betzig, E. (2016). High-density three-dimensional localization microscopy across large volumes. *Nat. Methods* **13**, 359-365.

Li, J. L., Goh, C. C., Keeble, J. L., Qin, J. S., Roediger, B., Jain, R., Wang, Y., Chew, W. K., Weninger, W. and Ng, L. G. (2012). Intravital multiphoton imaging of immune responses in the mouse ear skin. *Nat. Protoc.* **7**, 221-234.

Li, D., Shao, L., Chen, B.-C., Zhang, X., Zhang, M., Moses, B., Milkie, D. E., Beach, J. R., Hammer, J. A., Pasham, M. et al. (2015). Extended-resolution structured illumination imaging of endocytic and cytoskeletal dynamics. *Science* **349**, aab3500.

Lim, J., Lee, H. K., Yu, W. and Ahmed, S. (2014). Light sheet fluorescence microscopy (LSFM): past, present and future. *Analyst* **139**, 4758-4768.

Liu, Y.-J., Le Berre, M., Lautenschlaeger, F., Maiuri, P., Callan-Jones, A., Heuzé, M., Takaki, T., Voituriez, R. and Piel, M. (2015). Confinement and low adhesion induce fast amoeboid migration of slow mesenchymal cells. *Cell* **160**, 659-672.

Lye, C. M., Blanchard, G. B., Naylor, H. W., Muresan, L., Huisken, J., Adams, R. J. and Sanson, B. (2015). Mechanical coupling between endoderm invagination and axis extension in Drosophila. *PLoS Biol.* **13**, e1002292.

Maco, B., Holtmaat, A., Cantoni, M., Kreshuk, A., Straehle, C. N., Hamprecht, F. A. and Knott, G. W. (2013). Correlative in vivo 2 photon and focused ion beam scanning electron microscopy of cortical neurons. *PLoS ONE* **8**, e57405.

Maker, P. D. and Terhune, R. W. (1965). Study of optical effects due to an induced polarization third order in the electric field strength. *Phys. Rev.* **137**, 801-818.

Manley, S., Gillette, J. M., Patterson, G. H., Shroff, H., Hess, H. F., Betzig, E. and Lippincott-Schwartz, J. (2008). High-density mapping of single-molecule trajectories with photoactivated localization microscopy. *Nat. Methods* **5**, 155-157.

Mao, Y., Sun, Q., Wang, X., Ouyang, Q., Han, L., Jiang, L. and Han, D. (2009). In vivo nanomechanical imaging of blood-vessel tissues directly in living mammals using atomic force microscopy. *Appl. Phys. Lett.* **95**, 013704.

Marjoram, R. J., Guilluy, C. and Burridge, K. (2016). Using magnets and magnetic beads to dissect signaling pathways activated by mechanical tension applied to cells. *Methods* **94**, 19-26.

Masedunskas, A., Milberg, O., Porat-Shliom, N., Sramkova, M., Wigand, T., Amornphimoltham, P. and Weigert, R. (2012). Intravital microscopy: a practical guide on imaging intracellular structures in live animals. *BioArchitecture* **2**, 143-157.

Mercier, L., Böhm, J., Fekonja, N., Allio, G., Lutz, Y., Koch, M., Goetz, J. G. and Laporte, J. (2016). In vivo imaging of skeletal muscle in mice highlights muscle defects in a mouse model of myotubular myopathy. *IntraVital* **5**, e1168553.

Mick, D. U., Rodrigues, R. B., Leib, R. D., Adams, C. M., Chien, A. S., Gygi, S. P. and Nachury, M. V. (2015). Proteomics of primary cilia by proximity labeling. *Dev. Cell* **35**, 497-512.

Mickoleit, M., Schmid, B., Weber, M., Fahrbach, F. O., Hombach, S., Reischauer, S. and Huisken, J. (2014). High-resolution reconstruction of the beating zebrafish heart. *Nat. Methods* **11**, 919-922.

Minsky, M. (1961). Microscopy apparatus. U.S. Patent 3,013,467.

Müller-Reichert, T., Srayko, M., Hyman, A., O'Toole, E. T. and McDonald, K. (2007). Correlative light and electron microscopy of early Caenorhabditis elegans embryos in mitosis. *Methods Cell Biol.* **79**, 101-119.

Neuman, K. C. and Nagy, A. (2008). Single-molecule force spectroscopy: optical tweezers, magnetic tweezers and atomic force microscopy. *Nat. Methods* **5**, 491-505.

Nguyen, J. P., Shipley, F. B., Linder, A. N., Plummer, G. S., Liu, M., Setru, S. U., Shaevitz, J. W. and Leifer, A. M. (2016). Whole-brain calcium imaging with cellular resolution in freely behaving Caenorhabditis elegans. *Proc. Natl. Acad. Sci. USA* **113**, E1074-E1081.

Nixon, S. J., Webb, R. I., Floetenmeyer, M., Schieber, N., Lo, H. P. and Parton, R. G. (2009). A single method for cryofixation and correlative light, electron microscopy and tomography of zebrafish embryos. *Traffic* **10**, 131-136.

Ossola, D., Amarouch, M.-Y., Behr, P., Vörös, J., Abriel, H. and Zambelli, T. (2015). Force-controlled patch clamp of beating cardiac cells. *Nano Lett.* **15**, 1743-1750.

Paez-Segala, M. G., Sun, M. G., Shtengel, G., Viswanathan, S., Baird, M. A., Macklin, J. J., Patel, R., Allen, J. R., Howe, E. S., Piszczek, G. et al. (2015). Fixation-resistant photoactivatable fluorescent proteins for CLEM. *Nat. Methods* **12**, 215-218, 4 p following 218.

Pampaloni, F., Chang, B.-J. and Stelzer, E. H. K. (2015). Light sheet-based fluorescence microscopy (LSFM) for the quantitative imaging of cells and tissues. *Cell Tissue Res.* **360**, 129-141.

Pantazis, P., Maloney, J., Wu, D. and Fraser, S. E. (2010). Second harmonic generating (SHG) nanoprobes for in vivo imaging. *Proc. Natl. Acad. Sci. USA* **107**, 14535-14540.

Paszek, M. J., DuFort, C. C., Rossier, O., Bainer, R., Mouw, J. K., Godula, K., Hudak, J. E., Lakins, J. N., Wijekoon, A. C., Cassereau, L. et al. (2014). The cancer glycocalyx mechanically primes integrin-mediated growth and survival. *Nature* **511**, 319-325.

Peddie, C. J., Liv, N., Hoogenboom, J. P. and Collinson, L. M. (2014). Integrated light and scanning electron microscopy of GFP-expressing cells. *Methods Cell Biol.* **124**, 363-389.

Peralta, M., Steed, E., Harlepp, S., González-Rosa, J. M., Monduc, F., Ariza-Cosano, A., Cortés, A., Rayón, T., Gómez-Skarmeta, J.-L., Zapata, A. et al. (2013). Heartbeat-driven pericardial fluid forces contribute to epicardium morphogenesis. *Curr. Biol.* **23**, 1726-1735.

Pérez-Alvarez, A., Araque, A. and Martín, E. D. (2013). Confocal microscopy for astrocyte in vivo imaging: recycle and reuse in microscopy *Front. Cell Neurosci.* **7**, 51.

Perrault, C. M., Brugues, A., Bazellieres, E., Ricco, P., Lacroix, D. and Trepat, X. (2015). Traction forces of endothelial cells under slow shear flow. *Biophys. J.* **109**, 1533-1536.

Peticolas, W. L., Goldsborough, J. P. and Rieckhoff, K. E. (1963). Double photon excitation in organic crystals. *Phys. Rev. Lett.* **10**, 43-45.

Planchon, T. A., Gao, L., Milkie, D. E., Davidson, M. W., Galbraith, J. A., Galbraith, C. G. and Betzig, E. (2011). Rapid three-dimensional isotropic imaging of living cells using Bessel beam plane illumination. *Nat. Methods* **8**, 417-423.

Plodinec, M., Loparic, M., Monnier, C. A., Obermann, E. C., Zanetti-Dallenbach, R., Oertle P., Hyotyla, J. T., Aebi, U., Bentires-Alj, M., Lim, R. Y. and Schoenenberger, C. A. (2012). *Nat. Nanotechnol.* **11**, 57-65.

Raab, M., Gentili, M., de Belly, H., Thiam, H. R., Vargas, P., Jimenez, A. J., Lautenschlaeger, F., Voituriez, R., Lennon-Duménil, A. M., Manel, N. et al. (2016). ESCRT III repairs nuclear envelope ruptures during cell migration to limit DNA damage and cell death. *Science* **352**, 359-362.

Raman, C. V. and Krishnan, K. S. (1928). A new type of secondary radiation. *Nature* **121**, 501-502.

Ramspacher, C., Steed, E., Boselli, F., Ferreira, R., Faggianelli, N., Roth, S., Spiegelhalter, C., Messaddeq, N., Trinh, L., Liebling, M. et al. (2015). Developmental alterations in heart biomechanics and skeletal muscle function in desmin mutants suggest an early pathological root for desminopathies. *Cell Rep.* **11**, 1564-1576.

Rankin, B. R., Moneron, G., Wurm, C. A., Nelson, J. C., Walter, A., Schwarzer, D., Schroeder, J., Colón-Ramos, D. A. and Hell, S. W. (2011). Nanoscopy in a living multicellular organism expressing GFP. *Biophys. J.* **100**, L63-L65.

Rego, E. H., Shao, L., Macklin, J. J., Winoto, L., Johansson, G. A., Kamps-Hughes, N., Davidson, M. W. and Gustafsson, M. G. L. (2012). Nonlinear structured-illumination microscopy with a photoswitchable protein reveals cellular structures at 50-nm resolution. *Proc. Natl. Acad. Sci. USA* **109**, E135-E143.

Revach, O.-Y., Weiner, A., Rechav, K., Sabanay, I., Livne, A. and Geiger, B. (2015). Mechanical interplay between invadopodia and the nucleus in cultured cancer cells. *Sci. Rep.* **5**, 9466.

Reynaud, E. G., Kržič, U., Greger, K. and Stelzer, E. H. K. (2008). Light sheet-based fluorescence microscopy: more dimensions, more photons, and less photodamage. *HFSP J.* **2**, 266-275.

Ritsma, L., Steller, E. J. A., Beerling, E., Loomans, C. J. M., Zomer, A., Gerlach, C., Vrisekoop, N., Seinstra, D., van Gurp, L., Schäfer, R. et al. (2012). Intravital microscopy through an abdominal imaging window reveals a pre-micrometastasis stage during liver metastasis. *Sci. Transl. Med.* **4**, 158ra145.

Ritsma, L., Ellenbroek, S. I. J., Zomer, A., Snippert, H. J., de Sauvage, F. J., Simons, B. D., Clevers, H. and van Rheenen, J. (2014). Intestinal crypt homeostasis revealed at single-stem-cell level by in vivo live imaging. *Nature* **507**, 362-365.

Rossier, O., Octeau, V., Sibarita, J.-B., Leduc, C., Tessier, B., Nair, D., Gatterdam, V., Destaing, O., Albigès-Rizo, C., Tampé, R. et al. (2012). Integrins β1 and β3 exhibit distinct dynamic nanoscale organizations inside focal adhesions. *Nat. Cell Biol.* **14**, 1057-1067.

Journal of Cell Science • Advance article

Rust, M. J., Bates, M. and Zhuang, X. (2006). Sub-diffraction-limit imaging by stochastic optical reconstruction microscopy (STORM). *Nat. Methods* **3**, 793-796.

Salerno, D., Brogioli, D., Cassina, V., Turchi, D., Beretta, G. L., Seruggia, D., Ziano, R., Zunino, F. and Mantegazza, F. (2010). Magnetic tweezers measurements of the nanomechanical properties of DNA in the presence of drugs. *Nucleic Acids Res.* **38**, 7089-7099.

Scheul, T., Wang, I. and Vial, J.-C. (2014). STED-SPIM made simple. *Opt. Express* **22**, 30852.

Schneider, J., Zahn, J., Maglione, M., Sigrist, S. J., Marquard, J., Chojnacki, J., Kräusslich, H.-G., Sahl, S. J., Engelhardt, J. and Hell, S. W. (2015). Ultrafast, temporally stochastic STED nanoscopy of millisecond dynamics. *Nat. Methods* **12**, 827-830.

Schwarz, U. S. and Soiné, J. R. D. (2015). Traction force microscopy on soft elastic substrates: a guide to recent computational advances. *Biochim. Biophys. Acta Mol. Cell Res.* **1853**, 3095-3104.

Shao, L., Kner, P., Rego, E. H. and Gustafsson, M. G. L. (2011). Super-resolution 3D microscopy of live whole cells using structured illumination. *Nat. Methods* **8**, 1044-1046.

Shimozawa, T., Yamagata, K., Kondo, T., Hayashi, S., Shitamukai, A., Konno, D., Matsuzaki, F., Takayama, J., Onami, S., Nakayama, H. et al. (2013). Improving spinning disk confocal microscopy by preventing pinhole cross-talk for intravital imaging. *Proc. Natl. Acad. Sci. USA* **110**, 3399-3404.

Shu, X., Lev-Ram, V., Deerinck, T. J., Qi, Y., Ramko, E. B., Davidson, M. W., Jin, Y., Ellisman, M. H. and Tsien, R. Y. (2011). A genetically encoded tag for correlated light and electron microscopy of intact cells, tissues, and organisms. *PLoS Biol.* **9**, e1001041.

Skruzny, M., Desfosses, A., Prinz, S., Dodonova, S. O., Gieras, A., Uetrecht, C., Jakobi, A. J., Abella, M., Hagen, W. J. H., Schulz, J. et al. (2015). An organized co-assembly of clathrin adaptors is essential for endocytosis. *Dev. Cell* **33**, 150-162.

Smith, S. B., Cui, Y. and Bustamante, C. (1996). Overstretching B-DNA: the elastic response of individual double-stranded and single-stranded DNA molecules. *Science* **271**, 795-799.

Spiegelhalter, C., Tosch, V., Hentsch, D., Koch, M., Kessler, P., Schwab, Y. and Laporte, J. (2010). From dynamic live cell imaging to 3D ultrastructure: novel integrated methods for high pressure freezing and correlative light-electron microscopy. *PLoS ONE* **5**, e9014.

Stegmaier, J., Amat, F., Lemon, W. C., McDole, K., Wan, Y., Teodoro, G., Mikut, R. and Keller, P. J. (2016). Real-time three-dimensional cell segmentation in large-scale microscopy data of developing embryos. *Dev. Cell* **36**, 225-240.

Strick, T. R., Allemand, J.-F., Bensimon, D., Bensimon, A. and Croquette, V. (1996). The elasticity of a single supercoiled DNA molecule. *Science* **271**, 1835-1837.

Sugimura, K., Lenne, P.-F. and Graner, F. (2016). Measuring forces and stresses in situ in living tissues. *Development* **143**, 186-196.

Takasaki, K. T., Ding, J. B. and Sabatini, B. L. (2013). Live-cell superresolution imaging by pulsed STED two-photon excitation microscopy. *Biophys. J.* **104**, 770-777.

Tanase, M., Biais, N. and Sheetz, M. (2007). Magnetic tweezers in cell biology. *Methods Cell Biol.* **83**, 473-493.

Tartibi, M., Liu, Y. X., Liu, G.-Y. and Komvopoulos, K. (2015). Single-cell mechanics – An experimental–computational method for quantifying the membrane–cytoskeleton elasticity of cells. *Acta Biomater.* **27**, 224-235.

Tello, M., Spenlé, C., Hemmerlé, J., Mercier, L., Fabre, R., Allio, G., Simon-Assmann, P. and Goetz, J. G. (2016). Generating and characterizing the mechanical properties of cell-derived matrices using atomic force microscopy. *Methods* **94**, 85-100.

Theer, P., Hasan, M. T. and Denk, W. (2003). Two-photon imaging to a depth of 1000 µm in living brains by use of a Ti:Al2O3 regenerative amplifier. **28**, 1022-1024.

Théry, M., Pépin, A., Dressaire, E., Chen, Y. and Bornens, M. (2006). Cell distribution of stress fibres in response to the geometry of the adhesive environment. *Cell Motil. Cytoskeleton* **63**, 341-355.

Thiam, H.-R., Vargas, P., Carpi, N., Crespo, C. L., Raab, M., Terriac, E., King, M. C., Jacobelli, J., Alberts, A. S., Stradal, T. et al. (2016). Perinuclear Arp2/3-driven actin polymerization enables nuclear deformation to facilitate cell migration through complex environments. *Nat. Commun.* **7**, 10997.

Tomer, R., Khairy, K., Amat, F. and Keller, P. J. (2012). Quantitative high-speed imaging of entire developing embryos with simultaneous multiview light-sheet microscopy. *Nat. Methods* **9**, 755-763.

Truong, T. V., Supatto, W., Koos, D. S., Choi, J. M. and Fraser, S. E. (2011). Deep and fast live imaging with two-photon scanned light-sheet microscopy. *Nat. Methods* **8**, 757-760.

Truong Quang, B.-A., Mani, M., Markova, O., Lecuit, T. and Lenne, P.-F. (2013). Principles of E-cadherin supramolecular organization in vivo. *Curr. Biol.* **23**, 2197-2207.

Vangindertael, J., Beets, I., Rocha, S., Dedecker, P., Schoofs, L., Vanhoorelbeeke, K., Hofkens, J. and Mizuno, H. (2015). Super-resolution mapping of glutamate receptors in C. elegans by confocal correlated PALM. *Sci. Rep.* **5**, 13532.

Vartanian, K. B., Kirkpatrick, S. J., Hanson, S. R. and Hinds, M. T. (2008). Endothelial cell cytoskeletal alignment independent of fluid shear stress on micropatterned surfaces. *Biochem. Biophys. Res. Commun.* **371**, 787-792.

Versaevel, M., Grevesse, T. and Gabriele, S. (2012). Spatial coordination between cell and nuclear shape within micropatterned endothelial cells. *Nat. Commun.* **3**, 671.

Vicidomini, G., Moneron, G., Han, K. Y., Westphal, V., Ta, H., Reuss, M., Engelhardt, J., Eggeling, C. and Hell, S. W. (2011). Sharper low-power STED nanoscopy by time gating. *Nat. Methods* **8**, 571-573.

Villringer, A., Them, A., Lindauer, U., Einhaupl, K. and Dirnagl, U. (1994). Capillary perfusion of the rat brain cortex. *Circ. Res.* **75**, 55-62.

Wang, W., Wyckoff, J. B., Frohlich, V. C., Oleynikov, Y., Hüttelmaier, S., Zavadil, J., Cermak, L., Bottinger, E. P., Singer, R. H., White, J. G. et al. (2002). Single cell behavior in metastatic primary mammary tumors correlated with gene expression patterns revealed by molecular profiling. *Cancer Res.* **62**, 6278-6288.

Watanabe, S., Punge, A., Hollopeter, G., Willig, K. I., Hobson, R. J., Davis, M. W., Hell, S. W. and Jorgensen, E. M. (2011). Protein localization in electron micrographs using fluorescence nanoscopy. *Nat. Methods* **8**, 80-84.

Weber, M. and Huisken, J. (2011). Light sheet microscopy for real-time developmental biology. *Curr. Opin. Genet. Dev.* **21**, 566-572.

Weigelin, B., Bakker, G.-J. and Friedl, P. (2016). Third harmonic generation microscopy of cells and tissue organization. *J. Cell Sci* **129**, 245-255.

Weisshart, K. (2014). The basic principle of airyscanning. *Zeiss*.

Welf, E. S., Driscoll, M. K., Dean, K. M., Schäfer, C., Chu, J., Davidson, M. W., Lin, M. Z., Danuser, G. and Fiolka, R. (2016). Quantitative multiscale cell imaging in controlled 3D microenvironments. *Dev. Cell* **36**, 462-475.

Westphal, V., Rizzoli, S. O., Lauterbach, M. A., Kamin, D., Jahn, R. and Hell, S. W. (2008). Video-rate far-field optical nanoscopy dissects synaptic vesicle movement. *Science* **320**, 246-249.

Willig, K. I., Harke, B., Medda, R. and Hell, S. W. (2007). STED microscopy with continuous wave beams. *Nat. Methods* **4**, 915-918.

Willig, K. I., Steffens, H., Gregor, C., Herholt, A., Rossner, M. J. and Hell, S. W. (2014). Nanoscopy of filamentous actin in cortical dendrites of a living mouse. *Biophys. J.* **106**, L01-L03.

Wolf, S., Supatto, W., Debrégeas, G., Mahou, P., Kruglik, S. G., Sintes, J.-M., Beaurepaire, E. and Candelier, R. (2015). Whole-brain functional imaging with two-photon light-sheet microscopy. *Nat. Methods* **12**, 379-380.

Xiao, Y., Faucherre, A., Pola-Morell, L., Heddleston, J. M., Liu, T.-L., Chew, T.-L., Sato, F., Sehara-Fujisawa, A., Kawakami, K. and López-Schier, H. (2015). High-resolution live imaging reveals axon-glia interactions during peripheral nerve injury and repair in zebrafish. *Dis. Model. Mech.* **8**, 553-564.

Yamashita, N., Morita, M., Legant, W. R., Chen, B.-C., Betzig, E., Yokota, H. and Mimori-Kiyosue, Y. (2015). Three-dimensional tracking of plus-tips by lattice light-sheet microscopy permits the quantification of microtubule growth trajectories within the mitotic apparatus. *J. Biomed. Opt.* **20**, 101206-101206.

York, A. G., Parekh, S. H., Nogare, D. D., Fischer, R. S., Temprine, K., Mione, M., Chitnis, A. B., Combs, C. A. and Shroff, H. (2012). Resolution doubling in live, multicellular organisms via multifocal structured illumination microscopy. *Nat. Methods* **9**, 749-754.

York, A. G., Chandris, P., Nogare, D. D., Head, J., Wawrzusin, P., Fischer, R. S., Chitnis, A. and Shroff, H. (2013). Instant super-resolution imaging in live cells and embryos via analog image processing. *Nat. Methods* **10**, 1122-1126.

Zhong, M.-C., Wei, X.-B., Zhou, J.-H., Wang, Z.-Q. and Li, Y.-M. (2013). Trapping red blood cells in living animals using optical tweezers. *Nat. Commun.* **4**, 1768.

Zomer, A., Maynard, C., Verweij, F. J., Kamermans, A., Schäfer, R., Beerling, E., Schiffelers, R. M., de Wit, E., Berenguer, J., Ellenbroek, S. I. J. et al. (2015). In Vivo imaging reveals extracellular vesicle-mediated phenocopying of metastatic behavior. *Cell* **161**, 1046-1057.

1.6 Objectifs du travail de thèse

Après formation de la tumeur primaire, les cellules cancéreuses s'échappent de celle-ci en dégradant la membrane basale. Elles migrent dans la MEC et gagnent la circulation sanguine ou lymphatique par intravasation. Après avoir survécu aux forces de cisaillement dans la circulation sanguine les cellules vont être capables, par extravasation, de former des foyers cancéreux secondaires appelés métastases. La métastase constitue la première cause de mortalité des personnes affectées par cette maladie. La compréhension des phénomènes d'entrée de la cellule cancéreuse dans la circulation sanguine (intravasation) et de sa sortie (extravasation) afin d'envahir un organe à distance est une étape clé dans la lutte contre le cancer.

Les techniques de microscopie *in vivo* actuelles appliquées au petit animal permettent d'imager les différentes étapes qui conduisent à la formation de métastases de manière dynamique. Parmi ces techniques, la microscopie multiphotonique est la technique de prédilection pour imager en profondeur les tissus de façon non invasive. Cependant, cette technique n'offre pas la résolution spatiale nécessaire pour décrire l'ultrastructure de la machinerie cellulaire mise en jeu pour envahir l'organisme. La technique de microscopie corrélative (CLEM : Correlative Light and Electron Microscopy) permet de combiner les informations dynamiques obtenues grâce à la microscopie photonique à la très haute résolution spatiale fournie par la microscopie électronique. De nombreuses procédures de CLEM appliquées à de plus petits organismes (*C. elegans*, poisson zèbre) existent mais restaient jusqu'à tout récemment non-applicables aux petits mammifères.

Mon projet de thèse se divisait en trois axes majeurs :

1. Développement d'une méthode d'imagerie non invasive de xénogreffes de cellules tumorales chez la souris
2. Création d'une procédure de microscopie corrélative appliquée à la souris
3. Etude d'une structure impliquée dans l'invasion tumorale à l'échelle ultrastructurale à la fois *in vitro* et *in vivo*

2 Résultats

2.1 Microscopie intravitale dans l'oreille de souris

2.1.1 Contexte

Ce travail a été réalisé en collaboration avec l'équipe « Physiopathologie des maladies neuromusculaires » de J. Laporte à l'Institut de Génétique et de Biologie Moléculaire et Cellulaire (IGBMC, Illkirch, France).

Un des thèmes de recherche est l'étude des myopathies centronucléaires (CNM). Les CNM sont un groupe de myopathies congénitales définies par la présence d'un nombre anormalement élevé de fibres musculaires qui ont leurs noyaux situés au milieu de la fibre (Romero, 2010). Ces myopathies ont pour conséquence une faiblesse musculaire ainsi qu'une atrophie musculaire. Les caractéristiques histopathologiques de cette maladie est la position centrale du noyau dans les fibres musculaires ainsi qu'une hypotrophie des fibres musculaires.

Trois gènes codant pour trois protéines impliquées dans le remodelage membranaire sont responsables de cette maladie.

Le gène MTM1 code pour la 3'-phosphoinositides phosphatase myotubularin 1 (MTM1), une protéine qui contrôle le métabolisme des phospholipides membranaires, la mutation de cette protéine est responsable de la forme de CNM la plus sévère.

Le gène amphiphysin 2 (AMPH2/BIN1) est impliquée dans le remodelage, notamment la courbature, de la membrane ainsi que dans l'organisation des tubules T. Le degré de sévérité de CNM est intermédiaire.

Le gène dynamin-2 (DNM2) qui code une GTPase impliquée dans l'endocytose et le trafic membranaire. La mutation de DNM2 entraine une CNM moins sévère comparée aux deux premiers cas (Jungbluth and Gautel, 2014)

Le but de cette collaboration était de développer une méthode d'imagerie non invasive rapide à mettre en œuvre chez la souris. Cette technique doit permettre à l'équipe de recherche de réaliser un suivi longitudinal de la maladie afin de comprendre les premières étapes qui correspond à la réorganisation des organites et des noyaux dans la fibre musculaire.

2.1.2 Principaux résultats

L'oreille de la souris a été choisie car le pavillon contient des muscles striés squelettiques qui pourraient être facilement visualisable par microscopie multiphotonique à travers la peau. Cette méthode aurait pour avantage de ne pas à devoir exposer chirurgicalement le muscle tibial antérieur

(Musculum tibialis antérior), classiquement utilisé pour l'étude des CNM, permettant ainsi le suivi de l'évolution de la maladie au cours du temps.

Le pavillon de l'oreille de la souris a aussi d'autres avantages pour l'imagerie car c'est un tissu facilement accessible, fin et qui n'est pas soumis à des mouvements de contractions ou de respiration.

Un support spécifique imprimé en 3D (Figure 26) a été créé pour pouvoir facilement disposer la souris et son oreille sous l'objectif du microscope. Ce support permet de contrer la courbure naturelle du pavillon de l'oreille et de maintenir l'oreille plate sous l'objectif du microscope. Une ouverture présente dans le support permet de recoleter le signal SHG par un détecteur en position trans. Ce choix a été fait car le signal SHG est émis préférentiellement dans le sens de propagation du laser.
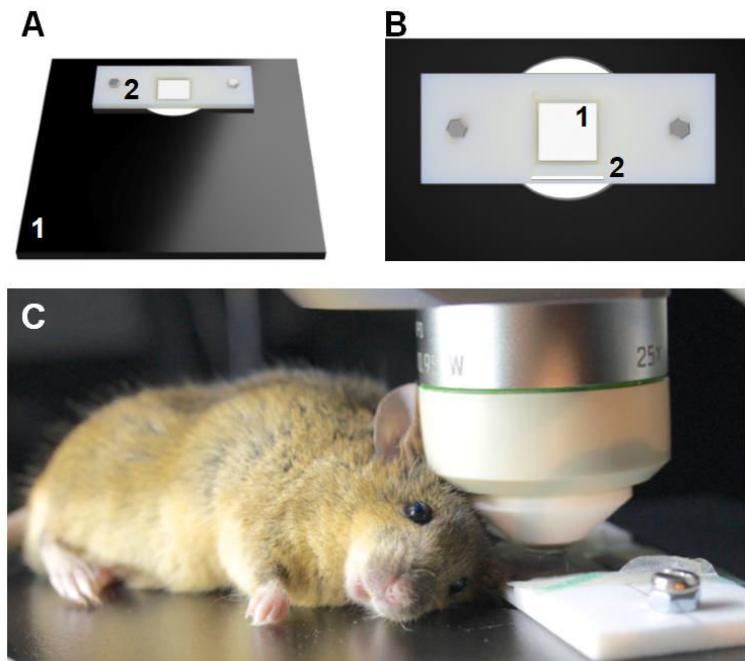
*Figure 26 : **Support spécifique permettant de maintenir la souris et son oreille sous l'objectif du microscope**. A : Le support est constitué de deux parties. 1 : permet de maintenir la souris anesthésiée. 2 : permet de maintenir le pavillon de l'oreille à plat sous l'objectif du microscope. B : Le support pour l'oreille comporte deux ouvertures. 1 : cette ouverture permet de récolter le signal SHG via un détecteur en position trans. Une lamelle de verre recouvre cette ouverture. 2 : l'oreille est glissée par cette fente qui va contraindre le pavillon à se maintenir à plat. C : La souris anesthésiée au cours d'une séance d'imagerie de son oreille.*

Une approche par microscopie multiphotonique a ensuite été validée par l'étude de l'organisation des fibres musculaires et des jonctions neuromusculaires chez des souris KO pour le gène MTM1.

2.1.3 Manuscrit n°2: In vivo imaging of skeletal muscle in mice highlights muscle defects in a model of myotubular myopathy

Taylor & Francis
Taylor & Francis Group

In vivo imaging of skeletal muscle in mice highlights muscle defects in a model of myotubular myopathy

Luc Mercier[a,b,c,d], Johann Böhm[b,d,e,f,g], Nina Fekonja[a,c,d], Guillaume Allio[a,c,d], Yves Lutz[b,e,f], Marc Koch[b,e,f], Jacky G. Goetz[a,c,d], and Jocelyn Laporte[b,d,e,f,g]

[a]Inserm U1109, MN3T, Strasbourg, France; [b]Institut de Génétique et de Biologie Moléculaire et Cellulaire (IGBMC), Illkirch, France; [c]LabEx Medalis, Université de Strasbourg, Strasbourg, France; [d]Fédération de Médecine Translationnelle de Strasbourg (FMTS), Strasbourg, France; [e]Institut National de la Santé et de la Recherche Médicale, U964, Illkirch, France; [f]Centre National de la Recherche Scientifique, UMR7104, Illkirch, France; [g]Collège de France, Chaire de Génétique Humaine, Illkirch, France

ABSTRACT

Skeletal muscle structure and function are altered in different myopathies. However, the understanding of the molecular and cellular mechanisms mainly rely on *in vitro* and *ex vivo* investigations in mammalian models. In order to monitor *in vivo* the intracellular structure of the neuromuscular system in its environment under normal and pathological conditions, we set-up and validated non-invasive imaging of ear and leg muscles in mice. This original approach allows simultaneous imaging of different cellular and intracellular structures such as neuromuscular junctions and sarcomeres, reconstruction of the 3D architecture of the neuromuscular system, and video recording of dynamic events such as spontaneous muscle fiber contraction. Second harmonic generation was combined with vital dyes and fluorescent-coupled molecules. Skin pigmentation, although limiting, did not prevent intravital imaging. Using this versatile toolbox on the *Mtm1* knockout mouse, a model for myotubular myopathy which is a severe congenital myopathy in human, we identified several hallmarks of the disease such as defects in fiber size and neuromuscular junction shape. Intravital imaging of the neuromuscular system paves the way for the follow-up of disease progression or/and disease amelioration upon therapeutic tests. It has also the potential to reduce the number of animals needed to reach scientific conclusions.

Introduction

Skeletal muscle represents nearly half of the dried body weight and is essential for movement, energy homeostasis and thermogenesis. Skeletal muscle fibers are syncytia containing hundreds of nuclei, span up to 20cm in human and are innervated through the neuromuscular junction. The sarcomere is the main unit of the contractile apparatus and is mainly composed of actin and myosin filaments.[1] At the neuromuscular junction (NMJ), the nerve action potential triggers the release of acetylcholine that binds to the acetylcholine receptors to create a depolarization of the muscle sarcolemma. Depolarization is sensed by voltage sensor channels located at the triad, the membrane structure sustaining excitation-contraction coupling, and induces the release of calcium from the sarcoplasmic reticulum store to the cytoplasm. Calcium binds and activates troponin followed by sliding of the actin and myosin filaments on each other.

Skeletal muscle structure and function are altered in a plethora of genetic diseases, as myopathies,[1] while progressive muscle loss as cachexia and sarcopenia are hallmarks of AIDS and cancer and a main sign of aging. Mutations in about 150 genes were implicated in myopathies and muscular dystrophies to date.[2] Among the most severe myopathies, myotubular myopathy (also called X-linked centronuclear myopathy, XLMTM, OMIM #310400) is associated with neonatal hypotonia, muscle weakness and breathing difficulties in male patients and is due to loss-of-function mutations in the *MTM1* gene.[3-7] Histopathological hallmarks comprise fiber hypotrophy and abnormal organelle positioning.[8] Different potential causes of the muscle weakness have been proposed for XLMTM, as triad structural defects,[9-11] unbalanced autophagy and protein homeostasis,[12-14] satellite cells alterations[15] or anomalies of the neuromuscular junction.[16,17] However,

monitoring cellular pathological hallmarks in living mammalian models of XLMTM was not achieved to date, and the knowledge of the cellular pathology of XLMTM mainly relies on *in vitro* or *ex vivo* observations in mammalian models,[9,13,18-21] or on data from more evolutionary-distant models as zebrafish,[10,17] drosophila,[22] C. elegans[23] or yeast.[18,24,25]

Monitoring the structure of muscles in place is thus of importance to follow disease progression and potential amelioration upon treatments. A few studies previously reported in vivo microscopy of skeletal muscle.[26,27] While some disease hallmarks can be recapitulated *in vitro*, intravital imaging (IVM) offers a window to the progression of the disease, and its associated cellular events such as subcellular membrane trafficking,[28] in a living animal.[29-31] Owing to its superior imaging property and its compatibility with non-linear optical processes, Two-Photon-Excitation-Microscopy (2PEM) allows simultaneous tracking of fluorescent events *in vivo* as well as detection of non-centrosymetric molecules by second harmonic generation (SHG) such as myosin in muscle,[32] and collagen in the extracellular matrix.[33,34] 2PEM and SHG were previously used to assess the structure of the contractile apparatus and tubular system in isolated mouse muscle fibers,[35] in preserved muscles from myopathic mice,[36,37] or in muscle in place in the animal after removal of the skin.[38] Minimally invasive imaging of muscle sarcomeres was achieved in mouse and human using microendoscopes.[39,40] However, non-invasive imaging of skeletal muscle under normal and pathological conditions in living mice was not extensively reported.

In order to monitor the intracellular structure of muscle fibers and the surrounding environment under normal and pathological conditions, we set-up and validated non-invasive imaging of ear and leg muscles, allowing simultaneous imaging of different cellular structures, reconstruction and visualization of the 3D architecture of the neuromuscular system in its environment, and video recording of dynamic events as muscle fiber contraction. Intravital analysis of a XLMTM murine model highlighted several pathological hallmarks of the disease.

Materials and methods

Animals

BALB/c and 129/SvPas mouse strains were used. 129/SvPas *Mtm1-/y* mice modeling XLMTM were previously described.[9] Animal experimentations were approved by IGBMC/ICS institutional review board (N° 2012-133).

Confocal macroscope imaging

Prior to imaging, the mice were either anesthetized via intra-peritoneal injection of a ketamine (100 mg/kg) and xylazine (10 mg/kg) mix, or sacrificed. When the skin was removed, the following dyes were applied in a 50% glycerol-PBS solution on the bare muscle: Hoechst 33342 (100 ug/ml), DiOC6 (100 uM), Cell Mask deep red (500 ug/ml), cresyl violet (0.3%), and α-Bungarotoxin (1 ug/ml). Anesthetized mice were kept at a constant temperature of 28°C for preserving the mouse body temperature around 37°C and positioned under the Leica Macrofluo confocal macroscope A rectal probe may also be used to monitor body temperature of the experimental mouse throughout the anesthesia and imaging session. To image muscle contraction, the macroscope was equipped with a Leica PLAN APO 5x lwd objective (NA: 0.5), a spinning disk head (Yokogawa CSU22) and an EMCCD camera (Andor, iXon+). Time-lapse acquisitions at 64–73 frames/s displaying significant muscle contraction were analyzed by tracking single sarcomeres over time (Fig. 4, movies S2-3). Relative muscle contraction was assessed by measuring the distance spanning 50 sarcomeres over time (Fig. 4).

2-Photon-excitation microscopy (2PEM) imaging

Before 2PEM imaging, the mice were first anesthetized through intra-peritoneal injection of a mixture of ketamine (100 mg/kg) and xylazine (10 mg/kg). The NMJ were stained by subcutaneous injection of α-bungarotoxin conjugate to green fluorochrome CF488A (Biotium, 00005) at 2,5 μg/ml. Evans Blue (100 μl , 10 mg/ml in PBS, E-2129 Sigma-Aldrich) was administrated via retro-orbital injection in order to allow imaging of the blood vasculature. Alternatively, fluorescent dextran can also be administrated as described previously.[41] The mouse was maintained anesthetised during the whole imaging process. The mouse ear was imaged as previously described.[41,42] The anesthetized mouse was mounted on a homemade holder.[41,43] The mice were then disposed on the stage of an upright Leica SP5X MP (Leica microsystems) and the temperature was set at 28°C for preserving the mouse body temperature around 37°C. A single excitation wavelength at 940 nm (Chameleon

Ultra II, Coherent) was used for 2PEM and recorded using a 25x 0.95 N.A. or 20x 1 N.A. water immersion objectives. Non-descanned detectors (NDD) were used to collect the emission signal of the CF488A at 510 nm and the Evans blue at 680 nm. Second harmonic generation was detected with a trans-detector through a single-band bandpass filter 470/22 nm. As described previously, second harmonic generation occurs mostly from *2PEM* of non-centrosymetric structures, and is restricted to collagen fibers and striated muscle myosin rod domains[44] in mammalian soft tissues. Consecutive images of 512 × 512 pixels (pixel size: 0.3 μm in x/y, 1 μm in z) were acquired at 0.4 frames/s.

Image processing, single particle tracking and analysis

The 2PEM datasets were analyzed using Fiji.[45] The module *Analyze Particles* was used to assess the morphology of the NMJ in 3D. Confocal acquisitions restricted to planes containing the NMJ were stacked onto a maximum z projection and circularity was analyzed on n = 11 NMJ for the WT and n = 12 for the KO mice. The measurements of the sarcomere length were determined by plotting the intensity profiles along a longitudinal line and measuring the distance between 2 consecutive SHG intensity peaks corresponding to myosin.

Results

Set-up for imaging different skeletal muscles

Two different muscles were used for imaging. The tibialis anterior (TA) in the lower hind limb is a mixed muscle containing oxidative and glycolytic fibers, is easily injectable and dissectable, and has been extensively studied in various murine myopathy models (Fig. 1B). As movement artifacts due to breathing significantly challenge IVM of the TA, we analyzed in parallel muscles of the outer ear. These three muscles stripes, which can be seen by backward lighting, are easily accessible and almost insensitive to breathing movements (Fig. 1A). They are thus suitable for non-invasive IVM of subcutaneous tissues and can be used for tracking tumor cell behavior *in vivo*,[41,43] where non-linear 2PEM can be used to track collagen-rich ECM fibers using SHG. We designed a specific holder to constrain the ear for imaging without interfering with

SHG signal detection (Fig. S1). Muscle imaging was performed with several microscopy approaches such as 2PEM for in-depth imaging, spinning disc microscopy for high speed acquisition, or macroconfocal microscopy allowing a good intracellular resolution with wide field of view and large distance between objective and sample (Fig. 1C and 1D). Hematoxilin-eosin staining revealed the general organization of TA and ear muscles (Fig. 1E and 1F), and electron microscopy highlighted the characteristic ultrastructure of muscle fibers with the contractile unit (sarcomere) composed of bands of different contrasts (Fig. 1G and 1H). The ear muscles, poorly described to date, are located on the outside surface of the ear close to the cartilage and underneath the skin and connective tissue. Overall, both ear and TA muscles display a classical skeletal muscle intracellular organization and are easily accessible for imaging. They represent an excellent model for tracking muscle by intravital imaging.

3D multi-color imaging of muscle fibers in their environment

In order to simultaneously label and record different tissues and intracellular structures, we used either non-invasive SHG muscle imaging (2PEM), or imaging upon injection of vital dyes and fluorescently labeled small molecules, or a combination of both approaches.

For ear imaging, blood vessels were visualized by an intravenous injection of Evans blue, neuromuscular junctions were stained with CF488-coupled bungarotoxin, and sarcomeres and collagen fibers were monitored with 2PEM-SHG (Fig. 2A and B). As expected, the NMJ are located at similar depth as the muscle fibers (Fig. 2C). 3D volume reconstruction offers access to the inner architecture of the muscle fibers and the relative position of the NMJ and the vasculature (Fig. 2D and Movie S1). Deep intracellular resolution can be achieved up to hundred micrometers.

For TA muscle, the cytosol was labeled with the cresyl violet, the plasma membrane with CellMask Deep Red, the nuclei with Hoechst, and mitochondria with DIOC6 (Fig. S2). Note that mitochondria labeling highlights the sarcomeric organization as they are enriched in the I-band between the Z-disc and the triad. All these structures can be imaged upon minimal surgery to expose the muscle and make it amenable for
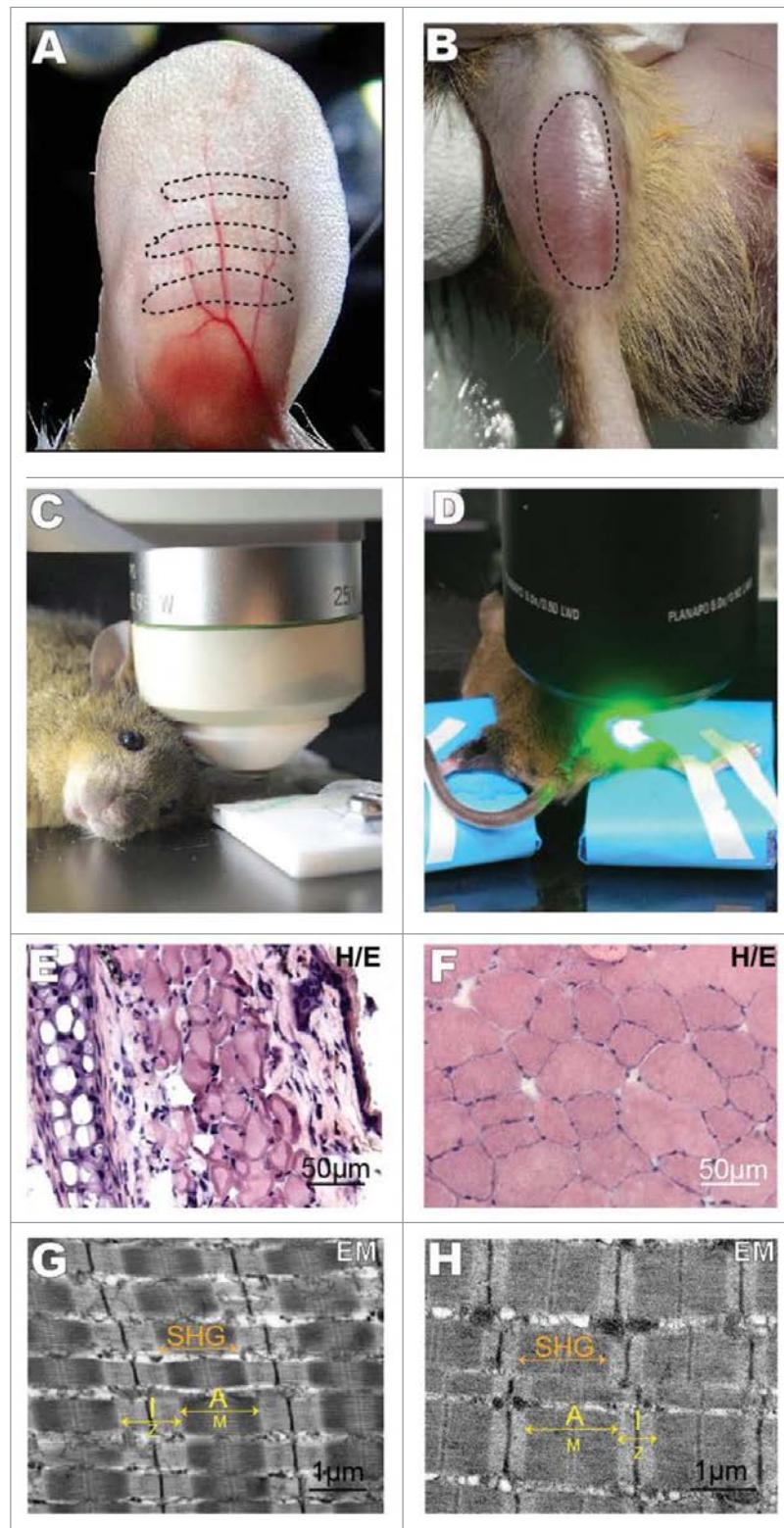
Figure 1. Assessing muscles with 2-photon excitation microscopy and confocal macroscopy. Imaging skeletal muscle in the ear (A, C, E, G), and in the anterior leg (B, D, F, H) of anesthetized mice. (A, B) Position of the ear and TA muscles. (C, D) Set-up for imaging ear muscles with a microscope (C) and TA muscles with a confocal macroscope (D). (E, F) Haematoxilin-eosin staining of transversal sections showing muscle fibers in pink and nuclei in blue. (G, H) Ultrastructure of myofibrils in longitudinal EM sections. The major sarcomeric components have been identified (M and Z lines, I and A bands). The A line is responsible for the SHG pattern.
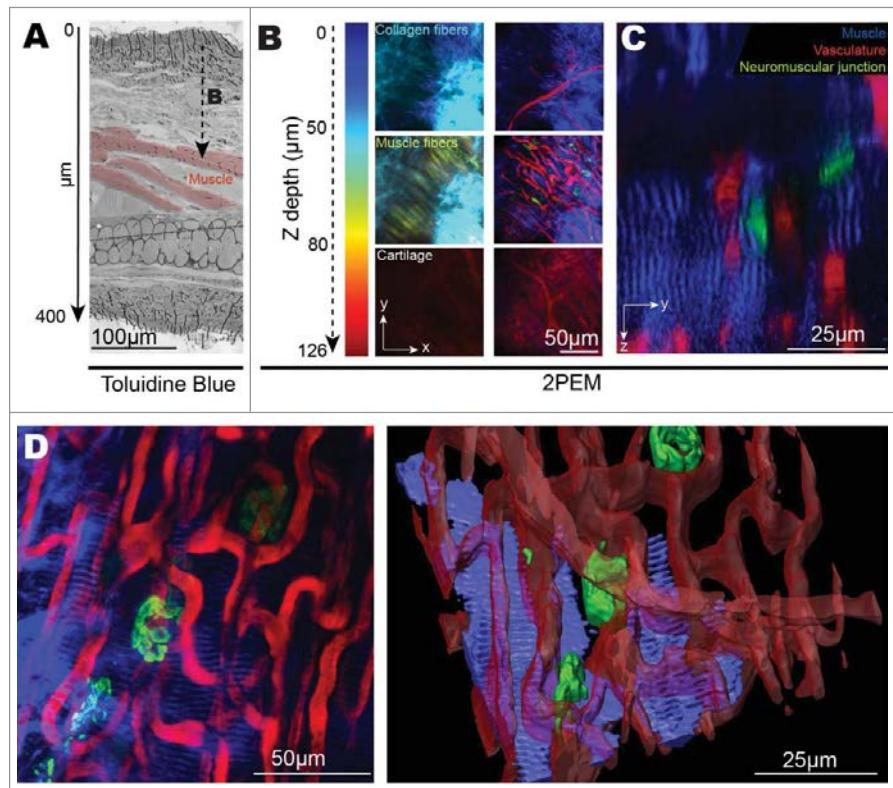
Figure 2. Muscle fibers and pre-labeled neuromuscular junctions can be imaged simultaneously. (A) Light microscopy picture of a section (toluidine blue staining) through the mouse ear. Muscle fibers are colored in pink. (B-D) Imaging of mouse ear structures across the skin. Evans Blue labels the blood flow (red), non-linear 2PEM (second harmonic generation) shows mainly collagen fibers and muscle sarcomeres (blue), and CF488-bungarotoxin labels the neuromuscular junctions (green). (B) Optical section at different Z-depths. The SHG signal (left panel) is color coded according to the z depth. The collagen rich layer of the skin appears in blue and the muscle fibers in yellow. The cartilage is the deepest structure that can be imaged. (C) Transversal imaging with 2PEM-SHG displaying the position of ear muscles relative to neuromuscular junctions and blood vessels. (D) 3D reconstruction of the architecture of the neuromuscular system in its environment. The neuromuscular junctions are in close proximity with the layer of muscle fibers. As the SHG signal drops at significant depth the muscle fiber connected to the upper right NMJ is barely visible.

microscopy. Co-labeling was used to assess the position of several structures in the same fiber.

Taken together, we show that different tissues and intracellular structures can be labeled simultaneously, imaged within a tissue-depth of up to 150 μm (with the Leica TCS LSI macroconfocal or with the upright Leica SP5X MP microscope), and visualized in 3D, thus offering a wide range of structural information.

Impact of skin pigmentation on imaging

We next assessed the impact of the skin and its pigmentation on the resolution and depth of intravital imaging. Intravital imaging of the ear muscles was performed as above using Evans blue for blood vessels (in case the skin was not peeled), 2PEM-SHG for sarcomeres and collagen fibers, and CF488-coupled bungarotoxin for the neuromuscular junctions (Fig. 3). The skin was either removed (Fig. 3A) or left intact (Fig. 3B and 3C). In addition, we performed imaging through the skin of albino BALB/c (white fur and light skin) or 129/SvPas (agouti fur and skin) mice. As expected, the overall image quality was better when performed after skin removal, which can be related to light absorption by pigmented layers of the skin. Of note, skin removal induces bleeding of small capillaries and is therefore incompatible with Evans blue injection. In contrast, image quality and resolution with intact skin was adequate to assess the position and shape of blood vessels and muscle fibers, the sarcomere organization, and the position and complexity of neuromuscular junctions. For example, 2PEM imaging of intact-skin ears allows monitoring of the mentioned structures to a depth of 150 μm (Fig. 2). The higher pigmentation of the agouti skin had a slight impact on image quality, albeit the same structures could be visualized. We noticed that
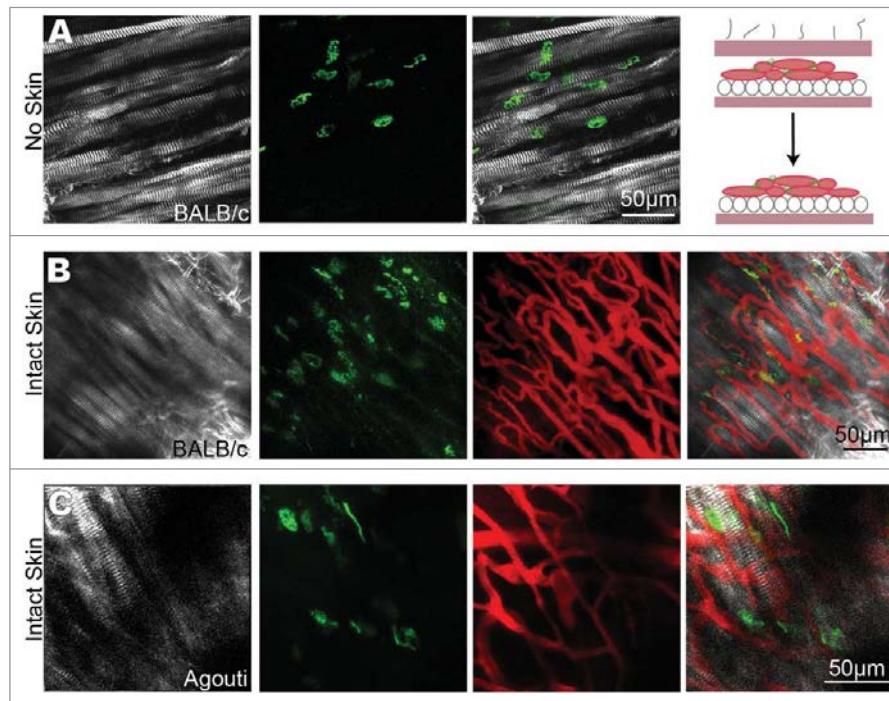
Figure 3. Skin pigmentation does not prevent imaging of muscle fibers and neuromuscular junctions. Intravital imaging of muscle sarcomeres (2PEM-SHG, white), neuromuscular junctions (CF488-bungarotoxin, green) and blood vessels (Evans Blue, red). Optical sections and merge photos on the last right column. (A) Imaging after skin removal of the dorsal surface of the mouse ear. (B) Imaging through the skin of a BALB/c mouse. The skin absorbed and scattered the excitation laser without preventing the imaging of the muscle fibers and labeled structures. (C) Imaging through the skin of an Agouti 129PAS mouse. The pigmentation of the skin has a main impact on the SHG signal noise.

strong skin pigmentation in C57BL/6 mice significantly impaired depth and quality of imaging across the skin, making non-invasive transcutaneous intravital imaging difficult in this specific genetic background (not shown).

The impact of the presence of the skin was also assessed on the TA leg muscle. To label the muscle fibers, we injected and electroporated a plasmid expressing a cytoplasmic GFP protein (Fig. S3). Individual muscle fibers can be clearly identified and imaged over the whole muscle length with the confocal macroscope both with and without the skin.

In conclusion, the murine neuromuscular system can be imaged and studied with a non-invasive protocol, and different labeling/detection methods as fluorescent dyes, SHG and recombinant fluorescent protein could be recorded through the skin, offering a wide palette for studying muscle function *in vivo*.

Recording and analysis of muscle fiber contraction

In vivo imaging can in principle allow recording of dynamic events as muscle contraction encompassing movements in space and through time, and representing a primary role of skeletal muscle. Quite serendipitously, we found single fibers contracting spontaneously and independently of neighboring fibers within the same muscle. The regular positioning of mitochondria within sarcomeres, and thus sarcomeric organization, was labeled with DIOC6 in the TA leg muscle and time recording performed with a spinning disc macroscope (Fig. 4 and Movie S2-3). A whole cycle of a spontaneous contraction lasted for a few seconds, based on the observation of several contractions of the same fiber. The displacement of specific intracellular tractable structures was followed through time for different fibers (Fig. 4C-E, Movie S2-3) and quantification of the total displacement distance confirmed that a single fiber significantly contracts compared to adjacent fibers that display no or weaker contraction. Pixel intensity along a longitudinal lane within a muscle fiber highlights the repetitive organization of sarcomeres (Fig. 4F and 4G). We measured the length of 50 successive sarcomeres through time
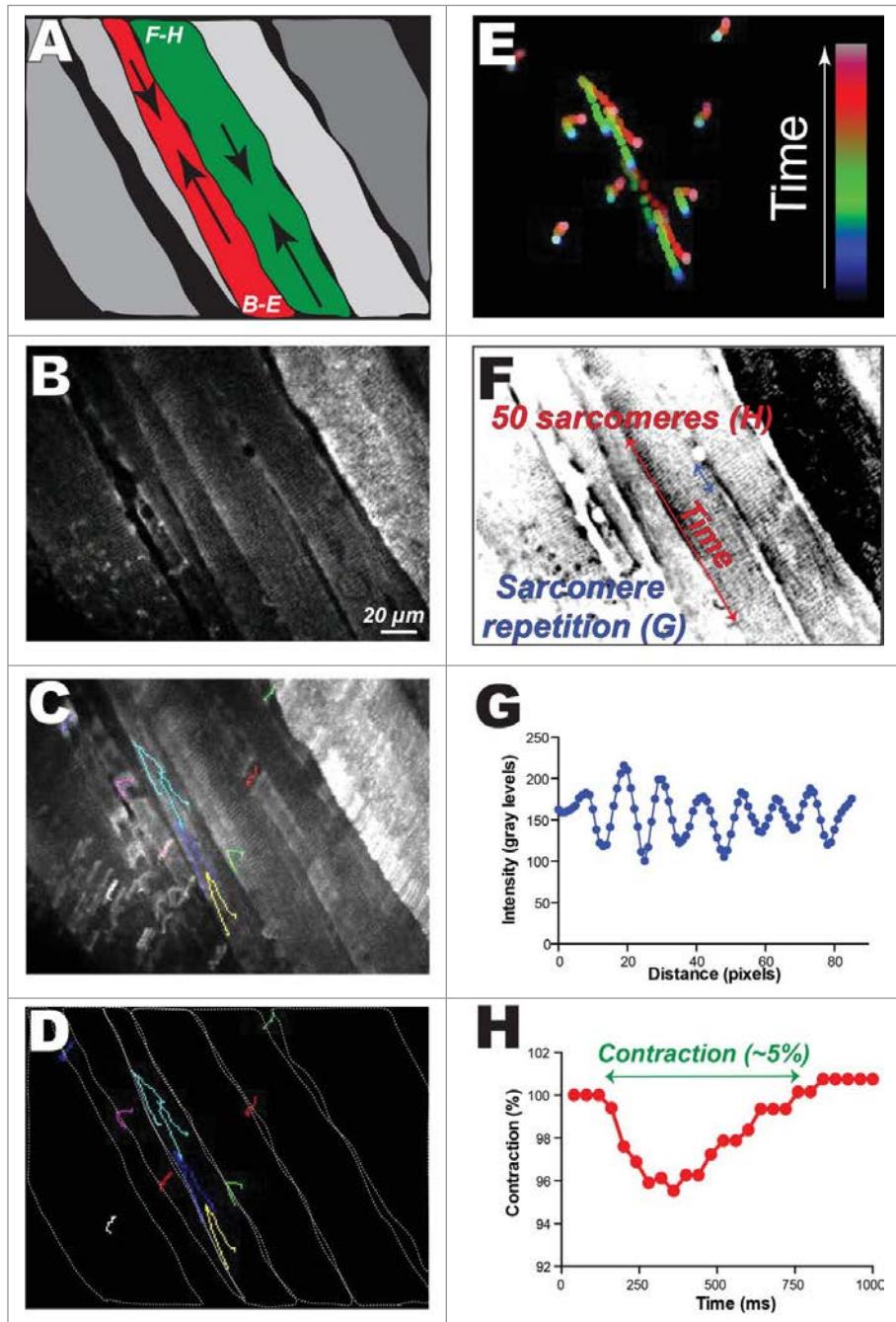
Figure 4. Dynamic monitoring of single muscle fiber contraction. (A) Schematic drawing of the muscle fiber contraction. (B) Image at the start of the video recording; myofiber sarcomeric organization was labeled with the vital dye DIOC6. (C-D) Total movement of regions of interest during the whole spontaneous contraction. (E) Positions of regions of interest through time. (F) Repetitive organization and contraction of sarcomeres assessed through time based on the total length of 50 contiguous sarcomeres. (G) Longitudinal scan line depicting the distance between several contiguous sarcomeres and highlighting their regular spacing. (H) Variation of sarcomere length through the contraction period. The full movie is shown in Video S2.

and calculated the maximal contraction to be 5% (Fig. 4H). The substantial contraction of the whole fiber is thus due to the fact that it contains a large number of sarcomeres.

Intravital analysis of neuromuscular defects in a murine model of myotubular myopathy

Using the different imaging modes, we assessed whether a neuromuscular phenotype can be detected in a mouse

model for myotubular myopathy. The *Mtm1*-/y mouse displays a progressive muscle atrophy and weakness starting at 3 w, and leading to death by 7-12 w.[9,20] Fiber hypotrophy and organelle mis-positioning were previously found in the TA leg muscle, and here we investigated the ear to assess whether this more accessible muscle can be used for disease phenotyping. Upon inspection with back lighting, the 3 muscle stripes of the back ear appeared thinner in the *Mtm1*-/y mouse compared to wild type mice.

Histological analysis with hematoxilin-eosin staining of transversal sections highlighted a typical CNM phenotype comprising thinner ears mainly due to a decrease in total muscle bulk, while other tissues like cartilage were not significantly affected. We also observed fiber size heterogeneity and an increased number of atrophic fibers, as well as abnormal nuclear centralization (Fig. 5A). Measuring the muscle fiber area confirmed that *Mtm1*-/y fibers are overall significantly thinner in the ear compared to WT (Fig. 5B).

Co-imaging of the sarcomeres with 2PEM-SHG, the neuromuscular junction with CF488-coupled bungarotoxin and blood vessels with Evans blue showed that the general organization of the tissues and the position of the muscles were conserved (Fig. 5C). Using SHG, we measured an average fiber width of 16.5 μm for wildtype and 14.7 μm for *Mtm1*-/y mice (Fig. 5E). Notably, there was a large distribution of
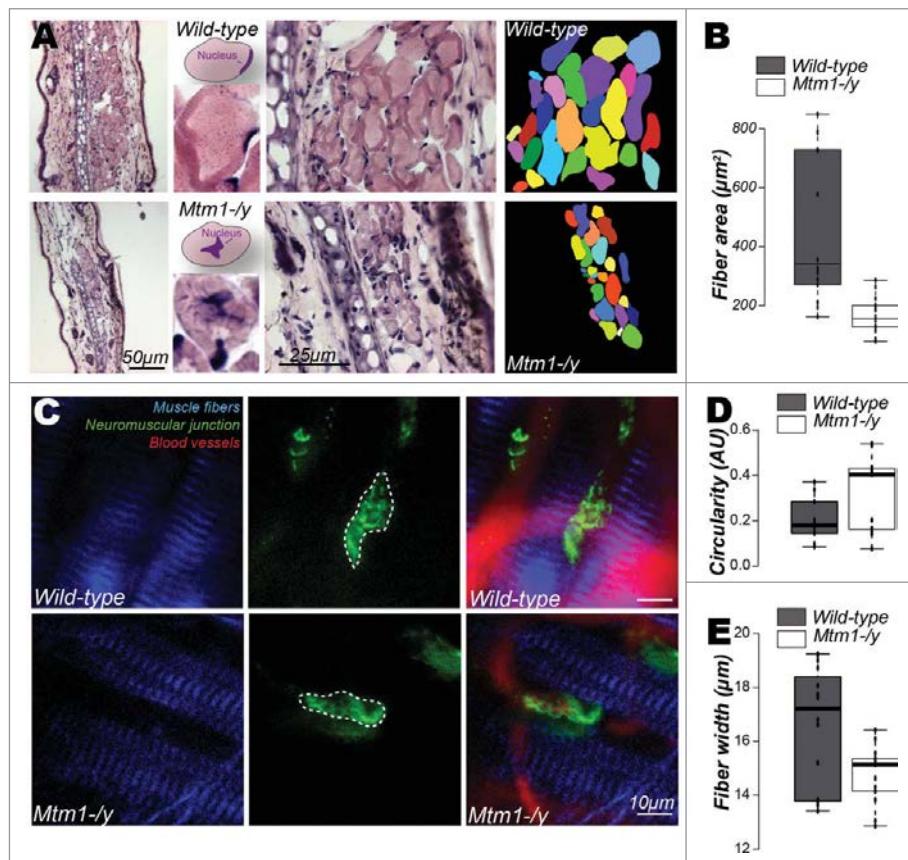
Figure 5. Intravital imaging highlights neuromuscular defects in a murine model of myotubular myopathy. Haematoxilin-eosin staining (A-B) or intravital imaging (C-E) to assess fiber size and neuromuscular junction shape in 5 week old 129/SvPas WT and *Mtm1*-/y mice. (A) The *Mtm1*-/y genotype displays decreased muscle mass, fiber size heterogeneity, a bias toward smaller fibers, and abnormal centralization of nuclei that are normally at the periphery of fibers. On the right, muscle fibers are color coded. (B) Measurement of the fiber area (WT n = 14; mean = 470,2. KO n = 14; mean = 167,7). (C) Intravital imaging of muscle sarcomeres (2PEM-SHG, white), neuromuscular junctions (CF488-bungarotoxin, green) and blood vessels (Evans Blue, red). Optical sections and merge photos in the right column. (D) To assess the shape of the neuromuscular junctions, a circularity coefficient was calculated with 0 representing a lane and 1 a circle (WT n = 10; mean = 0,20, KO n = 11; mean = 0,32). (E) Measurement of the fiber width (WT n = 16; mean = 16,54μm, KO n = 13; mean = 14,77μm). *Mtm1*-/y mice display smaller average fiber width both by histology and intravital imaging, and have rounder neuromuscular junctions. Distribution of the data is presented as whisker plots displaying both minimal and maximal values obtained over a single animal for each genotype.

fiber size in wildtype in the ear muscle, while the *Mtm1*-/y mice lacked the larger fibers. Taken together, both histological and IVM approaches revealed similar structural defects, suggesting that IVM is suitable for disease phenotyping. The neuromuscular junctions were further scrutinized (Fig. 5C-D). Their position compared to the neighboring tissue did not appear different in the *Mtm1*-/y or wildtype genotypes. In addition, we could not observe any obvious change in the density and distribution of neuromuscular junctions in the ears from Mtm1-/y mice. To get insight into their complexity, the shape was assessed and was found different between the 2 genotypes; a significant number of neuromuscular junctions was rounder in the *Mtm1*-/y genotype.

Altogether, these data show that we can detect and quantify significant alterations in the myotubular myopathy *Mtm1*-/y mouse model, especially concerning fiber size and neuromuscular junction shape, supporting that monitoring the ear muscle is a good marker to potentially follow the disease progression or amelioration.

Discussion

Here we describe a non-invasive analysis of the intracellular organization of skeletal muscle and the neuromuscular system in mice by multimodal microscopy combining SHG and fluorescence detection. We demonstrate that this approach is suitable to reveal disease hallmarks in a murine model of myotubular myopathy.

A versatile toolbox for intravital muscle imaging.

In order to analyze the architecture of the murine neuromuscular system *in vivo*, we focused on 2 main structures, the sarcomere and the neuromuscular junction. We monitored the tibialis anterior (TA) in the lower hind limb, as well as muscles in the outer ear. The TA muscle is well described and often used for *ex vivo* analysis, but we noted significant motion artifacts resulting from breathing and/or blood pressure, challenging the construction of image stacks and video recording. The ear muscle was seldomly investigated, but has the advantage to be easily accessible and insensitive to motion artifacts when the ear is constrained. As TA and ear muscles displayed similar structural neuromuscular defects in the myotubular myopathy mouse, we propose the ear muscle as new paradigm for intravital imaging of skeletal muscle.

Multimodal imaging, especially if achievable at the same excitation wavelength, is a powerful approach to combine the analysis of diverse tissues and even subcellular structures at different depths. Here we imaged blood circulation, neuromuscular junctions, collagen, cartilage, and muscle fibers at the same time. This versatility enables 3D reconstruction of specific cells and structures *in situ*, and paves the way to the study of the surface between 2 cell types like the neuromuscular junction in contact or close proximity with a myofiber. The intracellular organization of myofibers can be followed through detection of myosin molecules with SHG, and mitochondria, membranes and nuclei or other organelles that can be labeled fluorescently. It is possible to measure the distance between each sarcomere and thus to deduce the sarcomere length and organization, or the surface occupied by the neuromuscular junction.

In addition, we validated the use of a versatile imaging toolbox by combining SHG with chemical dyes, fluorescence-coupled molecules as bungarotoxin, and recombinant DNA constructs expressing fluorescent proteins. SHG does not require exogenous labeling as it is based on the fluorescence of non-centrosymmetric structures as myosin rod domains that are parallelly aligned in the sarcomere.[32,44,46] Chemical dyes have the advantage to cover a very large spectrum of structures and organelles, are easy to use, and are partially applied in clinical practice. The fluorescence-coupled molecules offer the possibility to tag and follow nearly any desirable molecule, and recombinant DNA constructs open the perspective to utilize advanced imaging modes as photoactivation and optogenetics.[47]

The depth of analysis is an important parameter for intravital imaging. The infrared light used in 2PEM deeply penetrates into the sample, allowing the visualization of muscle fibers beneath other tissues as the skin, collagen and blood vessels. Infrared wavelengths also have the advantage of reducing phototoxicity and photobleaching. Imaging the neuromuscular system is still feasible through an intact skin, even when using Agouti mice with colored skin, allowing fully non-invasive imaging. However, the mice need to be anesthetized before imaging and some labelings require the injection of dyes.

Monitoring dynamic events provides functional information in addition to intravital structure analysis. As a proof-of-concept, we followed spontaneous myofiber contraction. Sarcomere length decreased by

about 5%. Given the large number of sarcomeres per fiber, this decrease represents a substantial contraction of the whole myofiber. Our approach provides the possibility to study various parameters and kinetics of muscle contraction as time to maximal contraction or relaxation time under normal and pathological conditions.

Intravital monitoring of a muscle disease

To validate the intravital muscle imaging toolbox for the characterization of a disease state, we focused on a mouse model for myotubular myopathy. Previous *ex vivo* investigations of this model revealed different histopathological features including myofiber hypotrophy and structural abnormalities of the neuromuscular junction.[17,20,21] Using intravital imaging, we were indeed able to detect an increased proportion of atrophic fibers, and an abnormal shape of the neuromuscular junctions in the *Mtm1* knockout mice. Our *in vivo* observations support the notion that the muscle weakness correlates with hypotrophy, and that functional defects of the neuromuscular transmission represent one of the disease causes. Previous histopathological examinations mainly focused on the leg muscles, and here we describe similar defects in the ear muscle. This suggests that most skeletal muscles are affected in myotubular myopathy, whether or not they drive locomotor activities. To our knowledge, this is a first evidence that histological hallmarks of myotubular myopathy can be illustrated without muscle sectioning in a mammalian model.

Further in-depth analyses of this mouse model during pre-symptomatic age (before 3 w) might potentially reveal primary structural or/and functional defects preceding clinical manifestations and thus allows a better understanding of the pathological mechanisms underlying myotubular/centronuclear myopathies. Moreover, the possibility to monitor non-muscle tissues as blood vessels or connective tissues may reveal additional defects not considered before. For instance, it is known that patients with myotubular myopathy display non-muscle features as fatal liver hemorrhages that might relate to smooth muscle defect.[3]

In conclusion, multimodal intravital imaging of the neuromuscular system in time and space in mice, under healthy and diseased conditions, paves the way for the follow-up of disease progression or/and disease amelioration upon therapeutic tests, and has the potential to significantly reduce the number of animal needed to reach scientific conclusions.

Abbreviations

2PEM	2-photon microscopy
IVM	intravital imaging
NMJ	neuromuscular junction
SHG	second harmonic generation
XLMTM	X-linked myotubular myopathy

Acknowledgments

Funding

References

[1] Engel AG, Franzini-Armstrong C. Myology, Basic and Clinical. New York: McGraw-Hill, 2004.

[2] Kaplan JC, Hamroun D. The 2015 version of the gene table of monogenic neuromuscular disorders (nuclear genome). Neuromuscul Disord 2014; 24:1123–53; PMID:25625149; http://dx.doi.org/10.1016/j.nmd.2014.11.001

[3] Herman GE, Finegold M, Zhao W, de Gouyon B, Metzenberg A. Medical complications in long-term survivors with X-linked myotubular myopathy. J Pediatr 1999; 134:206–14; PMID:9931531; http://dx.doi.org/10.1016/S0022-3476(99)70417-8

[4] Jungbluth H, Wallgren-Pettersson C, Laporte J. Centronuclear (myotubular) myopathy. Orphanet J Rare Dis 2008; 3:26; PMID:18817572; http://dx.doi.org/10.1186/1750-1172-3-26

[5] Laporte J, Biancalana V, Tanner SM, Kress W, Schneider V, Wallgren-Pettersson C, Herger F, Buj-Bello A, Blondeau F, Liechti-Gallati S, et al. MTM1 mutations in X-linked myotubular myopathy. Hum Mutat 2000; 15:393–409; PMID:10790201; http://dx.doi.org/10.1002/(SICI)1098-1004

[6] Laporte J, Hu LJ, Kretz C, Mandel JL, Kioschis P, Coy JF, Klauck SM, Poustka A, Dahl N. A gene mutated in X-linked myotubular myopathy defines a new putative tyrosine phosphatase family conserved in yeast. Nat Genet 1996; 13:175–82; PMID:8640223; http://dx.doi.org/10.1038/ng0696-175

[7] Pierson CR, Tomczak K, Agrawal P, Moghadaszadeh B, Beggs AH. X-linked myotubular and centronuclear myopathies. J Neuropathol Exp Neurol 2005; 64:555–64; PMID:16042307; http://dx.doi.org/10.1097/01.jnen.0000171653.17213.2e

[8] Romero NB. Centronuclear myopathies: a widening concept. Neuromuscul Disord 2010; 20:223–8; PMID:20181480; http://dx.doi.org/10.1016/j.nmd.2010.01.014

[9] Al-Qusairi L, Weiss N, Toussaint A, Berbey C, Messaddeq N, Kretz C, Sanoudou D, Beggs AH, Allard B, Mandel JL, et al. T-tubule disorganization and defective excitation-contraction coupling in muscle fibers lacking myotubularin lipid phosphatase. Proc Natl Acad Sci U S A 2009; 106:18763–8; PMID:19846786; http://dx.doi.org/10.1073/pnas.0900705106

[10] Dowling JJ, Vreede AP, Low SE, Gibbs EM, Kuwada JY, Bonnemann CG, Feldman EL. Loss of myotubularin function results in T-tubule disorganization in zebrafish and human myotubular myopathy. PLoS Genet 2009; 5: e1000372; PMID:19197364

[11] Toussaint A, Cowling BS, Hnia K, Mohr M, Oldfors A, Schwab Y, Yis U, Maisonobe T, Stojkovic T, Wallgren-Pettersson C, et al. Defects in amphiphysin 2 (BIN1) and triads in several forms of centronuclear myopathies. Acta Neuropathol 2011; 121:253–66; PMID:20927630; http://dx.doi.org/10.1007/s00401-010-0754-2

[12] Al-Qusairi L, Prokic I, Amoasii L, Kretz C, Messaddeq N, Mandel JL, Laporte J. Lack of myotubularin (MTM1) leads to muscle hypotrophy through unbalanced regulation of the autophagy and ubiquitin-proteasome pathways. FASEB J 2013; 27:3384–94; PMID:23695157; http://dx.doi.org/10.1096/fj.12-220947

[13] Fetalvero KM, Yu Y, Goetschkes M, Liang G, Valdez RA, Gould T, Triantafellow E, Bergling S, Loureiro J, Eash J, et al. Defective autophagy and mTORC1 signaling in myotubularin null mice. Mol Cell Biol 2013; 33:98–110; PMID:23109424; http://dx.doi.org/10.1128/MCB.01075-12

[14] Jungbluth H, Gautel M. Pathogenic mechanisms in centronuclear myopathies. Front Aging Neurosci 2014; 6:339; PMID:25566070; http://dx.doi.org/10.3389/fnagi.2014.00339

[15] Lawlor MW, Viola MG, Meng H, Edelstein RV, Liu F, Yan K, Luna EJ, Lerch-Gaggl A, Hoffmann RG, Pierson CR, et al. Differential muscle hypertrophy is associated with satellite cell numbers and Akt pathway activation following activin type IIB receptor inhibition in Mtm1 p.R69C mice. Am J Pathol 2014; 184:1831–42; PMID:24726641; http://dx.doi.org/10.1016/j.ajpath.2014.03.003

[16] Ambler MW, Neave C, Singer DB. X-linked recessive myotubular myopathy: II. Muscle morphology and human myogenesis. HumPathol 1984; 15:1107–20; PMID:NOT_FOUND

[17] Dowling JJ, Joubert R, Low SE, Durban AN, Messaddeq N, Li X, Dulin-Smith AN, Snyder AD, Marshall ML, Marshall JT, et al. Myotubular myopathy and the neuromuscular junction: a novel therapeutic approach from mouse models. Dis Model Mech 2012; 5:852–9; PMID:22645112; http://dx.doi.org/10.1242/dmm.009746

[18] Amoasii L, Bertazzi DL, Tronchere H, Hnia K, Chicanne G, Rinaldi B, Cowling BS, Ferry A, Klaholz B, Payrastre B, et al. Phosphatase-dead myotubularin ameliorates X-linked centronuclear myopathy phenotypes in mice. PLoS Genet 2012; 8:e1002965; PMID:23071445

[19] Beggs AH, Bohm J, Snead E, Kozlowski M, Maurer M, Minor K, Childers MK, Taylor SM, Hitte C, Mickelson JR, et al. MTM1 mutation associated with X-linked myotubular myopathy in Labrador Retrievers. Proc Natl Acad Sci U S A 2010; 107:14697–702; PMID:20682747; http://dx.doi.org/10.1073/pnas.1003677107

[20] Buj-Bello A, Laugel V, Messaddeq N, Zahreddine H, Laporte J, Pellissier JF, Mandel JL. The lipid phosphatase myotubularin is essential for skeletal muscle maintenance but not for myogenesis in mice. Proc Natl Acad Sci U S A 2002; 99:15060–5; PMID:12391329; http://dx.doi.org/10.1073/pnas.212498399

[21] Pierson CR, Dulin-Smith AN, Durban AN, Marshall ML, Marshall JT, Snyder AD, Naiyer N, Gladman JT, Chandler DS, Lawlor MW, et al. Modeling the human MTM1 p.R69C mutation in murine Mtm1 results in exon 4 skipping and a less severe myotubular myopathy phenotype. Hum Mol Genet 2012; 21:811–25; PMID:22068590; http://dx.doi.org/10.1093/hmg/ddr512

[22] Velichkova M, Juan J, Kadandale P, Jean S, Ribeiro I, Raman V, Stefan C, Kiger AA. Drosophila Mtm and class II PI3K coregulate a PI(3)P pool with cortical and endolysosomal functions. J Cell Biol 2010; 190:407–25; PMID:20696708; http://dx.doi.org/10.1083/jcb.200911020

[23] Xue Y, Fares H, Grant B, Li Z, Rose AM, Clark SG, Skolnik EY. Genetic analysis of the myotubularin family of phosphatases in caenorhabditis elegans. J Biol Chem 2003; 278:34380–6; PMID:12788949

[24] Cebollero E, van der Vaart A, Zhao M, Rieter E, Klionsky DJ, Helms JB, Reggiori F. Phosphatidylinositol-3-phosphate clearance plays a key role in autophagosome completion. Curr Biol 2012; 22:1545–53; PMID:22771041; http://dx.doi.org/10.1016/j.cub.2012.06.029

[25] Parrish WR, Stefan CJ, Emr SD. Essential role for the myotubularin-related phosphatase Ymr1p and the synaptojanin-like phosphatases Sjl2p and Sjl3p in regulation of phosphatidylinositol 3-phosphate in yeast. Mol Biol Cell 2004; 15:3567–79; PMID:15169871; http://dx.doi.org/10.1091/mbc.E04-03-0209

[26] Webster MT, Manor U, Lippincott-Schwartz J, Fan CM. Intravital Imaging Reveals Ghost Fibers as Architectural Units Guiding Myogenic Progenitors during Regeneration. Cell Stem Cell 2016; 18:243–52; PMID:26686466; http://dx.doi.org/10.1016/j.stem.2015.11.005

[27] Oddoux S, Zaal KJ, Tate V, Kenea A, Nandkeolyar SA, Reid E, Liu W, Ralston E. Microtubules that form the stationary lattice of muscle fibers are dynamic and nucleated at Golgi elements. J Cell Biol 2013; 203:205–13; PMID:24145165; http://dx.doi.org/10.1083/jcb.201304063

[28] Shitara A, Weigert R. Imaging membrane remodeling during regulated exocytosis in live mice. Exp Cell Res 2015; 337:219–25; PMID:26160452; http://dx.doi.org/10.1016/j.yexcr.2015.06.018

[29] Ellenbroek SI, van Rheenen J. Imaging hallmarks of cancer in living mice. Nat Rev Cancer 2014; 14:406–18; PMID:24854083; http://dx.doi.org/10.1038/nrc3742

[30] Menard R, Tavares J, Cockburn I, Markus M, Zavala F, Amino R. Looking under the skin: the first steps in malarial infection and immunity. Nat Rev Microbiol 2013; 11:701–12; PMID:24037451; http://dx.doi.org/10.1038/nrmicro3111

[31] Weigert R, Porat-Shliom N, Amornphimoltham P. Imaging cell biology in live animals: ready for prime time. J Cell Biol 2013; 201:969–79; PMID:23798727; http://dx.doi.org/10.1083/jcb.201212130

[32] Campagnola PJ, Loew LM. Second-harmonic imaging microscopy for visualizing biomolecular arrays in cells, tissues and organisms. Nat Biotechnol 2003; 21:1356–60; PMID:14595363; http://dx.doi.org/10.1038/nbt894

[33] Provenzano PP, Eliceiri KW, Campbell JM, Inman DR, White JG, Keely PJ. Collagen reorganization at the tumor-stromal interface facilitates local invasion. BMC Med 2006; 4:38; PMID:17190588; http://dx.doi.org/10.1186/1741-7015-4-38

[34] Campagnola PJ, Millard AC, Terasaki M, Hoppe PE, Malone CJ, Mohler WA. Three-dimensional high-resolution second-harmonic generation imaging of endogenous structural proteins in biological tissues. Biophys J 2002; 82:493–508; PMID:11751336; http://dx.doi.org/10.1016/S0006-3495(02)75414-3

[35] Georgiev T, Zapiec B, Forderer M, Fink RH, Vogel M. Colocalization properties of elementary Ca(2+) release signals with structures specific to the contractile filaments and the tubular system of intact mouse skeletal muscle fibers. J Struct Biol 2015; 192:366–75; PMID:26431893; http://dx.doi.org/10.1016/j.jsb.2015.09.018

[36] Rehberg M, Krombach F, Pohl U, Dietzel S. Label-free 3D visualization of cellular and tissue structures in intact muscle with second and third harmonic generation microscopy. PLoS One 2011; 6:e28237; PMID:22140560; http://dx.doi.org/10.1371/journal.pone.0028237

[37] Rouede D, Coumailleau P, Schaub E, Bellanger JJ, Blanchard-Desce M, Tiaho F. Myofibrillar misalignment correlated to triad disappearance of mdx mouse gastrocnemius muscle probed by SHG microscopy. Biomed Opt Express 2014; 5:858–75; PMID:24688819; http://dx.doi.org/10.1364/BOE.5.000858

[38] Bruusgaard JC, Gundersen K. In vivo time-lapse microscopy reveals no loss of murine myonuclei during weeks of muscle atrophy. J Clin Invest 2008; 118:1450–7; PMID:18317591; http://dx.doi.org/10.1172/JCI34022

[39] Llewellyn ME, Barretto RP, Delp SL, Schnitzer MJ. Minimally invasive high-speed imaging of sarcomere contractile dynamics in mice and humans. Nature 2008; 454:784–8; PMID:18600262

[40] Sanchez GN, Sinha S, Liske H, Chen X, Nguyen V, Delp SL, Schnitzer MJ. In Vivo Imaging of Human Sarcomere Twitch Dynamics in Individual Motor Units. Neuron 2015; 88:1109–20; PMID:26687220; http://dx.doi.org/10.1016/j.neuron.2015.11.022

[41] Karreman MA, Mercier L, Schieber NL, Solecki G, Allio G, Winkler F, Ruthensteiner B, Goetz JG, Schwab Y. Fast and precise targeting of single tumor cells in vivo by multimodal correlative microscopy. J Cell Sci 2016; 129:444–56; PMID:26659665; http://dx.doi.org/10.1242/jcs.181842

[42] Li JL, Goh CC, Keeble JL, Qin JS, Roediger B, Jain R, Wang Y, Chew WK, Weninger W, Ng LG. Intravital multiphoton imaging of immune responses in the mouse ear skin. Nat Protoc 2012; 7:221–34; PMID:22240584

[43] Karreman MA, Mercier L, Schieber NL, Shibue T, Schwab Y, Goetz JG. Correlating intravital multi-photon microscopy to 3D electron microscopy of invading tumor cells using anatomical reference points. PLoS One 2014; 9:e114448; PMID:25479106

[44] Plotnikov SV, Millard AC, Campagnola PJ, Mohler WA. Characterization of the myosin-based source for second-harmonic generation from muscle sarcomeres. Biophys J 2006; 90:693–703; PMID:16258040; http://dx.doi.org/10.1529/biophysj.105.071555

[45] Schindelin J, Arganda-Carreras I, Frise E, Kaynig V, Longair M, Pietzsch T, Preibisch S, Rueden C, Saalfeld S, Schmid B, et al. Fiji: an open-source platform for biological-image analysis. Nat Methods 2012; 9:676–82; PMID:22743772; http://dx.doi.org/10.1038/nmeth.2019

[46] Freund I, Deutsch M. Second-harmonic microscopy of biological tissue. Opt Lett 1986; 11:94; PMID:19730544; http://dx.doi.org/10.1364/OL.11.000094

[47] Deisseroth K. Optogenetics: 10 years of microbial opsins in neuroscience. Nat Neurosci 2015; 18:1213–25; PMID:26308982; http://dx.doi.org/10.1038/nn.4091

2.1.4 Conclusions

Ce travail a permis d'imager les fibres musculaires ainsi que les jonctions neuromusculaires de façon non invasive par microscopie multiphotonique mettant en évidence des défauts dans l'organisation musculaire chez la souris KO MTM1. L'équipe de J. Laporte peut maintenant se servir de cet outil pour suivre l'évolution de la maladie chez des souris invalidées pour les autres gènes impliqués dans cette pathologie comme les gènes AMPH2 et DNM2. Une amélioration pourrait être l'implémentation de la THG ce qui permettrait d'imager les noyaux et donc suivre l'évolution de leur position dans la fibre musculaire au cours du temps (Rehberg et al., 2011).

L'imagerie non-invasive dans l'oreille de souris est rapide à mettre en œuvre car ne nécessitant pas de chirurgie au contraire des autres techniques d'imagerie intravitale où il est nécessaire de greffer une fenêtre optique.

D'autres groupes de recherche ont également utilisé l'oreille pour étudier par exemple la réponse immunitaire par imagerie multiphotonique (Li et al., 2012; Abtin et al., 2014).

Intéressé par l'étude de l'invasion tumorale nous avons par la suite adapté ce modèle pour l'imagerie de xenogreffes de cellules tumorales. Les cellules tumorales sont injectées en sous cutanée dans le pavillon de l'oreille et l'imagerie intravitale est réalisé sur plusieurs jours.

2.2 Protocole de CLEM intravitale

2.2.1 Contexte

Notre groupe est intéressé par l'étude de différentes étapes clés de la progression tumorale, notamment l'invasion et l'intra/extravasation des cellules tumorales. A l'heure actuelle seule la microscopie électronique permet d'avoir accès à l'ultrastructure cellulaire. Il nous faut donc pouvoir visualiser un évènement d'intérêt chez la souris vivante pour ensuite réaliser une imagerie par microscopie électronique afin de de déterminer au niveau ultra-structurale les mécanismes impliqués. En collaboration avec l'équipe de Y. Schwab (EMBL, Heidelberg) nous avons pour ce premier protocole décidé d'utiliser l'oreille de la souris comme base pour le développent du protocole de CLEM intravital.

En effet, l'oreille de souris est un organe facilement manipulable et accessible, ses caractéristiques anatomiques (taille, épaisseur, position) rendent la microscopie intravitale plus aisée. De plus, la technique d'imagerie a été mise en place au laboratoire (voir manuscrit n°1). Ainsi des cellules tumorales fluorescentes sont injectées en sous cutanée dans le pavillon de l'oreille et l'imagerie intravitale est réalisée sur plusieurs jours.

2.2.2 Principaux résultats

Une des difficultés dans la technique de CLEM est de conserver et retrouver la région d'intérêt visualisée dans l'animale vivant jusqu'aux coupes ultrafines réalisées pour la microscopie électronique. Nous avons ici adaptée la technique d'ablation laser appelée NIRB (Near Infra-Red Branding) (Bishop et al., 2011), développée à l'origine pour marquer des coupes de tissus fixés, au marquage de la peau de l'oreille de la souris vivante. Le NIRB consiste à créer des points de repère à la surface de l'échantillon, juste au-dessus de la ROI sans perturber ou endommager cette dernière. Ce marquage est à la fois visualisable sur le tissu vivant par autofluorescence mais aussi visualisable, par absence de matière, sur les coupes ultrafines.

Ce marquage c'est révélé comme une étape clé pour :

- Réaliser le prélèvement de la région d'intérêt avec précision
- Réduire la taille de l'échantillon à environ 1mm^3 pour permettre son inclusion dans la résine
- Retrouver la région d'intérêt lors de la réalisation des coupes semi fines (500nm d'épaisseurs)

La corrélation s'est faite sur des repères anatomiques constitués des vaisseaux sanguins, des follicules pileux mais également sur les fibres de collagènes imagées par SHG.

2.2.3 Manuscrit n°3: Correlating Intravital Multi-photon microscopy to 3D electron microscopy of invading tumor cells using anatomical reference points

RESEARCH ARTICLE

Correlating Intravital Multi-Photon Microscopy to 3D Electron Microscopy of Invading Tumor Cells Using Anatomical Reference Points

Matthia A. Karreman[1], Luc Mercier[2,3,4,5], Nicole L. Schieber[1], Tsukasa Shibue[6], Yannick Schwab[1]*, Jacky G. Goetz[2,3,4,5]*

1. European Molecular Biology Laboratory Heidelberg, Heidelberg, 69117, Germany, **2.** Inserm U1109, MN3T, Strasbourg, F-67200, France, **3.** Université de Strasbourg, Strasbourg, F-67000, France, **4.** LabEx Medalis, Université de Strasbourg, Strasbourg, F-67000, France, **5.** Fédération de Médecine Translationnelle de Strasbourg (FMTS), Strasbourg, F-67000, France, **6.** Whitehead Institute for Biomedical Research, Massachusetts Institute of Technology, Cambridge, Massachusetts, United States of America

*schwab@embl.de (YS); jacky.goetz@inserm.fr (JGG)

Abstract

Correlative microscopy combines the advantages of both light and electron microscopy to enable imaging of rare and transient events at high resolution. Performing correlative microscopy in complex and bulky samples such as an entire living organism is a time-consuming and error-prone task. Here, we investigate correlative methods that rely on the use of artificial and endogenous structural features of the sample as reference points for correlating intravital fluorescence microscopy and electron microscopy. To investigate tumor cell behavior *in vivo* with ultrastructural accuracy, a reliable approach is needed to retrieve single tumor cells imaged deep within the tissue. For this purpose, fluorescently labeled tumor cells were subcutaneously injected into a mouse ear and imaged using two-photon-excitation microscopy. Using near-infrared branding, the position of the imaged area within the sample was labeled at the skin level, allowing for its precise recollection. Following sample preparation for electron microscopy, concerted usage of the artificial branding and anatomical landmarks enables targeting and approaching the cells of interest while serial sectioning through the specimen. We describe here three procedures showing how three-dimensional (3D) mapping of structural features in the tissue can be exploited to accurately correlate between the two imaging modalities, without having to rely on the use of artificially introduced markers of the region of interest. The methods employed here facilitate the link between intravital and nanoscale imaging of invasive tumor cells, enabling correlating function to structure in the study of tumor invasion and metastasis.

Introduction

Electron Microscopy (EM) uniquely enables imaging the object of interest at high resolution in its structural context. In the study of metastatic processes, EM is the only technique to reveal the ultrastructure of both the invading cell and its microenvironment. When targeting rare and transient events like invasion, however, the small field of view of the EM and its restriction to image immobilized specimens are a disadvantage. *In vivo* studies of metastatic tumor cells have been successfully performed previously by intravital two-photon excitation microscopy (2PEM) of fluorescent tumor cells [1]. The infrared light used in 2PEM penetrates deep into the sample, and the effects of photo-bleaching and phototoxicity are reduced overall [2]. Moreover, using a single excitation wavelength, it is possible to simultaneously image fluorescent dyes, genetically expressed fluorescent proteins, and second or third harmonic signal generated by other features in the tissue like collagen fibers [3] and lipids [4]. Correlative light and electron microscopy (CLEM), exploits the advantages of both light microscopy and EM in the study of a single sample. When studying metastasis, 2PEM can monitor fluorescent tumor cells migrating through living tissue and image the process of invasion over time. Following fixation and processing, EM imaging then provides a snapshot of the fine structure and microenvironment of the tumor cells.

The main hurdle in CLEM is to keep track of the region of interest (ROI) while moving from the fluorescence to the electron microscope. Various procedures have been developed for the accurate retracing of the ROI in 2D organized samples. Registering the position of the ROI within a coordinate system of reference points can yield a precision of 100 nm [5–7]. Alternatively, by storing its xy-coordinates relative to the sample stage the correlation procedure can be partly automated [8–11]. However, in bulky and complex samples, like multicellular organisms and tissues, the retrieval of a rare event remains a challenge. Approaches were developed to mark the position of the ROI by Near Infrared Branding (NIRB) of the tissue [12–14], or by laser etching of the resin embedded sample [15]. The laser, however, looses power upon deep penetration into the sample, due to scattering. On brain tissue slices, precise marking of the ROI within the tissue was limited to a depth of 50 µm or less [12–14]. For larger specimens, it is thus only possible to create marks at the surface of the sample. These markings therefore reveal the xy-coordinates of the ROI with high precision, but fail to provide its z-position within a large 3D specimen. To accurately retrieve the ROI in three dimensions, these methods thus still require browsing through numerous z-sections of the sample. The ROI can then be recognized based on its position relative to structural features in the sample [16], often in conjunction with overlapping the outline of the EM structure with the shape of the fluorescent signal [17]. To help recognizing the cell or structure of interest, it is possible to use bimodal [18, 19] or photo-convertible [20, 21] probes that can be recognized first in FM and next in EM. Although facilitating its identification, the use of these markers can mask the ultrastructure of the ROI

[18], result in unspecific labeling [22] or may influence cellular processes [23]. To circumvent this, we set to evaluate different approaches that enable retrieval of the structure of interest imaged deep within a tissue without marking it with artificially introduced labels.

In this work, we employ CLEM to study early events of tumor invasion in mouse in order to correlate tumor cell behavior *in vivo* to their ultrastructural architecture in 3D. Metastasis formation is a multi-step process where tumor cells invade the surrounding tissue of a primary tumor, intravasate into the blood circulation, disseminate to anatomically distant organs and establish themselves in a new tissue microenvironment [24]. The complex bio-mechano-chemical processes leading to these events involve, amongst others, the formation of cellular protrusions, the turnover of cell-matrix contacts and local remodeling and degrading of the extra-cellular matrix surrounding the cells [25–28]. Previously, *in vitro* models have provided relevant information on the behavior of invading tumor cells, but there is currently no *in vivo* model system that can combine functional imaging of tumor cells in their microenvironment with their visualization in EM. 2PEM imaging can be performed directly on skin [29] or through an imaging window installed above the organ of interest [30–33]. Intravital fluorescence microscopy, however, does not provide detailed insight in the architecture of the imaged areas, stressing the missing link between the dynamics and the ultrastructure of metastatic events.

To enable correlating intravital 2PEM to 3D-EM of invading tumor cells *in situ*, we have used an approach that exploits both artificial and endogenous landmarks visible in the sample. Fluorescent tumor cells are injected in the mouse ear and imaged a few days later by 2PEM. The recording site is then marked by NIRB, at the level of the skin surface, so that the ROI could be retrieved and processed for EM. The ROI is then approached by ultramicrotomy. In this work, we make use of three variants of targeting using the reconstruction of the tissue anatomy from serial sections of the tissue embedded in the resin block. We show how we have made optimal use of tissue features, which are visible in each imaging modality, to achieve accurate correlation. Using the workflow we describe here, it was possible to successfully retrieve tumor cells injected in mouse ear, which enabled us to move from intravital dynamic 2PEM imaging to high-resolution 3D TEM tomography.

Methods

Mice handling

8 week old, female immuno-deficient mice (Rj:NMRI-Foxn1nu/Foxn1nu, Janvier labs) were transplanted with fluorescent tumor cells. For each experiment, a single mouse was subcutaneously injected into the ear with MDA-MB-231 cells expressing a cytoplasmic GFP [34] (~15000 cells/μL, Figures 1, 2, 3) or D2.0R cells expressing LifeAct-Ypet [35–38] (5000 cells/μL, Figures 4, 5) in a 1:1 mixture of phosphate buffered saline (PBS) and Matrigel (BD Biosciences). 8 mice were
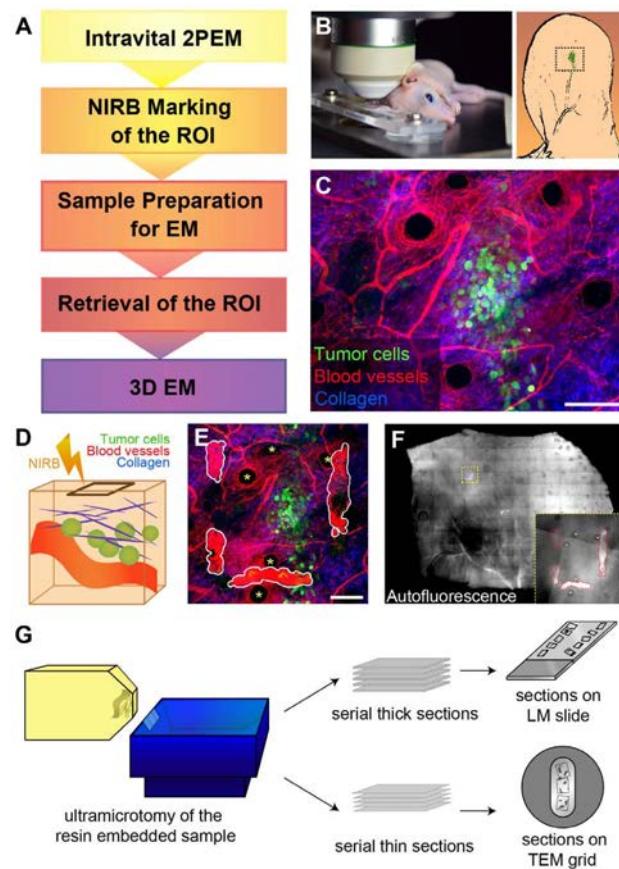
Figure 1. Outline of the Correlative Workflow. A. The flowchart lists the general steps involved in the correlative workflow. B. Left panel: installation of the anesthetized mouse on the LM stage. The ear with the transplanted fluorescent tumor cells (right panel, cartoon) is mounted in a custom-built holder. C. Z-projection of a typical 2PEM dataset obtained from the mouse ear that was injected with GFP-expressing tumor cells (green). SHG signal of the collagen fibers is shown in blue. Evans Blue stains blood vessels and is depicted in red. Scale bar: 100 μm. See Movie S1. D. Cartoon of the NIRB process representing the imaged volume containing a vessel (red), collagen fibers (blue), and tumor cells (green). Our NIRB-procedure entails drawing a frame at the surface of the skin with a high-powered laser, above and away from the ROI. The imaged volumes presented in this work were in between 60 and 200 μm in depth and ranging from 270 to 440 μm in xy. E. Following NIRB, the same volume is imaged again with 2PEM. The NIRB marks visible in this z-projection are traced in white. Scale bar: 100 μm. Asterisks point to hair follicles. See Movie S1. F. After chemical fixation of the mouse ear sample, NIRB markings remain temporarily autofluorescent and their location can be mapped. Asterisks pointing to hair follicles (as in E). G. Following EM processing, the embedded sample can be trimmed and sectioned by ultramicrotomy. Serial thick sections (500 nm) are placed on glass slides to be imaged by light microscopy ('sections on LM slide'). Serial thin sections (60 to 240 nm) are mounted on slot grids ('sections on TEM grid') allowing for TEM observation and/or electron tomography.

doi:10.1371/journal.pone.0114448.g001

imaged 2–3 days following injection with MDA-MB-231 cells. 3 mice, injected with D2.0R cells, were imaged after 7 days, upon tumor growth. In general, shortly before intravital imaging, the mouse was first anesthetized through intra-peritoneal injection of a mixture of ketamine (100 mg/kg) and xylazine (10 mg/kg). Then, to visualize the blood vessels with 2PEM, 100 μL of Evans Blue (10 mg/mL in PBS, E-2129 Sigma-Aldrich) was administered to the anesthetized mouse
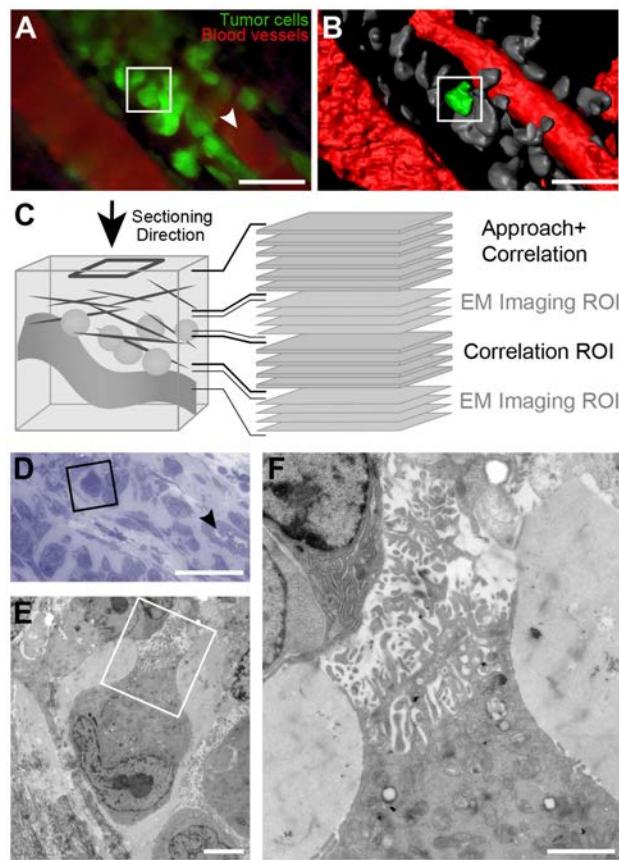
Figure 2. Correlation based on Sequential LM and EM imaging to Target a Single Tumor Cell. A. 3D view of a 2PEM z-stack of mouse ear skin tissue, 7 days post-injection with GFP-expressing tumor cells (green). Vessels are stained with Evans Blue (red). The arrowhead indicates the part of the blood vessel that is also visible in the thick section shown in panel D. The image is obtained using the 3D Viewer plugin in Fiji. Scale bar: 50 μm. See Movie S2. B. 3D model of the imaged volume. The cell of interest, boxed in panel A and B, is segmented in green, the other cells are segmented in grey. The vessels are shown in red. Scale bar: 50 μm. C. Cartoon of the sectioning procedure. The resin embedded sample is sectioned from the direction indicated with the arrow. To approach the ROI, 180 thick sections (500 nm) were obtained from the sample ('Approach and Correlation'). Next, 10 consecutive series of 10 thin (60 nm) and two thick (500 nm) sections were obtained from the ROI. Thick sections were used for correlation and the thin sections were imaged with EM. D. The cell of interest (box) was identified in a thick toluidine blue stained section of the ROI. The arrowhead points to a cross-section of the vessel depicted in A with a white arrowhead. Scale bar: 50 μm. E: Low magnification EM image of the cell boxed in panel D. The cell appears highly polarized and contains protrusive structures, showed at higher magnification in panel F. Scale bar in E: 5 μm, in F: 2 μm. See Movie S2.

doi:10.1371/journal.pone.0114448.g002

via retro-orbital injection. A gas anesthesia (isoflurane) system was used for performing time-lapse imaging shown in figures 4 and 5. The mouse studies were performed according to the Guide for Care and Use of Laboratory Animals (E67-6-482-21) and the European Directive with approval of the regional ethical committee (CREMEAS for Comité Régional d'Ethique en Matière d'Expérimentation Animale de Strasbourg, AL/73/80/02/13). Mice received food and water ad libitum, they were checked daily and tumor growth never exceeded a
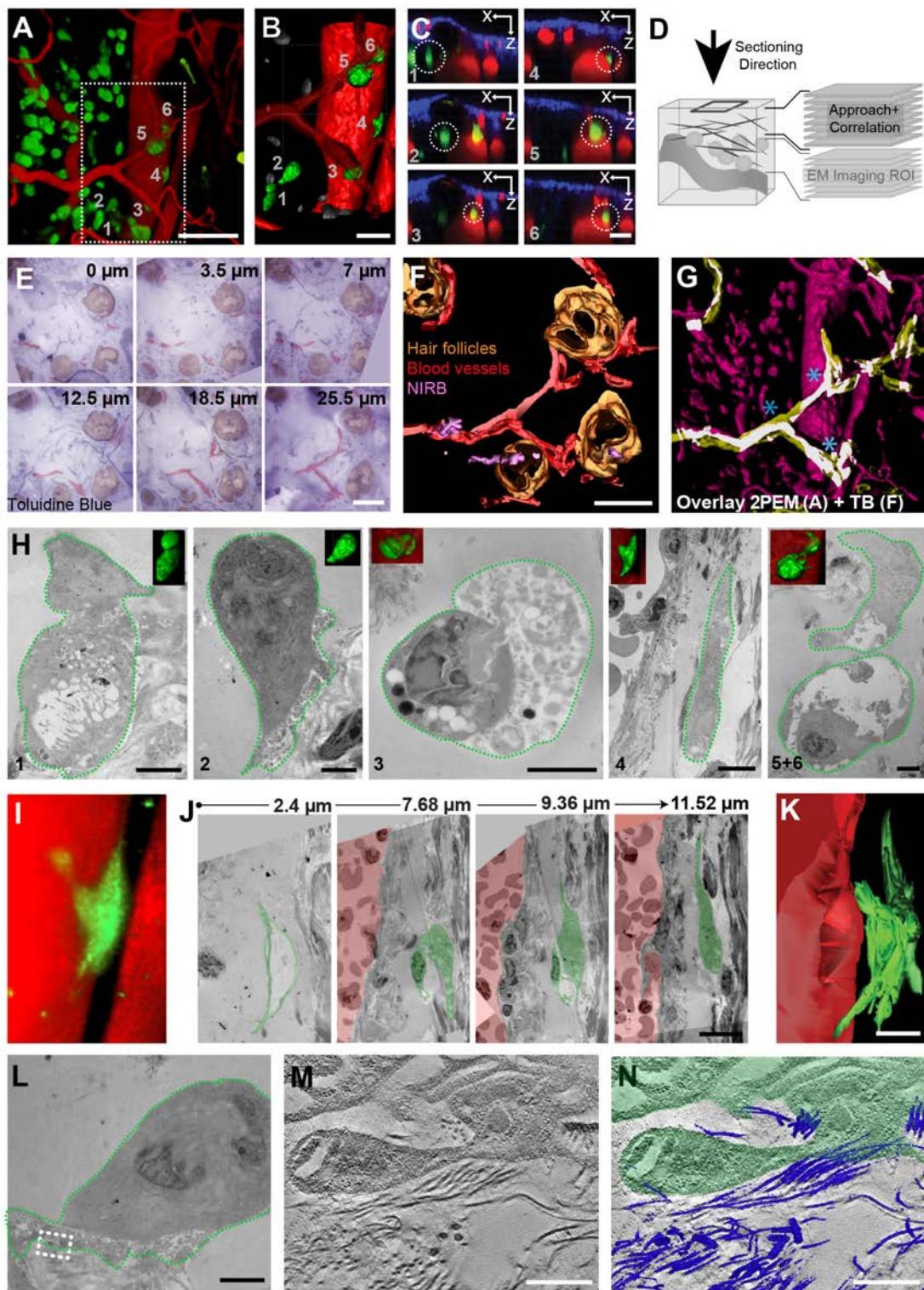
Figure 3. Full Volume Correlation of the ROI. A. 3D view of a 2PEM z-stack of mouse ear tissue, 7 days post-injection with GFP-expressing tumor cells (green). Vessels are stained with Evans Blue (red). Scale bar: 100 μm. See Movie S3. B. 3D model of the area that is indicated with a box in A. The cells of interest are segmented in green and numbered (1–6). The vessels are shown in red. The vessel bifurcation close to the skin surface is made transparent to reveal the cells underneath. Scale bar: 50 μm. C. X-Z slices through the 3D 2PEM volume, at the height of the cells of interest (circled). The numbers on the left bottom correspond to the numbers used in panel B to label the cells of interest. These views show the relative position of the cells with respect to the blood vessels (red) and the collagen-rich dermis (blue). D. Cartoon of the sectioning procedure. To approach the ROI and monitor the progression, serial thick sections were produced from the sample (the arrow indicates the sectioning direction) and imaged with LM ('Approach+Correlation'). Approximating the location of the cells of interest, 240 nm sections for electron tomography were obtained ('EM imaging ROI'). E. 500 nm toluidine-blue-stained sections that were obtained at different depths within the sample (the relative z-distance from the first section is indicated in top right corner of each panel). The vessels are segmented in red, hair follicles in brown. Scale bar: 100 μm. See Movie S3. F. 3D model of the hair follicles (brown), vessels (red) and NIRB markings (purple) segmented in the serial thick sections. Scale bar: 50 μm. See Movie S3. G. Overlay of a 3D model of the 2PEM z-stack (based on A, magenta) and a model of the vessels segmented in the serial thick sections (based on F, yellow). Overlapping areas are highlighted in white. Asterisks indicate vessel-forks that are visible in both datasets. Scale bar: 50 μm. See Movie S3. H. Correlation between 2PEM, LM and EM enabled retrieving the cells of interest (numbering in bottom right corner, as in B and C) in the sequence of serial thin sections. The electron transparent areas in proximity of the cells indicate a local absence of extracellular matrix components. The cause of this missing material remains to be elucidated. I. A selected area in the 2PEM dataset, showing a cell of interest (number 4 in B, C and H). J. Selection of the TEM images of cell 4, shown in panel I. The cell is modeled in green and the vessel lumen in red. For each image, we indicated the z-distance from the section where the cells was first spotted. Scale bar: 10 μm. K. Cell 4 (green) and the blood vessel lumen (red) are segmented in the serial sections (J). A 3D model of this segmentation reveals the shape of the cell, which closely resembles the 2PEM view of the same cell, shown in I. Scale bar: 10 μm. L-N: Electron tomography of a tumor cell (number 2 in B,C, and H), shown at low magnification in panel L. At the position of the box in L, a tomogram was obtained. Scale bar: 5 μm. See Movie S3. M. One selected virtual slice of the tomogram shows the complex architecture of the cell membrane and the fiber-like structure of extracellular matrix (ECM). N: The high image contrast of the ECM fibers enables semi-automatic segmentation of the fibers (shown in blue) within the 3D dataset. Scale bars in M and N: 500 nm. See Movie S3.

doi:10.1371/journal.pone.0114448.g003
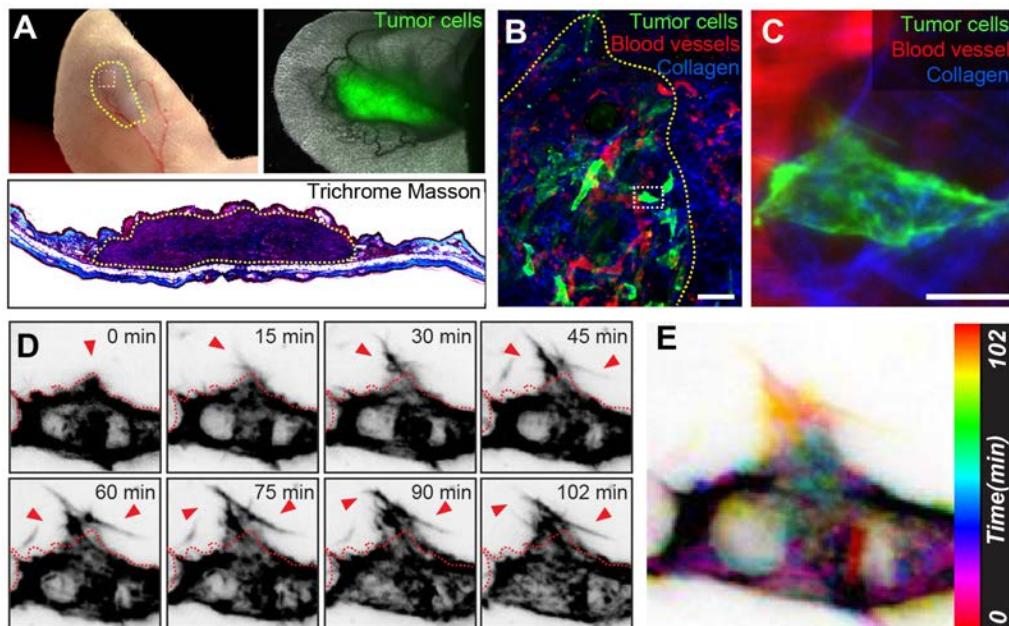
Figure 4. 2PEM Imaging of D2.0R Cells Xenotransplanted in Mouse Ear Skin. A. Two weeks after injection with LifeAct-Ypet expressing D2.0R cells, a tumor is formed in the mouse ear skin (top left panel, outlined in green). The green fluorescent signal of the D2.0R cells can be observed in the tumor region (top right panel). A histological cross-section through the tumor region was obtained from the second ear injected at the same time with the same cell type. The Trichrome Masson staining colors the collagen in blue (bottom panel). B. Maximum projection of a z-stack obtained from an area in the periphery of the invasive tumor (top left panel A, white square). The D2.0R cells are shown in green, and the tumor is outlined in yellow. A background signal from the Evans Blue (red) can be observed in the vicinity of the blood vessels, potentially caused by the 'leaky' nature of the tumor vessels, its uptake by residing immune cells and the repeated injections. Scale bar: 50 μm. See Movie S4. C. Higher magnification z-projection of the cell of interest boxed in B. Scale bar: 10 μm. D. Time-lapse imaging of a D2.0R tumor cell in vivo. The different panels depict, in black against a white background, the fluorescent signal of the actin in the cell at the indicated time-points. See Movie S4. E. Color-coded map of the structural changes of the cell of interest (boxed in B and C) over time. Scale bar: 10 μm.

doi:10.1371/journal.pone.0114448.g004
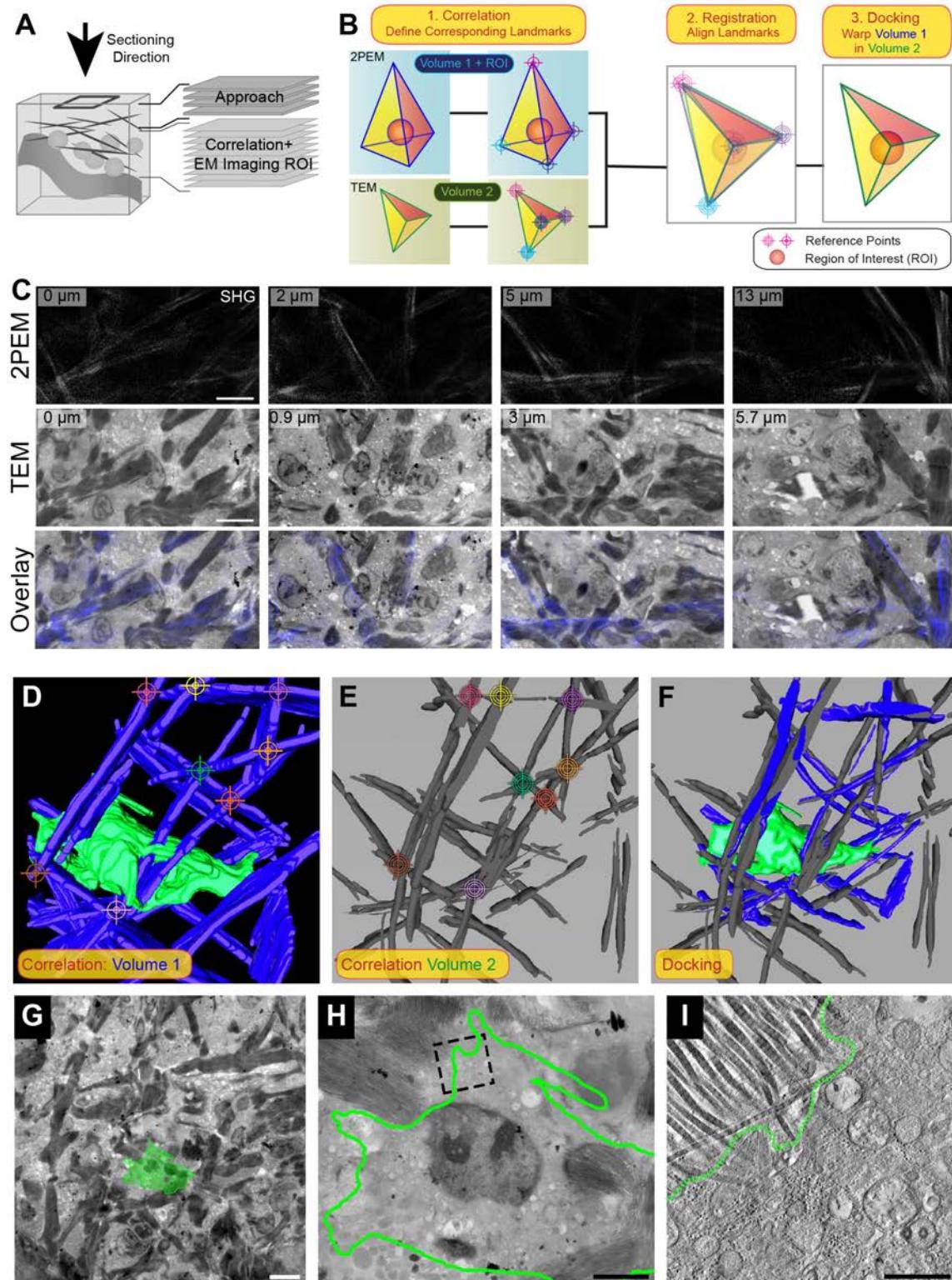
Figure 5. Correlating 2PEM to 3D EM of D2.0R Cells using Collagen Fibers as a Reference. A. Cartoon of the sectioning approach. Following 2PEM, NIRB and processing as described before, a few thick sections were produced from the sample to verify the orientation of the block and the presence of the NIRB markings ('Approach'). The sectioning direction is indicated with an arrow. As soon as the first NIRB marks were spotted in the thick sections, we proceeded with obtaining thin 240 nm sections for electron tomography ('Correlation+EM imaging ROI'). These sections were not only employed for EM imaging of the ROI, but also provided the structural features that were used for correlation between 2PEM and EM. B. Graphic representation of the landmark-based correlation procedure. The prisms with the blue and green ribs represent similar 3D volumes that differ in size, shape and orientation, representing the samples pre- and post-EM-processing. In order to predict the position of the ROI (ball, visible in volume 1) in volume 2, similar points (landmarks) in both datasets are identified ('Correlation'). These landmarks are overlaid in 3D ('Registration') enabling warping of volume 1 into volume 2 and thus also projecting the position of the ROI in volume 2 ('Docking'). C. Collagen fibers can be observed in both the 2PEM z-stack (top row panels, 2PEM) and the EM images of the serial sections (middle row, TEM). In the TEM images, the collagen is visible as electron dense fibers running in between the cellular material. Each column shows a 2PEM and an EM image obtained at a similar position in the sample, pre- and post EM processing. The numbers in the top left corner of the panels indicate their position in z to the image shown in the first column. The 2PEM dataset is stretched in z relative to the TEM dataset, causing the larger z-steps between the 2PEM images in the different rows. The bottom row shows the overlay of the 2PEM image (blue) and the TEM image (grey levels). Scale bars: 100 μm. D-F. The landmark-registration procedure is performed in Amira, using 3D models of collagen fibers as a reference. The selected landmarks (colored 'targets') indicate corresponding points in both datasets. D. 3D model of the collagen fibers (blue) and the cell of interest (green), obtained from a high magnification 2PEM z-stack of the cell of interest. E: 3D model of the collagen fibers (grey), obtained from a z-stack of EM images. F. The 3D visualization software Amira was used to overlay the landmarks and perform non-linear transformations to the 2PEM model to warp it into the EM model. G-I: Landmark-registration between the 2PEM and EM datasets enables retrieval and electron tomography of the cell of interest (green). G. Following the registration of the 2PEM in the EM dataset, the cell of interest could be docked within the z-stack of EM images. Scale bar: 10 μm. H. The docked cell of interest is outlined in green on a TEM section of the ROI. The nucleus of the cell is visible. Scale bar: 3 μm. K. Virtual slice through the tomogram obtained in the area that is boxed in I. The collagen fibers in the top left corner are clearly recognizable owing to their striated structure and high electron density. Scale bar: 500 nm. See Movie S4.

doi:10.1371/journal.pone.0114448.g005

week, leading to low-size tumors with no impact on the animal's health. All efforts were made to minimize suffering and euthanasia was performed using CO_2.

Intravital Two-Photon Excitation Microscopy (2PEM) and Near-Infrared Branding (NIRB)

The anesthetized mouse was mounted on a custom built holder inspired by Li *et al.* [29]. The holder keeps the ear flat under the lens of the microscope without interfering with second harmonic generation signal captured by a trans detector. The stage bearing the mouse was mounted on an upright confocal microscope (TCS SP8, Leica Microsystems, operating under Leica Application Suite Advanced Fluorescence (LAS AF) software), in an environmental chamber set to 28℃. 2PEM was performed by a single excitation wavelength at 940 nm (Chameleon Ultra II, Coherent), using a 25 × 0.95 N.A. water immersion objective. Emission wavelengths of 510 nm and 680 nm were chosen to collect the fluorescent signal of Life-Act (tumor cells) and Evans Blue (blood vessels), respectively, and the signal was collected by hybrid non-descanned photo-detectors (HyD, Leica Microsystems). The second harmonic generation (SHG, collagen) was imaged at a wavelength of 470 nm, using a photomultiplier detector (PMT, Leica Microsystems). The 2PEM datasets were captured at a scan speed of 400 Hz.

The ROI was marked by NIRB [12, 13], as described in the text. The frame contour was scanned with a pulsed laser at 800 nm (Coherent Chameleon Ultra II, coherent mean power 3,5W at 800 nm), and at a low scan speed (10 Hz, line average: 2, frame average: 2 and picture dimensions: 1024 × 1024 pixels) at the level of the skin surface, above the ROI. The branding was repeated until the square was clearly visible with transmitted light.

Sample Preparation for Electron Microscopy

Following 2PEM, the ear was dissected out and chemically fixed for 1 hour at room temperature in 2.5% glutaraldehyde (GA, Electron Microcopy Sciences) and 2% formaldehyde (FA, Electron Microcopy Sciences) in 0.1 M sodium cacodylate buffer. Fluorescence microscopy images were collected to map the position of the NIRB markings on the ear skin, and the sample was stored overnight in fixative, at 4°C. The following day, the fixative solution was replaced by cacodylate buffer and the sample was kept at 4°C until further processing. The ear was then trimmed close to the ROI. For the samples injected with MDA-MB-231 cells, post-fixation was performed in 0.05% malachite green oxalate (Sigma) and 2.5% GA (Electron Microcopy Sciences) in cacodylate buffer for 2 hours on ice, followed by 0.8% $K_3Fe(CN)_6$ (Merck) and 1.0% OsO4 (Electron Microscopy Sciences) in cacodylate buffer, for 1 hour on ice. Note that malachite green is used here to reduce the lipid extraction commonly associated to sample processing in EM ([39] and references cited, [40]). As a result, the osmium tetroxide has more substrate to interact with which leads to an improved contrast of cellular membranes. Following each fixation step, the samples were rinsed 4×5 min with cacodylate buffer. The samples were then stained with 1% aqueous tannic acid (Electron Microscopy Sciences), for 1 hour on ice. Following 3×5 min rinses with sodium cacodylate buffer, the samples were washed 5×5 min in water and stained with 0.5% aqueous uranyl acetate (UA, Serva), for 1 hour at room temperature. After 5×5 min washes in water, the samples were dehydrated in acetone, infiltrated with a graded series of Epon (Serva) and flat embedded in a 400 μm thick layer of epon as described before [15]. Following overnight polymerization at 60°, the thin sample was cut out and mounted on an empty resin block. The sample was oriented such that the side with the NIRB markings was exposed, and the backside of the sample was glued to the block using a drop of epon. The sample was then again polymerized in the oven overnight. In this way, the sample was mounted so that the ultramicrotomy sections would be parallel to the imaging plane.

A similar processing protocol was used for the sample injected with the D2.0R cells, however the processing after primary fixation with FA and GA was performed in a PELCO BioWave Pro microwave processor (Ted Pella, Inc.). The malachite green/GA and $K_3Fe(CN)_6$/OsO$_4$ fixation steps were done in the microwave, under vacuum, while exposing the sample to 14 minutes of 2 min 'power on/off'-cycles (100 W). Rinsing in between the steps was partly microwave-assisted: the first rinses were performed in the hood, the final 2 rinses for 40 seconds at 250 W. The samples were stained with aqueous UA for 7×1 minute 'power on/off'-cycles (150 W), under vacuum. The sample was then gradually dehydrated in 40 second steps of 25%, 50%, 75%, 90%, and 95% EtOH in water, at 250 W and at atmospheric pressure. Finally, the sample was rinsed twice in 100% EtOH (same settings). The sample was infiltrated with Epon by performing 7 steps (3 minutes at 250 W) where the concentration was increased from 25% Epon in EtOH to the 100% Epon, that was used for the last two washing-steps. The samples were then polymerized as described above. The

microwave-assisted processing is advantageous over the bench-protocols since it reduces the time required for the procedure from days to hours. More importantly, it is believed that the microwave improves the infiltration of the chemicals into the sample. Indeed, we previously observed improved ultra-structural quality in these and other samples (data not shown) when comparing bench and microwave processing [41]. Thick sections (500 nm) were mounted on Superfrost Plus glass slides (Fisherbrand) and stained with a mixture of 0.5% toluidine blue and 1% borax in water. Thin sections (60 nm, Figure 2E and F) and semi-thick sections for tomography (240 nm, Figure 3 and 5) were mounted on formvar-coated slot grids. These sections were stained for 5 minutes with 2% UA in 70% methanol and next for <3 min with lead citrate (Electron Microscopy Sciences).

Electron Microscopy Imaging

The thin sections were imaged with a CM120 transmission electron microscope (TEM, FEI Company) operating at 120 kV. Images were obtained with a Keen View CCD camera (Soft Imaging Solutions, Olympus), running under iTEM (Olympus) software. Electron tomography was performed with a Tecnai F30 Field Emission Gun TEM (FEI Company) operating at 300 kV and equipped with an Eagle 4K camera (FEI Company). The F30 was controlled by Tecnai User Interface (PEOUI) and Tecnai Acquisition (TIA) software. Single-axis tomograms were obtained using SerialEM [42], and reconstructed in eTomo, part of the IMOD software package [43] (Boulder Laboratory, University of Colorado).

Image Processing

Fluorescence images were processed in Fiji, part of ImageJ [44], IMARIS software (Bitplane), and in Adobe Photoshop CS6. Photoshop CS6 was also used to process the EM images. 3D registration of the serial sections and of the tomograms was performed in 3dmod, part of the IMOD software package [43] (Boulder Laboratory, University of Colorado), and the movies were produced in 3dmod, Fiji and Amira (FEI Company). Alignment, transformation and registration of the 3D models of the 2PEM and EM datasets were performed in Amira.

Results

Intravital imaging of tumor cells and branding the imaged area

In order to study *in vivo* tumor invasion events using intravital imaging, we employed a mouse model where fluorescent tumor cells were injected subcutaneously into the ear. The mouse ear was chosen as a model system since it enables non-invasive intravital microscopy through the skin. Moreover, the ear provides excellent imaging conditions for 2PEM since it is thin, easily accessible, and less prone to breathing-induced imaging artifacts. Figure 1A outlines the correlative workflow, the main steps of which are illustrated in panels B-G. After

injection of the tumor cells, the mice were anesthetized and mounted on a custom-made stage (Figure 1B). The stage was fitted with a holder in which the ear with the grafted cells was stabilized [29]. Figure 1C depicts a z-projection from a representative 2PEM stack (Movie S1), revealing fluorescent tumor cells in green (GFP), collagen fibers in blue (SHG) and the blood vessels in red (Evans Blue). Following 3D imaging, the position of the imaged area was marked at the skin level, above and sufficiently distant from the imaged cells to avoid any NIRB-induced damage [45, 46] (Figure 1D). Hereto, the contour of a square frame was slowly line-scanned using a high power pulsed laser. NIRB resulted in auto-fluorescent physical markings that could be seen upon imaging the same area after branding (Figure 1E, Movie S1). By performing NIRB on the living tissue, immediately after 2PEM imaging, the markings can be quickly and accurately created by simply changing the focus of the microscope to the level of the skin surface. Performing the NIRB post-fixation, as described by others [45, 46], would require a transfer of the mouse from the stage of the microscope to the bench for fixation and therefore jeopardize the tracking of the ROI position.

After chemical fixation, a low magnification fluorescence image was obtained to map the position of auto-fluorescent NIRB markings in the ear sample (Figure 1F). Based on this FM map, a smaller sample containing the imaged volume was produced and prepared for EM. Since the skin layer of the mouse ear significantly hinders the infiltration of the chemicals, we have overcome this issue by cutting down (using the NIRB mark) the sample as close as possible to the ROI. In the resin block, the sample was oriented so that subsequent sectioning could be performed parallel to the 2PEM-imaging plane (Figure 1G). The ROI was approached by producing serial sections from the resin embedded sample. Serial thick sections (500 nm), mounted on glass slides and stained with toluidine blue, can be inspected by light microscopy (LM). These images offer a quick overview of the structural features in the sample. Thin sections are mounted on slot grids and are imaged at high resolution by TEM (Figure 1G).

Sequential LM/EM to Retrieve the Cell of Interest

Although the NIRB markings outline the area of the sample that contains the ROI, they do not reveal how deep within the tissue the cells of interest can be found. To retrieve the tumor cells, it is therefore necessary to carefully monitor the progression to the ROI while serial sectioning through the sample. As an initial method to correlate between 2PEM and EM, we chose to use a classic approach for the correlation [47], consisting in alternating between semi-thin (500 nm) and ultra-thin (60 nm) sections of the area of interest. LM images of the semi-thin sections are used to visualize the global anatomy of the tissue, which can then be compared to the 2PEM dataset. When the cells of interest are localized on the semi-thin sections, they can be easily retrieved in the consecutive thin sections and imaged by EM.

Figure 2A and B show respectively a single plane and a 3D representation of a 2PEM z-stack of mouse ear tissue injected with tumor cells, which express

cytoplasmic GFP (Movie S2). As a target for EM imaging, we selected a single cell that had an apparent polarity and invasive morphology, with one side pointing towards the blood vessel (Figure 2A and B, square). Following NIRB, the sample was processed for EM (Figure 1, Methods). The 2PEM dataset revealed that the cell would be found>50 μm (data not shown) below the skin surface, giving an approximation of the depth of tissue to be trimmed. The ROI was first approached by producing 500 nm serial sections, which were imaged with LM (Figure 1G and Figure 2C, 'Approach + Correlation'). LM of the sections revealed the NIRB markings (data not shown) and other structural features of the tissue, including blood vessels. These features were also notable in the 2PEM dataset and could thus be used as reference points for correlating the volume acquired via 2PEM with the one from the resin embedded sample. While closely monitoring the progression through the sample, the vessels visible in the 2PEM stack (Figure 2A) were identified in the thick sections. From the 2PEM z-stack we could predict that our cell of interest should appear approximately 3.5 μm below this first set of serial sections. We then collected a sequence of thick and thin sections of the area of interest (Figure 2C). Overview images of the LM sections were correlated to the 2PEM z-stack (Figure 2A, Figure 2C, 'Correlation ROI', and D). Finally, the cell of interest was identified based on its shape and its position relative to one of the vessels (Figure 2A and 2D, arrowhead). Subsequently, this same cell was retrieved in the consecutive series of 60 nm sections (Figure 2C, 'EM Imaging ROI') and imaged at high resolution with EM (Figure 2E and F, Movie S2) revealing ultrastructural details of its protrusive region.

Serial EM of Invading Tumor Cells

The procedure described above (Figure 2C) is an efficient way to correlate FM and EM. However, it does not allow full three-dimensional reconstruction of the tumor cells with EM since it dedicates part of the volume of interest to sections for LM. In order to enable EM imaging of the complete ROI, it is necessary to obtain serial EM sections of the full volume. In this second approach we focused on tumor cells that were in close proximity to a large blood vessel (Figure 3A and Movie S3). For a better understanding of their distribution within the selected volume, the 2PEM dataset was segmented and the cells of interest rendered in green and numbered (Figure 3B). Orthogonal views (XZ) of the 2PEM dataset (Figure 3C) reveal the position of the cells of interest (circled) relative to the vessels (red, Evans Blue) and to the collagen-rich skin surface (blue, SHG). To approach the ROI (Figure 3D, 'Approach + Correlation'), serial thick sections were imaged by LM and aligned. The image stack was then segmented (Figure 3E and F, Movie S3) to highlight the NIRB marks (purple), hair follicles (orange) and vessels (red) using 3dmod [43]. The resulting 3D model of the sample features (Figure 3F) was then correlated to the model from the 2PEM dataset. We could monitor the block-face position within the sample by overlaying the two 3D models (Figure 3G and Movie S3). The three vessel bifurcations that could also be recognized in the 2PEM dataset (Figure 3G, asterisks, and Figure S1A, V1-3) were

key features to try to predict the position of the cells of interest. Three of the cells (3, 5 and 6) are in close proximity to these vessels, but slightly deeper into the tissue (about 1 to 2 µm as estimated from the measurements done on the 2PEM data-set). Having approached the cells of interest, we switched to producing serial EM sections (Figure 3D, 'EM imaging ROI').

Based on the 2PEM dataset, we could anticipate the cells of interest being within 50 µm in depth below the mentioned vessel bifurcations (in the z-range 73–123 µm of the imaged volume, Movie S3). To ensure that we could image all selected cells with EM, we obtained>170 serial sections, approximately 300 nm thick that were suitable for EM tomography. This 'library' of sections represented the complete volume in which the cells of interest could be expected. By aligning low magnification TEM images of these sections to the 2PEM z-stack using Photoshop, the xy positions of the cells could be determined. Using these coordinates as a guide, we could retrieve the selected tumor cells (Figure 3H, 1–6). The correlation was further confirmed by the shape similarity of the cells and their position relative to the vessel. Serial sectioning of the sample enabled us to reconstruct 3D EM models of the cells of interest through segmentation of the cells' plasma membrane (Figure 3I-K). This provided ultrastructural information of the tumor cells, and further confirmed the correlation of the two datasets (compare Figure 3I and K). Importantly, the gain of resolution between 2PEM and EM can be appreciated even though EM is performed here at low magnification (Figure 3I-K). For example, while the cell appears to be very close to the blood vessel in the 2PEM dataset (Figure 3I), serial EM reveals that it is actually still physically separated at least 5.5 µm, from the lumen of the vessel by both cellular and a-cellular material (Figure 3J and K).

Further gain in resolution can be achieved by electron tomography, which enables 3D visualization at nanoscale resolution. We selected a highly-polarized cell with protrusion-like extensions in close proximity to fibrous material, very likely extracellular matrix (ECM) fibers such as collagen (Figure 3L). A virtual slice from a tomogram, obtained at the site of these protrusions, shows the complex organization of the cell membrane in close proximity to the ECM fibers (Figure 3M, Movie S3). The latter are sufficiently electron dense to allow for semi-automatic segmentation throughout the reconstructed 3D volume (Figure 3N and Movie S3, blue). Altogether, this proves that we can potentially target any event/ cell of interest within the processed ROI and image/segment it at high resolution in 3D.

Identification of corresponding cells and other structural features (vessel branches) in both datasets allowed producing simplified 3D maps of the 2PEM z-stack and the serial section dataset. For both datasets, the relative positions of structural features, i.e. cells and vessel branches (Figure S1A), were plotted within a 3D coordinate system. In the 3D Analysis Software Amira, it was possible to simultaneously visualize both maps in 3D and to select common features, 'landmarks', in both datasets (Figure S1B). Together, the coordinates of the selected points form two paired 'landmark-sets', which are the basis of the correlation between the two datasets. Using Amira's *LandmarkWarp* module, we

performed a transformation of one map to fit into the other by attempting to overlay the paired landmarks in 3D. Applying a 'rigid' transformation method will optimize the warp without any deformations, but solely by translation and rotation of the dataset. The 'Bookstein' transformation method does allow additional non-linear transformations of the model, including stretching and scaling, in order to make both landmarks-sets overlap. Comparing the two different transformation approaches to fit the 2PEM in the serial sections model reveals the differences between both datasets. Using rigid transformations, it was not possible to overlay the landmarks in 3D (Figure S1C); this could only be achieved by the non-linear transformation enabled by the Bookstein method (Figure S1D). This finding confirms that, as expected, non-uniform changes are introduced while processing living tissues for EM. Therefore, the position of the cells of interest in the 2PEM dataset cannot be directly translated to their location into the resin block and therefore in the stack of serial sections. This further suggests the need for reliable correlation methods to allow the easy retrieval of events of interest in the EM processed sample.

Time-lapse imaging of invading tumor cells

One of the major advantages of intravital imaging is to follow tumor development over time. Here we show how to combine time-lapse 2PEM of fully mature tumors with 3D EM. D2.0R cells [38], expressing the fluorescent actin marker LifeAct-YPet [35, 36], were injected into the mouse ear tissue. We obtained fully-grown, invasive and vascularized tumors within 14 days after injection (Figure 4A, top left panel). While tumor size made 2PEM imaging more challenging, we could still analyze invasive regions at the tumor borders and record isolated invading cells (Figure 4B and C, Movie S4). Usage of LifeAct-Ypet allowed to dynamically record, through time-lapse imaging of the anesthetized mouse, invasive protrusions that resembled the filopodia-like protrusions (FLPs) previously characterized *in vitro* [35, 36] (Figure 4E, Movie S4). While the time-lapse acquisition of actin reveals how FLPs probe the surrounding environment, recording of SHG and the Evans Blue label allows to respectively visualize the collagen meshwork that engulf the imaged cell as well as the local hemodynamics (Movie S4). Following 2PEM of this cell, the imaged area was marked at the level of the skin surface using NIRB.

Using the collagen fibers meshwork to retrieve the ROI

In the previous experiments, the vasculature was used to retrace the position of the cells of interest within the tissue. In the case of mature tumors, the tumor-associated vasculature can be perturbed and therefore difficult to use as fiducial landmarks. Moreover, a mature tumor such as the one shown in figure 4 is enriched in fibrous and dense cellular material in which the cancer cells are evolving (Figure 4A). As a consequence, the strategy for targeting cannot rely on a 3D mapping by LM from semi-thin sections as shown previously. In the situation

illustrated in [Figures 4](#) and [5](#), the best strategy is therefore to perform a minimal approach of the region of interest by semi-thin sections (500 nm), that would expose the NIRB markings only, and then to collect the rest of the tissue by serial sections for TEM ([Figure 5A](#)).

Using this approach we obtained a complete 3D TEM dataset of the ROI and its surroundings, which enabled full volume correlation between 2PEM and TEM. From both the 2PEM and TEM dataset we could build precise 3D maps of the tissue, and the landmarks therein. Having identified corresponding landmarks, we could overlay the two datasets through 3D registration. A simplified cartoon of the steps involved in this approach is shown in [Figure 5B](#). As revealed by non-linear 2PEM (SHG) and TEM, the collagen fibers form dense bundles within the tissue ([Figure 5C](#)). They are distributed as an organized meshwork that can be used as landmarks in both modalities. As the 2PEM dataset also provides the position of the cell of interest relative to the collagen fibers ([Figure 5B](#), dashed lines), the registration transfers the predicted position of the cancer cell within the EM dataset. Using Amira, the collagen fibers were modeled from the 2PEM dataset and from the EM z-stacks ([Figure 5D and E](#)). Additionally, we also segmented the cell of interest in the 2PEM dataset ([Figure 5D](#)). Visualizing both 3D models in a shared 3D space in Amira enabled to identify corresponding points in both datasets, e.g. cross-points between collagen fibers. These similarities in both datasets could be selected with '*Landmark (2 sets)*'. Using Amira's *Landmarkwarp* module, the 2PEM collagen model with the ROI was then warped into the EM collagen model. This required non-linear transformations of the 2PEM model ([Figure 5F](#)). This finding is in agreement with our efforts to align a 2PEM and serial section 3D maps of structural reference points ([Figure S1](#)). Here, it was not possible to overlay the corresponding points from the pre- and post-EM-processing maps without performing non-linear transformations.

In Amira's virtual 3D space, the collagen models were linked to the image z-stacks from which they are segmented. Warping the 2PEM model to fit within the TEM model therefore also results in the projection of the ROI on the series of TEM images from the serial sections ([Figure 5G](#)). Having established the approximate position of the cell within the series of serial sections, high-resolution images could be made in this area ([Figure 5H](#)). Electron tomography of a selected area ([Figure 5J](#), dashed square, [Movie S4](#)) enables 3D EM imaging of the cell of interest. Moreover, a virtual section of the tomogram ([Figure 5I](#), [Movie S4](#)) has an improved z-resolution over the 2D projection of the full section, which is normally obtained with TEM. Here, the striations of the collagen fibrils, close to the cell membrane, are clearly visible, and the structure of the cancer cell can be studied in detail.

Discussion

Searching for individual cells of interest in complex tissues embedded in a resin block is a tedious task. In light microscopy, cells or regions of interest are

routinely tagged with fluorophores. Targeting to their specific location is thus fast and accurate even in complex organisms, provided that light microscopy allows imaging deep within intact tissues. To perform similar targeting in electron microscopy, several attempts have been made to preserve the signal from fluorescent proteins [48] or to add fluorescent dyes to the tissues [49] in resin embedded samples. These techniques rely on specific fixation methods (cryo-methods) and also on the use of hydrophilic resins (methacrylates). When the use of fluorescent probes is not possible, or when the selected procedures to prepare the sample for EM lead to a quenching of the fluorescent signal [8], other strategies need to be used [12, 13, 15, 16, 50, 51]. In this paper, we combine and synergize previously published strategies in order, for the first time, to perform accurate and reliable correlative light and electron microscopy of tumor cells in vivo upon non-invasive 2PEM imaging. One consists in recording the volume of the living sample to build a three-dimensional map of the region of interest [15, 52], which is used to predict its position in the resin block. Another relies on artificial landmarks produced with a near-infrared laser to highlight the region of interest directly on the hydrated sample [12–14]. Finally, we improved a strategy that we used before [15, 52] consisting of recapitulating the local anatomy of the tissue with serial sections in order to retrace the position of individual objects within the EM dataset [16].

Our method of correlation has three variations. With the first, sequences of thick and thin sections enable quick screening of the sample for the ROI, by comparing the 2PEM model to the 3D reconstruction built from the LM acquisitions of serial thick sections. Upon identification of the tumor cell in these sections, its ultrastructure is recorded by TEM from the adjacent thin section (Figure 2). A disadvantage of this approach is that it allocates a significant fraction of the ROI to the model reconstruction by serial LM imaging. Although these thick sections could in principle be re-embedded and re-sectioned for EM, full-cell reconstruction will not be possible and crucial structures may be lost. With the second strategy, a fraction of the embedded tissue is used to create a partial 3D model, which is correlated to the 2PEM dataset of the same area. The major advantage is the preservation of the cells of interest for further TEM imaging. Moreover, it facilitates an accurate estimation of the depth at which cells should be expected within the resin block. Full volume correlation allows determining the position of the ROI (Figure 5B). Using the 3D imaging software Amira [53], the registration of the two datasets required non-linear transformations of the 2PEM model to fit into the model obtained from the serial TEM images (Figure S1) reflecting the sample distortions caused by the preparation methods [54]. Chemical fixation, dehydration and resin embedding each influence the volume orientation of the sample. During chemical fixation, GA will cause around 5% shrinkage of the sample [55], whereas OsO_4 fixation will result in swelling [54, 56, 57]. Subsequent dehydration and resin embedding will cause further shrinkage to the specimen, which can be minimized by exposing the sample as briefly as possible to the solvents [55], e.g. by microwave assisted embedding. Importantly, the sample distortions are never homogenous throughout the tissue

due to differences in biological material and infiltration efficiency of the chemicals. This explains why the 2PEM dataset does not linearly corresponds to the TEM dataset. As a consequence, the prediction of the position of one particular structure inside the resin-embedded sample has a limited accuracy (in the order of 20 µm). Taking this into consideration, the progression through the sample has to be performed with great care and, upon approaching the ROI, thin sections for EM should be collected systematically. Similar concern is illustrated with the third approach, where the cells of interest are expected close to the surface of the sample (within the first 10 microns of the resin block). In that case and for preserving the cells of interest, systematic serial sections are collected and recorded by TEM. The correlation is then performed *a posteriori* by overlapping the 3D dataset from both imaging modalities. In this work, we show that endogenous landmarks can serve as fiducial for the volume registration. We have used blood vessels bifurcations as well as fluorescent cancer cells to build sets of points that were paired and matched together in Amira. The pairing can only be performed if the landmarks are clearly visible in both imaging modalities. Their detection is made possible in fluorescence microscopy by the use of dyes or of fluorescent proteins, while in EM, they show a straight forward pattern that can be identified unambiguously. In some instances though, tissues can be too dense or be perturbed by the onset of a large and vascularized tumor, making the vessels recognition difficult in both FM and EM. As illustrated in figure 5, in such conditions, the density of the tissue as observed by TEM hinders significantly the recognition of the targeted cell. Nevertheless, our approach was versatile enough to allow the use of other structures for the correlation, such as the collagen meshwork, which is again visible in both imaging modalities. Indeed, collagen fibers can be detected from living tissues using SHG, and appear as bundles of electron dense fibers in EM micrographs. The segmentation of these fibers on both datasets allowed a precise registration (after non-linear transformations) and a prediction of the position of the cell of interest.

The use of anatomical features as a basis for correlation can also be applied to studies of other biological questions in a wide range of samples and applications, making it a highly versatile approach. We have demonstrated correlation between FM, LM and EM based on different examples of intrinsic fiducials. Moreover, the approach described here could be extended by recently developed, advanced 3D EM approaches, including Focused Ion Beam Scanning EM [58] and serial block-face electron microscopy [59]. In both methods, numerous cycles of sequentially imaging and removing the sample surface result in voluminous 3D EM datasets. Correlation of the serial-sectioning dataset and the 2PEM model enables identification of the ROI within the sample, which can then be imaged either of these techniques.

With these improved methodologies for correlating dataset from multiphoton microscopy to 3D electron microscopy, we bring an accessible set of solutions to perform structure-function analysis upon intravital imaging of tumor behavior in a murine model. In this paper, we show that mouse intravital imaging of a tumor can be efficiently correlated to the ultrastructural analysis of selected cancer cells.

The subcutaneous graft model in the mouse ear has several advantages for studying the behavior of cancer cells in a native microenvironment, as it allows functional imaging over time, the capture of rare events at the single cell level. Moreover, our technique allows the recovery of the same cells for ultrastructural analysis. We therefore expect such methods will allow the study of fundamental features of the metastasis cascade within intact tissues.

Supporting Information

Figure S1. 3D Registration of 2PEM and Serial Section Datasets. A: Identification of features, 'landmarks', in the 2PEM dataset that could be retraced in the sequence of serial sections obtained from the EM processed sample. B. Front and side-view of 3D maps of the positions of the features in the 2PEM dataset (colored spheres) and the corresponding EM coordinates (colored squares). The vectors indicate for each EM position the magnitude (in µm) and the direction of the offset between the two datasets. In an attempt to overlay the 3D maps of both datasets, the 2PEM map (circles) was transformed to dock it in the serial-section dataset (squares). In Amira, it is possible to perform a 'rigid transformation' (C), which lowered the offset between the corresponding dataset, or to force the paired 'landmarks' (features) to overlap by performing a 'Bookstein Transform' (D).
doi:10.1371/journal.pone.0114448.s001 (TIF)

Checklist S1.
doi:10.1371/journal.pone.0114448.s002 (PDF)

Movie S1. 2PEM Imaging and NIRB. GFP-expressing tumor cells (green) are subcutaneously injected and imaged with 2PEM. Vessels are stained with Evans Blue (red) and collagen fibers are visualized through SHG (blue). The region of interest is then marked by NIRB (orange).
doi:10.1371/journal.pone.0114448.s003 (MP4)

Movie S2. Zooming in to the cell of interest. After injection with GFP-expressing tumor cells (green), the skin tissue was imaged with 2PEM. Vessels are shown in red. The z-stack moves into the tissue and then zooms in on a cell of interest. Following EM processing, thick and thin sections of the sample were correlated to the 2PEM z-stack, and the tumor cell was imaged at high magnification.
doi:10.1371/journal.pone.0114448.s004 (MP4)

Movie S3. Full Volume Correlation of the ROI Enables Electron Tomography of Tumor Cells *in vivo*. Mouse skin tissue injected with GFP-expressing tumor cells is imaged with 2PEM. Vessels are shown in red (Evans Blue dye) and collagen (SHG) is shown in blue. 500 nm sections through the EM processed sample are aligned segmented. The 3D models of the 2PEM and the serial section datasets are correlated to monitor the approach to the cells of interest. Upon retrieval of the cell of interest, electron tomography reveals its ultrastructure in 3D. Scale bar: 500 nm.
doi:10.1371/journal.pone.0114448.s005 (MP4)

Movie S4. Correlating Intravital Time-Lapse 2PEM to Electron Tomography of D2.0R Tumor Cells. The 2PEM z-stack reveals the position of LifeAct-Ypet expressing D2.0R cells injected in mouse ear skin. The vessels were injected with Evans Blue (red) and the collagen is visible through SHG (blue). The cells of interest were imaged over a period of 120 minutes (one image was acquired every three minutes), capturing the formation of actin-rich (LifeAct-Ypet signal, green) protrusions. Correlating 2PEM to EM enables to zoom in and perform electron tomography to reveal the ultrastructure of the cell of interest and the collagen fibrils in the extracellular matrix. Scalebar: 500 nm.
doi:10.1371/journal.pone.0114448.s006 (MP4)

Acknowledgments

Author Contributions

Conceived and designed the experiments: MAK LM YS JGG. Performed the experiments: MAK LM NS. Analyzed the data: MAK LM YS JGG. Contributed reagents/materials/analysis tools: NS TS. Wrote the paper: MAK LM YS JGG.

References

1. **Fein MR, Egeblad M** (2013) Caught in the act: revealing the metastatic process by live imaging. Dis Model Mech 6: 580–593.

2. **Denk W, Strickler JH, Webb WW** (1990) Two-photon laser scanning fluorescence microscopy. Science 248: 73–76.

3. **Freund I, Deutsch M** (1986) Second-harmonic microscopy of biological tissue. Opt Lett 11: 94.

4. **Debarre D, Supatto W, Pena AM, Fabre A, Tordjmann T, et al.** (2006) Imaging lipid bodies in cells and tissues using third-harmonic generation microscopy. Nat Methods 3: 47–53.

5. **Kukulski W, Schorb M, Welsch S, Picco A, Kaksonen M, et al.** (2011) Correlated Fluorescence and 3D Electron Microscopy with High Sensitivity and Spatial Precision. The Journal of Cell Biology 192: 111–119.

6. **Polishchuk RS, Polishchuk EV, Luini A** (2012) Visualizing live dynamics and ultrastructure of intracellular organelles with preembedding correlative light-electron microscopy. Methods Cell Biol 111: 21–35.

7. **Jimenez N, Van Donselaar EG, De Winter DA, Vocking K, Verkleij AJ, et al.** (2010) Gridded Aclar: preparation methods and use for correlative light and electron microscopy of cell monolayers, by TEM and FIB-SEM. J Microsc 237: 208–220.

8. **Karreman MA, Agronskaia AV, Verkleij AJ, Cremers FF, Gerritsen HC, et al.** (2009) Discovery of a new RNA-containing nuclear structure in UVC-induced apoptotic cells by integrated laser electron microscopy. Biol Cell 101: 287–299.

9. **Agronskaia AV, Valentijn JA, van Driel LF, Schneijdenberg CT, Humbel BM, et al.** (2008) Integrated fluorescence and transmission electron microscopy. J Struct Biol 164: 183–189.

10. **Lucas MS, Gunthert M, Gasser P, Lucas F, Wepf R** (2012) Bridging microscopes: 3D correlative light and scanning electron microscopy of complex biological structures. Methods Cell Biol 111: 325–356.

11. **Liv N, Zonnevylle AC, Narvaez AC, Effting AP, Voorneveld PW, et al.** (2013) Simultaneous correlative scanning electron and high-NA fluorescence microscopy. PLoS One 8: e55707.

12. **Bishop D, Nikić I, Brinkoetter M, Knecht S, Potz S, et al.** (2011) Near-infrared branding efficiently correlates light and electron microscopy. Nature Methods 8: 568–570.

13. **Maco B, Holtmaat A, Cantoni M, Kreshuk A, Straehle CN, et al.** (2013) Correlative in vivo 2 photon and focused ion beam scanning electron microscopy of cortical neurons. PloS one 8.

14. **Maco B, Cantoni M, Holtmaat A, Kreshuk A, Hamprecht FA, et al.** (2014) Semiautomated correlative 3D electron microscopy of in vivo-imaged axons and dendrites. Nat Protoc 9: 1354–1366.

15. **Kolotuev I, Schwab Y, Labouesse M** (2010) A precise and rapid mapping protocol for correlative light and electron microscopy of small invertebrate organisms. Biology of the Cell 102: 121–132.

16. **Goetz JG, Steed E, Ferreira RR, Roth S, Ramspacher C, et al.** (2014) Endothelial cilia mediate low flow sensing during zebrafish vascular development. Cell Rep 6: 799–808.

17. **Armer HE, Mariggi G, Png KM, Genoud C, Monteith AG, et al.** (2009) Imaging transient blood vessel fusion events in zebrafish by correlative volume electron microscopy. PLoS One 4: e7716.

18. **Giepmans BN, Deerinck TJ, Smarr BL, Jones YZ, Ellisman MH** (2005) Correlated light and electron microscopic imaging of multiple endogenous proteins using Quantum dots. Nat Methods 2: 743–749.

19. **Nisman R, Dellaire G, Ren Y, Li R, Bazett-Jones DP** (2004) Application of quantum dots as probes for correlative fluorescence, conventional, and energy-filtered transmission electron microscopy. J Histochem Cytochem 52: 13–18.

20. **Gaietta G, Deerinck TJ, Adams SR, Bouwer J, Tour O, et al.** (2002) Multicolor and electron microscopic imaging of connexin trafficking. Science 296: 503–507.

21. **Maranto AR** (1982) Neuronal mapping: a photooxidation reaction makes Lucifer yellow useful for electron microscopy. Science 217: 953–955.

22. **Deerinck TJ, Martone ME, Lev-Ram V, Green DP, Tsien RY, et al.** (1994) Fluorescence photooxidation with eosin: a method for high resolution immunolocalization and in situ hybridization detection for light and electron microscopy. J Cell Biol 126: 901–910.

23. **Saxton MJ, Jacobson K** (1997) Single-particle tracking: applications to membrane dynamics. Annu Rev Biophys Biomol Struct 26: 373–399.

24. **Valastyan S, Weinberg RA** (2011) Tumor metastasis: molecular insights and evolving paradigms. Cell 147: 275–292.

25. **Gaggioli C, Hooper S, Hidalgo-Carcedo C, Grosse R, Marshall JF, et al.** (2007) Fibroblast-led collective invasion of carcinoma cells with differing roles for RhoGTPases in leading and following cells. Nat Cell Biol 9: 1392–1400.

26. **Friedl P, Alexander S** (2011) Cancer invasion and the microenvironment: plasticity and reciprocity. Cell 147: 992–1009.

27. **Goetz JG, Minguet S, Navarro-Lerida I, Lazcano JJ, Samaniego R, et al.** (2011) Biomechanical remodeling of the microenvironment by stromal caveolin-1 favors tumor invasion and metastasis. Cell 146: 148–163.

28. **Cheung KJ, Gabrielson E, Werb Z, Ewald AJ** (2013) Collective invasion in breast cancer requires a conserved basal epithelial program. Cell 155: 1639–1651.

29. **Li JL, Goh CC, Keeble JL, Qin JS, Roediger B, et al.** (2012) Intravital multiphoton imaging of immune responses in the mouse ear skin. Nature protocols 7: 221–234.

30. **Kienast Y, von Baumgarten L, Fuhrmann M, Klinkert WE, Goldbrunner R, et al.** (2010) Real-time imaging reveals the single steps of brain metastasis formation. Nat Med 16: 116–122.

31. **Kedrin D, Gligorijevic B, Wyckoff J, Verkhusha VV, Condeelis J, et al.** (2008) Intravital imaging of metastatic behavior through a mammary imaging window. Nat Methods 5: 1019–1021.

32. **Alexander S, Koehl GE, Hirschberg M, Geissler EK, Friedl P** (2008) Dynamic imaging of cancer growth and invasion: a modified skin-fold chamber model. Histochem Cell Biol 130: 1147–1154.

33. **Ritsma L, Steller EJ, Beerling E, Loomans CJ, Zomer A, et al.** (2012) Intravital microscopy through an abdominal imaging window reveals a pre-micrometastasis stage during liver metastasis. Sci Transl Med 4: 158ra145.

34. **Goetz JG, Minguet S, Navarro-Lérida I, Lazcano JJ, Samaniego R, et al.** (2011) Biomechanical remodeling of the microenvironment by stromal caveolin-1 favors tumor invasion and metastasis. Cell 146: 148–163.

35. **Shibue T, Brooks MW, Inan MF, Reinhardt F, Weinberg RA** (2012) The outgrowth of micrometastases is enabled by the formation of filopodium-like protrusions. Cancer Discov 2: 706–721.

36. **Shibue T, Brooks MW, Weinberg RA** (2013) An integrin-linked machinery of cytoskeletal regulation that enables experimental tumor initiation and metastatic colonization. Cancer Cell 24: 481–498.

37. **Shibue T, Weinberg RA** (2009) Integrin beta1-focal adhesion kinase signaling directs the proliferation of metastatic cancer cells disseminated in the lungs. Proc Natl Acad Sci U S A 106: 10290–10295.

38. **Rak JW, McEachern D, Miller FR** (1992) Sequential alteration of peanut agglutinin binding-glycoprotein expression during progression of murine mammary neoplasia. Br J Cancer 65: 641–648.

39. **Griffiths G** (1993) 3.2.3.2: Extraction of Cellular Components by Buffers. In:, Griffiths G, . Fine Structure Immuno-cytochemistry. Heidelberg: Springer-Verlag. pp 60.

40. **Hayat MA** (1993) Stains and Cytochemical Methods. New York: Plenum Press. 455 p.

41. **Schieber NL, Nixon SJ, Webb RI, Oorschot VM, Parton RG** (2010) Modern approaches for ultrastructural analysis of the zebrafish embryo. In: Müller-Reichert T. Modern approaches for ultrastructural analysis of the zebrafish embryo. pp 425–442

42. **Mastronarde DN** (2005) Automated electron microscope tomography using robust prediction of specimen movements. Journal of structural biology 152: 36–51.

43. **Kremer JR, Mastronarde DN, McIntosh JR** (1996) Computer visualization of three-dimensional image data using IMOD. Journal of structural biology 116: 71–76.

44. **Schneider CA, Rasband WS, Eliceiri KW** (2012) NIH Image to ImageJ: 25 years of image analysis. Nature Methods 9: 671–675.

45. **Bishop D, Nikic I, Brinkoetter M, Knecht S, Potz S, et al.** (2011) Near-infrared branding efficiently correlates light and electron microscopy. Nat Methods 8: 568–570.

46. **Maco B, Holtmaat A, Cantoni M, Kreshuk A, Straehle CN, et al.** (2013) Correlative in vivo 2 photon and focused ion beam scanning electron microscopy of cortical neurons. PLoS One 8: e57405.

47. **Jones S, Chapman SK, Crocker PR, Carson G, Levison DA** (1982) Combined light and electron microscope in routine histopathology. J Clin Pathol 35: 425–429.

48. **Nixon SJ, Webb RI, Floetenmeyer M, Schieber N, Lo HP, et al.** (2009) A single method for cryofixation and correlative light, electron microscopy and tomography of zebrafish embryos. Traffic 10: 131–136.

49. **Biel SS, Kawaschinski K, Wittern KP, Hintze U, Wepf R** (2003) From tissue to cellular ultrastructure: closing the gap between micro- and nanostructural imaging. J Microsc 212: 91–99.

50. **Allegra Mascaro AL, Cesare P, Sacconi L, Grasselli G, Mandolesi G, et al.** (2013) In vivo single branch axotomy induces GAP-43-dependent sprouting and synaptic remodeling in cerebellar cortex. Proc Natl Acad Sci U S A 110: 10824–10829.

51. **Canty AJ, Huang L, Jackson JS, Little GE, Knott G, et al.** (2013) In-vivo single neuron axotomy triggers axon regeneration to restore synaptic density in specific cortical circuits. Nat Commun 4: 2038.

52. **Kolotuev I, Bumbarger DJ, Labouesse M, Schwab Y** (2012) Targeted ultramicrotomy: a valuable tool for correlated light and electron microscopy of small model organisms. Methods Cell Biol 111: 203–222.

53. **Handschuh S, Baeumler N, Schwaha T, Ruthensteiner B** (2013) A correlative approach for combining microCT, light and transmission electron microscopy in a single 3D scenario. Front Zool 10: 44.

54. **Hayat MA** (2000) Principles and Techniques of Electron Microscopy: Biological Applications. United States of America: Cambridge University Press. 564 p.

55. **Dykstra MJ, Reuss LE** (2003) Biological Electron Microscopy - Theory, Techniques, and Troubleshooting. New York: Kluwer Academic/Plenum Publishers. 534 p.

56. **Kushida H** (1962) A Study of Cellular Swelling and Shrinkage during Fixation, Dehydration and Embedding in Various Standard Media. J Electron Microsc 11: 135–138.

57. **Elbers PE** (1966) Ion permeability of the egg of Limnaea stagnalis L. on fixation for electron microscopy. Biochem Bophys Acta 112: 318–329.

58. **Heymann JA, Hayles M, Gestmann I, Giannuzzi LA, Lich B, et al.** (2006) Site-specific 3D imaging of cells and tissues with a dual beam microscope. J Struct Biol 155: 63–73.

59. **Denk W, Horstmann H** (2004) Serial block-face scanning electron microscopy to reconstruct three-dimensional tissue nanostructure. PLoS Biol 2: e329.

2.2.4 Conclusions

Ce protocole a permis pour la première fois d'effectuer de la CLEM sur tissu intact après imagerie intravitale non invasive. Ce protocole consiste à appliquer différentes stratégies qui avaient déjà été décrites auparavant. La première consiste à imager dans les trois dimensions l'échantillon vivant afin d'obtenir une cartographie 3D permettant la prédiction de la position des cellules d'intérêt dans le bloc de résine. La seconde consiste à ajouter des points de repères artificiels par ablation laser à la surface de l'échantillon pour toujours conserver la région d'intérêt au cours de la préparation pour la microscopie électronique. Finalement, l'utilisation des coupes sériées pour reconstruire les structures anatomiques présentes dans la région d'intérêt pour relocaliser précisément les cellules d'intérêts.

Cette technique nous a permis de valider l'approche et mettre en évidence les interactions des cellules cancéreuses avec la MEC ainsi qu'avec les vaisseaux sanguins à l'échelle nanométrique. L'étude de xénogreffes de cellules tumorales dans l'oreille de souris par CLEM devrait apporter de nouvelles connaissances dans l'invasion de la MEC ainsi que dans l'intravasation et l'extravasation des cellules tumorales.

Ce protocole a pour avantage de ne pas requérir d'autres appareils que ceux déjà présent pour réaliser l'imagerie intravitale et la microscopie électronique, rendant ce protocole accessible à de nombreux instituts de recherche. Cependant, la principale limitation réside dans la quantité et le temps de travail nécessaire pour approcher la région d'intérêt par coupes sériées. Le temps moyen pour préparer et imager la région d'intérêt par microscopie électronique était supérieur à 1 mois. De ce fait, ce protocole est limité à l'étude d'échantillon peux épais.

Nous avons donc cherché par la suite une façon de rendre ce protocole plus efficace et polyvalent.

2.3 Evolution du protocole de CLEM intravitale : plus efficace et polyvalent

2.3.1 Contexte

La procédure de CLEM intravitale précédente ne requière que peux d'équipements et peut être facilement mis en place dans un laboratoire possédant une plateforme d'imagerie.

Cependant, l'approche de la ROI par coupes sériés est une tache longue et fastidieuse, nécessitant de plus une grande expérience dans ce domaine. Ces limitations font que ce protocole n'est adapté qu'à des échantillons de faible volume où la ROI ne se situe pas en profondeur.

Intéressé par le fait de pouvoir aussi étudier les étapes finales de la formation de métastases plus particulièrement l'extravasation, une nouvelle collaboration a été établie avec l'équipe de F. Winkler (DKFZ, Heidelberg). Ce laboratoire a développé une méthode d'imagerie intravitale permettant de suivre la formation de micro-métastases dans le cerveau de la souris (Kienast et al., 2010). Une fenêtre optique est greffée sur le crâne de la souris, 3 semaines après l'opération des cellules métastatiques fluorescentes sont injectées dans la circulation sanguine de la souris. Certaines de ces cellules vont se retrouver très rapidement bloquer dans certain capillaires sanguins irrigant le cerveau. Il est alors possible par microscopie multiphotonique d'imager ces cellules *in vivo*.

Contrairement à l'oreille de souris, où les cellules cancéreuses étaient imagées à environ 80µm de profondeur, les cellules dans le cerveau étaient imagées à des profondeurs souvent supérieures à 400µm. Une approche de la ROI par coupes sériées comme décrit précédemment nécessiterait un travail titanesque consistant à réaliser des milliers de coupes à collecter et à corréler.

2.3.2 Principaux résultats

La première étape de CLEM pour ce type d'échantillon où la cellule d'intérêt se retrouve à des profondeurs 5 fois plus importante que dans l'oreille de souris est la même que précédemment. La technique de NIRB s'est encore révélée indispensable pour conserver et retrouver la ROI pendant la préparation de l'échantillon pour la microscopie électronique.

Une fois l'échantillon préparé et inclus dans le bloc de résine nous avons eu l'idée de réaliser l'imagerie du bloc de résine par tomographie aux rayons X (microCT). Cette idée est venue après avoir pris connaissance d'un article où les chercheurs décrivaient une méthode de CLEM où ils visualisaient par rayons X un échantillon juvénile de *Mytilus galloprovincialis* (Moule méditerranéenne) inclus dans la résine par microCT (Figure 27) (Handschuh et al., 2013).
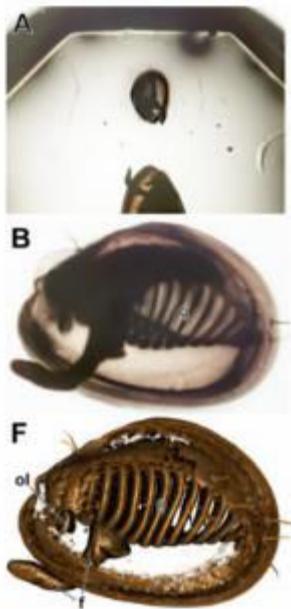
*Figure 27 : **Imagerie aux rayons X dans le bloc de résine**. **A** : vue de côté de l'échantillon inclus dans la résine. **B** : vue agrandie de l'échantillon dans le bloc de résine. **F** : reconstruction en 3D de l'échantillon visualisé par rayons X. D'après Handschuh et al., 2013.*

N'ayant pas ce type d'appareil au laboratoire nous avons ainsi collaboré avec l'équipe de B. Ruthensteiner (LMU, Münich) un des auteurs du travail sur *Mytilus galloprovincialis.*

Il s'est révélé que la fixation de la souris par perfusion cardiaque, qui vide le sang de la vasculature, et la post-fixation de l'échantillon par métaux lourds comme le tétroxyde d'osmium généraient suffisamment de contraste par microCT pour distinguer l'ensemble de la vasculature de l'échantillon.

La superposition des volumes obtenues par microscopie multiphotonique intravitale et microCT nous a permis de déterminer avec précision la position de la cellule d'intérêt directement dans le bloc de résine. L'approche par coupes sériées s'est alors révélée inutile.

2.3.3 Manuscrit n°4: Fast and precise targeting of single tumor cell *in vivo* by multimodal correlative microscopy

TOOLS AND TECHNIQUES

Fast and precise targeting of single tumor cells *in vivo* by multimodal correlative microscopy

Matthia A. Karreman[1], Luc Mercier[2,3,4,5], Nicole L. Schieber[1], Gergely Solecki[6,7], Guillaume Allio[2,3,4,5], Frank Winkler[6,7], Bernhard Ruthensteiner[8], Jacky G. Goetz[2,3,4,5,*] and Yannick Schwab[1,*]

ABSTRACT

Intravital microscopy provides dynamic understanding of multiple cell biological processes, but its limited resolution has so far precluded structural analysis. Because it is difficult to capture rare and transient events, only a few attempts have been made to observe specific developmental and pathological processes in animal models using electron microscopy. The multimodal correlative approach that we propose here combines intravital microscopy, microscopic X-ray computed tomography and three-dimensional electron microscopy. It enables a rapid (c.a. 2 weeks) and accurate (<5 μm) correlation of functional imaging to ultrastructural analysis of single cells in a relevant context. We demonstrate the power of our approach by capturing single tumor cells in the vasculature of the cerebral cortex and in subcutaneous tumors, providing unique insights into metastatic events. Providing a significantly improved throughput, our workflow enables multiple sampling, a prerequisite for making correlative imaging a relevant tool to study cell biology *in vivo*. Owing to the versatility of this workflow, we envision broad applications in various fields of biological research, such as cancer or developmental biology.

INTRODUCTION

Metastasis relies on a series of steps, including invasion of the tissue and circulation through the vasculature to reach a secondary distant site (Valastyan and Weinberg, 2011). Although relevant *in vitro* models have been created to study these processes (Gligorijevic et al., 2014), they have failed so far to recapitulate the complexity of living tissues. Intravital microscopy (IVM) of invasive tumor cells has enabled *in vivo* studies of the metastatic cascade (Gligorijevic et al., 2014; Kienast et al., 2010). Here, tumor progression can be imaged in various animal models upon, for example, orthotopic, subcutaneous or intra-circulation injection of tumor cells (Karreman et al., 2014; Leong et al., 2014; Sahai, 2007; Stoletov et al., 2010).

[1]Cell Biology and Biophysics Unit, European Molecular Biology Laboratory, Heidelberg 69117, Germany. [2]MN3T, Inserm U1109, Strasbourg 67200, France. [3]Université de Strasbourg, Strasbourg 67000, France. [4]LabEx Medalis, Université de Strasbourg, Strasbourg 67000, France. [5]Fédération de Médecine Translationnelle de Strasbourg (FMTS), Université de Strasbourg, Strasbourg 67000, France. [6]Department of Neurooncology, University Hospital Heidelberg, Heidelberg 69120, Germany. [7]Clinical Cooperation Unit Neurooncology, German Cancer Research Center (DKFZ), Heidelberg 69120, Germany. [8]Evertebrata Varia, Zoologische Staatssammlung München, Munich 81247, Germany.

*Authors for correspondence (jacky.goetz@inserm.fr; schwab@embl.de)

For that purpose, implementation of an imaging window allows for long-term deep-tissue monitoring of invasive behavior of tumor cells in living animals (Alexander et al., 2008; Beerling et al., 2011; Gligorijevic et al., 2014; Ritsma et al., 2013). We, and others, have successfully studied key steps of extravasation by performing IVM through a cranial window (Kienast et al., 2010). Extravasation is a crucial, yet rare and inefficient step in metastasis, which makes it difficult to study *in vivo*. There is, for example, no direct evidence as to how tumor cells arrest, adhere to the endothelium wall and cross the blood–brain barrier *in vivo* (Reymond et al., 2013). In addition, tumor cells use distinct mechanisms for invading the neighboring tissue (Friedl and Alexander, 2011). Understanding how cytoskeletal behavior, cell adhesion and proteolytic activity are integrated *in vivo* requires studying these events at the scale of a single cell, within its pathological context. IVM can capture dynamic metastatic events, but its resolution is insufficient to reveal subcellular events or the interactions of tumor cells with the surrounding tissue.

Correlating functional IVM to three-dimensional electron microscopy (3DEM) carries great potential in revealing the *in vivo* features of patho-physiological processes at nanometer resolution. The power of combining these imaging techniques is well established (Bishop et al., 2011; Briggman and Bock, 2012; Durdu et al., 2014; Goetz et al., 2014; Kolotuev et al., 2010; Maco et al., 2013). Because of a low throughput however (Karreman et al., 2014), intravital correlative microscopy has failed to provide the quantitative sampling needed for translational research.

The main bottleneck for intravital correlative microscopy is retrieving single objects in the electron-microscopy-processed sample. Unfortunately, processing tissue for 3DEM generally results in a loss of fluorescent signal, prohibiting the use of fluorescence microscopy to determine the position of the region of interest (ROI) in the volume of the electron microscopy sample. Moreover, the major sample distortions that result from fixation and resin embedding complicate the registration of the IVM into the electron microscopy datasets (Karreman et al., 2014). As a result, the targeted volume needs to be retrieved by correlating native or artificial landmarks that are encountered when serial-sectioning the sample, which in our experience (Karreman et al., 2014), can easily take more than 3 months. Moreover, such an approach is limited to relatively thin tissue samples, such as brain slices (Bishop et al., 2011; Maco et al., 2013) or skin (Karreman et al., 2014). Collecting quantitative electron microscopy data on multiple metastatic events *in vivo* therefore requires new strategies, endowed with an enhanced throughput. Here, we describe a novel method that exploits microscopic X-ray computed tomography (microCT) to precisely correlate the IVM volume with the electron-microscopy-processed resin-embedded sample, enabling the move from *in vivo* imaging to 3DEM within two weeks (Fig. 1). We developed and applied this approach to study single tumor cells that had been xenografted into a

Fig. 1. Workflow for multimodal correlative microscopy. Multimodal imaging of metastatic events observed *in vivo* requires specific sample and image processing methods. First, the event of interest is captured by using IVM (time, ~1–2 days). The position of the ROI is marked at the tissue surface with NIRB (1 h). Based on this macroscopic mark, a biopsy containing the ROI is dissected and processed for electron microscopy analysis (1 day+4 days). The resin-embedded sample is then imaged with microCT (2 h). The imaged volume obtained from the IVM is registered to the microCT volume by matching correlated pairs of landmarks in Amira software (1–2 days). 3D registration allows determination of the position of the resin-embedded ROI relative to the surface of the block. The resin block is accurately trimmed to expose the tumor cell for electron microscopy imaging (2 h). Finally, 3DEM of the ROI is performed (4–5 days). If all the steps are performed without interruption, the average duration of this workflow is thus roughly 2 weeks.

living mouse, showing the potential of this method to reveal key aspects of the plasticity and complexity of tumor cell invasion and metastasis. The versatility of this workflow is expected to enable a large range of applications in biology.

RESULTS

Intravital microscopy of metastasizing cells in the mouse brain cortex vasculature

Correlative imaging of the initial steps of tumor cell extravasation was performed on our established mouse model, in which we could reliably identify fluorescently labeled metastasizing tumor cells and track them over time. Upon intra-cardiac injection of GFP-labeled HER2-positive breast cancer cells (JIMT1), IVM analysis of the brain cortex was performed through a cranial window (Fig. 1, Fig. 2A). We labeled the blood vessel network with fluorescent dextran to create a stable 3D reference map of the area around the tumor cell. Tumor cells were arrested through physical occlusion in vessel bifurcations before extravasation (Kienast et al., 2010) and could be tracked over days by using IVM (Fig. 2B; Movie 1). IVM imaging of the volume allows recording of the position of the tumor cell relative to the local vasculature at the ROI. At a later stage in the workflow, the complex vessel network is exploited as a 3D roadmap to retrieve the tumor cell with 3DEM.

After fixation using intra-cardiac perfusion, the position of the ROI was immediately marked at the cortex surface using near-infrared branding (NIRB) (Bishop et al., 2011; Karreman et al., 2014; Maco et al., 2013) (Fig. 2C; Movie 1), enabling precise dissection of a small biopsy (<1 mm^3) containing the ROI. The sample was then processed for electron microscopy analysis and embedded in resin. This shows that we can reliably track metastatic events in the brain vasculature and, based on NIRB marking, biopsy the imaged region after fixation.

Retrieval of the tumor cell following electron microscopy processing

The high X-ray attenuation of the heavy metals used during electron microscopy processing (i.e. osmium tetroxide and uranyl acetate) enables the imaging of the resin-embedded sample with microCT (Bushong et al., 2015; Handschuh et al., 2013; Keene et al., 2014; Metscher, 2009; Sengle et al., 2013). MicroCT volumes of the samples were rendered in 3D to display the resin

block surface, the embedded tissue and its vascular network (Fig. 2D; Fig. S1). The models of the vascular network obtained from the IVM and the microCT datasets were then processed for non-linear 3D registration (Fig. 2E; Movie 2). Corresponding structural features, visible in both datasets, were used to seed pairs of landmarks (Fig. 2E, yellow and blue spheres) and were overlaid in 3D (see Materials and Methods for further details). Coarse 3D registration between the IVM (red) and the microCT (gray) volumes (Fig. 2E) was followed by fine registration using higher magnification IVM acquisitions (Fig. S2). Docking of the IVM model into the microCT dataset then enabled us to predict the position of the tumor cell, visible in the green IVM channel, within the resin block (Fig. 2F; Movie 2).

Knowing the distance between the block surface and the predicted position of the tumor cell allowed accurate block trimming to rapidly approach the ROI (Fig. 2F, bottom panel). This efficiently enabled us to expose the targeted cell to focused ion beam scanning electron microscopy (FIB-SEM). Because FIB-SEM can only effectively mill a depth of up to 60–90 µm into the resin sample, we trimmed the flank of the block (perpendicular to the FIB beam) to ~20 µm from the targeted tumor cell. Similarly, the distance between the block face and the ROI (Fig. 2D,F) should be trimmed to less than 5 µm (Bushong et al., 2015) to prevent unnecessary long milling times before reaching the cell of interest (Movie 3). To target the ROI with such precision, we collected a few thick sections as intermediate 'check points' when manually trimming to the targeted depth (Fig. S3). These sections were inspected by using light microscopy and compared to virtual sections extracted from the microCT dataset, thereby assessing the exact progression of the trimming. For trimming depths of around 500 µm, 3–5 check points were sufficient to correct for potential trimming inaccuracy (estimated to be between 5 and 10%, compared to the nominal settings of the ultramicrotome) and allowed a targeting precision of <5 µm. Thus, using microCT-based registration, we could accurately target a cell of interest within a millimeter-thick resin-embedded tissue.

3DEM of metastasizing cells arrested in the brain vasculature

We used FIB-SEM to collect 6350 serial images (8 nm pixel size in the x,y plane, and 8 nm milling depth in the z plane) of the tumor cell within the blood capillary (Fig. 3A,B; Movie 4). In addition, we
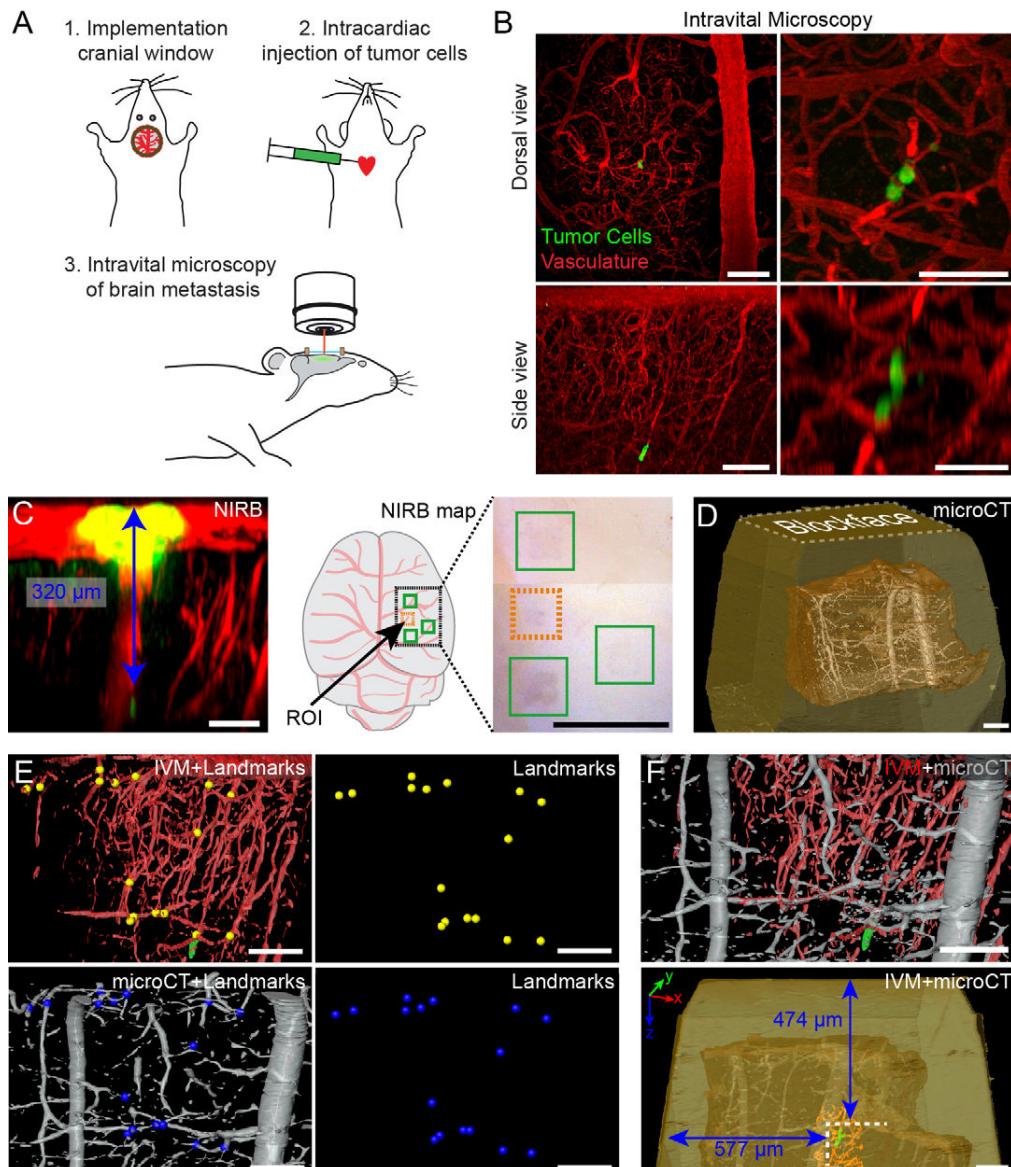
Fig. 2. IVM and microCT imaging of tumor cells in the mouse brain cortex, followed by 3D registration of both datasets. (A) A chronic cranial window is implanted 3 weeks before intravital imaging is performed. JIMT1 GFP-expressing cells are injected into the left ventricle of the mouse heart. For IVM analysis, the cranial window is mounted onto a customized stage that allows reproducible orientation, and thus imaging, of the same ROI over multiple days. (B) IVM analysis of an arrested tumor cell in the brain cortex vasculature. Dorsal views (top panels), z-projection of a large field of view around the ROI at 2 days post injection (top left panel) and of a smaller field of view, imaged 3 days post injection (top right panel). Side views (bottom panels), x,z-projection of the ROI, 2 days (left bottom panel) and 3 days (right bottom panel) post injection. Scale bars: 100 µm in left panels, 50 µm in right panels. (C) After IVM acquisition and perfusion fixation, the position of the ROI is marked by using NIRB at the surface of the brain, producing autofluorescence in both the green and red channel (yellow). The x,z projection shows the vasculature (red) and how the NIRB landmark is confined to the surface of the brain, distant (blue arrow) to the tumor cell (green). A cartoon and an image of the mouse brain show the relative positions of several NIRB landmarks. Aside from the landmark positioned above the ROI (orange box), three additional marks were created as references (green boxes) to facilitate targeting of the selected ROIs when dissecting the biopsies. Scale bars: 100 µm (left panel), 1 mm (right panel). (D) The microCT dataset shows the tissue biopsy (brown) within the resin block (yellow) and the blood vessels (gray). Scale bar: 100 µm. (E) 3D registration of the vasculature as segmented from the two imaging modalities – IVM (red) and microCT (gray). Corresponding points in both datasets are located and marked (yellow spheres for IVM and blue spheres for microCT). Scale bars: 100 µm. (F) Based on the landmarks shown in E, the IVM volume is registered into the microCT dataset with Amira software, which enables precise determination of the position of the tumor cell (green) within the resin block and relative to its surface (bottom panel in F). Scale bars: 100 µm.

acquired key frames (Fig. 3A) every 1 µm (50×50 µm², pixel size 24.4 nm, acquired every 1 µm) to obtain low-magnification overviews of the ROI showing surrounding cell nuclei and blood vessels (Narayan et al., 2014). To illustrate the efficiency of the multimodal correlation, the predicted position of the tumor cell within the resin block (as determined by registering the IVM

volume into the microCT volume; Fig. 3C, top panel) was compared to the manual segmentation of the key-frame-volume (Fig. 3C, bottom panel).

A second tumor cell, observed in a different region of the same brain, was also targeted and imaged with FIB-SEM (Fig. S4, Movie 5), demonstrating the reproducibility of our approach. Cell
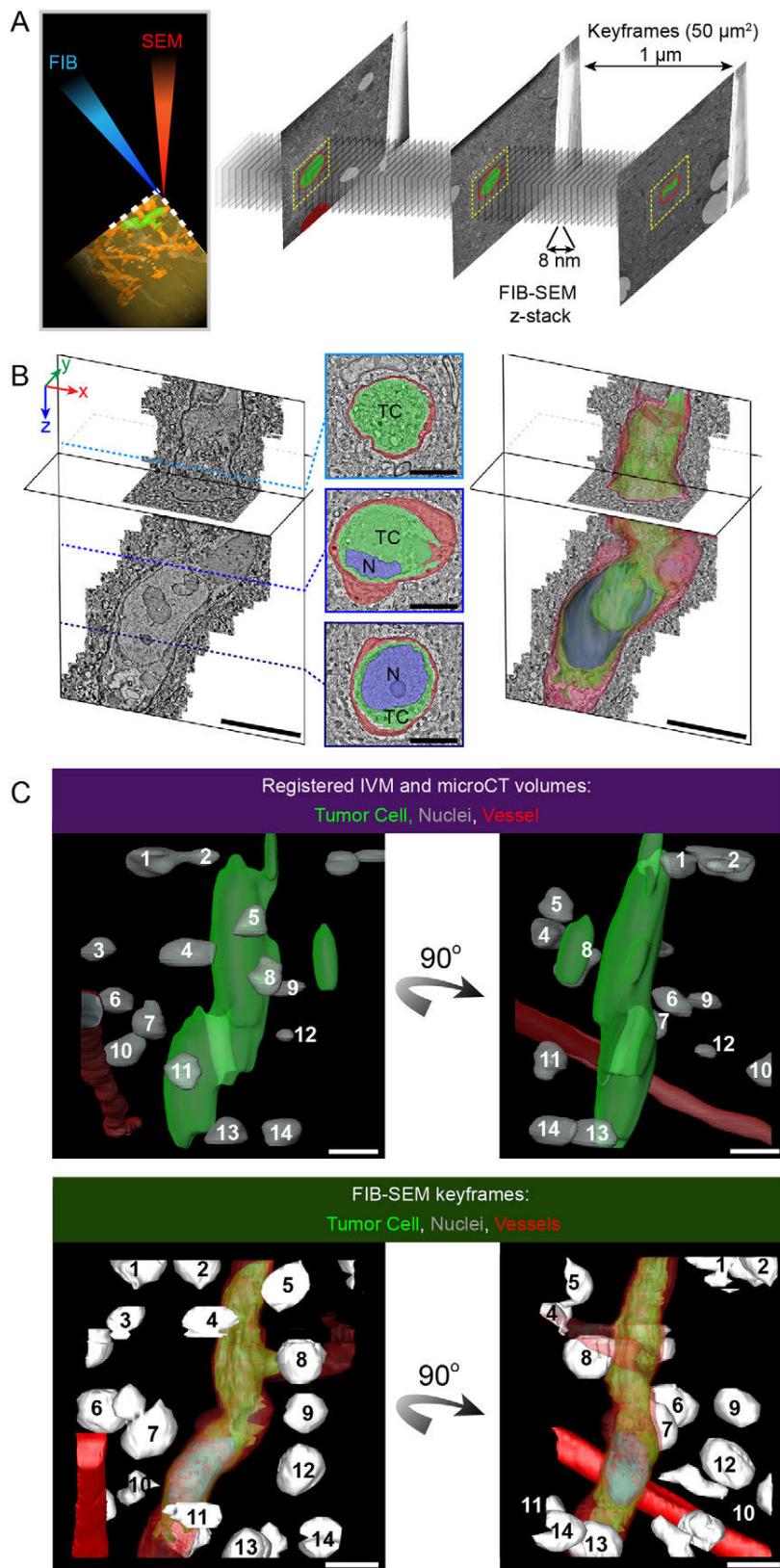
Fig. 3. FIB-SEM imaging of a tumor cell arrested in the vasculature of the brain. (A) Automated 3DEM. The resin block was precisely trimmed to expose the tumor cell for acquisition of data using FIB-SEM. During the course of the FIB-SEM data acquisition, low-magnification 'key frames' were obtained (z spacing ∼1 µm, size 50×50 µm). (B) The FIB-SEM z-stack (6350 frames, 8 nm isotropic voxel size) was used to study the fine organization of the tumor cell within the blood capillary. Frames of the FIB-SEM acquisition were segmented to show the tumor cell (TC, green), its nucleus (N, blue) and the capillary's endothelial cells and basal lamina (red). Scale bars: 10 µm (3D models), 5 µm (segmented sections). (C) Multimodal correlation – combining IVM, microCT and electron microscopy imaging to retrieve the tumor cell. Top panel, docking the IVM model in the microCT dataset enabled us to predict the position of the tumor cell (green, from IVM), relative to the nuclei (light gray, from microCT) and to a blood vessel (red, microCT). The nuclei and the vessel could be detected in the microCT scan because of their lower density relative to the surrounding tissue. Bottom panel, segmentation of the FIB-SEM key frames results in a 3D model of the nuclei (white), the vessels (red) and the tumor cell (green). Two views of the models are shown, rotated 90° with respect to each other. Comparing both models enabled us to correlate the positions of the nuclei that were visible with microCT and electron microscopy imaging. Matching nuclei are numbered in the top and bottom panels. Scale bars: 10 µm.

extensions were found to either intercalate between or to invaginate into endothelial cells of the capillary (Fig. 4; Movies 4 and 5). In addition to elucidating the ultrastructure of the tumor cell, this technique also gives access to the fine organization of the capillary, the parenchyme and the surrounding tissue (Fig. 5A; Movie 6). It therefore enables the study of potential alterations to the

447
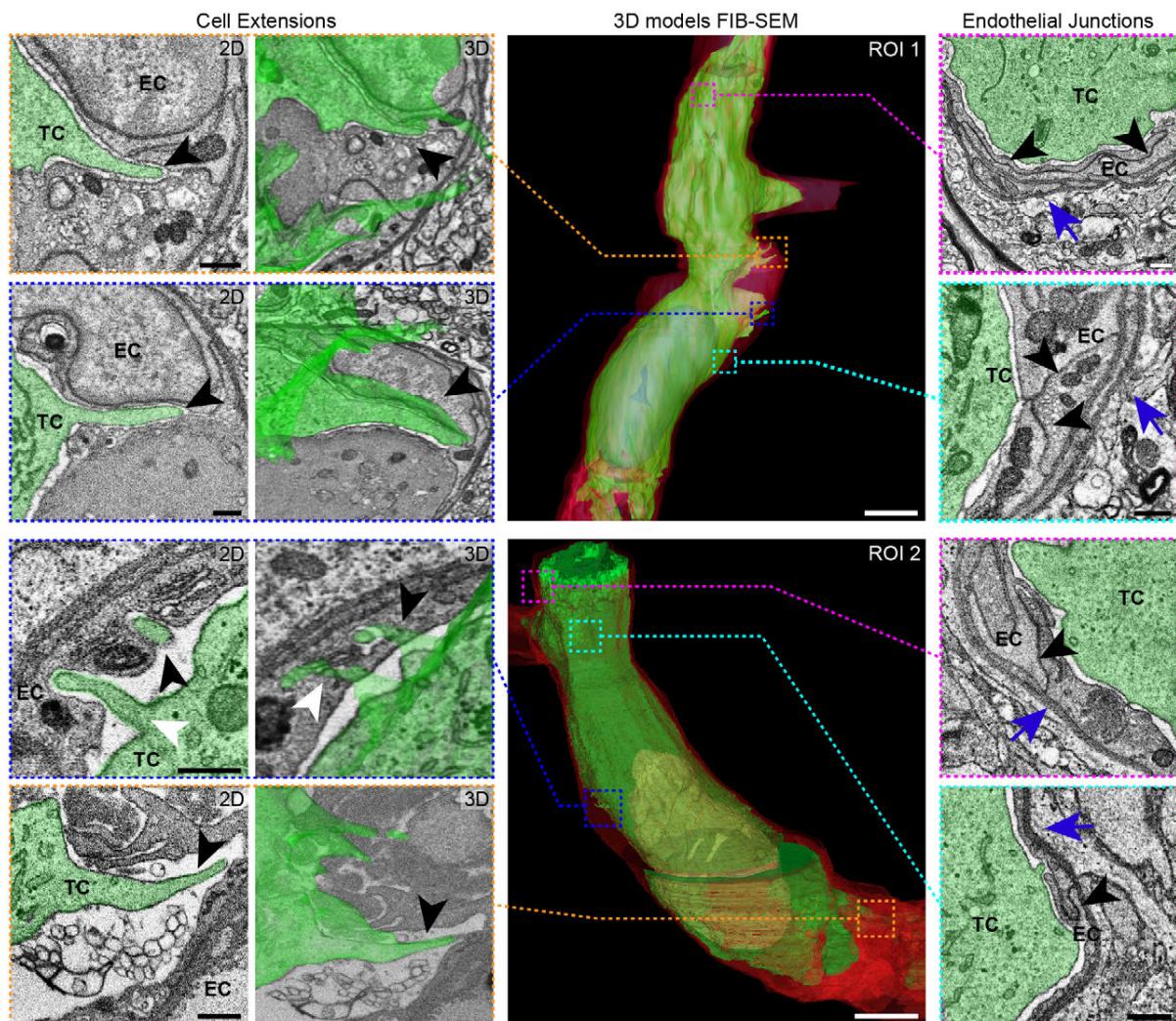
Fig. 4. 3DEM imaging of an arrested tumor cell in brain capillaries. 3DEM analysis reveals tumor cell (TC) extensions pointing towards and into the endothelial cell layer (EC) (first and second columns from the left, 2D and 3D views of the cell extensions, respectively; indicated with an arrowhead). Electron microscopy analyses revealed the junctions between endothelial cells (right-most column, arrowheads) and the basal lamina (right column, blue arrows). These ultrastructural features were observed in the FIB-SEM z-stacks obtained from two different tumor cells that were arrested in the vasculature of the brain (ROI1 and ROI2). The dotted lines and boxes in the 3D models of the FIB-SEM z-stack indicate from which regions of the tumor cells these images were obtained. Scale bars: 500 nm (electron microscopy images); 5 µm (3D models).

microenvironment of an arrested tumor cell that is initiating extravasation (Fig. 5A,B; Movie 6). Being able to systematically and repeatedly collect such data from multiple experiments will lead to a better understanding of the key steps of the metastasis cascade.

Intravital imaging of an invasive subcutaneous tumor xenograft

Unraveling the mechanisms and plasticity of metastatic pathways demands the establishment of a technology that enables the study of each step – from primary tumor invasion to metastasis formation. To validate its versatility, we decided to apply our approach to another *in vivo* model designed to track primary tumor invasion – invasive tumor xenografts in the mouse ear (Karreman et al., 2014). In this model, highly invasive fluorescent tumor cells (Shibue et al., 2013) are injected subcutaneously (Karreman et al., 2014). IVM revealed actin-rich protrusions at the edge of the tumor mass (Fig. 6A,B; Movie 7), and invasive regions of the tumor were recorded with time-lapse imaging (data not shown). We detected invasive cells

with visible morphological differences in the same invasive front (Fig. 6B), confirming that our model can recapitulate the established adaptability of tumor cell invasion (Friedl and Alexander, 2011). To analyze the ultrastructure of these invasive cells, we fixed the tissue and performed NIRB above the protrusions to mark the position of the ROI at the ear surface (Fig. 6C). The NIRB mark was then used to retrieve the ROI before further electron microscopy processing and resin embedding, which demonstrates that we could safely retrieve IVM-imaged ROIs from multiple tissues (brain and ear).

Targeting protrusions of invading tumor cells in the electron microscopy processed sample

The resin-embedded sample was scanned by using microCT (Fig. 6D; Fig. S1). The microCT volume revealed several anatomical features that could also be seen using IVM, such as hair follicles, blood vessels and nerve fibers. The IVM and microCT volumes were segmented to create 3D models (Fig. 6E; Movie 8). The IVM model was docked into the microCT volume (Fig. 6F;
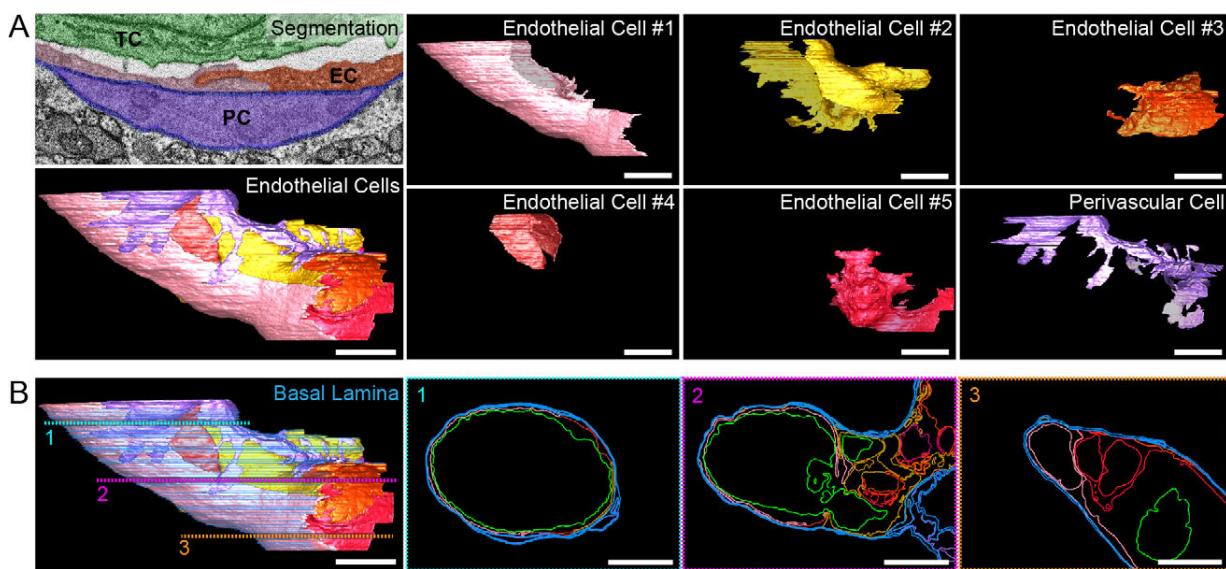
Fig. 5. 3DEM imaging allows dissection of the complex structural organization of the vessel containing an arrested tumor cell. (A) Each individual cell lining the tumor-cell-containing vessel, as well as the basal lamina and a perivascular cell we segmented. In the top left image ('segmentation'), a detailed image of a FIB-SEM slice is shown where two neighboring endothelial cells (EC, pink and red), a perivascular cell (PC, purple), the basal lamina (blue) and the tumor cell (TC, green) are segmented. The bottom left panel shows a 3D representation of all the cells lining the vessel that contains the lower part of the ROI2 tumor cell (Fig. 4). In the columns and rows on the right side, each cell is shown individually. Scale bar: 5 µm. (B) A 3D representation of the basal lamina (blue) is shown (left panel), together with the plasma membranes of endothelial cells (various colors), of the perivascular cell (purple) and the lower part of the ROI2 tumor cell (green; Fig. 4). The three panels on the right depict different sections through the model that reveal the contours of the basal lamina, the endothelial cells and the tumor cell. At the level of the vessel bifurcation, the organization of the endothelial cells and of the basal lamina displays complexity, highlighting potential endothelial remodeling in this area. Scale bar: 5 µm.

Movie 8) revealing that the invasive protrusions were at a distance of 415 µm relative to the surface of the resin block (Fig. 6F, bottom panel). As described above (Fig. 2), knowing the position of the cells of interest within the resin block allowed rapid and accurate trimming towards the ROI. Then, a series of 330 sections (thicknesses of 130 nm) was collected, imaged at low-magnification with TEM and aligned (Fig. 7A; Movie 9). The resulting stack of TEM images was segmented to generate a 3D model of the invasive structures of the tumor cells and the associated vasculature (Fig. 7B). As predicted, the targeted invasive front of the tumor was located within the TEM z-stack, as shown by correlation between the electron microscopy and the IVM 3D models (Fig. 7B). Only a 4.2 µm difference was calculated between the actual and predicted position of the first targeted protrusion (Fig. 7, arrowhead 1). Based on the time-lapse IVM analysis of the dynamic invasive front, we identified and successfully retrieved two invasive cells with obvious morphological differences (Figs 6B and 7; Movie 7). The first cell displayed two very long filament-rich protrusions that extended deep into the tissue (Fig. 7A). The perinuclear region of the cell lay between collagen bundles as well as between neighboring stromal cells (Fig. 8A–E; Movie 9). The second invasive cell sat deeper in the tissue and lay on a skeletal muscle fiber (Fig. 7A). This cell showed obvious differences in terms of morphology of the protrusive structures (Figs 7A and 8F–J; Movie 9). Taken together, these data demonstrate that we can reliably and rapidly visualize dynamic events of tumor invasion and resolve them in TEM sections from the resin-embedded tissue.

Zooming in on tumor cell protrusions and their micro-environment

Ultrastructural details of the two identified invasive cells (Fig. 7A, arrows 1 and 3) were imaged by using serial TEM and electron tomography (Fig. 8; Movies 9 and 10). Electron tomography

analysis allows the visualization of fine ultrastructural features, such as cytoskeleton fibers, local extracellular matrix components and intracellular organelles (Fig. 8). Serial TEM and reconstruction of the first invasive cell showed the overall cellular and nuclear morphology (Fig. 8A–C). This invasive cell displayed a deformed nucleus that could result from a constriction between a neighboring stromal cell and a collagen bundle (Fig. 8A–C; Movie 10). With electron tomography, we then zoomed further into subcellular regions of this invasive cell and observed that protrusions were enriched with cytoskeletal filaments (Fig. 8D). Electron tomography analysis of a perinuclear region close to a collagen bundle revealed a similar abundance of cytoskeletal filaments as well as intracellular vesicles, suggesting this region of the cell might react to some physical constraint that is imposed by the collagen bundle (Fig. 8E). These observations are in good agreement with recent findings (Wolf et al., 2013), suggesting that deformability of the nucleus is a key determinant of tumor cell invasion. A second cell was found to be intercalated between a skeletal muscle fiber and stromal cells (Fig. 8F–H). Although emanating from the same invasive front, this cell differed from the previous as it displayed several bleb-like protrusions all over its surface. As previously described in vitro (Charras and Paluch, 2008), electron tomography analysis revealed that these structures (Fig. 8I) displayed filament-free regions that contained, in some cases, many intracellular vesicles reminiscent of caveolae (Fig. 8J). Similar to the cell shown in Fig. 8A–E, close contacts with collagen bundles were observed (Fig. 8I). These results demonstrate the capacity of multimodal correlative imaging to resolve subcellular features of the dynamic and plastic processes of tumor invasion in native tissues.

DISCUSSION

Here, we report an efficient, rapid and reproducible approach for 3DEM imaging of tumor cells at crucial stages of the metastasis
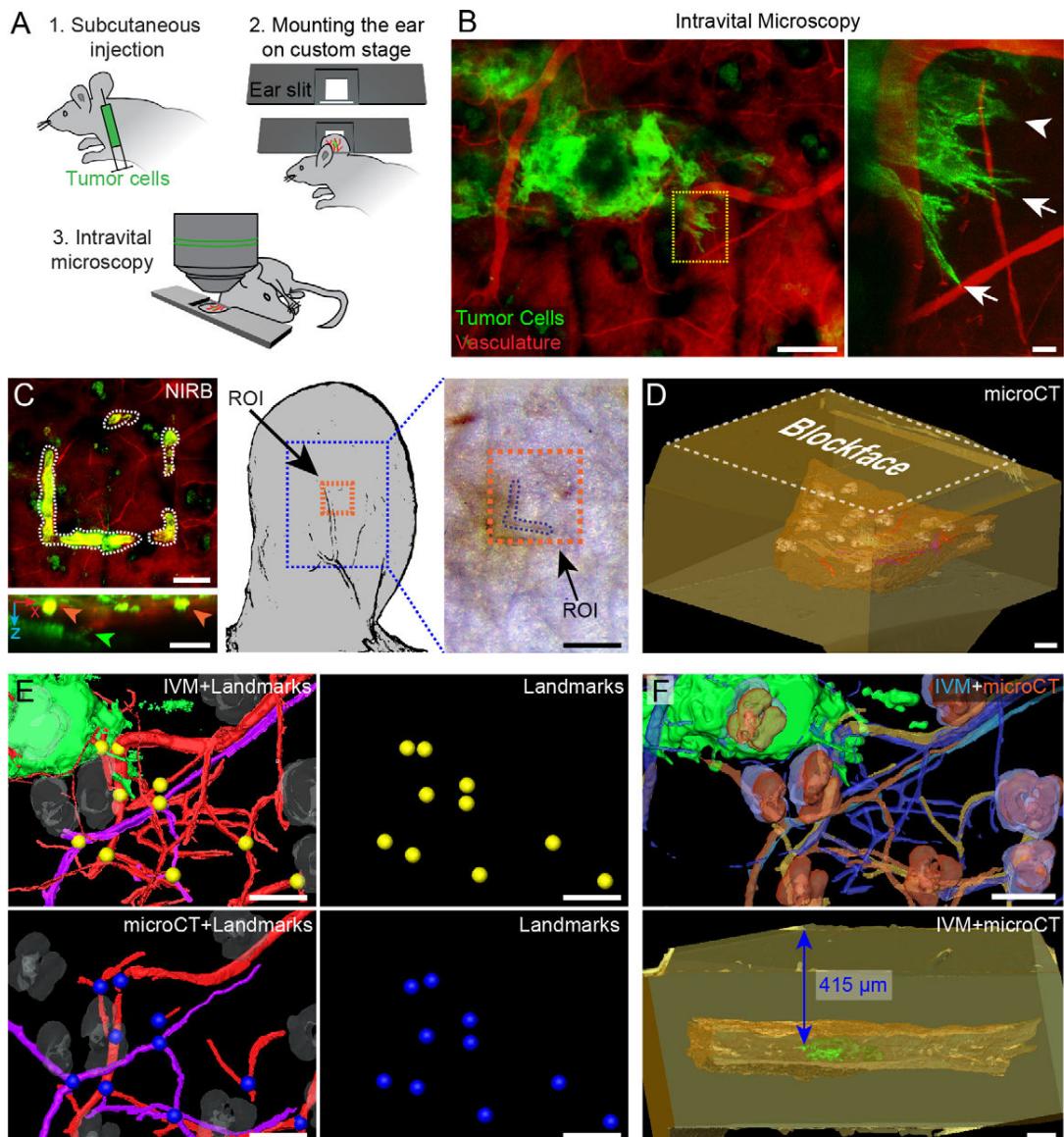
Fig. 6. IVM imaging of tumor cell protrusions of subcutaneous xenografts. (A) D2A1 LifeAct-YPet-expressing cells were injected subcutaneously into the mouse ear. After 2 weeks of tumor growth, the mouse was anesthetized and positioned on a custom-built stage. The ear slit in the stage kept the ear flat and still during intravital imaging. (B) z-projection of the IVM z-stack showing the tumor mass (Ypet, green), its invasive front and the vasculature (Evans Blue, red). The right panel shows a magnified view of the area boxed in the left panel and reveals invasive cells with distinct morphologies. Two cells have extended protrusions (arrows), whereas another one has smoother contours (arrowhead). Scale bars: 100 µm (left panel); 10 µm (right panel). (C) After IVM analysis, the area of interest was marked by using NIRB (white dotted line) at the skin surface. Bottom panel, x,z projection of the z-stack. The green arrowhead points to a tumor cell protrusion. The NIRB markings (orange arrowheads) are confined to the surface of the skin and are distant from the invasive front of the tumor mass. Following perfusion fixation, the NIRB markings (orange box) remain visible on the skin biopsy. Scale bars: 100 µm (left panels); 50 µm (right panel). (D) The resin-embedded sample was scanned by using microCT. The microCT dataset shows the skin tissue biopsy (brown), with the hair follicles (gray), nerves (purple) and blood vessels (red), within the resin block (yellow). Scale bar: 100 µm. (E) 3D registration of the tissue features as segmented from the two imaging modalities – IVM (top left panel) and microCT (bottom left panel). Corresponding points in both datasets were located and marked (yellow spheres for IVM and blue spheres for microCT, left and middle panels). Scale bars: 100 µm. (F) Top panel, based on the reference points shown in E, the IVM model (shown in blue and green) is registered to the microCT dataset (yellow and orange), which enabled us to determine the position of the ROI inside the resin block (bottom panel) and relative to the block surface (415 µm). Scale bars: 100 µm.

cascade, as determined by using IVM. Our multimodal correlative microscopy integrates microCT to accurately predict the position of *in vivo* imaged single cells inside large resin blocks. This enabled the routine retrieval of single tumor cells (Figs 3 and 7; Fig. S4) and their sub-cellular structures (Figs 4, 5 and 8) for 3DEM analysis in tissue samples. In this study, we show the results from two different regions in one mouse brain and from one region in a mouse ear skin sample.

Our approach combines well-established imaging modalities and sample preparation techniques. As a consequence, it suffers from the limitations brought by each one of them. Intravital imaging, for example, relies on the imaging of fluorescently labeled structures, and thus requires the introduction of dyes or genetically encoded fluorescent proteins. Xenografts of genetically engineered fluorescent cells can be extremely efficient tools to accurately
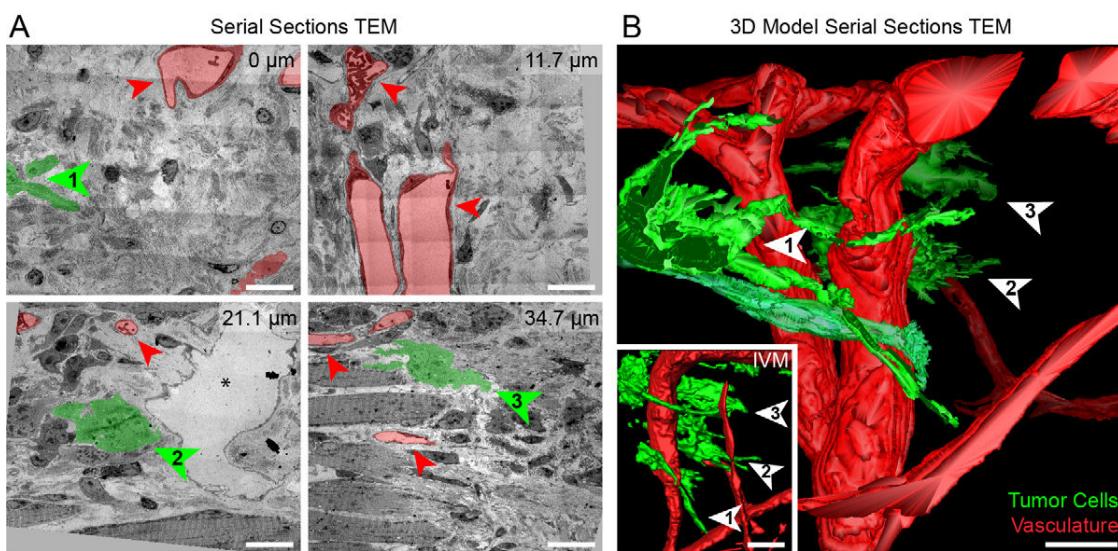
Fig. 7. Serial TEM imaging and correlation of tumor cell protrusions in skin tissue. (A) Large fields of view comprising stitched TEM micrographs from 130-nm thick sections of the volume of interest shown in Fig. 6. The blood vessels (red) and tumor cells (green) are highlighted. Four different depths (marked in µm relative to the first selected section) are shown to illustrate specific ultrastructural hallmarks of the tumor cells and their microenvironment. Three cells from the invasive front imaged with IVM have been retrieved and highlighted (numbered arrowheads). The electron-lucent area in the lower left panel, marked with an asterisk, is a lymphatic vessel. Scale bars: 20 µm. (B) 3D model of the tumor cell protrusions (green) and vessels (red), segmented from 330 serial TEM sections. Corresponding tumor cell protrusions in A and B are indicated with numbered arrowheads. 3D models and TEM images of the cells indicated with arrowheads 1 and 3 are shown in Fig. 8. The inset shows a 3D model of the same region, imaged by using IVM. Scale bars: 20 µm.

mimic patho-physiological situations, but these models can be a source of artifacts. Furthermore, preparing the samples for electron-microscopy-mediated visualization requires dedicated protocols. High-pressure freezing is the method of choice to preserve the ultrastructure of the sample, but this is currently only applicable to small samples (thickness of 200 µm or less). Large samples, such as whole organisms, require chemical fixation, but it is known that such fixation introduces structural artifacts into the sample (Korogod et al., 2015).

Intravital multimodal correlative microscopy provides unique insights into metastatic processes

Linking functional IVM analysis of tumor cells, and their microenvironment, to high-resolution imaging with electron microscopy will contribute to the understanding of the various cellular processes that lead to the spread of cancer. Using this workflow, we observed important sub-cellular features of arrested tumor cells. For example, in tumor cells that had been trapped in a blood vessel, we observed cellular extensions towards the vascular wall (Fig. 4). These observations suggest that tumor cells use active cellular protrusions to cross the physical barrier imposed by the endothelium and basal lamina. The protrusions could not be resolved through intravital imaging in the mouse brain (Movie 1) owing to the limited resolution of IVM. The formation of cellular extensions and the observed drastic remodeling of the endothelial layer close to the tumor cell (Fig. 5) are potentially the earliest steps in extravasation. Recently, invadopodia have been identified as key players in tumor cell extravasation in the chicken chorioallantoic membrane model (Leong et al., 2014).

Electron tomography analysis of invading tumor cells revealed protrusions that were massively populated with bundles of filaments, and we showed their tight interactions with the local extracellular matrix (Fig. 8). Furthermore, in the migrating tumor cells, we observed a clear deviation of the normal spindle-shaped

morphology of the nuclei (Fig. 8A–C,D,F). Other studies (Wolf and Friedl, 2011) have elegantly shown that cell migration through interstitial tissues is mostly controlled by the architecture of the extracellular matrix, in particular the matrix pore size. The nuclear deformability of cells can compensate for the small pore size and thus regulate the invasion abilities of cells (Friedl et al., 2011).

These observations confirm that this workflow has great potential in unraveling metastatic events at the nanoscale.

Practical considerations of intravital multimodal correlative microscopy

Although the presented workflow substantially speeds up the correlation between IVM and electron microscopy analysis, obtaining a significantly relevant number of observations still demands several months of work. To reveal the structural changes that a cell undergoes during extravasation, for example, might require 20 to 30 independent experiments. We estimate that such a study would take at least 7 months of full-time work for a single person, taking into account that some steps in the workflow can be performed in parallel. We believe, however, that for many *in vivo* studies, the unique gain in resolution will be worth the investment of time. Importantly, every single tumor cell (*n*=6, four are shown here) that has been targeted so far was successfully retrieved and imaged by using electron microscopy, illustrating the high success rate of the approach.

The multimodal correlative workflow requires access to a set of high-end equipment in order to perform the described analyses (intravital microscopy, microCT scanning, TEM tomography and/or FIB-SEM). After the intravital imaging, however, the sample is fixed and can be sent to collaborating laboratories where specific imaging could be performed. Therefore, if a laboratory does not possess the whole set of equipment, as in our case, this workflow is still achievable by establishing collaborations with other research groups or industry.
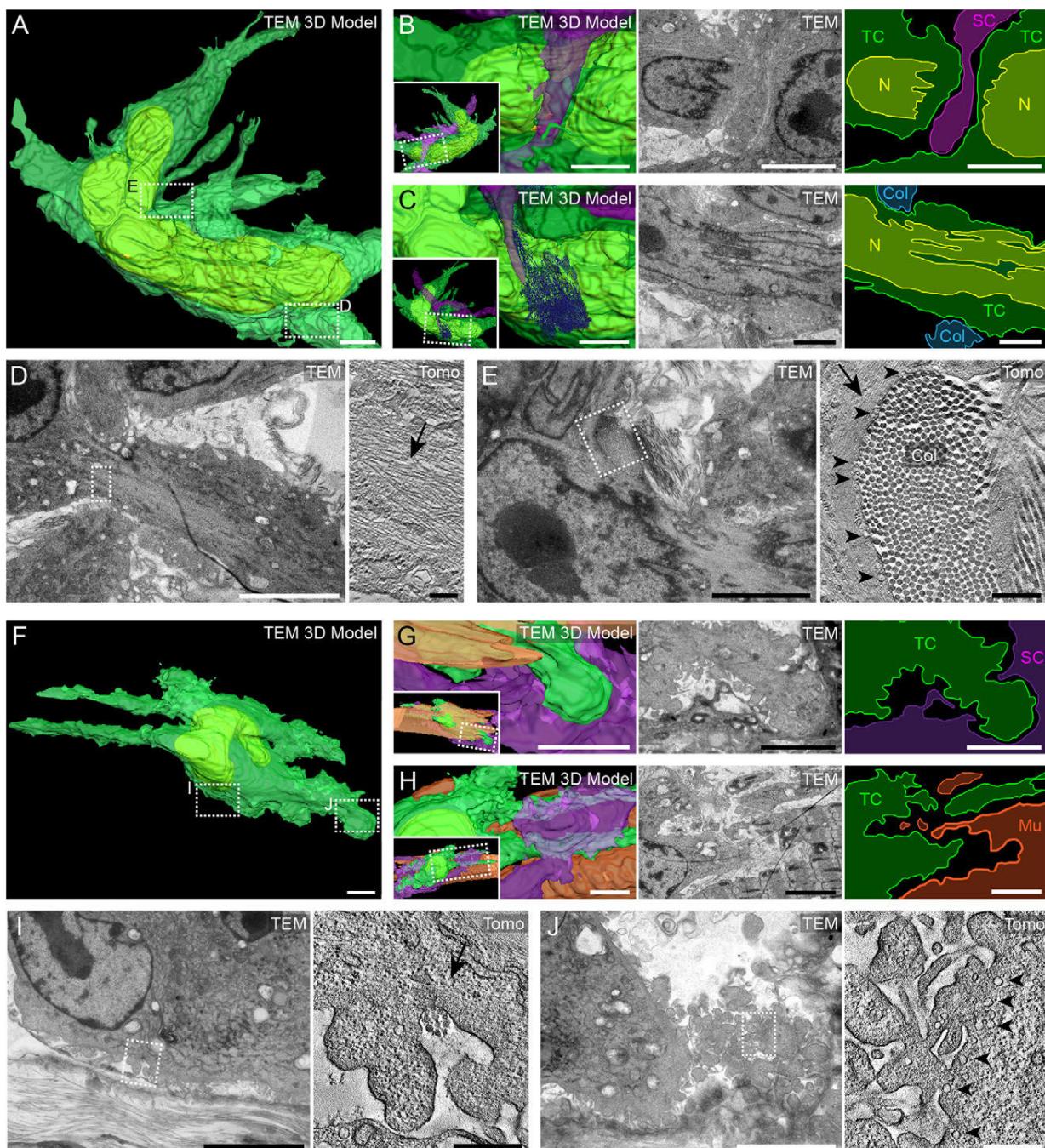
Fig. 8. Serial TEM and electron tomography analysis of tumor cell protrusions from subcutaneous xenografts. (A) 3D model obtained from serial TEM imaging of the cell body of the tumor cell 1 highlighted in Fig. 7. The nucleus (yellow) and plasma membrane (transparent green) of the tumor cell are segmented. Dashed boxes indicate where the higher magnification images shown in D,E were obtained. Scale bar: 5 µm. (B,C) The tumor cell (TC) is flanked by one stromal cell (B, 'SC', purple) and a bundle of collagen fibers (C, Col, blue) at a position where the ultrastructure indicates that the nucleus ('N') is slightly confined. The left panels show zoomed views of the 3D model, its orientation is shown in the insets. The middle panels show TEM images, and the right panels show color-coded maps of the middle panels. Scale bars: 5 µm. (D,E) Electron tomography analysis of the boxed areas in A. Scale bars: 5 µm (left panels); 200 nm (right panels). Electron tomography imaging revealed the presence of multiple cytoskeletal filaments (arrows) in a protrusion (D) and underneath the plasma membrane at the cell body (E). Moreover, groups of vesicles associated with the plasma membrane (arrowheads) can be recognized in the region where the tumor cells are in close proximity with collagen fibers (Col), a feature that can be observed in multiple regions. (F) 3D model from serial TEM imaging of tumor cell 3 shown in Fig. 7. Dashed boxes indicate where the higher-magnification images shown in I,J were obtained. Scale bar: 10 µm. (G,H) The tumor cell and its cellular and acellular microenvironment. The left panels show zoomed views of the 3D model, the orientations are shown in the insets. The middle panels show TEM images, and the right panels show color-coded maps of the middle panels. Scale bars: 5 µm. (G) A rounded blebbing protrusion of the tumor cell (green) is in close proximity to a neighboring stromal cell (purple). Scale bars: 5 µm. (H) One side of the tumor cell (green) is in close apposition to the skeletal muscle cell (Mu, orange). Scale bar: 5 µm. (I,J) Electron tomography analysis of the boxed areas in F. Electron tomography images reveal the filament network (arrow) at the base of the bleb-like protrusion (I), collagen fibrils (Col, I) and small intracellular vesicles reminiscent of caveolae (arrowheads, J). Scale bars: 5 µm (left panels); 500 nm (right panels).

Intravital multimodal correlative microscopy – other approaches and applications

Studying complex 3D samples with electron microscopy requires knowing the position of the ROI in the x, y and z planes. In order to identify the ROI within resin blocks, others have preserved the signal of fluorescent markers during electron microscopy processing (Lucas et al., 2012; Nixon et al., 2009). However, weak fluorescence signal is quenched when conventional electron microscopy processing methods are used. Moreover, the limited imaging depth and z-plane resolution of fluorescence microscopy hinders accurate visualization of the ROI inside the resin block. The approach presented here does not require a compromise in the electron microscopy processing protocols; by registering the IVM volume into the microCT scan of the processed sample, we could predict the position of our target with accuracy of <5 μm.

MicroCT imaging of resin-embedded samples has been used in previous studies to identify a ROI inside the resin block, in order to specifically target this area using electron microscopy (Burnett et al., 2014; Sengle et al., 2013). In these studies, however, the targeted ROIs were either clearly visible in the microCT scans or revealed by using electron-dense markers (Bushong et al., 2015). The former approach is therefore restricted to rather large and contrasted features, whereas the latter approach relies on photo-oxidation or an enzymatic reaction. This leads to dense precipitates (e.g. DAB) that mask the ultrastructure of the targeted cells. Our approach, however, predicts the position of the target without requiring its direct visualization by using microCT. Here, for the first time, microCT was employed to bridge IVM to electron microscopy, and 3D registration was performed to retrieve an *in vivo* observed event in a resin-embedded sample.

Other correlative methods have successfully targeted individual synapses within the mouse brain by introducing artificial landmarks with laser branding (Bishop et al., 2011; Maco et al., 2013). In this powerful approach, the retrieval of the ROI in the x, y and z planes solely relies on the positioning of the NIRB mark in the tissue – i.e. the branding was performed either right above or in the same plane as the ROI. NIRB efficiency, however, is highly sensitive to the scattering of light in deeper regions of the tissue. Therefore, NIRB can only be performed on 60- to 100-μm vibratome tissue sections that contain the ROI. Our method skips obtaining and screening such sections, and can address bulkier tissue pieces. We believe, therefore, that our approach can provide a complementary yet more versatile way to correlate intravital imaging with ultrastructure.

In conclusion, we have established a versatile and precise multimodal imaging approach that allows efficient correlation of *in vivo* imaging with volume electron microscopy. Applied here to cancer biology, this workflow has already provided informative and unexpected observations of the metastatic behaviors of single tumor cells within realistic pathological situations. We demonstrated our multimodal correlative imaging approach on mouse brain and skin tissue, but the workflow can be applied to many other cell biology events that can be imaged *in vivo*. The enhanced throughput of the method will allow routine use in translational research on animal models and holds great potential for understanding multiple biological processes at the ultrastructural level.

MATERIALS AND METHODS
Mouse handling
Mounting the cranial window, intracardiac injection of tumor cells and anesthesia
To perform intravital imaging of the cerebral cortex, a cranial window was grafted onto an 8–10-week-old immunodeficient female mouse (*Mus*

musculus) (NU/NU nude mouse, Charles River Laboratories International, Sulzfeld, Germany), as previously described. After a 3-week healing period, the mouse received a 100 μl solution of cytoplasmic GFP-expressing JIMT1 cells (1×10^7 cells/ml in PBS) through intracardiac injection through the left ventricle. Intravital imaging was performed immediately following injection, and on the second and third day post-injection. For imaging, the mouse was anesthetized by using isoflurane. To visualize the blood vessels, 100 μl of TRITC–dextran (500 kDa, Sigma-Aldrich) was administered to the mouse through injection into the tail vein. The mouse was placed on a custom-made holder (Deutsches Krebsforschungszentrum, Heidelberg, Germany) and remained anesthetized by using an isoflurane gas anesthesia system. All animal experiments were conducted in agreement with the regulations for animal experimentation dictated by the state Baden-Württemberg (Germany), and were approved by the state authorities.

Subcutaneous injection of tumor cells
An immunodeficient adult 8- to 10-week-old mouse (Rj:NMRI-Foxn1nu/Fox1nu, Janvier labs, Saint-Berthevin, France) was injected with the D2A1 Lifeact-YPet cell line, as previously described (Karreman et al., 2014).

Two-photon excitation IVM and NIRB
IVM and NIRB through the cranial window
The mouse was mounted on an upright confocal microscope (Zeiss LSM 7, controlled by the software Zen 2012, Carl Zeiss Microscopy GmbH, Jena, Germany) and kept at a steady temperature of 32°C by means of a heating pad. The holder kept the mouse head immobile and allowed analysis of the same imaging area over days by keeping track of the x,y coordinates of the microscope stage. IVM was performed at an excitation wavelength of 850 nm (680–1080 nm Chameleon Ultra II laser, Coherent, Santa Clara, CA) using a ×20 Zeiss W Plan Apochromat N.A. 1 objective (Carl Zeiss Microscopy GmbH). The GFP and TRITC emission wavelengths (510 and 573 nm, respectively) were collected by two hybrid non-descanned detectors. As the perfusion fixation leads to a wash out of the TRITC–dextran, fluorescent lectin from *Lycopersicon esculentum* (Sigma-Aldrich Chemie GmbH, Munich, Germany) was injected into the mouse tail vein in order to record the 3D organization of the blood vessels after fixation. The mouse was perfusion-fixed through intracardiac injection with 2.5% glutaraldehyde (Electron Microscopy Sciences, Hatfield, PA) and 2% formaldehyde (Electron Microscopy Sciences) in 0.1 M PHEM buffer (comprising 60 mM PIPES, 25 mM HEPES, 10 mM EGTA and 2 mM MgCl, pH adjusted to 6.9). Following fixation, the ROI was imaged again based on the stored stage x,y-coordinates. NIRB was performed with the same laser that had been used for IVM, tuned to a 750 nm wavelength. Above the ROIs, at the level of the brain surface, a 150×150 μm² area was scanned in a single focal plane until the NIRB square became clearly visible through emission of autofluorescence in the green channel. Around the ROI, three bigger 300×300 μm² NIRB squares were drawn in non-symmetric positions to facilitate orientation and retrieval of the ROI upon dissection (Fig. 2). The brain was removed from the skull and post-fixed by immersion in the same fixative at 4°C overnight. The following day, the fixative was replaced with 0.1 M PHEM buffer, and the brain was stored at 4°C until further processing.

IVM and NIRB analysis of subcutaneous tumors in the mouse ear
IVM and NIRB were performed as previously described (Karreman et al., 2014) on the anesthetized mouse. After the IVM data acquisition, the mouse was fixed through intracardiac perfusion of 2.5% glutaraldehyde and 2% formaldehyde in 0.1 M PHEM buffer. The ear was dissected and immersed in the same fixative at 4°C overnight. The next day, the ear biopsy was transferred to 0.1 M PHEM buffer and stored at 4°C until further processing.

Processing for electron microscopy
To improve the penetration of the chemicals during processing, small samples (<1 mm³) needed to be selected from the large brain and ear biopsies. Fixation and storage had not influenced the visibility of the NIRB markings on the surface, and small samples could be dissected

around these square shapes. The samples were processed in a PELCO Biowave Pro microwave (Ted Pella, Redding, CA), using a protocol based on previous work (Cantoni et al., 2010). The samples were washed four times, 5 min each in cacodylate buffer (pH 7.4), in a laminar flow hood. Primary post-fixation with 1% OsO_4 (Electron Microscopy Sciences, Hatfield, PA) and 1.5% $K_4Fe(CN)_6$ (Merck) in 0.1 M cacodylate buffer was performed in the microwave under a vacuum in seven consecutive 2-min steps, cycling between 100-W power on–off stages. The samples were then rinsed thoroughly in the laminar flow hood and twice for 40 s at 250 W in the microwave. Secondary post-fixation with 1% OsO_4 in 0.1 M cacodylate buffer was then performed under the same conditions as described for the primary post-fixation. Staining with 1% uranyl acetate (Serva Electrophoresis GmbH, Heidelberg, Germany), dehydration in ethanol and resin embedding were performed in the microwave, as described previously (Karreman et al., 2014). The mouse brain samples were mounted in commonly used resin molds and left to polymerize for 3 to 4 days at 60°C. The ear skin tissue was flat embedded between two sheets of aclar and mounted on an empty resin block the following day, as described before previously (Karreman et al., 2014). Following polymerization, the front face and the sides of the resin blocks were trimmed using a trimming diamond knife (20°, Diatome AG, Biel, Switzerland) to create a reference surface for future measurements (see text and below).

MicroCT imaging and reconstruction

MicroCT scanning was performed with a Phoenix Nanotom m (GE Sensing & Inspection Technologies, Fairfield, CT) operating under xs control and Phoenix datos|x acquisition software (both GE Sensing & Inspection Technologies). The resin-embedded biopsies were cut from the large resin block to achieve a small (<3 mm³) sample. This allowed mounting of the sample as close as possible to the X-ray source, which resulted in a higher magnification and resolution upon imaging. Scanning of the brain samples was performed at 50 kV and 500 µA for 1 h (1440 frames, average of 2, exposure time of 1 s). The skin sample was scanned in similar conditions, but with higher image averaging, which resulted in noise reduction and extended the scan time to 2 h. The voxel size of the resulting datasets was 0.75 µm in the x, y and z planes for the brain samples and 0.77 µm in the x, y and z planes for the ear skin sample. Reconstruction of the microCT volume was performed using Phoenix datos|x reconstruction software (GE Sensing & Inspection Technologies), and the volume was then further processed with VGStudio MAX software (Volume Graphics, Heidelberg, Germany).

3D registration of the IVM and microCT volumes in Amira software

The z-stacks (Fig. S1) were loaded into the digital space of Amira (FEI Company, Hillsboro, OR) and semi-automatically segmented using 'segmentation editor'. Hereto, pixels representing the features of interest were selected by global or local (using the 'magic wand') thresholding of gray values. Gaussian filtering and masking facilitated the automatic segmentation. The Amira feature 'normalize image' was used to minimize the effects of the intensity gradient in the dataset that had been caused by incomplete penetration of the heavy metals in deeper parts of the tissue. Segmentation artifacts were corrected by using manual segmentation.

3D surface models were generated from the label files and were simultaneously visualized in the Amira software. First, the IVM model was roughly fitted into the microCT model by manual displacement in 3D (rotation and translation). This first fitting helped to identify common features in both datasets. Second, using the 'landmark (2 sets)' module, the corresponding points in both datasets were selected (10–20 points). Using the 'Landmarksurfacewarp' module, the surface model of the IVM dataset was then warped into the microCT volume using rigid (affine) transformations. Generally, this first registration revealed more common points between both datasets, which could then be added to the 'landmark set', improving the final 3D registration.

Where the IVM dataset provided the position of the ROI with respect to the structural features within the biopsy, the microCT volume revealed the

orientation of the biopsy inside the resin block (see text). By combining both datasets, the location of the ROI inside the resin block could thus be predicted. Using Amira, the distance between the ROI and the surface and sides of the resin block was measured.

Trimming and approach at the ultramicrotome

The sample was mounted onto a Leica Ultracut S ultramicrotome (Leica Microsystems, Wetzlar, Germany) and trimmed using a 20° trimming diamond knife (Diatome AG, Biel, Switzerland). Before microCT scanning, a flat surface block face with parallel straight sides was trimmed. Following microCT and 3D registration of both datasets, the front face was trimmed to the calculated depth of the ROI. While trimming, the approach to the ROI could be monitored by obtaining a few thick sections (500 nm) from the sample. The sections were mounted onto a Superfrost ++ glass slide, stained with Toluidine Blue and imaged with light microscopy. The light-microscopy sections were correlated to the microCT virtual sections. To achieve this, an 'obliqueslice' was created in Amira software and aligned to be perfectly parallel with the trimmed block face in the microCT dataset, and thus also parallel to the trimming angle. The orientation of the 'obliqueslice' virtual sections then corresponded to the physical thick sections (500 nm) produced with the ultramicrotome.

It was determined, by visual inspection, which virtual section matched the best to the light-microscopy section. The position of this selected virtual section within the microCT dataset then enabled us to measure the distance between the newly trimmed surface and the ROI (Fig. S3). In practice, a small number of checkpoints are sufficient to obtain an accuracy of about 5 µm for the targeting. We have used from 2 to 5, evenly spread throughout the trimmed volume. Collecting more checkpoints might lead to a higher degree of accuracy but will also slow down the whole procedure.

For FIB-SEM imaging, both the front face and one flank of the block needed to be trimmed very close to the region of interest (see Results; Fig. S3). To achieve this, the front was trimmed to several micrometers (20–30 µm) just before reaching the tumor cell (as estimated from the microCT 3D map). Next, one flank was trimmed as close as possible to the tumor cell (maximum 20–30 µm), a new thick section was produced and compared to the microCT tomogram, to check the progression towards the ROI (Fig. S3). The front face, which would be the imaged surface in the FIB-SEM analysis, was then trimmed further to approach the cell as close as possible (3–5 µm). To enable mounting on the SEM stub, the trimmed tip of the resin block was cut away with a double-edged razor blade. The sample was mounted with an adhesive conductive carbon tab (PELCO Tabs, Ted Pella) onto a 0.5 'SEM pin stub' (Agar Scientific, Essex, United Kingdom) and stabilized with colloidal silver (liquid, Ted Pella). The sample on the stub was then sputter-coated with gold (60 s at 30 mA).

For serial sectioning of the resin-embedded subcutaneous tumor sample, the front face of the resin block was trimmed to the calculated depth of the region of interest. The flanks of the samples were trimmed to create a block face of approximately 300×600 µm². Approximately 330 thick serial sections (130 nm) were produced with a 45° histo diamond knife (Diatome AG, Biel, Switzerland) and mounted onto formvar-coated slot grids.

Electron microscopy and image analysis

The mouse brain samples were imaged in an Auriga 60 FIB-SEM instrument (Carl Zeiss Microscopy GmbH) operating under SmartSEM (Carl Zeiss Microscopy GmbH) and Atlas3D software (Fibics Incorporated, Ottowa, Ontario, Canada). The resulting datasets were aligned using TrakEM (Cardona et al., 2012) [ImageJ (Schindelin et al., 2012); http://imagej.nih.gov/ij/], and the image stack was segmented in 3dmod, part of the IMOD software package (Mastronarde, 2005) (Boulder Laboratory, University of Colorado, Denver, CO). The serial sections of the mouse ear skin tissue were screened and imaged with a Biotwin CM120 instrument (120 kV, FEI Company, Hillsboro, OR) equipped with a bottom-mounted 1 K Keen View CCD camera (Olympus Soft Imaging Solutions, Münster, Germany). Montaged images and tomograms were

acquired with a Tecnai F30 Field Emission Gun TEM (300 kV, FEI Company) equipped with an Eagle 4 K camera (FEI Company). The F30 was controlled using Tecnai User Interface (PEOUI) and Tecnai Acquisition (TIA) software. Tomograms and image montages were obtained using SerialEM software (Mastronarde, 2005), and the tomograms were reconstructed in eTomo, part of the IMOD software package (Kremer et al., 1996) (Boulder Laboratory). The electron microscopy images were processed using ImageJ (Schindelin et al., 2012) and Photoshop CS6 (Adobe). The figures were created in Illustrator CS6 (Adobe), and the supplementary material movies were made with Fiji (ImageJ), IMOD (Boulder Laboratory) and Amira (FEI Company).

Author contributions
Y.S., J.G.G. and M.A.K. designed the research; M.A.K., L.M., N.L.S., G.S. and G.A. conducted the experiments; B.R. and M.A.K. performed the microCT scans; F.W. established the cranial window mouse model. L.M. established the intravital imaging on the mouse ear. M.A.K. and L.M. processed and analyzed the data. M.A.K., J.G.G. and Y.S. wrote the manuscript; all authors commented on the manuscript.

Supplementary information
Supplementary information available online at
http://jcs.biologists.org/lookup/suppl/doi:10.1242/jcs.181842/-/DC1

References
Alexander, S., Koehl, G. E., Hirschberg, M., Geissler, E. K. and Friedl, P. (2008). Dynamic imaging of cancer growth and invasion: a modified skin-fold chamber model. *Histochem. Cell Biol.* **130**, 1147-1154.

Beerling, E., Ritsma, L., Vrisekoop, N., Derksen, P. W. B. and van Rheenen, J. (2011). Intravital microscopy: new insights into metastasis of tumors. *J. Cell Sci.* **124**, 299-310.

Bishop, D., Nikić, I., Brinkoetter, M., Knecht, S., Potz, S., Kerschensteiner, M. and Misgeld, T. (2011). Near-infrared branding efficiently correlates light and electron microscopy. *Nat. Methods* **8**, 568-570.

Briggman, K. L. and Bock, D. D. (2012). Volume electron microscopy for neuronal circuit reconstruction. *Curr. Opin. Neurobiol.* **22**, 154-161.

Burnett, T. L., McDonald, S. A., Gholinia, A., Geurts, R., Janus, M., Slater, T., Haigh, S. J., Ornek, C., Almuaili, F., Engelberg, D. L. et al. (2014). Correlative tomography. *Sci. Rep.* **4**, 4711.

Bushong, E. A., Johnson, D. D., Kim, K.-Y., Terada, M., Hatori, M., Peltier, S. T., Panda, S., Merkle, A. and Ellisman, M. H. (2015). X-ray microscopy as an approach to increasing accuracy and efficiency of serial block-face imaging for correlated light and electron microscopy of biological specimens. *Microsc. Microanal.* **21**, 231-238.

Cantoni, M., Genoud, C., Hébert, C. and Knott, G. (2010). Large volume, isotropic, 3D imaging of cell structure on the nanometer scale. *Microsc. Anal.* **24**, 13-16.

Cardona, A., Saalfeld, S., Schindelin, J., Arganda-Carreras, I., Preibisch, S., Longair, M., Tomancak, P., Hartenstein, V. and Douglas, R. J. (2012). TrakEM2 software for neural circuit reconstruction. *PLoS ONE* **7**, e38011.

Charras, G. and Paluch, E. (2008). Blebs lead the way: how to migrate without lamellipodia. *Nat. Rev. Mol. Cell Biol.* **9**, 730-736.

Durdu, S., Iskar, M., Revenu, C., Schieber, N., Kunze, A., Bork, P., Schwab, Y. and Gilmour, D. (2014). Luminal signalling links cell communication to tissue architecture during organogenesis. *Nature* **515**, 120-124.

Friedl, P. and Alexander, S. (2011). Cancer invasion and the microenvironment: plasticity and reciprocity. *Cell* **147**, 992-1009.

Friedl, P., Wolf, K. and Lammerding, J. (2011). Nuclear mechanics during cell migration. *Curr. Opin. Cell Biol.* **23**, 55-64.

Gligorijevic, B., Bergman, A. and Condeelis, J. (2014). Multiparametric classification links tumor microenvironments with tumor cell phenotype. *PLoS Biol.* **12**, e1001995.

Goetz, J. G., Steed, E., Ferreira, R. R., Roth, S., Ramspacher, C., Boselli, F., Charvin, G., Liebling, M., Wyart, C., Schwab, Y. et al. (2014). Endothelial cilia mediate low flow sensing during zebrafish vascular development. *Cell Rep.* **6**, 799-808.

Handschuh, S., Baeumler, N., Schwaha, T. and Ruthensteiner, B. (2013). A correlative approach for combining microCT, light and transmission electron microscopy in a single 3D scenario. *Front. Zool.* **10**, 44.

Karreman, M. A., Mercier, L., Schieber, N. L., Shibue, T., Schwab, Y. and Goetz, J. G. (2014). Correlating intravital multi-photon microscopy to 3D electron microscopy of invading tumor cells using anatomical reference points. *PLoS ONE* **9**, e114448.

Keene, D. R., Tufa, S. F., Wong, M. H., Smith, N. R., Sakai, L. Y. and Horton, W. A. (2014). Correlation of the same fields imaged in the TEM, Confocal, LM, and MicroCT by image registration: from specimen preparationto displaying a final composite image. In *Methods in Cell Biology* (ed. T. Mueller-Reichert and P. Verkade), pp. 391-417. Elsevier Inc.

Kienast, Y., von Baumgarten, L., Fuhrmann, M., Klinkert, W. E. F., Goldbrunner, R., Herms, J. and Winkler, F. (2010). Realtime imaging reveals the single steps of brain metastasis formation. *Nat. Med.* **16**, 116-122.

Kolotuev, I., Schwab, Y. and Labouesse, M. (2010). A precise and rapid mapping protocol for correlative light and electron microscopy of small invertebrate organisms. *Biol. Cell* **102**, 121-132.

Korogod, N., Petersen, C. C. H. and Knott, G. W. (2015). Ultrastructural analysis of adult mouse neocortex comparing aldehyde perfusion with cryo fixation. *eLife* **4**, 241.

Kremer, J. R., Mastronarde, D. N. and McIntosh, J. R. (1996). Computer visualization of three-dimensional image data using IMOD. *J. Struct. Biol.* **116**, 71-76.

Leong, H. S., Robertson, A. E., Stoletov, K., Leith, S. J., Chin, C. A., Chien, A. E., Hague, M. N., Ablack, A., Carmine-Simmen, K., McPherson, V. A. et al. (2014). Invadopodia are required for cancer cell extravasation and are a therapeutic target for metastasis. *Cell Rep.* **8**, 1558-1570.

Lucas, M. S., Günthert, M., Gasser, P., Lucas, F. and Wepf, R. (2012). Bridging microscopes: 3D correlative light and scanning electron microscopy of complex biological structures. In Methods in Cell Biology (ed. T. Mueller-Reichert and P. Verkade). New York: Elsevier.

Maco, B., Holtmaat, A., Cantoni, M., Kreshuk, A., Straehle, C. N., Hamprecht, F. A. and Knott, G. W. (2013). Correlative *in vivo* 2 photon and focused ion beam scanning electron microscopy of cortical neurons. *PLoS ONE* **8**, e57405.

Mastronarde, D. N. (2005). Automated electron microscope tomography using robust prediction of specimen movements. *J. Struct. Biol.* **152**, 36-51.

Metscher, B. D. (2009). MicroCT for comparative morphology: simple staining methods allow high-contrast 3D imaging of diverse non-mineralized animal tissues. *BMC Physiol.* **9**, 11.

Narayan, K., Danielson, C. M., Lagarec, K., Lowekamp, B. C., Coffman, P., Laquerre, A., Phaneuf, M. W., Hope, T. J. and Subramaniam, S. (2014). Multi-resolution correlative focused ion beam scanning electron microscopy: Applications to cell biology. *J. Struct. Biol.* **185**, 278-284.

Nixon, S. J., Webb, R. I., Floetenmeyer, M., Schieber, N., Lo, H. P. and Parton, R. G. (2009). A single method for cryofixation and correlative light, electron microscopy and tomography of zebrafish embryos. *Traffic* **10**, 131-136.

Reymond, N., d'Água, B. B. and Ridley, A. J. (2013). Crossing the endothelial barrier during metastasis. *Nat. Rev. Cancer* **13**, 858-870.

Ritsma, L., Vrisekoop, N. and van Rheenen, J. (2013). In vivo imaging and histochemistry are combined in the cryosection labelling and intravital microscopy technique. *Nat. Commun.* **4**, 2366.

Sahai, E. (2007). Illuminating the metastatic process. *Nat. Rev. Cancer* **7**, 737-749.

Schindelin, J., Arganda-Carreras, I., Frise, E., Kaynig, V., Longair, M., Pietzsch, T., Preibisch, S., Rueden, C., Saalfeld, S., Schmid, B. et al. (2012). Fiji: an open-source platform for biological-image analysis. *Nat. Methods* **9**, 676-682.

Sengle, G., Tufa, S. F., Sakai, L. Y., Zulliger, M. A. and Keene, D. R. (2013). A correlative method for imaging identical regions of samples by micro-CT, light

microscopy, and electron microscopy: imaging adipose tissue in a model system. *J. Histochem. Cytochem.* **61**, 263-271.

Shibue, T., Brooks, M. W. and Weinberg, R. A. (2013). An integrin-linked machinery of cytoskeletal regulation that enables experimental tumor initiation and metastatic colonization. *Cancer Cell* **24**, 481-498.

Stoletov, K., Kato, H., Zardouzian, E., Kelber, J., Yang, J., Shattil, S. and Klemke, R. (2010). Visualizing extravasation dynamics of metastatic tumor cells. *J. Cell Sci.* **123**, 2332-2341.

Valastyan, S. and Weinberg, R. A. (2011). Tumor metastasis: molecular insights and evolving paradigms. *Cell* **147**, 275-292.

Wolf, K. and Friedl, P. (2011). Extracellular matrix determinants of proteolytic and non-proteolytic cell migration. *Trends Cell Biol.* **21**, 736-744.

Wolf, K., te Lindert, M., Krause, M., Alexander, S., te Riet, J., Willis, A. L., Hoffman, R. M., Figdor, C. G., Weiss, S. J. and Friedl, P. (2013). Physical limits of cell migration: control by ECM space and nuclear deformation and tuning by proteolysis and traction force. *J. Cell Biol.* **201**, 1069-1084.

Special Issue on 3D Cell Biology

Call for papers

Submission deadline: January 16th, 2016

Journal of **Cell Science**

2.3.4 Conclusion et perspectives

La microCT aux rayons X, troisième modalité d'imagerie, permet d'imager l'échantillon inclus dans le bloc de résine. La position de la région d'intérêt est alors déterminée avec précision par rapport à la surface du bloc de résine. Lors de l'approche de l'échantillon par ultramicrotomie toute la partie supérieure du bloc est alors enlevée laissant la région d'intérêt effleuré la surface du bloc. Cette étape supplémentaire dans le protocole permet de cibler la région d'intérêt ce qui rend le protocole compatible avec des échantillons épais tout en le rendant plus efficace. Le processus de préparation pour la microscopie électronique est passé à 14 jours contre plus d'un mois pour le premier protocole.

Nous avons démontré l'application de ce protocole sur des échantillons épais (cerveau de souris) mais aussi sur des échantillons plus fin (oreille de souris), prouvant la polyvalence qui nous ouvre la voie à l'étude à l'échelle ultrastructurelle de toutes les étapes de la cascade métastatique dans la plupart des organes de la souris.

2.3.4.1 Etude de la dégradation de la membrane basale

En collaboration avec l'équipe de P. Chavrier (Institut Curie, Paris) cette technique a été appliquée à l'étude de l'implication de la métalloprotéinase MT1-MMP dans la dégradation de la membrane basale, première étape dans l'invasion par les cellules tumorales du tissu adjacent. Le modèle d'étude est le carcinome mammaire *in situ* évoluant vers un carcinome invasif (Lodillinsky et al., 2016).

Dans ce modèle des cellules MCF10DCIS.com sont injectées directement dans les canaux de la glande mammaire (Figure 28).
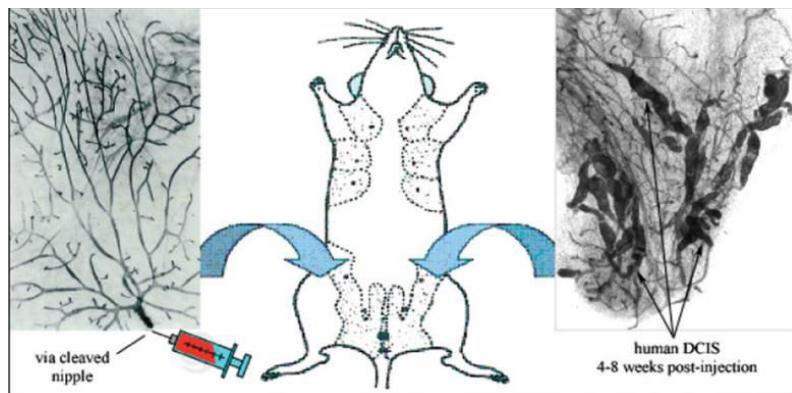
*Figure 28 : **Injection de cellules tumorales dans la glande mammaire de souris.** L'injection des cellules se fait directement via le mamelon pour former des carcinomes in situ dans la glande mammaire.*

Ces cellules expriment la metalloprotéinase MT1-MMP couplé au fluorochrome mCherry ou pHluorin. La protéine pHLuorin est une protéine GFP mutée la rendant sensible au pH (Miesenböck et al.,

1998). Pour des pH inférieurs à 6 la pHluorin n'émet pas de fluorescence, elle devient fluorescente à pH neutre.

La construction MT1-MMP-pHluorin permet ainsi de distinguer par absence de fluorescence les protéines MT1-MMP intracellulaires qui transit via la voie endosomale (Poincloux et al., 2009) des protéines MT1-MMP ancrées à la membrane cytoplasmique et exposées du côté extracellulaire.

L'imagerie intravitale est réalisée par microscopie multiphotonique à travers une fenêtre implantable au niveau de la glande mammaire de la souris.

La SHG permet d'imager les fibres de collagènes contenues dans la MEC, par son absence elle permet aussi de distinguer les glandes mammaires (zone sombre entourée par du collagène)
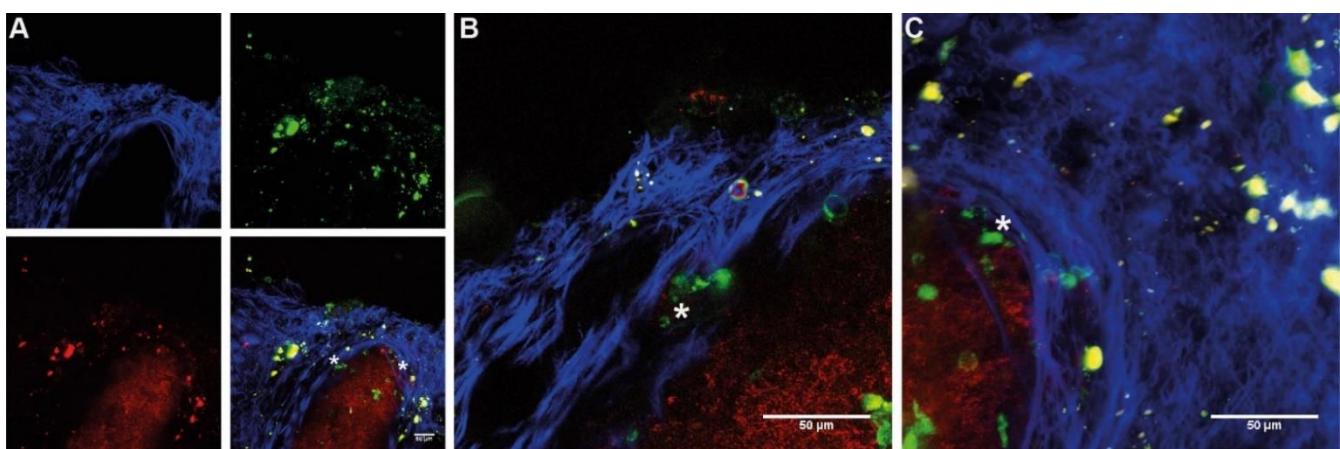
Figure 29 : **Imagerie des régions d'intérêts. A** : Projection en z d'une acquisition 3D d'une glande mammaire. En haut à gauche, Fibres de collagène imagées par SHG. En haut à droite, MT1-MMP exposée du côté extracellulaire. En bas à gauche, MT1-MMP intracellulaire. En bas à droite, Assemblage des trois images précédentes. Les deux régions d'intérêts sont localisés par des asterisque **B** : Projection en z de la permière région d'intérêt. **C** : Projection en z de la deuxème région d'intérêt.

Lors de cette expérience nous avons imagés deux zones d'intérêts (Figure 29) correspondant à des zones de micro invasion où MT1-MMP est exposée du côté extracellulaire (Fluorescence verte).

Pour repérer la région d'intérêt par microscopie électronique nous avons ajouté des points de repères par la technique de NIRB. Du fait que la glande mammaire ne soit pas plane (Figure 30) il nous était impossible de réaliser un cadre autour de la région d'intérêt. En effet, les zones hors focus n'auraient pas pu être marquées par NIRB, rendant le marquage imprévisible.
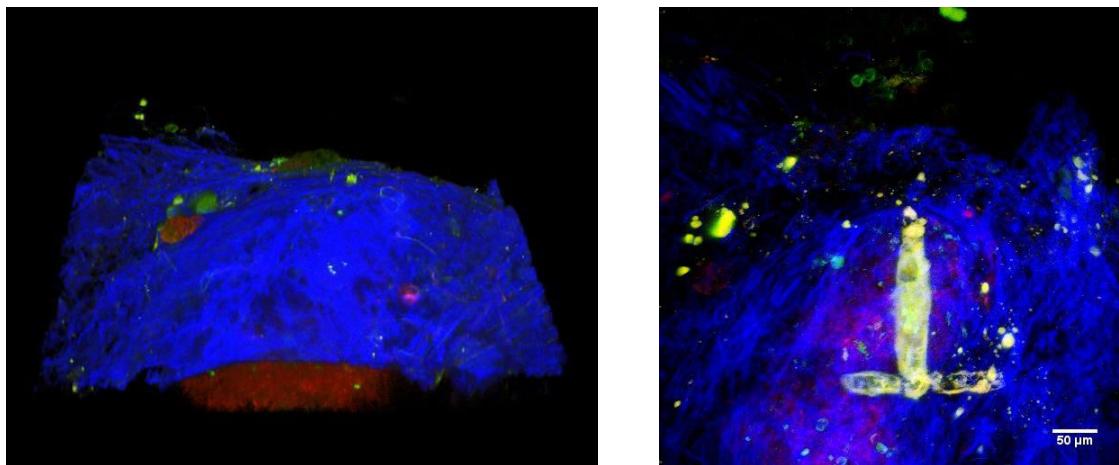
Figure 30 : **Vue en 3D dimension de la glande mammaire**. A gauche : vue 3D de la surface de la glande mammaire. A droite : surface de la glande mammaire après NIRB. Le « T » inversé jaune correspond à la marque faite par NIRB.

La solution a été de réaliser le marquage par NIRB en forme de « T » uniquement au sommet de la glande (Figure 30).

Une fois la souris sacrifiée l'ensemble du tissu mammaire a été fixé par immersion dans un mélange de Glutaraldehyde 2,5% + Paraformaldehyde 2% dans un tampon PHEM 0,1M.

La région d'intérêt a été retrouvé grâce à la marque créée par NIRB. Un morceau de tissu d'environ 1mm^3 a été biopsiées pour être ensuite traitée pour la microscopie électronique (Figure 31).
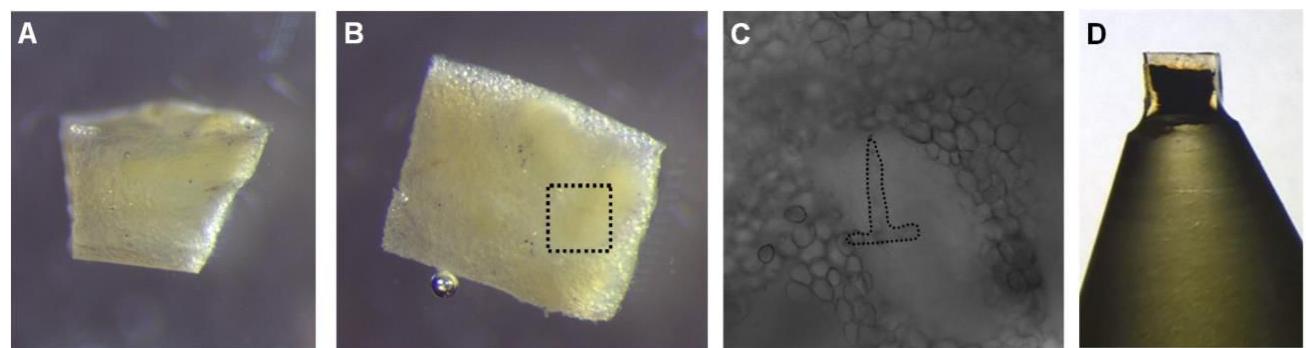
Figure 31 : **Préparation de l'échantillon pour la microscopie électronique. A** : Biopsie de la glande mammaire vue de côté. **B** : Biopsie de la glande mammaire vue de dessus. Le cadre noir désigne l'emplacement de la région d'intérêt. **C** : Vue du marquage réalisé par **NIRB** sur la glande mammaire. **D** : L'échantillon inclus dans le bloc de résine.

Une fois inclus dans le bloc de résine, le bloc a été imagé par tomographie aux rayons X (Figure 32) dans le but de déterminer la distance qui sépare la ROI de la surface du bloc. La segmentation de

l'imagerie aux rayons X avec le logiciel *Amira* nous permet de distinguer en 3D l'ensemble des structures constituant le tissu mammaire dont la ROI.
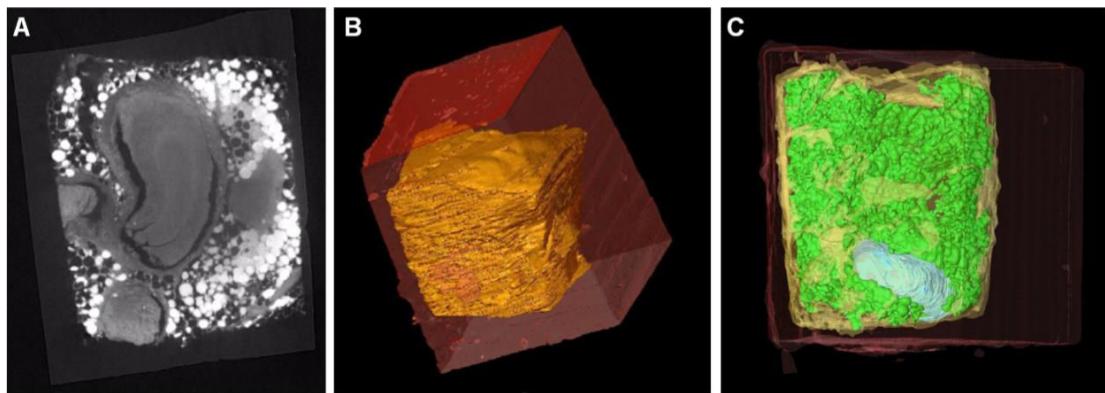
Figure 32 : **Tomographie aux rayons X du bloc résine contenant l'échantillon.** *A : Images brut de l'échantill0on inclus dans le bloc. Apparait en gris la glande mammaire, les structures sphériques d'aspect vide ou blanches correspondent aux adipocytes constituant le tissu mammaire. B : Image segmenté en rouge, le bloc de résine. En jaune, l'échantillon. C : Segmentation en vert des adipocytes. En bleu : la glande mammaire d'intérêt.*

La segmentation des données générées par microscopie multiphotonique sont aussi modélisées en 3D. Les deux volumes (multiphoton et rayons X) sont ensuite fusionnés (Figure 33). Cette étape permet de localiser avec précision la ROI dans le bloc de résine. La surface du bloc étant parfaitement plane, il est possible de calculer avec précision la position de la ROI avec la surface du bloc.
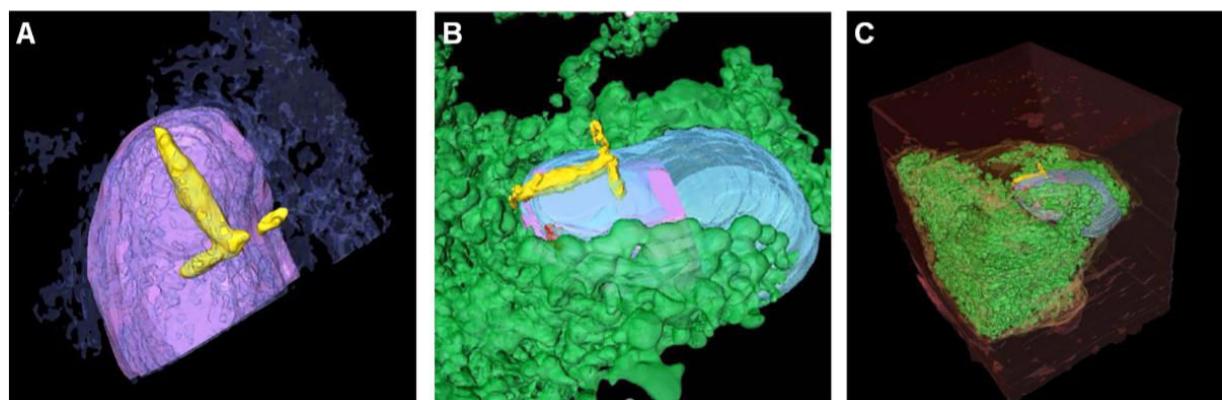
Figure 33 : **Assemblage des volumes générés par microscopie multiphotonique et rayons X. A** : *Le volume généré par microscopie multiphotonique est modélisé en 3D. La glande mammaire apparait en violet, la marque produite par la technique de NIRB est ici en jaune. B : Les deux volumes sont fusionnés. C : La ROI est positionnée avec précision dans le volume rayons X, permettant ainsi de déterminer sa position avec précision dans le bloc.*

Dans ce cas la ROI se situe à 295µm de la surface du bloc (Figure 34). Par sécurité les 290µm séparant la ROI de la surface du bloc ont d'abord été enlevée par ultramicrotomie, laissant 5µm

comme marge d'erreur. L'approche de la ROI s'est fait par coupes sériées d'une épaisseur de 500nm. La position dans l'échantillon a été vérifié en comparant les coupes épaisses colorées au bleu de toluidine et imagées par microscopie conventionnelle avec les données rayons X. Une fois la ROI atteinte, les coupes suivantes ont été réalisées à 100nm d'épaisseur pour être imagées par TEM (Figure 35).
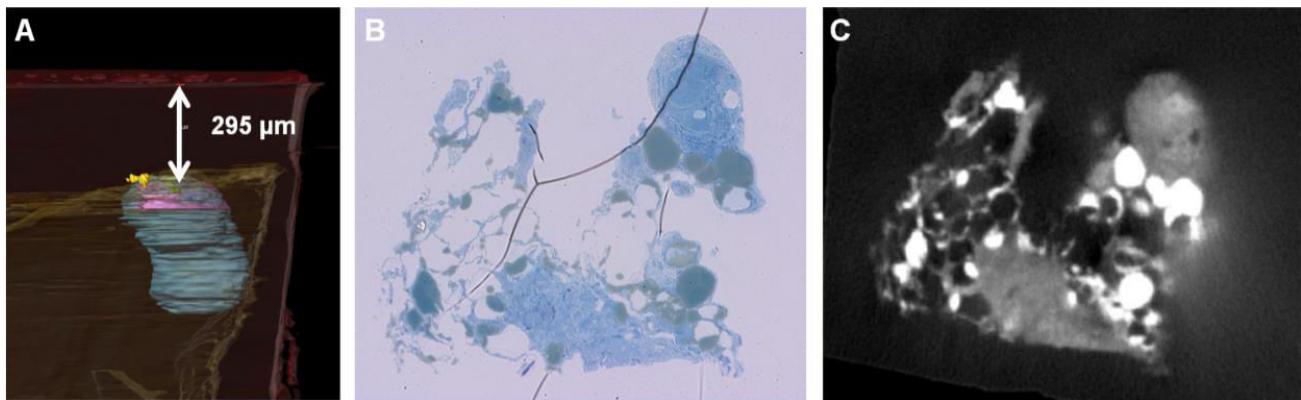
Figure 34 : **Approche de la ROI par ultramicrotomie. A** : La distance séparant la surface du bloc à la ROI est évaluée à295µm. **B** : Coupe de 500nm d'épaisseur colorée au bleu de toluidine, obtenue à 290m de la surface du bloc. **C** : L'approche de la ROI est vérifiée en comparant la coupe de 500nm aux données obtenues aux rayons X.

Figure 35 : **Microscopie électronqiue de la ROI**. **A** : Les données aux rayons X permettent de suivre la progression dans l'échantillon. La zone détourée en jaune correpond à la zone imagée par microscopie électronique en B. **B** : Image par microscopie de la ROI. La zone détourée en blanc correpond à la zone imagée en C. **C** : Image à fort grossissement de la ROI.
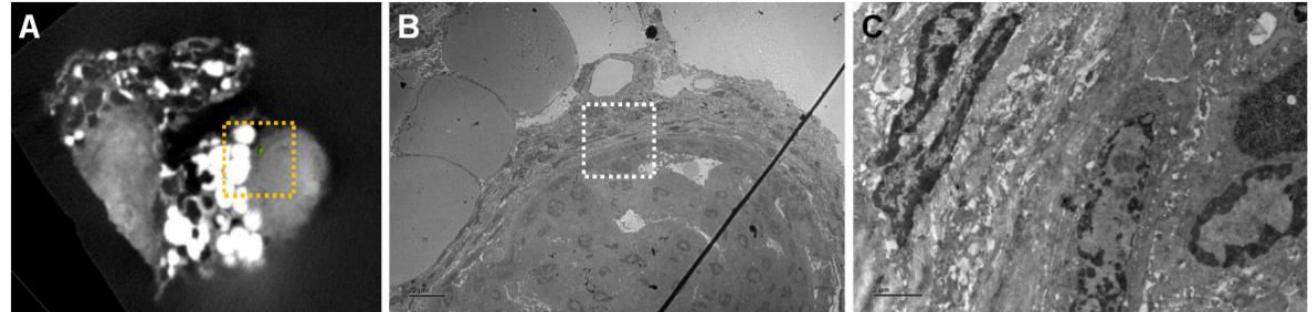
Cette première expérience de CLEM sur la glande mammaire de souris nous a permis de prouver sa faisabilité. La qualité de l'ultrastrucutre n'est ce pendant pas optimal. Ceci s'explique par la méthode de fixation par immersion choisie. Une fixation par injection intracardiaque permettrait d'améliorer l'ultrastrucure de l'échantillon.

Le tissu mammaire étant très riche en adipocytes, il serait possible d'utiliser leur forme et leur distribution pour améliorer l'étape de corrélation entre les données 2PEM et la tomographie aux rayon

X. En effet, les adipocytes sont parfaitement distinguable par rayons X (Figure 32) et peuvent aussi être imagés par THG (Figure 36).

En conclusion, ce protocole combinant l'imagerie multiphotonique intravitale, la tomographie aux rayons X et enfin la microscopie électronique a été appliqué jusqu'à présent à 3 types d'échantillons différents, le cerveau, l'oreille et le tissu mammaire de souris. Ce protocole ouvre la voie à l'étude à l'échelle ultrastructurale de l'invasion tumorales dans d'autres organes visualisables par microscopie multiphotonique (poumons, foie, peau) mais aussi à d'autres domaines d'études.
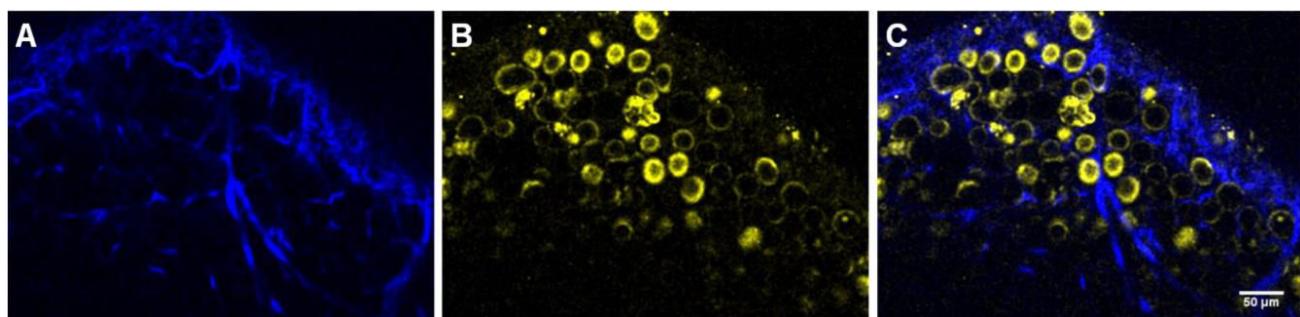
*Figure 36 : **Combinaison de l'imagerie par SHG et THG du tissu mammaire. A** : Le collagène est imagé par SHG. **B** : Les adipocytes sont imageables par THG. **C** : Combinaison de la SHG et de la THG.*

Ce papier de méthode présente la procédure à suivre pour réaliser le protocole de CLEM que nous avons mis en place dans le cerveau de souris.

Find your way with X-Ray: using microCT to correlate in vivo imaging with 3D electron microscopy

13

Matthia A. Karreman[*,1], **Bernhard Ruthensteiner**[§], **Luc Mercier**[¶,‖,#,**],
Nicole L. Schieber[*], **Gergely Solecki**[§§,¶¶], **Frank Winkler**[§§,¶¶],
Jacky G. Goetz[¶,‖,#,**], **Yannick Schwab**[*]

European Molecular Biology Laboratory, Heidelberg, Germany

§*Zoologische Staatssammlung München, Munich, Germany*

¶*MN3T, Inserm U1109, Strasbourg, France*

‖*Université de Strasbourg, Strasbourg, France*

#*LabEx Medalis, Université de Strasbourg, Strasbourg, France*

****Fédération de Médecine Translationnelle de Strasbourg (FMTS),
Université de Strasbourg, Strasbourg, France*

§§*University Hospital Heidelberg, Heidelberg, Germany*

¶¶*German Cancer Research Center (DKFZ), Heidelberg, Germany*

1*Corresponding author: E-mail: karreman@embl.de*

CHAPTER OUTLINE

Abstract

Combining in vivo imaging with electron microscopy (EM) uniquely allows monitoring rare and critical events in living tissue, followed by their high-resolution visualization in their native context. A major hurdle, however, is to keep track of the region of interest (ROI) when moving from intravital microscopy (IVM) to EM. Here, we present a workflow that relies on correlating IVM and microscopic X-ray computed tomography to predict the position of the ROI inside the EM-processed sample. The ROI can then be accurately and quickly targeted using ultramicrotomy and imaged using EM. We outline how this procedure is used to retrieve and image tumor cells arrested in the vasculature of the mouse brain.

INTRODUCTION

Intravital correlative light and electron microscopy (intravital CLEM) is a powerful approach to study developmental and pathological processes in animal models (Durdu et al., 2014; Karreman, Hyenne, Schwab, & Goetz, 2016; Maco et al., 2013). While in vitro model systems never fully recapitulate the complexity of living tissue, intravital microscopy (IVM) enables to monitor processes over time and in their native environment (Ellenbroek & van Rheenen, 2014; Follain, Mercier, Osmani, Harlepp, & Goetz, 2016). Extending IVM with electron microscopy (EM) reveals the process of interest at high resolution within its ultrastructural context.

The main challenge in intravital CLEM is to keep track of the region of interest (ROI) when moving from in vivo imaging to EM. For small organisms or embryos, it is possible to process and image the full sample in EM and retrieve the area of interest by browsing through the resulting images (Müller-Reichert, Srayko, Hyman, O'Toole, & McDonald, 2007; Zito, Parnas, Fetter, Isacoff, & Goodman, 1999). However, for larger model systems, a biopsy (e.g., a small piece of tissue or a vibratome section) containing the ROI needs to be selected and subsequently processed for EM. Retrieval of the ROI in the electron microscope is particularly difficult, due to the difference in image formation between IVM and EM, the small field of view (FOV) of EM and the deformation of the tissue that results from the EM sample preparation approaches.

In this chapter, we outline an approach that enables correlating IVM to three-dimensional (3D) EM of voluminous samples. As an example, we demonstrate how to retrieve single tumor cells inside mouse brain biopsies. Here, we aim to study how metastatic JIMT1 breast cancer cells cross the blood—brain barrier as part of the metastatic process (Karreman et al., 2016). We have developed a multimodal

correlative microscopy workflow that relies on microscopic X-ray computed tomography (microCT) imaging as a guide to retrieve the area(s) of interest inside the EM-processed sample (Karreman et al., 2016) (Fig. 1). The workflow starts out with IVM of fluorescent JIMT1 tumor cells inside the mouse brain, through a cranial window (Kienast et al., 2010). Following perfusion fixation, the position of the ROI is marked onto the mouse brain surface by near-infrared branding (NIRB) (Bishop et al., 2011). A small biopsy, which contains the area of interest, is then dissected from the fixed mouse brain. Next, the biopsy is prepared for EM by microwave-assisted processing, followed by embedding in resin. The sample is then imaged by microCT, enabling to get a 3D volume showing the resin block, the biopsy, and the structural features therein. The microCT data set of the processed sample is subsequently correlated to the IVM data set, which is the critical step in this correlative workflow because it translates the position of the target cell inside the volume of the opaque resin-embedded piece of tissue.

Using Amira software, 3D models of both the IVM and microCT volumes are generated by segmentation, and the corresponding points that can be found in each model are marked using the *Landmarks* module. The IVM volume, showing the vasculature and the tumor cell(s), is then registered into the microCT volume, which also shows the outlines of the resin block, the global topology of the biopsy and, importantly, the vasculature. Even though the fluorescent signal is lost during the sample preparation for EM, this warping procedure precisely positions the tumor cell inside the microCT data set, enabling to measure its location with respect to the
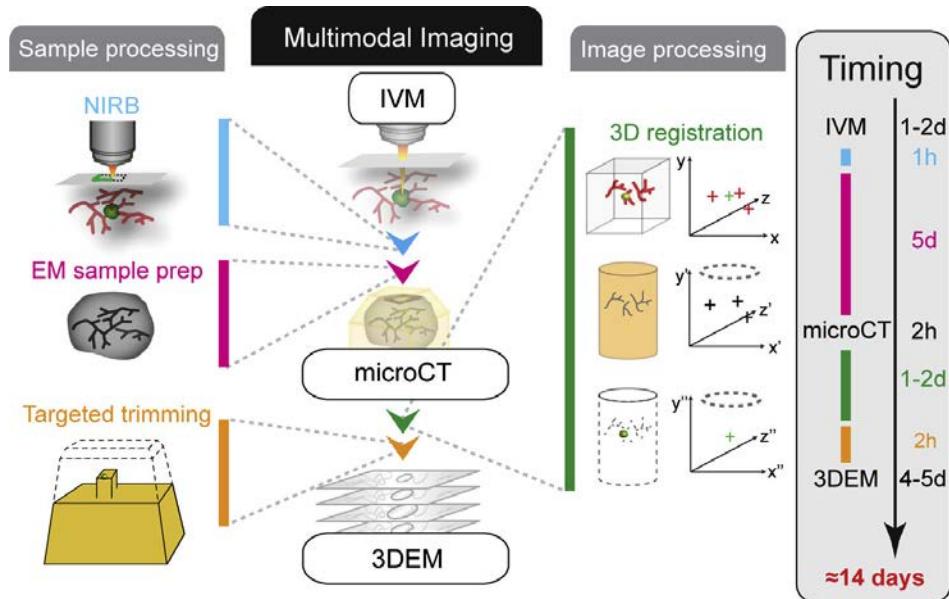
FIGURE 1

Overview of the multimodal correlative microscopy workflow. For a detailed description of the different steps involved, please refer to the main text. This figure appeared earlier in the original publication of the approach (Karreman et al., 2016). *EM*, electron microscopy.

resin block surface in x, y, and z. Based on these measurements, the resin block is accurately trimmed in an ultramicrotome to approach the position of the tumor cell. 3DEM is then performed, e.g., by focused ion beam−scanning electron microscopy (FIB-SEM), serial block face imaging or by serial section TEM (and serial electron tomography).

In this chapter, we outline step-by-step the protocol from taking the biopsy to accurately approaching the cell of interest using 3D-targeted trimming. In particular, we detail how both the IVM and the microCT data sets can be segmented and registered in 3D using Amira software and how this subsequently allows to sculpt the resin block to expose the target to 3DEM. The workflow is demonstrated here on mouse brain biopsies in which one or more tumor cells are retrieved. Importantly, this method can also be applied to other model systems, such as mouse skin tissue (Karreman et al., 2016) and starfish oocytes. The high success rate and improved throughput of this approach makes it highly suitable and promising for intravital CLEM. Moreover, its versatility allows its use in different fields, as it can be applied to retrieve any rare event from in vivo imaging to EM.

1. METHODS
1.1 PROCESSING FOR ELECTRON MICROSCOPY

A cranial window is grafted into 8- to 10-week-old nude mice and is followed by a 3-week healing period. Three or seven days before imaging, the mice are injected into the left heart ventricle with cytoplasmic GFP−expressing JIMT1 tumor cells. During IVM, described in more detail in our previous work (Karreman et al., 2016; Kienast et al., 2010), arrested and potentially extravasated tumor cells are targeted for imaging. On finding a cell of interest, a large-FOV z-stack (e.g., 600 μm × 600 μm × 500 μm) and a small-FOV z-stack (e.g., 200 μm × 200 μm × 250 μm) are acquired. In a later stage, both these IVM volumes are required for the correlation procedure (see Section 1.3). Following IVM, the anesthetized mouse is perfusion-fixed with 2.5% glutaraldehyde and 2% formaldehyde in PHEM buffer (60 mM PIPES, 25 mM HEPES, 10 mM EGTA, and 2 mM MgCl, pH adjusted to 6.9). The imaged volumes of interest are marked on the level of the brain surface by NIRB, and the brain is removed from the skull, immersed in the fixative, and stored overnight at 4°C. The next day, the fixative is replaced by 1% formaldehyde in PHEM buffer, for prolonged storage. For more details about IVM, perfusion fixation, and NIRB, please refer to earlier work (Bishop et al., 2011; Karreman et al., 2014, 2016).

During processing samples for EM, the effective infiltration of chemicals into the tissue is limited. For this reason, it is critical to dissect a small biopsy. The NIRB markings indicate the x-y position of the area of interest, and the IVM data set will roughly indicate the depth of the ROI inside the brain. Using this information as a guide, dissect a <600 μm × 600 μm × 900 μm biopsy (see Fig. 2).
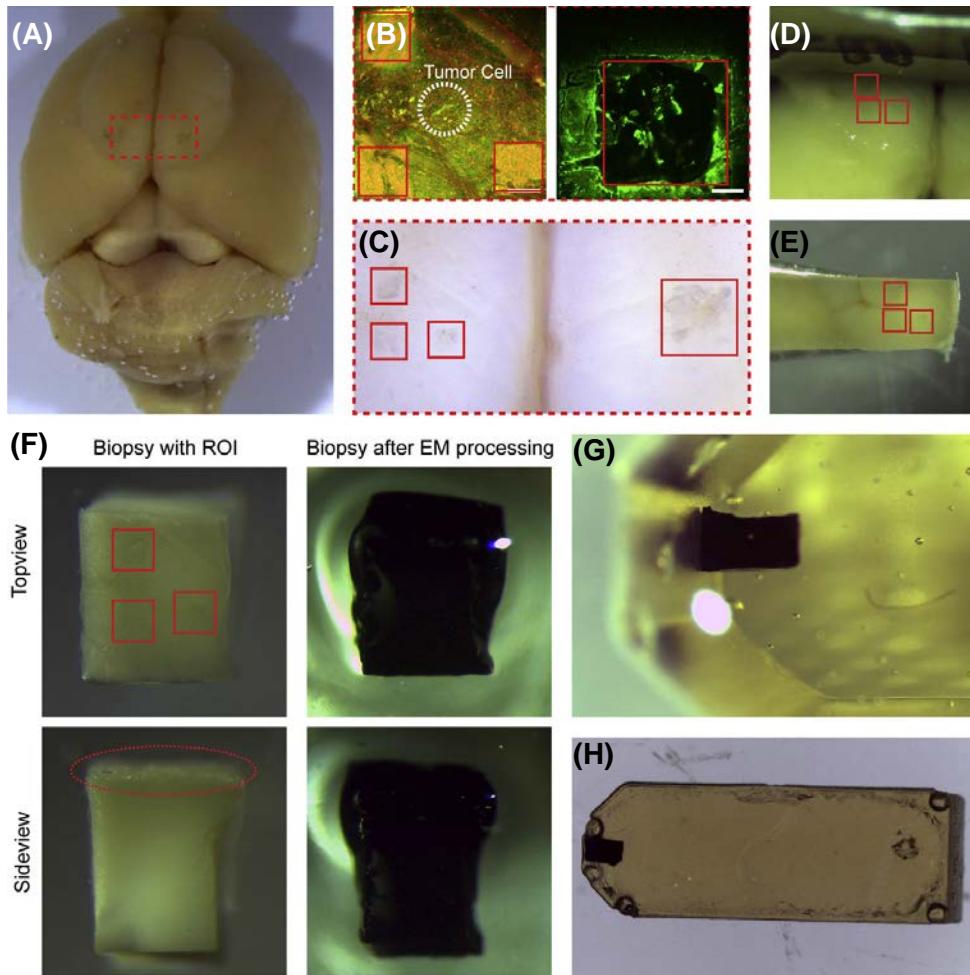
FIGURE 2

Dissecting and electron microscopy (EM) processing of the mouse brain biopsy containing the region of interest (ROI). (A) The position of the in vivo imaged tumor cell inside the mouse brain is marked by near-infrared branding (NIRB), visible inside the boxed area (see panel C). (B) Maximum intensity z-projections of the intravital microscopy data sets, showing in the left panel the position of the tumor cell (*dotted circle*) with respect to small NIRB markings (*boxes*). The right panel depicts a larger NIRB square that is generated on the opposing hemisphere to facilitate retrieval of the smaller markings around the tumor cell (see panel A and C). Scale bars: 100 μm. (C) On the brain surface, the small and large NIRB markings are visible as small scars (*boxes*). (D and E) A small biopsy is cut around the NIRB markings (*boxes*), using a razor blade. (F) Before EM processing (left panels, "Biopsy with ROI"), the NIRB markings are still visible (*boxes*, top of biopsy indicated in bottom left panel with *dotted oval*). During EM processing, the biopsy turns black due to osmification and the NIRB markings are no longer visible. (G and H) Due to the asymmetric shape of the biopsy, it can be positioned in the resin mold so that the NIRB markings are closest to the future block face.

Note: The NIRB markings are not always clearly recognizable on the brain surface, but their visibility is critical for this step of the workflow (Fig. 2C—F). Therefore, first test and optimize the NIRB conditions before embarking in the correlative studies. It is helpful to create an asymmetrically shaped biopsy, so that it is unambiguous which side of the sample is the brain surface with the NIRB marks. Following EM processing, the marks will no longer be visible (Fig. 2F—H) and the asymmetric shape will help position the biopsy during embedding.

The biopsy is prepared for EM imaging by microwave-assisted processing, which improves the infiltration of the solutions and greatly speeds up the procedure. The PELCO BioWave Pro (Ted Pella) can be preprogrammed, and we use the following steps and conditions:

1. Wash four times for 5 min in 0.1 M cacodylate buffer in the hood.
2. Primary postfixation: 1% OsO_4 + 1.5 $K_3Fe(CN)_6$ in 0.1 M cacodylate buffer, in the microwave: vacuum on, wash seven times for 2 min consecutive steps, 100 W cycling on—off.
3. Wash two to ten times briefly in 0.1 M cacodylate buffer; in the hood, and then in the microwave: wash two times for 40 s, 250 W, change buffer in between washes.
4. Secondary postfixation: 1% OsO_4 in 0.1 M cacodylate buffer, in the microwave: vacuum on, wash seven times for 2 min consecutive steps, 100 W cycling on—off.
5. Wash as described in step 3, but using water.
6. Staining with uranyl acetate (UA): 1% UA in water, in the microwave: vacuum on, wash seven times for 1 min consecutive steps, 100 W cycling on—off.
7. Wash in water as described in step 3.
8. Dehydration: Use a graded series of ethanol dilutions in water: 25%, 50%, 75%, 90%, 95%, in the microwave: 40 s of each step, 250 W. Finally, wash the sample two times for 40 s in 100% ethanol at 250 W.
9. Resin infiltration: Use a graded series of resin (Durcupan or Epon extra hard mix) in ethanol: 25%, 50%, 75%, 90%, in the microwave: vacuum on, wash seven times for 3 min, 250 W, cycling on—off.
   Here, we choose hard types of resin because they provide the required stability for FIB-SEM imaging. Our preferred choice is Durcupan. For serial sectioning TEM, other medium-hard Epon mixes would also be suitable.
10. Place the biopsy in the resin block mold, so that the surface with the NIRB mark will be close to the future block surface (Fig. 2G and H).
11. Polymerize the sample at 60°C for at least 48 h.

1.2 TRIMMING THE RESIN BLOCK AND microCT IMAGING

For microCT imaging, the sample should be trimmed to a small size (less the 2—5 mm in x, y, z). The microCT employed in our work (Borrego-Pinto, Somogyi, & Karreman, 2016; Karreman et al., 2016) uses a cone-shaped beam, and the

effective voxel size thus depends on the distance between the detector and the sample. Removing the excess of resin around the tissue will allow to position the object closer to the X-ray source, which will result in an improved voxel size and resolution. Mount the sample in a microtome and trim the sample using a razor blade (Fig. 3A and B) and a trimming diamond knife (or a glass knife). Trim the block as close as possible to the biopsy. Note: It is critical to create a flat block surface during this first trimming step. Trimming the sides with a knife will also be helpful for the 3D registration (see part 5), but it is not required to trim along the full depth of
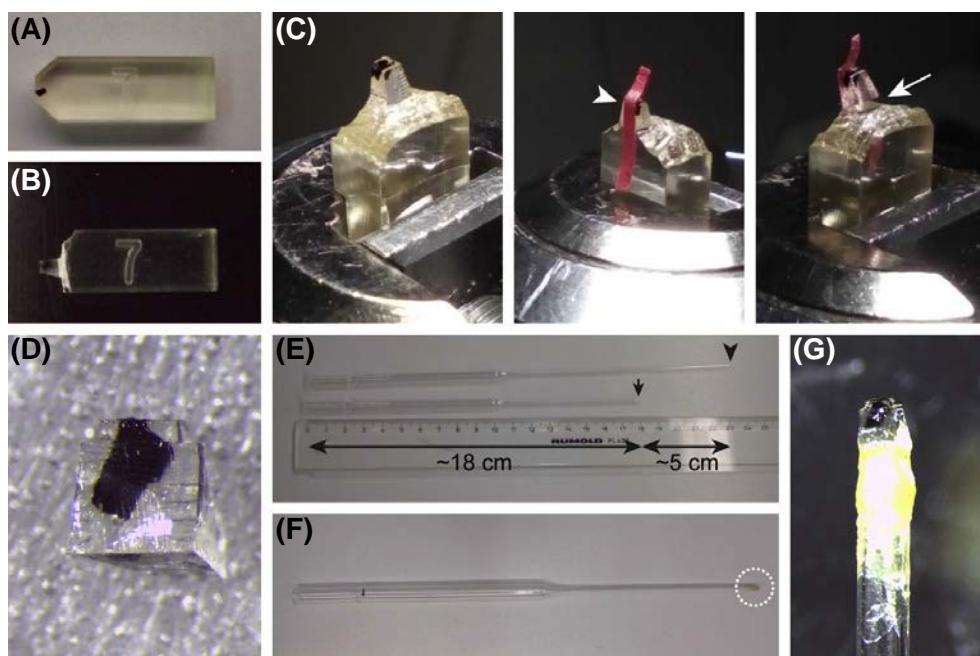
FIGURE 3

Trimming the sample for microCT imaging. (A) The untrimmed resin block, the brain biopsy is visible on the left side. (B) The resin block is roughly trimmed, using a razor blade, around the position of the biopsy. (C) The block surface and three out of four sides are trimmed using a 90-degree diamond knife (left panel). To ensure that the samples is not lost while cutting it off the large block, a small strip of tape (middle panel, red tape indicated with *white arrowhead*) is attached to the block that keeps the samples in place after separating it from the large block using a razor blade (*arrow* in right panel). (D) The small, chopped-off block can be placed on a strip of double-sided tape stuck to a glass slide. This allows to, if necessary, further trim the block with a razor blade. (E) For microCT imaging in the nanotom m, the sample is mounted on a glass rod. Hereto, take a long (approximately 23 cm) glass pipette and break off the tip (*arrowhead*) to remove approximately 5 cm of length (small *arrow*). Then, carefully round off the tip in a flame. (F) Mount the resin-embedded sample on the tip of the glass rod (*dotted circle*) using glue. (G) The sample is mounted on the tip of the glass rod.

the biopsy. The trimmed part with the biopsy can then be chopped off the larger block using a fresh razor blade (Fig. 3C and D).

For microCT imaging, the general steps include (1) mounting the sample on a holder that fits into the microCT setup, (2) aligning the sample to the center of the FOV in the microCT, (3) setting the imaging conditions (beam voltage and current, voxel size, exposure time, image averaging, etc.) and, finally, (4) reconstructing the data set. In our work, we have used the nanotom m (GE sciences), which operation is described here in more detail. First, the small sample is mounted on a holder for microCT imaging. For the nanotom m, rods can be used that are made from long glass Pasteur pipettes. Select a straight pipette; remove ∼5 cm from the tip; and round it off in a flame (Fig. 3E). The sample can be mounted on the tip using dental wax or glue (e.g., all-purpose glue, as long as it is removable after imaging) (Fig. 3F and G). Install the sample in the microCT setup and move it 10−15 cm away from the source. Start the X-ray beam at a low current (e.g., 45 μA) and 60 kV. In the microCT *xs control* software, position the sample in the center of the FOV by adjusting its vertical position. The sample will be fully rotated during acquisition and should remain centered during imaging. To achieve this, rotate the sample to 0, 90, 180, and 270 degrees, and position it to the middle of the FOV for each angle. Turn off the X-ray beam, open the machine, and position the sample as close as possible to the tube, while confirming that there is no risk of a collision with the tube while the sample rotates. The Phoenix *datos|x* software will indicate the voxel size, which should be in between 0.5 and 1.5 μm. Adjust the X-ray settings to the acquisition values: typically, we use 430 μA/60 kV [focus 3 (smallest) for a voxel size up to 0.7 μm, focus 2 (medium) for 0.7−1.3 μm]. To reduce the voxel size, the detector can be moved further backward (max 500 mm), but beware that this also reduces the signal count. It is recommended to perform the "centering 1" and the "Adjust Filament" procedure in the *xs|control* software before each scan. Next, store the position in *datos|x*, move the sample fully downward, and perform a detector calibration. After moving the sample back to its acquiring position, indicate the acquisition parameters: number of images (e.g., 1440), exposure time (e.g., 1000 ms), averaging (4), binning (e.g., 1), image size, etc. Indicate the filter (MolyB) and activate *Auto|Sco* (which allows to evaluate and compensate for sample movement during the scan) and *Shift* (which moves the detector slightly during the scan to prevent image artefacts generated by damaged pixels). Start the scan, which will take 1−2 h, depending on the image parameters. After completion, reconstruct the volume in the Phoenix *datos|x* reconstruction software.

1.3 SEGMENTATION AND 3D REGISTRATION IN AMIRA

The microCT imaging provides an image stack, which visualizes the structural features of the resin-embedded sample in 3D. In the current step, the IVM image volumes are correlated to this data set. In general, this requires the following steps:

1. segmentation of the biopsy and vasculature in the microCT data set,
2. segmentation of the vasculature and tumor cell(s) in the IVM data sets,

3. registration of the large-FOV IVM data set into the full microCT volume, cropping the microCT volume around the expected position of the tumor cell, and

4. finally, registration of the small-FOV IVM data set into the cropped microCT volume.

Since cropping the microCT data set preserves its coordinates with respect to the uncropped volume, it is then possible to measure the position of the tumor cell (from the registered small-FOV IVM data set) with respect to the resin block surface, visible in the uncropped microCT data set.

In this section, these steps are described in detail for the correlation of IVM and microCT imaging of mouse brain biopsies. Importantly, a similar approach can be applied for the correlation of different samples or tissues. However, this may rely on using different landmarks for the correlation between the two data sets, and the segmentation parameters should be adjusted accordingly.

1.3.1 Segmenting the microCT data set in Amira

1. Open Amira and start a blank project (Fig. 4)

2. Import the microCT volume in Amira (select "read full volume into memory") by dragging the file directly into Amira's Project View (indicate the voxel size in x, y, and z in the pop-up window, if applicable). Visualize the data set (Fig. 5) by creating a *Slice* or *Orthoslice*: left mouse click on the icon in the Project View, *Display > Slice* or *Orthoslice*. *Slice* can be rotated freely (in version 5 and older versions of Amira, this is called *Obliqueslice*).

3. The microCT can be resampled to speed up further processing steps. Left click on the data set, and select *Compute > Volume Operations > Resample*. In the Properties Area, change the voxel size to a higher value (between 1 and 2 μm). A novel file is generated and shown in the Project View with the extension "resampled" (Fig. 5A). Remove the original file from the project.

4. To facilitate the segmentation, filter the microCT data set. Apply a *Non-Local Means Filter* (*Image Processing > Smoothing and Denoising > Non-Local Means Filter*, Similarity Value: 0.5) (Fig. 5B).

5. Move to the "Segmentation" tab and select the filtered data set in "Image Data." A label data file is automatically generated with two "Materials": "Exterior" and "Inside" (Fig. 5D).

6. Select the pixels that depict biopsy inside the resin block, using the "Threshold" option. In "Display and Masking," select part of the histogram, so that the biopsy is highlighted in blue. In "Options" tick "All slices" to highlight the biopsy throughout the full data set. In "Action," click "Select."

7. Create a Material "Biopsy" in the label file. Add the selected pixels to this Material by selecting it, and click the red-circled plus button in "Selection" (Fig. 5D).
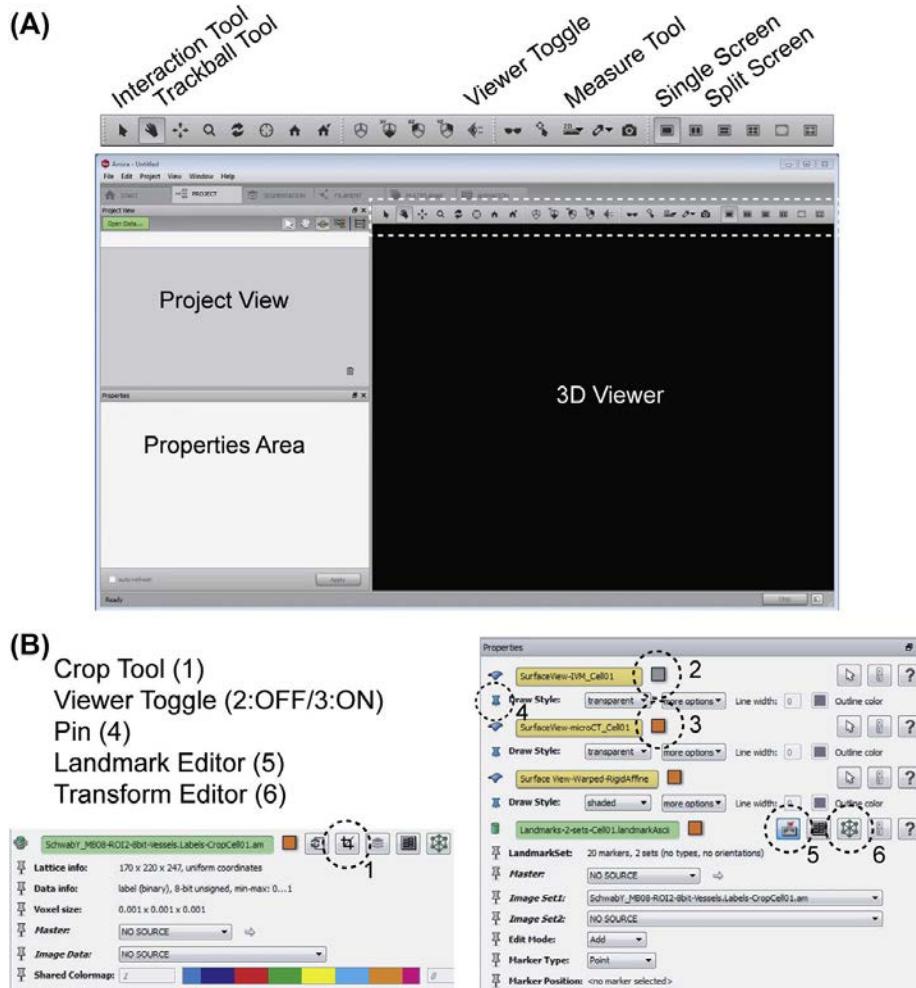
FIGURE 4

An overview of Amira's Project screen and the tools used for the workflow. (A) Amira's main Project screen shows the Project View, the Properties Area and the 3D viewer. The toolbar above the 3D viewer (boxed with a *dotted line*) has several useful tools to visualize and interact with the data. (B) When files or modules are selected in the Project View window, their properties and parameters are shown in the Properties Area (A). Here, also the conditions for specific modules can be set. Some tools that are used during the workflow are highlighted with *dotted circles*.

8. The vessels and nuclei inside the biopsy are not selected via thresholding since they appear darker than the surrounding tissue. Add these to the Material in the menu *Segmentation > Fill holes > All slices*.

9. Depending on the gray levels chosen for the thresholding, some parts outside the biopsy may be selected. These can be removed using the
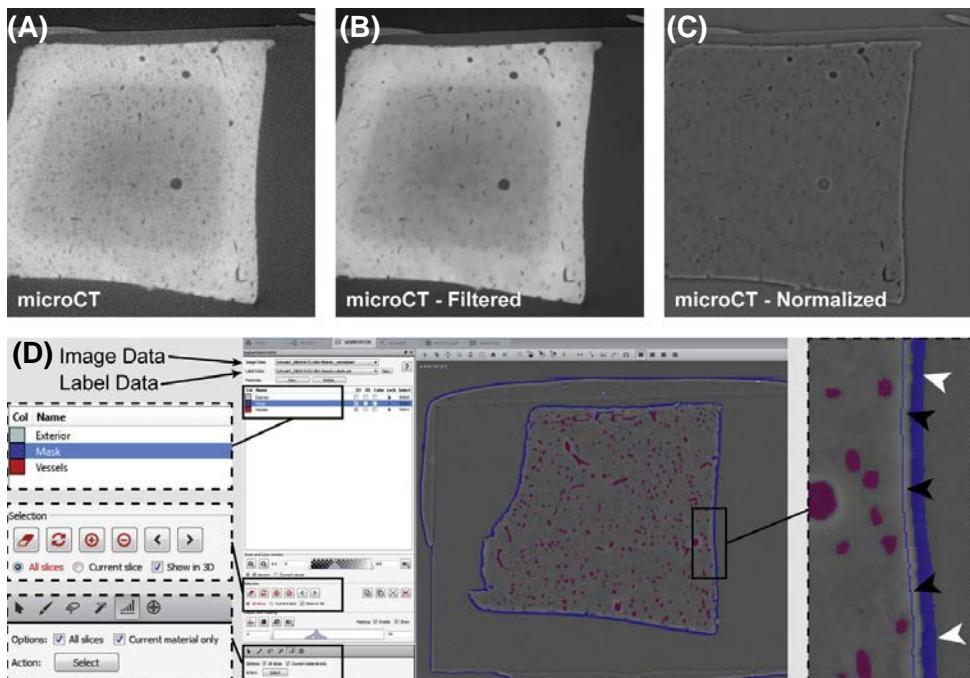
FIGURE 5

Segmentation of the microCT data set in Amira. (A) Visualization of a virtual section through the microCT data set. The biopsy appears in light/gray white, the vessels and nuclei are dark, and the outline of the resin block is dark gray. The outside of the sample (above) is shown in black/very dark gray. (B) A virtual section through the filtered microCT data set, at the same position as in A. (C) A virtual section through the filtered and normalized microCT data set, at same position as in A and B. (D) Segmentation of the filtered and normalized microCT data set. Commonly used tools are highlighted (left panels). The right panel shows the outline of the segmented biopsy (Mask, *thin line*, *black arrowheads*). The thresholded pixels that fall outside of the mask (*thick line, white arrowheads*) are not selected, but the thresholded pixels inside of the mask (left side, rounded structures that represent nuclei and vessel cross sections) are selected.

    Segmentation > Remove Islands. In the pop-up window "Remove Islands," choose size 1000−5000, tick "All Slices" and press "Select." The selection can be excluded from the Material by pressing "Remove." The brush tool, the magic wand, and *Selection > Interpolate* can be used to improve the segmentation.

10. To segment the vasculature, the Biopsy label file will be used as a mask in which the darker gray values of the emptied vessels can be selected by thresholding. Duplicate the Biopsy label file, which will function as the basis for the mask.

11. In case the infiltration of the heavy metals is not optimal, there might be a density gradient visible from the inside of the biopsy toward the outside.

However, the thresholding used to segment the vessels requires a homogeneous contrast—difference between the vessels and the surrounding tissue. To achieve this, use the *Normalize Image (Background Detection Correction)* module (Fig. 5C).

12. Go to the segmentation tab and select the normalized data set (Image Data) and the duplicated Biopsy label file (Fig. 5D).

13. Select the pixels in the Biopsy Material and shrink the volume by *Selection > Shrink > Volume* (repeat two to four times), so that the dark edges on the outside of the biopsy, visible in the normalized data set, are excluded from the selection. Add the selection now to a new Material "Mask" and delete "Biopsy" (Fig. 5D).

14. To select the vessels, choose a range of gray values, so that the vasculature is highlighted. Note: Since the nuclei are low in density, they will inadvertently also be selected during this procedure. Select the "Mask" material and tick "All Slices" and "Current Material Only" in the segmentation panel (Fig. 5D). Select these pixels and add these to a new material "Vessels."

15. Delete the "Mask" material, the label file now contains only the segmented vasculature and nuclei. To remove the nuclei, go back to the Project tab, select the label file in Project View and create a *Remove Small Spots* module (in *Image Segmentation*, Extension: XImagePAQ). Select in Interpretation "3D" and size 350 ($\sim$1 μm voxel size). This creates a new filtered label file. Alternatively, and much more time-consuming, is to go to the menu *Segmentation > Remove Islands* (Segmentation tab, select size 350 in "3D volume").

16. To visualize the segmentation, in Project View, create a *Generate Surface* module from the label file. The 3D surface visualization can be smoothed to different extends in the "Smoothing type" drop-down menu and is visualized using *Surface View.*

1.3.2 Segmenting the intravital microscopy z-stack

1. Import the IVM imaging stack (as an RGB tiff file) into Amira. In the pop-up window, select "Channel Conversion: All Channels" and provide the voxel size in x, y, and z. The file and the different channels are shown separately in the Project View.

2. Move to the Segmentation tab, and select channel 1 (red) in Image Data. Using the histogram tool, select the blood vessels and add these pixels to a new material "Vessels." Note: Due to light scattering and absorption deep into the tissue, there will be an intensity gradient along the z-axis of the data set. Manual selection of vessels might be required.

3. Get rid of noise by smoothing the labels (*Segmentation > Smooth Labels* 3, 3D Volume) and selecting and removing islands in 3D as described before.

4. Create a new Material for the tumor cell(s) in the same label file that contains the vessel segmentation. Select the green channel in "Image

Data," and segment the fluorescent tumor cell(s) using local thresholding with the magic wand tool.

5. The label file with the segmented vessels and the tumor cell(s) can be visualized by creating *Generate Surface* and *Surface View* in Project View.

1.3.3 Registration of the large-field of view intravital microscopy z-stack into the microCT volume

To register both data sets in 3D, the IVM surface file [vessels and tumor cell(s)] will be warped into the microCT surface file (vessels). Hereto, the *Landmark Surface Warp* module is used. Landmarks, shown as yellow and blue spheres, are manually placed in corresponding points in the two surface files, e.g., vessel forks or branches. To achieve higher accuracy, the landmark should be placed in the center of the vessel branch. For this, an Auto Skeleton view of the surface needs to be created, on which the landmarks can be placed (Fig. 6). To facilitate the docking, it is easiest to first perform a manual docking of the IVM surface into the microCT surface.

1. Open a new project for the 3D registration and load the label files of the microCT vessels segmentation and the IVM vessels and tumor cell(s) segmentation. Note: Display the vessels from the different imaging modalities in different colors (Fig. 7A).

2. Duplicate the IVM surface file, add "-PreWarp" to its name, and visualize it. Deactivate the display of the original IVM surface file using the viewer toggle (Fig. 4B).

3. Select the "-PreWarp" surface, and, in the Properties Area, click the Transform Editor (Fig. 4B). In the 3D Viewer, the IVM surface is now surrounded by a "transformation cube" that enables scaling, translation, and rotation, using the interact tool.
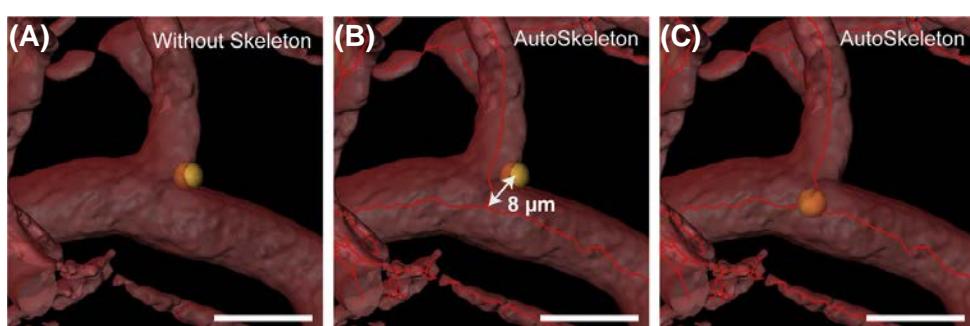
FIGURE 6

Placing the landmarks. (A) A view of the intravital microscopy surface file, showing a vessel bifurcation. Without the use of an *Auto Skeleton*, the landmark is placed on the surface. (B and C) In presence of an *Auto Skeleton*, the landmark can be positioned in the center of the bifurcation, improving the accuracy of the registration. The distance between the position of the landmark on the surface and on the *Auto Skeleton* is 8 μm. Scale bars: 20 μm.
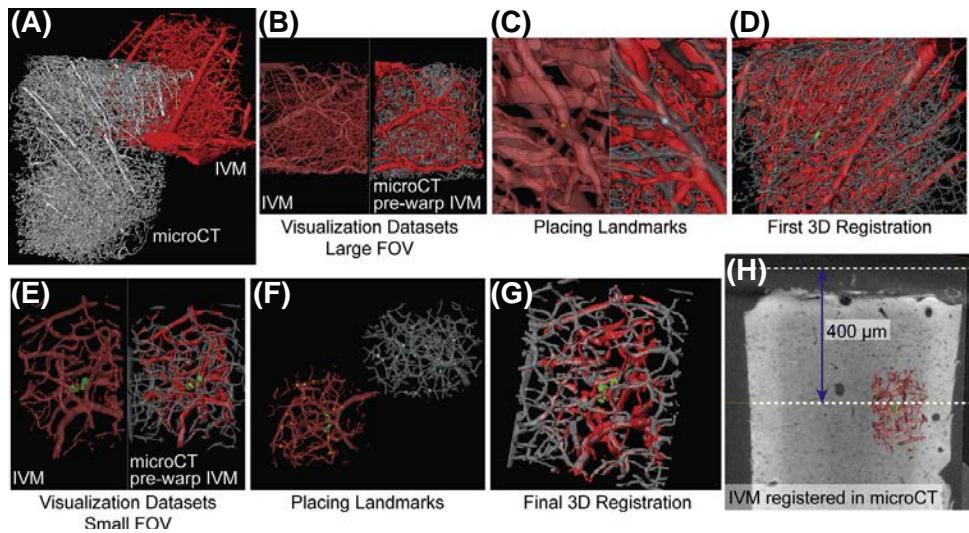
FIGURE 7

3D registration of the intravital microscopy (IVM) data sets into the microCT volume. (A) The IVM large-field of view (FOV) and microCT surface files are visualized in Amira's 3D viewer window. (B) Using a split screen, the IVM surface (left) and the prewarped IVM surface and cropped microCT surface (right) can be visualized simultaneously. (C) Landmarks (shown as small *spheres*) are placed in corresponding positions in the IVM and microCT data set. To improve accuracy of the registration, the landmarks are placed on the *Auto Skeleton* (see Fig. 6) that represents the core of the surface. (D) Based on the initial placement of 5—10 landmarks, a first 3D registration can be performed. (E) The first registration enables to crop the microCT label file to a small area around the prewarped position of the cell of interest (right panel). In a split screen, show the small-FOV Cell01 IVM surface (left), the prewarped IVM surface, and the microCT-CropCell01 surface. (F) Place the landmarks (*spheres*) so that these are evenly distributed around the tumor cell. (G) Perform the final registration of the small-FOV IVM surface into the microCT-CropCell01 surface. Since Amira preserves the coordinates of the data set during cropping, this registration also applies to the full, uncropped microCT data set. (H) Registration of the small-FOV Cell01 IVM surface in the microCT data set allows to measure the depth of the tumor cell with respect to the block surface (*top dotted line*).

4. By adjusting the position, rotation, and scale of the IVM data set, manually fit it inside the microCT data set. Then, inactivate Transform Editor and save the surface file (Fig. 7B).
5. The microCT vessel label file can be cropped around the area in which the IVM PreWarp surface is manually positioned. Activating the Crop Editor (Fig. 4B), a dialogue window appears and the outlines of the volume are shown in the 3D Viewer. Using the interaction tool, the volume can now be reduced around the area of interest by reducing the size of the box. Save the cropped label file under a new name, and visualize the segmentation.

1.3.3.1 Creating Auto Skeletons of the label files

6. The *Auto Skeleton* module (Extension: XSkeleton) shows the centerline and nodes of the label file. A simplified label file will generate less noisy centerlines; it is thus recommended to create a smoothened label file especially for the Auto Skeleton. Duplicate the label files, and add "-forSkeleton" to the name, in the Segmentation tab, select the new label file (in Label Data), and go to *Segmentation > Smooth Labels* (size 3, 3D volume). Do this for both the cropped microCT vessel label file and the IVM label file.

7. Select the "-forSkeleton" label files, and create an Auto Skeleton (*Image Processing > Skeletonization > Auto Skeleton*). A new *Spatial Graph View* appears, untick the box "Nodes" (Properties Window).

8. The *Surface Views* and *Spatial Graph Views* can be visualized simultaneously in Amira's 3D Viewer window. In the Properties Area, make the *Surface View* semitransparent by selecting *Draw Style: Transparent.* Change *Base Trans* to 0.6.

1.3.3.2 Placing the landmarks

9. Change the 3D viewer to a split screen (two viewers, vertical, Fig. 4A) to be able to visualize both data sets independently (Fig. 7B).

10. In the left screen, visualize the IVM vessels surface and Auto Skeleton. In the right screen, show the microCT vessels surface and Auto Skeleton and the prewarped IVM surface. The latter will function as a reference to identify corresponding points in the data sets (Fig. 7B).

11. Right-click into the Project View area, and select "Create Object…" in the menu and select *Points and Lines > Landmarks (2 sets).* Create two *Landmark View* modules (*Display > Landmark View*). Select the *Landmark View* and change *Point Set: Point Set 1* in the Properties Area. Limit its visualization to the left panel, using the viewer toggle. In the second *Landmark View2*, select *Point Set: Point Set 1* and show it only in the right panel.

12. To facilitate placing the landmarks, it is easier to pin a couple of useful objects in the Properties Area. Hereto, select the object and use the "pin" icon (Fig. 4B) to keep it visible in the Properties Area even though it is not selected. Pin the *Surface Views* of the IVM, the microCT (cropped), the prewarped IVM and the *Landmark-2-sets.*

13. To start placing the landmarks, select the Landmark Editor in the *Landmark-2-sets* (Properties Area). Select *Edit Mode: Add.*

14. Zoom into the right panel and identify a feature, i.e., vessel branches and bifurcations, which is visible in both the data sets. When a position is found, center the same area in the IVM surface in the left panel.

15. With *Landmark-2-sets* selected, place the first Landmark with the interact tool. Hereto, disable the visualization of the IVM surface and click on the appropriate position on the underlying Auto Skeleton. A yellow sphere appears in that position. Next, disable the visualization of the IVM prewarp surface and the microCT vessel surface, and click on the corresponding position on the

microCT vessel Auto Skeleton. A blue sphere appears. Change to Trackball mode, enable the visualization of the surfaces, and confirm if the Landmark spheres are placed correctly (Fig. 7C). Incorrectly placed landmarks can be moved or removed using the corresponding settings in *Edit Mode* (Properties *Landmark-2-sets,* Landmark Editor).

16. Seed five to seven well-spread Landmarks throughout the data set.
17. At this point, it makes sense to perform a first Landmark surface warp, to generate a reference prewarped surface, which is better than the manual fit (Fig. 7D). Hereto, select *Landmarks-2-sets* and create a *Landmark Surface Warp* (*Compute > Landmark Surface Warp*). Select in *Surface Data* the original IVM surface file, and choose *Direction 1>2*. These settings will result in the warping of the IVM surface into the microCT surface, by calculating the transformation of Point Set 1 into 2. Select *Method*: *Rigid* and choose *Affine*. This will enable translation, rotation of the surface file, and independent scaling of its x, y, and z dimensions. Visualize the new warped surface.
18. This warped surface provides an improved reference data set, enabling to place more Landmarks. If, however, the registration already looks satisfactory, it is possible to proceed from here with warping the smaller FOV IVM image volume(s) into the microCT data set (Fig. 7D).

1.3.4 Registration: small field of view around the tumor cells(s)

1. Start a new Amira Project, and import the small-FOV IVM imaging stack ("small-FOV Cell01"), which shows the ROI at a higher magnification.
2. Segment the vessels and the tumor cell(s) in the volume, and visualize the small-FOV Cell01 IVM surface.
3. Load the warped large-FOV IVM surface (Section 1.3.3) and the cropped microCT vessel surface file and label file.
4. Duplicate the cropped microCT vessel label file and further crop it around the tumor cell, to a similar volume as shown in the small-FOV Cell01 IVM surface. Save this microCT label file without overwriting the full-size file, e.g., by adding "-CropCell01" to its name.
5. Remove the warped IVM large-FOV surface, the tiff stack, the older microCT vessel surface file and label file from the network, but keep the new microCT-CropCell01 label file.
6. Create Auto Skeletons from both the IVM and the microCT label files (Figs. 6 and 7E).
7. Place Landmarks into the data sets, and warp the small-FOV Cell01 IVM surface into the microCT-CropCell01 surface. While placing the 7−20 Landmarks, ensure to find common points close to the tumor cell, and well dispersed in the space around it (Fig. 7F). Following warping, carefully check the fit of the IVM Cell01 surface into the microCT-CropCell01 surface, particularly around the tumor cell. The quality of the fit can be judged by the level of overlap between the segmented vessels visible in both the surfaces (Fig. 7G).

8. In a new project, load the resampled microCT z-stack (the full volume) and the warped IVM Cell01 surface file. The warped small-FOV Cell01 IVM surface is shown in its registered position within the microCT z-stack. By scrolling through the images, confirm that, indeed the vessels from the IVM surface, align with the vessels visible in the microCT. We emphasize here that cropping and reloading the label files and data sets *do not* influence where these are loaded in Amira's virtual coordinate system. This means that 3D registration of the small-FOV IVM volume in a cropped microCT volume also registers the IVM volume in the corresponding position within the full-sized microCT data set.

9. Align a *Slice* of the microCT z-stack with the top surface of the resin block. This can be done manually by *Options: Rotate* in the Properties Area. Use the Interact tool on the "Trackball" that appears on the *Slice* to rotate it to the desired orientation. Alternatively, use the *Options: Fit to points.* Using the Interact tool, click on three different positions on the top surface of the resin block (easily visible using a *Slice* that shows the side of the block in cross section). The *Slice* will then automatically align to the block face. In the Properties Area, select *Sampling: Finest* to achieve the highest resolution.

10. Duplicate the block face *Slice* and move it to a position 3−5 μm above the predicted position of the tumor cell. Note: Make sure that the 3D Viewer (Fig. 4A) is set to "Orthographic" and not "Perspective."

11. Measure the distance between the block face slice and the ROI (Fig. 7H). Hereto, use the 2D measurement tool.
    Note: In Amira 6.1 and later versions, the measurement tool is by default set to "3D measurements." This can lead to incorrect measurements of the distance between two slices. To change the measurement tool to 2D, type "measure useNewMeasureTools 0" into the console window and restart the software.

We have created a data package that contains Amira files, which allows the interested reader to interact with representative IVM, microCT, and registered data sets. A zipped folder, containing the data and a pdf file describing each of the files, can be downloaded at this link: https://www.embl.de/download/schwab/2017-Karreman_etal-MCB.zip.

1.4 TARGETED TRIMMING

Following registration of the IVM volume into the microCT data set, the sample can be trimmed in an ultramicrotome to approach the ROI (Fig. 8). Adhere to the small sample, imaged with microCT, to a blank resin block. When using resin to attach the sample, let it polymerize for 24−48 h at 60°C.

Mount the sample in an ultramicrotome, and ensure to keep track of its orientation, e.g., by noting which side of the resin block is facing up when it sits in the microtome. Here, it helps to have trimmed the sample asymmetrically. For targeted trimming, it is critical to be able to correlate the position of the sample in microtome to the 3D visualization of the microCT data set in Amira.
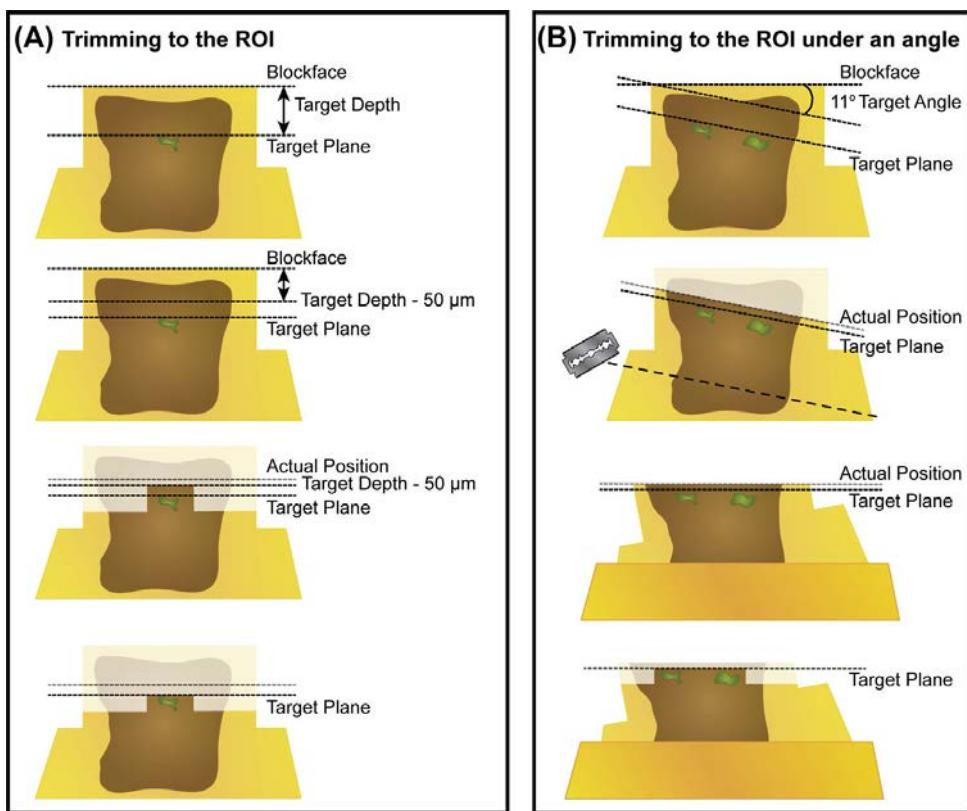
FIGURE 8

Trimming the resin block to expose the tumor cell for 3DEM. (A) Based on the 3D registration of the intravital microscopy data sets into the microCT volume, the distance between the block surface (*top dotted line*) and the tumor cell (*bottom dotted line*, Target Plane) can be measured: This is the Target Depth. Trim the front of the block to a depth of 50 μm above the Target Plane ("Target Depth—50 μm"), to stay at a safe distance of the tumor cell. Check the progression into the block based on an LM section, as described in the text and Fig. 9). Based on the prior knowledge of the position of the tumor cell with respect to the sides of the block, trim sides to reduce the block surface to ∼300 × 500 μm. Finally, approach the tumor cell in z. (B) In case multiple cells are targeted simultaneously, or the tumor cell is under a specific angle, it could be worthwhile to change the angle of the approach to the region of interest (ROI) (*bottom dotted line*). In this case, measure in Amira the angle between the block face and the desired angle (here 11-degree Target Angle). This angle can be created by tilting the trimming diamond knife (see Fig. 8). If the angle is too high, subsequent trimming and sectioning will be affected. In that case, cut the sample from the resin block (as shown in Fig. 2C) and trim its base with a razor blade, so that it is parallel to the new surface angle. Then, remount the sample on a new resin block and trim to the ROI as described in A.
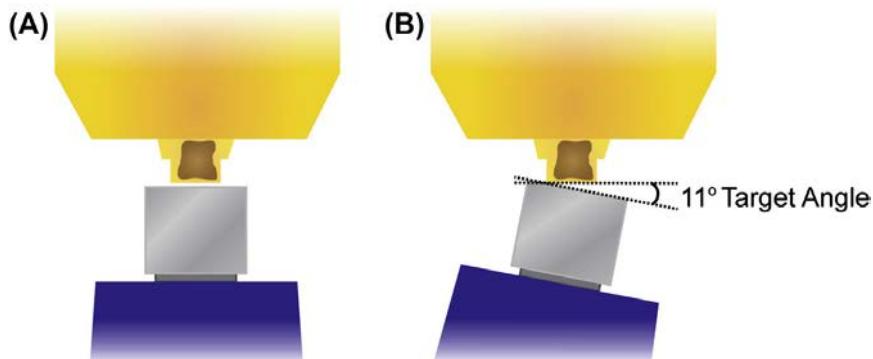
FIGURE 9

Creating an angled block surface. The sample should be mounted in the microtome, so that the angle can be introduced horizontally by rotating the trimming diamond. (A) To create a new, angled block surface, align the trimming diamond knife accurately to the resin block. Take particular care to align also the bottom and top side of the sample very well parallel to the cutting edge of the knife. (B) Change the rotation of the knife, so that the desired angle is achieved. Note: The knife could already be under an angle due to the alignment. Next, the knife will start cutting only one side of the block, creating an angled block surface.

Align a trimming diamond accurately to the block face. If required, an angle can be introduced to the block surface by rotating the knife following alignment (Fig. 8B: Target Angle, Fig. 9).

Trim to a depth that is 20—50 μm above the predicted ROI (Fig. 8, Target Plane), and check the progression into the resin block. Hereto, obtain a thick 300- to 500-nm section, and place it on a (Superfrost++) glass slide. Dry the section on a hot plate, stain it with toluene blue (or a comparable histological stain), and image it with a light microscope (LM, magnification 10—20×). Correlate the LM image to a virtual section (*Slice*) of the microCT data set, which is at the expected distance and angle with respect to the block surface (Fig. 8). Generally, the error margin of the microtome is around 5% (we experienced a similar offset with two different Leica UC7 microtomes); it removes less material than is indicated on the counter. When the knife is trimming under an angle (Fig. 9B), this error margin is even larger. By moving the *Slice* through the microCT data set, the best match to the LM image can be found. This enables to measure the actual progression toward the Target Plane (Figs. 8 and 10).

In Amira, determine how much material may be removed from the sides of the resin block to generate a smaller block face (Figs. 8 and 10C). Trim the desired amount of material using the straight side of a 90-degree diamond knife. To be on the safe side, the trimming can be performed to a limited depth, which is still above the ROI. Then, the dimensions of the new block face can be confirmed after trimming by correlating again an LM image of a thick section from the trimmed block to a virtual section in Amira. If this trim test is satisfactory, trim the sides further to below the volume of interest.
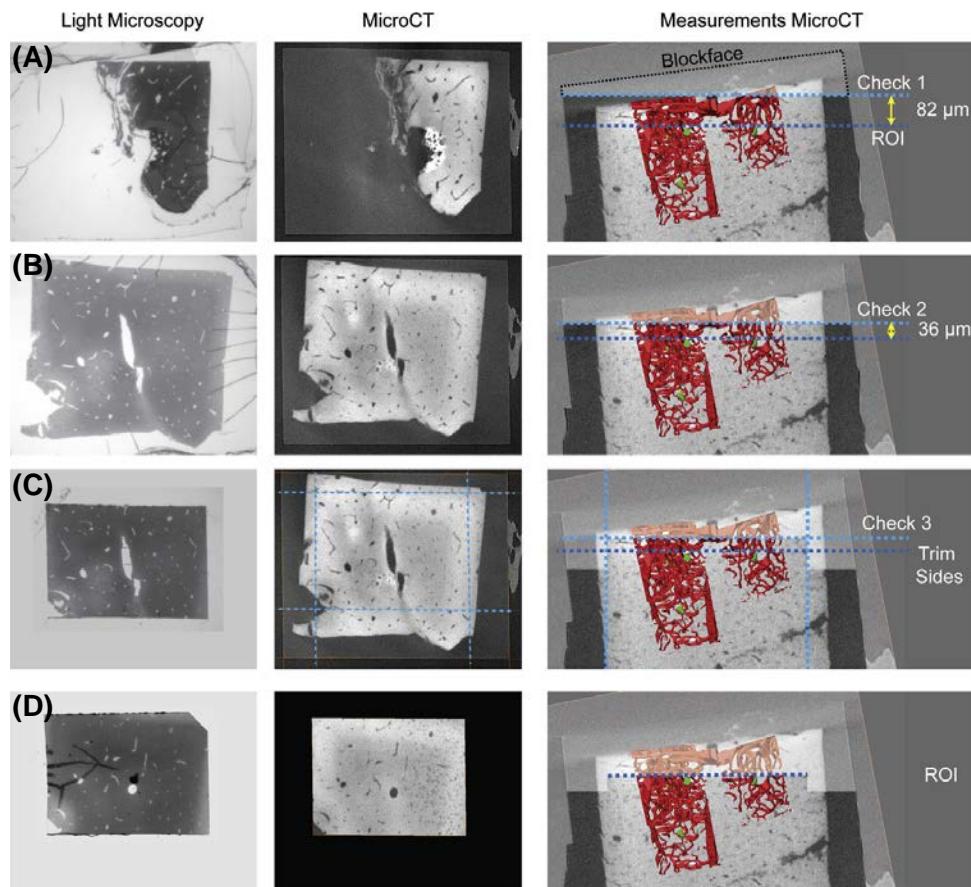
FIGURE 10

Checking the progression to the region of interest (ROI) as part of the targeted trimming procedure. (A) An angle is introduced to the block face, and a 300-nm section of the new surface is stained and imaged with LM (left panel). The matching section is found in the 3D volume of the microCT data set (middle panel) and is shown in the right panel as the top *thick dotted line* (Check 1). This confirms that the angle is correctly introduced (with respect to the original block face, *thin dotted outline*) and that the distance to the ROI (*bottom dotted line*, ROI) is 82 μm. (B) Following a second approach, the procedure described in A allows to determine that the current position is 36 μm from the ROI. This is a suitable position to start trimming the sides of the future block face. (C) Measure, based on the Amira 3D registration, how much material can be removed from each side and trim this using the straight sides of a 90-degree trimming diamond or glass knife. (D) After trimming the sides, carefully approach the ROI. Obtain a 300-nm section from the resin block before starting serial sectioning or mounting the block for SBF-SEM or FIB-SEM. *FIB-SEM*, focused ion beam—scanning electron microscopy; *SBF-SEM*, serial block face scanning electron microscopy.

Trim the block face up to approximately 3–5 μm above the predicted position of the ROI (Fig. 8, Target Plane). The approach to the ROI can be monitored as described before. It is helpful to obtain an LM image of the final 300- to 500-nm section that is taken from the block face, to correlate with the subsequent EM imaging (Fig. 10D). The resin block is now ready for serial sectioning or to be mounted on an SEM stub for FIB-SEM imaging or serial block face SEM (SBF-SEM).

2. INSTRUMENTATION AND MATERIALS

2.1 PROCESSING FOR ELECTRON MICROSCOPY

Instrumentation and Materials:

1. PELCO BioWave Microwave with Coldspot (Ted Pella)
2. Resin-embedding mold
3. Oven, set to 60°C

    Solutions and Reagents:

1. Glutaraldehyde (EM grade EMS cat#16220)
2. Formaldehyde (EM grade EMS cat#15710)
3. Cacodylate buffer (pH 7.2)
4. Osmium tetroxide in water (EM grade EMS cat#19150)
5. $K_3Fe(CN)_6$ (Merck, art. 4973)
6. UA (research grade, Serva lot 150126)
7. Ethanol
8. Resin: Durcupan (Sigma Cat# 44610) or Epon (Serva)

2.2 TRIMMING THE RESIN BLOCK AND microCT IMAGING

1. Razor blades
2. Ultramicrotome UC7 (Leica Microsystems)
3. Trimming diamond (TrimTool 90 degree, DiATOME) or glass knife
4. Long glass Pasteur pipettes
5. Wax or glue
6. MicroCT system (phoenix nanotom m, GE Sciences)
7. MicroCT data reconstruction and processing software

2.3 SEGMENTATION AND THREE-DIMENSIONAL REGISTRATION IN AMIRA

1. Amira v.6 (FEI visualization group, Thermo Fisher Scientific), with extensions XImagePAQ (optional) and XSkeleton (required).
2. 64-bit computer with Intel Xeon processor CPU 3.50 GHz, 32-bit RAM, and an NVIDIA Quadro K4000 graphics card, running Windows 7 professional. Minimal technical requirements to run Amira can be found on www.fei.com/software/amira-3d-for-life-sciences/.

2.4 TARGETED TRIMMING

1. "Dummy" blocks: blank resin block to remount the sample on
2. Ultramicrotome UC7 (Leica Microsystems)
3. Trimming diamond knife (TrimTool 90 degree, DiATOME) or glass knife
4. Histo diamond knife (DiATOME) or glass knife with attached boat
5. Superfrost++ glass slides and pick-up loops
6. Toluene blue stain
7. Hot plate, set to 100°C
8. Light microscope with 10× and 20× air objectives and digital camera

3. DISCUSSION

The method described here enables to reliably and easily correlate between IVM and 3DEM through an intermediate step of X-ray microCT imaging of the EM-processed sample. The power of the method can be found in its throughput and versatility; we are now routinely using this approach to study various model systems and biological questions that focus on monitoring and retrieving rare events in large voluminous samples. Moreover, it is applicable to prepare the sample for serial section TEM, FIB-SEM, and serial block face imaging.

Others demonstrated the use of microCT in the prescreening of a resin-embedded sample (Burnett et al., 2014; Bushong et al., 2014; Handschuh, Baeumler, Schwaha, & Ruthensteiner, 2013; Sengle, Tufa, Sakai, Zulliger, & Keene, 2013) and the correlation between fluorescence microscopy and EM (Bushong et al., 2014; Shami et al., 2016). MicroCT imaging provides a unique insight into the organization and orientation of the sample following EM processing. This information assists in retrieving the ROI postprocessing, as described in our work (Borrego-Pinto et al., 2016; Karreman et al., 2016) and that of others (Bushong et al., 2014; Shami et al., 2016). Moreover, it also enables adjusting the imaging orientation for 3DEM, which can be critical to study the organization of tissues and small organisms.

Multimodal intravital correlative microscopy as presented here is an approach that in principle can be relatively easily implemented since the different procedures described here are quickly learned. However, the method does require a range of high-end equipment and techniques, including IVM, a microCT setup, an ultramicrotome, and access to appropriate software (Amira) and to an electron microscope (TEM, FIB-SEM, or serial block face SEM). The application of this workflow thus may rely on establishing collaborations with different laboratories and/or companies that can offer access to, and experience with, one or more of these instruments. In our specific example, the IVM, microCT, and EM imaging were each performed at different research institutes.

Although this approach already offers a satisfying throughput and reliability (~14 days from IVM to EM), it is still possible to facilitate and speed up certain parts of the procedure. Most importantly, registration of both data sets could be

automated (in part) to gain time and improve the ease of use of the workflow. Currently, it takes on average 1−2 days to perform the segmentation and registration in Amira (see Section 1.3), depending also on the experience of the operator and the number of target areas. Further advancements of the software or the development of specialized plug-ins may allow to minimize the input of the operator and further simplify the protocol. In addition, the targeted trimming to approach the ROI may be subject to improved accuracy or even automation. The microCT data set and 3D registration of the IVM data set provide the exact dimensions of the resin block and the coordinates of the ROI inside (see Sections 1.3 and 1.4). Based on this information, an automated "sculpting" of the resin block to expose the ROI could thus be envisioned. Finally, the most time-consuming step of the full protocol is the EM imaging and subsequent processing of the data. The latter is a general problem for 3DEM, and software packages are currently developed to help and facilitate these steps (Belevich, Joensuu, Kumar, Vihinen, & Jokitalo, 2016; Schindelin et al., 2012; Sommer, Straehle, Kothe, & Hamprecht, 2011).

In summary, this chapter outlines the most critical and specific steps involved in the multimodal correlative microscopy workflow. This approach allows to quickly move from in vivo imaging of temporary, rare events in pathological or development models, to imaging these at high resolution using 3DEM. Although we demonstrate the approach here on a specific example, the study of tumor cells arrest in the vasculature of the mouse brain, the method is versatile and can be applied to different model systems and to answer a diversity of biological research questions.

ACKNOWLEDGMENTS

REFERENCES

Belevich, I., Joensuu, M., Kumar, D., Vihinen, H., & Jokitalo, E. (2016). Microscopy image browser: A platform for segmentation and analysis of multidimensional datasets. *PLoS Biology, 14*(1), e1002340. http://dx.doi.org/10.1371/journal.pbio.1002340.

Bishop, D., Nikić, I., Brinkoetter, M., Knecht, S., Potz, S., Kerschensteiner, M., & Misgeld, T. (2011). Near-infrared branding efficiently correlates light and electron microscopy. *Nature Methods, 8*(7), 568−570. http://dx.doi.org/10.1038/nmeth.1622.

Borrego-Pinto, J., Somogyi, K., & Karreman, M. A. (2016). Distinct mechanisms eliminate mother and daughter centrioles in meiosis of starfish oocytes. *The Journal of Cell*.

Burnett, T. L., McDonald, S. A., Gholinia, A., Geurts, R., Janus, M., Slater, T., … Withers, P. J. (2014). Correlative tomography. *Scientific Reports, 4*. http://dx.doi.org/10.1038/srep04711.

Bushong, E. A., Johnson, D. D., Kim, K.-Y., Terada, M., Hatori, M., Peltier, S. T., … Ellisman, M. H. (2014). X-ray microscopy as an approach to increasing accuracy and efficiency of serial block-face imaging for correlated light and electron microscopy of biological specimens. *Microscopy and Microanalysis, 21*(01), 231−238. http://dx.doi.org/10.1017/S1431927614013579.

Durdu, S., Iskar, M., Revenu, C., Schieber, N., Kunze, A., Bork, P., … Gilmour, D. (2014). Luminal signalling links cell communication to tissue architecture during organogenesis. *Nature, 515*(7525), 120−124. http://dx.doi.org/10.1038/nature13852.

Ellenbroek, S. I. J., & van Rheenen, J. (2014). Imaging hallmarks of cancer in living mice. *Nature Reviews Cancer, 14*(6), 406−418. http://dx.doi.org/10.1038/nrc3742.

Follain, G., Mercier, L., Osmani, N., Harlepp, S., & Goetz, J. G. (2016). Seeing is believing: Multi-scale spatio-temporal imaging towards in vivo cell biology. *Journal of Cell Science*. http://dx.doi.org/10.1242/jcs.189001. jcs.189001.

Handschuh, S., Baeumler, N., Schwaha, T., & Ruthensteiner, B. (2013). A correlative approach for combining microCT, light and transmission electron microscopy in a single 3D scenario. *Frontiers in Zoology, 10*(1), 1−16. http://dx.doi.org/10.1186/1742-9994-10-44.

Karreman, M. A., Hyenne, V., Schwab, Y., & Goetz, J. G. (2016). Intravital correlative microscopy: Imaging life at the nanoscale. *Trends in Cell Biology*. http://dx.doi.org/10.1016/j.tcb.2016.07.003.

Karreman, M. A., Mercier, L., Schieber, N. L., Shibue, T., Schwab, Y., & Goetz, J. G. (2014). Correlating intravital multi-photon microscopy to 3D electron microscopy of invading tumor cells using anatomical reference points. *PLoS One, 9*(12), e114448. http://dx.doi.org/10.1371/journal.pone.0114448.s006.

Karreman, M. A., Mercier, L., Schieber, N. L., Solecki, G., Allio, G., Winkler, F., … Schwab, Y. (2016). Fast and precise targeting of single tumor cells in vivo by multimodal correlative microscopy. *Journal of Cell Science, 129*(2), 444−456. http://dx.doi.org/10.1242/jcs.181842.

Kienast, Y., Baumgarten, von, L., Fuhrmann, M., Klinkert, W. E. F., Goldbrunner, R., Herms, J., & Winkler, F. (2010). Real-time imaging reveals the single steps of brain metastasis formation. *Nature Medicine, 16*(1), 116−122. http://dx.doi.org/10.1038/nm.2072.

Maco, B., Holtmaat, A., Cantoni, M., Kreshuk, A., Straehle, C. N., Hamprecht, F. A., & Knott, G. W. (2013). Correlative in vivo 2 photon and focused ion beam scanning electron microscopy of cortical neurons. *PLoS One, 8*(2), e57405. http://dx.doi.org/10.1371/journal.pone.0057405.g003.

Müller-Reichert, T., Srayko, M., Hyman, A., O'Toole, E. T., & McDonald, K. (2007). Correlative light and electron microscopy of early *Caenorhabditis elegans* embryos in mitosis. *Methods in Cell Biology, 79*, 101−119. http://dx.doi.org/10.1016/S0091-679X(06)79004-5.

Schindelin, J., Arganda-Carreras, I., Frise, E., Kaynig, V., Longair, M., Pietzsch, T., … Cardona, A. (2012). Fiji: An open-source platform for biological-image analysis. *Nature Methods, 9*(7), 676−682. http://dx.doi.org/10.1038/nmeth.2019.

Sengle, G., Tufa, S. F., Sakai, L. Y., Zulliger, M. A., & Keene, D. R. (2013). A correlative method for imaging identical regions of samples by micro-CT, light microscopy, and electron microscopy: Imaging adipose tissue in a model system. *The Journal of Histochemistry and Cytochemistry, 61*(4), 263−271. http://dx.doi.org/10.1369/0022155412473757.

Shami, G. J., Cheng, D., Huynh, M., Vreuls, C., Wisse, E., & Braet, F. (2016). 3-D EM exploration of the hepatic microarchitecture − lessons learned from large-volume in situ serial sectioning. *Scientific Reports, 6*(36744). http://dx.doi.org/10.1038/srep36744.

Sommer, C., Straehle, C., Kothe, U., & Hamprecht, F. A. (2011). Ilastik: Interactive learning and segmentation toolkit. In *Presented at the eighth IEEE international symposium on biomedical imaging (ISBI)* (pp. 230−233). http://dx.doi.org/10.1109/ISBI.2011.5872394.

Zito, K., Parnas, D., Fetter, R. D., Isacoff, E. Y., & Goodman, C. S. (1999). Watching a synapse grow: Noninvasive confocal imaging of synaptic growth in *Drosophila*. *Neuron, 22,* 719−729.

2.4 Des nanoparticules comme agents de contraste

2.4.1 Contexte

L'étape de corrélation se fait essentiellement grâce au réseau vasculaire à la fois visualisable *in vivo* par des marqueurs fluorescents (Bleu evans, Dextran-TRITC,FITC) injectés dans la circulation sanguine ou par rayons X lorsque l'échantillon est inclus dans le bloc de résine.

Cependant, les agents fluorescents injectées dans la circulation sanguine ont tendance à sortir de la vasculature au cours du temps et à augmenter le bruit de fond au niveau de la MEC rendant ainsi l'imagerie des vaisseaux situés profondément dans l'échantillon difficile.

Améliorer l'imagerie des vaisseaux *in vivo* améliorerai et faciliterai la corrélation. C'est dans cette optique que nous avons collaboré avec A. Klymchenko et N. Anton (Faculté de pharmacie, Illkirch, France) qui ont développé des nanoparticules lipidiques non toxiques (Li et al., 2013) renfermant une concentration très importante d'agents fluorescents.

Afin de caractériser le comportement de ces nanoparticules *in vivo* nous avons injectés les nanoparticules dans la circulation sanguine de la souris saine et de souris développant une tumeur dans le flanc. Les nanoparticules contiennent des fluorochromes proche infrarouge Cy5.5 et Cy7.5 qui ont la particularité d'être compatible pour l'imagerie FRET (Förster Resonance Energy Transfer). La technique de FRET a été utilisée pour mesurer l'intégrité des nanoparticules *in vivo* (Figure 37).
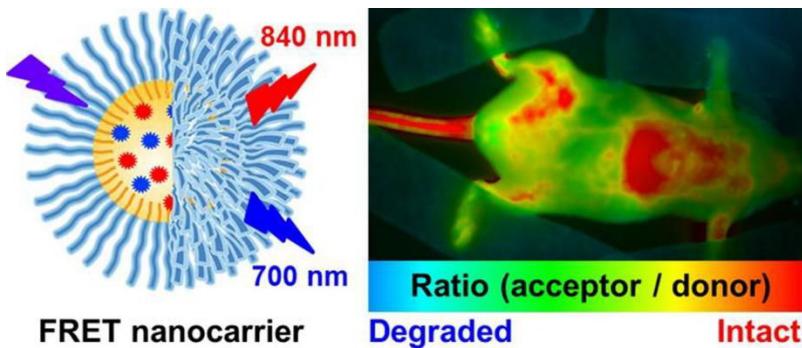
*Figure 37 : **Les nanoparticules lipidiques contiennent deux fluorochromes (Cy5.5 et Cy7.5) qui permettent de réaliser de l'imagerie FRET.** La présence de FRET indique que les nanoparticules sont intactes, l'absence ce FRET prouve que les nanoparticules ont été dégradées.*

2.4.2 Principaux résultats

Chez la souris saine, les nanoparticules permettent de visualiser la circulation sanguine au niveau de la queue, des pattes ainsi qu'au niveau d'organes tels que les poumons, le foie et le cœur. Les

nanoparticules s'accumulent au niveau du foie qui est le principal lieu de dégradation de ces particules.

Chez la souris développant une tumeur sous cutanée dans le flanc, les nanoparticules vont s'accumuler rapidement dans la tumeur où elles seront dégradées au cours du temps.

2.4.3 Manuscrit n°6: Integrity of lipid nanocarriers in bloodstream and tumor quantified by near-infrared ratiometric FRET imaging in living mice

Integrity of lipid nanocarriers in bloodstream and tumor quantified by near-infrared ratiometric FRET imaging in living mice

Redouane Bouchaala [a,b,1], Luc Mercier [c,1], Bohdan Andreiuk [a,d], Yves Mély [a], Thierry Vandamme [e], Nicolas Anton [e,*], Jacky G. Goetz [c,*], Andrey S. Klymchenko [a,*]

[a] Laboratoire de Biophotonique et Pharmacologie, UMR CNRS 7213, University of Strasbourg, 74 route du Rhin, 67401 Illkirch Cedex, France
[b] Laboratory of Photonic Systems and Nonlinear Optics, Institute of Optics and Fine Mechanics, University of Setif 1, 19000, Algeria
[c] MN3T, Inserm U1109, LabEx Medalis, Fédération de Médecine Translationnelle de Strasbourg (FMTS), University of Strasbourg, F-67200, France
[d] Organic Chemistry Department, Chemistry Faculty, Taras Shevchenko National University of Kyiv, 01601 Kyiv, Ukraine
[e] CNRS UMR 7199, Laboratoire de Conception et Application de Molécules Bioactives, University of Strasbourg, 74 route du Rhin, 67401 Illkirch Cedex, France

ABSTRACT

Lipid nanocarriers are considered as promising candidates for drug delivery and cancer targeting because of their low toxicity, biodegradability and capacity to encapsulate drugs and/or contrasting agents. However, their biomedical applications are currently limited because of a poor understanding of their integrity *in vivo*. To address this problem, we report on fluorescent nano-emulsion droplets of 100 nm size encapsulating lipophilic near-infrared cyanine 5.5 and 7.5 dyes with a help of bulky hydrophobic counterion tetraphenylborate. Excellent brightness and efficient Förster Resonance Energy Transfer (FRET) inside lipid NCs enabled for the first time quantitative fluorescence ratiometric imaging of NCs integrity directly in the blood circulation, liver and tumor xenografts of living mice using a whole-animal imaging set-up. This unique methodology revealed that the integrity of our FRET NCs in the blood circulation of healthy mice is preserved at 93% at 6 h of post-administration, while it drops to 66% in the liver (half-life is 8.2 h). Moreover, these NCs show fast and efficient accumulation in tumors, where they enter in nearly intact form (77% integrity at 2 h) before losing their integrity to 40% at 6 h (half-life is 4.4 h). Thus, we propose a simple and robust methodology based on ratiometric FRET imaging *in vivo* to evaluate quantitatively nanocarrier integrity in small animals. We also demonstrate that nano-emulsion droplets are remarkably stable nano-objects that remain nearly intact in the blood circulation and release their content mainly after entering tumors.

© 2016 The Authors. Published by Elsevier B.V. This is an open access article under the CC BY license (http://creativecommons.org/licenses/by/4.0/).

1. Introduction

Nanoscale vehicles (nanocarriers, NCs) become indispensable tools for *in vivo* imaging [1–3], drug delivery [4,5] and image-guided surgery [6,7]. One key requirement that any NC has to meet is to maintain its integrity until it reaches the target, for example a tumor [8,9]. This would ensure robust delivery of active molecules and/or provide the best signal to noise ratio when NCs are used as contrasting agents. However, suitable methods for assessing nanocarrier stability and the cargo leakage (such as dialysis, size exclusion chromatography, FCS, etc) are sparse and mostly operate *in vitro* [10]. Therefore, while providing

useful information, these model experiments cannot resolve fundamental issues such as the passage of NCs through the bloodstream, which includes shear forces, opsonization and uptake, and other undesirable interactions with off-target cells [11–13]. Moreover, in the context of tumor targeting, it is of utmost importance to assess whether NCs are capable of maintaining their load upon extravasation from the systemic circulation into the tumor (Fig. 1). Additionally, a reliable method for assessing their integrity can inform on the time scale of release of NCs' content upon tumor targeting through EPR (enhanced permeation and retention) effect [14,15]. Therefore, it is essential to monitor the integrity of the nanocarriers *in vivo*, preferably in real time. Current methods to study the integrity of the nanocarriers *in vivo* are very limited. In addition to radiolabelling assays [16], the highly promising approach is fluorescence imaging in the near-infrared (NIR) region, which now ranges from classical 2D imaging of small animals up to fluorescence-mediated tomography that enables quantitative 3D imaging

* Corresponding authors.
  E-mail addresses: nanton@unistra.fr (N. Anton), jacky.goetz@inserm.fr (J.G. Goetz), andrey.klymchenko@unistra.fr (A.S. Klymchenko).
[1] These authors contributed equally to this work.
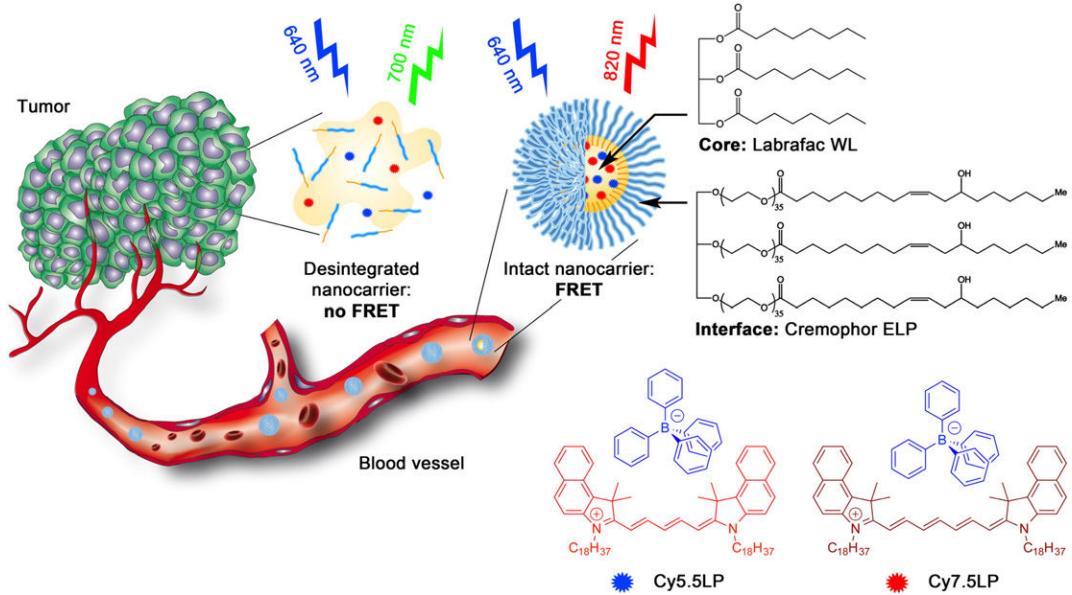
Fig. 1. Concept of FRET NCs that can report on their integrity by change in their emission color. Chemical structures of oil Labrafac WL (medium chain triglyceride) and Cremophor ELP (PEGylated surfactant) as well as lipophilic cyanine 5.5 and 7.5 dyes (Cy5.5LP and Cy7.5LP) with their bulky hydrophobic counterions are shown.

[17–20]. Importantly, optical imaging modality provides access to Förster Resonance Energy Transfer (FRET), which acts as a molecular ruler between the donor and acceptor dyes and has been extensively used to characterize properties of bio-/nano-materials and their response to biological environments [13,21–23]. It is particularly suitable to study the integrity of a nanocarrier, because of exquisite sensitivity of FRET to changes in the donor acceptor distance. Thus, encapsulation of both donor and acceptor inside a nanocarrier should ensure high FRET efficiency, while the loss of the nanocarrier integrity associated with the release of its components into the medium should result in the loss of the FRET signal. Moreover, when FRET occurs between two fluorescent dyes, dual emission of NCs can be obtained, which opens possibilities for quantitative ratiometric measurements using fluorescence detection in two distinct optical windows. It is only very recently that FRET imaging has been used for monitoring *in vivo* the integrity of NCs. It has been successfully applied to monitor biodistribution and integrity of polymer micelles [24], hybrid organic-inorganic nanoparticles [9] and nanoemulsion droplets [25]. However, these studies only showed global FRET signal from the mice or a tumor, without imaging directly the particle integrity in the blood circulation, where these nanocarriers are actually injected. For this purpose, only indirect *ex vivo* measurements and intravital microscopy, which requires complex dedicated setup, were realized to date [9,26,27]. Moreover, the studies were limited to qualitative evaluation and no quantification of nanocarrier integrity directly in living mice was reported to date. Quantitative *in vivo* fluorescence imaging of NCs integrity can be achieved only after some key limitations of existing fluorescent NCs are addressed. The first limitation is the insufficient fluorescence signal from NCs that is contaminated by the background from animal tissue. This could be overcome by high dye loading into NCs with minimal self-quenching of the encapsulated dyes and injecting large quantities of NCs into mice without toxic effects. Moreover, the loaded dyes should operate in the NIR region (>700 nm), where the absorption, light-scattering and auto-fluorescence of the tissue are minimal [28–30]. Second, intensity of the FRET signal was usually analyzed, making the assessment of nanocarrier integrity only qualitative. Quantification requires internal control, which can be realized by ratiometric FRET imaging, obtained by division of two images (*e.g.* acceptor/donor). In contrast to intensity, the measured ratio values are absolute, being independent of concentration of emissive species and light source intensity [31,32].

However, only one rare example used ratio imaging in application to analyze FRET of nanocarriers *in vivo* [33]. The problem is that in majority of examples FRET donor emits below near-infrared (NIR) window (<700 nm), so that its signal is strongly attenuated by tissue absorption and contaminated by light scattering and auto-fluorescence. Therefore, quantitative and reliable ratiometric *in vivo* imaging requires both donor and acceptor species to emit in the near-infrared (NIR) region above 700 nm.

Among the existing nanocarriers for drugs and contrasting agents in the biomedical research, lipid nano-emulsion emerged recently as a promising alternative [34–36]. Although nano-emulsions were mainly used for the last >20 years as template for nanoparticle preparation [37], only in the last years they attracted attention as nano-carriers in pharmacy and cosmetics application [38,39]. Nano-emulsifications enable preparation of lipid nanocarriers of well-defined size from FDA approved materials using direct approaches that do not use organic solvents [40]. This feature is particularly attractive for high quality fluorescence imaging as it enables injecting maximal amount of nanocarriers with minimal harm to an animal [34,35]. However, as nano-emulsions are essentially liquid objects, two major problems need to be addressed before they can be broadly used in drug delivery and/or as contrasting agents. First, efficient encapsulation of material and active compounds, without fast leakage, needs to be achieved. Second, *in vivo* stability is required to ensure proper delivery. Both issues are actively debated over the last years [25,41–43]. Recently, we introduced an original concept to improve the loading of cyanine dyes into the oil droplet, which is based on the use of hydrophobic counterions [44]. Cyanine dyes usually bear inorganic counterions such as perchlorate or iodide that are responsible for poor solubility of these dyes in oils. By replacing these ions with tetraphenyl borate (TPB), we were able to improve solubility >40-fold and create 90 nm lipid droplets bearing exceptional number of cyanine dyes (~12,000 per droplet, 8 wt% dye loading) that remained efficiently fluorescent [44]. The extreme brightness of these NCs enabled pioneer single particle tracking *in vivo* in a zebrafish embryo model. However, this unique counterion approach has never been applied to NIR cyanine dyes, required for *in vivo* imaging, and it has never been used to generate FRET inside nanocarriers, needed to assess the NCs integrity.

In the present work, we synthesized lipophilic cyanine 5.5 and 7.5 dyes bearing long alkyl chains and TPB counterion (Cy5.5LP and

Cy7.5LP, respectively, Fig. 1) and encapsulated them inside lipid nanocarriers at concentrations required for highly efficient FRET, *i.e.* 1% in oil. These dyes ideally fit the NIR spectral region for *in vivo* imaging, where, notably, our cyanine 7.5 is an apolar analogue of indocyanine green commonly used for *in vivo* imaging [45,46]. The obtained ultrabright FRET NCs were successfully injected and monitored in healthy and tumor-bearing mice. We were able, for the first time, to visualize and quantitatively assess lipid nanocarrier integrity directly in the bloodstream, liver and tumor of living mice. We showed that lipid NCs remain nearly intact in the blood circulation, and they can enter the tumor with minimal loss of their integrity followed by the release their content with a half-life of 4.4 ± 0.3 h. Thus, we provide a robust imaging methodology to follow the evolution of lipid NCs *in vivo*, showing their remarkable stability *in vivo* and capacity to deliver their content into the target cancer tissues.

2. Materials and methods

2.1. Materials

All chemicals and solvents for synthesis were from Sigma Aldrich. Cremophor ELP® (Kolliphor ELP®) was provided by BASF (Ludwigshafen, Germany), Labrafac WL® (medium chain triglycerides) by Gattefossé (Saint-Priest, France). Ultrapure water was obtained using a MilliQ® filtration system (Millipore, Saint-Quentin-en-Yvelines, France). Fetal bovine serum (FBS) was acquired from Lonza (Verviers, Belgium) and Gibco-Invitrogen (Grand Island, USA).

2.2. Synthesis of Cy5.5LP and Cy7.5LP

2.2.1. 1,1,2-trimethyl-3-octadecyl-1H-benzo[e]indol-3-ium iodide (1)

250 mL round-bottom flask equipped with magnetic stirring bar was charged with 1,1,2-trimethylbenz[e]indole (1 eq., 6.88 g, 32.9 mmol) and 1-iodooctadecane (2 eq., 25 g, 65.7 mmol), 100 mL of 2-butanone was added subsequently. Reaction mixture was refluxed for 24 h, then cooled down to r.t. Reaction mixture was cooled down to r.t., diethyl ether was added and formed solid part was filtered off and washed with 100 mL of diethyl ether. Obtained crystals of crude product were redissolved in DCM and precipitated back while by adding diethyl ether, afterwards filtered and washed with diethyl ether. Product was obtained as slightly green crystals in 76% yield (14.73 g).

^{1}H NMR (400 MHz, CDCl$_3$) δ 8.10 (d, $J = 8.7$ Hz, 1H), 8.08 (dd, $J = 8.0, 1.1$ Hz, 1H), 8.04 (dd, $J = 8.2, 1.3$ Hz, 1H), 7.76 (d, $J = 8.9$ Hz, 1H), 7.72 (ddd, $J = 8.3, 6.9, 1.4$ Hz, 1H), 7.65 (ddd, $J = 8.1, 6.9, 1.2$ Hz, 1H), 4.78 (t, $J = 7.7$ Hz, 2H), 3.19 (s, 3H), 1.97 (p, $J = 7.8$ Hz, 2H), 1.87 (s, 6H), 1.52–1.41 (m, 2H), 1.40–1.30 (m, 2H), 1.28–1.19 (m, 26H), 0.85 (t, $J = 7.0$ Hz, 3H).

^{13}C NMR (100 MHz, CDCl$_3$) δ 195.25, 138.34, 137.29, 133.82, 131.56, 130.17, 128.77, 127.97, 127.74, 122.96, 112.59, 56.04, 50.56, 32.00, 29.77, 29.76, 29.73, 29.70, 29.65, 29.55, 29.43, 29.41, 29.24, 28.26, 26.92, 22.85, 22.76, 17.03, 14.18.

HRMS (m/z): [M]$^+$ calcd for C$_{33}$H$_{52}$N 462.40943; found 462.40854.

2.2.2. Dioctadecylcyanine 5.5 chloride (2)

1,1,2-trimethyl-3-octadecyl-1H-benzo[e]indol-3-ium iodide (1) (1 eq., 2 g, 3.39 mmol) was placed in 50 mL round-bottom flask. 10 mL of dry pyridine was added *via* syringe. Then, 1,1,3,3-tetramethoxypropane (1.5 eq., 0.835 g, 0.838 mL, 5.09 mmol) was quickly added dropwise to the boiling solution of indoleninium salt using syringe. Reaction mixture was stirred under reflux for 3 h. After cooling down to room temperature solvent was removed under reduced pressure. To the obtained residue 50 mL of dichloromethane were added. Obtained solution was washed three times with 1 N HCl, then with brine and water. The crude product was purified by flash column chromatography on silica gel using ethyl acetate/dichloromethane

(9:1) mixture as eluent. Cyanine was obtained as dark blue-greenish viscous oil in 76% yield (2.8 g).

^{1}H NMR (400 MHz, CDCl$_3$) δ 8.55 (t, $J = 13.0$ Hz, 2H), 8.20 (d, $J = 8.5$ Hz, 2H), 7.90 (d, $J = 8.6$ Hz, 4H), 7.64–7.54 (m, 2H), 7.44 (t, $J = 7.5$ Hz, 2H), 7.32 (d, $J = 8.8$ Hz, 2H), 6.74 (t, $J = 12.4$ Hz, 1H), 6.24 (d, $J = 13.7$ Hz, 2H), 4.14 (t, $J = 7.5$ Hz, 4H), 2.12 (s, 12H), 1.83 (p, $J = 7.6$ Hz, 4H), 1.46 (p, $J = 7.6, 7.0$ Hz, 4H), 1.40–1.33 (m, 4H), 1.30–1.18 (m, 52H), 0.85 (t, $J = 6.7$ Hz, 6H).

^{13}C NMR (100 MHz, CDCl$_3$) δ 174.60, 153.33, 139.40, 134.46, 131.81, 130.44, 129.94, 128.32, 127.83, 125.11, 122.65, 110.44, 103.10, 51.53, 44.64, 32.00, 29.79, 29.77, 29.74, 29.70, 29.66, 29.55, 29.48, 29.44, 27.93, 27.80, 27.08, 22.77, 14.21.

HRMS (m/z): [M]$^+$ calcd for C$_{69}$H$_{103}$N$_2$ 959.81158; found 959.8098.

2.2.3. Dioctadecylcyanine 7.5 chloride (3)

1,1,2-trimethyl-3-octadecyl-1H-benzo[e]indol-3-ium iodide (1) (2.2 eq., 1029 mg, 1.75 mmol) and glutaconaldehydedianil hydrochloride (1 eq., 226 mg, 0.794 mmol) were mixed in 10 mL of pyridine, afterwards Ac$_2$O (13.4 eq., 1087 mg, 1 mL, 10.6 mmol) was added and the reaction mixture was heated to 60 °C while stirring and left for 3 h. After reaction was finished, solvents were evaporated at vacuum, and the crude product was dissolved in DCM, washed with 0.1 N HCl (3 times), brine and water. DCM layer was dried over Na$_2$SO$_4$, the solvent was evaporated and the product was purified by column chromatography on silica (gradient DCM/MeOH 99/1–95/5). Product was obtained as a green solid (926 mg, 0.906 mmol, 52%).

^{1}H NMR (400 MHz, CDCl$_3$): δ 8.16 (d, $J = 8$ Hz, 2H), 8.06 (t, $J = 12$ Hz, 2H), 7.97 (bs, 1H), 7.92 (d, $J = 8$ Hz, 4H), 7.61 (t, $J = 7$ Hz, 2H), 7.46 (t, $J = 7$ Hz, 2H), 7.35 (d, $J = 9$ Hz, 2H), 6.67 (t, $J = 12$ Hz, 2H), 6.25 (d, $J = 12$ Hz, 2H), 4.14 (bs, 4H), 2.04 (s, 12H), 1.87 (m, $J = 7$ Hz, 4H), 1.49 (m, $J = 7$ Hz, 4H), 1.39 (m, $J = 7$ Hz, 4H), 1.26 (bs, 52H), 0.88 (t, $J = 7$ Hz, 6H).

^{13}C NMR (100 MHz, CDCl$_3$): δ 173.07, 157.04, 151.02, 139.74, 133.98, 131.83, 130.59, 130.09, 128.41, 127.87, 126.27, 125.06, 122.47, 110.56, 103.39, 51.155, 44.76, 32.06, 29.842, 29.807, 29.76, 29.72, 29.60, 29.53, 29.50, 27.86, 27.14, 22.82, 14.26.

HRMS (m/z): [M]$^+$ calcd. For C$_{71}$H$_{105}$N$_2^+$ 985.8272; found 985.8290.

2.2.4. Dioctadecylcyanine 5.5 tetraphenylborate (Cy5.5LP)

Dioctadecylcyanine 5.5 chloride (1 eq., 100 mg, 0.1 mmol) was dissolved in 5 mL of DCM, sodium tetraphenylborate (3 eq., 103 mg, 0.301 mmol) was added and the dispersion was sonicated for 5 min. TLC control has shown full conversion. Afterwards, the mixture was purified on a silica column, eluent DCM/MeOH 95/5 (product goes almost with front). Dioctadecylcyanine 5.5 tetraphenylborate (109.2 mg, 0.085 mmol, 85%) was obtained as blue-green viscous oil and used without further characterisation.

2.2.5. Dioctadecylcyanine 7.5 tetraphenylborate (Cy7.5LP)

Dioctadecylcyanine 7.5 chloride (1 eq., 200 mg, 0.18 mmol) was dissolved in 5 mL of DCM, sodium tetraphenylborate (3 eq., 184 mg, 0.539 mmol) was added and the dispersion was sonicated for 5 min. TLC control has shown full conversion. Afterwards, the mixture was purified on a silica column, eluent DCM/MeOH 95/5 (product goes almost with front). Dioctadecylcyanine 7.5 tetraphenylborate (218 mg, 0.167 mmol, 93%) was obtained as green viscous oil and used without further characterisation.

2.3. Formulation and characterisation of lipid nanocarriers

Dye loaded nanoemulsions were produced by spontaneous nano-emulsification. Briefly, the dyes (Cy5.5LP and Cy7.5LP) were firstly dissolved in Labrafac WL® (56 mg) at concentrations ranging from 0.1 to 1% by weight. Then, Cremophor ELP® (also called Kolliphor ELP®) was added (44 mg), and the mixture was homogenized under magnetic stirring at 37 °C for 10 min up to complete homogenisation. Finally,

nanoemulsions were generated with the addition of ultrapure (Milli-Q) water (230 mg). Size distributions were determined by dynamic light scattering using a Zetasizer Nano series DTS 1060 (Malvern Instruments S.A).

2.4. Fluorescence spectroscopy

Absorption and fluorescence spectra were recorded on a Cary 4 spectrophotometer (Varian) and a Fluoromax 4 (Jobin Yvon, Horiba) spectrofluorometer, respectively. Fluorescence emission spectra were performed at room temperature with 670 and 760 nm excitation wavelengths for Cy5.5LP and Cy7.5LP loaded nanocarrier, respectively. The emission spectra were corrected from for the wavelength-dependent response of the detector. All fluorescence measurements were done using solutions with absorbance ≤0.1 at the wavelength of excitation. The relative fluorescence quantum yield was measured using DiD dye in methanol (QY = 33%) as reference using excitation at 630 nm [47].

2.5. FRET-based stability test

The stability of lipid nanocarriers was estimated using Forster resonance Energy transfer (FRET) between two encapsulated dyes, 1% of Cy5.5LP (with respect to Labrafac WL®) as energy donor and 1% of Cy7.5LP as energy acceptor were used. The NCs were diluted 10,000 times from the original formulation and incubated in water and 100% of fetal bovine serum (FBS). High dilution was needed to avoid saturation of serum by lipids of NCs. The donor in the nanocarriers was excited at 670 nm. The semi-quantitative parameter of FRET efficiency was calculated according to the following equation E = A/(A + D) [48], where A and D are the maximum of fluorescence intensity of the acceptor and donor, respectively.

2.6. Cytotoxicity studies

In 96-well plates, HeLa cells were seeded at a concentration of 1×10^4 cells per well in 200 μL of the DMEM growth medium and then incubated overnight at 37 °C in humidified atmosphere containing 5% CO_2. Next, we add the lipid Nanocarriers (1% Cy5.5LP–Cy7.5LP), by substituting the culture medium for a similar one containing variable dilutions of the Nanocarriers. After incubation for 24 h, the medium was removed. Then, the wells were filled with cell culture medium containing MTT, incubated for 4 h at 37 °C, and the formazan crystals formed were dissolved by adding 100 μL of DMSO and shaked for 10 min. We measure the absorbance at 570 nm with a microplate reader (Xenius, Safas). Experiments were carried out in triplicate, and expressed as a percentage of viable cells compared to the control group.

2.7. Subcutaneous tumor grafting and administration of FRET nanocarriers

Adult (10 months) immuno-deficient mice (NMRI-Foxn1nu/Fox1nu, Janvier labs, 1) were anesthetized via gas anesthesia (isoflurane) system prior to tumor cell grafting. Anesthetized mice were injected subcutaneously (in the flank) with 100 μL of a solution made of 50% PBS and 50% Matrigel containing 1.10^6 of D2A1 (murine mammary carcinoma) cells [49]. Tumors were grown over a period of 20 days before administrating lipid nanocarriers. The mouse studies were performed according to the Guide for Care and Use of Laboratory Animals (E67-6-482-21) and the European Directive with approval of the regional ethical committee (CREMEAS for Comité Régional d'Ethique en Matière d'Expérimentation Animale de Strasbourg, AL/73/80/02/13). Mice received food and water ad libitum; they were checked daily and tumor growth never exceeded 20 days, leading to low-size tumors with no impact on the animal's health. All efforts were made to minimize suffering and euthanasia was performed using CO2. General health status was monitored regularly by

independent observers. Sacrifice of the animal was effectuated when reaching limit ethical endpoints. Before administration of the nanocarriers solution, mice were anesthetized by intraperitoneal injection of a mixture of ketamine (100 mg/kg) and xylazine (10 mg/kg). The nanocarriers were administrated by retro-orbital injection (100 μL) as previously performed for other purposes [50].

2.8. In vivo whole animal FRET imaging

Whole- and live-animal imaging of the FRET signal in healthy and tumor-bearing mice was performed by using a luminograph (NightOwl, Berthold Technologies). Anesthetized mice (isoflurane) were placed repeatedly in the luminograph, and positioned either on the flank or the back. Mice were imaged using a halogen lamp, (75 W, 340–750 nm) and emission of the two dyes was collected separately using separate filters sets (630/700 nm for Cy5.5LP, and 630/820 nm for Cy7.5LP). The experiments with healthy and tumor bearing mice were repeated three times.

2.9. Calibration of the ratiometric response of NCs to disintegration

To calibrate the ratiometric response of NCs to disintegration in our in vivo imaging setup, we model the disintegration NCs by mixing intact FRET NCs with NCs containing separately donor and acceptor at low concentration, with the preservation of the same concentration of dyes: 100% integrity corresponds to FRET NCs (1% of Cy5.5LP and 1% of Cy7.5LP) diluted in PBS 1000-fold from the original formulation, while 0% integrity corresponds to a mixture of NCs containing separately donor (0.1% of Cy5.5LP) and acceptor (0.1% Cy7.5LP), both diluted at 100-fold in PBS. Intermediate mixtures were made, where the level of integrity (%) is defined as the fraction of Cy5.5LP/Cy7.5LP dyes in the FRET NCs with respect to the total amount of these dyes. They were placed into 96-well plate and imaged using the NightOwl setup. The measurements were done in triplicate. The obtained values of the A/(A + D) ratio were plotted vs % of integrity and the data were fit with an exponential function (1):

$$y = a + be^{cx} \tag{1}$$

where $a = 0.14572$; $b = 0.1254$; $c = 0.01748$, y is A/(A + D) and x is FRET pair concentration (wt%).

As another model of the complete disintegration of NCs, solution FRET NCs diluted 1000-fold in dioxane was placed into 1 mL Eppendorf® tube and imaged by the NightOwl setup.

2.10. Image analysis of the FRET signal in the living mice

The ratiometric images were built using a homemade plugin (developed by Romain Vauchelles) under ImageJ that divides the image of the 840 nm channel by that of the 700 nm channel. For each pixel, a pseudocolor scale is used for coding the ratio, while the intensity is defined by the integral intensity recorded for both channels at the corresponding pixel. Image analysis was performed by using the ImageJ software [51]. The tail vein, liver and tumor were manually delimitated and the mean intensity of the delimitated region was determined for each respective time point and channel for three healthy and three tumor-bearing mice. For both donor and acceptor channels, the signal was corrected for the background using the mice before injection (in the corresponding region of interest). Then the corrected values of A/(A + D) were converted into the FRET pair concentration using Eq. (1). The obtained values of FRET pair concentration were then plotted vs time and fitted using a logistic function (2):

$$y = a_2 + \frac{(a_1 - a_2)}{\left(1 + \left(\frac{x}{x_0}\right)\right)^p} \tag{2}$$

where y is the FRET pair concentration (wt%); x is time; other parameters were calculated during the fitting procedure. This fit was further used to calculate the integrity half-life.

2.11. Statistical analysis

Student's t-test was used to evaluate the statistical significance between two sample groups. The differences between the results were considered to be significant when the p-values were <0.05.

3. Results and discussion

Nanoemulsions were selected as NCs for several reasons. First, they are very efficient at encapsulating materials. Second, nanoemulsions can be easily formulated by spontaneous emulsification with non-toxic compounds compatible with the parenteral administration route, so that they can be intravenously injected at high concentrations into mice with minimal harm [34,35]. The latter is particularly attractive to achieve superior contrast for imaging nanocarriers directly in the blood circulation. Cyanines 5.5 and 7.5 dyes were selected for encapsulation, because they are an excellent FRET couple with ideal spectral properties for *in vivo* whole-animal imaging. Indeed, cyanine 5.5 derivatives are among the most commonly used NIR imaging agents with convenient excitation 650–700 nm and emission in NIR region (>700 nm). Moreover, cyanine 7.5 absorption spectrum overlaps perfectly with the emission spectrum of cyanine 5.5 (Fig. S2), while its emission in NIR region at 840 nm is perfectly separated from the emission of cyanine 5.5, making this couple perfectly tailored for ratiometric FRET imaging. To achieve both strong brightness and highly efficient FRET inside NCs, cyanines 5.5 and 7.5 should be encapsulated at very high concentrations up to 1 wt% in oil, as we earlier showed for other FRET pair [41]. Therefore, their hydrophobic analogues, dioctadecylcyanines 5.5 (**2**) and 7.5 (**3**), were synthesized bearing long alkyl chains to ensure their high lipophilicity. Nevertheless, their solubility in labrafac oil (medium chain triglycerides) was only 0.15 and 0.05 wt%, for **2** and **3**, respectively. Therefore, we replaced their inorganic counterion (chloride) with bulky hydrophobic tetraphenylborate, which, according to our earlier study, improved drastically the solubility of the cyanine 3 dye DiI [44]. The obtained new salts, Cy5.5LP and Cy7.5LP (Fig. 1), showed much higher solubility in labrafac, 7 and 4 wt%, respectively. Then, nano-emulsions (lipid NCs) were generated by the spontaneous emulsification of dye-loaded oil and non-ionic surfactant (Cremophor® ELP), giving rise to fluorescent PEGylated droplets sizing around 90–100 nm (Table S1). To generate FRET NCs, we prepared NCs encapsulating increasing amount of Cy5.5LP and Cy7.5LP. As expected, the emission spectra recorded after excitation of the energy donor showed strong dependence on the concentration of the FRET pair (Fig. 2A). Thus, at 0.1% of dyes, the emission spectrum was very close to that of Cy5.5LP alone, while at higher concentrations, a long wavelength emission, corresponding to the FRET acceptor, appeared and became dominant at ≥0.5% of the dyes. It should be noted that the emission maximum of Cy7.5LP shifted gradually to the red with increase in the dye content (Fig. 2A). Similar concentration-dependent red shifts were previously observed for Cy3 dye in lipid droplets [44]; they could be related to some aggregation of the dyes, homo-FRET, as well as to small changes in the oil core properties at higher dye concentrations. Remarkably, the total (donor + acceptor) fluorescence quantum yield (QY) of NCs encapsulating FRET pair at 1% loading of each dye was 11%. Although this value was lower than the QY of NCs with 1% of Cy5.5LP alone (27%), it remained relatively high to ensure high brightness to these NCs, important for *in vivo* imaging. For comparison, QY of NIR dye indocyanine green measured in phosphate-buffered saline (PBS) is 2.4% [52]. Here, we achieved much higher QY already for the FRET system. Moreover, because NCs minimize potential interactions of loaded dyes with tissues *in vivo*, they allow the use of higher dye concentrations, which is essential for achieving optimal imaging contrast for NIR imaging.

Then, to verify the response of our FRET NCs to their disintegration, we forced this process by adding excess of water miscible organic solvent dioxane, which should destroy NCs by solubilizing its components. As a result, a strong emission of Cy5.5LP dye was observed, while the emission of Cy7.5LP was fully hampered (Fig. 2B). This result confirmed that integrity of NCs, where Cy5.5LP and Cy7.5LP are in very close proximity within the NCs, can be assessed based on FRET signal. We next assessed the stability of these FRET NCs by incubating them in serum (100%), used as model of a biological medium *in vivo*. As a semi-quantitative parameter of FRET efficiency, we used the band intensity ratio of acceptor to the sum of acceptor and donor, $A/(A + D)$, so-called proximity ratio [48,53]. This ratio showed only a mild decrease over 24 h of incubation in serum (Fig. 2C) and nearly no change in water, demonstrating the relative stability of our FRET NCs. Therefore, we concluded that these new FRET NCs, owing to good stability and relative ease in monitoring their integrity, should be perfectly suited for whole-animal NIR imaging through intravenous injection.

Before testing the integrity of our NCs *in vivo*, we evaluated cytotoxic effects of NCs by performing a cell viability assay *in vitro* on tumor cells. In the dilution range between 10,000 and 500, blank and dye-loaded FRET NCs did not show any significant cytotoxicity (Fig. S3). NCs were however cytotoxic when used at a 200-fold (and below) dilution. Importantly, the presence of both dyes (Cy5.5LP and Cy7.5LP) in the NCs had no added cytotoxic effect. It should be noted that the dilution factor that we further used in our mice experiments corresponded to ~1000-
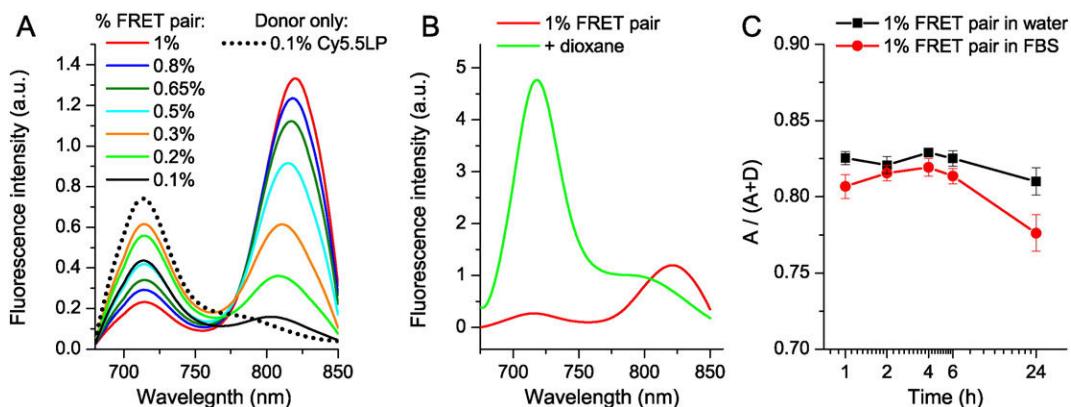
Fig. 2. FRET in the lipid NCs. (A) Fluorescence spectra of dye-loaded NCs as a function of weight % of FRET pair (corresponds to % of each dye). The spectra were recorded for the same 1000-fold dilution of NCs in water. (B) Disintegration of NCs by dioxane: fluorescence spectra of NCs encapsulating 1% of Cy5.5LP and 1% of Cy7.5LP diluted 1000-fold in water or in dioxane. (C) Stability of FRET NCs in serum: FRET signal, expressed as $A/(A + D)$ ratio, for different incubation times in 100% serum or water at 37 °C. To avoid saturation of serum by lipids of NCs, 10,000-fold dilution from original formulation was used. Excitation wavelength was systematically 670 nm.

fold, which is well in the low cytotoxicity range according to the present data.

We then performed whole-animal *in vivo* NIR imaging of anesthetized and immobilized nude mice (Fig. S4) upon parenteral venous administration (retro-orbital) of the FRET NCs suspension, diluted to 50-fold in PBS (the dye concentration in the injected solution was 0.16 mM). We used 630 nm illumination in order to excite Cy5.5LP dye. Emission was collected at two wavelengths: at 700 nm to observe emission of the FRET donor Cy5.5LP, and at 820 nm to observe emission of the FRET acceptor Cy7.5LP (Fig. 3). In order to evaluate directly FRET changes independently of concentration, we also generated ratio images where emission of the acceptor was divided by the emission of the donor (A/D, Fig. 3). Before injection, only low fluorescence was observed for 700 nm channel and negligible signal at 820 nm (Fig. 3A). Right after injection (15 min), the emission of Cy7.5LP corresponding to FRET increased significantly, while emission intensities collected in the Cy5.5LP channel remained very close to auto-fluorescence levels observed before injection (Fig. 3B). This strong FRET fluorescence suggested that the integrity of our FRET NCs was well preserved *in vivo* 15 min after their parenteral injection. Even more importantly, we obtained high imaging contrast in the FRET channel, where blood circulation could be distinguished, notably in the tail and in the back legs vasculature (see arrows 1 and 2 in Fig. 3B). Strikingly, efficient FRET (high A/D ratio in red) highlighted strongly vascularized organs,

Fig. 3. FRET imaging of healthy nude mice before (A) and after (B) injection of NIR-FRET lipid NCs (1% of Cy5.5LP and Cy7.5LP each). Left panels present intensity images of the Cy5.5LP channel (700 nm), middle panels present images of Cy7.5LP channel (820 nm), while the right panels present ratiometric images (acceptor/donor). The excitation wavelength was 630 nm. Numbers of arrows show vasculature of tail (1) and back leg (2) as well as liver (3) and lungs (4).

particularly liver. Other organs sitting above the liver, such as the lungs and potentially thyroid glands, were also resolved with our FRET NCs. Thus, the use of ratiometric imaging of whole living mice with our FRET NCs provided remarkably high resolution, where both the blood circulation and several important organs were easily revealed.

Further time-course imaging experiment revealed that fluorescence intensities of our NIR dyes and the associated ratio underwent dramatic evolution. The fluorescence intensity gradually increased in the Cy5.5LP channel, and became significant after 6 h, reaching maximal values only after 24 h. On the contrary, overall FRET intensity gradually decreased, so that after 24 h it was much lower than that at Cy5.5LP channel (Fig. 4). The ratio (A/D) imaging confirmed the continuous decay of the FRET signal as the initial red pseudo-color changed to green, and reached the lowest levels (blue) 24 h post-injection (Fig. 4 and S5). Remarkably, this color switch corresponded to ~30-fold decrease in the A/D ratio within 24 h, indicating profound changes of FRET in our NCs as well as high sensitivity and dynamic range of the ratio imaging. This experiment reveals, using FRET imaging, the time-course of disintegration of our NCs. When the control NCs, containing only Cy5.5LP were injected, the emission at the donor (Cy5.5LP) channel was much higher than that at the acceptor one, whatever the post-injection time (Fig. 4 and S7). The obtained ratio images gave very similar blue pseudo-coloring all over the mice body for different post-injection times (Fig. S7), in agreement with total absence of FRET in the control NCs. They matched well with the images obtained at 24 h post-injection of the FRET NCs, where the FRET signal was lost (Fig. 4). Interestingly, we obtained high-quality contrast in the Cy5.5LP channel 15 min after injection of our control donor dye-loaded NCs, and could easily discern both the vasculature network as well as highly-vascularized organs such as the liver. However, in contrast to the ratio imaging with FRET NCs, fewer details were observed (*i.e.* no lungs and less blood vessels). The time-lapse experiment showed a gradual decay of the fluorescence intensity from the tail vasculature (tail vein) with complete disappearance of the signal after 24 h (Fig. 4 and S8).

To provide connection between observed pseudo-color and the integrity of our NCs, we performed a calibration of our imaging set-up with diluted solutions of NCs containing mixtures modeling different integrity levels. As our dyes did not show significant leakage in serum even within 24 h, we consider that disintegration of NCs observed *in vivo* results in the destruction of the droplets themselves. The latter would lead to the dilution of the liberated dyes in the surrounding tissue especially in their lipid structures (lipid membranes and droplets), producing the loss of FRET. In this case, to model fully disintegrated NCs, we mixed NCs containing separately donor and acceptor dyes at low concentration (0.1%). The final concentration of each dye in this model mixture was identical to that in our FRET NCs, but in this case donor and acceptors dyes were isolated from each other and diluted in the oil of NCs. This system should mimic disintegrated NCs, where liberated donors/acceptor dyes are highly diluted in lipid environments of the tissue. We also prepared mixtures of FRET NCs and NCs containing separated FRET partners, where % of integrity was defined as the fraction of the dyes in the intact FRET NCs with respect to total amount of dyes in the mixture. Decrease in the integrity level produced drastic variation of the two-band emission of NCs with rapid increase in the donor emission and less pronounced decrease in the acceptor emission (Fig. 5B). These changes were expected as the fraction of non-FRET NCs increased. Then, using our *in vivo* imaging setup, we observed that a decrease in the NCs integrity correlated with a rapid increase in the donor channel, with only minor decrease in the acceptor one (Fig. 5C), in line with the spectroscopic data. Ratiometric images of the intact FRET NCs appeared in red, which reliably matched the blood circulation of healthy mice at 15 min after injection (Fig. 4). Subsequently, the decrease in the NCs integrity level produced gradual change of the pseudo-color to yellow, green and then to blue, reflecting the drop of the A/D ratio (Fig. 5C). Remarkably, changes in the pseudo-color of our calibrating solution followed the same trend as those in the ratiometric images

Fig. 4. FRET imaging of healthy nude mice at different times after injection with NIR-FRET lipid NCs (1% of Cy5.5LP and Cy7.5LP each) and control NCs containing only Cy5.5LP dye (1%). Upper panels present intensity images of the Cy5.5LP channel (700 nm), middle panels present images of Cy7.5LP channel (820 nm), while the lower panels present ratiometric images (acceptor/donor). The excitation wavelength was 630 nm. Experiment was repeated on three mice, the set of data for the other two mice (15 min post-injection) is reported in the Supplementary information section (Fig. S6).

of mice in the course of 24 h. The same color switch to blue was observed once the NCs were diluted in dioxane (Fig. 5C), which was an additional model of NCs disintegration. Based on the calibration results, the ratio images obtained in living mice could directly be correlated to NCs integrity in vivo. To realize quantitative analysis of the changes in the NCs integrity, we first corrected the data from the background signal in liver and tail vein for both 700 and 820 nm channels, and used them to obtain the $A/(A + D)$ ratio, which is used here as a semi-quantitative measure of the overall FRET efficiency in our samples. This ratio remained stable for 2–3 h post-injection in the tail vein (Fig. 6B), indicating remarkable stability of NCs in the blood circulation. In sharp contrast, this ratio showed significant drop in the liver, indicating significant loss of FRET and thus NCs integrity on the time scale of 2–3 h. Although we cannot provide absolute values of FRET efficiency simply based on the $A/(A + D)$ ratio [48,53,54], we could directly correlate this ratio with the integrity level of NCs (Fig. 5D) using calibration images in Fig. 5C, recorded by the same imaging setup with identical emission filters. The obtained plot of $A/(A + D)$ ratio vs integrity level of NCs was fitted using a non-linear equation and then used as our calibration curve. Consequently, this allowed us to estimate integrity of our NCs over time for liver and tail vein, directly in living mice (Fig. 6C). This analysis revealed dramatic difference in the stability of NCs in blood circulation and liver. At 6 h of post-administration, the integrity of NCs in the liver decreased to $66 \pm 2\%$, whereas in blood circulation NCs remained practically intact with integrity level reaching $93 \pm 2\%$ (Fig. 6C) ($p < 0.0003$, n = 3). The integrity half-life of NCs was 8.2 ± 0.4 h in the liver of healthy mice. Unfortunately, this parameter could not be assessed for the blood circulation since NCs were cleared from the blood on the shorter time scale. Indeed, our experiments with NCs containing only donor dye (Cy5.5LP) (Fig. S7) confirmed that the circulation half-time was 3 ± 1 h (Fig. S8). Therefore, after 6 h, most of NCs were cleared from the blood circulation, so the detected signal in the tail region was produced mainly by surrounding tissues. Thus, the lipid NCs remain stable until their clearance from the blood. On the

other hand, our data suggest that liver can disintegrate lipid NCs on the time scale of hours.

Next, because NCs bear great potential in tumor targeting, we administrated our FRET NCs to tumor-bearing animals, where murine tumor cells (D2A1) were subcutaneously xenografted in the flank of nude mice 20 days before NCs injection (see photo of one tumor bearing mice in Fig. S4). Thus, assuming that EPR would lead to accumulation of NCs in tumors, the basic question we asked was whether the NCs enter tumor in their intact or disintegrated form. Upon administration of NCs, we observed a significant targeting of the microenvironment of the tumor by our NCs, which led to fluorescence around tumor in the FRET channel and almost negligible fluorescence in the Cy5.5LP channel (Fig. 7A and Fig. S9). This fluorescence signal corresponded to high A/D ratio (observed in red), indicating efficient FRET, similar to that in the tail vessel. Thus, the fluorescence observed in the peri-tumoral region can be assigned to the tumor-associated vasculature, which contains high concentration of intact FRET NCs. Already at 1 h post-injection, the tumor region displayed very strong FRET signal, even though signal collected in the Cy5.5LP channel remained very low (Fig. 7A). In this case, the absolute intensity of the donor channel was only 5.7 ± 1.3 (arbitrary units, a. u.), whereas for control NCs with only donor Cy5.5LP, the intensity in the tumor region at 1 h injection was 26 ± 2 (a. u.). This much lower intensity of the donor channel suggested the efficient FRET-based quenching of the donor inside the FRET NCs accumulated in the tumor. Ratio image at 1 h showed mainly yellow-red color in the tumor region, which indicated that after accumulation in the tumor the FRET remained very high despite a small decrease. These observations suggested that (i) the lipid NCs underwent a specific, rapid and efficient accumulation into the xenografted tumor, through the tumor-associated vasculature, and (ii) they remain, to a large extent, intact for at least 1 h within tumor region. Intensity of the FRET signal in tumor reached maximum values 2 h post-injection and then remained stable over the time-course of the experiment. In contrast, the fluorescence intensity in the donor channel increased slowly over the first
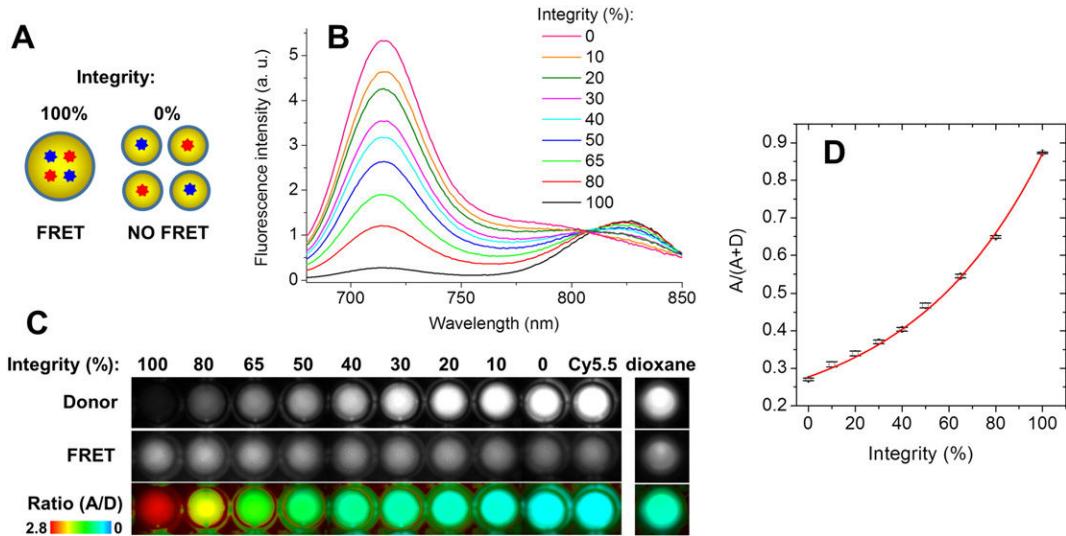
Fig. 5. Calibration of ratiometric *in vivo* images using mixtures of intact FRET NCs with NCs containing separately donor and acceptor at low concentration. The mixing is done to preserve the same concentration of dyes: 100% integrity corresponds to FRET NCs (1% of Cy5.5LP and 1% of Cy7.5LP) diluted in PBS 1000-fold from the original formulation, while 0% integrity corresponds to a mixture of NCs containing separately donor (0.1% of Cy5.5LP) and acceptor (0.1% Cy7.5LP), both diluted at 100-fold in PBS. The latter mixture models the disintegrated NCs, where donor and acceptor separate and get diluted in the tissue (A). (B) Fluorescence spectra of the obtained solutions. (C) Fluorescence images of these mixtures acquired with the *in vivo* imaging set-up: donor (Cy5.5LP) channel (upper panels), acceptor (Cy7.5LP) FRET channel (middle panels), and the acceptor/donor ratio images (lower panels). NCs containing only donor dye (Cy5.5LP) and FRET NCs diluted 1000-fold in dioxane (second model of the complete disintegration) are also shown. (D) Calibration curve of A/(A + D) ratio *vs* the level of integrity of NCs obtained based on data in (C) panel. The error bars represent the standard error of the mean ($n = 3$).

6 h post-injection, but drastically increased 24 h post-injection. The ratiometric imaging showed that relative intensity of the FRET acceptor decreased continuously with time, reaching the lowest values after 24 h of incubation. Experiments with control NCs containing only donor dye Cy5.5LP confirmed rapid accumulation of NCs into the tumor region already at 1 h post-injection (Fig. 7A). The acceptor channel remained dim in the tumor region, in line with expected absence of FRET. The intensity in the donor channel continued to gradually increase over time, reaching saturation after 24 h, whereas in the acceptor channel the intensity remained poor (Fig. S11). Imaging of mice organs (Fig. S12) dissected from animals at 24 h post-administration revealed that fluorescence of tumor was slightly brighter than that of liver (by 30%, $p = 0.02$, n = 4). By contrast, fluorescence of other studied organs (spleen, lungs, heart and kidneys) was many-fold lower ($p \leq 0.0002$, n = 4), suggesting that both tumors and liver are the main targets for accumulation of our NCs, in line with the whole animal *in vivo* imaging data.

After accounting for the background fluorescence, we quantified the FRET proximity ratio in tumor-bearing mice by analyzing the A/(A + D) ratio (Fig. 7B) and then converted it to the NCs integrity level for different post-administration times (Fig. 7C). Importantly, after 2 h, when the signal of NCs from the tumor region was already very strong (Fig. 7A), the integrity of NCs was still at 77 ± 1% (Fig. 7C), indicating that they

could enter the tumor with minimal loss of integrity. Nevertheless, the loss of integrity was faster than in the blood circulation. Indeed, in tail vein after 6 h NCs integrity was at 71 ± 3%, whereas for tumor it dropped already to 40 ± 4% (Fig. 7C) ($p < 0.003$, n = 3). The integrity half-life for our NCs in tumor was 4.4 ± 0.3 h, which was even faster than in the liver of healthy mice (8.2 ± 0.4 h, $p < 0.001$, n = 3). We provide the first evidence for the kinetics of disintegration of lipid NCs in tumor bearing mice *in vivo* and show that the lipid NCs preserve their content in the blood circulation, then they can enter tumors with minimal loss of integrity and finally after accumulation in the tumors they disintegrate on the time scale of hours. One should also note that disintegration of NCs inside blood circulation of tumor bearing mice was considerably faster than in healthy mice, which can be seen from the integrity levels at 6 h of post-administration (71 ± 3% *vs* 93 ± 2%, $p < 0.003$, n = 3). On the other hand, the clearance from blood circulation, measured using control NCs bearing only Cy5.5LP (Fig. S11) in tumor-bearing mice was similar to that in healthy mice (Fig. S8).

In conclusion, we propose here an original approach to obtain near-infrared lipid nanocarriers with efficient FRET and excellent brightness. It is based on hydrophobic counterions that increase many-fold the solubility of cyanines dyes in oil and thereby enable their high loading inside NCs, required for FRET. We provide here clear demonstration that these new NCs allow reliable imaging and monitoring NCs' integrity *in*
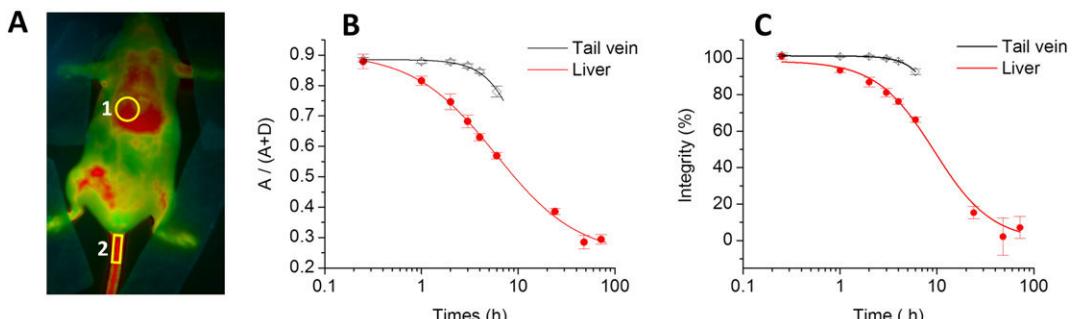
Fig. 6. Quantitative analysis of NCs integrity in living mice. (A) Ratio image of healthy mice showing the regions of interest: liver (1) and tail vein (2). (B, C) Analysis of the A/(A + D) ratio (B) and integrity (C) of NCs in different regions of healthy mice as a function of post-administration time. Ratio analysis in the tail vein was done until 6 h, because after that the signal was too low. Three mice were analyzed, the error bars represent the standard error of the mean (n = 3).
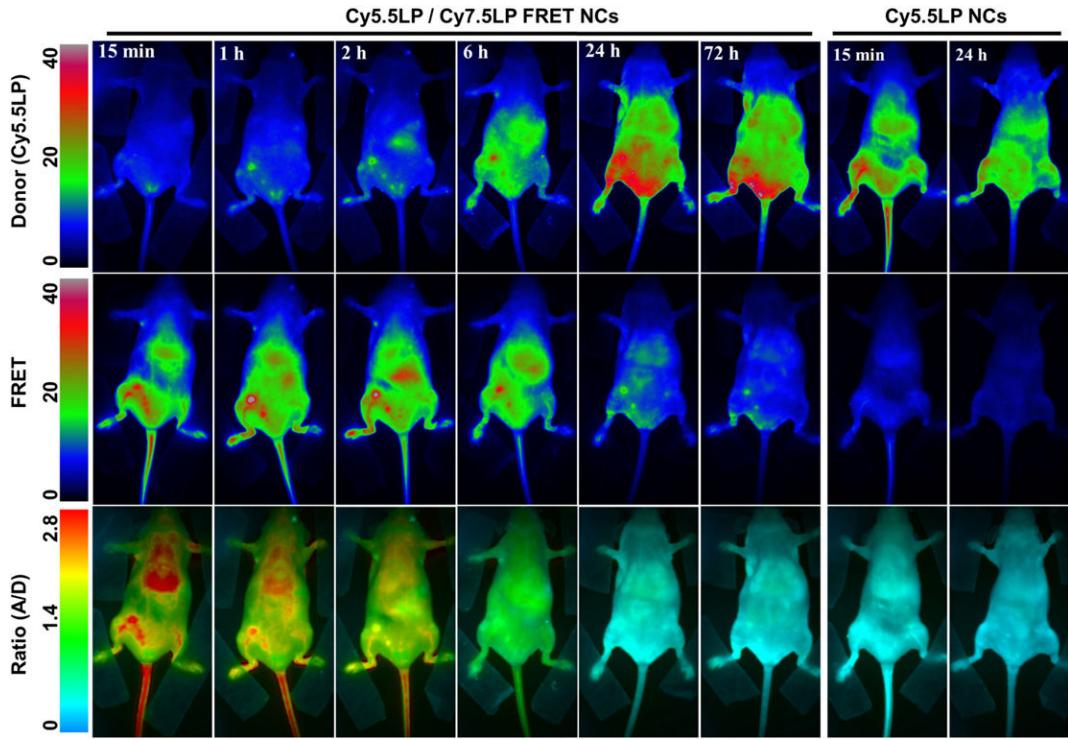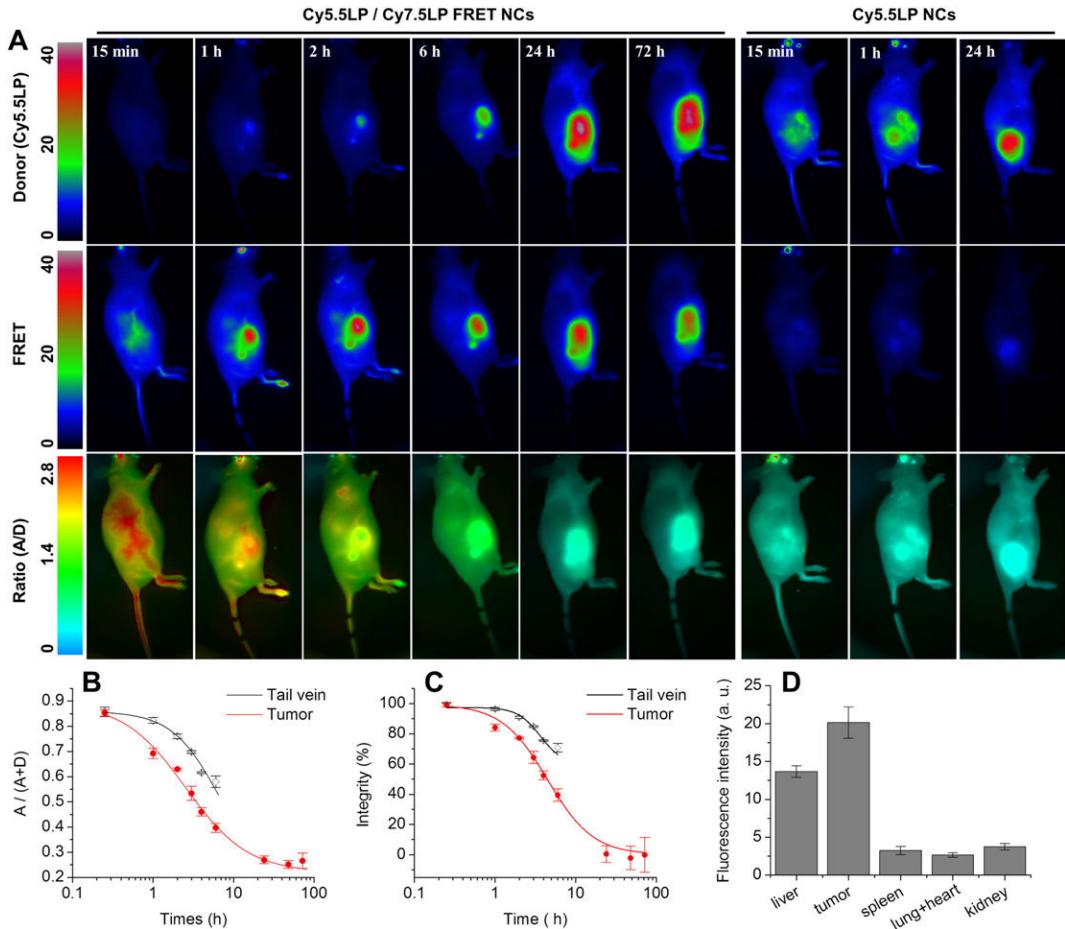
Fig. 7. (A) FRET imaging of tumor-bearing nude mice at different times after injected with NIR-FRET lipid NCs (1% of Cy5.5LP and Cy7.5LP each) or control NCs with donor dye only (1% of Cy5.5LP dye). Upper panels present intensity images of the Cy5.5LP channel (700 nm), middle panels present images of Cy7.5LP channel (820 nm), while the lower panels present ratiometric images (acceptor/donor). The excitation wavelength was 630 nm. Experiment was repeated on three mice, the set of data for the other two mice is reported in the Supplementary information section (Fig. S10). (B, C) Analysis of the A/(A + D) ratio (B) and integrity (C) of NCs in different regions of tumor-bearing mice as a function of post-administration time. Three mice were analyzed, the error bars represent the standard error of the mean (n = 3). (D) Fluorescence intensity of organs dissected from animals at 24 h post-administration with NCs containing 1% of Cy5.5LP dye. The error bars corresponds to standard error of the mean (n = 4). Images of organs are presented in Fig. S12.

vivo. Notably, we provide here whole-animal imaging with apparently higher resolution compared to existing FRET systems for *in vivo* imaging [9,24,25]. Importantly, we were able to accurately resolve the follow-up of NCs integrity directly in the blood circulation of living mice, which was possible before only by using dedicated intravital microscopy [9,27]. The high-quality of the obtained images is probably due to relatively high fluorescence quantum yield, dye-loading and injection dose, as well as optimal NIR spectral excitation and emission windows of our FRET NCs. Moreover, by dividing two emission channels, we generated high quality ratiometric images capable of resolving some features of the vascular system and tissues that are usually not assessable by live whole-animal fluorescence imaging. The intensity ratio is the absolute parameter, which is almost independent on the concentration of the imaging agent and excitation light intensity [31,32,55,56]. Therefore, the ratio signal provides quantitative information about the changes in the emission spectra of the probe in the imaged system. In our case, due to calibration of the spectral response of the FRET NCs directly under the *in vivo* imaging setup, we achieved a reliable read-out of the integrity of our NCs by ratiometric analysis, which would not be possible using absolute intensity measurements. It should be noted that in addition to calibration of the imaging system, this method requires subtraction of the background, which is relatively high in small animal fluorescence imaging. One important point that is difficult to take into account is the difference in the penetration depth for 700- and 820-nm light [30], which may affect the precision of the quantitative analysis.

The described methodology enabled, for the first time, to quantify by *in vivo* fluorescence imaging the integrity of NCs in different regions of healthy and tumor-bearing mice. It revealed that injected NCs remain nearly intact after 6 h in the blood circulation of healthy mice, whereas their integrity significantly dropped to 66 ± 2% in the liver of healthy mice, and up to 40 ± 4% in tumors. Nevertheless, lipid NCs appeared remarkably stable as they could enter tumors rapidly with minimal loss of integrity, showing for instance 77 ± 1% of the integrity at 2 h of post-injection. Thus, NCs can preserve their content in the blood circulation, enter tumors in nearly intact form and then release this content on the time scale of hours. This data shows the strong potential of NCs as efficient carriers of drugs and contrast agents. The remarkable stability of lipid NCs is an important finding of this work. Commonly, nanoemulsions are considered as liquid systems that should not be stable enough *in vivo* and require, for instance, specially designed surface of lipids with long PEG chains [25,36]. However, in the present work, we showed for the first time that nanoemulsion droplets built only from oil (medium chain triglycerides) and a surfactant (Cremophor® ELP) exhibited no signs of disintegration in blood circulation for hours. This result contrasts strongly with the poor capacity of these NCs to keep medium polar molecules like Nile Red, which is rapidly released in biological media [41,57].

Our NCs showed remarkably efficient accumulation in tumors, which can be clearly assigned to the EPR effect originating from the leaky nature of the tumor vesicles [15,58]. The efficiency of the passive EPR tumor accumulation is generally proportional to the circulation

time of the agent in the bloodstream. In this respect, our NCs present dense PEG shell which is known to prolong the circulation time of nano-particles [59].

Finally, the key finding that has never been shown for lipid NCs is their capacity to accumulate in tumors in nearly intact form. This prop-erty is known for polymer nanoparticles, which are established drug de-livery vehicles into tumors [60,61], and inorganic nanoparticles, such as quantum dots covered with robust organic shell [9,62]. The capacity of our nano-emulsion droplets to preserve their integrity after accumula-tion in tumors is particularly remarkable given the liquid nature of their core. This result shows the strong potential of these lipid NCs as nanoscale platform for *in vivo* imaging, drug delivery and image guided surgery.

Acknowledgments

Appendix A. Supplementary data

Supplementary data to this article can be found online at http://dx.doi.org/10.1016/j.jconrel.2016.06.027.

References

[1] D.E. Lee, H. Koo, I.C. Sun, J.H. Ryu, K. Kim, I.C. Kwon, Multifunctional nanoparticles for multimodal imaging and theragnosis, Chem. Soc. Rev. 41 (2012) 2656–2672.

[2] P.D. Howes, R. Chandrawati, M.M. Stevens, Colloidal nanoparticles as advanced bio-logical sensors, Science 346 (2014) 1247390.

[3] A. Reisch, A.S. Klymchenko, Fluorescent Polymer Nanoparticles Based on Dyes: Seeking Brighter Tools for Bioimaging, Small 12 (2016) 1968–1992.

[4] J.-W. Yoo, D.J. Irvine, D.E. Discher, S. Mitragotri, Bio-inspired, bioengineered and bio-mimetic drug delivery carriers, Nat. Rev. Drug Discov. 10 (2011) 521–535.

[5] D. Peer, J.M. Karp, S. Hong, O.C. FaroKhzad, R. Margalit, R. Langer, Nanocarriers as an emerging platform for cancer therapy, Nat. Nanotechnol. 2 (2007) 751–760.

[6] E. Locatelli, I. Monaco, M.C. Franchini, Hard and soft nanoparticles for image-guided surgery in nanomedicine, J. Nanopart. Res. 17 (2015) 1–17.

[7] L. Bu, B. Shen, Z. Cheng, Fluorescent imaging of cancerous tissues for targeted sur-gery, Adv. Drug Deliv. Rev. 76 (2014) 21–38.

[8] H.S. Choi, W. Liu, F. Liu, K. Nasr, P. Misra, M.G. Bawendi, et al., Design considerations for tumour-targeted nanoparticles, Nat. Nanotechnol. 5 (2010) 42–47.

[9] Y.M. Zhao, I. van Rooy, S. Hak, F. Fay, J. Tang, C.D. Davies, et al., Near-infrared fluores-cence energy transfer imaging of nanoparticle accumulation and dissociation kinet-ics in tumor-bearing mice, ACS Nano 7 (2013) 10362–10370.

[10] S.S. D'Souza, P.P. DeLuca, Methods to assess in vitro drug release from injectable polymeric particulate systems, Pharm. Res. 23 (2006) 460–474.

[11] D.E. Owens, N.A. Peppas, Opsonization, biodistribution, and pharmacokinetics of polymeric nanoparticles, Int. J. Pharm. 307 (2006) 93–102.

[12] A.E. Nel, L. Maedler, D. Velegol, T. Xia, E.M.V. Hoek, P. Somasundaran, et al., Under-standing biophysicochemical interactions at the nano-bio interface, Nat. Mater. 8 (2009) 543–557.

[13] Y. Li, M.S. Budamagunta, J. Luo, W. Xiao, J.C. Voss, K.S. Lam, Probing of the assembly structure and dynamics within nanoparticles during interaction with blood pro-teins, ACS Nano 6 (2012) 9485–9495.

[14] S. Hak, E. Helgesen, H.H. Hektoen, E.M. Huuse, P.A. Jarzyna, W.J.M. Mulder, et al., The effect of nanoparticle polyethylene glycol surface density on ligand-directed tumor targeting studied in vivo by dual modality imaging, ACS Nano 6 (2012) 5648–5658.

[15] J. Fang, H. Nakamura, H. Maeda, The EPR effect: unique features of tumor blood ves-sels for drug delivery, factors involved, and limitations and augmentation of the ef-fect, Adv. Drug Deliv. Rev. 63 (2011) 136–151.

[16] W.G. Kreyling, A.M. Abdelmonem, Z. Ali, F. Alves, M. Geiser, N. Haberl, et al., In vivo integrity of polymer-coated gold nanoparticles, Nat. Nanotechnol. 10 (2015) 619–623.

[17] V. Ntziachristos, C. Bremer, R. Weissleder, Fluorescence imaging with near-infrared light: new technological advances that enable in vivo molecular imaging, Eur. Radiol. 13 (2003) 195–208.

[18] J.V. Frangioni, In vivo near-infrared fluorescence imaging, Curr. Opin. Chem. Biol. 7 (2003) 626–634.

[19] J.H. Rao, A. Dragulescu-Andrasi, H.Q. Yao, Fluorescence imaging in vivo: recent ad-vances, Curr. Opin. Biotechnol. 18 (2007) 17–25.

[20] C. Darne, Y.J. Lu, E.M. Sevick-Muraca, Small animal fluorescence and bioluminesce-cence tomography: a review of approaches, algorithms and technology update, Phys. Med. Biol. 59 (2014) R1–R64.

[21] E.A. Jares-Erijman, T.M. Jovin, FRET imaging, Nat. Biotechnol. 21 (2003) 1387–1395.

[22] K.E. Sapsford, L. Berti, I.L. Medintz, Materials for fluorescence resonance energy transfer analysis: beyond traditional donor-acceptor combinations, Angew. Chem. Int. Ed. 45 (2006) 4562–4588.

[23] T. Skajaa, Y. Zhao, D.J. van den Heuvel, H.C. Gerritsen, D.P. Cormode, R. Koole, et al., Quantum dot and Cy5.5LP labeled nanoparticles to investigate lipoprotein biointeractions via Forster resonance energy transfer, Nano Lett. 10 (2010) 5131–5138.

[24] S.W. Morton, X. Zhao, M.A. Quadir, P.T. Hammond, FRET-enabled biological charac-terization of polymeric micelles, Biomaterials 35 (2014) 3489–3496.

[25] A.L. Laine, J. Gravier, M. Henry, L. Sancey, J. Bejaud, E. Pancani, et al., Conventional versus stealth lipid nanoparticles: formulation and in vivo fate prediction through FRET monitoring, J. Control. Release 188 (2014) 1–8.

[26] S. Hak, N.K. Reitan, O. Haraldseth, Davies CdL. Intravital microscopy in window chambers: a unique tool to study tumor angiogenesis and delivery of nanoparticles, Angiogenesis 13 (2010) 113–130.

[27] H. Chen, S. Kim, W. He, H. Wang, P.S. Low, K. Park, et al., Fast release of lipophilic agents from circulating PEG-PDLLA micelles revealed by in vivo Förster resonance energy transfer imaging, Langmuir 24 (2008) 5213–5217.

[28] Z.Q. Guo, S. Park, J. Yoon, I. Shin, Recent progress in the development of near-infra-red fluorescent probes for bioimaging applications, Chem. Soc. Rev. 43 (2014) 16–29.

[29] S.L. Luo, E.L. Zhang, Y.P. Su, T.M. Cheng, C.M. Shi, A review of NIR dyes in cancer targeting and imaging, Biomaterials 32 (2011) 7127–7138.

[30] H. Kobayashi, M. Ogawa, R. Alford, P.L. Choyke, Y. Urano, New strategies for fluores-cent probe design in medical diagnostic imaging, Chem. Rev. 110 (2010) 2620–2640.

[31] A. H-w, K.L. Hazelwood, M.W. Davidson, R.E. Campbell, Fluorescent protein FRET pairs for ratiometric imaging of dual biosensors, Nat. Methods 5 (2008) 401–403.

[32] X.F. Zhou, F.Y. Su, H.G. Lu, P. Senechal-Willis, Y.Q. Tian, R.H. Johnson, et al., An FRET-based ratiometric chemosensor for in vitro cellular fluorescence analyses of pH, Bio-materials 33 (2012) 171–180.

[33] K.K. Ng, M. Takada, C.C.S. Jin, G. Zheng, Self-sensing porphysomes for fluorescence-guided photothermal therapy, Bioconjug. Chem. 26 (2015) 345–351.

[34] M.F. Attia, N. Anton, M. Chiper, R. Akasov, H. Anton, N. Messaddeq, et al., Biodistribution of X-ray iodinated contrast agent in nano-emulsions is controlled by the chemical nature of the oily core, ACS Nano 8 (2014) 10537–10550.

[35] X. Li, N. Anton, G. Zuber, M.J. Zhao, N. Messaddeq, F. Hallouard, et al., Iodinated alpha-tocopherol nano-emulsions as non-toxic contrast agents for preclinical X-ray imaging, Biomaterials 34 (2013) 481–491.

[36] N.T. Huynh, C. Passirani, P. Saulnier, J.P. Benoit, Lipid nanocapsules: a new platform for nanomedicine, Int. J. Pharm. 379 (2009) 201–209.

[37] N. Anton, J.-P. Benoit, P. Saulnier, Design and production of nanoparticles formulated from nano-emulsion templates - a review, J. Control. Release 128 (2008) 185–199.

[38] J.M. Gutierrez, C. Gonzalez, A. Maestro, I. Sole, C.M. Pey, J. Nolla, Nano-emulsions: new applications and optimization of their preparation, Curr. Opin. Colloid Interface Sci. 13 (2008) 245–251.

[39] K. Hormann, A. Zimmer, Drug delivery and drug targeting with parenteral lipid nanoemulsions - a review, J. Control. Release 223 (2016) 85–98.

[40] N. Anton, T.F. Vandamme, The universality of low-energy nano-emulsification, Int. J. Pharm. 377 (2009) 142–147.

[41] A.S. Klymchenko, E. Roger, N. Anton, H. Anton, I. Shulov, J. Vermot, et al., Highly lipo-philic fluorescent dyes in nano-emulsions: towards bright non-leaking nano-drop-lets, RSC Adv. 2 (2012) 11876–11886.

[42] J. Gravier, L. Sancey, S. Hirsjaervi, E. Rustique, C. Passirani, J.-P. Benoit, et al., FRET im-aging approaches for in vitro and in vivo characterization of synthetic lipid nanopar-ticles, Mol. Pharm. 11 (2014) 3133–3144.

[43] J. Merian, R. Boisgard, P.-A. Bayle, M. Bardet, B. Tavitian, I. Texier, Comparative biodistribution in mice of cyanine dyes loaded in lipid nanoparticles, Eur. J. Pharm. Biopharm. 93 (2015) 1–10.

[44] V.N. Kilin, H. Anton, N. Anton, E. Steed, J. Vermot, T.E. Vandamme, et al., Counterion-enhanced cyanine dye loading into lipid nano-droplets for single-particle tracking in zebrafish, Biomaterials 35 (2014) 4950–4957.

[45] B.E. Schaafsma, J.S.D. Mieog, M. Hutteman, J.R. Van Der Vorst, P.J.K. Kuppen, C.W.G.M. Löwik, et al., The clinical use of indocyanine green as a near-infrared fluo-rescent contrast agent for image-guided oncologic surgery, J. Surg. Oncol. 104 (2011) 323–332.

[46] T. Ishizawa, N. Fukushima, J. Shibahara, K. Masuda, T. Tamura, T. Aoki, et al., Real-time identification of liver cancers by using indocyanine green fluorescent imaging, Cancer 115 (2009) 2491–2504.

[47] I. Texier, M. Goutayer, A. Da Silva, L. Guyon, N. Djaker, V. Josserand, et al., Cyanine-loaded lipid nanoparticles for improved in vivo fluorescence imaging, J. Biomed. Opt. 14 (2009) 054005.

[48] S. Preus, L.M. Wilhelmsson, Advances in quantitative FRET-based methods for studying nucleic acids, Chembiochem 13 (2012) 1990–2001.

[49] T. Shibue, M.W. Brooks, R.A. Weinberg, An integrin-linked machinery of cytoskeletal regulation that enables experimental tumor initiation and metastatic colonization, Cancer Cell 24 (2013) 481–498.

[50] M.A. Karreman, L. Mercier, N.L. Schieber, T. Shibue, Y. Schwab, J.G. Goetz, Correlating intravital multi-photon microscopy to 3D electron microscopy of invading tumor cells using anatomical reference points, PLoS One 9 (2014) e114448.

[51] J. Schindelin, I. Arganda-Carreras, E. Frise, V. Kaynig, M. Longair, T. Pietzsch, et al., Fiji: an open-source platform for biological-image analysis, Nat. Methods 9 (2012) 676–682.

[52] T.J. Russin, E.Ï. Altmoğlu, J.H. Adair, P.C. Eklund, Measuring the fluorescent quantum efficiency of indocyanine green encapsulated in nanocomposite particulates, J. Phys. Condens. Matter 22 (2010) 334217.

[53] E. Nir, X. Michalet, K.M. Hamadani, T.A. Laurence, D. Neuhauser, Y. Kovchegov, et al., Shot-noise limited single-molecule FRET histograms: comparison between theory and experiments, J. Phys. Chem. B 110 (2006) 22103–22124.

[54] J.A. Broussard, B. Rappaz, D.J. Webb, C.M. Brown, Fluorescence resonance energy transfer microscopy as demonstrated by measuring the activation of the serine/threonine kinase Akt, Nat. Protoc. 8 (2013) 265–281.

[55] V.V. Shynkar, A.S. Klymchenko, C. Kunzelmann, G. Duportail, C.D. Muller, A.P. Demchenko, et al., Fluorescent biomembrane probe for ratiometric detection of apoptosis, J. Am. Chem. Soc. 129 (2007) 2187–2193.

[56] Y. Kurishita, T. Kohira, A. Ojida, I. Hamachi, Rational design of FRET-based ratiometric chemosensors for in vitro and in cell fluorescence analyses of nucleoside polyphosphates, J. Am. Chem. Soc. 132 (2010) 13290–13299.

[57] G. Bastiat, C.O. Pritz, C. Roider, F. Fouchet, E. Lignieres, A. Jesacher, et al., A new tool to ensure the fluorescent dye labeling stability of nanocarriers: a real challenge for fluorescence imaging, J. Control. Release 170 (2013) 334–342.

[58] S.K. Hobbs, W.L. Monsky, F. Yuan, W.G. Roberts, L. Griffith, V.P. Torchilin, et al., Regulation of transport pathways in tumor vessels: role of tumor type and microenvironment, Proc. Natl. Acad. Sci. U. S. A. 95 (1998) 4607–4612.

[59] J.V. Jokerst, T. Lobovkina, R.N. Zare, S.S. Gambhir, Nanoparticle PEGylation for imaging and therapy, Nanomedicine 6 (2011) 715–728.

[60] R. Devulapally, R. Paulmurugan, Polymer nanoparticles for drug and small silencing RNA delivery to treat cancers of different phenotypes, Wiley Interdiscip. Rev. Nanomed. Nanobiotechnol. 6 (2014) 40–60.

[61] A. Schadlich, H. Caysa, T. Mueller, F. Tenambergen, C. Rose, A. Gopferich, et al., Tumor accumulation of NIR fluorescent PEG PLA nanoparticles: impact of particle size and human xenograft tumor model, ACS Nano 5 (2011) 8710–8720.

[62] X.H. Gao, Y.Y. Cui, R.M. Levenson, L.W.K. Chung, S.M. Nie, In vivo cancer targeting and imaging with semiconductor quantum dots, Nat. Biotechnol. 22 (2004) 969–976.

2.4.4   Conclusion

Ces nanoparticules lipidiques ont l'avantage de rester dans la circulation sanguine au cours du temps et de permettre l'imagerie des vaisseaux sanguins par luminographie grâce à leur fluorescence intense (Figure 38).
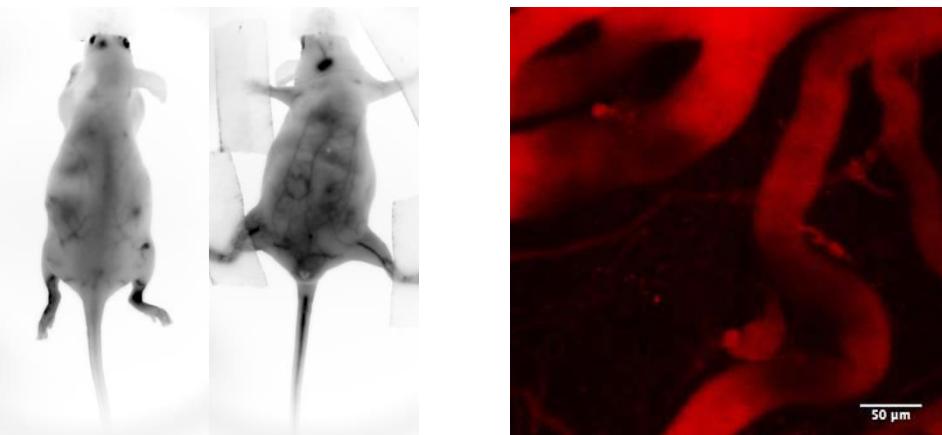
*Figure 38 : **Angiographie par fluorescence.** La forte intensité de fluorescence des nanoparticules permettent de générer des images de type angiographie sur l'animal entier (Image de gauche). Les nanopartiicules sont aussi compatibles avec l'imagerie intravitale et permettent ici d'imager la vascularisation de l'oreille de souris (Image de droite).*

De plus ces nanoparticules sont compatibles avec la microscopie multiphotonique. Elles ont été testées pour l'imagerie de vascularisation de l'oreille de souris (Figure 38).

Dans des études précédentes ces nanoparticules ont été chargées avec un composé iodé rendant ainsi possible leur détection par rayons X (Li et al., 2013; Attia et al., 2014). Afin de faciliter la corrélation lors de la procédure de CLEM *in vivo*, ces nanoparticules pourraient devenir bimodal en contenant à la fois des fluorochromes pour la microscopie intravitale ainsi que de l'iode pour l'imagerie aux rayons X. La difficulté ici est la conservation des nanoparticules dans les vaisseaux sanguins lors de la fixation intracardiaque de la souris.

Une autre propriété de ces nanoparticules est de s'accumuler et de se dégrader au niveau de la tumeur. De ce fait ces nanoparticules pourraient devenir une nouvelle méthode pour délivrer des drogues anti tumorales au cœur de la tumeur.

2.5 Caractérisation de l'ultrastructure des invadopodes *in vitro* & *in vivo*

2.5.1 Contexte

Par des approches de biologie moléculaire il a été démontré *in vivo* que les invadopodes favorisent l'invasion tumorale en conférant aux cellules tumorales un pouvoir invasif plus important. Ainsi les invadopodes sont nécessaires à la dégradation de la membrane basale, à la migration dans la MEC, l'intravasation et l'extravasation dans un organe à distance de la tumeur primaire.

Cependant depuis la première description des invadopodes *in vitro* dans les années 80, l'étude de la structure des invadopodes a essentiellement été étudiées *in vitro*. Actuellement très peu d'études ont permis de mettre en évidence la présence des invadopodes *in vivo* et aucune ne décrit l'ultrastructure des invadopodes *in vivo*.

Etant donné que les protocoles de CLEM que nous avons créés fonctionnent en routine, ils seraient pertinents de les appliquer à l'étude de l'ultrastructure des invadopodes *in vivo*.

En collaboration avec l'équipe de F. Saltel (INSERM, Bordeaux) nous avons généré différentes lignées cellulaires exprimant à la fois Tks5, protéine d'échafaudage des invadopodes, et le peptide LifeAct (Riedl et al., 2008) qui se lie à l'actine, couplés tous les deux à des protéines fluorescentes. La combinaison de ces deux marqueurs nous permet de visualiserles invadopodes.

Cette étude est en cours de réalisation. Les données présentées ci-dessous représente l'état d'avancement actuel de ce travail.

2.5.2 Etude *in vitro*

Dans un premier temps nous nous sommes intéressés à la caractérisation des invadopodes *in vitro*. Les cellules A431 (Carcinome épidermoïde humain) et NIH 3T3 (Fibroblastes d'embryon de souris) ont été cultivées sur différents substrats. Un substrat composé de gélatine permettant la formation d'invadopodes dans le cas des A431 et de rosettes dans le cas des NIH 3T3. Le deuxième substrat constitué de collagène fibrillaire de type 1 induit la formation d'invadopodes linéaires. Après imagerie confocale les cellules ont été fixées et préparées pour la microscopie électronique.

2.5.2.1 Matériel et méthode

Culture cellulaire sur substrat de gélatine et de collagène

Pour réaliser la CLEM sur cellules nous avons utilisé des films d'aclar microgravés (Spiegelhalter et al., 2014). Ces films ont été déposés dans des boites de 24 puits. Une solution de gélatine à 0.5 mg/ml a été incubée dans chaque puits pendant 5 min. Le surplus de solution a ensuite été aspiré et les films ont séchés à l'air libre. Pour la condition collagène, une solution de collagène type 1 a été

diluée à 1,5 mg/ml dans du PBS et le collagène a été marqué par ajout dans la solution de Succinimidyl Ester-AlexaFluor 647 dilué au 1000ème. La solution déposée dans les puits a été incubée 4h à 37°C. Le surplus de collagène polymérise a ensuite été enlevé par aspiration. Les cellules ont ensuite été déposées à une concentration de 20 000 cellules/ml et ont été incubées toute la nuit sur collagène.

CLEM in vitro

Les cellules sur films d'aclar ont été transférées dans des boites de 35mm à fond de verre (MatTek P35G-1.0-20-C) pour l'imagerie confocale (Leica SP2) avec un objectif 63x (NA:1.32, Leica microsystems). Des images à fort grossissement des cellules et des structures d'intérêts (Invadopodes, invadopodes linéaires et rosettes) ont été acquises ainsi que des images à faible grossissement pour positionner les cellules d'intérêt en fonction des points de repères visibles en lumière transmise. Une fois imagées les cellules ont été fixées dans une solution constitué de 2.5% Paraformaldehyde (EMS 15713) et 2.5% Glutaraldehyde (GA, EMS 16220) dilué dans un tampon cacodylate 0.1M (EMS 11652) 1 h température ambiante. Les cellules ont ensuite été post-fixées dans un mélange constitué de Tétraoxyde d'osmium à 1% (EMS 19150) dilué dans un tampon cacodylate 0,1M pendant 1 h sur glace. Après rinçage à l'eau 3x10 min, les cellules ont été contrastées dans de l'acétate d'uranyl à 2% puis déshydratées dans des bains séquentiels d'alcool et infiltrées par de l'epon (résine). Des capsules d'enrobage (EMS 69910-05) ont été déposées sur le film d'aclar au-dessus des cellules d'intérêts. Les échantillons ont ensuite été mis à polymériser à 60°C toute la nuit. Le lendemain les capsules ont été remplies d'epon et repolymérisées à 60°C toute la nuit. Pour relocaliser les régions d'intérêts la surface du bloc de résine a été imagée à l'aide d'un stéréomicroscope permettant de relocaliser précisément la position des cellules par rapport aux points de repères. Le bloc de résine a ensuite été taillé précisément autour de la cellule d'intérêt. Finalement le bloc de résine a été coupé de façon sériée (épaisseur de la coupe 70nm), toutes les sections ont été collectées sur des grilles de microscopie électronique à fente. Les sections ont été imagées sur un microscope électronique à transmission CM12 (FEI company) avec une caméra CCD (Orius, Gatan). Les images de fluorescence ont été analysées avec Fiji (Schindelin et al., 2012) et les images de microscopie électronique ont été alignées et repositionnées en z avec TrakEM2 (Cardona et al., 2012) (Plugin dans Fiji). Les rendus 3D ont été réalisés avec Imod (Kremer et al., 1996).

2.5.2.2   Résultats

2.5.2.2.1   Formation d'invadopodes linéaires sur collagène

Les cellules A431 expriment à la fois la protéine Tks5-GFP et le peptide LifeAct-tdTomato tandis que les cellules NIH-3T3 expriment seulement le peptide LifeAct-mRuby. La colocalisation des différents

marquages permettent d'identifier la formation d'invadopodes linéaires sur une matrice constituée de fibres de collagène 1 (Figure 39 et Figure 40). Après fixation et préparation pour la microscopie électronique, l'échantillon est coupé et toutes les sections sont récoltées. L'examen de l'échantillon par TEM nous a permis de mettre en évidence pour les deux types cellulaires un remodelage important de la membrane cytoplasmique autour des fibres de collagènes. Les deux types cellulaires ont créé une dépression que ce soit sous la face ventrale pour les A431 ou au contact périphérique pour les NIH-3T3. Des vésicules de 100nm de diamètre sont observables au contact des fibres de collagènes dans l'échantillon NIH-3T3. Ces vésicules pourraient correspondre à des exosomes sécrétés au niveau du LI. Cette hypothèse pourrait être vérifiée par marquage fluorescent de la tétraspanine CD63, une protéine à quatre domaines transmembranaires enrichie dans les exosomes.
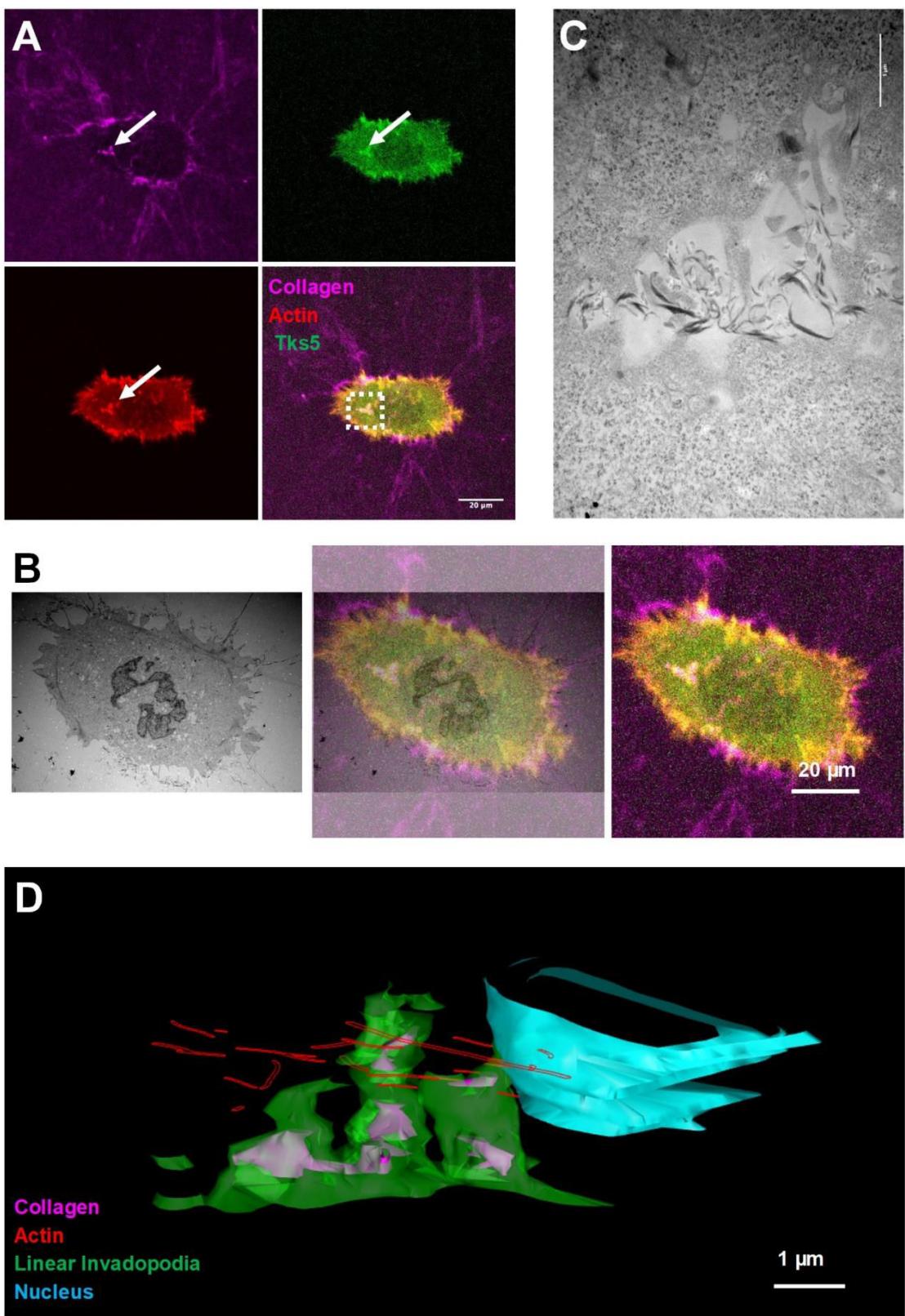
*Figure 39 : **Cellules A431 sur fibres de collagène 1. A** : Acquisition confocale d'une cellule sur collagène. La flèche indique la position de l'invadopode linéaire. Le cadre représente la zone imagée par microscopie électronique. **B** : Corrélation entre microscopie électronique et confocale. **C** : Image par microscopie électronique de l'invadopode linéaire. Les structures fibrillaires foncées correspondent aux fibres de collagène 1. **D** : Modélisation en 3D de l'invadopode linéaire.*
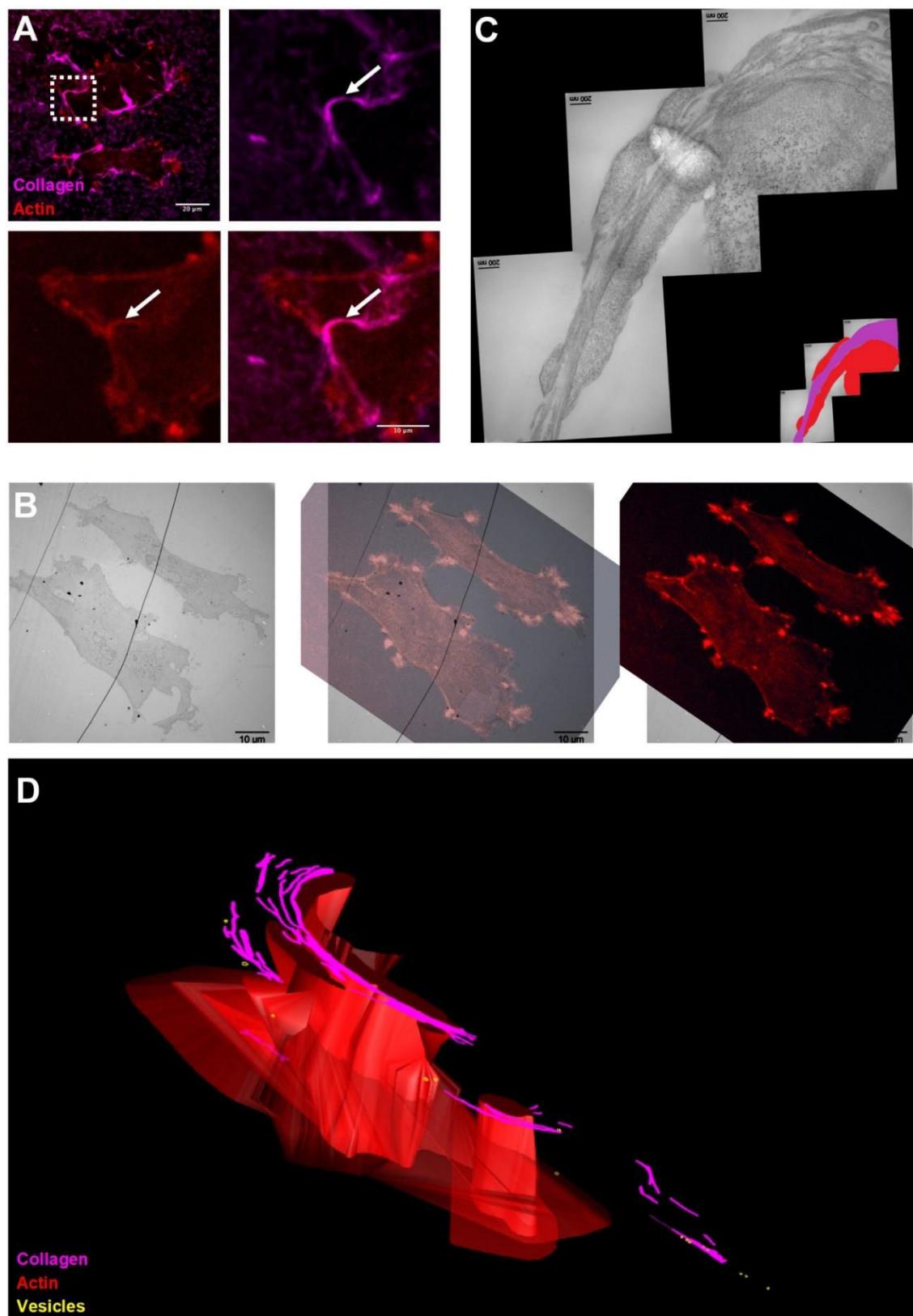
*Figure 40 : : **Cellules NIH-3T3 sur fibres de collagène 1. A** : Acquisition confocale d'une cellule sur collagène. La flèche indique la position de l'invadopode linéaire. Le cadre représente la zone imagée par microscopie électronique. **B** : Corrélation entre microscopie électronique et confocale. **C** : Image par microscopie électronique de l'invadopode linéaire. L'insert permet d'identifier les fibres de collagènes en violet et la structure correspondante à l'invadopode linéaire en rouge. **D** : Modélisation en 3D de l'invadopode linéaire.*

179

Les cellules NIH-3T3 au contact de la gélatine forment un type d'invadosome appelé rosettes. Les rosettes apparaissent comme des structures presque indépendantes de la cellule car elles sont connectées à la cellule sur une zone bien spécifique et leur contenue est totalement différent du cytoplasme. En effet, on observe à la jonction entre la rosette et la cellule une délimitation nette entre les deux compartiments. Les rosettes ne contiennent aucun organite mais on observe un enrichissement en ribosomes à la périphérie de la rosette signe d'une production protéique importante (Figure 41).
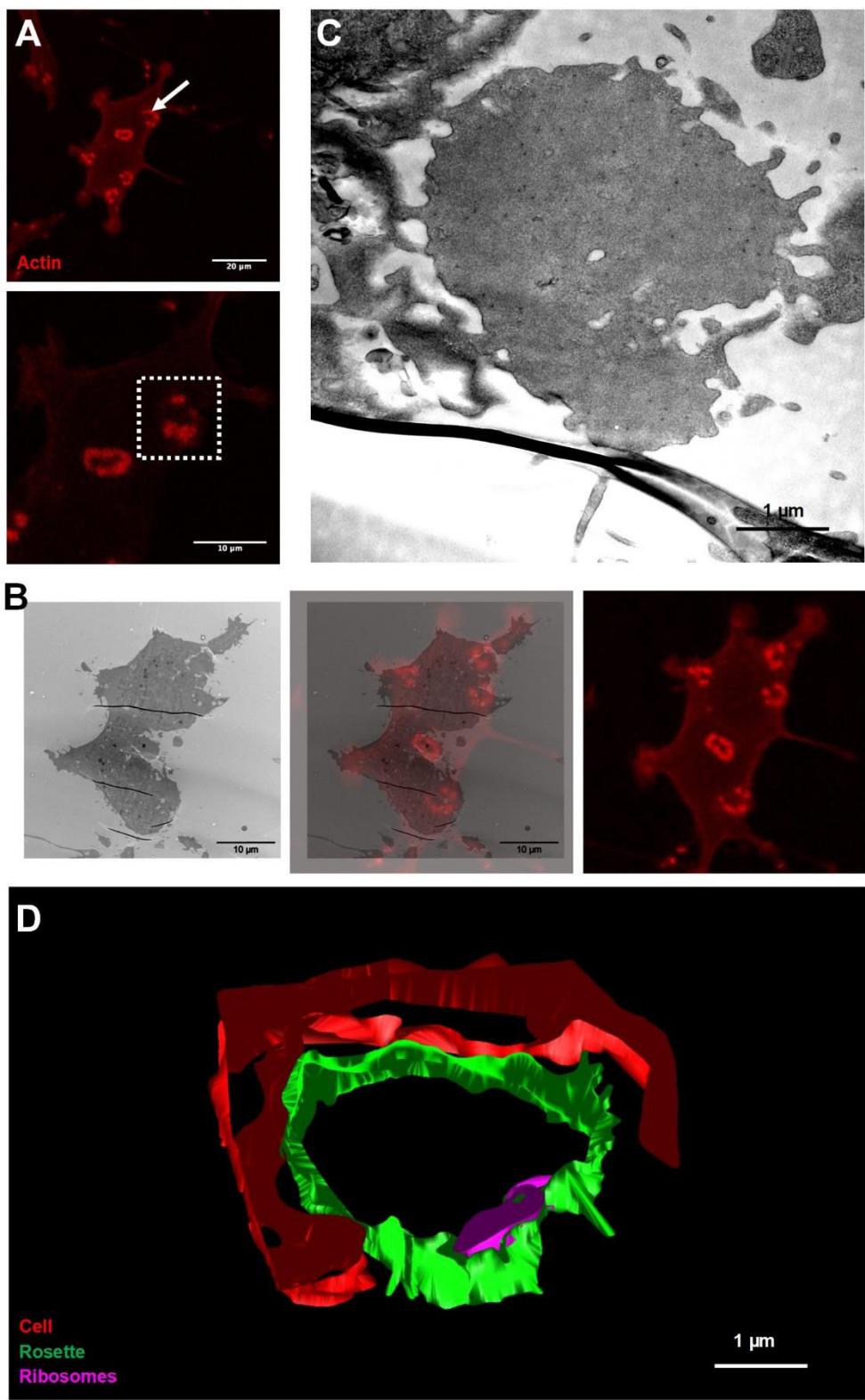
*Figure 41 : **Cellules NIH-3T3 sur gélatine. A** : Acquisition confocale d'une cellule sur gélatine. La flèche indique la position d'une rosette. Le cadre représente la zone imagée par microscopie électronique. **B** : Corrélation entre microscopie électronique et confocale. **C** : Image par microscopie électronique de la rosette. **D** : Modélisation en 3D de la rosette.*

Bien que les cellules A431 forment des invadopodes sur un substrat de gélatine, il n'a pas été pour l'instant possible de retrouver ces invadopodes par microscopie électronique.

2.5.3 Etude *in vivo*

Xenogreffe de cellules tumorales

Après trypsinisation et comptage les cellules ont été resuspendues à une concentration de 15 000 cellules/µl dans une solution contenant 50% de PBS et 50% de matrigel. Conservées sur glace, environ 150 000 cellules ont été injectées en sous cutané dans le pavillon de l'oreille de souris. L'imagerie intravitale est réalisée 48h après injection.

Imagerie Intravitale

La souris a été anesthésiée par injection intrapéritonéale d'une mixture Ketamine/Xylazine. L'oreille et la souris ont été disposées sur un support spécifique (Mercier et al., 2016). L'anesthésie a ensuite été poursuivie par l'utilisation d'un système anesthésie gazeuse (Isoflurane).

L'excitation à 940nm permet d'imager les fibres de collagène contenue dans la peau par génération de seconde harmonique ainsi que les fluorophores tel que la GFP ou td-Tomato. Le signal SHG est récolté par un détecteur positionné en position trans alors que le signal émis par les protéines fluorescentes GFP et td-Tomato est récolté par des détecteurs non descanés.

Une première partie de l'étude est consacrée à l'imagerie intravitale de cellules A375 issues d'un mélanome humain exprimant la protéine Tks5-GFP. Plusieurs séances d'imageries sur plusieurs souris différentes ont permis de visualiser le comportement de ces cellules dans l'oreille de souris. Une première quantification du nombre d'invadopodes formés par ces cellules a été réalisée sur les cellules de la masse tumorale ou selon leur morphologie. La quantification des invadopodes a été réalisée sur l'intensité de fluorescence de la protéine Tks5-GFP. Il s'agit d'une quantification test permettant de voir s'il était possible de réaliser ce type de mesure *in vivo (*Figure 42*)*.
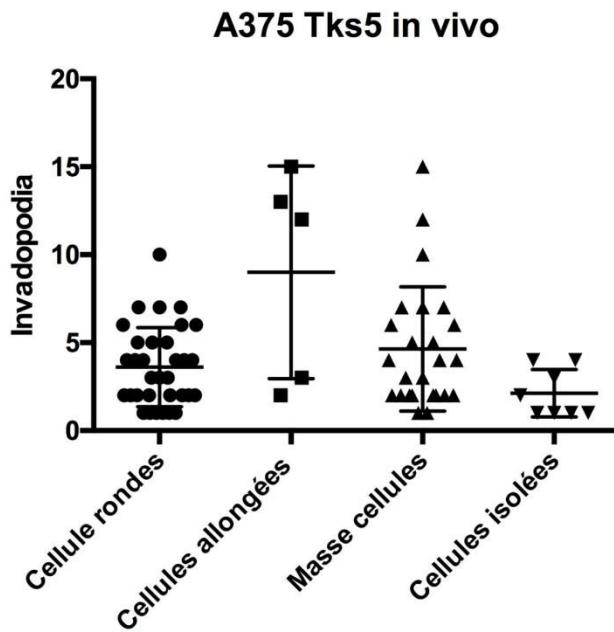
*Figure 42 : **Quantification du nombres d'invadopodes formées par les cellules A375 in vivo.***

On peut voir se dégager une certaine tendance où les cellules rondes qui pourraient migrer de façon amiboïde forment moins d'invadopodes que les cellules allongées de type mesenchymales. Cette tendance est en accord avec ce qui a été publié sur ce type de migration où les cellules amiboïdes ont moins recours à la dégradation de la MEC que les cellules mésenchymales (voir paragraphe 1.1.2). Autre observation concernant le nombre d'invadopodes formées dans un ensemble de cellules comparé aux invadopodes formés par des cellules isolées. La masse de cellule a recours plus souvent à la formation d'invadopodes alors que les cellules isolées en forment moins. Pour se frayer un chemin dans la MEC les cellules qui migrent de manière collective dégradent la MEC au niveau du front d'invasion mais aussi autour de la masse cellulaire pour élargir le passage. Les cellules isolées qui migrent de manière mesenchymale ou amiboïde forment moins d'invadopodes pour migrer dans la MEC.

La création des cellules A431 qui expriment à la fois la protéine Lifeact-tdTomato et Tks-GFP a permis l'observation d'invadopodes linéaires au niveau du derme de l'oreille riche en collagène de type 1 (Figure 43).
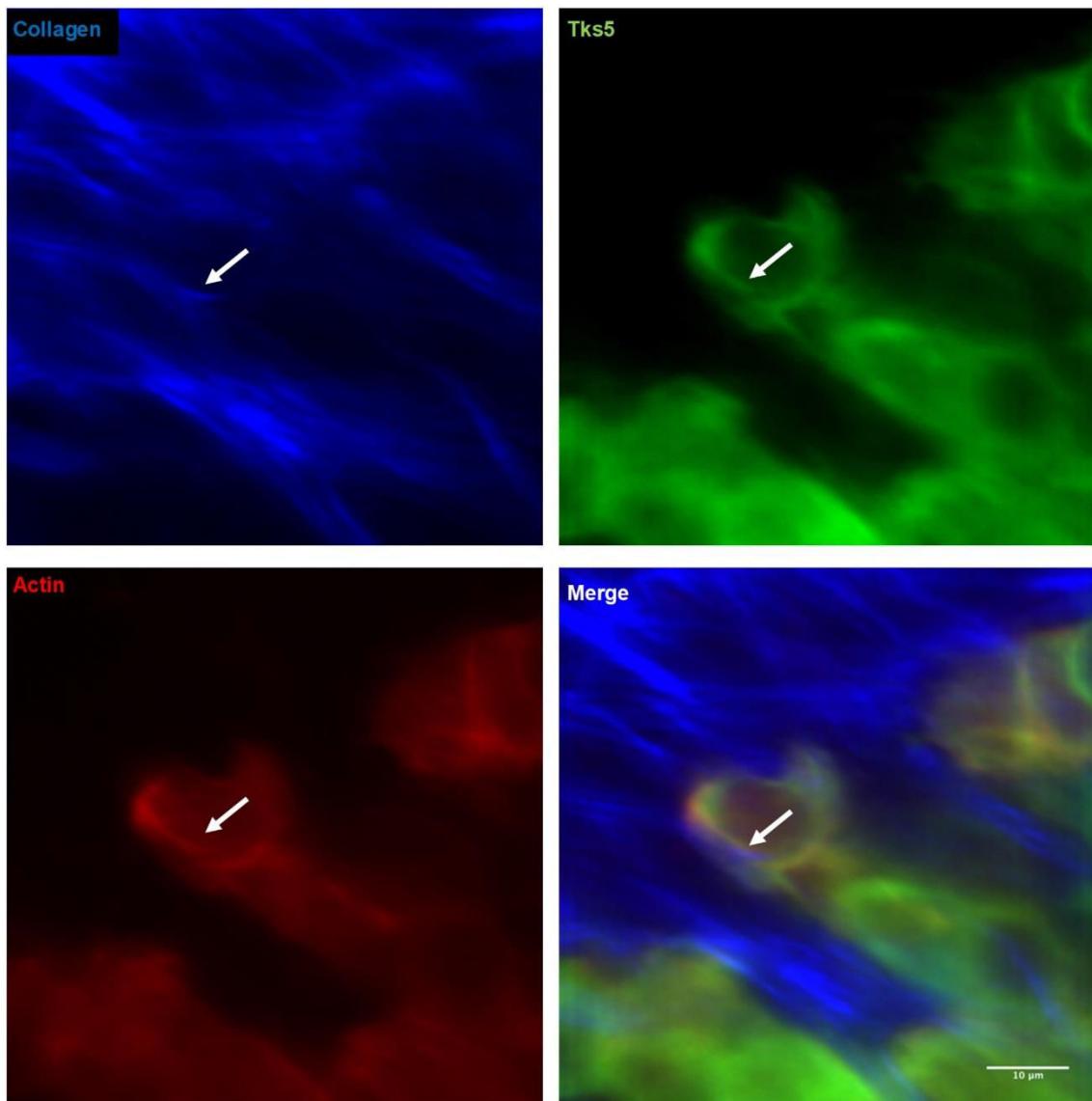
*Figure 43 : **Formation d'un invadopode linéaire in vivo.** Observation par microscopie multiphotonique de cellules A431 Tks5-GFP LifeAct-tdTomato dans l'oreille de souris. Le collagène (bleu) a été imagé par SHG. L'actine apparait rouge et Tks5 vert. La colocalisation du collagène, de l'actine et de la protéine Tks5 permet l'identification d'un invadopode linéaire. La flèche indique la position de l'invadopode linéaire.*

2.6 Etude protéomique des invadopodes

2.6.1 Contexte

L'équipe de F. Saltel (INSERM 1053, Bordeaux) a développé une technique automatisée de microdissection laser permettant de récolter suffisamment de matériel biologique pour réaliser une étude par spectrométrie de masse. Pour démontrer l'efficacité de leur technique, ils ont étudié dans un premier temps le contenu protéique des rosettes formées par les cellules NIH 3T3. J'ai pu dans ce contexte leur apporter par la technique de CLEM *in vitro* mise en place dans notre laboratoire la visualisation de la localisation des ribosomes dans les rosettes.

Ce manuscrit a été soumis pour publication.

2.6.2 Manuscrit n°7 : Combined laser micro-dissection and mass spectrometry for targeted subcellular proteomics

Combined laser micro-dissection and mass spectrometry for targeted sucellular proteomics.

Zakaria Ezzoukhy[1,2#†], Elodie Henriet[1,2#], Fabrice P. Cordelières[2,3], Jean-William Dupuy[2,4], Marlène Maître[5], Nathan Gay[1,2], Luc Mercier[6], Jacky Goetz[6], Marion Peter[7], Frédéric Bard[8], Violaine Moreau[1,2], Anne-Aurélie Raymond[1,2,9*] and Frédéric Saltel[1,2,9*§]

[1] INSERM, UMR1053, BaRITOn Bordeaux Research in Translational Oncology, F-33000 Bordeaux, France

[2] Université de Bordeaux, Bordeaux F-33076 Bordeaux, France
[3] Bordeaux Imaging Center, UMS 3420 CNRS-Université de Bordeaux-US4 INSERM, Pôle d'imagerie photonique, Bordeaux F-33000, France
[4] Plateforme Protéome, Centre de Génomique Fonctionnelle, F-33000 Bordeaux, France
[5] Neurocentre Magendie U1215, INSERM, F-33000 Bordeaux, France
[6] Inserm U1109, MN3T, Strasbourg, France; Université de Strasbourg, Strasbourg, France; LabEx Medalis, Université de Strasbourg, Strasbourg, France
[7] Institut de Génétique Moléculaire de Montpellier, UMR 5535 CNRS, 1919 route de Mende, 34293 Montpellier cedex 5, France

[8] Institute of Molecular and Cell Biology, 61 Biopolis Drive, Proteos, Singapore
[9] Oncoprot, INSERM U1053-TBM Core US005, F-33000 Bordeaux, France
[†] Current position, Mohammed VI University of Health Sciences (UM6SS)

Running title: mass spectrometry analysis of subcellular compartments

§ Correspondence to FS, frederic.saltel@inserm.fr

INSERM U1053, Bariton
Université Bordeaux Segalen
146 rue Léo Saignat
33076 Bordeaux cedex, France
Tel : +33 (0)5 57 57 17 71 Fax: +33 (0)5 56 51 40 77

Abstract

To understand cellular processes it is crucial to decipher the proteome of subcellular complexes. This goal is currently hindered by the difficulty in maintaining integrity during the isolation of protein complexes. In addition, classical purification methods usually lead to contaminations and consequently difficulties for data validation. To solve these problems, we developed a method combining laser capture and mass spectrometry analysis consistent with a low amount of material, allowing the analysis of subcellular complexes in their native state. As a proof of concept, we applied this strategy to invadosomes, which are F-actin-based structures involved in extracellular matrix degradation and cell invasion. Using this new analysis process, in addition to known invadosome markers, we identified components of the translational machinery, leading to the characterization of a local and critical mRNA translation activity.

Introduction

The identification of proteins forming subcellular complexes improves our understanding of their functions and more generally of cellular mechanisms. Currently, the association of mass spectrometry (MS)-based proteomics with biochemical fractionation or immunoprecipitation are the classical approaches for characterization of protein interactions in subcellular complexes [1, 2]. Typically, cell homogenates prepared by mechanical homogenization contain a mixture of various organelle types or cellular compartments such as cytoplasmic membranes and cytoskeletal portions that can be then fractionated by centrifugation and/or density gradient centrifugation [2]. Isolation of specific subcellular organelles, structures, or protein complexes is particularly challenging due to the mechanical cellular lysis that disrupts them directly. This is the case for example for adhesive structures (focal adhesions or invadosomes), cell-cell junctions or cytoskeleton structures (filopodia, stress fibers, lamellipodia), which are disassembled during cell lysis. Various strategies were developed to conserve the integrity of these subcellular organizations but it has been difficult to isolate them specifically [3, 4].

The growing need of accuracy in identifying protein complexes and subcellular compartment proteomes requires (i) better enrichment techniques, (ii) lower levels of contaminating proteins and (iii) high-sensitivity analytical techniques compatible with very low amount of biological material.

In this study, we developed a new procedure combining laser capture and mass spectrometry for subcellular proteomic analyses on fixed cells. At first, laser microdissection enables to access precisely to the subcellular compartment. Fluorescent-labeled protein or dyes are necessary to visualize and select region of interest from fixed cells under microscope guidance. We designed a method to automate the capture, which greatly facilitated the collection of the subcellular compartments or structures of interest. Then, the sensitivity of the last generation mass spectrometers is currently adequate to analyze very small amount of material. Bias of this greater sensibility is to identify also undesirable contaminating proteins that originate from the laboratory, from either the user (e.g. keratin from hair and skin) or reagents [5]. For this reason, we previously labeled cell proteins by metabolic isotopic labeling (SILAC) [6] to discriminate proteins coming for laser capture to contaminant from the environment and so guaranteeing the specificity of identifications. In the end, this method

allowed us to identify several hundred of labeled proteins from only nanograms of collected compartments.

We decided to test our protocol on adhesive structures, the invadosomes. Invadosomes is a general term enclosing podosomes and invadopodia observed respectively in normal and cancer cells. They consist in dynamic F-actin structures involved in different functions such as adhesion, mechanotransduction, signalization; but the specific role for invadosomes is their capacity to degrade extracellular matrix. Depending on the cell type, this matrix degradation activity is associated in various cellular functions, such as angiogenesis for endothelial cells or bone resorption for osteoclasts [7]. Invadosomes were also described *in vivo*, and their presence in cancer cells is correlated with invasiveness [8, 9]. So it is crucial to determine their molecular composition to investigate their *modus operandi*. A primary difficulty is that there are different forms of invadosomes, depending on the cell type and the cellular microenvironment. Indeed, cytokines stimulation, the composition and the organization of the extracellular matrix can modulate invadosome formation and organization as individual dots, aggregates, rosettes or linear invadosomes [10, 11].

The second challenge about invadosomes is the difficulty in purifying these structures. Indeed, invadosomes are F-actin structures among others actin structures in cells such as lamellipodia, filopodia, stress fibers and membrane ruffles. All of them share common components. For example, focal adhesions associated with actin stress fibers share common molecular elements with invadosomes such as talin, vinculin, paxillin. Several studies have focused on the focal adhesion proteome [12, 4, 13]. By contrast, only a few studies attempted to elucidate the invadosome protein composition [14-17]. They relied on conventional differential cell lysis or subcellular fractionation with their well-known limitations.

In this study, our main goal was to minimize contamination of other actin structures while maintaining the cell and the invadosome integrity. We analyzed the proteome of microdissected and collected invadosomes, and confirmed the enrichment of identified proteins by a label free quantification against a total cell lysate. Among the 312 proteins identified with more than 2 peptides and for which we confirmed the enrichment; we were surprised to notice a majority of proteins involved in mRNA

translation. After validation of their presence into invadosomes, we established for the first time that invadosomes concentrated mRNA and exhibit their own translation activity.

On line method

Cell culture

NIH-3T3 WT and NIH-3T3-Src cells were a generous gift from Sara A. Courtneidge (Burnham Institute for Medical Research, LaJolla, CA). The cells were maintained in Dulbecco's modified Eagle's medium with 4.5 g/l glucose Glutamax-I (Invitrogen) supplemented with 10% fetal calf serum (Sigma Aldrich) and 100 U/ml penicillin-streptomycin (Invitrogen).

Transfection

Caprin-myc, Eif3L-myc, S100A4-myc and eEF2-GFP were purchase form Origene. Those plasmids were transfected (1µg) using JetPrime (PolyPlus Transfection) following the manufacturer's instructions.

siRNA oligonucleotides (60nM) were transfected using the Lipofectamine RNAiMax (Invitrogen) according to the manufacturer's instructions. The sequences are listed in the **supplementary table 1**

Antibodies and reagents

The anisomycin and the cycloheximide were purchase from Sigma-Aldrich. The GM6001 was purchase from EMD Millipore. PP2, eEF1A1 antibody (EPR9470) and anti-GFP (LGB-1) were purchase from Abcam. Anti-Myc (9E10) was purchase from Santa Cruz Biotechnology, Inc. Anti-EiF3H (D9C1) was purchase from Cell Signaling Technology. Secondary antibodies FluoProbes 488 and 547H anti-rabbit and anti-mouse were purchase from Interchim. Hoechst 34580 (Invitrogen) was used to stain nuclei. For the endoplasmic reticulum localization, cells were incubated with 1µM of ER-Tracker™ green (BOPIDY™ FL Glibenclamide) (Molecular Pobes™) for 30 min at 37°C. Then the cells were fixed in 4% PFA before confocal imaging.

In situ zymography assay

Coverslips were coated with Oregon green gelatin (Invitrogen), fixed with 0.5% glutaraldehyde (Electron Microscopy Sciences), and washed with PBS (Invitrogen). Cells were seeded on coated coverslips and incubated 24 h before fixation and staining.

Immunofluorescence

Cells were fixed with 4% paraformaldehyde (PFA), pH 7.2, for 10 min, permeabilized with 0.2% Triton X-100 for 10 min and incubated with various antibodies. Cells were imaged with an SP5 confocal microscope (Leica) using a 63x/NA 1.4 Pla Neofluor objective lens. To prevent contamination between fluorochromes, each channel was imaged sequentially using the multitrack recording module before merging.

smiFISH

Single molecule inexpensive FISH (smiFISH) was performed as described [18]. Briefly, cells were fixed with 4% PFA and permeabilized in 70% ethanol. Cells were then hybridized using two types of probes: (i) 24 unlabelled primary probes containing both a beta-actin mRNA targeting sequence and a shared sequence (FLAP); (ii) a secondary probe conjugated to two Cy3 moieties, pre-hybridized *in vitro* to the primary probes *via* the FLAP sequence. All probes were purchased from Integrated DNA Technologies. The probe sequences are listed in **supplementary table 2**. Following smiFISH, cells were permeabilized with 0.1% Triton-X100 and stained with anti-beta-actin (clone AC-15, Sigma A5441) and goat anti-mouse-FITC (Jackson ImmunoResearch 115-095-062) antibodies [18].

Microscopy

Three-dimensional image stacks were captured on a wide-field microscope (Zeiss Axioimager Z1) equipped with a 63x 1.4 NA objective and a sCMOS camera (Zyla 4.2 MP, Andor Technology) and controlled with Metamorph (Molecular Devices). Maximum intensity projections of image stacks were obtained with ImageJ (Rasband, W.S., ImageJ, U. S. National Institutes of Health, Bethesda, Maryland, USA, https://imagej.nih.gov/ij/, 1997-2016). For **confocal microscopy,** cells were imaged as previously described [11]. Cells were imaged with a SP5 confocal microscope (Leica, Leica microsystems GmbH, Wetzlar, German) using a 63x/numerical aperture (NA) 1.4 Plan Neofluor objective lens. To prevent contamination between fluorochromes, each channel was imaged

sequentially using the multitrack recording module before merging. Z-stack pictures were obtained using LAS AF, Leica software. Three-dimensional reconstructions were obtained from Z-cut pictures, by using leica software (LAS AF, Leica software, Germany). **Correlative microscopy,** for performing CLEM of rosettes, we used laser micro-patterned aclar films as previously described [19]. The aclar films were pre-coated with 0.5 mg/ml of gelatin in a 24 well-plate. NIH-3T3 cells were seeded at 20 000 cells/ml and incubated overnight. The next day, the aclar film was transferred to a 35 mm glass bottom dish (MatTek P35G-1.0-20-C) for confocal imaging (Leica SP2) using a 63x objective (NA:1,32, Leica microsystems). High-magnification fluorescent pictures of cells and rosettes were acquired. In addition, low-magnification images were acquired for mapping the position of the cell in relation to the micropatterns that are visible using transmitted light (see experiment workflow). Once imaged, cells were fixed in 2,5% Paraformaldehyde (EMS 15713) and 2,5% Glutaraldehyde (GA, EMS 16220) in 0,1M cacodylate buffer (EMS 11652) for 1h at room temperature. The cells were post-fixed in 1% OSO_4 (EMS 19150) in cacodylate buffer 0,1M for 1h on ice. After 3x10 min water rinses, cells were stained with 2% uranyl acetate. The cells were dehydrated in sequential gradient alcohol baths and infiltrated with epon (resin). Plastic embedding capsule (EMS 69910-05) were mounted over the aclar film following overnight polymerization at 60°C. The following day, the capsules were filled with epon and polymerized again overnight at 60°C.

For relocating the region of interest, the surface of the resin block was imaged using a stereomicroscope allowing accurate positioning of the cell of interest according to the micro-pattern. Precise trimming was performed around the cell of interest. Finally, the resin block was serially sectioned (thickness: 70nm) and all the sections were collected on electron microscope slot grids. Sample sections were imaged on a CM12 transmitted electron microscope (FEI company) with a CCD camera (Orius, Gatan). For the image processing, fluorescent images were processed in Fiji [20] and electron microscopy images were aligned and stacked with TrakEM2 [21]. 3D rendering of the electron microscopy acquisitions were performed with Imod [22].

SILAC labeling

Src-NIH-3T3 cells were grown in DMEM without lysine and arginine (Gibco) supplemented with 10% dialyzed foetal bovine serum (Gibco), 200mg/L L-proline (Sigma-Aldrich), and 84mg/L $^{13}C6$ L-Arginine (R) and 146mg/L $^{13}C6$ L-Lysine (K) (both from Eurisotop) at 37°C in a humidified incubator in a 5% CO2 atmosphere. The total incorporation of the labeling was checked by mass spectrometry after 6 cycles of cellular doubling.

Laser microdissection

Invadosomes were microdissected from PFA fixed src-NIH-3T3 cells with a PALM type 4 (Zeiss) automated laser microdissector. Five analyses were performed with an increasing number of microdissected invadosomes (100, 350, 3000, 10 000, 40 000). The four first ones were manually made. The microdissection of 40 000 rosettes was made using the system of automation which we developed.

Assisted invadosomes laser microdissection

An ImageJ macro toolset was used to automatically segment invadosomes and export the regions of interest to be isolated toward the PALM Zeiss microdissector. While the sample is being scanned, the ImageJ toolset monitors the arrival of newly saved images. For each single image, pre-processing and segmentation steps are performed as follows. First the channels from the RGB images are split: only the red image is retained. A median filtering is applied (radius: 2 pixels), and a background subtraction is performed using the rolling-ball algorithm (radius: 20 pixels). To isolate invadosomes from background, automated thresholding is applied, morphological closing and hole filling performed. Finally, structures are delineated by connexity analysis (ImageJ analyse particles function). Morphological parameters, strictly defined on well-identified structures, are used to only retain structures of interest: objects' area should be at least 10 µm^2, with a circularity enclosed within the 0.35-1 range. This analysis output takes the form of regions of interest (ROI), stored within the ImageJ RoiManager. All ROIs are exported as an "Element file", using an in-house developed ImageJ plugin.

High Content Analysis

Images for HCA were collected using an inverted Leica DMI 6000 microscope (Leica Microsystems, Wetzlar, Germany) equipped with a HC PLAN APO 20x/0.7 objective, a Lumencor spectra 7 illumination device (Lumencor, Beaverton, USA) and a HQ2 CCD camera (Photometrics, Tucson, USA). This system was under the control of the MetaMorph software (Molecular Devices, Sunnyvale, USA), under which a serie of journal has been created to automate the acquisitions over a multi-well plate (24 wells/plate, 25 fields imaged/well). Automated image analysis has been performed using an in-house developed workflow, using the CellProfiler software [23]. Briefly, for both the invadosomes and nuclei images a correction for uneven illumination has been performed. Invadosomes were first enhanced by top-hat filtering. Candidate structures were isolated using the "Identify primary objects" function, then submitted to a refined identification by filtering based on morphological parameters (area, major/minor axis length and solidity). Nuclei identification was performed using only the primary object detection. For both channels, an image of the objects' outlines was saved to visual assess the segmentation efficiency. All morphological parameters were extracted and saved as a SQLite database for further reviewing and analysis using the Cell Profiler Analyst software [24].

Range of protein quantity of total cellular extract

SILAC labeled src-NIH-3T3 cells were lysed in RIPA buffer (Sigma) supplemented with protease inhibitor cocktail (Roche). Protein concentrations were measured using the Bio-Rad protein assay.

Sample preparation for mass spectrometry

Microdissected invadosomes and whole cells extracts were incubated in a Tris-HCl pH 6,8 solution for 2 hours at 95°C. Samples were loaded on a 10% acrylamide SDS-PAGE gel. Migration was stopped when the samples entered the resolving gel and the proteins were visualized by colloidal blue staining. The SDS-PAGE band was cut into 1 mm x 1 mm gel pieces. Gel pieces were destained in 25 mM ammonium bicarbonate (NH_4HCO_3), 50% acetonitrile (ACN) and shrunk in ACN for 10 min. After ACN removal, the gel pieces were dried at room temperature. The proteins were first reduced

in 10 mM dithiothreitol, 100 mM NH$_4$HCO$_3$ for 30 min at 56°C then alkylated in 100 mM iodoacetamide, 100 mM NH$_4$HCO$_3$ for 30 min at room temperature and shrunk in ACN for 10 min. After ACN removal, the gel pieces were rehydrated with 100 mM NH$_4$HCO$_3$ for 10 min at room temperature. Before protein digestion, the gel pieces were shrunk in ACN for 10 min and dried at room temperature. The proteins were digested by incubating each gel slice with 10 ng/µL of trypsin (T6567, Sigma-Aldrich) in 40 mM NH$_4$HCO$_3$, 10% ACN, rehydrated at 4°C for 10 min, and were finally incubated overnight at 37°C. The resulting peptides were extracted from the gel in three steps: the first incubation was in 40 mM NH$_4$HCO$_3$, 10% ACN for 15 minutes at room temperature and two subsequent incubations were in 47.5 % ACN, 5% formic acid for 15 min at room temperature. The three collected extractions were pooled with the initial digestion supernatant, dried in a SpeedVac, and re-suspended with 20 µL of 0.1% formic acid before nanoLC-MS/MS analysis.

Mass spectrometry analysis

Online nanoLC-MS/MS analyses were performed using an Ultimate 3000 RSLC Nano-UPHLC system (Thermo Scientific, USA) coupled to a nanospray Q-Exactive hybrid quadrupole-Orbitrap mass spectrometer (Thermo Scientific, USA). Ten microliters of the peptide extract were loaded on a 300 µm ID x 5mm PepMap C18 precolumn (Thermo Scientific, USA) at a flow rate of 20 µL/min. After 5 min desalting, peptides were separated on a 75µm ID x 25cm C18 Acclaim PepMap® RSLC column (Thermo Scientific, USA) with a 4-40% linear gradient of solvent B (0.1% formic acid in 80% ACN) in 108 min. The separation flow rate was set at 300 nL/min. The mass spectrometer operated in positive ion mode at a 1.8kV needle voltage. Data were acquired using Xcalibur 3.1 software in a data-dependent mode. MS scans (m/z 350-1600) were recorded at the resolution of R = 70000 (@ m/z 200) and an AGC target of 3 x 106 ions collected within 100ms. Dynamic exclusion was set to 30s and top 12 ions were selected from fragmentation in HCD mode. MS/MS scans with a target value of 1 x 105 ions were collected with a maximum fill time of 100 ms and a resolution of R = 17500. Additionally, only +2 and +3 charged ions were selected for fragmentation. The other settings were as follows: no sheath and no auxiliary gas flow, heated capillary temperature, 200°C; normalized HCD collision energy of 27% and an isolation width of 2 m/z.

Database search, MS results processing and quantification.

For protein identification, we used the Mascot 2.5 algorithm available with Proteome Discoverer 1.4 Software (Thermo Fisher Scientific Inc.). It was used in batch mode by searching against the UniProt *Mus musculus* database (45 172 entries, Reference Proteome Set, release 2016_03) from http://www.uniprot.org/website. Two missed enzyme cleavages were allowed. Mass tolerances in MS and MS/MS were set to 10 ppm and 0.02 Da. Oxidation of methionine, acetylation of lysine and deamidation of asparagine and glutamine were looked for dynamic modifications. Carbamidomethylation on cysteine was searched as static modification. $^{13}C(6)$ (K) or $^{13}C(6)$ (R) labeling was searched as variable modification for contaminating analyses and as fixed modification for invadosomal proteome analyses.

For the enrichment analysis compared with the total cellular proteome, raw LC-MS/MS data were imported in Proline Studio (http://proline.profiproteomics.fr/) for feature detection, alignment, and quantification. Protein identification was only accepted with at least 2 specific peptides with a pretty rank=1 and with a protein FDR value less than 1.0% calculated using the "decoy" option in Mascot [25]. Label-free quantification of MS1 level by extracted ion chromatograms (XIC) was carried out using the parameters indicated in **Supplementary Table 3**. Protein ratios were normalized by sum of peak intensities. Proteins with invadosomes/total ratios ≥1.5 were considered as enriched in comparison with the whole cellular proteome.

Bioinformatics analysis

Proteins listed in the **Supplementary table 4** were used for analyses of Gene Ontology (Protein class) classification from the PANTHER (http://pantherdb.org) database.

Ribopuromycylation (RPM) method

To visualize newly synthetized proteins within cells, we used the RPM method as described by David et al. [26]. NIH3T3-Src cells grown on coverslips were incubated for 15 min at 37°C in complete H12 medium supplemented with 208 mM emetin (EMD, Sigma). In protein synthesis inhibitor control

experiments, cells were pretreated with 40 mM anisomycin (Sigma) for 30 min at 37°C before incubation with EMD. Cells were then treated with 355 mM cycloheximide (Sigma) for 2 min on ice in permeabilization buffer (50 mM Tris-HCl, pH 7.5, 5 mM MgCl2, 25 mM KCl, 0.015% digitonin, EDTA-free protease inhibitor, 10 U/ml RNaseOut (Invitrogen). Cells were then washed and incubated in polysome buffer (50 mM Tris-HCl, pH 7.5, 5 mM MgCl2, 25 mM KCl, 0.2 M sucrose, EDTA-free protease inhibitor, 10 U/ml RNaseOut (Invitrogen) supplemented with 91mM puromycin (PMY, Sigma) for 10 min on ice. After rapid washing in polysome buffer, cells were fixed in 4% formaldehyde for 15 min at room temperature. After fixation, cells were washed twice with PBS and immunostaining with anti-PMY antibody was performed as described above.

Results

A new procedure combining automated laser capture and mass spectrometry for subcellular proteomic analysis.

The necessity of ultrasensitive and specific identification of protein complexes and cellular compartment proteomes prompted us to develop a new procedure combining laser capture and mass spectrometry for subcellular proteomic analyses (**Figure 1a**). First, cells were labeled by a metabolic isotopic labeling (SILAC) to discriminate proteins coming from laser capture to undesirable contaminating proteins that originate from the laboratory or from reagents. This first step guarantees the specificity of identifications. To precisely visualize and select the compartments to be microdissected, they must be labeled using fluorescent-labeled protein or dyes and the cells fixed using PFA. Immunolabeling is not recommended because the immunoglobulins could mask the MS signal.

Laser microdissection enables to isolate the region of interest minimizing contaminations from the other cellular elements. Performing micro-dissection implied manual delineation of the structures of interest. A laser beam was used to cut the selected region and the same laser propels and collects the subcellular compartments into a tube cap. Isolating subcellular complexes or compartments for proteomic analysis implies dissecting thousands of structures to get enough material. When

performed manually, a confirmed experimenter could expect to dissect at best 200 structures per hour. This task is cumbersome and time consuming. To speed up the process, we therefore developed a strategy taking benefit of image processing automation using the ImageJ software. As a first step, under the Zeiss PALM software, the user located a field of interest. An image was taken, that was automatically imported under the ImageJ software (**Figure 1b**). Using a homemade plugin, metadata were extracted. This information allowed getting access to the precise stage location where the acquisition took place, expressed as a calibrated set of coordinates. A homemade ImageJ toolset took benefit of those coordinates to calculate a matrix of points placed at the center of adjacent field. Thanks to the plugin, this matrix was exported as an "Element file", a proprietary file format from Zeiss, and manually imported into the PALM software. The micro-dissection system was then operated to move the stage at each of the coordinates, and to acquire an image for each visited field. The dissection process was finally achieved, based on automatically segmented regions (**Figure 1b**). When performed semi-automatically, a confirmed experimenter could expect to dissect on average 900 structures per hour, which represents a 4-fold improvement compared to the manual procedure. Once collected, proteins were extracted and the fixation reversed. The proteins were then digested by trypsin in-gel and the peptides analyzed by LC-MS/MS on a last generation mass spectrometer (Q-exactive, Thermo) whose sensitivity was compatible with small quantities of material. Database searching with ^{13}C(6) K or ^{13}C(6) R labeling as fixed modification uniquely identified proteins coming from microdissected elements. Finally, in order to confirm the enrichment of identified proteins in comparison with the total cellular proteome and thus the significant presence of these proteins in the compartment of interest, we performed a relative label free quantification between the microdissected fraction and the total extract of labeled cells.

Overall, this association of several advanced technologies was aimed at lowering the level of contaminants and increase the level of sensitivity for subcellular proteomics.

Process application to the invadosome proteome study

We chose to apply our method to invadosome structures. We used Src-transformed mouse fibroblasts (NIH-3T3-Src cells) as invadosome model [27]. This model presented the advantage to form large

invadosomes rosettes (diameter up to 5-7 µm) with a high frequency (at least one structure per cell) (**Figure 2a**). Since the position of these invadosome rosettes was random, some localized under the nucleus or near the central core of the cell or at the extremity of membrane protrusions (**Figure 2a**). An orthogonal view of invadosome rosettes shows that these structures occupied a large part of the cell thickness (**Figure 2a**). We confirmed a matrix degradation activity associated with the invadosome rosettes using an *in situ* zymography assay with fluorescent gelatin (**Figure 2a**). For this study, we generated a NIH-3T3-Src cell line stably expressing mRuby-LifeAct to detect invadosomes without exogenous staining. It is important to work with fixed cell due to the dynamics of these invadosome rosettes (see movie 1). Following our experimental pipeline, identified F-actin structures were then laser-captured and collected into a tube cap (**Figure 2b**). We started experiments with a manual collection of 100 rosettes. After protein extraction, fixation reversion and protein digestion, the LC-MS/MS analysis identified only 2 proteins with 5 ^{13}C peptides. Since one of these proteins was actin, we were reassured on our approach but also concluded that we didn't collect enough material. We increased the number of manually collected rosettes and identified each time more ^{13}C proteins (**Figure 2c**). A database search analysis with ^{13}C(6) K or ^{13}C(6) R labeling as variable modification allowed to state that a large majority (67% to 97%) of identified peptides in the first experiment was not ^{13}C labeled and thus came from contaminations. The part of contaminating proteins decreased as we brought more cellular material and became minority (5% for 40 000 rosettes collected) as soon as we exceeded the sensitivity threshold of the mass spectrometer (**Figure 2c**). This result demonstrated the relevance of isotopic labeling before laser microdissection to guarantee the specificity of protein identifications.

Once we manually collected 10 000 rosettes, the task of microdissection became too heavy and time consuming. Thus, we developed the described automation system that allowed us to save time, collect more comfortably 40 000 rosettes and identify 2286 ^{13}C-peptides corresponding to 570 proteins identified with at least one specific peptide or 366 proteins identified with at least 2 specific peptides (**Figure 2c and Figure 3a**). We compared the proteins identified in each experiment and found overlaps between 59 and 76% (**Figure 2d**) suggesting a good reproducibility of the entire process.

Finally, we wanted to confirm the enrichment of proteins in the rosette samples in comparison with the total cellular proteome. With such small amount of collected material, we could not measure the protein concentration and thus analyze directly an equal amount of total extract proteins. We opted for the analysis by LC-MS/MS of a dilution range of a total extract of ^{13}C labeled NIH-3T3-Src cells for which we measured the protein concentration. We used the sum of surface area of all detected ^{13}C peptides as readout to evaluate the injected peptide quantities. We have deduced a value of 72 ng for the peptide quantity contained in the sample of 40 000 rosettes and chose 100 ng as the closest point of the total protein quantity range (**Figure 3a and b**). We then normalized MS abundances on the sum of detected peaks and performed a relative label free quantification between proteins identified in the rosette sample and in the whole proteome (**Figure 3c**). Among the 366 proteins identified with at least 2 peptides in the rosette sample, 312 proteins were enriched with a rosette/total proteome abundance ratio ≥1.5, indicating the significant presence of these proteins in the rosettes (**Figure 3c**, Sup **Table 4**).

As expected, we found cytoskeletal proteins flagged by the Gene Ontology (26). We then compared in detail our result with published data (**Figure 3d**). Thirty-seven proteins were already described into invadosomes and, more widely, 131 proteins (42%) were associated to tumor invasion (**Table 1 and Figure 3d**) reinforcing the relevance of our findings and providing new opportunities to identify new keys members not yet described. With the aim of associating biological functions with identified proteins, we classified the 312 enriched proteins according to the GO categories (**Figure 3e**). Interestingly, we also found a large proportion of nucleic acid binding proteins (22% 70 proteins) and more precisely RNA binding proteins (19%, 60 proteins) (**Figure 3e**). The identification of several ribosomal proteins (27), ribonucleoproteins (8), mRNA processing factors (14) and translation factors (12) into the invadosome proteome suggested dedicated protein synthesis machinery associated with these structures.

Validation and localization of proteins enriched in the invadosome proteome

The spatio-temporal control of protein translation is necessary to ensure protein production at the right time and place [28]. This point was already established in neurons and for focal adhesion [29, 30].

Translational control is also crucial in cancer development, especially the selective control of the translation of specific mRNAs that promote tumor progression including invasion and metastasis [31]. Our data suggested that invadosomes concentrated a protein translational machinery.

To test this hypothesis, first, we tested the impact of translation inhibitors into invadosome formation. Anisomycin and cycloheximide (CHX) treatment in a concentration range and time course assays impact invadosome formation (**Figure 4a and Supplementary Figure 1a**). This effect seems to specific to invadosome in comparison to other F-actin structure such as stress fibers or lamellipodia [32, 33]. Secondly, we tested whether identified and mostly enriched proteins from the translational machinery were localized in invadosome. Using immunofluorescence approach we demonstrated that caprin 1, *eukaryotic elongation factor 2 (eEF2) and* eukaryotic translation elongation factor 1 alpha 1 (eEF1A1) colocalized with invadosome (**Figure 4b**). Interestingly, depending the protein tested, the localization could be different. Indeed, some colocalized with the F-actin such as eEF2 and eEF1A1, while caprin 1 concentrated in the center and at the periphery of the rosette. Moreover, a dynamic observation of eEF2 showed that the localization of this protein could evolve during the maturation process of the invadosome rosette (**Supplementary Figure1b**)

Depletion of eEF2 and eEF1A using siRNA promoted a decrease of invadosomes formation, at the opposite caprin1 expression did not affect the number of invadosome per nuclei (**Figure 4c**). In parallel, we measured the degradation activity of the cells in the same conditions and all cases tested we obtained a decrease in the matrix degradation capacity of the cells (**Figure 4d**).

To validate our methodology into a larger number of proteins, we realized a screen using two independent siRNAs, knocked-down 18 proteins chosen according to their enrichment ratio and/or in line with the literature. Twenty eight % of the siRNA tested, and 36% of the siRNA targeting translation related protein impact invadosome formation in our assay (**Supplementary Figure 1c**). These data, were completed by the localization in invadosomes of other protein of the lists, demonstrating that eukaryotic translation initiation factor 3 subunit H and L (EIF3H, EIF3L) and S100A4 (a calcium binding protein and RNA binding protein) respectively involved in translation initiation and invasion colocalize also with invadosomes [34] (**Supplementary Figure 1d**). All these data confirmed the robustness of our approach to identify the invadosome proteome.

A protein translation activity associated with invadosome rosettes

To investigate the presence of an intrinsic and specific translational activity within rosettes, first, we analyzed the endoplasmic reticulum (ER) organization associated with invadosome rosette. Interestingly, we noticed a concentration of ER in the rosette center (**Figure 5a**). An orthogonal view of the ER demonstrated that the ER forms an extension, which reaches the center of the rosette from the top. Moreover, we observed a fine staining that surround the inner and outer part of the F-actin (**Figure 5a**). A similar pattern was observed for several protein enriched in invadosomes such as the initiation factor 4E (eIF4E), a major translation initiation factor (Supplementary **Figure 2a**). To perform translation, several elements are necessary, ribosomes and mRNA. Correlative microscopy was used to show the presence of ribosome into the center of the invadosome rosettes (**Figure 5b**). In parallel, using oligo-dT probes and oligo-dA as control we confirmed the accumulation of mRNA in these invasive structures (**Supplementary Figure 2b**). Actin is the main structural component of these structures, so, we decided to test the presence of actin mRNA into invadosomes. Using single molecule inexpensive FISH (smiFISH) [18], we found a specific accumulation of actin mRNA into invadosome rosettes in NIH-3T3-Src cells (**Figure 5c**).

In some cases mRNA translation is inhibited and they can be accumulated and stored at the invadosomes without translation. To directly visualize translation into live cells, we used the ribopuromycylation method (RPM). RPM is based on incorporation of puromycin (PMY) into nascent polypeptidic chains, whose association with ribosomes is maintained by the presence of the chain elongation inhibitor emetine [18]. We found a strong PMY signal around the nuclei but also into invadosome rosettes demonstrating that active protein translation took place into rosettes (**Figure 5d**). This signal was abolished using anisomycin, which is a translation inhibitor. Consequently, we demonstrated that an internal protein translational activity was an inherent property of these invasive structures and was important for their maintenance. Invadosome rosettes are composed by F-actin in constant polymerization-depolymerization to ensure the generation, the maturation, the stabilization and the collapse of the structure. Overall, these data suggest that podosomes require a localized synthesis of actin to maintain their structure.

Discussion

With our new process combining laser microdissection and mass spectrometry, we answer to subcellular proteomics challenges guaranteeing specificity and sensitivity. We bring so alternative to the classical biochemical fractionations known for their limitations both in term of contaminations by other organelles and in the impossibility to analyze robustly membranes structures or other elements destabilized or destroyed by the cell lysis. We bring also new solutions for protein complexes analyses classically investigated by immunoprecipitation. Indeed, our method allows to analyze and to decipher the proteome of targeted subcellular compartments in their native state.

Herein, we provided the proof-of-concept using an invadosome proteome study for which these limits applied. There were only very few studies about the definition of the invadosome proteome due to their dynamics and problems encountered for their isolation. All the previous studies used a MS-based discovery approach. Cervero *et al.* used a protocol of adhesive fraction from primary human macrophages allowing enrichment of the ventral membrane of the cells containing podosomes. After SILAC labeling, they compared preparations of ventral membranes from macrophages bearing podosomes versus ventral membranes from PP2-treated macrophages that did not form podosomes. They identified 203 proteins (identified with ≥1 peptide) comprising 33 established podosomes proteins and highlighted WDR1/AIP-1 and hnRNP-K as new components that localised to the core structure of macrophage podosomes [14]. In another study, Attanasio *et al.* compared invadopodia-enriched sub-cellular fractions with either cytosolic fractions or whole cell lysates by a Difference Gel Electrophoresis (DIGE) - MALDI approach. Among the 58 identified proteins, their revealed new components of invadopodia (14-3-3ε, G protein β1 subunit, GAPDH, G6PD, LDHA and PKM) [17], which, unfortunately were not validated in further studies. Even if these studies did not use the same invadosome models and methodologies, we found proteins commonly identified (12 proteins (21%) with Attanasio *et al.* and 71 proteins (35%) with Cervero *et al.*) (**Supplementary Figure 3**). Beyond the demonstration of the better capacity of identification of our method (570 proteins identified with ≥1 peptide, 366 proteins identified with ≥2 peptides), the laser microdissection selectivity allows to be

confident on the interpretation of the obtained results. Indeed, Cervero *et al* also identified several ribonuclear components and RNA binding proteins but expressed reservation about this result that it could come from a defect of their preparation [14].

Thanks to our approach, we highlighted and demonstrated for the first time an internal protein translational activity into the invadosomes. This relocation of the translation is coherent with the dynamics of these structures and was already described for other subcellular compartments in neurons for example [35]. Indeed, the local concentration of protein is a limitation to cellular processes [36]. Also, translational control is a crucial component of cancer development and progression. The control of protein synthesis and the selection of specific mRNAs are involved in cancer invasion and metastasis [31]. Notably, some mRNA binding proteins identified with our methodology are already associated with cancer progression, invasion (**Supplementary Table 5**). In the future, this new invadosome feature could pave the way for the identification of a translation signature for tumor cell invasion, which could be then targeted pharmacologically.

In this study, we used for the first time the combination of laser microdissection and mass spectrometry for subcellular proteomics analyses. The only comparable approach was the proteome study of Lewy bodies, whose size was as large as one or several cells [37]. Thanks to the SILAC labeling guaranteeing the specificity of identification in case of very small amount of material, to the automation of the laser microdissection, and the sensitivity of the last generation mass spectrometers, we can now analyze the proteome of very small compartments even sub-organellar compartments. It raises also new possibilities for other membrane structures as for example the cellular junctions whose studies were slowed down by technological locks. Moreover, as this methodology is suitable on fixed samples, our method brings other advantages. For example, concerning dynamics or evolutive structures such as invadosomes, it allows analysing a specific maturation step correlated with a specific morphology of the rosette. Also, to increase the specificity of the analysis of the targeted sub-cellular structure, it is possible to use z sections of the cells, and then reduce contaminations due to elements below or above the region of interest.

In the future, our process could be competed by the MALDI-imaging (MALDI IMS). Indeed, spatial MS analysis could provide a new dimension for cellular analyses. But unfortunately, current MALDI

IMS instruments can now achieve spatial resolutions at just below 20 µm making impossible or very coarse for the moment a sub-cellular analysis [38]. Moreover, the associated MS-identification method (top-down) is still in its infancy and allows at best identifying only proteins with very low molecular weight without possibilities of quantification [39]. While waiting for, it is possible with our method to quantify the identified proteins and compare different conditions (mutants, maturation steps, treated with an inhibitor, pathologic, etc..), and thus find applications in many fields of study to give precious information to better understand molecular and cellular processes.
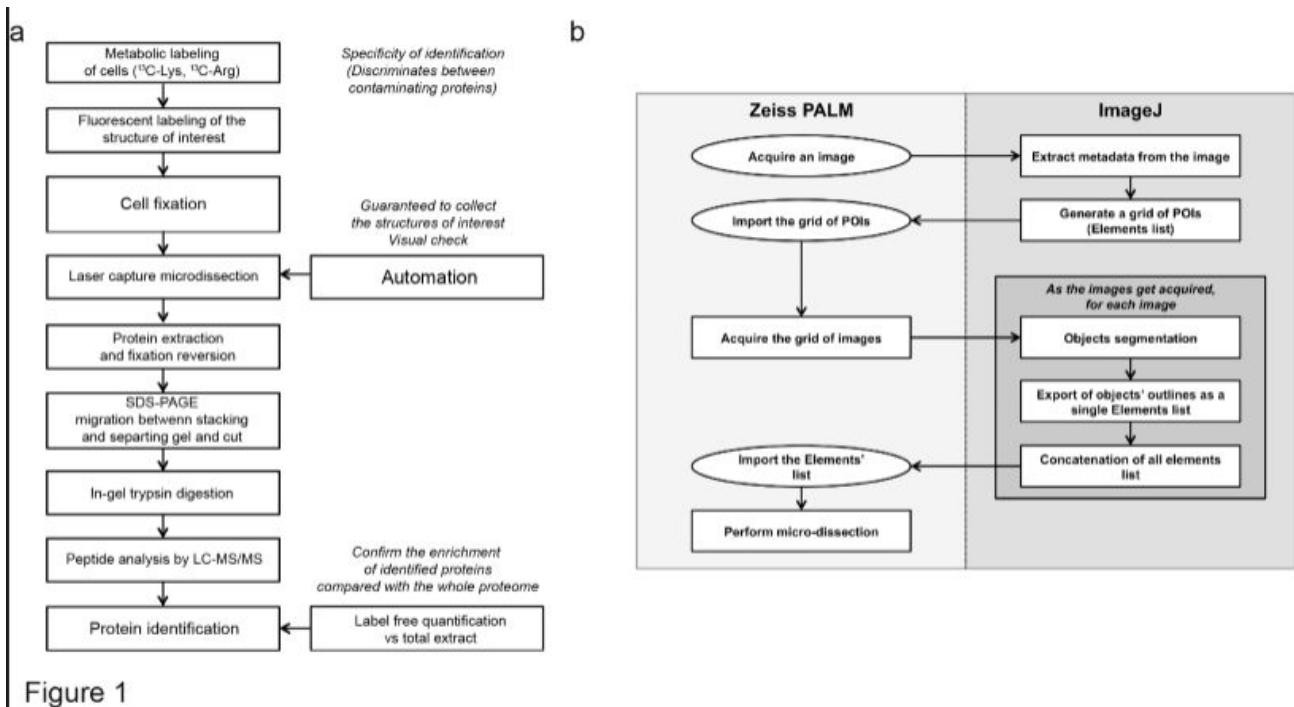
Figure 1

Figure 1: Flowchart of the analytical process combining assisted laser microdissection and LC-MS/MS for subcellular proteomics.

(a) Technical flow chart including the metabolic labeling of the proteins to ensure the specificity of identification, the isolation and the collection of fluorescent-labeled structures of interest with an automated laser capture, and finally, the proteins identification by LC-MS/MS analysis and the enrichment quantification by a label free approach (B) Detailed workflow of the automated laser capture. A first image is acquired from the Zeiss PALM software. Its positional informations are extracted and used by an ImageJ plugin in order to generate a grid of coordinates, covering adjacent field to be explored. For each field, an image is acquired and automatically analysed by ImageJ to recover the structures of interest's outlines. Structures contours are exported from the ImageJ software as a Zeiss PALM compatible file. The microdissection step is started upon this file's import. Automatic steps are indicated in squares and manual steps in circles.

(b) Assisted invadosome microdissection workflow: A first image is acquired from the Zeiss PALM software. Its positional information is extracted and used by an ImageJ plugin in order to generate a

grid of coordinates, covering adjacent field to be explored. For each field, an image is acquired and automatically analysed by ImageJ to recover the structures of interest's outlines. Structures contours are exported from the ImageJ software as a Zeiss PALM compatible file. The microdissection step is started upon importing this file.
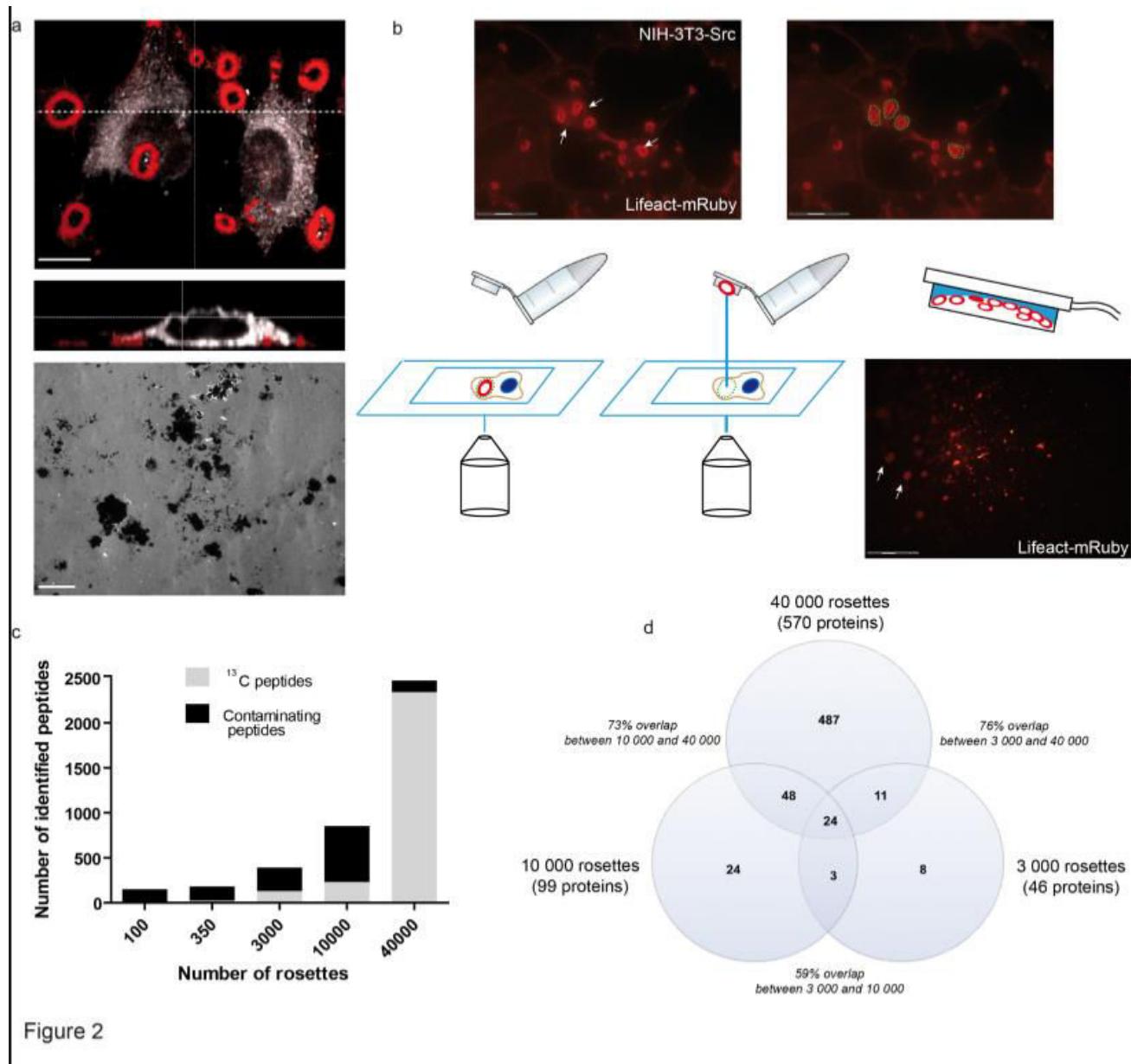
Figure 2

Figure 2: Laser capture and collection of rosettes, global identification values and reproducibility of identification.

 (a) Representative confocal images of NIH-3T3-Src cells with podosome rosettes revealed with the Lifeact-mRuby (red). Z-Cut section shows the thickness of those structures. Below, a representative

image of an *in situ* zymography assay shows the degradation capacity of the cells when seeded on a fluorescent gelatin matrix. Scale bars: 10µm.

(b) (b, upper panel) Representative confocal images of NIH-3T3-Src cells with rosettes. On right image, the dotted circles surround the rosettes that will be microdissected (scale bar: 30µm). (b, below panel) Schematic representation of the microdissection process. The laser will cut the region of interest, which will then be propelled into the cap of a tube. The last panel shows microdissected rosettes (Lifeact-mRuby, red) collected into the cap of the tube (scale bar: 300µm).

(c) Number of identified peptides according to the number of collected rosettes. Thanks to previous metabolic isotopic labelling, peptides coming from dissected invadosomes were identified with ^{13}C modifications (^{13}C peptides) and discriminated from external contamination (contaminating peptides).

(d) Proteins identified in each experiment (increasing number of collected invadosomes) were compared to estimate the reproducibility of identification.
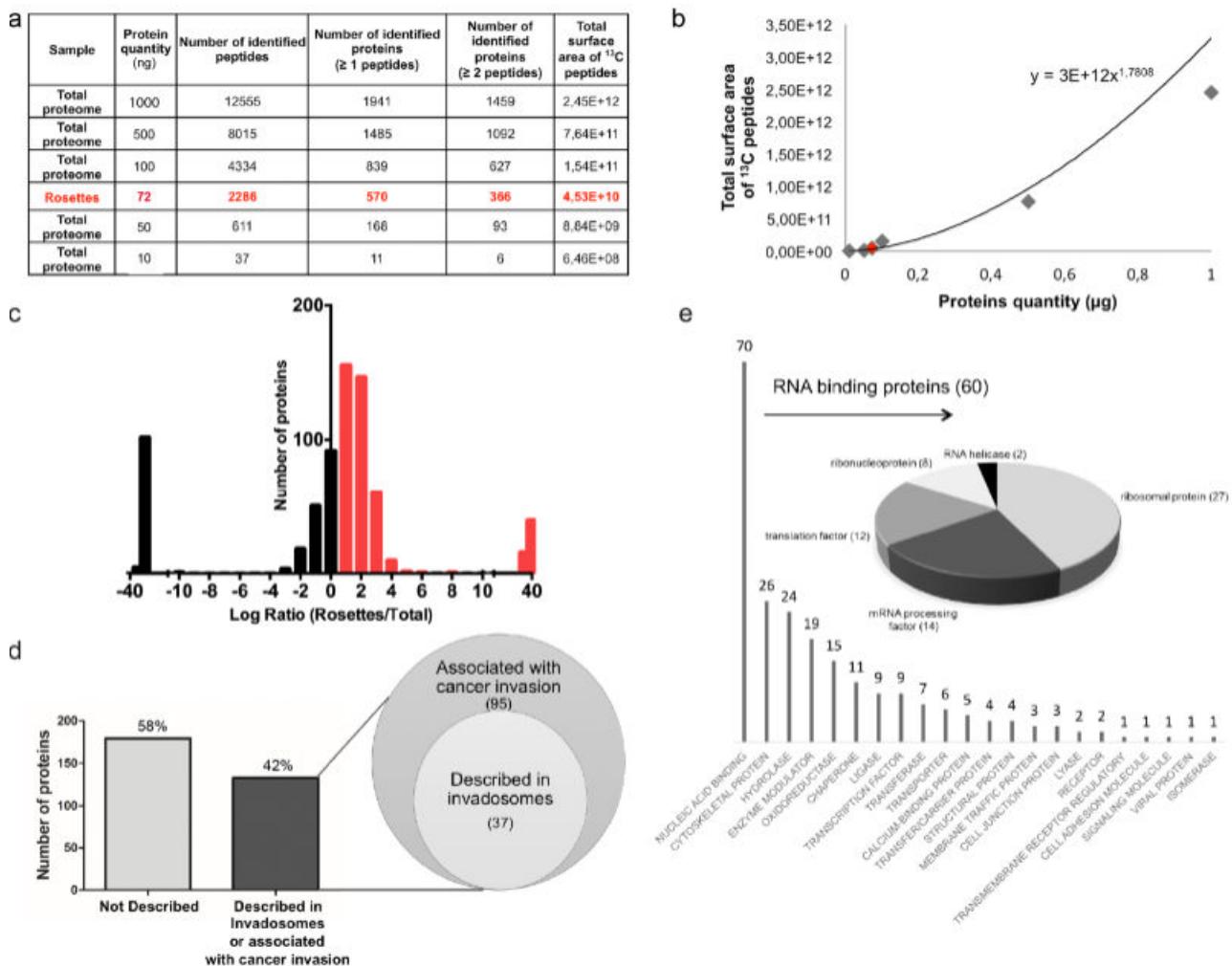
Figure 3: Enrichment analysis and functional classification of proteins. (a) The table recapitulates the number of identified peptides, the corresponding number of identified proteins with at least 1 or 2 specific peptides and the associated sum of MS intensities of all ¹³C peptides detected according to a range of proteins quantity from ¹³C labelled NIH-3T3-Src cells. The sum of intensities of all detected ¹³C peptides was used to deduce the protein quantity from the 40 000 rosettes sample (in red in the table and in the graphical representation (b)). The closest point of the total proteins quantity range (100ng) was chose to compare the MS relative abundances after normalisation. (c) Among the 366 proteins identified with at least 2 peptides in the rosettes sample, 312 proteins were enriched with a rosettes/total proteome abundance ratio ≥1.5 (log ratio≥0.6 in red). (d) The bart chart represents the classification of the 312 enriched proteins according to the GO categories ("Protein

class" classification from the PANTHER database). Among the 70 nucleic acid proteins, 60 proteins were sub-classified as RNA binding proteins whose functional assignments distribution is represented into the pie chart.
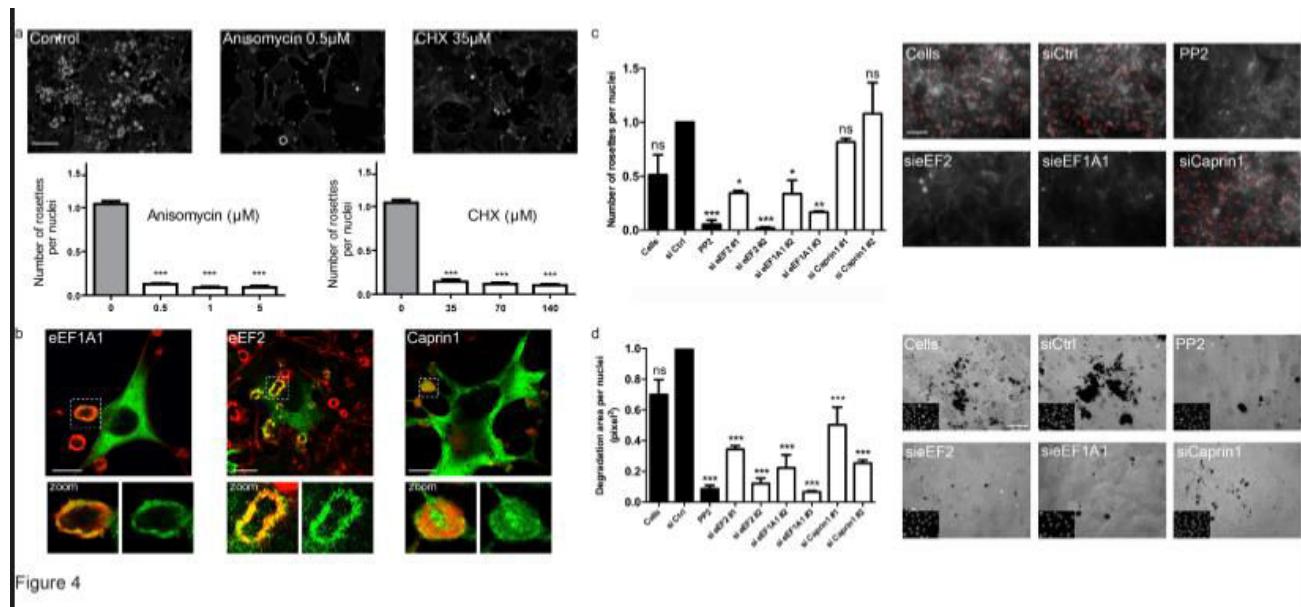
Figure 4

Figure 4:

(a) Dose response of the number of rosette per nuclei after translation inhibitor treatment. NIH-3T3-Src cells were treated with the indicated doses of anisomycin or cycloheximide (CHX) for 24 h. Panel on the top shows representative images of the cells for which there is an effect with the minimum dose. The bar graph represents the number of rosettes per nuclei. Error bars represent the SEM (n=20 fields, three independent experiments; ***, P < 0.001 as compared to the non-treated cells as control). Scale bar: 50µm.

(b) Confocal images of NIH-3T3-Src cells transfected with Caprin1-myc (green) or eEF2-myc (green) and eEF1A1 (green) revealed by indirect immunofluorescence. Panels on the right show enlarged views of the boxed regions. Scale bars: 10µm, 20 µm and 10µm respectively.

(c) NIH-3T3-Src cells were transfected with a siRNA control (siCtrl) or two independent siRNA targeting eEF2, eEF1A1 or Caprin1 involved in translation activity. As controls the cells were treated with the Src inhibitor PP2 (5 µM). Bar graph shows the number of rosettes per nuclei. The black bars represent the control conditions of the experiment. Error bars represent the SEM (n=75 fields, three

independent experiments; ns, not significant; *, P <0.05; **, P < 0.005; ***, P < 0.001 as compared to the siRNA control). The right panel shows representative images of the rosette number determined by the mask applied by the software (red areas). Scale bar: 50µm.

(d) NIH-3T3-Src cells transfected with a siRNA control (siCtrl) or two independent siRNA targeting eEF2, eEF1A1 or Caprin1 were seeded on a fluorescent gelatin matrix. As a control, cells were treated with PP2 (5 µM). Bar graph shows the gelatin area degraded per cells after 24h. The black bars represent the control conditions of the experiment. Error bars represent the SEM (n=30 fields, three independent experiments; ns, not significant, **, P < 0.005; ***, P < 0.001 as compared to the control siRNA). The right panel shows representative images of the degraded area (black), insets on the bottom show the nuclei associated. Scale bar: 50µm.

a ER-Tracker | merge | ER-Tracker | merge

b Actin | Confocal microscopy | Electron microscopy | Merge

Ribosomes Membrane | Ribosomes Membrane

c NIH-3T3 WT | zoom 1 | 2 | FISH-Act
NIH-3T3-Src | zoom 1 | 2

d PMY | zoom 1 | 2 | Anisomycin
PMY | 1 zoom | 2
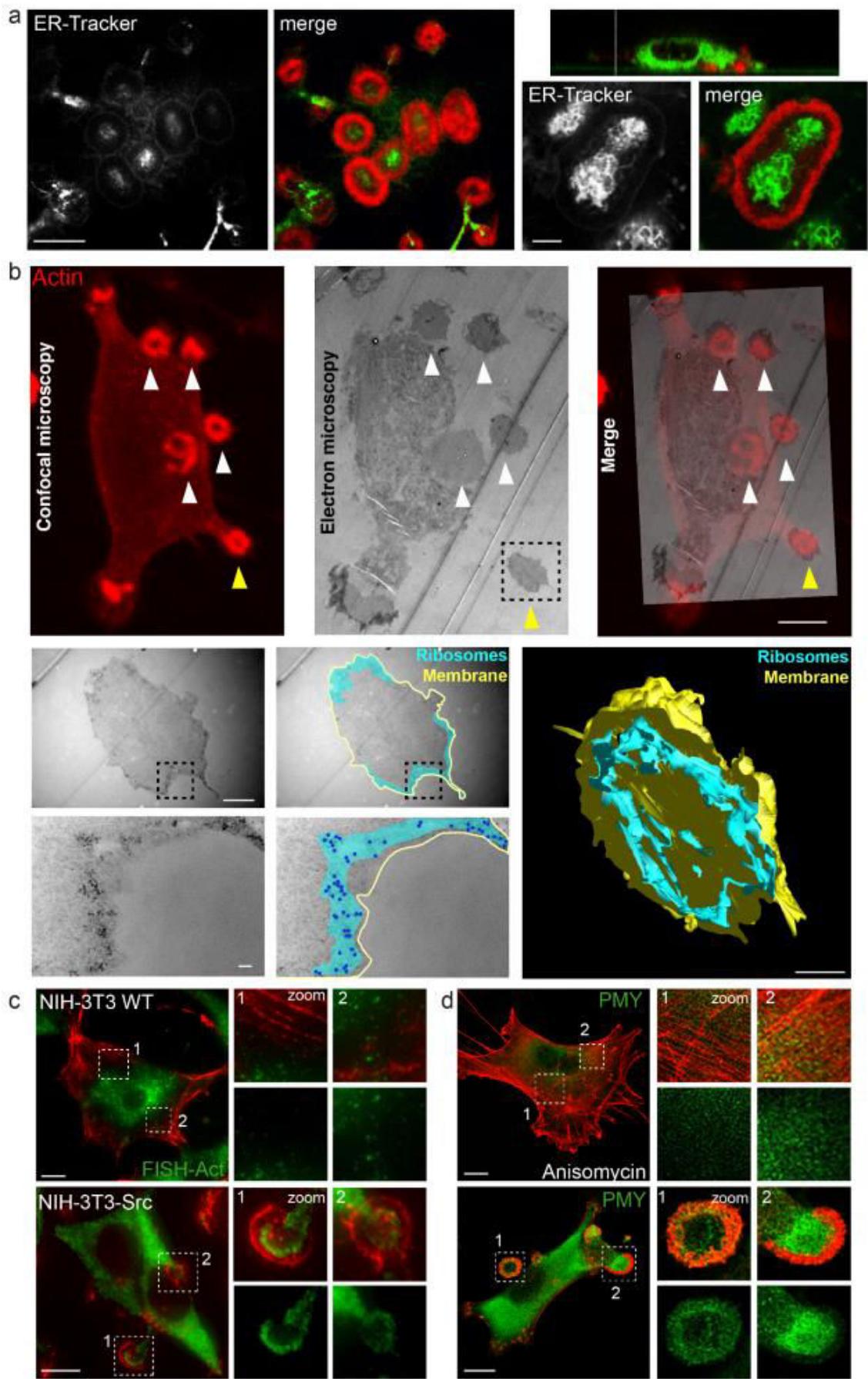
Figure 5

Figure 5:

(a) NIH-3T3-Src cells were stained with an ER tracker. Representative images confocal images are shown. On the left panel a Z-stack reconstruction shows an invagination of the ER into a podosome rosette. A magnification of a rosette shows the ER organization into this structure. Scale bars: 10µm (right panel), 2µm (left panel).

(b, upper panel) Correlative light and electron microscopy (CLEM) *in vitro*. First a confocal acquisition of NIH-3T3-Src cell Lifeact-mRuby forming rosettes (arrow heads) is taken. Then, the exact same cell is imaged by transmitted electron microscopy (TEM). Next, the position of rosettes are correlated between confocal and electron microscopy (arrowheads). The dashed square represents the area imaged in the panel below Scale bar: 5µm. (Bottom panel) TEM micrographs of the rosette outlined in the upper panel (box, yellow arrow head). The boxed region is displayed at higher magnification in the bottom images. The area containing ribosomes is highlighted in blue. Single or small groups of ribosomes are represented by individual blue dots. Outline of the rosettes is marked in yellow. The images on the right are a 3D reconstruction of the rosette with ribosomes located at the periphery of the full rosette. The 3D model is 1.54µm thick and composed of 22 sections. Scale bars: first line 1µm, second line 100nm; 3D reconstruction: 1µm.

References

1.   Larance, M. & Lamond, A.I. Multidimensional proteomics for cell biology. *Nat Rev Mol Cell Biol* **16**, 269-280 (2015).
2.   Satori, C.P., Kostal, V. & Arriaga, E.A. Review on recent advances in the analysis of isolated organelles. *Anal Chim Acta* **753**, 8-18 (2012).
3.   Bezrukov, L., Blank, P.S., Polozov, I.V. & Zimmerberg, J. An adhesion-based method for plasma membrane isolation: evaluating cholesterol extraction from cells and their membranes. *Anal Biochem* **394**, 171-176 (2009).
4.   Kuo, J.C., Han, X., Hsiao, C.T., Yates, J.R., 3rd & Waterman, C.M. Analysis of the myosin-II-responsive focal adhesion proteome reveals a role for beta-Pix in negative regulation of focal adhesion maturation. *Nat Cell Biol* **13**, 383-393 (2011).
5.   Hodge, K., Have, S.T., Hutton, L. & Lamond, A.I. Cleaning up the masses: exclusion lists to reduce contamination with HPLC-MS/MS. *J Proteomics* **88**, 92-103 (2013).
6.   Ong, S.E. et al. Stable isotope labeling by amino acids in cell culture, SILAC, as a simple and accurate approach to expression proteomics. *Mol Cell Proteomics* **1**, 376-386 (2002).
7.   Linder, S., Wiesner, C. & Himmel, M. Degrading devices: invadosomes in proteolytic cell invasion. *Annu Rev Cell Dev Biol* **27**, 185-211 (2011).

8.   Eddy, R.J., Weidmann, M.D., Sharma, V.P. & Condeelis, J.S. Tumor Cell Invadopodia: Invasive Protrusions that Orchestrate Metastasis. *Trends Cell Biol* (2017).

9.   Genot, E. & Gligorijevic, B. Invadosomes in their natural habitat. *Eur J Cell Biol* **93**, 367-379 (2014).

10.   Di Martino, J. et al. The microenvironment controls invadosome plasticity. *J Cell Sci* **129**, 1759-1768 (2016).

11.   Juin, A. et al. Discoidin domain receptor 1 controls linear invadosome formation via a Cdc42-Tuba pathway. *J Cell Biol* **207**, 517-533 (2014).

12.   Horton, E.R. et al. Definition of a consensus integrin adhesome and its dynamics during adhesion complex assembly and disassembly. *Nat Cell Biol* **17**, 1577-1587 (2015).

13.   Schiller, H.B., Friedel, C.C., Boulegue, C. & Fassler, R. Quantitative proteomics of the integrin adhesome show a myosin II-dependent recruitment of LIM domain proteins. *EMBO Rep* **12**, 259-266 (2011).

14.   Cervero, P., Himmel, M., Kruger, M. & Linder, S. Proteomic analysis of podosome fractions from macrophages reveals similarities to spreading initiation centres. *Eur J Cell Biol* **91**, 908-922 (2012).

15.   Havrylov, S. & Park, M. MS/MS-based strategies for proteomic profiling of invasive cell structures. *Proteomics* **15**, 272-286 (2015).

16.   Artym, V.V. et al. Dense fibrillar collagen is a potent inducer of invadopodia via a specific signaling network. *J Cell Biol* **208**, 331-350 (2015).

17.   Attanasio, F. et al. Novel invadopodia components revealed by differential proteomic analysis. *Eur J Cell Biol* **90**, 115-127 (2011).

18.   Tsanov, N. et al. smiFISH and FISH-quant - a flexible single RNA detection approach with super-resolution capability. *Nucleic Acids Res* **44**, e165 (2016).

19.   Spiegelhalter, C., Laporte, J.F. & Schwab, Y. Correlative light and electron microscopy: from live cell dynamic to 3D ultrastructure. *Methods Mol Biol* **1117**, 485-501 (2014).

20.   Schindelin, J. et al. Fiji: an open-source platform for biological-image analysis. *Nat Methods* **9**, 676-682 (2012).

21.   Cardona, A. et al. TrakEM2 software for neural circuit reconstruction. *PLoS One* **7**, e38011 (2012).

22.   Kremer, J.R., Mastronarde, D.N. & McIntosh, J.R. Computer visualization of three-dimensional image data using IMOD. *J Struct Biol* **116**, 71-76 (1996).

23.   Carpenter, A.E. et al. CellProfiler: image analysis software for identifying and quantifying cell phenotypes. *Genome Biol* **7**, R100 (2006).

24.   Jones, T.R. et al. CellProfiler Analyst: data exploration and analysis software for complex image-based screens. *BMC Bioinformatics* **9**, 482 (2008).

25.   Vandenbrouck, Y. et al. Looking for Missing Proteins in the Proteome of Human Spermatozoa: An Update. *J Proteome Res* **15**, 3998-4019 (2016).

26.   David, A. et al. Nuclear translation visualized by ribosome-bound nascent chain puromycylation. *J Cell Biol* **197**, 45-57 (2012).

27.   Seals, D.F. et al. The adaptor protein Tks5/Fish is required for podosome formation and function, and for the protease-driven invasion of cancer cells. *Cancer Cell* **7**, 155-165 (2005).

28.   Buxbaum, A.R., Haimovich, G. & Singer, R.H. In the right place at the right time: visualizing and understanding mRNA localization. *Nat Rev Mol Cell Biol* **16**, 95-109 (2015).

29.   Holt, C.E. & Schuman, E.M. The central dogma decentralized: new perspectives on RNA function and local translation in neurons. *Neuron* **80**, 648-657 (2013).

30.   Katz, Z.B. et al. beta-Actin mRNA compartmentalization enhances focal adhesion stability and directs cell migration. *Genes Dev* **26**, 1885-1890 (2012).

31.   Silvera, D., Formenti, S.C. & Schneider, R.J. Translational control in cancer. *Nat Rev Cancer* **10**, 254-266 (2010).

32.   Flickinger, K.S. & Culp, L.A. Aging-related changes and topology of adhesion responses sensitive to cycloheximide on collagen substrata by human dermal fibroblasts. *Exp Cell Res* **186**, 158-168 (1990).

33.   Sundell, C.L. & Singer, R.H. Actin mRNA localizes in the absence of protein synthesis. *J Cell Biol* **111**, 2397-2403 (1990).

34.   Cadamuro, M. et al. Low-Dose Paclitaxel Reduces S100A4 Nuclear Import to Inhibit Invasion and Hematogenous Metastasis of Cholangiocarcinoma. *Cancer Res* **76**, 4775-4784 (2016).
35.   Shigeoka, T. et al. Dynamic Axonal Translation in Developing and Mature Visual Circuits. *Cell* **166**, 181-192 (2016).
36.   Liu, Y., Beyer, A. & Aebersold, R. On the Dependency of Cellular Protein Levels on mRNA Abundance. *Cell* **165**, 535-550 (2016).
37.   Xia, Q. et al. Proteomic identification of novel proteins associated with Lewy bodies. *Front Biosci* **13**, 3850-3856 (2008).
38.   Gessel, M.M., Norris, J.L. & Caprioli, R.M. MALDI imaging mass spectrometry: spatial molecular analysis to enable a new age of discovery. *J Proteomics* **107**, 71-82 (2014).
39.   Padula, M.P. et al. A Comprehensive Guide for Performing Sample Preparation and Top-Down Protein Analysis. *Proteomes* **5** (2017).

3   Annexe n°1 : Travaux dans le cadre de collaborations

L'équipe MN3T est aussi spécialisée dans l'étude de la matrice extracellulaire et notamment de l'étude des effets de la MEC sur la progression tumorale.

Une manière d'étudier la MEC est de générer *in vitro* des matrices dérivées de cellules (CDM : Cell derived matrix). Cette technique consiste à mettre en culture confluente les cellules d'intérêts, généralement des fibroblastes, sur plusieurs jours. Les cellules vont sécréter les composants constituants la MEC et seront extraites par traitement chimique à la fin de l'expérience pour ne conserver que la MEC (Franco-Barraza et al., 2016).

Cette technique a été utilisée au laboratoire pour étudier l'angiogenèse sur des matrices sécrétées par des fibroblastes exprimant et n'exprimant pas la Ténacine C (Rupp et al., 2016). Elle a aussi été utilisée pour étudier l'implication de l'expression de la cavéoline-1 dans le remodelage de la MEC (Goetz et al., 2011).

Je me suis ainsi intéressé au début de ma thèse à la différence de rigidité entre des CDM produites par des fibroblastes normaux et d'autres CDM produites par des fibroblastes associés au cancer (CAF). La rigidité de ces matrices a été mesurée par microscopie à force atomique (AFM).

La maitrise de cette technique m'a permis de collaborer avec l'équipe de P. Mangin (EFS, Strasbourg) pour étudier l'effet de la fibronectine sur l'agrégation plaquettaire (Manuscrit n°8).

J'ai aussi participé à la rédaction d'une revue récapitulant les techniques d'études des CDM par AFM (Manuscrit n°9).

3.1 Manuscrit n°8: Fibrillar cellular fibronectin supports efficient platelet aggregation and procoagulant activity

Fibrillar cellular fibronectin supports efficient platelet aggregation and procoagulant activity

Eric Maurer[1,2,3,4]; Mathieu Schaff[1,2,3,4]; Nicolas Receveur[1,2,3,4]; Catherine Bourdon[1,2,3,4]; Luc Mercier[5,6]; Bernhard Nieswandt[7,8]; Christophe Dubois[9,10]; Martine Jandrot-Perrus[11,12]; Jacky G. Goetz[5,6]; François Lanza[1,2,3,4]; Christian Gachet[1,2,3,4]; Pierre H. Mangin[1,2,3,4]

[1]Unité mixte de recherche (UMR)_S949, Inserm, Strasbourg, France; [2]Etablissement Français du Sang-Alsace (EFS-Alsace), Strasbourg, France; [3]Fédération de Médecine Translationnelle de Strasbourg (FMTS), Strasbourg, France; [4]Université de Strasbourg, Strasbourg, France; [5]UMR_S1109, Inserm, Strasbourg, France; [6]CHU Hautepierre, Strasbourg, France; [7]University Hospital Würzburg, Würzburg, Germany; [8]Rudolf Virchow Center, DFG Research Center for Experimental Biomedicine, University of Würzburg, Würzburg, Germany; [9]UMR_S1076, Inserm, Marseille, France; [10]Faculté de Pharmacie, Marseille, France; [11]UMR_S1148, Inserm, France; [12]CHU Bichat, Paris, France

Summary

The ability of cellular fibronectin, found in the vessel wall in a fibrillar conformation, to regulate platelet functions and trigger thrombus formation remains largely unknown. In this study, we evaluated how parietal cellular fibronectin can modulate platelet responses under flow conditions. A fibrillar network was formed by mechanically stretching immobilised dimeric cellular fibronectin. Perfusion of anticoagulated whole blood over this surface resulted in efficient platelet adhesion and thrombus growth. The initial steps of platelet adhesion and activation, as evidenced by filopodia extension and an increase in intracellular calcium levels (419 ± 29 nmol/l), were dependent on integrins α5β1 and αIIbβ3. Subsequent thrombus growth was mediated by these integrins together with the GPIb-V-IX complex, GPVI and Toll-like receptor 4. The involvement of Toll-like receptor 4 could be conveyed via its binding to the EDA region of cellular fibronectin. Upon thrombus formation, the platelets became procoagulant and generated fibrin as revealed by video-microscopy. This work provides evidence that fibrillar cellular fibronectin is a strong thrombogenic surface which supports efficient platelet adhesion, activation, aggregation and procoagulant activity through the interplay of a series of receptors including integrins α5β1 and αIIbβ3, the GPIb-V-IX complex, GPVI and Toll-like receptor 4.

Keywords

Platelets, arterial thrombosis, haemostasis, fibronectin

Correspondence to:
Pierre H. Mangin
UMR_S949, INSERM
Etablissement Français du Sang-Alsace (EFS-Alsace)
10, rue Spielmann, BP 36, F-67065 Strasbourg Cedex, France
Tel.: +33 3 88 21 25 25, Fax: +33 3 88 21 25 21
E-mail: pierre.mangin@efs.sante.fr

Introduction

Platelet adhesion, activation and aggregation at a site of vascular injury result in the formation of a plug which stops blood loss (1). In contrast, rupture of an atherosclerotic plaque in a diseased artery can lead to an occlusive thrombus resulting in life-threatening pathologies like myocardial infarction or stroke (2). The initial step of plug or thrombus formation depends on the interaction of platelets with numerous adhesive proteins present in the vessel wall such as von Willebrand factor (VWF), collagens, thrombospondins, laminins and fibronectin (FN).

FN is an extracellular matrix protein which interacts with many different cell types, thereby regulating various functions such as adhesion, migration, growth and differentiation (3). Its crucial importance in vertebrate development is evidenced by the early embryonic lethality observed in FN-deficient mice (4). FN is a 500 kDa glyco-protein containing two monomers linked by disulfide bonds, each being composed of 12 type I, 2 type II and 15 to 17 type III modules (3). FN is encoded by a single gene which, through alternative mRNA splicing, generates 20 variants differing by inclusion or exclusion of the type III_{15} homology connecting segment, the extra domains A (EDA) and B (EDB) and the presence of the region V, variable in length. EDA is recognised as an important site for cell interaction since it binds various receptors including α4β1 and α9β1 integrins and the Toll-like receptor 4 (TLR4), (5, 6). FN can be subdivided in two main types, namely plasma FN (pFN) and cellular FN (cFN). pFN, which is secreted by hepatocytes, lacks the EDA and EDB sequences and circulates at concentrations ranging from 230 to 650 µg/ml (7). pFN can be incorporated into the vessel wall where it assembles in fibrils. cFN is synthesised by endothelial cells, smooth muscle cells and fibroblasts and is present as insoluble fibrils in the extracellular matrix (8, 9). cFN contains the EDA and EDB

sequences in variable proportions and is particularly highly expressed under conditions of atherosclerosis (10).

When pFN is immobilised on a surface, this glycoprotein supports modest levels of platelet adhesion under both static and flow conditions (11–13). The interaction between platelets and pFN is known to depend on integrins α5β1 and αIIbβ3 (11, 13) and on the GPIb-V-IX/VWF axis (12). More recently, it was proposed that the collagen receptor GPVI also supports platelet adhesion through its binding to pFN (14). The role of dimeric pFN in platelet aggregation and thrombus formation remains controversial with numerous *in vitro* and *in vivo* studies reporting either prothrombotic (15–19) or antithrombotic properties (20–23). To date, the thrombogenicity of parietal cFN remains largely unknown. The aim of this study was thus to characterize *in vitro* the ability of fibrillar cFN to trigger different platelet responses.

We provide evidence that fibrillar cFN efficiently supports platelet adhesion under various flow conditions. Adherent platelets become activated and form thrombi, a process relying on integrins α5β1 and αIIbβ3, together with the GPIb-V-IX complex, GPVI and TLR4. Finally, the platelets become procoagulant on this glycoprotein, resulting in fibrin formation.

Materials and methods

Materials

Materials, antibodies and synthetic peptides are described in the Supplementary Material (available online at www.thrombosis-online.com).

Sources and characterisation of fibronectins

Human cellular fibronectin (cFN) was from Sigma-Aldrich (ref: 2518), (Lyon, France) and plasma fibronectin (pFN) was isolated in our laboratory according to a previously described method (24). Characterisation of cFN and pFN by Western blotting (anti-FN antibody: ab23750; anti-EDA domain: ab6328 (Abcam)) revealed that cFN, but not pFN, contained the EDA domain (data not shown). We provided evidence that the two types of FN used in this study were not contaminated with endotoxins (Suppl. Figure 1, available online at www.thrombosis-online.com). Their purity was evidenced by an overloaded gel followed by silver staining, and by liquid chromatography-mass spectrometry/mass spectrometry (Suppl. Figure 2, available online at www.thrombosis-online.com) indicating high degree of purity. Dose-response flow experiments were performed with dimeric pFN to determine the concentration allowing maximal platelet adhesion (Suppl. Figure 3, available online at www.thrombosis-online.com). Based on this experiment, a FN concentration of 300 μg/ml was chosen for each flow assay on pFN and cFN, used in a dimeric or fibrillar form. We showed that cFN under its fibrillar form supported thrombus formation not only at elevated concentrations (300 μg/ml), but also at much lower concentrations (5 μg/ml), suggesting that platelet adhesion was not due to the presence of contaminants (Suppl. Figure 4, available online at www.thrombosis-online.com). Impor-

tantly, no other adhesive protein than collagen, present in the plasma or in the vessel wall, has so far been reported to support thrombus growth in a flow chamber. As a control, we showed that fibrillar cFN allows thrombus formation in diverse flow devices (Suppl. Figure 5, available online at www.thrombosis-online.com).

Mice

αIIb-null (αIIb$^{-/-}$) mice have been previously described (25). C57BL/6 WT mice were obtained from Charles River (L'Arbresle, France). β1$^{fl/fl}$ mice, obtained from Dr. R. Fässler (Max Planck Institute, Martinsried, Germany), were mated with PF4-Cre$^+$ animals obtained from Radek Skoda (University Hospital Basel, Basel, Switzerland) (26, 27), and GPVI-null (GPVI$^{-/-}$) mice by Dr. B. Nieswandt (University of Würzburg, Germany) (28). TLR4-null mice were purchased from Charles Rivers France (L'Arbresle, France). Unless otherwise indicated, we used 8- to 10-week-old mice, anesthetised intraperitoneally with a mixture of xylazine (20 mg/kg, Rompun®, Bayer, Leverkusen, Germany) and ketamine (100 mg/kg, Imalgene 1,000®, Merial, Lyon, France). All experiments were carried out in conformity with the French legislation for animal experimentation and followed the recommendations of the Guide for the Care and Use of Laboratory Animals.

Immunohistofluorescence of mouse carotid arteries

Immunohistofluorescence experiments were adapted from Takaku (29) and are described in detail in the Suppl. Materials and methods (available online at www.thrombosis-online.com).

Preparation of microfluidic devices

Microfluidic devices were made from poly-(dimethylsiloxane) (PDMS) by standard soft lithography techniques (30) and are described in details in the Suppl. Materials and methods (available online at www.thrombosis-online.com).

In vitro flow-based adhesion assay

Flow-based assays were performed as previously described by Schaff et al. (31). Briefly, the microfluidic devices were coated with purified pFN (300 μg/ml), cFN (300 μg/ml), fibrinogen (300 μg/ml), VWF (20 μg/ml) or collagen (2.5 mg/ml) overnight at 4°C and blocked with phosphate buffered saline (PBS)-HSA (10 mg/ml) for 30 minutes (min) at room temperature (RT). The wall shear rates in the microfluidic devices were calculated by using the equation: wall shear rate = $6 \times Q / (w \times h^2)$, where Q is the flow rate (cubic meters per second), w the width in meter and h the height in meter, as previously described by Kroll et al. (32).

Method of mechanical stretching of FNs

The method of mechanical stretching of FN was adapted from a previously described technique (33). The microfluidic flow devices were coated with purified pFN or cFN (300 μg/ml) overnight at

4°C and blocked with phosphate buffered saline (PBS)-HSA (10 mg/ml) for 30 min at RT. Silicon tubes (VWR International S. A.S, Fontenay-sous-Bois, France) were connected to the inlet and outlet of each flow device. The inlet was then connected to a vacuum diaphragm pump (VWR International S. A.S) while the outlet was clamped. The pump was switched on for one minute at 100 mbar and the clamp on the outlet tube was then opened very slowly to apply a tensile force to the surface and allow the FN to multimerise through mechanical stretching. The microfluidic devices were then disconnected from the vacuum diaphragm pump and placed in the *in vitro* flow system described above.

Cell-derived extracellular matrices (CDMs) produced by immortalised fibroblasts

Three-dimensional matrices modelling *in vivo* extracellular matrices (ECM) were prepared as published (34, 35). As previously described (35), these CDMs are highly enriched in fibrillar fibronectin, which is their major ECM component (upon proteomic characterisation). Here, Ibidi μ-Slide I$^{0.2}$ Luer chambers were coated with 1 % Gelatin for 1 hour (h) at 37 °C and crosslinked with 1 % glutaraldehyde. Upon glutaraldehyde quenching with Glycine (1 mol/l, for 20 min) and several washes with PBS, 440,000 cells (tumour-associated fibroblasts isolated from murine squamous cell carcinoma) were plated (close to confluency) and maintained highly confluent for seven days. Cells were supplemented every 24 h with 50 μg/ml fresh L-ascorbic acid to stabilise ECM components and facilitate collagen secretion. Cells were removed from the deposited matrix by alkaline detergent extraction (20 mmol/l NH$_4$OH, 0.5 % Triton-X-100 in PBS) overnight at 4 °C. Finally, CDMs were gently washed several times with PBS before perfusion with anticoagulated blood.

Microscopic observations of the FN fibers

The fibers of the FN coat were examined by scanning electron microscopy (SEM), (see below), by differential interference contrast (DIC) or fluorescence microscopy after immunolabelling with ab23750 followed by a Cy3-coupled goat anti-rabbit secondary antibody (1 μg/ml), (36). A Leica DMI 4000 B microscope (Leica Microsystems) was employed, with a Leica EL6000 fluorescent lamp and a 40x, 1.4 numerical aperture oil objective. Images were acquired with a Photometrics charge-coupled device (CCD) camera (CoolSNAP HQ Monochrome, Photometrics, Tucson, AZ, USA) and analyzed with ImageJ software (National Institute of Health, Bethesda, MD, USA).

Measurement of the thrombus volume

The technique to measure the thrombus volume has been described in details in the Suppl. Materials and Methods (available online at www.thrombosis-online.com).

SEM analysis of platelet shape change after adhesion to FN

Hirudinated (100 U/ml) whole blood was perfused for 5 min at 300 s^{-1} through glass microcapillaries coated with fibrillar cFN. The capillaries were then washed with phosphate-buffered saline (PBS) at 300 s^{-1} for 3 min and the adherent platelets were fixed with glutaraldehyde (25 mg/ml) in cacodylate buffer (0.1 mol/l, pH 7.3) containing sucrose (20 mg/ml) for 45 min. The capillaries were then bisected by using a razor blade. Scanning electron microscopy (SEM) was performed as described elsewhere (36). Platelet shape change was defined as the transformation of a resting discoid platelet into an activated spherical cell with filopodial projections more than 0.2 μm in length.

Analysis of cytosolic Ca²⁺ changes in adherent platelets

Intracellular calcium changes upon platelet adhesion to fibrillar cFN were monitored using a quantitative dual-dye ratiometric assay as previously described (31).

Measurement of annexin V binding

Hirudinated (100 U/ml) whole blood was perfused for 35 min at 300 s^{-1} through glass microcapillaries coated with fibrillar cFN. After washing with PBS at 300 s^{-1} for 10 min, the capillaries were perfused with PBS containing Alexa 568-conjugated annexin V (1/10) for 10 min (37). Activated annexin V-positive platelets were visualised by DIC or fluorescence microscopy under a Leica DMI 4000 B microscope (Leica Microsystems) using a Leica EL6000 fluorescent lamp and a 63x, 1.4 numerical aperture oil objective. Images were acquired with a Photometrics CCD camera (CoolSNAP HQ Monochrome).

Fibrin formation on fibrillar cFN under flow conditions

To generate thrombin and observe real-time fibrin formation, human blood was collected on citrate before being recalcified. Citrated human blood labelled with CellTrace Calcein green-AM (10 μmol/l) and recalcified with 7.5 mmol/l calcium and 3.7 mmol/l magnesium was perfused at 300 s^{-1} through flow devices coated with VWF (20 μg/ml), fibrinogen (300 μg/ml) or fibrillar cFN (300 μg/ml). Confocal microscopy was employed to detect fibrin formation using the Alexa 647-coupled anti-human fibrin antibody 59d8 (38).

Statistical analyses

All values are reported as the mean ± SEM unless otherwise indicated. Data were compared by the Mann-Whitney test. Differences were considered to be significant at p<0.05 and all tests were performed using Prism software (GraphPad, La Jolla, CA, USA).
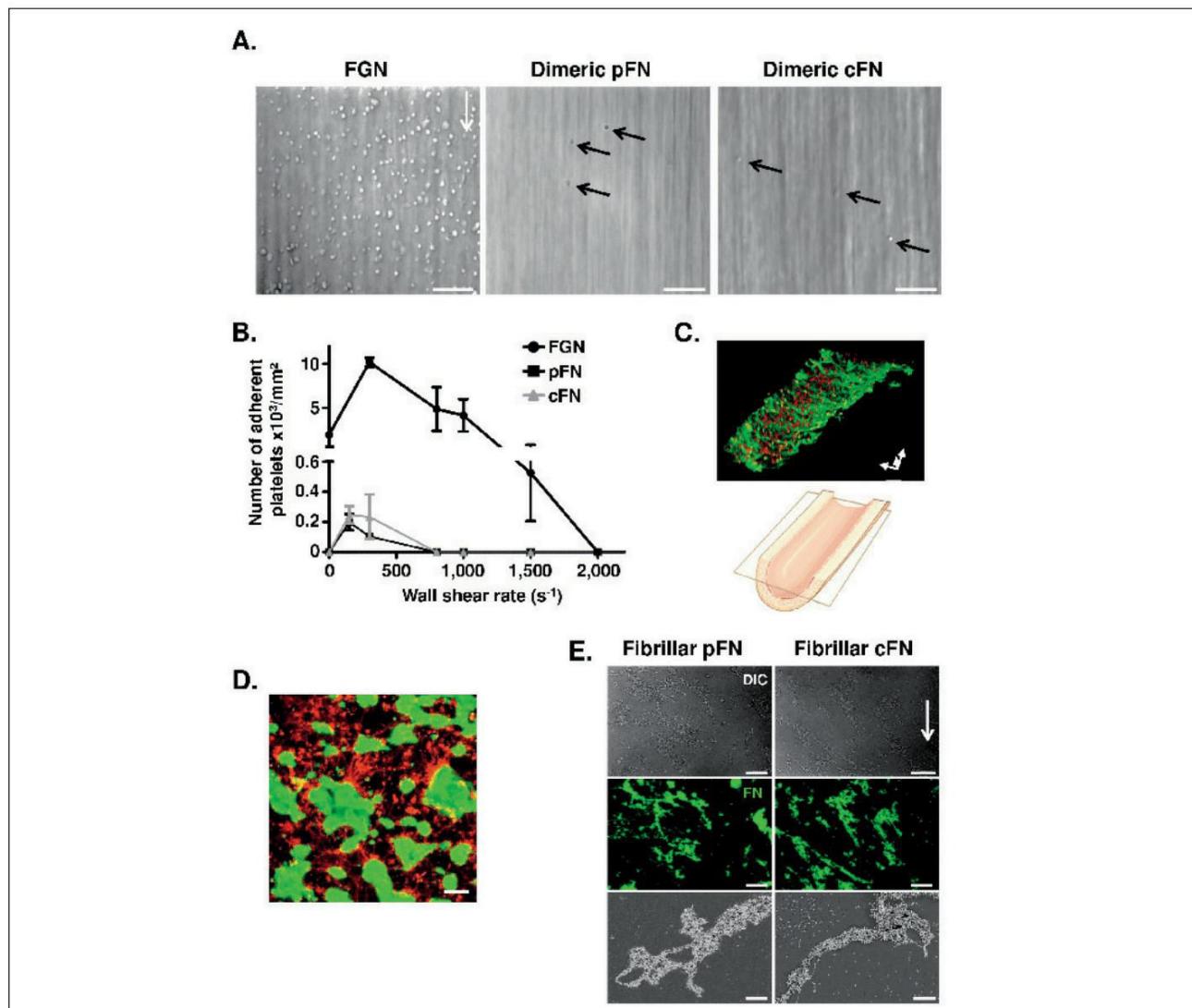
Figure 1: Fibrillar FN supports efficient platelet adhesion and thrombus formation. A-B) Hirudinated human whole blood was perfused at various wall shear rates over FGN, dimeric pFN or dimeric cFN (coated 300 µg/ml). Platelet adhesion was observed in real time using DIC microscopy. A) Representative DIC microscopy images illustrating platelets adhering to FGN, dimeric pFN and dimeric cFN after 3 min of perfusion at 300 s^{-1}. The white and the black arrows indicate respectively the direction of blood flow and the adherent platelets. Scale bar 10 µm. B) The total number of adherent platelets was counted in one random field after 3 min of perfusion and was expressed as a function of the wall shear rate. The results are presented as the mean ± SEM in three independent experiments for each condition. C) Representative confocal immunofluorescence image of a WT mouse carotid stained with an anti-FN antibody (green) and nuclear DAPI (red). Scale bar 50 µm. D) Hirudinated human whole blood was perfused at 300 s^{-1} over a fibroblast derived matrix for 20 min. Representative immunofluorescence image depicting the thrombi in green (DIOC6: 1 µmol/l) and the FN network in red. This experiment has been performed with three different blood donors. Scale bar: 50 µm. E) Representative DIC (top), epifluorescence (middle) and scanning electron (bottom) microscopy images of pFN (left) or cFN (right) coated on the inside of flow devices and made fibrillar by application of surface tension with a vacuum pump. The fibres were stained with an anti-FN antibody followed by an Alexa488-coupled goat anti-rabbit secondary antibody (green). For DIC, epifluorescence and scanning electron microscopy the scale bars represent 40 µm, 40 µm and 2 µm, respectively. F-H) Hirudinated human whole blood was perfused at 300 s^{-1} over fibrillar pFN or fibrillar cFN (coated at 300 µg/ml). F) Platelet adhesion was visualised in real time in one random field by DIC microscopy and the number of adherent platelets was calculated over a 3 min period. G) Left: representative scanning electron microscopy image showing the thrombi formed on fibrillar cFN (1,250x). Right: closer view of a thrombus containing tightly packed platelets (4,000x). Scale bars: 10 µm. H) Representative DIC microscopy images depicting platelet accumulation on fibrillar pFN or fibrillar cFN after 30 min of blood perfusion. The black arrow indicates the flow direction. Scale bar 20 µm. I) Bar graphs represent the total volume of the thrombi after 30 min of perfusion as measured by confocal microscopy. The thrombus volumes are the mean ± SEM in eight random fields, in four separate experiments performed with different blood donors (***P<0.001). J-K) Hirudinated human blood incubated with the fluorescent dye DIOC6 (1 µmol/l) was perfused for 30 min over fibrillar cFN (coated at 300 µg/ml) at various wall shear rates. J) Representative 3D reconstructions from confocal images of thrombi obtained after 30 min of blood perfusion at 150, 300, 500 and 750 s^{-1}. K) Bar graphs represent the volume of the platelet thrombi as a function of the wall shear rate (mean ± SEM) in eight random fields, in six separate experiments performed with different blood donors.
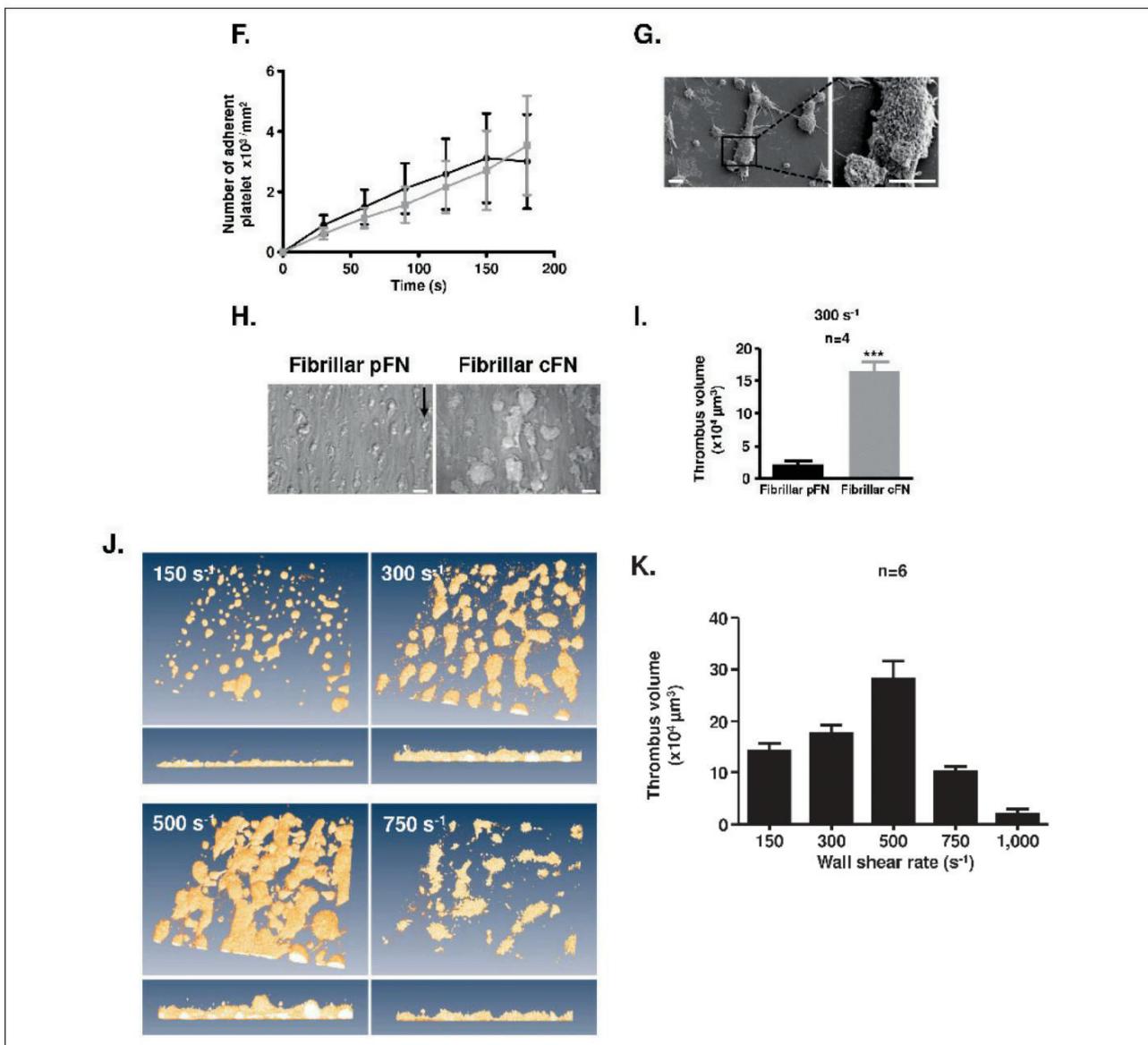
Figure 1: Continued.

Results

Fibrillar cFN supports efficient thrombus formation under various flow conditions

We first assessed the thrombogenic potential of pFN and cFN in their dimeric form and found that both FNs formed a very weak adhesive surface supporting only marginal platelet adhesion at 300 s^{-1} as compared to fibrinogen (▶ Figure 1A and B). It is well established that neither form of FN is dimeric in the vessel wall, but exists rather in a polymerised fibrillar conformation (39, 40). Consistent with these findings, epifluorescence images of a mouse carotid artery showed that FN was organised as a dense network within the vessel wall (▶ Figure 1C). To assess the thrombogenic potential of this glycoprotein in its fibrillar form, hirudinated

human whole blood was perfused over a cFN-rich matrix generated by fibroblasts. Platelets rapidly adhered and accumulated on cFN fibers (red) and formed large thrombi (green) (▶ Figure 1D). This result suggests that FN, under its fibrillar conformation, could be a reactive surface. Since fibroblast-derived matrices contain other adhesive proteins than cFN which might be responsible for platelet aggregation, we decided to reproduce this result with purified proteins. The FNs were deposited on the walls of a flow chamber in their dimeric form and polymerised through an established method which promotes the stretching of (glyco)proteins through application of surface tension with a vacuum pump (41). Observation of the flow channel by differential interference contrast (DIC), epifluorescence and scanning electron microscopy showed that both FNs formed a fibrillar network on the surface of
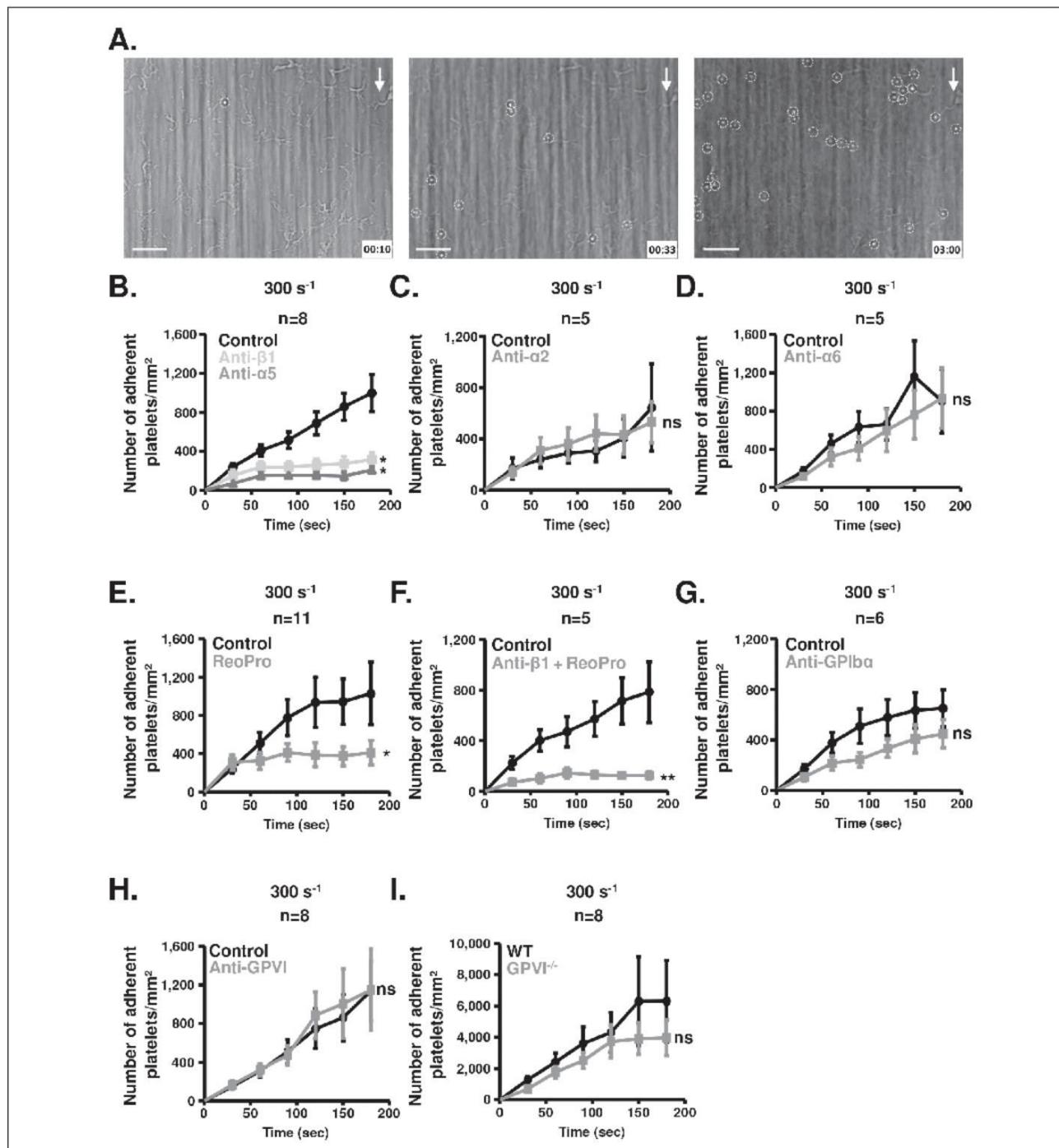
Figure 2: Integrins α5β1 and αIIbβ3 ensure the initial phase of platelet adhesion to fibrillar cFN. A-H) Hirudinated human blood was pretreated or not (A) with blocking antibodies against integrin β1 (anti-β1: 10 µg/ml), (B), integrin α5 (anti-α5: 10 µg/ml), (B), integrin α2 (anti-α2: 10 µg/ml), (C), integrin α6 (anti-α6: 10 µg/ml), (D), integrin β3 (ReoPro: 40 µg/ml), (E), integrins β1 and β3 (anti-β1 + ReoPro: 10 µg/ml and 40 µg/ml, respectively), (F), GPIbα (anti-GPIbα: 10 µg/ml), (G) or GPVI (anti-GPVI: 50 µg/ml), (H), or with irrelevant mouse IgG (Control: 10 µg/ml), (B-G) or Fab fragments (Control), (50 µg/ml), (H) and perfused through flow chambers coated with fibrillar cFN at 300 s⁻¹. A) Representative DIC images of platelets adhering to fibrillar cFN over time. Single adherent platelets are circled in white. The white arrows indicate the flow direction. Scale bars represent 40 µm. I, Hirudinated blood from WT (WT) or GPVI-null (GPVI⁻/⁻) mice was perfused over fibrillar cFN at 300 s⁻¹. B-I) Platelet adhesion was visualised in real time in one random field by DIC microscopy and the number of adherent platelets was calculated over a 3 min period. Data are the mean ± SEM in 5–11 separate experiments as detailed on each panel (*P<0.05; **P<0.01 and ns: P>0.05).

the flow chamber (►Figure 1E). Perfusion of anticoagulated whole blood at 300 s^{-1} led to efficient platelet adhesion which was equivalent on both protein networks (►Figure 1F). At later stages, whereas large thrombi composed of tightly packed platelets formed on fibrillar cFN, its plasma fibrillar counterpart was much less reactive allowing the formation of small aggregates, with a 87% reduction in thrombus volume as compared to fibrillar cFN (n=4, p<0.0001) (►Figure 1G-I). We next determined the range of wall shear rates at which fibrillar cFN supports thrombus formation. Three dimensional (3D) reconstructed confocal images showed that numerous small, mostly round-shaped thrombi formed at 150 s^{-1} (►Figure 1J). The thrombi became voluminous at 300 and 500 s^{-1}, while smaller aggregates were observed at 750 s^{-1}. Maximal thrombus volumes were attained at 300 s^{-1} ($17.6 \pm 1.3 \times 10^4$ µm^3) and 500 s^{-1} ($28.6 \pm 2.7 \times 10^4$ µm^3), whereas almost no thrombi formed above 1,000 s^{-1} ($1.8 \pm 0.8 \times 10^4$ µm^3) (►Figure 1K). These results indicated that fibrillar cFN supports efficient platelet adhesion and thrombus formation under rheological conditions ranging from 150 s^{-1} to 750 s^{-1}, found in veins, arteries and in the post-stenotic areas of atherosclerotic plaques.

Integrins α5β1 and αIIbβ3 ensure the initial phase of platelet adhesion to fibrillar cFN

To obtain insight into the mechanism of thrombus formation on fibrillar cFN, we explored the first stages of platelet capture by real-time video microscopy, to identify the receptors involved in initial platelet attachment to the surface (►Figure 2A). Blocking antibodies against the α5 or β1 subunits reduced by 78% (n=8, p=0.047) and 67% (n=8, p=0.029), respectively, the number of human platelets adhering to fibrillar cFN during the first 3 min of flow (300 s^{-1}) (►Figure 2B). Blocking integrin α2 or α6 did not affect adhesion to the cFN surface (►Figure 2C-D). ReoPro, which targets αIIbβ3, decreased platelet adhesion by 61% (n=11, p=0.038) (►Figure 2E). A combination of anti-β1 and anti-β3 blocking antibodies further reduced adhesion, suggesting complementary roles of α5β1 and αIIbβ3 (►Figure 2F). AK2, a mAb against GPIbα, did not significantly reduce adhesion, indicating that this receptor does not play a critical role under these rheological conditions (►Figure 2G). Blockade or absence of GPVI, which has been reported to bind dimeric pFN(14), did not decrease adhesion of human or mouse platelets (►Figure 2H-I). Altogether, these results suggested that integrins α5β1 and αIIbβ3 have an additive effect in supporting platelet adhesion to fibrillar cFN under flow conditions.

Investigation of platelet activation on fibrillar cFN and identification of the receptors involved

To determine whether fibrillar cFN could promote platelet activation, the morphological changes of adherent human platelets were studied, as a readout for activation, following their perfusion at 300 s^{-1} over the protein surface. Scanning electron microscopy images showed that the vast majority of adherent platelets became spherical and extended filopodia (►Figure 3A-B). As calcium

mobilisation is required for this process, the degree of platelet activation was further evaluated using a dual-dye calcium assay. Most of the human platelets attaching to fibrillar cFN exhibited an increase in intracellular calcium levels, with an average maximal concentration of about 419 ± 29 nmol/l at 300 s^{-1}, as compared to 45 ± 4 nmol/l (n=3, p<0.0001) for resting platelets settling on HSA (►Figure 3C). Taken individually, these platelets displayed a sequence of repeated calcium spikes (►Figure 3D). Blocking human integrin β3, β1 or α5, but not α2 (data not shown), reduced the maximal increase in intracellular calcium by 59% (n=6, p<0.0001), 56% (n=5, p<0.0001) and 54% (n=3, p<0.0001), respectively, as compared to the control, suggesting that both αIIbβ3 and α5β1 initiate platelet activation on fibrillar cFN (►Figure 3E). Moreover, treating human platelets with aspirin in combination with the P2Y$_1$ and P2Y$_{12}$ antagonists MRS2500 and ARC69931MX strongly reduced calcium signalling (by 46%; n=3, p=0.0006), highlighting an important role of the soluble agonists thromboxane A2 (TxA2) and ADP (►Figure 3F). In contrast, blockade of GPVI with 9O12 or absence of this receptor in GPVI$^{-/-}$ platelets did not prevent calcium signalling (n=4, p=0.280; n=3, p=0.640, respectively), further indicating that GPVI is not a receptor for fibrillar cFN (►Figure 3G-H).

Integrin α5β1, but not integrin α2β1 or α6β1, is important for *in vitro* thrombus formation on fibrillar cFN

Once human or mouse platelets had adhered to fibrillar cFN and become activated, they progressively formed large thrombi (►Figure 1G; Suppl. Figure 6, available online at www.thrombosis-online.com). Integrin α5β1 had been found to ensure the initial phase of platelet adhesion and activation on fibrillar cFN. To evaluate its role in thrombus formation, the aggregate volumes were measured by confocal microscopy after blood perfusion at 300 s^{-1} during 30 min for humans and 15 min for mice. Blockade of human integrin β1 reduced the thrombus volume by 60% as compared to the control (n=3, p<0.0001) (►Figure 4A). Stronger inhibition was observed when perfusing blood from β1$^{-/-}$ mice, with a 91% reduction in thrombus volume with respect to the control (n=5, p=0.0159) (►Figure 4B). Use of further blocking antibodies revealed that human integrin α5β1 (n=3, p<0.0001), but not integrin α2β1 (n=5, p=0.130) or α6β1 (n=6, p=0.231), played a critical role in thrombus formation on fibrillar cFN (►Figure 4C-E).

Integrin αIIbβ3, the GPIb-V-IX complex and GPVI play key roles in *in vitro* thrombus formation on fibrillar cFN

Blocking integrin αIIbβ3, but not the GPIb-V-IX complex or GPVI, prevented platelet adhesion to cFN (►Figure 2). ReoPro also reduced the thrombus volume by 79% with respect to the control (n=3, p<0.0001) (►Figure 5A). Similarly, there was a marked reduction in thrombus volume when perfusing blood from αIIb$^{-/-}$ as compared to WT mice (n=5, p=0.0079), confirming the key role of αIIbβ3 (►Figure 5B). To assess the involvement of

© Schattauer 2015
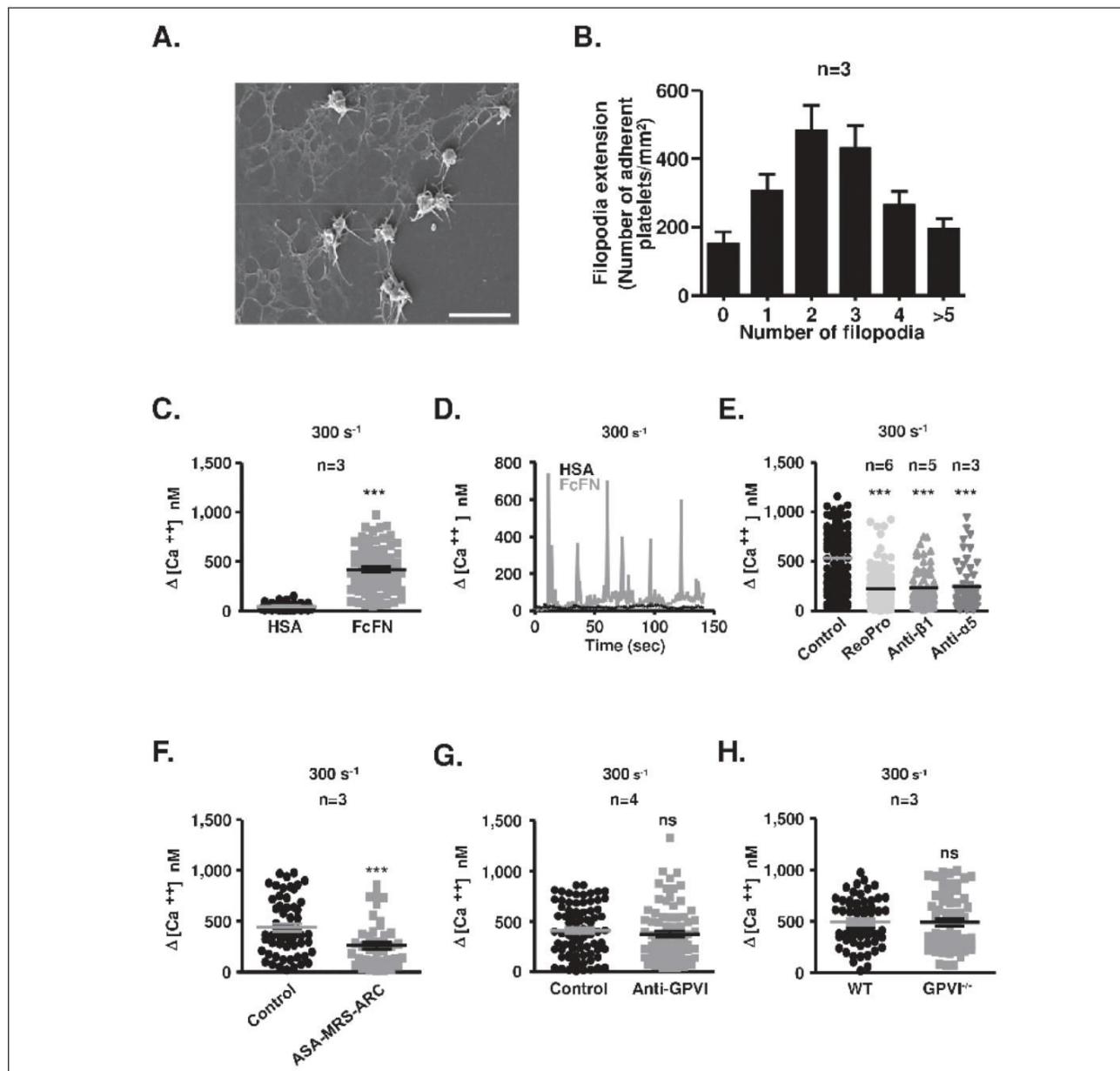
Figure 3: Platelet adhesion to fibrillar cFN leads to morphological changes and an increase in intracellular calcium levels. A-B) Hirudinated human whole blood was perfused over fibrillar cFN at 300 s^{-1} for 5 min. The flow chambers were washed for 3 min with PBS and the adherent platelets were fixed and examined by scanning electron microscopy. A) Representative scanning electron microscopy image. Scale bars 5 μm. B) The number of platelets extending 0, 1, 2, 3, 4 or >5 filopodia was counted in at least ten fields and expressed as number of adherent platelets per surface unit. Results are the mean ± SEM in three independent experiments. C-H) Washed platelets loaded with Oregon-green BAPTA-AM and Calcein red orange were reconstituted with 50% (vol/vol) autologous washed red blood cells and perfused over fibrillar cFN at 300 s^{-1}. The changes in fluorescence of individual adherent platelets were monitored for 5 min by confocal microscopy and Ca^{2+} concentrations were determined. C, E-H) Dot plot distributions of the maximal increase in cytosolic intracellular Ca^{2+} concentration in individual platelets adhering to fibrillar cFN. C-D) HSA refers to washed platelets allowed to adhere to coverslips coated with non-reactive HSA (10 mg/ml). D) Typical time-course Ca^{2+} profile of one representative platelet adhering to fibrillar cFN or deposited on HSA. Experiments were performed in the presence of blocking antibodies against integrins β3 (anti-β3: 40 μg/ml), β1 (anti-β1: 10 μg/ml) and α5 (anti-α5: 10 μg/ml), (E) a combination of aspirin (1 mmol/l), MRS2500 (10 μmol/l) and ARC69931MX (10 μmol/l), (F) or an antibody blocking GPVI (anti-GPVI: 50 μg/ml), (G). Controls corresponded to an irrelevant mouse IgG (Control: 10 μg/mL), (E) or to saline (F) or Fab fragments (Control: 50 μg/mL), (G). H, Dot plot distribution of the maximal increase in cytosolic Ca2+ in individual platelets from WT or GPVI$^{-/-}$ mice. The results are presented as the mean ± SEM in 3-5 independent experiments for each condition (***P< 0.001 and ns: P>0.05).

the GPIb-V-IX complex, flow experiments were performed at 300 s^{-1} and 500 s^{-1}. The OS-1 peptide, which blocks the VWF binding site on human GPIbα, decreased the thrombus volume by 34% (n=3, p=0.0151) and 70% (n=3, p<0.0001) at 300 s^{-1} and 500 s^{-1}, respectively, as compared to a scrambled peptide (►Figure 5C). AK2, which did not prevent platelet adhesion, reduced the thrombus volume by 46% (n=3, p=0.0007) and 93% (n=3, p=0.0002) at 300 s^{-1} and 500 s^{-1}, respectively (►Figure 5D), confirming the role of GPIbα in fibrillar cFN induced platelet aggregation. The role of the GPIb-V-IX complex appears to be indirect and mediated by VWF because 701, an anti-VWF A1 domain monoclonal antibody blocking GPIbα binding, reduced thrombus formation on fibrillar cFN by 56% at 500 s^{-1} (n=3, p=0.0002) (►Figure 5E). The anti-human GPVI agent 9O12, which had no effect on platelet adhesion or activation on cFN, dramatically decreased the thrombus volume as compared to a Fab control (88% reduction; n=5, p<0.0001) (►Figure 5F). This result was confirmed in GPVI$^{-/-}$ mice, with a 94% reduction in thrombus volume with respect to

WT animals (n=5, p=0.0079), highlighting an unexpected role of GPVI in the process of platelet/platelet interaction (►Figure 5G).

TLR4, an EDA binding receptor, participates in platelet aggregation on fibrillar cFN

The striking difference of thrombogenicity between the two forms of fibrillar FNs (►Figure 1H) could have its origin in the inclusion of few alternatively spliced regions in cFN. We hypothesised that the EDA region, a known ligand of TLR4, could explain the differences, since this receptor is expressed at the platelet surface (42, 43). Blockade of TLR4 with two distinct anti-TLR4 antibodies reduced the thrombus volume by 69% (n=8, p<0.0001) and 67% (n=3, p<0.0001) on fibrillar cFN, suggesting that this receptor participates in fibrillar cFN-induced platelet aggregation (►Figure 5H). Blockade of TLR4 with both antibodies impaired the initial growth phase of the thrombus as evidenced by the reduced slope of platelet accumulation (►Figure 5I-J), without preventing the
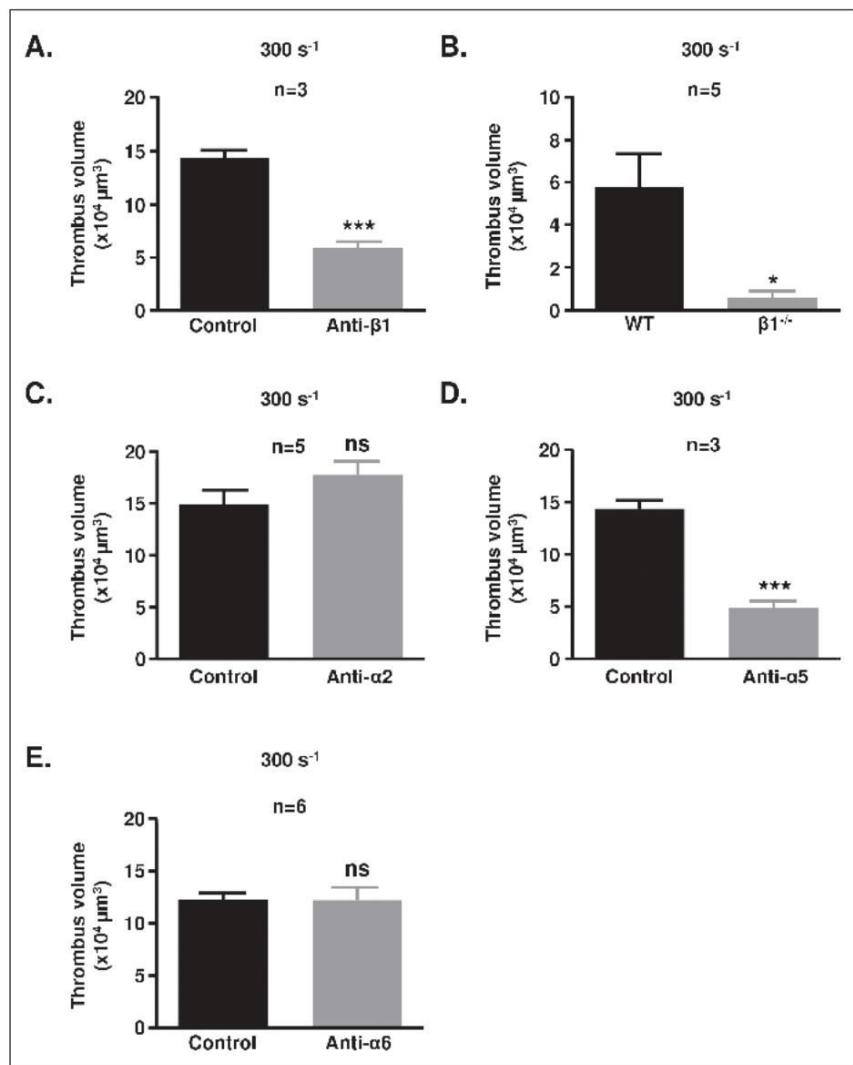
Figure 4: Integrin α5β1 mediates thrombus growth on fibrillar cFN. A, C-E) Hirudinated human whole blood incubated with DIOC6 (1 µmol/l) was pretreated with blocking antibodies (10 µg/ml) against integrin β1 (anti-β1) (A), integrin α2 (anti-α2) (C), integrin α5 (anti-α5) (D) integrin α6 (anti-α6) (E) or with an irrelevant mouse IgG (Control: 10 µg/ml) (A, C-E) and perfused over fibrillar cFN (300 µg/ml) at 300 s^{-1} for 30 min. B) Hirudinated whole blood from WT or β1-null (β1$^{-/-}$) mice labelled with DIOC6 (1 µmol/l) was perfused over fibrillar cFN (coated at 300 µg/ml) at 300 s^{-1} for 15 min. A-E) Bar graphs represent the total thrombus volume as measured by confocal microscopy. The thrombus volumes are the mean ± SEM in eight random fields, in 3-4 separate experiments as detailed on each panel (*P<0.05; ***P<0.001 and ns: P>0.05).
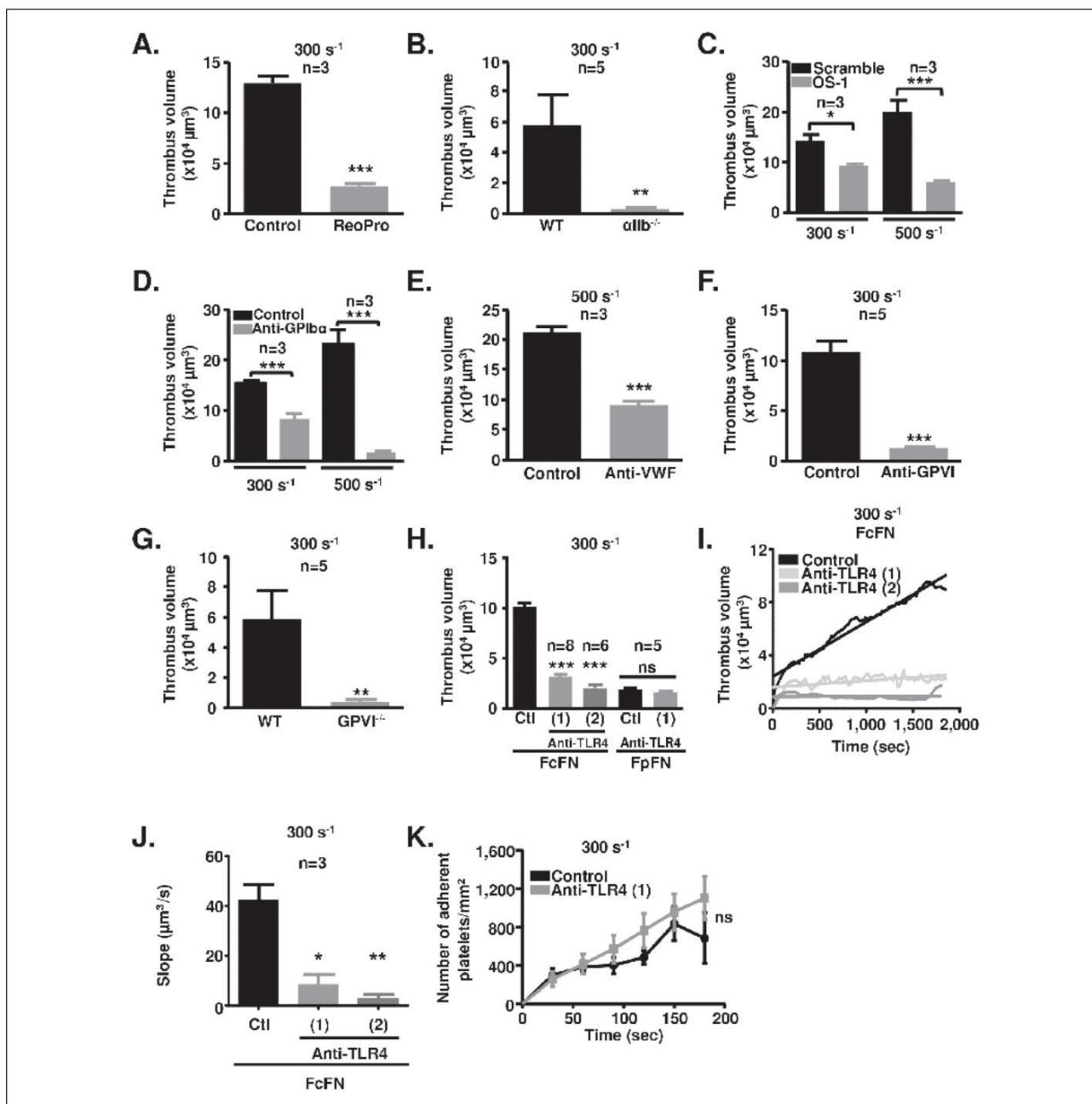
Figure 5: Integrin αIIbβ3, the GPIb-V-IX complex, GPVI and TLR4 mediate thrombus formation on fibrillar cFN. Hirudinated human whole blood incubated with DIOC6 (1 µmol/l) was perfused over fibrillar cFN (A, C-F, H-K) or fibrillar pFN (H), (coated at 300 µg/ml) at 300 or 500 s⁻¹ for 30 min, after pretreatment with an integrin β3 blocker (ReoPro: 40 µg/ml) (A), the anti-human GPIbα peptide OS-1 (500 nM) (C), an anti-human GPIbα antibody (anti-GPIbα: 10 µg/ml) (D), the anti-VWF A1 domain antibody (anti-VWF: 10 µg/ml) (E), the anti-human GPVI antibody (anti-GPVI: 50 µg/ml) (F) or with two distinct TLR4 blocking antibodies (Anti-TLR4: 10 µg/ml) (H-J). Controls were performed with saline (A), a scrambled peptide (Scramble: 500 nM) (C) or an irrelevant mouse IgG (Control or Ctl: 10 µg/ml) (D-E, H-K) or a Fab fragments (Control: 50 µg/ml) (F). L) Hirudinated human whole blood incubated with DIOC6 (1 µmol/l) was perfused over collagen (2.5 mg/ml) at 300 s⁻¹ for 10 min after pretreat-

ment with a TLR4 blocking antibody (Anti-TLR4: 10 µg/ml). Control was performed with an irrelevant mouse IgG (Control: 10 µg/ml) (L). B, G, M) Hirudinated whole blood from WT, αIIb-null (αIIb⁻/⁻) (B), GPVI-null (GPVI⁻/⁻) (G) or TLR4-null (TLR4⁻/⁻) (M) mice incubated with DIOC6 (1 µmol/l) was perfused over fibrillar cFN (coated at 300 µg/ml) at 300 s⁻¹ for 15 min. A-H, J, L-M) Bar graphs represent the total thrombus volume measured by confocal microscopy after 15 min (mouse) or 30 min (human) of whole blood perfusion. The thrombus volumes are the mean ± SEM in eight random fields, in 3-8 separate experiments as detailed on the figures (*P< 0.05; **P< 0.01; ***P< 0.001 and ns: P> 0.05). I) Representative curves and slopes of the thrombus volume measured in real time in one random field by confocal microscopy. J) Bar graphs represent the mean slope (± SEM) of platelet accumulation in one random field, in three separate experiments (*P< 0.05).

Figure 5: Continued.

Figure 6: Fibrillar cFN supports the procoagulant activity of platelets and fibrin formation. A) Hirudinated human whole blood was perfused over fibrillar cFN at 300 s^{-1} for 30 min. The flow devices were rinsed with PBS for 10 min and perfused with Alexa 568-conjugated annexin-V (1/10) for 10 min at 300 s^{-1}. Procoagulant platelets were detected by their annexin-V positivity (green platelets) using epifluorescence microscopy. B) Recalcified citrated human whole blood loaded with Calcein green-AM (10 µmol/l) was perfused over VWF (coated at 20 µg/ml), fibrinogen (coated at 300 µg/ml) or fibrillar cFN (coated at 300 µg/ml) at 300 s^{-1}, in the presence of the specific Alexa 647-coupled anti human fibrin antibody 59d8 (5 µg/ml). Representative confocal microscopy images depicting platelet accumulation (green) and fibrin formation (red) on VWF, fibrinogen or fibrillar cFN after 10 min of blood perfusion. A-B) Images are representative of at least three independent experiments and the white arrows indicate the flow direction. Scale bar 10 µm. C) Bar graphs represent fibrin formation expressed in MFI (mean fluorescence intensity) measured by confocal microscopy, in four independent experiments (*P<0.05).

recruitment of individual platelets to fibrillar cFN (n=6, p=0.173), (►Figure 5K). This result suggests a role of TLR4 in promoting activation of the first platelet monolayer. Conversely, blockade of TLR4 did not reduce the thrombus volume on fibrillar pFN or collagen, which both lack an EDA domain (n=5, p>0.05 and n=7, p>0.05, respectively) (►Figure 5H, L). These results were confirmed when perfusing blood from TLR4$^{-/-}$ mice, which resulted in a 31% reduction in thrombus volume as compared to WT animals (n=8, p=0.0499) (►Figure 5M).

Role of fibrillar cFN in regulating the procoagulant activity of platelets and fibrin formation

Platelets adhering to collagen expose phosphatidylserine at their surface and become procoagulant (44). We assessed the procoagulant potential of fibrillar cFN by monitoring annexin-V binding. Epifluorescence images showed that many of the human platelets adhering to this surface at 300 s^{-1} became positive for annexin-V (►Figure 6A). Such cells were mainly observed at the periphery of aggregates and exhibited the typical smooth, round-shaped morphology of Sustained Calcium-Induced Platelet (SCIP) or Collagen and Thrombin-activated (COAT) platelets (37, 44). The ability of fibrillar cFN to support fibrin formation was evaluated by perfusing citrated recalcified blood in comparison with two recognised platelet adhesive proteins, fibrinogen and VWF. A dense fibrin network was observed around the platelets adherent on fibrillar cFN, while this network was much smaller on immobilised fibrinogen and did not form on VWF even after 10 min of perfusion (►Figure 6B). Interestingly, fibrin formation was 5.8- and 26.1-fold more important on fibrillar cFN as compared to FGN and VWF, respectively (p<0.05). These results provide evidence that fibrillar cFN promotes efficient platelet procoagulant activity compared to FGN and VWF, resulting in fibrin formation.

Discussion

The main finding of this study is that fibrillar cFN represents a potent thrombogenic component of the subendothelium. Fibrillar cFN supports efficient platelet adhesion and activation under arterial flow conditions, which promotes thrombus formation *in vitro* and procoagulant activity. The initial phase of platelet adhesion and activation is mediated by integrins α5β1 and αIIbβ3. These integrins, together with the GPIb-V-IX complex, GPVI and TLR4, also contribute to subsequent thrombus growth.

The adhesive proteins of the vessel wall are commonly subdivided into two groups according to their reactivity. To date, only fibrillar collagens have been considered to be highly thrombogenic. On the other hand, VWF, fibrinogen, laminins, thrombospondins and pFN are considered to be weakly reactive, allowing only single platelet adhesion (11, 45–47). Our data provide evidence that cFN in its fibrillar form is also thrombogenic because it promotes efficient platelet adhesion, activation, aggregation and procoagulant activity. This is probably a consequence of its fibrillar structure, since it supported only marginal platelet adhesion in its dimeric

form. The importance of the multimeric structure of certain platelet ligands for their reactivity has been well described for collagens, IgGs, venom proteins and even synthetic peptides such as CRP (48–50). One explanation for the higher reactivity of the fibrillar forms is that multimerisation enhances the avidity of the ligands, providing stronger platelet interaction and recruitment of signalling partners.

Interestingly, pFN in its fibrillar form was much less reactive than fibrillar cFN. Since this difference in reactivity does not appear to be due to the structure or the number of fibers formed, which are very similar in both types of FN, we hypothesised that the difference could lie at the molecular level, in the nature of the glycoproteins themselves. cFN differs from pFN by the inclusion of alternatively spliced EDA and EDB domains and the type III homology connecting segment. Our study provides evidence that blockade or absence of TLR4, which binds to EDA, significantly reduced the aggregate volume on fibrillar cFN, suggesting that this receptor participates in thrombus growth and could, at least in part, explain the differences in reactivity between fibrillar cFN and pFN (51, 52). This observation appears in agreement with the work of Chauhan et al. who described a prothrombotic effect of fibronectin isoforms containing the EDA domain (53). Moreover, our *in vitro* data were recently supported by a work published by Prakash et al., who demonstrated *in vivo* that cellular FN expressing the EDA region promotes arterial thrombosis specifically through TLR4 expression on platelets (54). These results suggest that targeting TLR4 would represent an interesting antithrombotic strategy. Whether TLR4 interaction with fibrillar cFN is also important in platelet function beyond hemostasis, notably in platelet-mediated immune responses in conditions of infection or sepsis will need further investigations (42, 43, 55, 56).

Our results indicate that platelets only marginally adhere to dimeric pFN, which contrasts with several reports in the literature (11, 12, 14, 57). The reason for this discrepancy is unclear but could arise from differences in experimental conditions, notably in the method used to coat surfaces with FN. Some groups employed a spray-based technique, which could promote a certain degree of polymerisation, thereby increasing the reactivity of the protein (11, 12). Similarly as in these latter studies, we found that initial platelet adhesion to fibrillar cFN depended on integrins α5β1 and αIIbβ3. Conversely, the GPIb-V-IX complex did not seem to be required for platelet tethering to fibrillar cFN (12). This could be explained by a higher affinity and/or avidity of integrins α5β1 and αIIbβ3 for fibrillar cFN, which might hide a potential role of GPIb. A second difference in the mechanism of platelet interaction with pFN as compared to fibrillar cFN lies in the importance of GPVI. Whereas Bultmann et al. reported an important role of GPVI in platelet adhesion to pFN under flow conditions (14), our data indicate that this receptor was not necessary for adhesion to fibrillar cFN. Interestingly, we found that GPVI was essential for thrombus build-up on fibrillar cFN. Although the molecular mechanism is still unclear, one could speculate that GPVI might interact with a counter-receptor or an adhesive plasma protein at the surface of thrombus-bound activated platelets, thereby contributing to sustain platelet activation and promote thrombus growth. This

hypothesis is in agreement with a previous *in vivo* observation showing that GPVI-deficient mice exhibit a defect during the later stages of thrombus formation rather than in the initial step (28). Further studies will be needed to precisely define the role of GPVI in platelet-platelet interaction during the growth of the thrombus and identify its counter-receptor or the plasma protein involved in this process.

Thrombus growth on fibrillar cFN was efficient at wall shear rates between 300 s^{-1} and 500 s^{-1}, as can be found in large arteries like the carotid or coronary vessels, or in the post-stenotic region of advanced atherosclerotic plaques where recirculation occurs (58). Therefore, one may hypothesise that exposure of cFN to flowing blood is likely to contribute to the haemostatic response under normal conditions, and to the growth of a thrombus in a pathological setting. To date, only fibrillar collagens have been described to promote such a range of platelet responses. Histological studies nevertheless indicated that fibrillar collagens are mainly located in the deeper layers of the vessel wall and would be exposed exclusively after severe damage (59). More superficial layers contain non fibrillar collagens like type IV collagen, but the reactivity of these molecules is relatively low (57, 60). cFN is found in all layers of the vessel wall, which also contain FN derived from plasma (61), and both are in a reactive fibrillar form (61, 62). FNs therefore represent interesting alternative matrices for the efficient adhesion and activation of platelets after a superficial injury and the formation of a haemostatic plug. A role of FN in arterial thrombosis after plaque erosion or rupture is also highly probable in view of its strong expression in atherosclerotic plaques (63).

In conclusion, this study provides evidence that the fibrillar cFN present in the vessel wall is a thrombogenic surface promoting a range of platelet responses including adhesion, activation, release of soluble agonists, aggregation and procoagulant activity. Hence its exposure to blood after injury of the vessel wall is likely to contribute to haemostasis, thereby helping to prevent blood loss, but also to the thrombotic process after erosion or rupture of an atherosclerotic plaque.

Conflicts of interest
None declared.

What is known about this topic?

- Cellular fibronectin is an adhesive protein which is found in all layers of the vessel wall and is overexpressed in atherosclerotic plaques.
- Whereas plasma fibronectin has been described to support platelet adhesion and activation through integrins α5β1 and αIIbβ3, and the GPIb/VWF axis, the adhesive properties of cellular fibronectin is unknown.
- GPVI has been proposed to be a platelet receptor for plasma fibronectin.

What does this paper add?

- This study highlights the thrombogenicity of cFN under its fibrillar form, as it is found in all layers of the vessel wall.
- The fibrillar structure of cellular fibronectin is important for its reactivity and allows efficient platelet adhesion, activation, aggregation and procoagulant activity.
- Thrombus formation on fibrillar cFN relies on the same receptors involved in platelet adhesion to pFN, namely integrins α5β1 and αIIbβ3 and the GPIb-V-IX complex.
- GPVI is not a key receptor for platelet adhesion and activation on fibrillar cFN, but appears to play a novel role in platelet/platelet interaction.
- TLR4 participates in platelet aggregation on fibrillar cFN, and represents a potential novel anti-thrombotic target.

References

1. Versteeg HH, Heemskerk JW, Levi M, et al. New fundamentals in hemostasis. Physiol Rev 2013; 93: 327–358.
2. Jackson SP. Arterial thrombosis--insidious, unpredictable and deadly. Nature Med 2011; 17: 1423–1436.
3. Pankov R, Yamada KM. Fibronectin at a glance. J Cell Sci 2002; 115: 3861–3863.
4. George EL, Georges-Labouesse EN, Patel-King RS, et al. Defects in mesoderm, neural tube and vascular development in mouse embryos lacking fibronectin. Development 1993; 119: 1079–1091.
5. Erridge C. Endogenous ligands of TLR2 and TLR4: agonists or assistants? J Leukoc Biol 2010; 87: 989–999.
6. Liao YF, Gotwals PJ, Koteliansky VE, et al. The EIIIA segment of fibronectin is a ligand for integrins alpha 9beta 1 and alpha 4beta 1 providing a novel mechanism for regulating cell adhesion by alternative splicing. J Biol Chem 2002; 277: 14467–14474.
7. Zerlauth G, Wolf G. Plasma fibronectin as a marker for cancer and other diseases. Am J Med 1984; 77: 685–689.
8. Peters JH, Sporn LA, Ginsberg MH, et al. Human endothelial cells synthesize, process, and secrete fibronectin molecules bearing an alternatively spliced type III homology (ED1). Blood 1990; 75: 1801–1808.
9. Glukhova MA, Frid MG, Shekhonin BV, et al. Expression of extra domain A fibronectin sequence in vascular smooth muscle cells is phenotype dependent. J Cell Biol 1989; 109: 357–366.
10. van Keulen JK, de Kleijn DP, Nijhuis MM, et al. Levels of extra domain A containing fibronectin in human atherosclerotic plaques are associated with a stable plaque phenotype. Atherosclerosis 2007; 195: e83–91.
11. Beumer S, Ijsseldijk MJ, de Groot PG, et al. Platelet adhesion to fibronectin in flow: dependence on surface concentration and shear rate, role of platelet membrane glycoproteins GP IIb/IIIa and VLA-5, and inhibition by heparin. Blood 1994; 84: 3724–3733.
12. Beumer S, Heijnen HF, Ijsseldijk MJ, et al. Platelet adhesion to fibronectin in flow: the importance of von Willebrand factor and glycoprotein Ib. Blood 1995; 86: 3452–3460.
13. McCarty OJ, Zhao Y, Andrew N, et al. Evaluation of the role of platelet integrins in fibronectin-dependent spreading and adhesion. J Thromb Haemost 2004; 2: 1823–1833.
14. Bultmann A, Li Z, Wagner S, et al. Impact of glycoprotein VI and platelet adhesion on atherosclerosis--a possible role of fibronectin. J Mol Cell Cardiol 2010; 49: 532–542.

15. Bastida E, Escolar G, Ordinas A, et al. Fibronectin is required for platelet adhesion and for thrombus formation on subendothelium and collagen surfaces. Blood 1987; 70: 1437–1442.

16. Nievelstein PF, D'Alessio PA, Sixma JJ. Fibronectin in platelet adhesion to human collagen types I and III. Use of nonfibrillar and fibrillar collagen in flowing blood studies. Arteriosclerosis 1988; 8: 200–206.

17. Cho J, Mosher DF. Enhancement of thrombogenesis by plasma fibronectin cross-linked to fibrin and assembled in platelet thrombi. Blood 2006; 107: 3555–3563.

18. Ni H, Yuen PS, Papalia JM, et al. Plasma fibronectin promotes thrombus growth and stability in injured arterioles. Proc Natl Acad Sci USA 2003; 100: 2415–2419.

19. Matuskova J, Chauhan AK, Cambien B, et al. Decreased plasma fibronectin leads to delayed thrombus growth in injured arterioles. Arterioscler Thromb Vasc Biol 2006; 26: 1391–1396.

20. Santoro SA. Inhibition of platelet aggregation by fibronectin. Biochem Biophys Res Commun 1983; 116: 135–140.

21. Moon DG, Kaplan JE, Mazurkewicz JE. The inhibitory effect of plasma fibronectin on collagen-induced platelet aggregation. Blood 1986; 67: 450–457.

22. Tanabe J, Fujita H, Iwamatsu A, et al. Fibronectin inhibits platelet aggregation independently of RGD sequence. J Biol Chem 1993; 268: 27143–27147.

23. Reheman A, Yang H, Zhu G, et al. Plasma fibronectin depletion enhances platelet aggregation and thrombus formation in mice lacking fibrinogen and von Willebrand factor. Blood 2009; 113: 1809–1817.

24. Miekka S. Rapid methods for isolation of human plasma fibronectin. Thromb Res 1982; 24: 1–14.

25. Tronik-Le Roux D, Roullot V, Schweitzer A, et al. Suppression of erythro-megakaryocytopoiesis and the induction of reversible thrombocytopenia in mice transgenic for the thymidine kinase gene targeted by the platelet glycoprotein alpha IIb promoter. J Exp Med 1995; 181: 2141–2151.

26. Tiedt R, Schomber T, Hao-Shen H, et al. Pf4-Cre transgenic mice allow the generation of lineage-restricted gene knockouts for studying megakaryocyte and platelet function in vivo. Blood 2007; 109: 1503–1506.

27. Potocnik AJ, Brakebusch C, Fassler R. Fetal and adult hematopoietic stem cells require beta1 integrin function for colonizing fetal liver, spleen, and bone marrow. Immunity 2000; 12: 653–663.

28. Bender M, Hagedorn I, Nieswandt B. Genetic and antibody-induced glycoprotein VI deficiency equally protects mice from mechanically and FeCl(3) -induced thrombosis. J Thromb Haemost 2011; 9: 1423–1426.

29. Takaku T, Malide D, Chen J, et al. Hematopoiesis in 3 dimensions: human and murine bone marrow architecture visualized by confocal microscopy. Blood 2010; 116: e41–55.

30. McDonald JC, Duffy DC, Anderson JR, et al. Fabrication of microfluidic systems in poly(dimethylsiloxane). Electrophoresis 2000; 21: 27–40.

31. Schaff M, Receveur N, Bourdon C, et al. Novel function of tenascin-C, a matrix protein relevant to atherosclerosis, in platelet recruitment and activation under flow. Arterioscler Thromb Vasc Biol 2011; 31: 117–124.

32. Kroll MH, Hellums JD, McIntire LV, et al. Platelets and shear stress. Blood 1996; 88: 1525–1541.

33. Steward RL, Jr., Cheng CM, Ye JD, et al. Mechanical stretch and shear flow induced reorganisation and recruitment of fibronectin in fibroblasts. Scientific Rep 2011; 1: 147.

34. Goetz JG, Minguet S, Navarro-Lerida I, et al. Biomechanical remodeling of the microenvironment by stromal caveolin-1 favors tumor invasion and metastasis. Cell 2011; 146: 148–163.

35. Beacham DA, Amatangelo MD, Cukierman E. Preparation of extracellular matrices produced by cultured and primary fibroblasts. Curr Prot Cell Biol 2007; 10: 10.9.

36. Mangin P, Yuan Y, Goncalves I, et al. Signaling role for phospholipase C gamma 2 in platelet glycoprotein Ib alpha calcium flux and cytoskeletal reorganisation. Involvement of a pathway distinct from FcR gamma chain and Fc gamma RIIA. J Biol Chem 2003; 278: 32880–32891.

37. Kulkarni S, Jackson SP. Platelet factor XIII and calpain negatively regulate integrin alphaIIbbeta3 adhesive function and thrombus growth. J Biol Chem 2004; 279: 30697–30706.

38. Hui KY, Haber E, Matsueda GR. Monoclonal antibodies to a synthetic fibrin-like peptide bind to human fibrin but not fibrinogen. Science 1983; 222: 1129–1132.

39. Hocking DC, Titus PA, Sumagin R, et al. Extracellular matrix fibronectin mechanically couples skeletal muscle contraction with local vasodilation. Circ Res 2008; 102: 372–379.

40. To WS, Midwood KS. Plasma and cellular fibronectin: distinct and independent functions during tissue repair. Fibrogen Tissue Rep 2011; 4: 21.

41. Lemmon CA, Chen CS, Romer LH. Cell traction forces direct fibronectin matrix assembly. Biophys J 2009; 96: 729–738.

42. Berthet J, Damien P, Hamzeh-Cognasse H, et al. Human platelets can discriminate between various bacterial LPS isoforms via TLR4 signaling and differential cytokine secretion. Clin Immunol 2012; 145: 189–200.

43. Cognasse F, Hamzeh H, Chavarin P, et al. Evidence of Toll-like receptor molecules on human platelets. Immunol Cell Biol 2005; 83: 196–198.

44. Heemskerk JW, Vuist WM, Feijge MA, et al. Collagen but not fibrinogen surfaces induce bleb formation, exposure of phosphatidylserine, and procoagulant activity of adherent platelets: evidence for regulation by protein tyrosine kinase-dependent Ca2+ responses. Blood 1997; 90: 2615–2625.

45. Savage B, Saldivar E, Ruggeri ZM. Initiation of platelet adhesion by arrest onto fibrinogen or translocation on von Willebrand factor. Cell 1996; 84: 289–297.

46. Schaff M, Tang C, Maurer E, et al. Integrin alpha6beta1 is the Main Receptor for Vascular Laminins and Plays a Role in Platelet Adhesion, Activation and Arterial Thrombosis. Circulation 2013; 128: 541–552.

47. Jurk K, Clemetson KJ, de Groot PG, et al. Thrombospondin-1 mediates platelet adhesion at high shear via glycoprotein Ib (GPIb): an alternative/backup mechanism to von Willebrand factor. FASEB J 2003; 17: 1490–1492.

48. Savage B, Ginsberg MH, Ruggeri ZM. Influence of fibrillar collagen structure on the mechanisms of platelet thrombus formation under flow. Blood 1999; 94: 2704–2715.

49. Morton LF, Peachey AR, Zijenah LS, et al. Conformation-dependent platelet adhesion to collagen involving integrin alpha 2 beta 1-mediated and other mechanisms: multiple alpha 2 beta 1-recognition sites in collagen type I. Biochem J 1994; 299: 791–797.

50. Luo Y, Lu Z, Raso SW, et al. Dimers and multimers of monoclonal IgG1 exhibit higher in vitro binding affinities to Fcgamma receptors. MAbs 2009; 1: 491–504.

51. Okamura Y, Watari M, Jerud ES, et al. The extra domain A of fibronectin activates Toll-like receptor 4. J Biol Chem 2001; 276: 10229–10233.

52. Zhang G, Han J, Welch EJ, et al. Lipopolysaccharide stimulates platelet secretion and potentiates platelet aggregation via TLR4/MyD88 and the cGMP-dependent protein kinase pathway. J Immunol 2009; 182: 7997–8004.

53. Chauhan AK. Prothrombotic Effects of Fibronectin Isoforms Containing the EDA Domain. Arterioscl Thromb Vasc Biol 2008; 28: 296–301.

54. Prakash P, Kulkarni PP, Lentz SR, et al. Cellular fibronectin containing extra domain A promotes arterial thrombosis in mice through platelet toll-like receptor 4. Blood 2015; 14;125:3164–3172.

55. Semeraro F, Ammollo CT, Morrissey JH, et al. Extracellular histones promote thrombin generation through platelet-dependent mechanisms: involvement of platelet TLR2 and TLR4. Blood 2011; 118: 1952–1961.

56. Brown GT, Narayanan P, Li W, et al. Lipopolysaccharide stimulates platelets through an IL-1beta autocrine loop. J Immunol 2013; 191: 5196–5203.

57. Polanowska-Grabowska R, Simon CG, Jr., Gear AR. Platelet adhesion to collagen type I, collagen type IV, von Willebrand factor, fibronectin, laminin and fibrinogen: rapid kinetics under shear. Thromb Haemost 1999; 81: 118–123.

58. Nesbitt WS, Westein E, Tovar-Lopez FJ, et al. A shear gradient-dependent platelet aggregation mechanism drives thrombus formation. Nature Med 2009; 15: 665–673.

59. Farquharson C, Robins SP. Immunolocalisation of collagen types I and III in the arterial wall of the rat. Histochem J 1989; 21: 172–178.

60. Parsons TJ, Haycraft DL, Hoak JC, et al. Interaction of platelets and purified collagens in a laminar flow model. Thromb Res 1986; 43: 435–443.

61. Moretti FA, Chauhan AK, Iaconcig A, et al. A major fraction of fibronectin present in the extracellular matrix of tissues is plasma-derived. J Biol Chem 2007; 282: 28057–28062.

62. Singh P, Carraher C, Schwarzbauer JE. Assembly of fibronectin extracellular matrix. Ann Rev Cell Developm Biol 2010; 26: 397–419.

63. Matter CM, Schuler PK, Alessi P, et al. Molecular imaging of atherosclerotic plaques using a human antibody against the extra-domain B of fibronectin. Circ Res 2004; 95: 1225–1233.

3.2 Manuscrit n°9: Generating and characterizing the mechanical properties of cell-derived matrices using atomic force microscopy
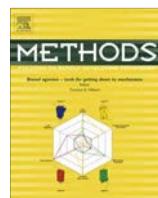
Generating and characterizing the mechanical properties of cell-derived matrices using atomic force microscopy

Marta Tello [a,1,2], Caroline Spenlé [b,c,d,e,2], Joseph Hemmerlé [c,e,g], Luc Mercier [b,c,d,e], Roxane Fabre [f], Guillaume Allio [b,c,d,e], Patricia Simon-Assmann [b,c,d,e,*,2], Jacky G. Goetz [b,c,d,e,*,2]

[a] Instituto de Microelectrónica de Madrid, CSIC, Isaac Newton 8, 28760, Tres Cantos, Madrid, Spain
[b] Inserm U1109, MN3T, Strasbourg F-67200, France
[c] Université de Strasbourg, Strasbourg F-67000, France
[d] LabEx Medalis, Université de Strasbourg, Strasbourg F-67000, France
[e] Fédération de Médecine Translationnelle de Strasbourg (FMTS), Strasbourg F-67000, France
[f] Centre d'Immunologie de Marseille – Luminy, Parc Scientifique et Technologique de Luminy, F-13288 Marseille, France
[g] Inserm U1121, Strasbourg F-67200, France

ARTICLE INFO

ABSTRACT

Mechanical interaction between cells and their surrounding extracellular matrix (ECM) controls key processes such as proliferation, differentiation and motility. For many years, two-dimensional (2D) models were used to better understand the interactions between cells and their surrounding ECM. More recently, variation of the mechanical properties of tissues has been reported to play a major role in physiological and pathological scenarios such as cancer progression. The 3D architecture of the ECM finely tunes cellular behavior to perform physiologically relevant tasks. Technical limitations prevented scientists from obtaining accurate assessment of the mechanical properties of physiologically realistic matrices. There is therefore a need for combining the production of high-quality cell-derived 3D matrices (CDMs) and the characterization of their topographical and mechanical properties. Here, we describe methods that allow to accurately measure the young modulus of matrices produced by various cellular types. In the first part, we will describe and review several protocols for generating CDMs matrices from endothelial, epithelial, fibroblastic, muscle and mesenchymal stem cells. We will discuss tools allowing the characterization of the topographical details as well as of the protein content of such CDMs. In a second part, we will report the methodologies that can be used, based on atomic force microscopy, to accurately evaluate the stiffness properties of the CDMs through the quantification of their young modulus. Altogether, such methodologies allow characterizing the stiffness and topography of matrices deposited by the cells, which is key for the understanding of cellular behavior in physiological conditions.

© 2015 Elsevier Inc. All rights reserved.

1. Introduction: definition, terminology and rationale for studying cell-derived matrices (CDMs)

Interactions between cells and the extracellular matrix (ECM) are key and vital drivers of embryonic development and adult organ homeostasis. Mis-regulation or impairment of this process leads to a plethora of disorders including developmental malformations, fibrosis and cancer, among others. *In vivo*, cells naturally encounter cell-derived extracellular matrices (CDMs). The interaction of cells with the surrounding ECM is essential for their proper function, as well as the maintenance of tissue architecture and homeostasis. The ECM provides a physico-chemical scaffold in which cells adhere, anchor and function, shaping tissue architecture and homeostasis. The ECM provides also a signaling support which regulates cellular functions such as growth and survival [1,2]. Cells have developed a large repertoire of receptors capable of binding to the ECM [3,4]. They provide a physical link to the ECM and allow them to transduce signals emanating from the ECM by adapting their behavior to the properties of this complex microenvironment. Noteworthy, cell behavior is affected by the composition, the topography and the mechanical properties of the ECM [5]. In addition, ECM is a potent reservoir of growth

---

factors that can drastically affect cellular functions [6]. Finally, the ECM is commonly deregulated and disorganized in diseases such as cancer [7].

It is therefore of utmost importance to mimic as much as possible the reality by developing *in vivo*-like 3D CDMs. By definition, *in vitro* CDMs are ECM molecules that are deposited and organized by the cells themselves. They are eventually decellularized and represent 3D composites of ECM proteins. CDMs have been developed for many years and not surprisingly have led to several terminologies: cell-free matrix, cell-secreted matrix, cell-derived matrix, acellular matrix, decellularized ECM or decellularized matrix, immobilized ECM surface, cell-driven matrix. Here, for the sake of simplicity, we will use a common nomenclature, which is cell-derived matrix (CDM). When derived from a tissue, they can be named cell-free-organ-derived ECM (ex: cell-free-bone marrow-derived ECM) or tissue-derived matrices (TDMs).

Such matrices, when used as substrate for other cells, allow the characterization of a plethora of cellular functions with high physiological relevance and which drastically differs from culturing cells on artificial 2D substrates *in vitro* [8]. They further allow mimicking *in vivo* situations since ECM does not function merely as an inert structural role but rather plays an active role in the control of cell growth and differentiation [9]. In addition, CDMs allow to reproduce *in vitro* the micro-heterogeneity of the basement membranes, or more generally of the ECMs, that is known to regulate cellular functions or to establish niches suitable for the growth of stem or progenitor cells. They further allow taking into account the tissue-specificity of the ECM and thus to better replicate and mimic cell-specific features of the ECM architecture. They naturally allow to present associated bioactive factors such as growth factors and are advantageous for the culture of anchorage-dependent cells that fail to attach properly to available substrates, or that are not capable to produce their own matrix. They also provide a way to study the synthesis and asymmetrical deposition of the ECM. Finally, they are perfectly suitable for the characterization of their mechanical properties (stiffness and viscoelastic properties) and allow thus to study their biomechanical contribution to cell behavior.

2. Preparation of CDMs

The ultimate goal of developing and using CDMs is to allow the cells to produce and deposit their own ECM and then to use extraction procedures to remove the cell layer but, importantly, leaving the underlying deposited-ECM intact, free of cellular debris and firmly attached to the culture dish. While it is unfortunately impossible to clearly identify optimal experimental conditions for producing CDMs of high-quality, multiple laboratories over the world have developed a wide range of protocols with the idea of optimizing the methodology: this includes priming of the substrate before seeding of the cells, usage of various cell types, culture timings and conditions (such as presence of cytokines, growth factors, oxygen tension) and cell extraction protocols. All these parameters will strongly influence the composition, the organization, and the mechanical properties of the matrices, and thereby modulate differentially the phenotype of cells seeded on them. Importantly, cells will secrete and deposit the ECM molecules basally as a function of time. Intuitively, the more cells are seeded in a confluent state, the higher the amount of ECM should be deposited on the surfaces by cells that were seeded on. Yet if cells are too confluent, detachment and/or contraction of CDMs can occur.

The common feature of each workflow is to achieve efficient lysis of ECM-producing cells. For this purpose, several scenarios have been developed [10,11]. While some experimental strategies rely on physical detachment of cells using freeze–thaw cycles (formation of intracellular crystals that disrupt cell membrane and cause cell lysis), the most-commonly used methods are based on chemical or enzymatic approaches (Fig. 1):

- *Removal of cells using alkaline buffers:* They are used to solubilize the cytoplasmic components of the cells as well to remove nucleic acids (RNA, DNA). The most common used is ammonium hydroxide (NH_4OH); yet this molecule may dissociate glycosaminoglycans from collagens [10].
- *Removal of cells using detergents:* (i) non-ionic detergents with the most commonly used being Triton X-100 (disruption of lipid–lipid and lipid–protein interactions); Tween-20 or NP-40 have been also used but to a lesser extent; (ii) ionic detergents such as sodium deoxycholate (DOC) that will disrupt protein–protein interactions and solubilize cytoplasmic and nuclear membranes. Combined use of Triton X-100 with NH_4OH is often realized.
- *Removal of cells using denaturing agents:* Such as urea.
- *Removal of cells using hypotonic treatment:* Osmotic shock with a hypotonic solution such as deionized water or low ionic strength solution is used to lyse the cells.
- *Removal of cells using chelating agents:* EDTA or EGTA for disrupting the cell–cell junction. The advantage here will be that EDTA inhibits metalloproteases and therefore may contribute to ECM preservation [11].
- *Removal of cells using enzymatic methods:* Enzymatic detachment of the cells from the deposited ECM can be done using trypsin; the major drawback is the possible damage of the remaining ECM and its bound factors.

Which method to use is a rather difficult assumption/choice to make and one should carefully consider the existing protocols, which we will review in the subsequent sections, according to cell subtypes.

2.1. Endothelial cell-derived matrices

Generation of matrices derived from endothelial cells have led to several protocols detailed below. They are historically the first cells that had been used to produce CDMs and have led to multiple observations. ECM produced by cultured endothelial cells closely resembles the sub-endothelium *in vivo*, in its morphology and molecular composition. Endothelial CDMs have been used to study the adhesion- and growth-promoting properties, but also as substrate to assess cell differentiation potential (for a review see [12]). Importantly, cells maintained on CDMs produced by corneal endothelial cells proliferated rapidly and no longer required FGF to reach confluence [13]:

a. *Original method using detergents:* The first description of a technique that allows isolating ECM deposited by cells in culture was from Gospodarowicz's team [13,14]. The original technique used only Triton X-100 to prepare CDMs from bovine endothelial cells. Briefly, once the cultures became confluent (ordinarily within 6 days) the media were renewed, and the cultures were further incubated for 6 days. After washing with PBS, cells were exposed for 30 min to 0.5% Triton X-100. In this condition, only a few cytoskeletons and nuclei were associated with the intact ECM (as defined by a thick layer of amorphous material) that coated the entire dish as shown by scanning electron microscope (SEM). The remaining nuclei and cytoskeletons were removed either by pipetting [15] or by adding subsequently 0.025 N NH_4OH (2–3 min exposure) to the CDM [16].
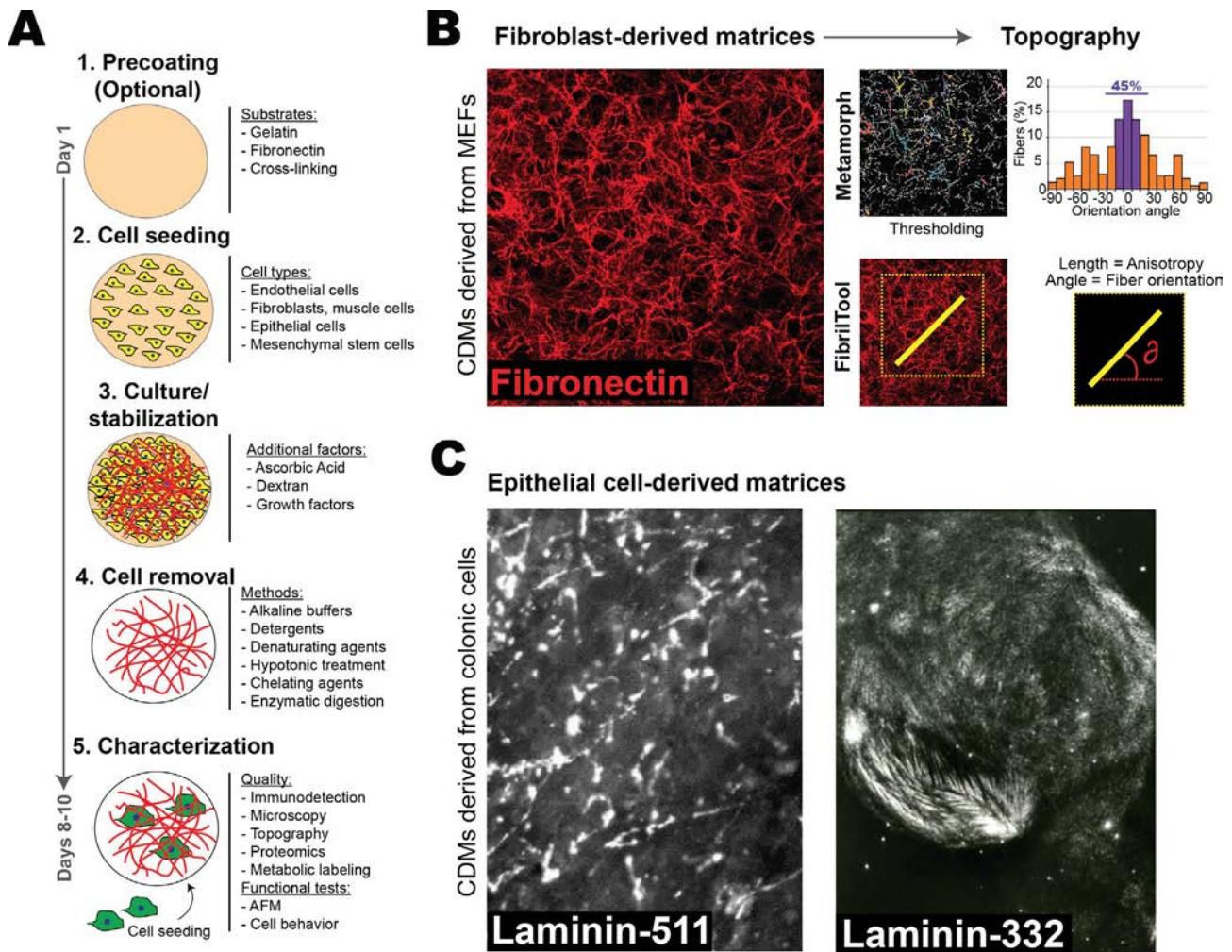
Fig. 1. Workflow for generating and characterizing CDMs. (A) Schematic for the generation of cell-derived matrices consisting in five major steps: (1) optional pre-coating of plastic or glass dishes with reinforced substratum such as fibronectin; (2) cell seeding; (3) cell culture to allow matrix secretion and stabilization using additional factors; (4) cell removal using various approaches, among which addition of alkali, detergents, denaturing agents and (5) finally, characterization of CDMs for assessing their quality as well as for performing functional tests. (B) Once CDMs have been produced, specific ECM can be stained and their topography assessed using image processing methods such as Metamorph (as described in [65]). We recently applied a Fiji plugin called *Fibriltool* [86], which has proven to be very useful for fast quantification of both the mean orientation as well as the anisotropy of immunolabeled-CDMs. (C) Immunodection of laminin-511 and of laminin-332 deposited by colonic cancer cells respectively by Caco2 [34] and HT29 MTX [38] cells.

b. *Alkaline treatment:* CDMs produced by bovine or human endothelial (HUVEC, HMEC) cells could also be recovered by alkaline treatment [17–19]. Confluent cells were washed/lysed with distilled water and then exposed to 20 mM NH_4OH in distilled water for 5 min, followed by washing with PBS. Bovine aortic endothelial-cell derived matrix could also be isolated by lysing cells with an aqueous solution of 0.2 M ammonia at room temperature for 1 h [20]. CDMs treated with 0.5% Triton X-100 or 20 mM NH_4OH were shown to be equally capable of supporting the growth of various cell types seeded on them [17,21].

c. *Optimal protocol:* Currently, the best and more convenient protocol is to incubate endothelial cells directly for 3–5 min with a combined 0.5% (v/v) Triton X-100/20 mM NH_4-OH lysis solution [12]. The pre-warmed lysis solution has to be added for 10–20 min at 37 °C (incubation with detergents at 37 °C may induce subtle proteolysis). In that case, gelatin-coated dishes can be used to improve the plating efficiency of cells. Furthermore, dextran T40 was added to the culture medium to increase its viscosity and activates the exocytosis of the cells; by this way, the amount of ECM secreted and deposited can be increased at least by 2-fold.

d. *Exceptions, usage of denaturating agents:* In certain cases use of Triton X-100 and NH_4OH should be avoided. This was the case for experiments that aimed to prove that bFGF was deposited into the ECM (prior to the actual denudation of the CDM) [21] as this procedure does not require lysis of cells. For this purpose, cells which had been confluent for 7 days were removed with 2 M urea in DMEM for 10–20 min at 37 °C. After cells had retracted, they were removed from their substrate by gently adding DMEM supplemented with 2 M urea and the medium containing the cells was aspired; this step was repeated four times, leaving the underlying CDM firmly bound to the culture dish [21].

e. *Alternate protocols:* CDMs from bovine corneal endothelial cells were produced upon (i) hypotonic treatment of cells with cold sterile distilled water for half an hour [22], (ii) use of 0.5% NP-40 detergent in hypotonic buffer [23], (iii) pre-incubation of cells with medium containing 5% dextran (for 7 days) and treatment of cells with 20 mM NH_4OH [24], (iv) alternatively, CDMs from HUVECs have recently been derived upon two cell incubations with 0.5% DOC at 4 °C [25].

The first *in vitro* studies using CDMs isolated from endothelial cells showed that cell interactions with a naturally produced 'basement membrane-like' matrix could induce dramatic effects on cell shape, growth characteristics as well as on response to growth factors and hormones [16]. More recently, such endothelial-derived matrices have been shown to trigger mesenchymal stem cell differentiation towards the vascular cell lineages with some possible implications for vascular tissue regeneration or engineering [19].

2.2. Epithelial cell-derived extracellular matrices

In vivo, epithelial cells are resting on the basement membrane (BM) that mediates communication with other cells types found in the surrounding microenvironment. The BM appears early during development and guides important physiological events such as migration and differentiation [1,26]. The majority of the BM components such as laminins, collagen IV, heparan sulfate proteoglycan are secreted by epithelial cells. However, the assembly and deposition of a complete BM required presence of fibroblasts [27]. This explains at least partly why normal epithelial cells, when grown as monolayers on classical tissue culture plastic, often lose their morphological and differentiation markers. Matrices derived from epithelial cells can be isolated from normal and cancer cell lines although they may not be representative of tissues. We and others have established and used multiple methods to produce CDMs from epithelial cells, which should be considered more as basement membrane-like matrices, by using the methods listed below:

(a) The most common method used is based on lysis of cells with NH_4OH as described previously for endothelial cells [17]. This protocol has been used either for the mouse-derived PFHR-9 endodermal cells [28], rat bladder epithelial cells [29,30] but also for colon [31–35] and breast [36] cancer cell lines. The NH_4OH concentration used was 20 mM as in the original paper of Gospodarowicz et al. [17], although it can be increased up to 25 mM [31,33]. A slight modification of the original technique of Gospodarowicz et al. [17] was provided for preparation of CDMs from mouse parietal yolk sac carcinoma (PYS-2) cells that includes pre-treatment of cells with 5% dextran before lysis of cells with 20 mM NH_3 [24]. To reinforce the adhesion of endodermal cells that are usually less adherent to plastic than cancer cells, one can plate the cells on pre-coated fibronectin dishes [28].

(b) Alternatively, CDMs from PFHR-9 endodermal cells could be prepared using NP-40 non-ionic detergent to lyse the cells [23,37]. Again here, cells were grown onto fibronectin-coated dishes and cultured to superconfluent densities for 10 days with ascorbic acid (25–50 μg/ml). After rinsing with a hypotonic buffer (8–10 min, 37 °C), extraction was performed by two incubations with 0.5% NP-40 in hypotonic buffer at 37 °C.

(c) Native CDM can also be prepared from colon cancer cells using Triton X-100. Removal of cells from dishes was performed with 0.5% Triton X-100 for 10 min [31] or with a solution containing 1% Triton X-100, 10 mM EDTA and 25 mM Tris–HCl, pH 7.5 [38–40]. Otherwise Triton-X100 can be combined with NH_4OH; in that case colon cancer cells were incubated with PBS-0.5% Triton X-100 for 30 min at 37 °C and then with 2.4 mM NH_4OH 10 min at room temperature; washings were performed with 20 mM Tris–HCl, 0.15 mM NaCl and 0.05% Tween 20 [41].

(d) To study cell interactions with ECM, the group of Carter [42] has produced CDM deposited on culture dishes by human foreskin keratinocytes that synthesized large amounts of laminin-332 (formerly named laminin-5). In the first paper, keratinocytes were removed from glass coverslips by sequential extraction with 1% (v/v) Triton X-100 in PBS, 2 M urea in 1 M NaCl, and 8 M urea [42]. Later on, they used a combination of trypsin/EDTA with cells being removed from their matrix by a 5–10 min treatment with 0.05% trypsin and 1 mM EDTA in PBS [43,44]. The CDM was then treated with 0.1 mg/ml soybean trypsin inhibitor, blocked with 1 mg/ml BSA in PBS, and used for cell adhesion studies. The laminin-enriched CDM prepared in this way was more effective at inducing cell adhesion than surfaces prepared by differential extraction [42] or by coating with purified laminin-332. Yet this method has a major drawback as any left-over of trypsin may cleave the underlying deposited CDM and liberate some cryptic sites on the laminin molecule that could trigger other functions compared to the native entire molecule.

(e) The freeze–thaw protocol has been used for preparation of CDM from MDCK cells (Madin-Darby canine kidney cell line), a commonly used non-transformed epithelial cell line. At 5–11 days post-confluence, cells were removed from culture dishes by pouring off the medium and immediately immersing the entire dish into liquid nitrogen. After thawing, the dishes were sheared with a stream of distilled water until no cell remnants could be visualized by phase microscopy. These CDMs were used within 8 h [45].

(f) Kruk and Auersperg [46] have examined three used preparative techniques to prepare CDM of a rat ovarian surface epithelial cell line (ROSE 199): chemical treatments with NH_4OH (20 mM, 5 min) or with 1% DOC (for 1–2 min) and the non-chemical procedure involving repeated freeze–thaws (three cycles: −70 °C to room temperature). All three treatments supported the adhesion, spreading and growth of cells of endodermal, mesodermal and ectodermal origin although some slight differences existed regarding the presence of residual nuclei.

In contrast to CDMs isolated from fibroblast cells, epithelial-derived CDMs are mostly non-fibrillar, due to the relatively poor levels of collagen I and fibronectin [46]. They share common features (nature of the ECM molecules secreted) with matrices derived from endothelial cells. Epithelial-derived CDMs represent valuable models as they provide structural and functional context for examining biological activities such as migration and differentiation of normal and cancer cells. As an example, we were able to show that laminin 511-enriched CDMs from colon epithelial cells prevent apoptosis of cells via a PI3Kinase-dependent pathway [39].

2.3. Fibroblast- and muscle-derived extracellular matrices

The ECM of an organism is organized into a so-called connective tissue made of fibroblasts and other differentiated cells that are closely related. Fibroblasts derive from the primitive mesenchyme and represent the most abundant cells of the connective tissue. In addition to other closely-related connective-tissue cells such as cartilage and bone cells, adipocytes and smooth/skeletal muscle cells, fibroblasts are specialized for the secretion, the remodeling, the degradation of most of the components of the ECM and are thus responsible for the shaping of the architectural framework of an organism [47]. Upon tissue injury, fibroblasts are recruited to the injured site and activated into myofibroblasts by neo-expression of smooth muscle actin, which is responsible for their high adhesive and contractile activity. Indeed, contractility of scar tissue is largely driven by myofibroblasts during both physiological (wound healing) and pathological (fibrosis) tissue repair [48]. Very interestingly, physiological wound healing and tumor progression share many intriguing similarities. While wounded skin (or any other epithelium) is characterized by concomitant disruption of

the epithelium and dysfunction of the underlying connective tissue, neoplastic transformation and progression of an epithelium is accompanied by a strong stromal reaction called desmoplasia [49]. This active stroma compartment is essential for tumor onset and progression and is actively enriched in myofibroblasts, which behave as architects of the tumor microenvironment and rely heavily on adhesion to and remodeling of the scaffolding connective tissue they secrete. Indeed, fibroblasts are capable of secreting components and regulators of the ECM. They not only synthesize matrix proteins such as collagens, fibronectins, laminins, proteoglycans, elastins, tenascins, fibrillins, matricellular proteins, they also expose plasma membrane receptors able to bind to those molecules while they secrete (and expose) matrix metalloproteinases and tissue inhibitors of metalloproteinases that remodel the ECM. By doing so, fibroblasts, through adhesion, are guarantors of the structural, mechanical and chemical integrity of the ECM, in both physiological and pathological scenarios.

Matrices derived from fibroblasts have been extensively used and, in comparison to matrices derived from endothelial cells, can be generated using a variety of techniques that we will detail in the following sections.

2.3.1. Primary cultures of embryonic fibroblasts

a. *CDMs from chick embryo fibroblasts:* Confluent cells were first washed with Ca^{2+}/Mg^{2+}-free PBS, then with buffer containing 0.1 M Na_2HPO_4, 2 mM $MgCl_2$ and 2 mM EGTA (pH 9.6). Cells were then incubated with lysis buffer containing 8 mM Na_2HPO_4, 1% NP40 (pH 9.6) for 10–20 min. After withdrawing the lysis buffer, cells were further incubated with fresh lysis buffer for 1 h. Five repeated cycles of washings with 0.3 M KCl were performed allowing the removal of most of the cellular structures. If nuclei still remained they could be removed either by 0.5% DOC for biological experiment or with 0.1% SDS for gel analysis [50].

b. *CDMs from mouse and human embryonic fibroblasts:* They can be generated using DOC or Triton X-100 as detergents. For mouse embryonic fibroblasts (MEFs) from 12.5 day mouse embryos [51] and human embryonic skin fibroblasts [52], CDMs were prepared by DOC extraction. When the cultures had become dense, cell monolayers were rinsed in PBS and the cells were incubated in 0.5% DOC (eventually with 1 mM PMSF) in 10 mM Tris–HCl, pH 8.0 on ice for 30 min, rinsed with PBS or with a low ionic strength buffer [51,52]. For generation of CDMs from MEFs and from syndecan-null MEFs (primary fibroblasts isolated from 13.5 day mouse embryos) [53] or immortalized caveolin-1-null/WT MEFs [54], cells were cultured with ascorbic acid to stabilize matrix fibrils. The matrices were denuded of fibroblasts by lysis with 0.5% (v/v) Triton X-100/ 20 mM NH_4OH [54] followed by a 30 min digestion with 10 µg/ml DNase I [53].

c. *CDMs from intestinal mesenchymal cells:* Isolated stromal cells [55] were incubated with PBS/Triton-X100 0.5% for 30 min at 37 °C and then with 2.4 mM NH_4OH 10 min at room temperature; washings were performed with 20 mM Tris–HCl, 0.15 mM NaCl and 0.05% Tween 20 [41,56].

2.3.2. Established NIH3T3 embryonic fibroblast cell line

The standard 3T3 fibroblast cell line (NIH3T3) which has been established from a Swiss albino mouse embryo tissue can also be used to derive CDMs on which epithelial cells can be re-seeded. To adopt an optimal phenotype for matrix production, cells should be adapted to grow in 10% fetal bovine serum rather than calf serum for a minimum of 20 passages to overcome their normal contact growth inhibition [57]. In general cells were cultured every other day for 8 days with ascorbic acid (50 µg/ml) and cell-free

CDMs were obtained after classical alkaline detergent treatment using 0.5% (v/v) Triton X-100/20 mM NH_4OH followed by PBS washings [58–60]. In some cases, cells were plated beforehand on chemically cross-linked 0.2% gelatin coating to improve cell attachment [54]. This method has also been applied to mouse embryonic fibroblasts [54].

2.3.3. Normal and cancer-associated fibroblasts

Adult fibroblasts can be derived from various normal tissues or from tumoral tissues owing to define suitable techniques [61,62]. The protocol largely used here to generate CDMs is based on Vlodavsky's technique [12] using the Triton X-100/NH_4OH combination. It was applied to a large panel of primary fibroblasts [57] including human foreskin fibroblasts and lung fibroblasts [63–65], to tumor-associated fibroblasts [59,61,65] and also to immortalized cancer-associated fibroblasts [66]. Although not strictly required both gelatin coating (0.2% solution incubated 1 h at 37 °C or overnight at 4 °C) and cross-linking of gelatin with glutaraldehyde (1% for 30 min at room temperature and blocking with 1 M ethanolamine [8,57]) stabilize the attachment of matrices to the culture dish surface and greatly improve the final CDM yield. In general, ascorbic acid (50 µg/ml) was added at confluent cells every 2 days. At day 8, the pre-heated extraction buffer containing the 0.5% (v/v) Triton X-100/20 mM or 50 mM NH_4OH is then added. Fibroblasts should be lysed after 5–10 min. In some cases, pre-coating of gelatin and addition of ascorbic acid were omitted from the protocol [8,64,67].

2.3.4. Smooth and skeletal muscle cells

(a) CDMs elaborated from rat aortic smooth muscle cells [23]. Cells were seeded on fibronectin and then treated with ascorbic acid (50 µg/ml; added every 24 h). After rinsing of the cells in a hypotonic solution, lysis of cells was performed at 37 °C using 0.5% NP-40 detergent in hypotonic buffer (two brief extractions of 1 min each). This protocol has been applied to other cell types including skin fibroblasts [23].

(b) *CDMs from immortalized myometrial smooth muscle cells:* Here, a cold-EDTA decellularization method was used [11], method which is described in detail in the next section (Section 2.4). In that case, they used mCherry as a cytoplasmic marker allowing them to assess the proper removal of cellular debris on the remaining CDMs. In contrast, removal of the cells with Triton X-100 detergent led to contamination of the CDM with unidentified debris.

(c) *CDMs from skeletal muscle cells:* CDMs derived from the immortalized 129CB3 cell line was performed by a successive incubation of cells with 0.5% Triton X-100 in PBS for 30 min and then with 2.4 mM NH_4OH (10 min at room temperature); washings were performed with 20 mM Tris–HCl, 0.15 mM NaCl and 0.05% Tween 20 [41].

Altogether, fibroblasts and muscle cells are able to produce large amounts of ECM that retain the ability to alter the phenotype of subsequently seeded cells, and therefore to closely recapitulate the conditions encountered *in vivo* [68]. The most important goals are to preserve the native mechanical properties of the fibroblasts, as well as their biological features. Interestingly, such 3D fibroblast-derived matrices can be be locally compressed to reform a 2D environment in order to compare cell adhesive structures such as focal and fibrillary adhesions [8].

2.4. Extracellular matrices derived from mesenchymal stem cells

Human mesenchymal stem cells (MSCs) are bone marrow-derived multipotent cells that give rise to many cell types includ-

ing stromal cells, osteoclasts and adipocytes. It is hypothesized that the marrow ECM could provide important microenvironmental cues for cell survival/expansion of various cell types including marrow-derived mesenchymal progenitor cells [69]. Homeostasis of the native mechanical properties of the matrix is important to maintain stemness. In particular matrix elasticity was shown to direct stem cell lineage specification being more selective than soluble factors [70]. The specific ECM proteins involved remain to be identified. ECM from mesenchymal stem cells can be decellularized via the combination of mechanical and chemical methods, freeze–thaw cycling and DNAse treatment [71]:

(a) *Main protocol:* Adherent stromal cells obtained from human or murine bone marrow were cultured in general for 2 weeks with fresh media replacement every 2–3 days. Ascorbic acid (at a 50 μM final concentration) was added to the media for the last 8 days of culture to increase the production of ECM in particular collagen synthesis. Cells were removed from the ECM by incubation with 0.5% (v/v) Triton X-100 and 20 mM NH_4OH in PBS for 5 min at 37 °C [72] as described previously for endothelial cells [12]. The CDMs were then treated with DNAse (100 units/ml) for 1 h at 37 °C. This protocol is the one being largely used by various groups although pre-treatment of cells with ascorbic acid was not general [73–75]. The stable CDMs produced by human MSCs after 15 days of culture appeared as a white gel-like material and can even be collected by scraping [76]. Yet, Grünert et al. [77] produced a decellularized matrix obtained solely by chemical cell lysis [28] from pre-osteoblast cells. Cells were cultured with 5 mM β-glycerol phosphate and 25 μl/ml ascorbic acid 2-phosphate for 8 days. To generate the osteoblast-specific matrix, 20 mM NH_4OH was applied on cells for 5 min at 25 °C.

(b) *Preventing CDMs detachment using fibronectin pre-coating:* The preparation of such culture-derived decellularized matrices can result sometimes in undesired partial detachment of the CDM from the culture dish carrier. To circumvent this problem, the simplest way is to precoat the plastic dishes with fibronectin (FN) before seeding the cells [64]. Prewitz et al. have developed a newly anchoring method to generate native CDM [78]. The stabilization method begins with the fibronectin immobilization on glass surface through a glass-immobilized maleic anhydride copolymer. MSCs were then seeded on this anchorage platform allowing the binding of the cell-deposited ECMs to FN via its binding domains. The classical protocol can then be applied: addition of ascorbic acid (50 μg/ml), decellularization process via the combined 0.5% (v/v) Triton X-100/20 mM NH_4OH treatment. It is important to note that this will potentially affect the mechanical properties of the CDMs (see Section 6.4) that may then modify the differentiation of stem cells.

(c) *Removal of cells using EDTA:* A cold-EDTA decellularization method starting from undifferentiated human MSCs, osteogenic human MSCs but also from two smooth muscle cell lines was tested on naïve MSC growth and differentiation as the authors stated that using CDMs decellularized by Triton X-100 lysis yielded poor and highly variable results [11]. After specified culture time periods, the cultures were washed twice with pre-chilled PBS (4 °C) and then incubated in 1 mM EDTA-PBS for 12–24 h at 4 °C which caused cell rounding. The rounded cells were detached by agitating the culture dish and gently rinsing with fresh cold-EDTA. After aspirating the detached cells, the surface was washed once with cold PBS before the CDM can be used.

(d) *Removal of cells using freeze–thaw cycles:* Decellularized matrices derived from mesenchymal stem cells can also be obtained by a freeze–thaw process. Once the cells had been cultured for the desired time period, they were subjected first to rapid freeze–thaw cycling to disrupt the cellular membranes: cells were frozen in −80 °C freezer for 20 min and then thawed at room temperature for 20 min; this process was repeated three times and followed with DNase treatment (1 mg/ml DNase for 30 min at 37 °C) to remove cellular debris. This process was also successful to derive CDM produced by human amniotic fluid stem cells [71].

The use and derivation of CDMs from MSCs is a promising approach as it allows the expansion of stem cells that retain their self-renewal capacity. They also represent natural scaffold that trigger, in certain precise culture conditions, the differentiation into specific cell lineages. For example, stepwise osteogenesis-mimicking matrices derived from MSCs allowed expression of osteogenic genes accompanied by modifications in transcription factor levels [73].

3. Factors that may influence the production, quality and organization of CDMs

In all the cases described in the previous sections, the production, the quality and the organization of the resulting CDMs is strongly influenced by several parameters. These are listed below and one should pay attention to each of them. Importantly, it is rather important to avoid using trypsin to detach the cells, as it might degrade the secreted and deposited matrix proteins:

(a) *Cell passage number:* Thickness and homogeneity of CDMs is improved with secondary or early passages of bovine endothelial cells [12]. This is also the case for MSCs cells between early and late passages possibly due to the fact that cells reach senescence faster in the later passages [79].

(b) *Culture duration:* As we already mentioned in the introduction of this chapter, cells will secrete and deposit the ECM molecules basally as a function of culture time. The time required for each cell type to produce CDMs may however vary. Therefore, this time period should ideally be determined for each cell type and according to the cell culture conditions. Increased synthesis and organization of ECM with time was confirmed by gel electrophoresis of CDMs extracted from hepatic stellate cell line. For example, FN displayed a maximal enrichment after 2 weeks of culture, while fibrillin maximal levels were already reached after 11 days [80]. Interestingly CDMs derived from macrovascular endothelial cells collected at different time culture periods (from 2 to 10 days) were able to modify functional markers of cells embedded in the produced CDMs [19]. Precisely, expression of endothelial cell markers (such as CD31/PECAM) was significantly increased for mesenchymal stem cells seeded in CDMs that had been produced from longer culture periods.

(c) *Presence of growth factors:* These may influence the spatial organization of the CDMs. For example, colorectal cancer cells seeded on CDMs derived from TGFβ1-treated fibroblasts attached along pre-formed tracks whereas on bFGF-treated CDMs cells showed a random distribution [66].

(d) *Additional factors:* Addition of ascorbic acid (generally 50 μg/ml) is often added to the culture medium in particular for fibroblasts and mesenchymal stem cells mostly to activate collagen production, crosslinking and subsequently to other ECM molecules.

4. Tips for assessing and improving the quality of the CDMs

4.1. Removal of residual nuclear and cytoskeletal components

Upon detachment or lysis of the cells that had secreted the matrices of interest, remaining cellular contaminants such as nuclei and cellular debris, among which cytoskeletal or focal-adhesion associated molecules that have tendency to adhere to ECM proteins, can be discarded by treating the extracted matrices with:

(a) Detergents such as 0.5% DOC [50] or 0.05% Tween 20 [56].
(b) DNAse I to minimize contaminating DNA; this was performed on matrices derived from MSCs (100 units/ml for 1 h at room temperature; [76]; or at 37 °C; [72]), fibroblasts (10 µg/ml for 30 min; [53]) and epithelial cells (50 µg/ml for 15 min at room temperature [81]; 10 µg/ml for 30 min [42]).
(c) A combination of DNase I (100 µg /ml) and RNAse A (100 µg /ml) for 1 h at 37 °C [73].

4.2. Assessing the absence of residual cellular components

High-quality decellularized matrices are characterized by a total absence of cellular debris on the deposited extracellular fibers, which can be assessed by phase contrast microscopy. Labeling and screening of potential viable cells on the CDMs with the vital polyanionic dye calcein can also be performed. In addition, quantification of contaminating cells is possible owing the Live/Dead Viability/Cytotoxicity kit. In case some cells are labeled (^{3}H thymidine, fluorescent dyes such as mCherry or GFP [11]), a proper experiment should lead to a total absence of labeling on the resulting CDMs upon cell removal/lysis. One can also verify the absence of released cytoskeleton or focal adhesion molecules by staining the produced CDMs with phalloidin (for actin), or with antibodies directed against cytoskeletal molecules (such as myosin or vimentin) or against focal adhesion molecules. Alternatively, this can also be assessed biochemically by SDS/PAGE of the CDMs. Finally, the absence of nuclei or of DNA on CDMs can be checked rapidly with either DAPI, Hoechst 33342 or 33258, or even quantified using a PicoGreen DNA dye [77].

4.3. Stabilization of the structure of the CDMs

CDMs that are continuously secreted overtime can be further stabilized with specific treatments upon lysis/removal of the cells or during the cell culture:

(a) *Fixation and crosslinking:* Matrices can be treated with 0.1% glutaraldehyde in PBS for 6 h at 4 °C to stabilize the secreted fibers, and then with 0.1 M glycine [73] or with 1 M ethanolamine for 30 min [57]. This approach however involves cross-linking of de-cellularized matrices leading to rigidified CDMs [8] which is of utmost importance if one wants to characterize their mechanical properties. Moreover, such chemical treatments could affect the native characteristics of the generated CDMs, and lead to potential toxicity upon cell seeding.
(b) *Viscosity of the medium:* Addition of 5% (w/v) dextran T-20 [24] or 4–5% dextran T-40 [12,82] to the culture medium of endothelial cells will increase its viscosity and thereby enhance the amount (thickness) of ECM deposited by at least 2-fold [12].
(c) *Precoating with other ECM molecules:* To enforce a firm adhesion of cells to the plastic substratum, it is sometimes necessary to precoat the culture dishes with FN. This method

was used to prepare CDMs from the mouse endodermal PF-HR9 cell line [12] or to derive CDMs from endothelial cells (HUVECs) using a pre-incubation of culture dishes with 50 µl/ml FN solution overnight at 4 °C [78]. It is important to note that this technical aspect can potentially affect mechanical properties of the CDMs (see Section 6.4) that may further modify the differentiation of stem cells.

4.4. Storage

One major advantage of the production of CDMs is that one can store them for later use. The CDMs have proven to be remarkably stable [51]. The CDM-containing plates can be dehydrated, kept in PBS and antibiotics, or frozen. In order to preserve the integrity of CDMs, several means exist to ensure proper storage:

(a) Place the CDMs-coated dishes under a UV lamp (254 nm) and/or under a laminar flow hood [56,83].
(b) CDMs can be stored for 3 weeks up to 1 month at 4 °C. For longer time periods (up to 4 months), one can add antibiotics (50 µg/ml gentamicin or 100 U/ml penicillin with 100 µg/ml streptomycin) and /or 0.25 µg/ml fungizone [65,72,75].
(c) CDMs can be also frozen at −20 °C at least 1 month with no loss of efficiency or at −80 °C until use [73].
(d) Klimanskaya et al. [51] have showed that CDMs could be very stable as the plates could be dehydrated, treated with paraformaldehyde (2–4%), heat-pasteurized (60 °C for 20 h) or γ-irradiated (10–25 kGy) without any major changes in human stem cell performance. *Of note:* Some growth factors presented by CDMs may be inactivated during heat-pasteurization or sterilization [51].

4.5. Assessing the organization and composition of the CDMs

The success and quality of the de-cellularization method with respect to both cellular removal and matrix integrity can be assessed in a variety of ways. This is an important step for the conduction and understanding of functional studies related to CDMs-embedded cell behavior. While there is no optimal or unique method to ensure the quality of the CDMs, we think that combination of multiple assays (described below) should be performed before embarking in functional studies:

(a) *Microscopy:* The morphological appearance of the CDMs can be analyzed by transmission or scanning electron microscopy (T/SEM) [14,72]. Gospodarowicz et al. [14] have shown that the entire surface of the matrices derived from endothelial cells displayed a thick and uniform layer of material. Confocal Raman Microscopy can be used to check the composition of cell-free CDMs generated by cultured bone marrow cells (from either young versus old mice) thereby providing some information on the deposition of minerals [84].
(b) *Staining of ECM molecules:* This can be assessed by Coomassie Brilliant Blue staining for proteins [73,74], by Alcian Blue staining for glycosaminoglycans [74,77], by the Blyscan assay for sulfated ones [85], by light green colorant (component of the Masson Trichrome staining) for collagen [77].
(c) *Immunodetection of specific ECM proteins:* Immunodetection of specific molecules can be performed owing to specific antibodies against individual ECM among which collagens, laminins and fibronectin [15,34,38,60,72] (Fig. 1). Matrix imaging of the CDM is then acquired by classical fluorescence or confocal microscopy. Additionally, reflection microscopy,

as well as second harmonic generation (SHG, obtained with two-photon microscopy), can also be used provided that CDMs of interest are capable of secreting high amounts of type I collagen (in the case of SHG). Three-dimensional reconstructions after immunolabeling allow to define the structure and topography of the constitutive proteins as exemplified by differential arrangements between tenascin and fibronectin [64].

(d) *Topographical analysis:* The aspect and orientation of the fibers deposited by cells can be measured after labeling of the CDMs with antibodies as exemplified for FN-labeled fibers deposited by fibroblasts [54,65] (Fig. 1). Orientation of the fibers can be measured using available image processing methods described [54,65]. We recently also used the Fibriltool plugin (FIJI, [86]) for fine anisotropy measurements of the CDMs (Fig. 1).

(e) *Thickness:* The thickness of the CDMs can be determined by fluorescence/confocal microscopy (subtracting the distance between the top and bottom sections of assembled fibronectin matrix, [54,65]) or by TEM [72]. The thickness observed often varied from 5 to 20 μm [54,64,65,57,75] but could reach 100 μm in the case of MSCs as determined by TEM [72]. Relatively thin CDMs (20 nm) have also been described [78].

(f) *Metabolic labeling:* Radioactive metabolically labeled CDMs can be prepared by adding labeled sulfate ($Na_2^{35}SO_4$), amino acids (^3H proline or ^{14}C glycine) or sugars (^{14}C glucosamine) to the culture medium [12]. Such metabolically-labeled CDMs can be used to study for example the ability of metastatic cells to degrade sulfate-containing macromolecules present in the CDMs [16].

(g) *Protein content and amounts:* The total amount of protein content in CDMs can be determined using the RC/DC protein assay or the microBCA assay [84]. The composition and molecular weights of the separated CDMs-associated proteins, as well as potential proteolytic products, can be achieved using SDS–PAGE [80,87]. Proteins are extracted using lysis buffer containing 7 M urea, 2 M thiourea, 2% CHAPS, 50 mM DTT, and 40 mM Tris (pH 8.8) followed by sonication [84]. Alternatively, if one wants to resolve CDMs-containing proteins using SDS–PAGE, SDS can also be used to detach and lyse the cells that have produced the matrices.

(h) *Proteomic analysis:* Proteins contained in the CDMs of interested can be studied and separated by Liquid Chromatography and Tandem Mass Spectrometry. Labeling of digested peptides with iTRAQ reagents allows quantification of protein content between different CDMs [54]. The latter could be very useful in assessing proteolytic events during CDMs preparation. Protein levels between CDMs derived from osteogenic MSCs and CDMs where collagen secretion has been stimulated with ascorbic acid was performed on SDS–PAGE extracts subjected to mass spectrometry [78]. In that case, although these CDMs lead to functional differences, differential secretion levels of specific ECM proteins could not explain them.

5. Preparation of tissue-derived matrices (TDMs)

While cells naturally produce matrices with significant physiological relevance, it lacks the complexity of tissues that contain several cell types and thus are producers of ECM molecules. Therefore, extracellular matrices derived from normal and tumoral tissues (TDMs) potentially mimic better the complex and native extracellular microenvironment that comprises different cell types. The first and most famous example of TDM is the specific

extraction of BM molecules from the mouse EHS (Engelbreth–Holm–Swarm) tumor [88], which is now commercially available as Matrigel™ (BD Biosciences). Although this complex protein mixture (that contains also growth factors) has major advantages (such as promoter of cell differentiation and angiogenesis [89]), it has some drawbacks. Besides the fact that Matrigel™ is derived from tumor tissue, it displays poor mechanical properties certainly due to the fact that its components do not exhibit cross-linking [90].

To circumvent such limitations, complex three-dimensional substrata have been successfully derived from normal tissues [10,91,92]. Although very powerful, the use of tissue-specific coatings has only begun in the last decade. Methods of decellularization on various tissues as well as advantages /disadvantages of such methods have been nicely reviewed in Gilbert et al. [10], and more recently in Rana et al. [93]. The main objective of these methods is again to remove cells without affecting the composition, integrity and biological activity of the remaining ECM [10,93]. Because tissues contain multiple distinct components, the protocols often combine physical, enzymatic and chemical treatments. Once de-cellularized, these tissue-derived scaffolds offer multiple applications such as stem cell-driven tissue engineering [93]. Interestingly, de-cellularized TDMs allow differentiation of stem cells into the cells and structures indicative of that tissue [88]. Here, we limit the discussion to only few examples of methods allowing the decellularization of tissues (for more comprehensive reviews, see [10,93]):

(a) DeQuach et al. [85] have generated matrix coatings derived from porcine skeletal and cardiac tissues. Tissue pieces were de-cellularized using the detergent SDS (1% in PBS) until the tissue was completely white and then rinsed thoroughly to remove detergents. If needed, the tissue can be further incubated in 1% (v/v) Triton X-100 for 30 min for final cell removal [94]. Confirmation of de-cellularization can be achieved by histological staining of tissue sections. The de-cellularized matrix was then lyophilized and milled in a fine powder that can be kept at −80 °C. To generate tissue-specific matrix coatings, the ECM powder needs to be solubilized using pepsin (1 mg/ml in 0.1 M HCl for 2 days) and kept at acidic pH to prevent assembly. This solution was used to coat tissue culture plates for 1 h at 37 °C. Such matrices were showed to contain a complex mixture of ECM components as showed by mass spectroscopy composition analysis [85].

(b) Tissue-derived 3D matrices have been obtained from detergent-extracted mouse embryo sections [8]. Practically, 10- to 15-μm cryosections of mouse craniofacial tissue were treated with alkaline detergent [12] to obtain a well-organized fibrillary extracellular matrix network. This was used as a system for culturing fibroblastic cells which showed more than 6-fold rates of cell attachment compared to classical purified molecules such as fibronectin, collagen I or laminin [8,95].

(c) Decellularization of embryoid bodies was assessed using physical disruption methods such as lyophilization or freeze–thaw cycling [91,93], or by testing various solvent extraction methods [96]. Overall, acellularization using mechanical disruption techniques (coupled with DNAse) was capable to produce CDMs with slightly increased protein content compared to CDMs using solvent such as Triton X-100 extraction [92].

(d) Lü et al. [97] have recently developed an acellular tumor ECM that can be used for future tumor engineering. Xenografted pulmonary adenocarcinoma cells were sliced into sheets and were subsequently decellularized owing to four different procedures: peroxyacetic acid (PAA), trypsin/

TritonX-100, Tris/trypsin/Triton and SDS. They conclude that while the two latter methods allowed a complete decellular removal, the multistep treatment (Tris/trypsin/Triton) was the better by maintaining optimal 3D tumor cell proliferation and repopulation.

(e) ECM-containing biological scaffold material: Biological scaffold materials composed of ECM have been shown to facilitate the constructive remodeling of many tissues in both preclinical animal studies and in human clinical applications [91]. The goal is to get procedures for *ex vivo* expansion of mesenchymal stem cells (which are multipotent) using their own derived matrix to provide the ideal microenvironment for future grafting. For this, MSCs can be expanded on different scaffolds composed of titanium or of PCL microfibers [98,99]. To avoid methods that may affect the mechanical integrity and eventually the biological activity of the desired tissue from expanding MSCs, the freezing–thawing method is used to de-cellularize the deposited CDMS.

6. Protocols: measuring the Young modulus of CDMs

The development of high-resolution physical techniques has made possible to touch and manipulate matter at the nanometer scale, including soft biological samples in their native environment. The invention and development of Scanning Probe Microscopy (SPM) has played a major role in Molecular Biology allowing high resolution characterization not only of topographical features, but mechanical and compositional properties as well [100]. Among the SPM techniques, the atomic force microscopy (AFM) is the most widely used for Biophysics and Molecular Biology research as it combines nanometer resolution with easy sample preparation and preservation. The AFM maps the surface in the three spatial axes by measuring the interaction between a tip and the sample. The success of AFM imaging in biology has

been extensively reported in the literature [101,102]. The AFM technique offers several unique features that are very useful for biological studies. First, the sample preparation and topographical analysis are quite straightforward. Second, it is less destructive than other techniques commonly used in biology (such as Electron Microscopy). And finally, it can operate in different environments, including air, vacuum and liquid. Moreover, the AFM will permit the direct measurement of the elastic modulus or the interaction forces between biomolecules by the so-called force spectroscopy [102]. Atomic force spectroscopy performs force curves on a surface by approaching the AFM tip to the sample and retracting it afterwards. The profile of the curve will be specific for each biomolecule and can yield information about interaction forces as well as the Young modulus of the probed sample.

In this section we will focus our attention to the ability of the AFM to estimate the value of the force constant of CDMs using the above-mentioned Force Spectroscopy technique. In Section 6.1 we will present the force spectroscopy results using a sharp tip attached at the end of a cantilever. As it will be commented below the tip radius is on the order of 10–20 nm. Section 6.2 will show a similar protocol but using a bead instead of a sharp tip. The radius of the beads is on the 10 μm range. In Section 6.3 we will briefly comment on differences between both protocols. Finally, we will discuss the potential impact of the distinct CDMs protocols on AFM data robustness in Section 6.4.

6.1. Force spectroscopy using a multimode AFM with a nanoscope V controller

The final resolution in the *XY* axis depends mostly on the radius of the tip apex, which is usually on the range of 10–20 nm, although tips with radius as low as 2 nm are also commercially available. Fig. 2 shows a diagram of the proposed method that
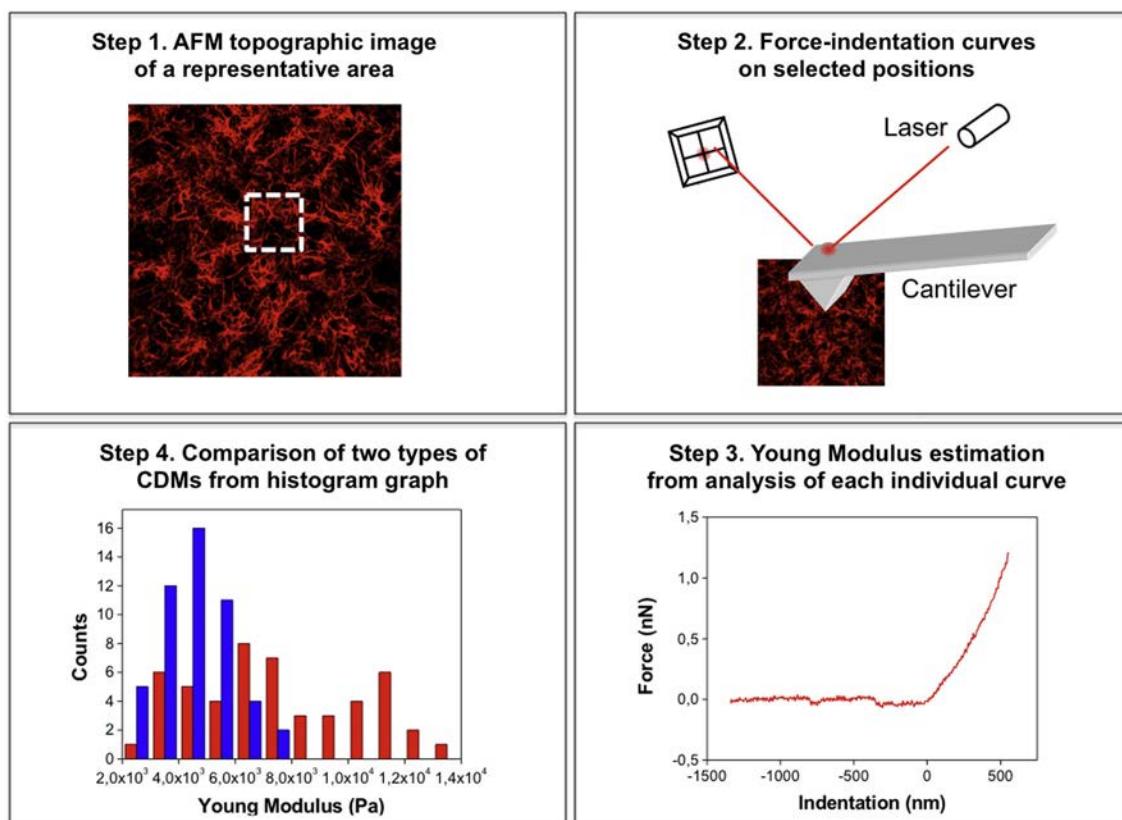
Fig. 2. Diagram of the force spectroscopy method using a cantilever with a sharp tip at the end.

we have used in the past for characterizing the Young modulus of CDMs derived from mouse embryonic fibroblasts [54]. In this section we will describe the procedure involved during each individual step:

1. The experiments described here were performed with a Multimode AFM with a Nanoscope V controller (Veeco Digital Instruments) though other microscopes of similar characteristics could be employed as well. Imaging and force spectroscopy of CDMs from mouse embryonic fibroblasts [54] (the protocol used for CDMs' extraction is detailed in Section 2.3.2) were carried out in the AFM contact mode. All the measurements were performed in liquid in a 0.01 M PBS (pH 7.4) with the idea of mimicking the biological conditions in the living cells. To minimize damage to the CDMs, we selected cantilevers with a low nominal force constant as given by the manufacturer of $k \approx 0.01$ N/m (Olympus BL-RC150VB-C1). To get an accurate value for the force constant the cantilevers were calibrated using the thermal tuning method [103]. The sensitivity of the photodiode was calibrated as well by performing a deflection versus distance curve on a mica substrate (36.14 nm/V). Prior to measurements, the CDMs were rinsed with distilled water and subsequently mounted into the fluid cell of the microscope.

The cell was filled with 100 µl of PBS. The amount of liquid was checked throughout the experiment to prevent the matrices from being dry.

2. To acquire the force curves, first a 30 µm × 30 µm image of a representative area of the sample was recorded. Fig. 3 shows a topographical AFM image of two types of CDMs, established from mouse embryonic fibroblasts (wild-type and KO for caveolin-1 [54]). Once the area is selected, the points on the fibers where force spectroscopy measurements are going to be taken are chosen. These points are indicated by white arrows in Fig. 2 and in both images they lay along on a fiber on the CDMs.

3. Afterwards, the force curves were acquired manually by approaching and retracting the tip towards the sample by 2 µm at a rate of 1 Hz. Each curve has 512 × 512 points. To prevent damage to fibers, tip excursion was stopped when the force reached 2 nN. Fig. 4 shows a sketch of the dependence of the applied force on the indentation as the tip approaches the sample. The Young modulus can be derived from the force curve by using the Hertz model for a parabolic tip [102,104]:

$$F = \frac{4}{3}R\frac{E}{1-v^2}\delta^{3/2} \tag{1}$$
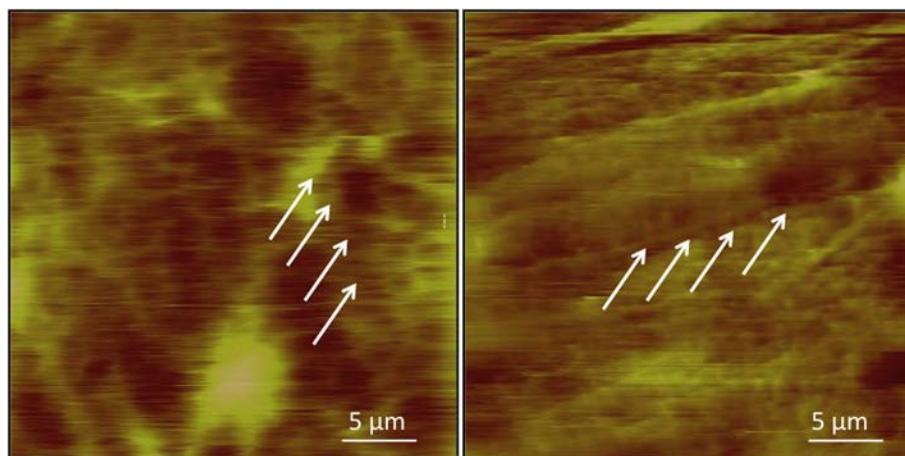
Fig. 3. AFM images of CDMs from caveolin-1 WT-MEFs (left) and caveolin-1 KO-MEFs (right). The force-indentation curves were taken on the points indicated by the white arrows.
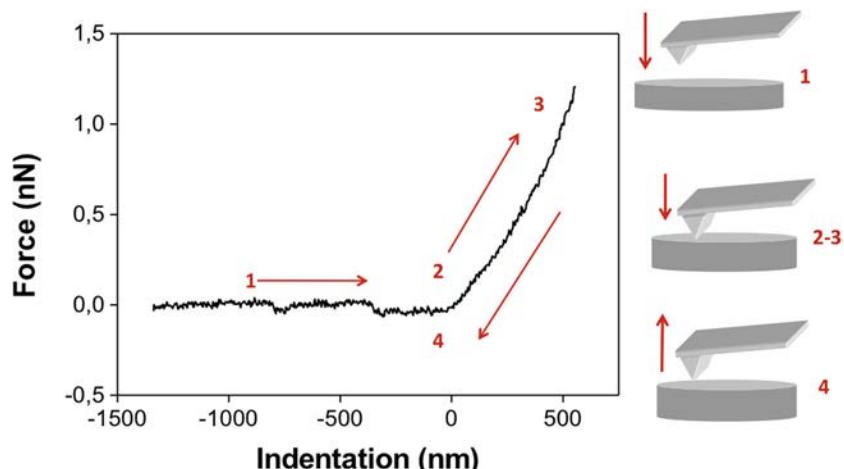
Fig. 4. Force indentation curve and position of the cantilever over the sample at different steps. In the first point the cantilever approaches the sample and the interaction is negligible. At position 2 the cantilever gets in contact with the CDMs and the force starts increasing. The tip continues indenting the sample in position 3. Finally in step 4 the tip is retracted. Information about the mechanical properties of the sample can be obtained by analyzing these curves.

where F is the applied load, R the tip radius ($R = 20$ nm), E the effective Young modulus of the tip-sample interface, v the Poisson ratio (0.5 for soft materials) and δ the indentation. As the AFM probe is several orders of magnitude stiffer than the ECMs we can make the approximation $E \approx E_{\text{CDM}}$.

4. In order to apply Eq. (1), some rearrangements are required. The data we obtained from the AFM measurements show the cantilever deflection dependence on sample displacement. In order to determine the Young modulus of the CDM (E_{CDM}) we need to plot a force vs. indentation graph and derive the value of E_{CDM} from the gradient of this curve [105]. Therefore we need to transform the deflection-displacement curves into force versus indentation curves. This is accomplished by calculating the force using Hooke's law $F = -k(z - z_0)$ and determining the indentation from:

$$\delta = (S_{\text{p}} - S_0) - (z - z_0) \qquad (2)$$

where S_{p} is the piezo movement, S_0 the contact point as determined from the curves, z the deflection recorded by the photodiode and z_0 the deflection's offset.

5. Each curve must be analyzed individually. To make the experiment as fair as possible, we decided to discard those curves that showed either unstable behavior, usually due to thermal drift after a certain time has elapsed or those which presented features beyond the scope of the research. Fig. 5 shows two examples of the type of force-indentation curves that were analyzed. They were performed on WT and KO CDMs (from [54]) and it is clearly seen that the matrices derived from WT MEFs are stiffer (have a higher slope) as compared to the ones derived from KO MEFs. This result was consistently observed in the rest of the recorded curves.

6. Knowing the value of the applied force and the indentation it is possible to estimate the value for the Young modulus using Eq. (1). To minimize errors a statistical analysis has to be performed over a significant number or curves. In this experiment [54], we used one hundred different curves and estimated the value of the Young Modulus for each of them. The results were afterwards plotted in a histogram to get a direct comparison. The Student's t-test was used as a mean to compare both values. The final data show that the WT matrices are stiffer than the KO ones, as expected from the behavior of the individual curves. The distribution is also broader in the case of the WT matrices compared to the KO [54]. This is in agreement with previous results reported in the literature.
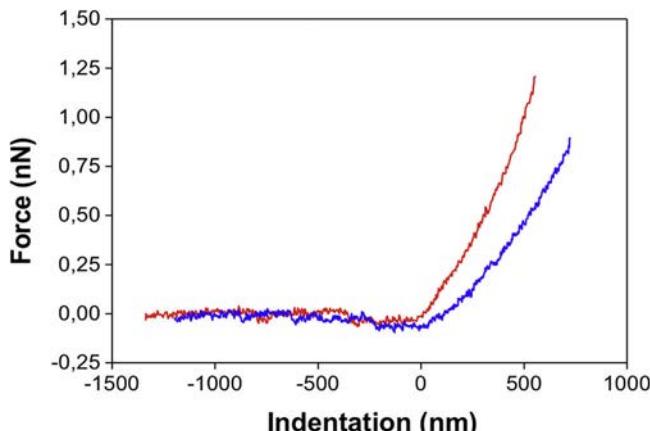
Fig. 5. Force-indentation curves of CDMs from caveolin-1 WT-MEFs (red line) and caveolin-1 KO-MEFs (blue line). WT CDMs have a higher slope and hence a higher Young modulus than the KO CDMs, in agreement with the experimental results obtained by other techniques.

7. Therefore this method reveals the potential of the AFM not only to image the structure of a sample with molecular or even sub-molecular resolution, but to probe the mechanical properties of the substrate mimicking their native conditions by performing the experiments in a liquid environment.

6.2. Determining the elastic modulus of biological samples using the BioScope Catalyst atomic force microscope

In this section, we will describe how the mechanical properties (elastic modulus E) of the CDMs can also be measured conveniently by using a BioScope Catalyst (Bruker Corporation, Santa Barbara, CA, USA) atomic force microscope (BioAFM) that is equipped with a nanomechanics package. As this BioAFM is designed to integrate with an inverted light microscope, it allows superior optical and physical accesses to the sample. We have recently used this technology to probe the Young modulus of matrices derived from colonic epithelial cells that lacked or expressed the laminin-α1 chain [40]:

1. Colon cancer epithelial cells expressing or not the laminin-α1 chain were cultured for 10 days. CDMs were isolated following removal of the cells by a combined 1% Triton X-100/10 mM EDTA treatment. This protocol is detailed in Section 2.2.c and the associated reference [40].

2. Force measurements are usually performed on many different areas directly in the culture dishes at room temperature. For each culture dish, between 10 and 30 areas are probed in different regions of more or less 50×50 μm squares of the CDMs. The MIRO (Microscope Image Registration and Overlay) software is used to select the areas of interest and target discrete points for "Point and Shoot" force measurements.

3. The ECM deposited by the cells is indented with borosilicate beads, 10 μm in diameter, mounted on silicon nitride AFM probes (Novascan Technologies, Ames, IA, USA). The manufacturer reports a nominal spring constant value of 0.06 N/m. Modified AFM probes arrive sealed individually under argon to remain protected from contamination. The probes are removed from their protective environment just before being used.

4. In order to measure indentation accurately, a precise knowledge of the cantilever's spring constant is necessary. The cantilever spring constant is determined with the thermal fluctuation method [103]. Experiments are achieved at constant approach and withdrawal velocities.

5. Quantitative measurements of matrix stiffness are obtained by fitting the force-indentation curves to the Hertz model [104] for the elastic indentation of a flat and soft sample by an undeformable sphere. The Young's modulus can be extracted by fitting the Hertz law to the approach curve from the contact point up to a point corresponding to an indentation not exceeding a few percent of the radius of the colloidal probe (Fig. 6).

6. To characterize the micro-scale stiffness of the CDMs, the captured force curves are processed manually using the commercial NanoScope Analysis software (Bruker Corporation, Santa Barbara, CA, USA), which offers a full suite of force curve analysis tools, including baseline correction and indentation analysis. Because the CDMs are mostly composed of water, that is incompressible, the sample Poisson's ratio is set to 0.5.

Using this methodology, we were able to measure accurately the Young modulus of matrices derived from colonic epithelial cells. These cells are capable of depositing basement membrane molecules and produce stiffer matrices when they express (and thus secrete) the laminin-α1 chain [40].
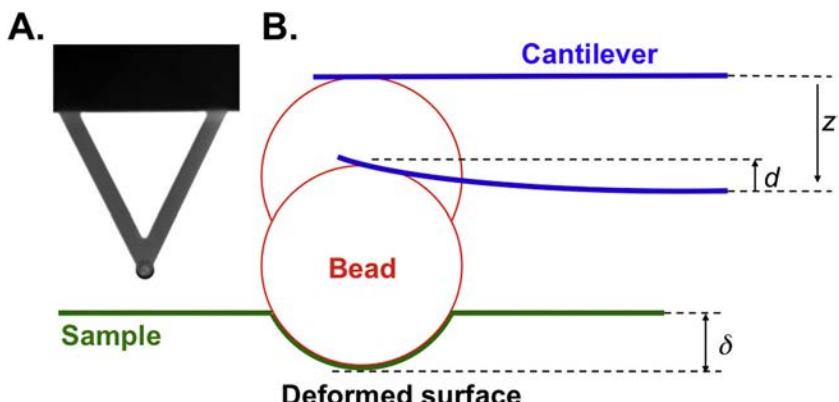
Fig. 6. (A). Picture of a cantilever with a bead. (B) Diagram of the force spectroscopy method using a cantilever with a bead at the end. The cantilever is moved towards the sample by a distance *z*. After contact with the sample's surface, the cantilever bends in the opposite direction (*d*). The Young's modulus of the spherical indenter is considerably larger than the modulus of the biological sample. *δ* corresponds to the indentation depth.

6.3. Comparison between the two techniques: pros and cons

Although the methods described so far rely on sensing the mechanical properties of a sample by the use of an atomic force microscope there are slight differences that will be briefly commented in this section. As previously mentioned both make use of the interaction between a probe and the sensing substratum, in this case CDMs derived from either mouse embryonic fibroblasts or colonic epithelial cells. While the physics behind the setup and data recording is the same in both cases, the major difference arises in the size of the sensor:

1. In the first method (Section 6.1) a tip is attached to the end of a cantilever. The estimated radius of the tip is around 10–20 nm. This allows the characterization of the surface of the sample at the nanometer scale. In fact a high-resolution image of the area to be analyzed is taken before performing any force-indentation curves. Specific points will be selected on the image where the force curves are going to be taken. Thanks to the low drift ensured by the experimental conditions and the resolution offered by the tip, we can be almost certain that the experiments were performed on the fibers. This is a major advantage of this method as it allows high resolution mapping of the mechanical properties of a sample. When instead of a sharp tip we have a bead attached to the end of the cantilever (Section 6.2), an optical image is taken before proceeding with the analysis. While the optical image suffices to give a clear idea of the suitability of the sample, the resolution is less than the one offered by the AFM. Thus, by using a bead we would expect a more averaged result as we cannot be certain where the tip is indenting. Nevertheless, due to the size of the bead and the structure of the matrices we can also be certain that we are getting an average result as the bead will be mostly indenting on the fibers.
2. In addition, the method described in Section 6.1 permits the indentation of the tip in a small area (less than 100 nm^2), whereas the method described in Section 6.2 the use of a bead will clearly imply the sensing of a much bigger area. However this might entail some advantages as even if the measurements are not performed on a single fiber, they could be considered as an average over different parts of the CDMs. Hence, the use of a bead at the end of the tip would most likely allow a narrower histogram with a sharper tip. In addition, the use of the tip might produce higher damage as the mechanical stress might be increased as compared to the use of a bead [106]. A possible extension to this experiment would be to change the stress applied in both cases and see how this affects the resulting data.

Both methods allow a direct comparison between two types of matrices derived from cells where single genes have been depleted. They thus mimic native conditions and offer a straightforward way to estimate differences in the mechanical properties of the CDMs. Although the experiments were not performed exactly on the same samples, we believe they provide good agreement within the experimental results. It is left as a future experiment to perform measurements on the same sample, and whenever possible on a same region using both protocols. That would require an adequate patterning of the sample to be able to locate a probing area and a need to ensure that the pattern does not interfere with the structure of the matrices. We believe that the results yielded by such an experiment would reinforce those reported so far.

6.4. Impact of CDMs protocol on AFM data robustness

Although various protocols have been described for proper decellularization of the CDMs, there is very little information as how these distinct methods could affect the mechanical properties of matrices derived from single cell sources. This should ideally be explored in the future since technical details in the protocols are indeed prone to mechanical variations. For example, cross-linking CDMs with glutaraldehyde upon decellularization leads to a significant increase in the Young modulus of fibroblast-derived matrices [107,108]. Usage of fixative, which favors CDM's stability and preservation, should thus be done accordingly. Interestingly, ascorbic acid, which favors secretion and crosslinking of type I collagen [109], does not necessarily alter the mechanical properties of the fibroblast-derived matrices [107]. We made similar observations with matrices derived from tumor epithelial cells. However, matrices produced from similar cells, but overexpressing the laminin-α1 chain, displayed a significant increase in the Young modulus upon treatment with ascorbic acid (personal communication, data not shown), suggesting that increased deposition of type I collagen could alter the mechanical properties of the derived matrices. While confluency and culture duration have been shown to significantly affect the quality and content of the matrices [80], which is very likely to affect their mechanical properties, there is to our knowledge no study which specifically addressed this issue. Pre-coating with stabilized matrix molecules (in particular FN), which prevents delamination of the matrices during the decellularization [78], allows to generate stable and soft matrices derived from multiple cell types and potentially result in notable changes in their Young modulus. Here again, although this elegant study demonstrates that stable anchorage of cell-secreted ECM yields thin and soft ECMs, the contribution of the coating has not been addressed

[78]. In conclusion, while many efforts have been put in optimizing protocols for generating CDMs of high quality, there is so far only limited knowledge on how they would alter their mechanical properties. This should be explored in the future.

7. On the utility of measuring the Young modulus of extracellular matrices

Because compliance of the extracellular environment is capable of regulating important cellular functions such as migration, proliferation and morphogenesis, it is essential to carefully and accurately measure the elastic properties of matrices naturally produced by cells. AFM has been used to probe the mechanical properties of multiple substrates. Specialized BM have been assessed for both imaging and quantification of elastic modulus [110–112]. Matrigel, a commercially available tumor BM-like substrate widely used, has also been probed via AFM technologies [113,114]. AFM can also be used to measure the elastic modulus of artificial and tunable substrates such as natural polyelectrolyte films [115] or polydimethylsiloxane (PDMS) and polyacrylamide (PAAm) hydrogel surfaces [116]. The elastic moduli of soft and thin substrates that resemble and mimic natural biological environments have been measured [117,118,70]. These substrates more reliably resemble environments encountered *in vivo* compared to plastic or glass surfaces whose Young modulus approach the GPa range. Fine measurement of the micro-elastic properties of matrices derived from lung cells revealed that their stiffness did not scale with collagen I content, but rather with the cross-linking of extracellular matrix molecules [107]. Recently, AFM measurements allowed discriminating the mechanical properties of 3D collagen gels, from gelatin and collagen substrates, and from a recently-developed high-density fibrillar collagen [63]. These measurements were instrumental in understanding the behavior of cells, and in particular their subcellular protrusions called invadopodia, in response to distinct physical and chemical substrates. AFM studies performed in parallel on CDMs and conventional cell culture substrates confirmed that ECM secreted by cells displayed soft elastic properties, which differ from one cell type to another [78]. Using basement membranes isolated from human eyes, Halfter et al. showed that their epithelial side was stiffer than the stromal one [119]. This suggests that the bi-functional organization of basement membranes, in addition to other factors, contributes to frame the basic tissue architecture.

Measurement of stiffness profiles has been very useful in understanding pathological phenomena such as cancer. During tumor progression, stromal changes including ECM remodeling and stiffening disturb the homeostatic dynamics of the tumor and drive its aggressiveness. AFM has thus been widely used to probe mechanical changes during cancer progression. For example, AFM has been used *in situ* to probe the mechanical properties of sectioned tissues, including tumor-associated stroma of melanoma [120] and mammary tumors [121]. Sheets of acellular tumor extracellular matrices derived from *in vivo* tumors were probed with AFM to assess the quality of the decellularization method and proved to be ideal and mechanically-favorable environments for the growth of tumor cells [97]. Indentation-type atomic force microscope (IT-AFM) has been used to assess stiffness profiles of human breast biopsies and revealed that those displayed a broad distribution resulting from tissue heterogeneity [122]. Noteworthy, Young modulus increased when moving from the core to the periphery of the tumor, suggesting again that tumor-associated is stiff, while cancer cells are relatively soft. Interestingly, AFM-probed metastatic cancer cells have been shown to be significantly softer than benign cells, further suggesting that nanomechanical analysis of tumors could be used as a new way to probe and detect cancer [123].

8. Conclusion

The recent discoveries have shown that both ECM elasticity and topography drive important cell behavior, *in vitro* and *in vivo*. Researchers thus need to have access to reliable and physiologically relevant substrates, cell- or tissue-derived, in addition to reliable and accurate methods for quantifying their mechanical properties. We have provided here a thorough methodological review of protocols designed to generate high-quality cell-derived matrices, and detailed two protocols that we have developed successfully for assessing their Young modulus. Further efforts in the future should be invested to compare the impact of the various CDMs protocols (for a single cell source) on their mechanical properties, as well as thoroughly and carefully compare different AFM methods on CDMs generated similarly. Further efforts in the future should be invested in the creation of reproducible workflow for deriving and characterizing ECM from normal and pathological tissues as they represent a fertile avenue for understanding cell behavior in the most realistic microenvironmental context. Altogether, these methodologies will further increase our understanding of how cell behavior and fate is influenced by both topographical and mechanical cues of the ECM, and, ultimately, lead to the design of reliable biomimetic materials with therapeutic potential.

Acknowledgements

References

[1] C. Bonnans, J. Chou, Z. Werb, Remodelling the extracellular matrix in development and disease, Nat. Rev. Mol. Cell Biol. 15 (2014) 786–801, http://dx.doi.org/10.1038/nrm3904.

[2] R.O. Hynes, The extracellular matrix: not just pretty fibrils, Science 326 (2009) 1216–1219, http://dx.doi.org/10.1126/science.1176009.

[3] R.O. Hynes, Cell adhesion: old and new questions, Trends Cell Biol. 9 (1999) M33–M37.

[4] M.R. Morgan, M.J. Humphries, M.D. Bass, Synergistic control of cell adhesion by integrins and syndecans, Nat. Rev. Mol. Cell Biol. 8 (2007) 957–969, http://dx.doi.org/10.1038/nrm2289.

[5] C.M. Nelson, M.J. Bissell, Of extracellular matrix, scaffolds, and signaling: tissue architecture regulates development, homeostasis, and cancer, Annu. Rev. Cell Dev. Biol. 22 (2006) 287–309, http://dx.doi.org/10.1146/annurev.cellbio.22.010305.104315.

[6] M.F. Brizzi, G. Tarone, P. Defilippi, Extracellular matrix, integrins, and growth factors as tailors of the stem cell niche, Curr. Opin. Cell Biol. 24 (2012) 645–651, http://dx.doi.org/10.1016/j.ceb.2012.07.001.

[7] P. Lu, V.M. Weaver, Z. Werb, The extracellular matrix: a dynamic niche in cancer progression, J. Cell Biol. 196 (2012) 395–406, http://dx.doi.org/10.1083/jcb.201102147.

[8] E. Cukierman, R. Pankov, D.R. Stevens, K.M. Yamada, Taking cell–matrix adhesions to the third dimension, Science 294 (2001) 1708–1712, http://dx.doi.org/10.1126/science.1064829.

[9] B. Weigelt, C.M. Ghajar, M.J. Bissell, The need for complex 3D culture models to unravel novel pathways and identify accurate biomarkers in breast cancer, Adv. Drug Deliv. Rev. 69–70 (2014) 42–51, http://dx.doi.org/10.1016/j.addr.2014.01.001.

[10] T.W. Gilbert, T.L. Sellaro, S.F. Badylak, Decellularization of tissues and organs, Biomaterials 27 (2006) 3675–3683, http://dx.doi.org/10.1016/j.biomaterials.2006.02.014.

[11] S. Rao Pattabhi, J.S. Martinez, T.C.S. Keller, Decellularized ECM effects on human mesenchymal stem cell stemness and differentiation, Differ. Res. Biol. Divers. 88 (2014) 131–143, http://dx.doi.org/10.1016/j.diff.2014.12.005.

[12] I. Vlodavsky, Preparation of extracellular matrices produced by cultured corneal endothelial and PF-HR9 endodermal cells, in: Board Juan Bonifacino Al (Ed.), Curr. Protoc. Cell Biol. Editor, 2001 (Chapter 10, Unit 10.4). http://dx.doi.org/10.1002/0471143030.cb1004s01.

[13] D. Gospodarowicz, C. Ill, Extracellular matrix and control of proliferation of vascular endothelial cells, J. Clin. Invest. 65 (1980) 1351–1364, http://dx.doi.org/10.1172/JCI109799.

[14] D. Gospodarowicz, D. Delgado, I. Vlodavsky, Permissive effect of the extracellular matrix on cell proliferation in vitro, Proc. Natl. Acad. Sci. USA 77 (1980) 4094–4098.

[15] I. Vlodavsky, G.M. Lui, D. Gospodarowicz, Morphological appearance, growth behavior and migratory activity of human tumor cells maintained on extracellular matrix versus plastic, Cell 19 (1980) 607–616.

[16] I. Vlodavsky, Y. Ariav, R. Atzmon, Z. Fuks, Tumor cell attachment to the vascular endothelium and subsequent degradation of the subendothelial extracellular matrix, Exp. Cell Res. 140 (1982) 149–159.

[17] D. Gospodarowicz, K. Hirabayashi, L. Giguère, J.P. Tauber, Factors controlling the proliferative rate, final cell density, and life span of bovine vascular smooth muscle cells in culture, J. Cell Biol. 89 (1981) 568–578.

[18] K. Pavelic, M.A. Bulbul, H.K. Slocum, Z.P. Pavelic, Y.M. Rustum, M.J. Niedbala, et al., Growth of human urological tumors on extracellular matrix as a model for the in vitro cultivation of primary human tumor explants, Cancer Res. 46 (1986) 3653–3662.

[19] T.P. Lozito, C.K. Kuo, J.M. Taboas, R.S. Tuan, Human mesenchymal stem cells express vascular cell phenotypes upon interaction with endothelial cell matrix, J. Cell. Biochem. 107 (2009) 714–722, http://dx.doi.org/10.1002/jcb.22167.

[20] F.E. Wren, A.M. Schor, S.L. Schor, M.E. Grant, Modulation of smooth muscle cell behaviour by platelet-derived factors and the extracellular matrix, J. Cell. Physiol. 127 (1986) 297–302, http://dx.doi.org/10.1002/jcp.1041270217.

[21] D. Gospodarowicz, R. Gonzalez, D.K. Fujii, Are factors originating from serum, plasma, or cultured cells involved in the growth-promoting effect of the extracellular matrix produced by cultured bovine corneal endothelial cells?, J Cell. Physiol. 114 (1983) 191–202, http://dx.doi.org/10.1002/jcp.1041140208.

[22] J. Tassin, E. Jacquemin, Y. Courtois, Interaction of bovine epithelial lens (BEL) cells with extracellular matrix (ECM) and eye-derived growth factor (EDGF). I. Effects on short-term adhesiveness and on long-term organization of the culture, Exp. Cell Res. 149 (1983) 69–84.

[23] R.H. Kramer, K.G. Bensch, P.M. Davison, M.A. Karasek, Basal lamina formation by cultured microvascular endothelial cells, J. Cell Biol. 99 (1984) 692–698.

[24] T. Matsubara, S. Tsutsumi, H. Pan, H. Hiraoka, R. Oda, M. Nishimura, et al., A new technique to expand human mesenchymal stem cells using basement membrane extracellular matrix, Biochem. Biophys. Res. Commun. 313 (2004) 503–508.

[25] N. Beckouche, M. Bignon, V. Lelarge, T. Mathivet, C. Pichol-Thievend, S. Berndt, et al., The interaction of heparan sulfate proteoglycans with endothelial transglutaminase-2 limits VEGF165-induced angiogenesis, Sci. Signal. 8 (2015) ra70, http://dx.doi.org/10.1126/scisignal.aaa0963.

[26] P.D. Yurchenco, Basement membranes: cell scaffoldings and signaling platforms, Cold Spring Harb. Perspect. Biol. 3 (2011), http://dx.doi.org/10.1101/cshperspect.a004911.

[27] P. Simon-Assmann, C. Spenle, O. Lefebvre, M. Kedinger, The role of the basement membrane as a modulator of intestinal epithelial–mesenchymal interactions, Prog. Mol. Biol. Transl. Sci. 96 (2010) 175–206, http://dx.doi.org/10.1016/B978-0-12-381280-3.00008-7.

[28] D. Gospodarowicz, J. Lepine, S. Massoglia, I. Wood, Comparison of the ability of basement membranes produced by corneal endothelial and mouse-derived endodermal PF-HR-9 cells to support the proliferation and differentiation of bovine kidney tubule epithelial cells in vitro, J. Cell Biol. 99 (1984) 947–961.

[29] M. Langhofer, S.B. Hopkinson, J.C. Jones, The matrix secreted by 804G cells contains laminin-related components that participate in hemidesmosome assembly in vitro, J. Cell Sci. 105 (1993) 753–764.

[30] G. Plopper, J. Falk-Marzillier, S. Glaser, M. Fitchmun, G. Giannelli, T. Romano, et al., Changes in expression of monoclonal antibody epitopes on laminin-5r induced by cell contact, J. Cell Sci. 109 (1996) 1965–1973.

[31] F. Bellot, J. Luis, A. el Battari, J. Secchi, P. Cau, J. Marvaldi, et al., Extracellular material secreted by human colonic adenocarcinoma cell lines promotes spreading in serum-free medium and induces neurite outgrowth of PC-12 cells, Int. J. Cancer 36 (1985) 609–615.

[32] D. Boyd, G. Florent, S. Chakrabarty, D. Brattain, M.G. Brattain, Alterations of the biological characteristics of a colon carcinoma cell line by colon-derived substrata material, Cancer Res. 48 (1988) 2825–2831.

[33] A.E. Levine, B. Black, M.G. Brattain, Effects of N,N-dimethylformamide and extracellular matrix on transforming growth factor-beta binding to a human colon carcinoma cell line, J. Cell. Physiol. 138 (1989) 459–466, http://dx.doi.org/10.1002/jcp.1041380304.

[34] N. Turck, I. Gross, P. Gendry, J. Stutzmann, J.-N. Freund, M. Kedinger, et al., Laminin isoforms: biological roles and effects on the intracellular distribution of nuclear proteins in intestinal epithelial cells, Exp. Cell Res. 303 (2005) 494–503, http://dx.doi.org/10.1016/j.yexcr.2004.10.025.

[35] N. Turck, O. Lefebvre, I. Gross, P. Gendry, M. Kedinger, P. Simon-Assmann, et al., Effect of laminin-1 on intestinal cell differentiation involves inhibition

[36] B.H. Sung, X. Zhu, I. Kaverina, A.M. Weaver, Cortactin controls cell motility and lamellipodial dynamics by regulating ECM secretion, Curr. Biol. 21 (2011) 1460–1469, http://dx.doi.org/10.1016/j.cub.2011.06.065.

[37] G. Parry, B. Cullen, C.S. Kaetzel, R. Kramer, L. Moss, Regulation of differentiation and polarized secretion in mammary epithelial cells maintained in culture: extracellular matrix and membrane polarity influences, J. Cell Biol. 105 (1987) 2043–2051.

[38] V. Orian-Rousseau, D. Aberdam, P. Rousselle, A. Messent, J. Gavrilovic, G. Meneguzzi, et al., Human colonic cancer cells synthesize and adhere to laminin-5. Their adhesion to laminin-5 involves multiple receptors among which is integrin alpha2beta1, J. Cell Sci. 111 (1998) 1993–2004.

[39] L. Ritié, C. Spenlé, J. Lacroute, A.-L. Bolcato-Bellemin, O. Lefebvre, C. Bole-Feysot, et al., Abnormal Wnt and PI3Kinase signaling in the malformed intestine of lama5 deficient mice, PLoS One 7 (2012) e37710, http://dx.doi.org/10.1371/journal.pone.0037710.

[40] C. Spenlé, O. Lefebvre, J. Lacroute, A. Méchine-Neuville, F. Barreau, H.M. Blottière, et al., The laminin response in inflammatory bowel disease: protection or malignancy?, PLoS One 9 (2014) e111336, http://dxdoi.org/10.1371/journal.pone.0111336.

[41] C. Schreider, G. Peignon, S. Thenet, J. Chambaz, M. Pinçon-Raymond, Integrin-mediated functional polarization of Caco-2 cells through E-cadherin–actin complexes, J. Cell Sci. 115 (2002) 543–552.

[42] W.G. Carter, M.C. Ryan, P.J. Gahr, Epiligrin, a new cell adhesion ligand for integrin alpha 3 beta 1 in epithelial basement membranes, Cell 65 (1991) 599–610.

[43] Y. Xia, S.G. Gil, W.G. Carter, Anchorage mediated by integrin alpha6beta4 to laminin 5 (epiligrin) regulates tyrosine phosphorylation of a membrane-associated 80-kD protein, J. Cell Biol. 132 (1996) 727–740.

[44] D.E. Frank, W.G. Carter, Laminin 5 deposition regulates keratinocyte polarization and persistent migration, J. Cell Sci. 117 (2004) 1351–1363, http://dx.doi.org/10.1242/jcs.01003.

[45] A.J. Milici, M.B. Furie, W.W. Carley, The formation of fenestrations and channels by capillary endothelium in vitro, Proc. Natl. Acad. Sci. USA 82 (1985) 6181–6185.

[46] P.A. Kruk, N. Auersperg, A line of rat ovarian surface epithelium provides a continuous source of complex extracellular matrix, In Vitro Cell. Dev. Biol. Anim. 30A (1994) 217–225.

[47] M. Jacob, L. Chang, E. Puré, Fibroblast activation protein in remodeling tissues, Curr. Mol. Med. 12 (2012) 1220–1243.

[48] F. Klingberg, B. Hinz, E.S. White, The myofibroblast matrix: implications for tissue repair and fibrosis, J. Pathol. 229 (2013) 298–309, http://dx.doi.org/10.1002/path.4104.

[49] M. Otranto, V. Sarrazy, F. Bonté, B. Hinz, G. Gabbiani, A. Desmoulière, The role of the myofibroblast in tumor stroma remodeling, Cell Adhes. Migr. 6 (2012) 203–219, http://dx.doi.org/10.4161/cam.20377.

[50] L.B. Chen, A. Murray, R.A. Segal, A. Bushnell, M.L. Walsh, Studies on intercellular LETS glycoprotein matrices, Cell 14 (1978) 377–391.

[51] I. Klimanskaya, Y. Chung, L. Meisner, J. Johnson, M.D. West, R. Lanza, Human embryonic stem cells derived without feeder cells, Lancet 365 (2005) 1636–1641, http://dx.doi.org/10.1016/S0140-6736(05)66473-2.

[52] K. Hedman, M. Kurkinen, K. Alitalo, A. Vaheri, S. Johansson, M. Höök, Isolation of the pericellular matrix of human fibroblast cultures, J. Cell Biol. 81 (1979) 83–91.

[53] M.D. Bass, K.A. Roach, M.R. Morgan, Z. Mostafavi-Pour, T. Schoen, T. Muramatsu, et al., Syndecan-4-dependent Rac1 regulation determines directional migration in response to the extracellular matrix, J. Cell Biol. 177 (2007) 527–538, http://dx.doi.org/10.1083/jcb.200610076.

[54] J.G. Goetz, S. Minguet, I. Navarro-Lérida, J.J. Lazcano, R. Samaniego, E. Calvo, et al., Biomechanical remodeling of the microenvironment by stromal caveolin-1 favors tumor invasion and metastasis, Cell 146 (2011) 148–163, http://dx.doi.org/10.1016/j.cell.2011.05.040.

[55] C. Fritsch, V. Orian-Rousseaul, O. Lefebvre, P. Simon-Assmann, J.M. Reimund, B. Duclos, et al., Characterization of human intestinal stromal cell lines: response to cytokines and interactions with epithelial cells, Exp. Cell Res. 248 (1999) 391–406, http://dx.doi.org/10.1006/excr.1999.4414.

[56] J. Le Beyec, F. Delers, F. Jourdant, C. Schreider, J. Chambaz, P. Cardot, et al., A complete epithelial organization of Caco-2 cells induces I-FABP and potentializes apolipoprotein gene expression, Exp. Cell Res. 236 (1997) 311–320.

[57] D.A. Beacham, M.D. Amatangelo, E. Cukierman, Preparation of extracellular matrices produced by cultured and primary fibroblasts, in: Board Juan Bonifacino Al (Ed.), Curr. Protoc. Cell Biol., 2007 (Chapter 10, Unit 10.9). http://dx.doi.org/10.1002/0471143030.cb1009s33.

[58] I. Serebriiskii, R. Castelló-Cros, A. Lamb, E.A. Golemis, E. Cukierman, Fibroblast-derived 3D matrix differentially regulates the growth and drug-responsiveness of human cancer cells, Matrix Biol. 27 (2008) 573–585, http://dx.doi.org/10.1016/j.matbio.2008.02.008.

[59] R. Castelló-Cros, D.R. Khan, J. Simons, M. Valianou, E. Cukierman, Staged stromal extracellular 3D matrices differentially regulate breast cancer cell responses through PI3K and beta1-integrins, BMC Cancer 9 (2009) 94, http://dx.doi.org/10.1186/1471-2407-9-94.

[60] K.M. Hakkinen, J.S. Harunaga, A.D. Doyle, K.M. Yamada, Direct comparisons of the morphology, migration, cell adhesions, and actin cytoskeleton of fibroblasts in four different three-dimensional extracellular matrices, Tissue Eng. Part A 17 (2011) 713–724, http://dx.doi.org/10.1089/ten.TEA.2010.0273.

[61] R. Castelló-Cros, E. Cukierman, Stromagenesis during tumorigenesis: characterization of tumor-associated fibroblasts and stroma-derived 3D matrices, Methods Mol. Biol. (Clifton NJ) 522 (2009) 275–305, http://dx.doi.org/10.1007/978-1-59745-413-1_19.

[62] J. Tommelein, L. Verset, T. Boterberg, P. Demetter, M. Bracke, O. De Wever, Cancer-associated fibroblasts connect metastasis-promoting communication in colorectal cancer, Front. Oncol. 5 (2015) 63, http://dx.doi.org/10.3389/fonc.2015.00063.

[63] V.V. Artym, S. Swatkoski, K. Matsumoto, C.B. Campbell, R.J. Petrie, E.K. Dimitriadis, et al., Dense fibrillar collagen is a potent inducer of invadopodia via a specific signaling network, J. Cell Biol. 208 (2015) 331–350, http://dx.doi.org/10.1083/jcb.201405099.

[64] P.A. Soucy, L.H. Romer, Endothelial cell adhesion, signaling, and morphogenesis in fibroblast-derived matrix, Matrix Biol. 28 (2009) 273–283, http://dx.doi.org/10.1016/j.matbio.2009.04.005.

[65] M.D. Amatangelo, D.E. Bassi, A.J.P. Klein-Szanto, E. Cukierman, Stroma-derived three-dimensional matrices are necessary and sufficient to promote desmoplastic differentiation of normal fibroblasts, Am. J. Pathol. 167 (2005) 475–488, http://dx.doi.org/10.1016/S0002-9440(10)62991-4.

[66] M. Van Bockstal, K. Lambein, M. Van Gele, E. De Vlieghere, R. Limame, G. Braems, et al., Differential regulation of extracellular matrix protein expression in carcinoma-associated fibroblasts by TGF-β1 regulates cancer cell spreading but not adhesion, Oncoscience 1 (2014) 634–648.

[67] R. Pankov, Y. Endo, S. Even-Ram, M. Araki, K. Clark, E. Cukierman, et al., A Rac switch regulates random versus directionally persistent cell migration, J. Cell Biol. 170 (2005) 793–802, http://dx.doi.org/10.1083/jcb.200503152.

[68] M.L. Kutys, A.D. Doyle, K.M. Yamada, Regulation of cell adhesion and migration by cell-derived matrices, Exp. Cell Res. 319 (2013) 2434–2439, http://dx.doi.org/10.1016/j.yexcr.2013.05.030.

[69] N.Z. Kuhn, R.S. Tuan, Regulation of stemness and stem cell niche of mesenchymal stem cells: implications in tumorigenesis and metastasis, J. Cell. Physiol. 222 (2010) 268–277, http://dx.doi.org/10.1002/jcp.21940.

[70] A.J. Engler, S. Sen, H.L. Sweeney, D.E. Discher, Matrix elasticity directs stem cell lineage specification, Cell 126 (2006) 677–689, http://dx.doi.org/10.1016/j.cell.2006.06.044.

[71] E.R. Deutsch, R.E. Guldberg, Stem cell-synthesized extracellular matrix for bone repair, J. Mater. Chem. 20 (2010) 8942–8951, http://dx.doi.org/10.1039/C0JM01070G.

[72] X.-D. Chen, V. Dusevich, J.Q. Feng, S.C. Manolagas, R.L. Jilka, Extracellular matrix made by bone marrow cells facilitates expansion of marrow-derived mesenchymal progenitor cells and prevents their differentiation into osteoblasts, J. Bone Miner. Res. 22 (2007) 1943–1956, http://dx.doi.org/10.1359/jbmr.070725.

[73] T. Hoshiba, N. Kawazoe, T. Tateishi, G. Chen, Development of stepwise osteogenesis-mimicking matrices for the regulation of mesenchymal stem cell functions, J. Biol. Chem. 284 (2009) 31164–31173, http://dx.doi.org/10.1074/jbc.M109.054676.

[74] M.L. Decaris, J.K. Leach, Design of experiments approach to engineer cell-secreted matrices for directing osteogenic differentiation, Ann. Biomed. Eng. 39 (2011) 1174–1185, http://dx.doi.org/10.1007/s10439-010-0217-x.

[75] Y. Lai, Y. Sun, C.M. Skinner, E.L. Son, Z. Lu, R.S. Tuan, et al., Reconstitution of marrow-derived extracellular matrix ex vivo: a robust culture system for expanding large-scale highly functional human mesenchymal stem cells, Stem Cells Dev. 19 (2010) 1095–1107, http://dx.doi.org/10.1089/scd.2009.0217.

[76] H. Lin, G. Yang, J. Tan, R.S. Tuan, Influence of decellularized matrix derived from human mesenchymal stem cells on their proliferation, migration and multi-lineage differentiation potential, Biomaterials 33 (2012) 4480–4489, http://dx.doi.org/10.1016/j.biomaterials.2012.03.012.

[77] M. Grünert, C. Dombrowski, M. Sadasivam, K. Manton, S.M. Cool, V. Nurcombe, Isolation of a native osteoblast matrix with a specific affinity for BMP2, J. Mol. Histol. 38 (2007) 393–404, http://dx.doi.org/10.1007/s10735-007-9119-0.

[78] M.C. Prewitz, F.P. Seib, M. von Bonin, J. Friedrichs, A. Stißel, C. Niehage, et al., Tightly anchored tissue-mimetic matrices as instructive stem cell microenvironments, Nat. Methods 10 (2013) 788–794, http://dx.doi.org/10.1038/nmeth.2523.

[79] C.P. Ng, A.R.M. Sharif, D.E. Heath, J.W. Chow, C.B.Y. Zhang, M.B. Chan-Park, et al., Enhanced ex vivo expansion of adult mesenchymal stem cells by fetal mesenchymal stem cell ECM, Biomaterials 35 (2014) 4046–4057, http://dx.doi.org/10.1016/j.biomaterials.2014.01.081.

[80] S.T. Rashid, J.D. Humphries, A. Byron, A. Dhar, J.A. Askari, J.N. Selley, et al., Proteomic analysis of extracellular matrix from the hepatic stellate cell line LX-2 identifies CYR61 and Wnt-5a as novel constituents of fibrotic liver, J. Proteome Res. 11 (2012) 4052–4064, http://dx.doi.org/10.1021/pr3000927.

[81] I. Leivo, K. Alitalo, L. Risteli, A. Vaheri, R. Timpl, J. Wartiovaara, Basal lamina glycoproteins laminin and type IV collagen are assembled into a fine-fibered matrix in cultures of a teratocarcinoma-derived endodermal cell line, Exp. Cell Res. 137 (1982) 15–23.

[82] D. Gospodarowicz, Charles III, The extracellular matrix and the control of proliferation of corneal endothelial and lens epithelial cells, Exp. Eye Res. 31 (1980) 181–199.

[83] W.W. Carley, A.J. Milici, J.A. Madri, Extracellular matrix specificity for the differentiation of capillary endothelial cells, Exp. Cell Res. 178 (1988) 426–434.

[84] Y. Sun, W. Li, Z. Lu, R. Chen, J. Ling, Q. Ran, et al., Rescuing replication and osteogenesis of aged mesenchymal stem cells by exposure to a young

[85] J.A. DeQuach, V. Mezzano, A. Miglani, S. Lange, G.M. Keller, F. Sheikh, et al., Simple and high yielding method for preparing tissue specific extracellular matrix coatings for cell culture, PLoS One 5 (2010) e13039, http://dx.doi.org/10.1371/journal.pone.0013039.

[86] A. Boudaoud, A. Burian, D. Borowska-Wykręt, M. Uyttewaal, R. Wrzalik, D. Kwiatkowska, et al., FibrilTool, an ImageJ plug-in to quantify fibrillar structures in raw microscopy images, Nat. Protoc. 9 (2014) 457–463, http://dx.doi.org/10.1038/nprot.2014.024.

[87] M. Bignon, C. Pichol-Thievend, J. Hardouin, M. Malbouyres, N. Bréchot, L. Nasciutti, et al., Lysyl oxidase-like protein-2 regulates sprouting angiogenesis and type IV collagen assembly in the endothelial basement membrane, Blood 118 (2011) 3979–3989, http://dx.doi.org/10.1182/blood-2010-10-313296.

[88] D. Philp, S.S. Chen, W. Fitzgerald, J. Orenstein, L. Margolis, H.K. Kleinman, Complex extracellular matrices promote tissue-specific stem cell differentiation, Stem Cells (Dayt Ohio) 23 (2005) 288–296, http://dx.doi.org/10.1634/stemcells.2002-0109.

[89] H.K. Kleinman, G.R. Martin, Matrigel: basement membrane matrix with biological activity, Semin. Cancer Biol. 15 (2005) 378–386, http://dx.doi.org/10.1016/j.semcancer.2005.05.004.

[90] A.L. Willis, F. Sabeh, X.-Y. Li, S.J. Weiss, Extracellular matrix determinants and the regulation of cancer cell invasion stratagems, J. Microsc. 251 (2013) 250–260, http://dx.doi.org/10.1111/jmi.12064.

[91] S.F. Badylak, D.O. Freytes, T.W. Gilbert, Extracellular matrix as a biological scaffold material: structure and function, Acta Biomater. 5 (2009) 1–13, http://dx.doi.org/10.1016/j.actbio.2008.09.013.

[92] A.V. Ngangan, T.C. McDevitt, Acellularization of embryoid bodies via physical disruption methods, Biomaterials 30 (2009) 1143–1149, http://dx.doi.org/10.1016/j.biomaterials.2008.11.001.

[93] D. Rana, H. Zreiqat, N. Benkirane-Jessel, S. Ramakrishna, M. Ramalingam, Development of decellularized scaffolds for stem cell-driven tissue engineering, J. Tissue Eng. Regener. Med. (2015), http://dx.doi.org/10.1002/term.2061.

[94] J.M. Singelyn, J.A. DeQuach, S.B. Seif-Naraghi, R.B. Littlefield, P.J. Schup-Magoffin, K.L. Christman, Naturally derived myocardial matrix as an injectable scaffold for cardiac tissue engineering, Biomaterials 30 (2009) 5409–5416, http://dx.doi.org/10.1016/j.biomaterials.2009.06.045.

[95] K.M. Yamada, R. Pankov, E. Cukierman, Dimensions and dynamics in integrin function, Braz. J. Med. Biol. Res. 36 (2003) 959–966.

[96] R. Nair, A.V. Ngangan, T.C. McDevitt, Efficacy of solvent extraction methods for acellularization of embryoid bodies, J. Biomater. Sci. Polym. Ed. 19 (2008) 801–819, http://dx.doi.org/10.1163/156856208784522056.

[97] W.-D. Lü, L. Zhang, C.-L. Wu, Z.-G. Liu, G.-Y. Lei, J. Liu, et al., Development of an acellular tumor extracellular matrix as a three-dimensional scaffold for tumor engineering, PLoS One 9 (2014) e103672, http://dx.doi.org/10.1371/journal.pone.0103672.

[98] N. Datta, H.L. Holtorf, V.I. Sikavitsas, J.A. Jansen, A.G. Mikos, Effect of bone extracellular matrix synthesized in vitro on the osteoblastic differentiation of marrow stromal cells, Biomaterials 26 (2005) 971–977, http://dx.doi.org/10.1016/j.biomaterials.2004.04.001.

[99] J. Liao, X. Guo, D. Nelson, F.K. Kasper, A.G. Mikos, Modulation of osteogenic properties of biodegradable polymer/extracellular matrix scaffolds generated with a flow perfusion bioreactor, Acta Biomater. 6 (2010) 2386–2393, http://dx.doi.org/10.1016/j.actbio.2010.01.011.

[100] R. Garcia, E.T. Herruzo, The emergence of multifrequency force microscopy, Nat. Nanotechnol. 7 (2012) 217–226, http://dx.doi.org/10.1038/nnano.2012.38.

[101] N.C. Santos, M.A.R.B. Castanho, An overview of the biophysical applications of atomic force microscopy, Biophys. Chem. 107 (2004) 133–149, http://dx.doi.org/10.1016/j.bpc.2003.09.001.

[102] H.-J. Butt, Force measurements with the atomic force microscope: technique, interpretation and applications, Surf. Sci. Rep. 59 (2005) 1–152, http://dx.doi.org/10.1016/j.surfrep.2005.08.003.

[103] H.-J. Butt, M. Jaschke, Calculation of thermal noise in atomic force microscopy, Nanotechnology 6 (1995) 1, http://dx.doi.org/10.1088/0957-4484/6/1/001.

[104] H. Hertz, Über die Berührung fester elastischer Körper, ournal für die reine und angewandte Mathematik 92 (1881) 156–171.

[105] D.J. Müller, Y.F. Dufrêne, Atomic force microscopy: a nanoscopic window on the cell surface, Trends Cell Biol. 21 (2011) 461–469, http://dx.doi.org/10.1016/j.tcb.2011.04.008.

[106] S. Nawaz, P. Sánchez, K. Bodensiek, S. Li, M. Simons, I.A.T. Schaap, Cell visco-elasticity measured with AFM and optical trapping at sub-micrometer deformations, PLoS One 7 (2012) e45297, http://dx.doi.org/10.1371/journal.pone.0045297.

[107] P.A. Soucy, J. Werbin, W. Heinz, J.H. Hoh, L.H. Romer, Microelastic properties of lung cell-derived extracellular matrix, Acta Biomater. 7 (2011) 96–105, http://dx.doi.org/10.1016/j.actbio.2010.07.021.

[108] A.J. Engler, M. Chan, D. Boettiger, J.E. Schwarzbauer, A novel mode of cell detachment from fibrillar fibronectin matrix under shear, J. Cell Sci. 122 (2009) 1647–1653, http://dx.doi.org/10.1242/jcs.040824.

[109] F. Grinnell, H. Fukamizu, P. Pawelek, S. Nakagawa, Collagen processing, crosslinking, and fibril bundle assembly in matrix produced by fibroblasts in long-term cultures supplemented with ascorbic acid, Exp. Cell Res. 181 (1989) 483–491.

[110] S.M. Thomasy, V.K. Raghunathan, M. Winkler, C.M. Reilly, A.R. Sadeli, P. Russell, et al., Elastic modulus and collagen organization of the rabbit cornea: epithelium to endothelium, Acta Biomater. 10 (2014) 785–791, http://dx.doi.org/10.1016/j.actbio.2013.09.025.

[111] P. Mestres, L.L. Gomez, T.N. Lopez, G. del Rosario, S.W. Lukas, U. Hartmann, The basement membrane of the isolated rat colonic mucosa. A light, electron and atomic force microscopy study, Ann. Anat. Anat. Anz. 196 (2014) 108–118, http://dx.doi.org/10.1016/j.aanat.2014.01.001.

[112] C.H. Chen, H.G. Hansma, Basement membrane macromolecules: insights from atomic force microscopy, J. Struct. Biol. 131 (2000) 44–55, http://dx.doi.org/10.1006/jsbi.2000.4252.

[113] S.S. Soofi, J.A. Last, S.J. Liliensiek, P.F. Nealey, C.J. Murphy, The elastic modulus of Matrigel as determined by atomic force microscopy, J. Struct. Biol. 167 (2009) 216–219, http://dx.doi.org/10.1016/j.jsb.2009.05.005.

[114] J. Alcaraz, R. Xu, H. Mori, C.M. Nelson, R. Mroue, V.A. Spencer, et al., Laminin and biomimetic extracellular elasticity enhance functional differentiation in mammary epithelia, EMBO J. 27 (2008) 2829–2838, http://dx.doi.org/10.1038/emboj.2008.206.

[115] J. Zhang, B. Senger, D. Vautier, C. Picart, P. Schaaf, J.-C. Voegel, et al., Natural polyelectrolyte films based on layer-by layer deposition of collagen and hyaluronic acid, Biomaterials 26 (2005) 3353–3361, http://dx.doi.org/10.1016/j.biomaterials.2004.08.019.

[116] B. Trappmann, J.E. Gautrot, J.T. Connelly, D.G.T. Strange, Y. Li, M.L. Oyen, et al., Extracellular-matrix tethering regulates stem-cell fate, Nat. Mater. 11 (2012) 642–649, http://dx.doi.org/10.1038/nmat3339.

[117] J. Domke, M. Radmacher, Measuring the elastic properties of thin polymer films with the atomic force microscope, Langmuir 14 (1998) 3320–3325, http://dx.doi.org/10.1021/la9713006.

[118] E.K. Dimitriadis, F. Horkay, J. Maresca, B. Kachar, R.S. Chadwick, Determination of elastic moduli of thin layers of soft material using the atomic force microscope, Biophys. J. 82 (2002) 2798–2810.

[119] W. Halfter, C. Monnier, D. Müller, P. Oertle, G. Uechi, M. Balasubramani, et al., The bi-functional organization of human basement membranes, PLoS One 8 (2013) e67660, http://dx.doi.org/10.1371/journal.pone.0067660.

[120] M.S. Samuel, J.I. Lopez, E.J. McGhee, D.R. Croft, D. Strachan, P. Timpson, et al., Actomyosin-mediated cellular tension drives increased tissue stiffness and β-catenin activation to induce epidermal hyperplasia and tumor growth, Cancer Cell 19 (2011) 776–791, http://dx.doi.org/10.1016/j.ccr.2011.05.008.

[121] J.I. Lopez, I. Kang, W.-K. You, D.M. McDonald, V.M. Weaver, In situ force mapping of mammary gland transformation, Integr. Biol. (Camb) 3 (2011) 910–921, http://dx.doi.org/10.1039/c1ib00043h.

[122] M. Plodinec, M. Loparic, C.A. Monnier, E.C. Obermann, R. Zanetti-Dallenbach, P. Oertle, et al., The nanomechanical signature of breast cancer, Nat. Nanotechnol. 7 (2012) 757–765, http://dx.doi.org/10.1038/nnano.2012.167.

[123] S.E. Cross, Y.-S. Jin, J. Rao, J.K. Gimzewski, Nanomechanical analysis of cells from cancer patients, Nat. Nanotechnol. 2 (2007) 780–783, http://dx.doi.org/10.1038/nnano.2007.388.

4 Annexe n°2 : Participation à d'autres thématiques du laboratoire

Une des autres thématiques de l'équipe est l'étude de l'impact du flux sanguin sur l'arrêt et l'extravasation des cellule tumorales dans la circulation sanguine de l'embryon du poisson zèbre.

J'ai participé ici à la construction de la figure 7 qui est construite à partir de données provenant de l'imagerie intravitale de cellules métastatiques dans le cerveau de souris. J'ai aussi conduit une expérience pour évaluer l'effet du remodelage des vaisseaux sanguins sur l'extravasation. Dans cette expérience nous avons traité un groupe de souris avec du Sunitinib qui inhibe, entre autres les récepteurs au VEGF. Nous avons ensuite réalisé une injection intra-cardiaque de cellules tumorales Jimt1-tdTomato (métastasant dans le cerveau). Après 5 jours de traitement au Sunitinib les souris ont été fixées par perfusion intracardiaque, les cerveaux prélevés pour être ensuite coupés au vibratome. Les sections de cerveau ont ensuite été traitées par immunofluorescence pour le marquage de CD31, marqueur des cellules endothéliales. Les acquisitions confocales des différentes cellules retrouvées dans les cerveaux traités au Sunitinib et les cerveaux contrôles nous permettent de quantifier l'implication des récepteurs au VEGF sur le remodelage de l'endothélium lors de l'extravasation. Ces expériences sont actuellement en cours d'analyse.

4.1 Manuscrit n°10: Hemodynamic forces tune the arrest, adhesion and extravasation of circulating tumor cells

Hemodynamic forces tune the arrest, adhesion and extravasation of circulating tumor cells

Gautier Follain[1-4], Naël Osmani[1-4], Sofia Azevedo[1-4], Guillaume Allio[1-4], Luc Mercier[1-4], Matthia A. Karreman[5], Gergely Solecki[6], Nina Fekonja[1-4], Claudia Hille[7], Vincent Chabannes[8], Guillaume Dollé[8], Thibaut Metivet[8], Christophe Prudhomme[8], Bernhard Ruthensteiner[9], André Kemmling[10], Susanne Siemonsen[11], Tanja Schneider[11], Jens Fiehler[11], Markus Glatzel[12], Frank Winkler[6], Yannick Schwab[5], Klaus Pantel[7], Sébastien Harlepp[2,13-14], Jacky G. Goetz[1-4*]

[1]INSERM UMR_S1109, MN3T, Strasbourg, F-67200, France.

[2]Université de Strasbourg, Strasbourg, F-67000, France.

[3]LabEx Medalis, Université de Strasbourg, Strasbourg, F-67000, France.

[4]Fédération de Médecine Translationnelle de Strasbourg (FMTS), Strasbourg, F-67000, France.

[5]Cell Biology and Biophysics Unit, European Molecular Biology Laboratory, Heidelberg, 69117, Germany.

[6]Department of Neurooncology, University Hospital Heidelberg, Heidelberg, 69120, Germany and Clinical Cooperation Unit Neurooncology, German Cancer Research Center (DKFZ), Heidelberg, 69120, Germany.

[7]Institute of Tumor Biology, University Medical Center Hamburg-Eppendorf, Martinistrasse 52, Hamburg, 20246, Germany.

[8]LabEx IRMIA, CEMOSIS, Université de Strasbourg, Strasbourg, F-67000 France.

[9]Zoologische Staatssammlung München, Munich, 81247, Germany.

[10]Department of Neuroradiology, University Medical Center Schleswig-Holstein, Campus Lübeck, 23535 Lübeck, Germany

[11]Department of Diagnostic and Interventional Neuroradiology, University Medical Center Hamburg-Eppendorf, 20246 Hamburg, Germany

[12]Center for Diagnostics, Institute of Neuropathology, University Medical Center Hamburg-Eppendorf, 20246 Hamburg, Germany

[13]CNRS UMR7504, Institut de Physique et Chimie des Matériaux de Strasbourg (IPCMS), Strasbourg, F-67000, France.

[14]LabEx NIE, Université de Strasbourg, Strasbourg, F-67000, France.

ABSTRACT

Metastatic seeding is driven by cell-intrinsic and environmental cues, yet the contribution of biomechanics is poorly known. We aim to elucidate the impact of blood flow on the arrest and the extravasation of circulating tumor cells (CTCs) *in vivo*. Using the zebrafish embryo, we show that arrest of CTCs occurs mostly in vessels with favorable flow profiles where flow forces control the adhesion efficacy of CTCs to the endothelium. We biophysically identified the threshold values of flow and adhesion forces allowing successful arrest of CTCs. In addition, flow forces fine-tune tumor cell extravasation by impairing the remodeling properties of the endothelium. Importantly, we also observe endothelial remodeling at arrest sites of CTCs in mouse brain capillaries. Finally, we observed that human supratentorial brain metastases preferably develop in areas with low perfusion. Altogether, these results demonstrate that hemodynamic profiles at metastatic sites regulate key steps of extravasation preceding metastatic outgrowth.

KEYWORDS

INTRODUCTION

Metastatic progression is a complex process resulting in the formation of lethal secondary tumors at distance of its origin[1]. Metastatic cancer cells disseminate very efficiently throughout the body upon intravasation in the blood circulation. Recent work on breast cancer suggests that about 80% of metastases originate from early disseminated cancer cells[2,3]. Once in the blood stream, circulating tumor cells (CTCs) may find a location favoring arrest and stable adhesion before extravasating, and avoiding the hostile shear forces[4,5]. After extravasation, metastatic cells either remain dormant[6] or grow successfully into life-threatening secondary tumors[7]. Although multiple mechanisms have been postulated for successful extravasation and outgrowth of metastatic cells[7-10], there are only little informations on the role played by mechanical cues encountered in the blood, the main route for hematogenous metastatic dissemination.

Biomechanical forces are known to have a major impact on tumor progression, leading to metastatic growth. For example, tumor cells sense and respond to stiffening of the surrounding stroma by increasing their invasive potential[11-13]. High extravascular stress caused by tumor growth[14,15] and interstitial fluid pressure[16] leads to vascular compression that impairs perfusion and eventually promotes tumor progression, immunosuppression, and treatment resistance. Locally, invading tumor cells need to overcome physical tissue constraints by cellular and nuclear deformability[17,18], possibly inducing nuclear envelope rupture and DNA damage[19] leading eventually to inheritable genomic instability[20]. Overall, while the impact of biomechanics on tumor growth and invasion are mechanistically relatively well understood, the *in vivo* mechanisms driving arrest, survival and successful extravasation of CTCs, preceding metastatic growth, remain to be elucidated.

Indeed, very little is known about how CTCs arrest and adhere to the endothelium of small capillaries and leave the blood stream by crossing the vascular wall. While the "seed and soil" concept states that metastasis will occur at sites where the local microenvironment is favorable[21], the "mechanical" concept argues that arrest and metastasis of CTC occur at sites of optimal flow patterns[22]. CTCs in the blood circulation are subjected to vascular routing[23], collisions and associations with blood cells[24], hemodynamic shear forces[25] and physical constraints imposed by the vessel architecture[7,9]. Only CTCs capable of overcoming or exploiting the deleterious effects of shear forces will eventually arrest, adhere to and exit the vasculature to form a

secondary tumor[26]. Interestingly, upon arrest in lung microvessels, shear flow disrupts CTCs into microparticles that prime and recruit myeloid cells thereby stimulating successful metastasis from surviving CTC[9]. Nevertheless, a direct contribution of mechanical cues to the arrest and successful extravasation of CTCs has only been poorly studied so far[26]. Therefore, new *in vivo* models, where modeling, visualization and biophysical quantification of the extravasation parameters are easily performed, are of utmost importance for assessing whether biomechanics regulate metastatic extravasation.

Here, we aim to address the direct impact of the blood flow on the arrest and extravasation of CTCs *in vivo*. We developed an original experimental approach to measure and modulate blood flow with intravascular injection of CTCs within zebrafish (ZF) embryos. We observed that blood flow controls the sequential steps of arrest, adhesion and extravasation of CTCs *in vivo*. In parallel, using microfluidics and optical tweezers, we identified the critical adhesion force (80 pN) that CTCs require to initiate adhesion to the endothelium which rapidly stabilizes under shear flow. This value matches the threshold dragging force measured *in vivo* at extravasation sites. Finally, we used our recently-developed intravital correlative light and electronic microscope (CLEM)[27–29], to identify endothelial remodeling as one of the major extravasation mechanisms *in vivo*, and that endothelial remodeling scales with flow velocities. Overall our studies demonstrate that blood flow forces at metastatic sites regulate key steps of extravasation preceding metastatic outgrowth.

RESULTS

Arrest and adhesion of CTC is favored by permissive flow velocities

In order to test the impact of blood flow on the arrest, adhesion and extravasation of CTCs, we experimentally modeled metastatic seeding in endothelium-labeled ZF embryo (*Tg(Fli1a:EGFP)*) at 2 days post-fertilization (dpf) by injecting fluorescently-labeled tumor cells (D2A1 LA-RFP) in the duct of Cuvier (Figure 1A,B). While metastatic extravasation can be successfully tracked in this model[30], the ZF embryo further allows to combine biophysical characterization and manipulation of blood flow parameters with long-lasting and high-resolution imaging of tumor cells *in vivo*. We first quantified and mapped the position of arrested and stably adherent tumor cells in the ZF vasculature and noticed that CTCs preferentially arrested (and extravasated) in the caudal plexus (CP) (Figure 1C). Although arrest and extravasation can be also observed in inter-somitic vessels (ISV) (Figure 1C) and in the brain of ZF embryos (Figure 1C, Figure S1, Movie 1), the majority of the tumor cells arrest in the caudal plexus. We exploited the highly stereotyped vasculature of this region for compiling 20 embryos and quantitatively identifying a major hotspot of arrest in this region (Figure 1D), that sits in between the caudal artery and the venous plexus. Using fast imaging of the blood flow (100 fps) within the entire ZF embryo, combined with PIV (Particle Image Velocimetry) analysis, we observed decreasing flow values in the vascular region that is permissive for the CTC arrest (Figure 1E-F, Movie 2). Accurate dissection of blood flow profiles using PIV analysis showed that flow velocity progressively decreases from the anterior dorsal aorta (Position 1, maximal velocity, v_{max} = 2500 µm/sec, Figure 1E-F), to a minimal flow in its most posterior region (Positions 5 to 6, v_{max} = 500 µm/sec), which we named the arterio-venous junction (AVJ). We have shown in the past that blood flow dissipates along the vascular network of the ZF embryo[31]. In addition, the mass conservation implies that ramification of the vessels in the AVJ further contributes to the blood flow decrease. We thus set out to model this phenomenon *in silico* using mathematical simulation of the blood flow in the CP. To do so, we modelled a simplified geometry of the CP in 3D based on fine 3D confocal microscopy segmentation. Simulation experiments reproduced the flow drop observed in the most posterior region of the CP (Figure S2, Movie 3). Besides, to determine whether flow velocity can impact CTCs arrest, we developed an *in vitro* approach to mimic *in vivo* flow profiles in microfluidic channels previously coated with endothelial cells (EC, Figure 1G). We observed that adhesion

of CTCs to the endothelial layer was favored by low flow profiles (peak velocities of 100 to 400 µm/sec) (Figure 1G), similar to those measured *in vivo* in the AVJ (Figure 1D-E). Using high flow profiles that mimic flow values obtained in the anterior DA prevented efficient adhesion of CTCs to the endothelial layer (Figure 1G), as observed *in vivo* where no adhesion could be observed in the DA between position 1 and 4 (Figure 1D-E). Finally, similar flow profiles were measured in vessels favoring extravasation of CTCs in the ZF brain (Figure S1C, Movie 1). Taken together, these data suggest that low flow profiles are permissive for stable adhesion of CTCs to the endothelium, and that the threshold velocity value for efficient adhesion of CTCs ranges from 400 to 600 µm/sec.

Permissive flow profiles promote stable adhesion of CTCs to the endothelium

Adhesion of CTCs to the endothelium is an important feature that precedes their extravasation[32]. Furthermore, mechanical constraints imposed by cell size and vessel topology likely favor the initial arrest of CTCs[7,33,34]. We set out to test whether such features also contribute to arrest and adhesion in the ZF embryo by accurately measuring both CTC and vessel diameters, with a high-resolution reconstruction of the CP lumen (Movie 4). We measured an average diameter of ~10 µm for the tumor cells (D2A1) in suspension, mimicking CTCs (Figure 2A). We validated this model by comparing this value to average diameters of human CTCs isolated from breast and lung cancer patients (ranging from 7 to 29 µm)(Figure 2A). The diameters of the DA, the AVJ and the caudal vein (CV) each displayed a minimal value of ~15 µm (Figure 2B), suggesting that size limitation is not the main cause for successful arrest of CTCs, when circulating as single cells. This led us to test the role of adhesion molecules in driving successful, flow-dependent, arrest of CTCs. We have observed that intravascular CTCs are capable of efficiently crawling on the vessel wall, suggesting that CTCs establish firm adhesions with the endothelium (Movie 5). In addition, we took advantage of our *in vitro* microfluidic approach and used the optical tweezers (OT) technology to trap and stick CTCs to the EC monolayer. Doing so, we identified an average value of 80 pN for the very early adhesion forces (less than 1 min after adhesion of the CTC to the endothelial layer) required for the attachment of CTCs to ECs (Figure S3A, Movie 6). Interestingly, applying the Stokes law to measure the correspondence between flow and force intensity, we noted that a value of 80 pN represents an average flow value of 450 µm/sec, which agrees with

threshold flow values that we measured both *in vivo* and *in vitro* (Figure 1). Thus, CTCs establish very quickly adhesion forces that allow them to sustain flow velocities of 450 µm/sec.

To test the role of adhesion molecules, we targeted ß1 integrins (ITGB1), known to play a central role in tumor metastasis[35] and promote stable adhesion of CTC to the endothelium before extravasation[36,37]. We determined whether compromising stable adhesion mediated by ß1 integrins would affect the ability of CTC to arrest under permissive flows. We depleted ITGB1 in our cells using a siRNA approach (Figure 2C) and assessed their stable adhesion 3hpi using a heatmapping procedure (see supplementary methods) over several embryos. Interestingly, the adhesion pattern showing an adhesion hotspot in the AVJ is conserved (Figure 2D) but the overall number of adhesion event is significantly reduced (Figure 2E). Similar observations were made in our microfluidic system where only 20% of ITGB1-depleted CTCs stably adhere to the EC monolayer using the same perfusion parameters (Figure 2F). Comparable values were obtained when adhesion (or detachment) of perfused CTCs to (from) ECs was forced using OT in microfluidic channels (Figure S3B, Movie 7) indicating, that permissive flow profiles, combined with proper adhesion forces, allow stable adhesion of CTCs to the endothelium.

To further support this hypothesis, we assessed whether adhesion events could be observed *in vivo* using intravital CLEM[38], which allows to combine live imaging of xenografted CTCs in the ZF embryo with Transmission Electron Microscopy (TEM) and Electron tomography (ET). Interestingly, CTCs that were arrested in the ZF vasculature only 15 mpi displayed finger-like adhesive contacts with endothelial cells (Figure 2G). In addition, ECs displayed long protrusions when in contact with arrested CTCs (upper panels, Figure 2G). These observations suggest that integrin-dependent adhesion forces between early arrested CTCs and ECs are quickly exceeding stripping forces from the blood flow. We aimed to further demonstrate the contribution of early adhesion forces to flow-dependent arrest of CTCs and we performed OT *in vivo.* Although OT can very efficiently trap circulating red blood cells (RBCs) in the vasculature of living ZF embryo (Movie 8) and detach adhered CTCs from ECs *in vitro* (Figure S3B), OT was inefficient for detaching arrested CTCs *in vivo* (Figure 2H, Movie 8). The inability to detach >35 arrested CTCs with OT, demonstrates that early adhesion forces rapidly exceed 200 pN (which is the technical limit of our OT set-up). Altogether, these results suggest that low flow

forces (~80pN) enable the arrest and stable adhesion of CTCs *in vivo*, and ITGB1 mediates stable adhesion (and subsequent increase in adhesion forces) of CTCs to ECs.

Pharmacological tuning of hemodynamic forces modulates pacemaker activity

Since arrest of CTCs occurs at site of permissive flow patterns, we investigated whether tuning flow forces would impact arrest efficacy. We first took advantage of the possibility to tune the ZF pacemaker activity and subsequent flow forces using pharmacological treatments. We selected lidocain[39] and Isobutylmethylxanthine (IBMX)[40] to decrease or increase the pacemaker activity (PMA), respectively (Figure 3A,G). Upon treatment, we assessed cardiac PMA and measured an average decrease and increase of 20% for lidocain and IBMX respectively. Using fast imaging combined with PIV analysis we determined the resulting velocities in 3 positions of the DA for several embryos (ISV 1, 4 and 8) and observed that lowering or increasing PMA with lidocain and IBMX, respectively, significantly altered flow profiles (Figure 3B,H, Movie 9). In brief, while lidocain treatments led to lower velocities with longer times under 400 µm/sec (Fig.3B,S4A), IBMX significantly increased the maximum velocities of flow pulses and decreased the overall duration of the flow under 400 µm/sec (Fig.3H, S4A). We confirmed the impact of the two drugs on flow profiles using *in silico* 3D flow simulation (Fig.S5, Movie 10). We further assessed the impact of tuning PMA on hemodynamic forces by trapping RBCs using OT in the AVJ region *in vivo* (Figure S4B, Movie 11). We measured the forces exerted on trapped RBCs, both at the vessel wall and in its center, and extracted the corresponding flow profile based on the Poiseuille law for each condition (Figure S4B). While lidocain significantly reduced flow forces in the center of the vessel, IBMX increased flow forces at the vessel wall and in the center (Figure 3C,I). Importantly, before taking on experiments aiming to study the behavior of CTCs in distinct flow profiles, we demonstrated that our pharmacological treatments had no impact on the vasculature architecture and permeability (Figure S6A to D, Movie 12), and the migratory and adhesive properties of tumor cells (TCs) *in vitro* (Fig.S6E to G).

Low flow promotes early arrest of CTCs

We then assessed the impact of modulating flow forces on the arrest of CTCs using live and instantaneous intravital imaging upon injection (Figure 3D,J, Movie 13). As

expected, CTCs mostly arrest in the AVJ in normal flow profiles (Figure 3D-E, J-K, Vehicle). Interestingly, decreasing flow profiles with lidocain induced arrest of CTCs in anterior regions of the DA, decreased the number of CTCs in the blood flow over a period of 5 minutes post-injection (mpi) and significantly increased their mean arrest time over the imaging period (Figure 3D-F). In contrast, increasing flow profiles with IBMX drastically abrogated the arrest of CTCs in the blood flow over a period of 5 mpi and reduced their mean arrest time (Figure 3J-L). Altogether, these results show that while low flow forces enhance the arrest probability of CTCs, high flow profiles are capable of impeding their early arrest.

Hemodynamic forces tune the stable intravascular adhesion of CTCs

Because extravasation of CTCs requires stable adhesion to the vessel wall, we investigated whether tuning flow profiles would impact stable adhesion of CTCs to ECs *in vivo*. We first assessed the number and location of arrested CTCs 3 hpi in a large number of embryos, making use of our heatmapping protocol and the stereotyped vasculature of the ZF caudal plexus (Figure 4A, D). While normal flow conditions favored the definitive arrest in the AVJ, decreasing flow forces with lidocain stimulated the stable adhesion of CTCs in more anterior regions of the DA and reduced the proportion of CTCs arresting in the AVJ (Figure 4A-C). On the contrary, increasing flow forces with IBMX impaired the stable arrest in the DA and AVJ regions, and shifted definitive arrest towards venous regions of the caudal plexus (Figure 4D-F). We further consolidated this observation by using two additional drugs known to decrease (nifedipin[41]) and increase (norepinephrine [40]) PMA (Figure S7A,F). Decreasing flow forces with nifedipin favored the arrest of CTCs in more anterior regions of the DA, increasing flow forces with norepinephrine significantly favored the stable adhesion of CTCs in the CV region of the caudal plexus (Figure S7B-C, G-I). Reassuringly, none of these drugs altered the adhesion or migration properties of TCs *in vitro* (Figure S7D-E, H-J). Altogether, these data suggest that flow forces finely tune the adhesive capacity of CTCs, independently of the vessel architecture.

High flow promotes extravasation of CTCs

Once stably attached to the vessel wall, CTCs need to withstand the shear forces and undergo extravasation for metastatic outgrowth. We thus further investigated

whether flow forces could impact the extravasation abilities of arrested CTCs and assessed the location and ratio of extravascular cells 24 hpi. Most of the arrested CTCs eventually undergo extravasation in normal flow conditions, while impairing flow forces with lidocain drastically reduced the number of extravascular cells. More than 60% of cells remained fully intravascular, in particular along anterior regions of the DA where CTCs mostly arrested in low flow conditions (Figure 5A-B). Using our CLEM protocol, we confirmed that the TCs were extravascular in normal flow conditions using serial TEM (Figure 5E, Movie 14). Similar experiments conducted on lidocain-treated embryos showed that the vast majority of the cells remain indeed fully intravascular (Figure 5E). In contrast, increasing flow forces with IBMX further increased the ratio of extravascular cells (close to 100%) (Figure 5C-D), and favored the formation of micrometastasis foci that were surrounded by the local vasculature, as depicted in the 3D view (Figure 5C). Overall, these results show that blood flow forces enhance the extravasation abilities of CTCs.

Flow-dependent endothelial remodeling drives extravasation of CTCs

We noticed that ECs could react very quickly to the presence of arrested CTCs (Figure 2G) and that extravasation of CTCs induces massive remodeling of the local vasculature (Figure 5C). In addition, our drugs had no effect on the behavior of the TCs (Figure S6-7), which prompted us to investigate whether flow forces could impact extravasation via ECs. We thus set up long-lasting (15h) intravital recordings of the behavior of arrested CTCs during extravasation using 3D confocal microscopy (Figure 6A, Movie 15). Unexpectedly, image analysis revealed that a majority of CTCs extravasated by indoctrinating the local vasculature rather than by actively transmigrating through the vessel wall by diapedesis, which is nevertheless also observed (Figure 6B-D). Indeed, ECs actively remodeled around the arrested CTCs by slowly protruding and establishing tight connections with other ECs. During this process, endothelial cells progressively engulf single or cluster of arrested CTCs, allowing full reperfusion of the vessel while inducing extravasation of CTCs. In order to gain further structural insights into this phenomenon, we took advantage of our intravital CLEM procedure on ZF embryos only 9 hpi, which allows us to dissect the behavior of CTCs and associated ECs that are engaged in extravasation (Figure 6E). 3D TEM analysis revealed that clusters of arrested CTCs are indeed fully surrounded by ECs (Figure 6F-G, Movie 16). High-resolution images performed via ET (Electron

Tomography) showed that ECs could establish tight contact around the cluster of arrested CTCs (Figure 6H), suggesting that ECs are also actively participating to the extravasation of CTCs.

We further examined embryos 3, 9 and 24 hpi and documented the behavior of the associated ECs (pocketing) over a high number of arrested CTCs (Figure 6I), over time, and in dependence of the blood flow profiles. Interestingly, impairing flow forces *in vivo* with lidocain significantly impaired the ability of ECs to engage pocketing over arrested CTCs (Figure 6J-K) suggesting that blood flow is essential for maintaining the remodeling ability of the endothelium. Remarkably, in normal flow conditions, injected CTCs that are fully intravascular are rapidly (≈3hpi) accompanied by a massive EC pocketing that drives successful extravasation of TCs (Figure 6J). On the contrary, low flow significantly delays the pocketing behavior of ECs (≈9hpi) impairing efficient extravasation of intravascular TCs (Figure 6K). We then wondered whether this flow-dependent phenomenon could be reproduced *in vitro* and set out a microfluidic experiment where CTCs were perfused over a monolayer of ECs for 10 minutes and incubate 16h under perfusion (or not) before assessing the behavior of ECs. We observed that flow stimulated the transmigration of TCs. Interestingly, TCs that transmigrated through the HUVECs monolayer were mostly engulfed by ECs, mimicking the pocketing phenomenon we had observed *in vivo* (Figure 6L-M). As a consequence, TCs that successfully transmigrated in absence of flow were rarely surrounded by ECs suggesting that they crossed the monolayer by diapedesis. Altogether, these results demonstrate that the extravasation of CTCs occurs via indoctrination of the associated endothelium, and that flow forces are essential for maintaining the remodeling abilities of the vasculature.

Micrometastasis develop from mouse brain capillaries with low flow profiles

We next investigated whether blood flow forces could explain the location of successful extravasation and micrometastasis formation in another model, the mouse brain. We used our intravital imaging set-up[7] to quantify the vascular arrest, extravasation, and successful growth vs. regression in the mouse brain over weeks after intra-cardiac injection of highly metastatic tumor cells (Figure 7A). By analyzing >5000 arrested tumor cells from four different cell lines (JIMT1br3, A2058br, PC14PE6br, H1), we discovered that tumor cells that successfully mastered all step of brain metastatic cascade in microvessels of a specific diameter, shape and depth

(Figure 7B). Next, we measured the associated blood flow velocities of these vessels, and compared them to flow velocities within blood vessels where arrest and extravasation of CTCs never occurred (Figure 7B). Strikingly, the mean flow velocity in metastasis-proficient vessels was 628±46 µm/sec, which is very close to the permissive flow values we had identified in the ZF embryo. In contrast, mean flow velocity of metastasis-deficient vessels was much higher (5880±716 µm/sec). Together, this data suggests that flow-mediated arrest of CTCs could be a universal determinant of tumor metastasis.

Similar to the ZF embryo experiments, we took advantage of our intravital CLEM procedure[28,29] and investigated whether ECs were also influenced by arrested CTCs in the mouse brain. We thus conducted intracardiac injections of Jimt1 cells and recorded the position of arrested CTCs only 3 dpi, where most of the CTCs are still intravascular (Figure 7C). Our workflow driven by X-ray micro-computed tomography (mCT) allowed us to successfully retrieve arrested CTCs in the vasculature of the mouse brain. This enabled us to document, using serial section TEM, the ultrastructure of the arrested TC (Figure 7C-D), of its associated vessel (Figure 7C-D) and of neighboring vessels where no CTC could be observed (Figure 7C,E). Blood vessels where no arrested CTC could be observed displayed a smooth vascular wall (Figure 7E). However, ECs from the vessel containing an arrested CTC displayed a remodeling phenotype, possibly in response to the presence of the arrested cell (Figure 7D). Indeed, multiple endothelial cells could be observed protruding within the vessel lumen, establishing contacts with other cells of the vessel wall and enwrapping the arrested tumor cell while maintaining a lumenized vessel. Altogether, these results obtained in the context of brain metastasis in the mouse suggest that permissive flow profile is a very relevant mechanism driving the arrest of CTCs, leading to successful micrometastasis growth. In addition, the observation of early vascular remodeling in the presence of arrested CTCs further suggest an active reaction of the endothelium to arrested cancer cells during the brain metastatic cascade, which could speak for mechanisms similar to what we have observed in zebrafish.

Blood perfusion controls the location of human brain metastasis (BM)

We next investigated whether blood flow perfusion would control the location of BM in humans. For this purpose, we analyzed a randomly selected cohort of 100 patients

with BM (n=580) in the supratentorial region of the brain (Fig.8A). The BM of each patient were segmented on contrast-enhanced T1-weighted imaging and the sum mask of all patients (Fig.8B) was co-registered with a computed tomography perfusion atlas of a healthy cohort (Fig.8C). We then performed a voxel-wise comparison of regions containing BM (BM+) and those who did not (BM-) (Fig.8D). Strikingly, BM preferably develop in regions with lower cerebral blood flow (CBF, 51±36-61 vs 58±41-76 ml/100g/min, p<0.001) and higher mean transit time (MTT, 4.6±4.3-5.1 vs 4.5±4.2-5.0 seconds, p<0.001) (Fig.8C,D). These results indicated that occurrence of BM is favored in brain regions with low perfusion, further demonstrating that blood flow patterns are key determinants of metastatic outgrowth.

DISCUSSION

In this work, we have unraveled for the first time the contribution of flow forces *in vivo* on mediating arrest, adhesion and successful extravasation of CTCs, preceding metastatic outgrowth. Using the multiple advantages of the ZF embryo, we have identified a threshold of hemodynamic profiles (400-600 µm/s) that allows stable arrest of CTCs in permissive vascular regions, a prerequisite for metastasis formation (Fig.8E). These values were further confirmed *in vitro* and *in silico* using a combination of microfluidic and 3D flow simulation approaches, which were developed upon accurate *in vivo* measurements of hemodynamic forces. We have shown that these permissive flow profiles promote the formation of transient protrusions establishing integrin-dependent adhesion of CTCs to the endothelium. This fast and weak adhesion is then quickly stabilized (less than a minute *in vitro*) to reach adhesion forces exceeding the shear forces generated by such permissive flow values. This process is impaired in regions with high shear values, where forces are significantly higher than the initial adhesion forces CTCs are able to produce. Reduced or low flow forces favor arrest and metastasis in the zebrafish embryo, but also in mouse brain capillaries. Importantly, we made similar observations in humans where a significant reduction of blood perfusion is observed in pro-metastatic brain regions. Thus, low or reduced flow profiles favor the stable arrest of CTCs preceding metastatic outgrowth (Fig.8E). Once arrest of CTCs within blood vessels is consolidated (through integrins), arrested TCs engage in a second step where blood flow remains essential. Indeed, we have observed that blood flow is required to stimulate endothelial remodeling and subsequent pro-metastatic extravasation. However, although low flow allows arrest of CTCs, it impedes the remodeling potential of ECs, and significantly impairs extravasation of arrested TCs. Thus, pro-metastatic vascular regions are characterized by intermediate flow profiles that are sufficiently low (or reduced) to favor the arrest of CTCs, and sufficiently high to stimulate endothelial remodeling, which could be a fundamental mechanism driving metastasis formation.

While much attention has been given to the contribution of biomechanics to tumor growth and tumor invasion[26,42], only few evidence suggest that biomechanics could also modulate one of the most important steps of tumor progression, namely extravasation and metastatic outgrowth. However, CTCs are shed in the blood

circulation and must survive in a very hostile environment, such as blood shear forces that could induce cell cycle arrest[25] or even necrotic cell death[5]. In addition, CTCs frequently collide with other components of the blood and the vascular wall, reaching capillary-like vascular regions that appear often occlusive[7,9,36]. Size-mediated arrest of CTCs in capillaries occurs in multiple organs such as the lung, the liver and the brain[43]. Moreover, cellular and nuclear rigidity[18] and integrity[19,20] was recently shown to be key drivers of tumor invasion and metastasis. Our work suggests that, in addition to physical occlusion, permissive flows are sufficient to facilitate arrest of CTCs. In the ZF embryo, 50% of arrested TCs did so in vascular regions where diameter of the vessel exceeds diameter of TCs, excluding occlusion mechanisms. In addition, full occlusion of mouse brain capillaries is rarely observed suggesting that blood flow or physical constraints, although they could impact synergistically, are sufficient to promote the arrest of CTCs, preceding metastatic outgrowth. Further work is required to investigate the mutual contribution of cell stiffness/size and the blood flow as determinant factors in arrest and extravasation of CTCs. Interestingly, recent work demonstrates that clusters of CTCs, whose arrest would be favored by physical occlusion, are more potent in driving tumor metastasis[44–46]. Besides, we frequently observed a remarkable behavior of arrested CTCs that do not occlude the blood vessel: they stably crawl counter-flow along the endothelium in fully perfused vessels and tend to cluster intravascularly before extravasating (Movie 5). This process occurs without compromising blood flow and suggests that TCs establish cell-cell contact that could favor successful extravasation.

A fundamental observation made in our study is that low blood flow favors arrest of CTCs in any species (ZF, mouse and human), preceding metastatic outgrowth. Indeed, we first identified a threshold flow velocity value of 400-600 µm/s that favors the arrest of CTCs in the vasculature of the ZF embryo. Using intravital imaging and flow profiling in the mouse brain, we further confirmed that brain capillaries perfused with low flow velocities (around 600 µm/s) are favorable to extravasation and outgrowth of TCs. Finally, we analyzed a cohort of 100 patients with brain metastasis and observed that they preferably develop in regions with lower cerebral blood perfusion. Altogether, these results obtained in various organisms indicate that occurrence of metastasis is favored in vascular regions with reduced perfusion, further demonstrating that blood flow patterns are key determinants of metastatic

outgrowth in the brain. Interestingly, human brain metastasis had been shown to occur preferentially in vascular border zones as well as in the gray and white matter junction[47]. These regions are located at the most distal part of the arterial tree and display sudden drops in vessel diameter, blood pressure and blood flow, making them very susceptible to infarction and ischemia. Our results further demonstrate that such vascular networks are favorable environments for metastatic extravasation.

Another key observation from our work is that low flow promotes arrest of CTCs, by favoring the establishment of intravascular TC-EC adhesions. Indeed, successful arrest of CTCs can be observed in anterior regions of the DA, when flow values are decreased and depletion of ITGB1 drastically impedes the successful arrest of CTCs. We identified an initial TC-EC adhesion force of 80 pN, likely mediated by a few integrin molecules. While ITBGB1 favors TC protrusion into the subendothelial matrix thereby favoring metastatic outgrowth[48], integrin-mediated arrest of CTCs could be favored by interaction between ITGB1 and endothelial adhesion molecules, or extracellular matrix molecules localized on the luminal side of the vascular wall. Indeed, *in vitro* data suggest that CTCs hijack the leukocyte adhesion machinery and arrest using $\alpha4\beta1$ integrins to bind the VCAM-1 receptor present at the surface of endothelial cells[49]. Furthermore, *in vivo* imaging of liver metastasis has demonstrated that although lumen occlusion by CTCs is rather frequent, it does not account fully for the efficient extravasation as blocking adhesion with ITGB1-blocking antibody significantly impaired stable cell arrest of CTCs[36]. CTCs can escape mechanical entrapment in the lungs[50] and adhesion-mediated arrest of CTCs has been observed without signs of mechanical entrapment[51]. This suggests that although capillary size can stop CTCs, active adhesion between CTCs and the vascular wall is required for efficient extravasation, and subsequent metastasis. Even if we have not directly visualized this in our experiments, we cannot exclude the CTCs undergo rolling, that could activate ITGB1, before stably arresting. Further work will be required to investigate whether arrest of CTCs follows rules that are commonly used by immune cells before extravasation.

Another important observation of our work is the route used by arrested CTCs to undergo extravasation. Indeed, in most of the cases, extravasation of CTCs engages massive endothelial remodeling, which encapsulate single or clusters of arrested CTCs. This phenomenon has been observed during extravasation of neutrophils and allows the vessel to reduce vascular permeability[52]. We observed that pocketing or

encapsulation of arrested CTCs occurs by the formation of endothelial domes, reminiscent of the ones observed for extravasation of neutrophils[53], that are tightly connected through EC-EC junctions (Figure 6). Recent work performed in ZF embryos has shown that stem cells use similar mechanisms to undergo extravasation[54]. Interestingly, using our intravital CLEM technology, we observed that vascular regions of arrested TCs in the mouse brain also engage massive endothelial remodeling in vessels with permissive flow profiles, suggesting it could drive successful extravasation of brain metastatic cells. Altogether, this reinforces the view that CTCs require a very active contribution of the endothelium to perform successful transmigration of the vascular wall, and challenge the classical idea that CTCs mostly use diapedesis for successful extravasation[55–57]. Along this line, arrested CTCs have been observed to proliferate attached to the luminal wall of lung blood vessels, leading to intraluminal metastatic foci that eventually passively rupture the endothelial barrier[58]. Recent work suggest that arrested CTCs are also capable of driving TC-mediated necroptosis of EC and subsequent metastasis[10], further suggesting that the vascular wall is a key contributor to efficient metastatic outgrowth. While endothelium remodeling of arrested CTCs had been observed *in vivo* in the past[30,59], its importance during metastatic extravasation is still not fully appreciated[60]. We now provide evidence that blood flow actively regulates endothelial remodeling thus promoting successful extravasation. Indeed, both *in vivo* pocketing and *in vitro* endothelial dome formation are increased by flow. As blood flow is known to be key regulator of vascular homeostasis[61,62] and angiogenesis[38,63], it is likely that it is required during extravasation by maintaining its remodeling behavior.

In conclusion, we provide the first *in vivo* demonstration that blood flow, which carries tumor-shed CTCs, actively participates in both CTC stable arrest and extravasation, preceding metastatic outgrowth. Our work identified pro-metastatic vascular regions that are characterized by intermediate flow profiles which are sufficiently low (or reduced) to favor the arrest of CTCs, and sufficiently high to stimulate endothelial remodeling. From our *in vivo* observations, this latter mechanism is fundamental in driving metastasis formation. Our current work aims to identify the molecular mechanisms that are driven by blood flow to successfully encapsulate arrested CTCs. Altogether, this work suggests that therapies that target endothelial remodeling might be useful to impede extravasation, and subsequent outgrowth, of metastatic cells.

AUTHOR CONTRIBUTIONS

G.F. performed most of the experiments and analysis, and wrote the paper. N.O. performed the siITGB1 experiments and analysis, and contributed to Fig.3 and Fig.6. S.A. initiated the project, and performed experiments and analysis. G.A. developed the heatmapping protocol and contributed to blood flow analysis, as well as processing of EM images. L.M. participated to the mouse experiments. M.K. and Y.S. performed EM of the mouse brain metastasis. G.S. and F.W. performed 2PEM imaging of the mouse brain metastasis. C.H. and K.P. isolated and characterized human CTCs. N.F. performed EM in the ZF embryo. V.C, G.D., T.M. and C.P. developed the flow simulation with input from G.F., S.H. and J.G. B.R. and M.K. performed mCT experiments. A.K., S.S., T.S., J.F and K.P. analyzed human brain metastases and blood perfusion patterns on imaging. S.H. supervised the study, performed OT experiments and analysis. J.G. conceived the project, supervised the study, performed experiments and analysis, and wrote the paper with input from G.F., S.H., and N.O.

ACKNOWLEDGMENTS

REFERENCES

1. Nguyen, D. X., Bos, P. D. & Massagué, J. Metastasis: from dissemination to organ-specific colonization. *Nat. Rev. Cancer* **9,** 274–284 (2009).
2. Hosseini, H. *et al.* Early dissemination seeds metastasis in breast cancer. *Nature* (2016). doi:10.1038/nature20785
3. Harper, K. L. *et al.* Mechanism of early dissemination and metastasis in Her2(+) mammary cancer. *Nature* (2016). doi:10.1038/nature20609
4. Valastyan, S. & Weinberg, R. A. Tumor Metastasis: Molecular Insights and Evolving Paradigms. *Cell* **147,** 275–292 (2011).
5. Regmi, S., Fu, A. & Luo, K. Q. High Shear Stresses under Exercise Condition Destroy Circulating Tumor Cells in a Microfluidic System. *Scientific Reports* **7,** 39975 (2017).
6. Sosa, M. S., Bragado, P. & Aguirre-Ghiso, J. A. Mechanisms of disseminated cancer cell dormancy: an awakening field. *Nat. Rev. Cancer* **14,** 611–622 (2014).
7. Kienast, Y. *et al.* Real-time imaging reveals the single steps of brain metastasis formation. *Nat. Med.* **16,** 116–122 (2010).
8. Chen, Q. *et al.* Carcinoma-astrocyte gap junctions promote brain metastasis by cGAMP transfer. *Nature* **533,** 493–498 (2016).
9. Headley, M. B. *et al.* Visualization of immediate immune responses to pioneer metastatic cells in the lung. *Nature* **531,** 513–517 (2016).
10. Strilic, B. *et al.* Tumour-cell-induced endothelial cell necroptosis via death receptor 6 promotes metastasis. *Nature* **536,** 215–218 (2016).
11. Paszek, M. J. *et al.* Tensional homeostasis and the malignant phenotype. *Cancer Cell* **8,** 241–254 (2005).
12. Levental, K. R. *et al.* Matrix crosslinking forces tumor progression by enhancing integrin signaling. *Cell* **139,** 891–906 (2009).
13. Mouw, J. K. *et al.* Tissue mechanics modulate microRNA-dependent PTEN expression to regulate malignant progression. *Nat. Med.* **20,** 360–367 (2014).
14. Stylianopoulos, T. *et al.* Causes, consequences, and remedies for growth-induced solid stress in murine and human tumors. *Proc. Natl. Acad. Sci. U.S.A.* **109,** 15101–15108 (2012).
15. Chauhan, V. P. *et al.* Angiotensin inhibition enhances drug delivery and potentiates chemotherapy by decompressing tumour blood vessels. *Nat Commun* **4,** 2516 (2013).
16. Provenzano, P. P. *et al.* Enzymatic targeting of the stroma ablates physical barriers to treatment of pancreatic ductal adenocarcinoma. *Cancer Cell* **21,** 418–429 (2012).
17. Wolf, K. *et al.* Physical limits of cell migration: control by ECM space and nuclear deformation and tuning by proteolysis and traction force. *J. Cell Biol.* **201,** 1069–1084 (2013).
18. Harada, T. *et al.* Nuclear lamin stiffness is a barrier to 3D migration, but softness can limit survival. *J. Cell Biol.* **204,** 669–682 (2014).
19. Denais, C. M. *et al.* Nuclear envelope rupture and repair during cancer cell migration. *Science* **352,** 353–358 (2016).
20. Irianto, J. *et al.* DNA Damage Follows Repair Factor Depletion and Portends Genome Variation in Cancer Cells after Pore Migration. *Curr. Biol.* (2016). doi:10.1016/j.cub.2016.11.049
21. Paget, S. The distribution of secondary growths in cancer of the breast. 1889. *Cancer Metastasis Rev.* **8,** 98–101 (1989).
22. Weiss, L. Comments on hematogenous metastatic patterns in humans as

revealed by autopsy. *Clin. Exp. Metastasis* **10,** 191–199 (1992).

23. Chambers, A. F., Groom, A. C. & MacDonald, I. C. Dissemination and growth of cancer cells in metastatic sites. *Nat. Rev. Cancer* **2,** 563–572 (2002).

24. Labelle, M., Begum, S. & Hynes, R. O. Platelets guide the formation of early metastatic niches. *Proc. Natl. Acad. Sci. U.S.A.* **111,** E3053–3061 (2014).

25. Chang, S.-F. *et al.* Tumor cell cycle arrest induced by shear stress: Roles of integrins and Smad. *PNAS* **105,** 3927–3932 (2008).

26. Wirtz, D., Konstantopoulos, K. & Searson, P. C. The physics of cancer: the role of physical interactions and mechanical forces in metastasis. *Nat. Rev. Cancer* **11,** 512–522 (2011).

27. Follain, G., Mercier, L., Osmani, N., Harlepp, S. & Goetz, J. G. Seeing is believing – multi-scale spatio-temporal imaging towards in vivo cell biology. *J Cell Sci* **130,** 23–38 (2017).

28. Karreman, M. A., Hyenne, V., Schwab, Y. & Goetz, J. G. Intravital Correlative Microscopy: Imaging Life at the Nanoscale. *Trends Cell Biol.* **26,** 848–863 (2016).

29. Karreman, M. A. *et al.* Fast and precise targeting of single tumor cells in vivo by multimodal correlative microscopy. *J Cell Sci* **129,** 444–456 (2016).

30. Stoletov, K. *et al.* Visualizing extravasation dynamics of metastatic tumor cells. *J Cell Sci* **123,** 2332–2341 (2010).

31. Anton, H. *et al.* Pulse propagation by a capacitive mechanism drives embryonic blood flow. *Development* **140,** 4426–4434 (2013).

32. Reymond, N., d'Água, B. B. & Ridley, A. J. Crossing the endothelial barrier during metastasis. *Nat. Rev. Cancer* **13,** 858–870 (2013).

33. Cameron, M. D. *et al.* Temporal progression of metastasis in lung: cell survival, dormancy, and location dependence of metastatic inefficiency. *Cancer research* **60,** 2541–2546 (2000).

34. Luzzi, K. J. *et al.* Multistep nature of metastatic inefficiency: dormancy of solitary cells after successful extravasation and limited survival of early micrometastases. *The American journal of pathology* **153,** 865–873 (1998).

35. Seguin, L., Desgrosellier, J. S., Weis, S. M. & Cheresh, D. A. Integrins and cancer: regulators of cancer stemness, metastasis, and drug resistance. *Trends Cell Biol.* **25,** 234–240 (2015).

36. Gassmann, P., Hemping-Bovenkerk, A., Mees, S. T. & Haier, J. Metastatic tumor cell arrest in the liver–lumen occlusion and specific adhesion are not exclusive. *International Journal of Colorectal Disease* **24,** 851–858 (2009).

37. Schlesinger, M. & Bendas, G. Contribution of very late antigen-4 (VLA-4) integrin to cancer progression and metastasis. *Cancer Metastasis Rev.* **34,** 575–591 (2015).

38. Goetz, J. G. *et al.* Endothelial Cilia Mediate Low Flow Sensing during Zebrafish Vascular Development. *Cell Reports* **6,** 799–808 (2014).

39. Vermot, J. *et al.* Reversing blood flows act through klf2a to ensure normal valvulogenesis in the developing heart. *PLoS Biol.* **7,** e1000246 (2009).

40. Luca, E. D. *et al.* ZebraBeat: a flexible platform for the analysis of the cardiac rate in zebrafish embryos. *Scientific Reports* **4,** 4898 (2014).

41. Brennan, C. Acetylcholine and calcium signalling regulates muscle fibre formation in the zebrafish embryo. *Journal of Cell Science* **118,** 5181–5190 (2005).

42. Kai, F., Laklai, H. & Weaver, V. M. Force Matters: Biomechanical Regulation of Cell Invasion and Migration in Disease. *Trends Cell Biol.* **26,** 486–497 (2016).

43. Azevedo, A. S., Follain, G., Patthabhiraman, S., Harlepp, S. & Goetz, J. G. Metastasis of circulating tumor cells: favorable soil or suitable biomechanics, or

both? *Cell Adh Migr* **9,** 345–356 (2015).

44. Cheung, K. J. & Ewald, A. J. A collective route to metastasis: Seeding by tumor cell clusters. *Science* **352,** 167–169 (2016).

45. Cheung, K. J. *et al.* Polyclonal breast cancer metastases arise from collective dissemination of keratin 14-expressing tumor cell clusters. *Proc. Natl. Acad. Sci. U.S.A.* **113,** E854–863 (2016).

46. Aceto, N. *et al.* Circulating tumor cell clusters are oligoclonal precursors of breast cancer metastasis. *Cell* **158,** 1110–1122 (2014).

47. Hwang, T. L., Close, T. P., Grego, J. M., Brannon, W. L. & Gonzales, F. Predilection of brain metastasis in gray and white matter junction and vascular border zones. *Cancer* **77,** 1551–1555 (1996).

48. Chen, M. B., Lamar, J. M., Li, R., Hynes, R. O. & Kamm, R. D. Elucidation of the Roles of Tumor Integrin β1 in the Extravasation Stage of the Metastasis Cascade. *Cancer Res.* **76,** 2513–2524 (2016).

49. Klemke, M., Weschenfelder, T., Konstandin, M. H. & Samstag, Y. High affinity interaction of integrin alpha4beta1 (VLA-4) and vascular cell adhesion molecule 1 (VCAM-1) enhances migration of human melanoma cells across activated endothelial cell layers. *J. Cell. Physiol.* **212,** 368–374 (2007).

50. Glinskii, O. V. *et al.* Mechanical entrapment is insufficient and intercellular adhesion is essential for metastatic cell arrest in distant organs. *Neoplasia* **7,** 522–527 (2005).

51. Enns, A. *et al.* Integrins can directly mediate metastatic tumor cell adhesion within the liver sinusoids. *J. Gastrointest. Surg.* **8,** 1049–1059; discussion 1060 (2004).

52. Petri, B. *et al.* Endothelial LSP1 is involved in endothelial dome formation, minimizing vascular permeability changes during neutrophil transmigration in vivo. *Blood* **117,** 942–952 (2011).

53. Phillipson, M., Kaur, J., Colarusso, P., Ballantyne, C. M. & Kubes, P. Endothelial domes encapsulate adherent neutrophils and minimize increases in vascular permeability in paracellular and transcellular emigration. *PLoS ONE* **3,** e1649 (2008).

54. Allen, T. A. *et al.* Angiopellosis as an Alternative Mechanism of Cell Extravasation. *Stem Cells* **35,** 170–180 (2017).

55. Heyder, C. *et al.* Realtime visualization of tumor cell/endothelial cell interactions during transmigration across the endothelial barrier. *J. Cancer Res. Clin. Oncol.* **128,** 533–538 (2002).

56. Khuon, S. *et al.* Myosin light chain kinase mediates transcellular intravasation of breast cancer cells through the underlying endothelial cells: a three-dimensional FRET study. *J Cell Sci* **123,** 431–440 (2010).

57. Tremblay, P.-L., Huot, J. & Auger, F. A. Mechanisms by which E-selectin regulates diapedesis of colon cancer cells under flow conditions. *Cancer Res.* **68,** 5167–5176 (2008).

58. Al-Mehdi, A. B. *et al.* Intravascular origin of metastasis from the proliferation of endothelium-attached tumor cells: a new model for metastasis. *Nat Med* **6,** 100–102 (2000).

59. Lapis, K., Paku, S. & Liotta, L. A. Endothelialization of embolized tumor cells during metastasis formation. *Clinical & experimental metastasis* **6,** 73–89 (1988).

60. Lambert, A. W., Pattabiraman, D. R. & Weinberg, R. A. Emerging Biological Principles of Metastasis. *Cell* **168,** 670–691 (2017).

61. Franco, C. A. *et al.* Dynamic endothelial cell rearrangements drive developmental vessel regression. *PLoS Biol.* **13,** e1002125 (2015).

62. Gebala, V., Collins, R., Geudens, I., Phng, L.-K. & Gerhardt, H. Blood flow drives lumen formation by inverse membrane blebbing during angiogenesis in vivo. *Nat. Cell Biol.* **18,** 443–450 (2016).

63. Potente, M., Gerhardt, H. & Carmeliet, P. Basic and therapeutic aspects of angiogenesis. *Cell* **146,** 873–887 (2011).

64. Shibue, T., Brooks, M. W. & Weinberg, R. A. An integrin-linked machinery of cytoskeletal regulation that enables experimental tumor initiation and metastatic colonization. *Cancer Cell* **24,** 481–498 (2013).

65. Osswald, M. *et al.* Brain tumour cells interconnect to a functional and resistant network. *Nature* **528,** 93–98 (2015).

66. Prud'Homme, C. *et al.* Feel++: A Computational Framework for Galerkin Methods and Advanced Numerical Methods. *ESAIM: Proceedings* **38,** 429–455 (2012).

67. Burman, E. & Fernández, M. A. Explicit strategies for incompressible fluid-structure interaction problems: Nitsche type mortaring versus Robin-Robin coupling. *International Journal for Numerical Methods in Engineering* **97,** 739–758 (2014).

68. Hvichia, G. E. *et al.* A novel microfluidic platform for size and deformability based separation and the subsequent molecular characterization of viable circulating tumor cells. *Int. J. Cancer* **138,** 2894–2904 (2016).

69. Chudziak, J. *et al.* Clinical evaluation of a novel microfluidic device for epitope-independent enrichment of circulating tumour cells in patients with small cell lung cancer. *Analyst* **141,** 669–678 (2016).

70. Magbanua, M. J. M. *et al.* A Novel Strategy for Detection and Enumeration of Circulating Rare Cell Populations in Metastatic Cancer Patients Using Automated Microfluidic Filtration and Multiplex Immunoassay. *PLoS ONE* **10,** e0141166 (2015).

71. Robb, R. A. The biomedical imaging resource at Mayo Clinic. *IEEE Trans Med Imaging* **20,** 854–867 (2001).

72. Nudelman, K. N. H. *et al.* Altered cerebral blood flow one month after systemic chemotherapy for breast cancer: a prospective study using pulsed arterial spin labeling MRI perfusion. *PLoS ONE* **9,** e96713 (2014).

73. Schwarzbach, C. J. *et al.* Stroke and cancer: the importance of cancer-associated hypercoagulation as a possible stroke etiology. *Stroke* **43,** 3029–3034 (2012).

74. Feyen, L. *et al.* Standardization of Dynamic Whole-Brain Perfusion CT: A Comprehensive Database of Regional Perfusion Parameters. 189–220 (2010).

75. Abels, B., Klotz, E., Tomandl, B. F., Kloska, S. P. & Lell, M. M. Perfusion CT in Acute Ischemic Stroke: A Qualitative and Quantitative Comparison of Deconvolution and Maximum Slope Approach. *American Journal of Neuroradiology* **31,** 1690–1698 (2010).

76. Kemmling, A. *et al.* Decomposing the Hounsfield unit: probabilistic segmentation of brain tissue in computed tomography. *Clin Neuroradiol* **22,** 79–91 (2012).

FIGURE LEGENDS

Figure 1: Arrest and stable adhesion of CTCs are favored by permissive blood flow profiles in the ZF embryo. (A-B) Experimental design and workflow. xpi: minutes or hours post-injection. (C) Representative images (*Head, head region; CP,* Caudal Plexus) and quantification of arrested CTCs (red) in the vasculature (green) of the ZF embryo at 3 hpi (See also Movie 1). Ant., Mid and Post.: Anterior, mid and posterior plexus as depicted in D. (D) High-magnification image of the vascular caudal plexus, the associated regions, and heatmap of arrested CTCs at 3 hpi (n=20 embryos). *AVJ*: arterio-venous junction. *DA*: Dorsal aorta. *CV*: Caudal veins. Arrows indicate blood flow direction. (E) Blood flow velocity measurements (PIV) in the indicated region (red and blue squares 1 to 8) of the ZF embryo. Arrows indicate blood flow direction (See also Movies 2&3). (F) Minimum, maximum and mean values of the blood flow velocity are plotted over the 8 different regions (n=3 embryos). (G) Experimental set-up, representative images and quantification of the microfluidic approach. CTCs (green) are perfused over a monolayer of HUVECs (ECs, red) and adhesion is quantified (n=5 to 6 independent channel per conditions). Pulsatile flow corresponds to 0.3 sec perfusion/0.3 sec stop of the peristatique pump. Values in (C), (E), (F) and (G) are mean ±SD (gray area in E). *p <0,05, **p < 0.01, ***p <0.001. Kruskal-Wallis test and Dunn's multiple comparisons post-test.

Figure 2: Arrest of CTCs depends on early cellular adhesion forces. (A) Quantification of the diameters of human CTCs (gray, five breast cancer patients and one lung cancer patient) and D2A1 cells (red) in suspension (number of cells quantified is provided). Representative images of D2A1 and of human CTCs are also provided. Human CTCs are labeled with Pan-Keratin (CTC marker), CD45 and DAPI (nucleus). Red dotted line shows the mean diameter of D2A1 cells. (B) Representative confocal Z-projection image of the caudal plexus and orthoslices from indicated position (yellow line) used to measure the diameter of the dorsal aorta (DA), the arterio-vascular junction (AVJ) and the caudal vein (CV). Quantification all along the caudal plexus (13 ISV: Inter segmental vessels) (see also Movie 4). (C) Experimental workflow and depletion of ITGB1 via siRNA in D2A1 cells: control siRNA (siCTL), and two distinct sequences of the siRNA targeting ITGB1 (siITGB1#1, siITGB1#2). Representative western-blot (WB) and immunofluorescent

images are shown. Quantification of ITGB1 levels using WB is also provided (n=3). (D) Heatmaps of arrested CTCs after 3hpi are shown for CTCs transfected with siRNAs (n=77, 63, 55, respectively). (E) Quantification of the ratio of arrested CTCs in the indicated region is provided. Norm.: normalized to siCTL AVJ. (F) Graph depicts the number of adhesion events (CTCs to HUVECs) quantified in our microfluidic approach (n=3 independent experiment) (See also Movies 6&7). Norm.: normalized to siCTL. (G) Experimental set-up of intravital CLEM performed on arrested CTCs only 15 mpi (minutes post-injection). Representative EM images of arrested CTCs (red) in vascular lumen (green) are provided from two different sections (top and bottom). A reconstruction of an Electron Tomogram is provided. (H) Experimental set-up, representative image and quantification of optical tweezing experiments of arrested CTCs in the AVJ (n=37 arrested cells, n>10 embryos) (see also Movie 8). Values in (A), (C), (E) and (F) are mean ±SD. *p <0,05, **p < 0.01, ***p <0.001. Mann-Whitney test for (E), Krustal-Wallis test and Dunn's multiple comparisons post-test for (F).

Figure 3: Modulating blood flow forces regulates arrest of CTCs. ZF embryos were treated with vehicles, lidocain (A-F) or IBMX (G-L). (A,G) Experimental workflow. Heart pacemaker activity is quantified for each condition. CTL: Breeding water. An additional kymograph analysis is provided. (B,H) (top) Images extracted from fast imaging and PIV analysis of the blood flow in the caudal plexus (region boxed in A,G) (see also Movies 9&10). (Bottom) Quantification of the flow profile in the center of the dorsal aorta analyzed at position ISV 8, ISV 4 and ISV1 (n=4 to 5 embryos per condition). (C,I) Orthogonal flow velocity profile and quantification extracted from optical tweezing of RBCs in the dorsal aorta under ISV 1 (W,Wall; C,Center) (See also Movie 11). (D,J) Experimental workflow and representative images of the residency time of CTCs in the caudal plexus over a period of 5 min (See also Movies 13). Arrow heads indicate long lasting arrested cells (white color). (E,K) Spatio-temporal quantification of the residency time of CTCs in the CP using heatmapping on a representative embryo. (F,L) Quantification of the ratio of CTCs as well as the mean arrest time over a period of 5 min for embryos treated with vehicle or the indicated drug. Norm.: normalized to vehicle mean. Values in (A-C), (F), (G-I) and (L) are mean ±SD. *p <0,05, **p < 0.01, ***p <0.001, ****p <0.0001. Mann-

Whitney test for (C,F,I,L), Kruskal-Wallis and Dunn's multiple comparisons post-test for (A,G).

Figure 4: Modulating blood flow forces regulates stable intravascular adhesion of CTCs. ZF embryos were treated with vehicles, lidocain (A-C) or IBMX (D-F). (A,D) Experimental workflow and representative images of arrested CTCs (red) in the caudal plexus (green) of vehicle- or drug-treated embryos. (B,E) Quantification of the number and location of arrested CTCs in the caudal plexus of 3hpi vehicle- or drug-treated embryos, through heatmapping. (C,F) Quantification of the number of arrested CTCs per embryo as well as the ratio of arrested CTCs per region in vehicle- or drug-treated embryos, 3 hpi. Data normalized to vehicle AVJ mean ratio. Values in (C) and (F) are mean ±SD. *p <0,05, **p < 0.01, ****p <0.0001. Mann-Whitney test.

Figure 5: Blood forces control the extravasation of CTCs. ZF embryos were treated with vehicle, lidocain (A-B) or IBMX (C-D). (A,C) Representative images of TCs (red) in the caudal plexus (green) of 24 hpi vehicle- or drug-treated embryos are shown. 3D reconstruction and scheme of the boxed region is also provided. (B,D) Quantification of the number and location of intra- and extravascular TCs in the caudal plexus of 24hpi vehicle- or drug-treated embryos, through heatmapping. Quantification of the ratio of extravascular TCs is also provided. Data normalized to vehicle mean ratio. (E) Experimental workflow and CLEM analysis of 24 hpi vehicle- or lidocain-treated embryos is used for further assessing the vascular location of TCs (yellow stars) intravascular (red) or extravascular (blue) (See also Movie 14). CLEM: Correlative light and electron microscopy. Values in (B) and (D) are mean ±SD. *p <0,05, ****p <0.0001. Mann-Whitney test.

Figure 6: Extravasation of CTCs occurs via flow-dependent endothelial remodeling. (A) Experimental workflow. (B) Extracted Z-projection image from 3D time-lapse analysis of the behavior of arrested TCs (red) in the caudal plexus vasculature (green) over a period of 15h (See also Movie 15). (C) Multiple sequential images, over a period of 800 min, of the region boxed in B are displayed and commented (yellow arrowheads point to the location of the associated comment (left panel)). (D) Multiple sequential images, over a period of 150 min, of the region boxed

in B are displayed and commented (yellow arrowheads point to the location of the associated comment). (E) Experimental workflow and CLEM analysis of a 9hpi vehicle-treated embryo. Extracted images of confocal analysis of extravasating TCs (red) at 9hpi is performed. (F) TEM image of the region of interest boxed in E, retrieved in the electron microscopy volume. A representative section is shown and color-coded for TCs (red) and vascular lumen (green) (see also Movie 16). (G) 3D reconstruction of the serial section TEM performed over the entire ROI, depicting TCs (red) and associated ECs (green) (See also Movie 16). (H) Electron tomography image extracted from 3D reconstruction over the boxed region in F (TC: red, ECs: green) (see also Movie 16). (I) Representative images of TCs (red) and the associated vasculature (green) in 9 hpi embryos are shown. (J-K) Quantification and kinetic analysis of the mean number of events over time for vehicle and lidocain treated embryos. The number of events (intravascular, pocketing and extravascular) was quantified at 3hpi (vehicle: n=16, 72 events and Lidocain: n=21, 78 events), 9 hpi (vehicle: n=22, 95 events and Lidocain: n=23, 110 events) and 24 hpi (vehicle: n=20, 94 events and Lidocain: n=20, 104 events). Immunostaining (L) of TCs (LifeAct, red) arrested on a monolayer of HUVECs (PECAM, green) is shown, in two flow conditions (0 and 400/sec). Height of associated HUVECs is color-coded and displayed. (M) Quantification of the number of transmigrated TCs and of transmigrated TCs with remodeled HUVECs. Values in (M) are mean ±SD. *p <0,05, ***p <0.001, ****p <0.0001. Fisher test for (M).

Figure 7: Permissive flow profiles favor formation of micrometastasis in the mouse brain. (A) Experimental workflow and representative images of micrometastases in 7 dpi mice injected with Jimt1-GFP cells (2PM: Two-photon microscopy). (B) Experimental workflow and 3D reconstruction of representative vascular network of the healthy brain. Quantification of the mean blood flow velocity in brain capillary with a diameter of 5 to 10 µm (highlighted in green, where extravasation preferentially takes place) and with higher diameter (highlighted in red, where extravasation is not expected). Work done over more than 5,000 tumor cells from four different tumor cell lines were quantified (JIMT1br3, A2058br, PC14PE6br, H1). A total of 51-96 vessels from 12-13 regions (dimensions: 607.28x607.28x372.00 µm) of 3-6 animals per group were quantified. Box plots representing median values with 10th, 25th, 75th and 90th percentiles. ***p <0.001 (Mann-Whitney test). (C)

Experimental workflow of intravital CLEM of 3dpi arrested JIMT1br3 cells. Maximum Z-projections showing an arrested JIMT1br3 cell (GFP, green) and the associated vasculature (TRITC-dextran, red). Merged images of the micro-computed x-ray tomography (mCT) and the intravital imaging (IVM) volume. Vessels containing the TC is circled in green (TC) and dissected using serial section TEM in D, normal neighboring vessels are circled in blue (#1-3) and dissected in E. (D) Serial section TEM images and segmentation of the tumor cell (green), its nucleus (blue) and ECs (red colors) are shown. 3 different z heights are provided. (E) TEM images and segmentation of the ECs (red colors) of normal neighboring vessels are shown.

Figure 8: Blood perfusion controls the location of human brain metastases (BM). (A) Number of BM and number of patients are provided for the entire cohort. BM originate from various tumor types including lung cancer (n=51), skin cancer (n=17), breast cancer (n=10), genitourinary (GU) cancer (n=10), gastrointestinal (GI) cancer (n=4), sarcoma (n=2) and cancer of unknown primary origin (n=6). (B,C) BM of the 100 patients were segmented semi-manually and co-registered on a CT perfusion mask from a control brain template consisting of 107 healthy patients. The cerebral blood flow (CBF) mask is displayed with red indicating a lower CBF and yellow a higher CBF. The cumulative BM is overlaid to the perfusion mask. (D) Mean CBF (cerebral blood flow) and MTT (mean transit time) is displayed for the brain metastases (BM, +) and the corresponding area without any BM (BM, -). Bars indicate standard deviations. Paired sample t-test (voxel-wise analysis) was used to compare the perfusions values of the BM+ and BM- regions. (E) Graphical abstract of our study: we identified a threshold of flow velocities that are permissive for the arrest of CTCs, a prerequisite for metastasis formation. Below blood flow velocities of 400-600 µm/s, arrest and adhesion of CTCs to the endothelium is favored. This is the case *in vitro* (microfluidics), in zebrafish embryos and in mouse brain capillaries. Similar results are obtained in humans where a significant reduction of blood perfusion is observed in pro-metastatic regions. In a second step, blood flow is required to stimulate endothelial remodeling and subsequent pro-metastatic extravasation. However, although low flow allows arrest of CTCs, it impairs extravasation of arrested TCs. Thus, pro-metastatic vascular regions are characterized by flow profiles that are sufficiently low (or reduced) to favor the arrest of CTCs, and sufficiently high to stimulate endothelial remodeling.

METHODS

Cell culture and siRNA-mediated knock-down

D2A1 stably expressing LifeAct-RFP or LifeAct-YPET, kindly provided by Robert A. Weinberg (MIT), were grown as previously described[64], in DMEM with 4.5 g/l glucose (Dutscher) supplemented with 5% FBS, 5% NBCS, 1% NEAA and 1% penicillin-streptomycin (Gibco). Human Umbilical Vein Endothelial Cells (HUVEC) (PromoCell) were grown in ECGM (PromoCell) supplemented with supplemental mix (PromoCell C-39215) and 1% penicillin-streptomycin (Gibco). To maximize the reproducibility of our experiments, we always used these cells at 4th passage in the microfluidic channels. siRNAs were transfected into D2A1 cells using Lipofectamine RNAiMAX (Invitrogen) following the manufacturer's instructions. Experiments were performed between 72 h and 96h post-transfection. siRNA sense sequences are the following: siCTL: GCA AAT TAT CCG TAA ATC A, siITGB1 #1: CCA CAG AAG UUU ACA UUA A, siITGB1 #2: GUG UGU AGG AAG AGA GAU A.

Zebrafish handling

Tg(fli1a:eGFP) Zebrafish (*Danio rerio*) embryos from a Tübingen background used in the experiments were kindly provided by the group of F.Peri from EMBL (Heidelberg, Germany). Embryos were maintained in Danieau 0.3X medium (17,4 mM NaCl, 0,2 mM KCl, 0,1 mM $MgSO_4$, 0,2 mM $Ca(NO_3)_2$) buffered with HEPES 0,15 mM (pH = 7.6), supplemented with 200 µM of 1-Phenyl-2-thiourea (Sigma-Aldrich) to inhibit the melanogenesis, as previously described[38].

Pharmacological treatments

Drugs were added in the breeding water (Danieau 0.3X + PTU) of the embryos before mounting and injection. IBMX (3-isobutyl-1-methylxanthin)[40], lidocain[39], nifedipin and norepinephrine[40] (Sigma) were used at 100 µM in DMSO (incubation time: 20h), 640µM in ethanol (inc. time: 2h), 5 µM in DMSO (inc. time: 2h) and 500 µM in water (inc. time: 1h) respectively.

High-speed microscopy for pacemaker activity and blood flow profiling

To measure the heart pacemaker activity and the associated blood flow profiles, we used the USB 3.0 uEye IDS CCD camera (IDEX) mounted on a DMIRE2 inverted

microscope (Leica) using transmitted light. Heartbeats were acquired at 80 frames per second (fps) and blood flow in the tail region at 200 fps. For the whole-embryo high-speed recordings of the blood flow, acquisitions were done using an Orca Flash 4.0 cMOS camera (Hamamatsu) mounted on an IX-73 inverted microscope equipped with a UPLFLN 10X/0.3 objective (Olympus). Heartbeats were manually counted to compute the pacemaker activity. The blood flow intensity profile over time at each positions in the vasculature was analyzed using an adapted Particle Image Velocimetry (PIV) protocol from ImageJ software that is available online (https://sites.google.com/site/qingzongtseng/piv).

Intravascular injection of CTCs in the ZF embryo

48 hour post-fertilization (hpf) *Tg(Fli1a:eGFP)* embryos were mounted in 0.8% low melting point agarose pad containing 650 µM of tricain (ethyl-3-aminobenzoate-methanesulfonate) to immobilize the embryos. D2A1 LifeAct-RFP cells were injected with a Nanoject microinjector 2 (Drummond) and microforged glass capillaries (25 to 30 µm inner diameter) filled with mineral oil (Sigma). 23nL of a cell suspension at 100.10^6 cells per ml were injected in the duct of Cuvier of the embryos under the M205 FA stereomicroscope (Leica), as previously described[30].

Confocal imaging and analysis

Confocal imaging was alternatively performed with an upright TCS SP5 or SP8 confocal microscope with a HC FLUOTAR L 25X/0,95 W VISIR (Leica), or with a SP2 confocal head mounted on a DMIRE2 stage with HC PL APO 20X/0,7 IMM CORR CS objective (Leica). The caudal plexus region (around 50µm width) was imaged with a z-step of less than 1.5 µm for at least 20 embryos per conditions from at least 3 independent experiments. Cells dispersion was manually counted and localized (using the stereotype patterning of ISVs as reference) in the caudal plexus. The data were compiled to generate heatmaps using a custom-made MATLAB plug in (see next section). Post-processing was performed using Imaris (Bitplane), Amira (FEI) and IMOD (Boulder Laboratory, University of Colorado) for segmentation and 3D reconstruction. For the permeability assay, embryos were pharmacologically treated (as described above) and injected in the duct of Cuvier with 18,4 nl of Dextran-TRITC (500kDa), 3 hours before confocal imaging of the caudal plexus. For assessing the endothelial remodeling *in vivo*, cells were sorted in 3 groups

(intravascular, pocketing and extravascular) based on confocal imaging. A kinetic analysis for the individual groups, in vehicle- and lidocain-treated embryos, was performed based on a Michaelis-Menten model, where the arrested tumor cells (TC) interact with endothelial cells (EC) that initiate pocketing (P) before undergoing extravasation (Ex):

$$[EC] + [TC] \rightleftharpoons [P] \rightarrow [Ex]$$
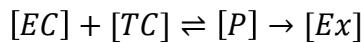
Heatmaps

The heatmaps were generated using ImageJ (https://imagej.nih.gov/ij/index.html) and MATLAB (MathWorks) softwares. The adhesion/extravasation events are identified for each fish after the analysis of the confocal z-stacks with ImageJ. The position of these events is manually reported on a gray-level support image of a 2.5 days post-fertilization zebrafish plexus. Then, all the support images representing each embryo for one condition were put together in an image stack using ImageJ. The stack is read layer by layer in MATLAB and the dots representing the localization are automatically detected with the function Hough circles (Yuan-Liang Tang, Department of Information Management, Chaoyang University of Technology, Taichung, Taiwan) (https://fr.mathworks.com/matlabcentral/fileexchange/22543-detects-multiple-disks--coins--in-an-image-using-hough-transform) using the Circular Hough Transform based algorithm, giving in output the coordinates of the detected dots. Gaussian spots are then created at these coordinates. The amplitude of each Gaussian spot is equal to 1. The different layers of one condition are added each other by making a sum projection, and a black and white mask created with the gray level support image is applied to this sum projection. The gaussian spot amplitudes of each layers are summed to produce the heatmap. The areas of the sum projection where the gaussian spot amplitudes are higher corresponds to high density areas of adhesion/extravasation events. To produce the final heatmap, a custom colormap, inspired by the jet colormap, is applied to the sum projection. The colormap goes from black (no event) to red (high density areas).

Sample preparation for Electronic microscopy of ZF embryos

Correlative Light and Electron Microscopy was performed as previously described[38]. To describe ultra structural characteristics of CTCs and the endothelium in the ZF embryo, chosen ZF embryos were chemically fixed with 2,5% glutaraldehyde and 4%

paraformaldehyde in 0.1 M Cacodylate buffer (fish tails cut off in the fixative). Samples were kept in fixative at room temperature for 1-2h and stored in fixative at 4°C overnight or until further processing. Samples were rinsed in 0.1M Cacodylate buffer for 2x5min and post-fixed using 1% OsO4 in 0.1 M Cacodylate buffer, for 1h at 4°C. Then, samples were rinsed for 2x10min in 0.1M Cacodylate buffer and secondary post-fixed with 4% water solution of uranyl acetate, 1h at room temperature. Rotation was used at all steps of sample processing. Followed by 5min wash in MiliQ water, the samples were stepwise dehydrated in Ethanol (25%, 50% each 15min, 95%, 3X100% each 20min) and infiltrated in a graded series of Epon (Ethanol/Epon 3/1, 1/1, 1/3, each 45min). Samples were left in absolute Epon (EmBed812) overnight. The following day, samples were placed in a fresh absolute Epon for 1h and polymerized (flat embedded) at 60°C for 24-48h. Once polymerized, most surrounding Epon was cut off using razorblade and samples were mounted on empty Epon blocks (samples flat on the top of the blocks) and left at 60 °C for 24h-48h. Semi-thin sections (200nm) were serially sectioned using ultramicrotome (Leica Ultracut UCT), collected on formvar-coated slot grids and stained with 4% water solution of uranyl acetate for 10min and Reynolds lead citrate for 3min. Semi-thin sections (200nm) were imaged with a CM120 transmission electron microscope (Philips Biotwin) operating at 120 kV. Images were recorded with Veleta 2k x 2k (Olympus-SIS) camera using iTEM software. On the same sections, Electron tomography was performed with a Tecnai F30 Field Emission Gun TEM (FEI) operating at 300 kV and equipped with an Eagle 4K camera (FEI). The F30 was controlled by Tecnai User Interface (PEOUI) and Tecnai Acquisition (TIA) software. Single-axis tomograms were obtained using SerialEM and reconstructed in eTomo, part of the IMOD software package (Boulder Laboratory, University of Colorado).

Microfluidic experiments

Quantification of the flow-dependent adhesion of CTCs was done using six channels μ-slides VI^{0,4} pre-coated with fibronectin (IBIDI). HUVEC cells were seeded at 21 000 cells per channel (Volume = 30µl). Medium was changed twice a day until they reach maximal confluency (3 to 4 days). D2A1 LifeAct-GFP cells were diluted to maintain the concentration of 150 000 cells/ml of cells between the different speed conditions and perfused using a REGLO Digital MS-2/12 peristaltic pump (Ismatec) and Tygon

LMT-55 tubing (IDEX) for 10 minutes before fixation with 4% PFA (Electronic Microscopy Sciences) and stainings (see below).

For endothelial remodeling experiments *in vitro*, two μ-slides I$^{0.4}$ Luer (IBIDI) coated with fibronectin from bovine plasma at 10μg/ml (Sigma F-1141) were used in parallel for each experiment. After seeding the HUVEC cells, one channel was cultured under a flow of 400μm/sec using REGLO pump and Tygon tubbing and for the other channel (no flow condition), medium was changed twice a day. At confluence, D2A1 LifeAct-RFP cells were added at a concentration of 200 000 cells/ml for 10 min. Then, tumor cells were washed using fresh medium and incubated for 16h with or without flow. Z position of the tumor cells relative to the HUVEC monolayer was determined using the piezzo stage of the confocal microscope.

Optical tweezers

Optical tweezing experiments were performed as previously described[31]. Briefly, OT behaves as a picodynanometer where stiffness and the displacement from the steady position can be computed to extract the applied force. Optical tweezing experiments *in vitro* were performed in single channel I$^{0.4}$ Luer μ-slides pre-coated with fibronectin (IBIDI). HUVEC cells were cultured until confluence before the experiment as described above. D2A1 were perfused at 10^4 cells/ml at a low speed to maximize the cell trapping and avoid collision effects by other CTC. A 1064 nm laser (Navigator 1064-7Y Spectra Physics) was used to generate optical tweezers mounted on a thermostated inverted microscope equipped with a UPLFLN-P 100X/1.3 objective (Olympus). D2A1 cells attached to the HUVEC monolayer were trapped in the beam and moved away from the HUVEC monolayer by displacing a computer-controlled piezzo stage (PI P545 PNano) along the X/Y axis. The fluctuations of the cell in the trap were recorded on a quadrant diode (Thorlabs PDQ30C) and the associated spectral power density allowed the calibration of the trap stiffness. The detachment of D2A1 cells from the HUVEC monolayer was recorded using a Cmos camera (Thorlabs DCC3240C). The movies were analyzed to access the center of mass of the cell in each image. This position compared to the steady position of the cell in the trap is proportional to the force exerted on the cellular adhesion. The rupture force between D2A1 and HUVEC gave rise to a drop in the position of the trapped cell steady state and allowed to access the rupture force.

Optical tweezing experiments in the zebrafish embryo were performed as previously described[31], with slight modifications: We implemented the setup with a thermoregulated chamber ensuring the embryos to remain at 28°C. We acquired the displacement with the camera at high frame rates 200fps after having established the power spectrum from the photodiode at 20kHz resolution to calibrate the setup.

Mice experiments and surgical procedures

8-10 weeks old female Nu/Nu mice (Charles River, Sulzfeld, Germany) were used to study the extravasation cascade. All efforts were made to minimize animal suffering and to reduce the number of animals used. The operation of the chronic cranial window was done as previously described[7,65]. Three weeks after window implantation a 100µl cell suspension, containing 500,000 tumor cells (JIMT1br3, A2058br, PC14PE6br, H1), was injected intracardially. *In vivo* imaging was done on day 3 and day 7 after the heart injection. After imaging, the mouse was perfusion-fixed through intracardiac injection with 2.5% glutaraldehyde (Electron Microscopy Sciences, Hatfield, PA) and 2% formaldehyde (Electron Microscopy Sciences) in 0.1 M PHEM buffer (comprising 60 mM PIPES, 25 mM HEPES, 10 mM EGTA and 2 mM MgCl, pH adjusted to 6.9). Following fixation, the regions of interest (ROIs) were imaged again based on the stored stage *x,y*-coordinates. NIRB was performed with the same laser that had been used for *in vivo* microscopy, tuned to 800 nm wavelength, as previously described[29]. Above the ROIs, at the level of the brain surface, a 150×150 µm^2 area was scanned in a single focal plane until the NIRB square became clearly visible through emission of autofluorescence in the green channel. Around the ROI, three bigger 300×300 µm^2 NIRB squares were drawn in non-symmetric positions to facilitate orientation and retrieval of the ROI upon dissection. The brain was removed from the skull and post-fixed by immersion in the same fixative at 4°C overnight. The following day, the fixative was replaced with 0.1 M PHEM buffer, and the brain was stored at 4°C until further processing[29]. All animal procedures were performed in accordance with the institutional laboratory animal research guidelines after approval of the Regierungspräsidium Karlsruhe, Germany (governmental authority).

***In vivo* multiphoton laser scanning microscopy (MPLSM).**

In vivo imaging was performed with a Zeiss 7MP microscope (Carl Zeiss Microscopy, Jena, Germany) provided with a Coherent Chameleon UltraII laser (Coherent,

Glasgow, UK) with a 500-550 nm and a 575-610 nm band pass filter. With the wavelength of 850 nm GFP and TRITC-dextran were detected. To prevent phototoxic effects, laser power was always kept as low as possible. During the imaging process animals were anaesthetized with a low gas narcosis including 1.5% isoflurane (Baxter, Unterschleißheim, Germany) and 98.5% oxygen (Guttroff, Heidelberg, Germany). During imaging body temperature was kept constantly at 37°C by a heating pad. To acquire angiographies of brain blood vessel, 0.1 ml TRITC-dextran (500 kDa, 10 mg.ml^{-1}, Sigma-Aldrich, Munich, Germany) was injected.

Blood flow velocity measurements and visualization of MPLSM data.

The blood flow velocity was measured by a line scan with a minimum length of 10 µm, detecting 2000 events in microvessels. At least 16 randomly chosen vessels were measured per animal. The resulting scan identifies single erythrocytes as angular black lines, where the x-axis is according to the length of the detected distance and the y-axis is the elapsed time of the measurement. The angle is converging more and more to 90° when the cells are static. By knowing the resolution of both parameters and by the measurement of the slope of 30 randomly chosen red blood cells a calculation of the mean velocity is possible, by inversion of the result.

Western blotting

For western blotting analysis, extracts corresponding to similar cell numbers were loaded on 4-20% polyacrylamide gels (Biorad) and run under denaturing conditions. The following primary antibodies were used: ITGB1 (Millipore AB1952; rabbit), GAPDH (V-18; Goat). HRP-conjugated secondary antibodies were used with ECL (GE Healthcare) for reading using using a PXi system (Syngene). Intensities were normalized over cellular GAPDH levels.

Immunofluorescent staining in the microfluidic channels

Cells were fixed using 4% PFA (Electronic Microscopy Sciences), permeabilized with 0.2% Triton-X100 (Sigma) and quenched with 2mg/ml NaBH$_4$ (Sigma) 10 min at room temperature before using the following primary antibodies: rat anti-mouse CD29 (9EG7, BD), mouse anti-human CD31 monoclonal primary antibody (MEM-5, Invitrogen). Following secondary antibodies were used: goat anti-rat or mouse

coupled with Alexa Fluor 488 (Invitrogen). Cells were mounted using Vectashield (Vector Laboratories). For fluorescent labelling of the HUVEC cells (Fig.1), Alexa Fluor 568 Phalloidin (Life-technologies) and DAPI (Sigma) were used.

In vitro migration and adhesion assays

For wound healing assay, cells were cultured until confluence in 6-wells plate. The monolayer was scratched with a 20 µl tips and medium was changed with medium supplemented with the corresponding pharmacological treatments. Pictures were taken at time = 0h, 3h, 6h, 9h and 24h. Wound closure was analyze using ImageJ.

For adhesion assay, cells were plated at 20 000 cells/ml in 96-well plate filled with culture medium supplemented with the corresponding pharmacological treatments. After 30 min incubation, wells were washed with PBS, fixed in 4% PFA and stain with 1% violet crystal (VC, Sigma) for 1h at room temperature. VC was washed with PBS and pure DMSO was added to solubilized VC for 30 min under gentle moving. Optical density at 590nm was measured using TriStar^2 plate reader (Berthold).

Statistical analysis from zebrafish, mouse and microfluidic experiments.

Statistical analysis of the results was performed using the GraphPad Prism program version 5.04. The Shapiro-Wilk normality test was used to confirm the normality of the data. The statistical difference of Gaussian data sets was analyzed using the Student unpaired two-tailed t test, with Welch's correction in case of unequal variances. For data not following a Gaussian distribution, Kruskal-Wallis and Dunn's multiple comparisons post-test or the Mann-Whitney test was used. For qualitative data, the Fisher test was used. Illustrations of these statistical analyses are displayed as the mean +/- standard deviation (SD). p-values smaller than 0.05 were considered as significant. *, $p<0.05$, **, $p < 0.01$, ***, $p < 0.001$, ****, $p < 0.0001$.

Mathematical modeling and numerical methods for *in silico* experiments

The *in silico* experiments are developed in the framework of Finite Element Embedded Library in C++, Feel++[66]. To reproduce the blood flow in the ZF arterial and venous systems, we followed these steps: *(i)* build manually using a computer aided design software and generate a discrete computational domain where the entry point is ISV8 (Figure S2C), *(ii)* set up a fluid-structure interaction model between the blood and the endothelium in Feel++ and *(iii)* extract numerical flow rates and

compare with in-vivo experiments. *(i)* The computational domain could not be obtained directly from the *in vivo* measurements. We built the model using a computer aided design software and reproduced an idealized geometry. The discrete computational domain is built of 884221 tetrahedrons. The computational domain is in millimeters and the units of the physical quantities used hereafter are accordingly adapted. *(ii)* In order to simulate the blood flow in the system, we have to consider the interaction between the blood and the endothelium. The blood flow is modeled using the incompressible Navier-Stokes equations and the endothelium is modeled using the linear elasticity model formulated in displacement/pressure due to the quasi-incompressible nature of the endothelium, both models are supplemented by boundary conditions. Regarding the blood flow: *(i)* a Poiseuille flow in the aorta at ISV8 giving by a fit of the experimental data *(ii)* free outflow boundary conditions at the outlet of the venous system. Regarding the endothelium: *(i)* clamped at the inlet of the aorta (ISV8), *(ii)* free-stress at the outlets of the venous system and *(iii)* Robin type condition elsewhere to constrain the endothelium by the surrounding tissues (the elastance coefficient is taken as constant). Finally, the model is completed by coupling conditions at the interface between the fluid and the structure stating the continuity of the velocity and the normal stress. The coupling between both is handled using a so-called Robin-Robin scheme[67]. Finally, we use the following setting for the physical parameters: For the blood: Viscosity, f = 2.2e-6 kg.mm^{-1}.s^{-1}; Density, f = 1.0e-6 kg/mm^3. For the endothelium: Density, s = 1.2e-6 kg/mm^3; Young Modulus, E = 3 kg/(mm*s^2); Poisson Coefficient = 0.49 (dimensionless). *(iii)* Regarding the space discretization, we use the finite element method to discretize the model described above. We use continuous piecewise polynomials of order 2 for the velocity and order 1 for the pressure in the fluid and we use continuous piecewise polynomials of order 1 for the displacement and order 1 for the pressure in the solid. Regarding the time discretization, we use for the fluid an BDF2 scheme and for the solid we use the Newmark scheme, both are second order in time. The time step is fixed to 5e-3s and the final time is at 4s. The algebraic representation of the fluid and solid model are solved using iterative methods preconditioned with algebraic-factorization type preconditioners enabling fast solves. The fluid-structure interaction coupling is handled with a Picard method that iterates between the fluid and the solid models until the relative increment between two non-linear iterations reaches 1e-5.   We conducted the study for the different

pharmacological treatment (IBMX, EtOH, Lidocain, DMSO). Each condition requires high performance computing to solve the equation set. We used 48 cores to solve each configuration to simulate 4s of blood flow. The later ensures that the flow is correctly established.

Patient blood collection for CTC size analysis

Patient blood samples were acquired in accordance to the World Medical Association Declaration of Helsinki and the guidelines for experimentation with humans by the Chambers of Physicians of the State of Hamburg ("Hamburger Ärztekammer"). All patients gave informed, written consent prior to blood draw. Samples were collected from 5 metastatic breast cancer patients into standard 7.5 ml ethylenediaminetetraacetic acid (EDTA) vacutainers and transferred to TransFix® (Cytomark) tubes within 2 h of sample draw. Blood was also collected from a metastatic non-small lung cancer patient directly into either CellSave® (Menarini-Silicon Biosystems), Cell-free DNA BCT® (Streck) or TransFix® preservatives for further analysis. Circulating tumor cells were isolated from whole blood sample by two size based enrichment systems: Both methods have been validated within a large European consortium of 36 partners from academia and industry, CANCER-ID (www.cancer-id.eu). The Parsortix™ system (ANGLE plc, UK) enriches tumor cells from a wide variety of blood tubes and has been described in detail in previous publications[68,69]. In short, the device passes blood into a disposable cassette. This cassette narrows down to a critical gap of 6.5 µm at which all larger cells are retained while smaller cells pass through into the waste, thus drastically reducing white blood cell and erythrocyte background. Due to their larger size and higher rigidity, tumor cells are retained at the gap and can be extracted by reversing the flow within the chamber. The enriched cell fraction is harvested into a cytospin funnel and spun down (190 x g, 5 min). Upon drying overnight, samples can either be frozen at -80 °C or directly stained by immunocytochemistry (ICC). The second size based enrichment system used to process cancer patient samples, was a novel microfluidic filtration device provided by Siemens Healthcare Diagnostics (Elkhart, IN, USA). The system uses a Hamilton STARlet™ robot (Hamilton Company, Reno Nevada) with a specifically developed software allowing for automated enrichment and staining of CTCs from whole blood[70]. Briefly, the blood is passed through a membrane containing pores of 8 µm, enriching for all larger cells. For this, EDTA blood samples

were transferred into TransFix® preservation tubes and incubated overnight. The blood was then transferred to the device together with all reagents necessary for ICC staining of CTCs. Cytospins generated following Parsortix™ enrichment were stained using fluorescently labeled antibodies. ICC included fixation with 4 % PFA, permeabilization with 0.1 % Triton X-100 and blocking using serum albumin. Two pan-Keratin antibodies (clone AE1/AE3, eBioScience and clone C11, Cell Signaling) were combined with a CD45 targeting antibody (REA747, Miltenyi Biotec) and DAPI for cell detection. Cytospins were cover slipped using ProLong® Gold antifade reagent (Invitrogen). For the filtration device, we performed a single ICC staining step using a cocktail of fluorescently labeled antibodies, followed by cover slipping with ProLong® Gold antifade reagent (Invitrogen). Tumor cells were detected by targeting Dy550 labelled keratins (Pan CK – clone AE1/AE3, CK8/18 – clone UCD / PR10.11, CK19 – clone A53-B/A2), multiple Dy650 labelled white blood cell markers (CD45 – clone 9.4, CD66b – clone G10F5) and DAPI, all provided directly by Siemens Healthcare Diagnostics. Cytospins and filtration membranes were evaluated and enumerated manually by fluorescence microscopy. CTCs were classified as pan-keratin positive, CD45 negative and DAPI positive cells. They were photographed using the AxioVision LE64 microscope software (Zeiss) which allows for measurement of lengths with its respective processing tools.

Brain metastasis and blood flow perfusion study

Human patient data showing the link between brain metastasis (BM) and perfusion pattern were obtained on a single-center cohort. The retrospective study was conducted in compliance with the local ethics committee (Ethik-Kommission der Ärztekammer Hamburg, WF-018/15) with a waiver of informed consent. To collect cases, all MRI studies from 01/2014 to 12/2016 were screened for the presence of untreated malignant intra-axial brain tumors (no previous brain surgery or radiation). In total, 407 patients met the inclusion criteria. From the entire cohort, we randomly selected 100 patients (37 women and 63 men).

MRI was performed using a 1.5 Tesla (Magnetom® Sonata, Siemens Healthcare, Erlangen, Germany; Magnetom® Symphony, Siemens Healthcare, Erlangen, Germany, and Magnetom® Avanto, Siemens Healthcare, Erlangen, Germany) in 94 patients or a 3 Tesla scanner (Magnetom® Skyra, Siemens Healthcare, Erlangen, Germany; Ingenia, Philips Medical Systems, Best, The Netherlands) in 6 patients.

Imaging protocol always included axial T1w spin echo with flow compensation and/or three-dimensional T1w gradient echo sequences following weight-adjusted Gadolinium injection (T1w+). If both sequences were acquired the latter one was used for further analysis. Sequence parameters (repetition time, echo time, inversion time, field of view, matrix, pixel size, slice thickness, interslice gap, and number of slices) varied among the different scanners. All BM were subsequently segmented semi-manually using the Analyze Software System 11.0 (Biomedical Imaging Resource, Mayo Clinic, Rochester, MN, USA)[71]. Axial T1w+ MR images of all patients were then automatically co-registered to the Montréal Neurological Institute (MNI) brain by using the FMRIB Software Library (Analysis Group, Oxford, UK) linear registration tool. Correct registration of all T1w+ images and the segmented BM to the MNI brain was secured by visual inspection. Cluster maps comprising all BM of the respective cohort were calculated (Figure 8). Computed tomography was used to build the brain perfusion atlas. Since cancer patients often show an altered cerebral blood flow due to paraneoplastic changes or chemotherapy administration, we decided to use computed tomography (CT) perfusion data from a healthy cohort as reference[72,73]. In brief, 107 patients were triaged by CT perfusion for symptoms of transient ischemic attack but without evidence of ischemia or any perfusion abnormality, infarction or symptoms on follow up, or vascular abnormality as reported elsewhere[74]. Quantitative perfusion maps were obtained for CBF and MTT[75]. All perfusion raw data were processed in a central core-lab on a workstation dedicated for perfusion analysis (Syngo mmwp VE52A with VPCT-Neuro; Siemens Healthcare, Forchheim, Germany) with motion correction and low band temporal noise removal. Non-parenchymal voxels corresponding to bone, vasculature, calcification and cerebrospinal fluid were automatically excluded by adaptive intensity thresholding. Perfusion parameter maps were calculated based on a deconvolution model by least mean squares fitting. All perfusion maps were then affine registered to 1 mm MNI standard space by a precise registration model between the baseline time average of each CT perfusion dataset and a custom CT template in standard space using the FMRIB Software Library 5.0[76]. Mean voxel-wise perfusion parameter maps normalized to standard space were then registered to each individual patient in our study cohort to obtain voxel specific normal perfusion values. Absolute mean cerebral blood flow (CBF in ml/100g brain tissue/min) and mean transit time (MTT in sec) values of all BM were calculated for each voxel of the perfusion mask and each

voxel with a BM. Statistical analysis was conducted using IBM SPSS Statistics®
software (IBM® 2011, version 20, Armonk, New York, USA) and R (The R
Foundation, version 3.3.1. Vienna, Austria). The differences in CBF and MTT
between all BM and BM- voxels were compared by the independent t-test. Voxels
with more than one BM were weighted according to the number of BM occurring
within the voxel. The paired samples t-test was used to compare the perfusion values
and the volume of the BM. If not otherwise indicated, data are given as median ±
interquartile range.

Figure 1_Follain et al.

A CTC diameter (μm) plot — Breast (#1 n=2, #2 n=12, #3 n=1, #4 n=53, #5 n=10), Lung (n=7), D2A1 (n=90). D2A1 (Tumor cells), 10 μm. Human CTCs: Pan-Keratin, CD45, DAPI, 50 μm, 10 μm.

B Vessel diameter all along the plexus. Diameter measurements using orthoslices. DA, AVJ, CV. Tumor cells (CTCs). ISV number from AVJ.

C 2dpf, 15mpi, 3hpi, 24 hpi. CTCs Injection, CTCs Arrest, CTCs Adhesion, CTCs Extravasation. siITGβ1 Tumor cells (2.10³). D2A1 cells: β1-integrin, GAPDH, CTL #1 #2 siRNA (72h). ITGB1 expression (WB): CTL, #1, #2 siRNA (72h). siCTL, siITGB1#1,2, ITGB1.

D Cell density 20–0. siCTL, siITGB1 #1, siITGB1 #2.

E Norm. ratio of arrested cells: siCTL, siITGB1 #1, siITGB1 #2. DA, AVJ, CV.

F Norm. number of adhesion events: siCTL, siITGB1 #1, siITGB1 #2.

G 2dpf, 15mpi, 3hpi, 24 hpi. CTCs Injection, CTCs Arrest, CTCs Adhesion, CTCs Extravasation. Tumor cells (2.10³). CLEM 15mpi. Tumor cells / Vessel lumen, Tumor cells / Endothelium, 1 μm, 20 μm, 2 μm. Tomogram - 3D reconstruction: Endothelial cell and nucleus, Tumor cell and nucleus.

H Tumor cells. Optical tweezing of Arrested CTC. Arrested TC, Circulating RBCs. Non-detachable adherent tumor cells (n=37): 1 2 3 4 5.

Figure 2_Follain et al.

Figure 3_Follain et al.

Figure 4_Follain et al.

A

Tg (Fli1a:egfp) Tumor cells   Lidocain

24 hpi

25 µm

Intravascular

Tumor cells Vasculature

DA

CV

B

Extravascular   Intravascular

Vehicle (n=20)

Cell density   Cell density
0   25   0   5

Lidocain (n=20)

Normalized ratio of extravasated cells

****

Veh.   Lidocain

C

Tg (Fli1a:egfp) Tumor cells   IBMX

24 hpi

25 µm

Extravascular

Tumor cells Vasculature

DA

CV

D

Extravascular   Intravascular

Vehicle (n=24)

Cell density   Cell density
0   25   0   5

IBMX (n=23)

Normalized ratio of extravasated cells

**

Veh.   IBMX

E

2dpf   5mpi   3hpi   24 hpi
CTCs Injection   CTCs Arrest   CTCs Adhesion   CTCs Extravasation

Tumor cells (2.10³)

CLEM

Embedded sample

Grid x
Grid x+1
Grid x+2

Vehicle, 24 hpi

Tg (Fli1a:egfp) Tumor cells

25 µm

Intravascular   Extravascular

Lidocain, 24 hpi

*Figure 5*_Follain et al.*

A

Time lapse

2dpf 5mpi 3hpi 24 hpi

CTCs Injection
CTCs Arrest
CTCs Adhesion
CTCs Extravasation

Tumor cells

B

20 μm

Tumor cells
Endothelium

C

t=0min t=100min t=200min
t=300min t=400min t=500min
t=600min t=700min t=800min

10 μm

D

t=0min t=80min t=150min

Pocketing Split Reperfusion

Flow

Time-lapse analysis of C

t=0min
Arrested cluster of tumor cells

t=100min
Endothelial cells split above the tumor cells

t=200min
Cells start moving to the bottom space

t=300min
Endothelial cells migrate to the inside of the lumen

t=500min
Cells trapped in an endothelial pocket

t=800min
Majority of the cluster extravasated

E

2dpf 5mpi 3hpi 9hpi

CTCs Injection
CTCs Arrest
CTCs Adhesion
Extravasating CTCs

CLEM (F-H)

Tumor cells

Quantification (I-K)

Tumor cells
Endothelium

25 μm

3D EM

Endothelium

Tumor cells

F

DA

x
y
H

2 μm

G

DA

3D TEM

x
y
z

Tumor cells
Endothelium

H

E. Tomography

I

Tumor cell / Endothelium   Tumor cell   Endothelium

Intra.

Pocketing   Early
Late

Extra.

10 μm

J

Vehicle

0hpi 3hpi 9hpi 24 hpi
Intravascular
Pocketing
Extravascular

Extravascular
Pocketing
Intravascular

Normalized Reaction Progress
Time (hpi)

K

Lidocain

0hpi 3hpi 9hpi 24 hpi
Intravascular
Pocketing
Extravascular

Intravascular
Pocketing
Extravascular

Normalized Reaction Progress
Time (hpi)

L

0 μm.s⁻¹ / 16 h

400 μm.s⁻¹ / 16 h

5 μm

0 μm.s⁻¹

Tumor cells
HUVEC (PECAM)

10 μm

0 Height (μm) 18,5

400 μm.s⁻¹

Tumor cells
HUVEC (PECAM)

0 Height (μm) 18,5

M

400 μm.s⁻¹
0 μm.s⁻¹

Transmigrated cells ratio

****

Trans. + remodeling ratio

Figure 6_Follain et al.

A

CTCs → 2PM → 7 dpi → Micrometastasis / Blood vessels

Micrometastasis / *Blood vessels*

Jimt1

100 μm / 20 μm

B

Blood vessels * Velocity measurements (line scanning)

100 μm

blood flow velocity (μm/s)

***

628±46   5880±716

Extravasation
No extravasation

C

CTCs → 2PM → 3 dpi

Arrested tumor cell / Blood vessels

Blood vessels / Tumor cell

ssTEM(E) / ssTEM(D)

CLEM

IVM+mCT / IVM+mCT

#1 #2 #3 TC

D

Tumor cell *Nucleus*
Endothelial cells

Lumen

2 μm

E

#2 #1 #3 TC

TEM

#1

Lumen

Endothelial cells

2 μm

#2 #3

*Figure 7*_Follain et al.

A Human Brain Metastasis
(Supratentorial area)

Primary tumor type
(number of patients)
- Lung (51)
- Skin (17)
- Breast (10)
- GU (10)
- Unknown (6)
- GI (4)
- Sarcoma (2)

100 patients, 580 metastases

B Brain metastasis Heatmap

100 patients, 580 metastases

z

Side view   Top view

C

z

BM mask

CBF

High

Low

D

Brain Metastasis

−   +

p<0.001

CBF (ml/100g/min)

120

100

80

60

40

20

0

Brain Metastasis

−   +

p<0.001

MTT (seconds)

6.0

5.5

5.0

4.5

4.0

3.5

3.0

E

400-600 μm/sec

Blood flow/perfusion

HIGH   LOW

>1000 μm/sec   <100 μm/sec

❶ ARREST & ADHESION

Inhibitory hemodynamics   *Arrest of CTCs by permissive flow velocity*

Flow

Circulating Tumor Cell   *Endothelial cells*

Flow-activated endothelial remodeling

❷ EXTRAVASATION

Extravasated   *Pocketing*   *Intravascular*

Flow

Metastatic outgrowth

Figure 8_ Follain et al.

A

2dpf · 15mpi · 3hpi · **24 hpi**

CTCs Injection
CTCs Arrest
CTCs Adhesion
CTCs Extravasation

Imaging

Tumor cells (2.10³)

B

50 µm

20 µm

10 µm

C

10 µm

OUT

Hemodynamics of extravasation site

Red Blood Cell

- #1
- #2
- #3
- #4
- #5
- #6
- #7

Velocity (µm/s) vs Time (ms)

Supplemental Figure 1_Follain et al.

A Tg(fli1a:egfp)
50 µm
Confocal imaging

B 3D Reconstruction

C CAO model
ISV8　ISV4　ISV1　Junction
CV

D 3D Flow simulation
Velocity (µm/sec)
0　1400

E

ISV8 — Velocity (µm/sec) vs Time (sec)

ISV4 — Velocity (µm/sec) vs Time (sec)

ISV1 — Velocity (µm/sec) vs Time (sec)

Junction — Velocity (µm/sec) vs Time (sec)

CV — Velocity (µm/sec) vs Time (sec)

F Velocity (µm/sec)
Minimum
Mean
Maximum
ISV8　ISV4　ISV1　Junction　CV

Supplemental Figure 2_Follain *et al.*

A

Optical trapping

1 Optical trapping
2 Imposed contact until active adhesion
3 Detachment and adhesion force measurment

Tumor cells

Endothelial monolayer

Microfluidic channel

Force (pN)

Optical tweezers

| 0 sec | 0.52 sec | 0.91 sec | 1.14 sec |

5 µm

F

| Adhesion rupture 1.31 sec | Recoil 1.48 sec | Recoil 1.65 sec | Equilibrium 1.82 sec |

F

B

1 - Trapping to impose contact **2 - Trapping to detach adherent cells**

Optical trapping of circulating cells

Imposed contact with endothelium

Try to break the adhesion by moving the OT

Trap adherent cells

Perfusion of siRNA transfected cells

siCTL
silTGB1 #1
silTGB1 #2

Tumor cells

Endothelial monolayer

Microfluidic channel

5 minutes post-adhesion

n = 15   n = 23   n = 14

% of adhesion
n = 12   n = 13   n = 15

siCTL   silTGB1 #1 **   silTGB1 #2 *
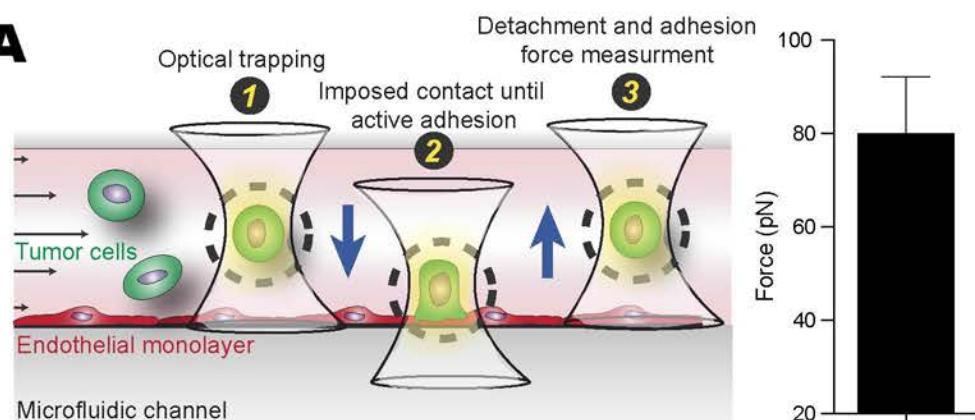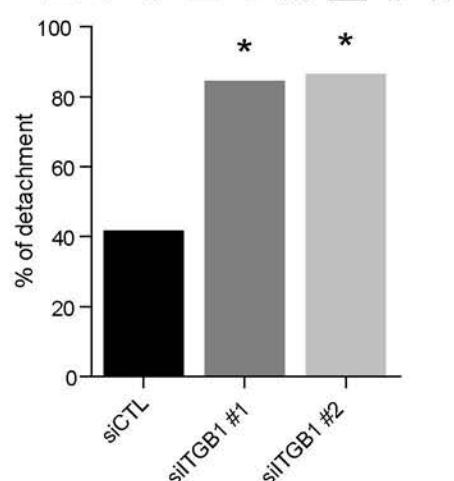
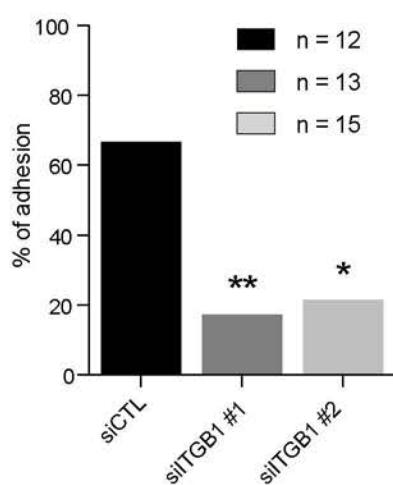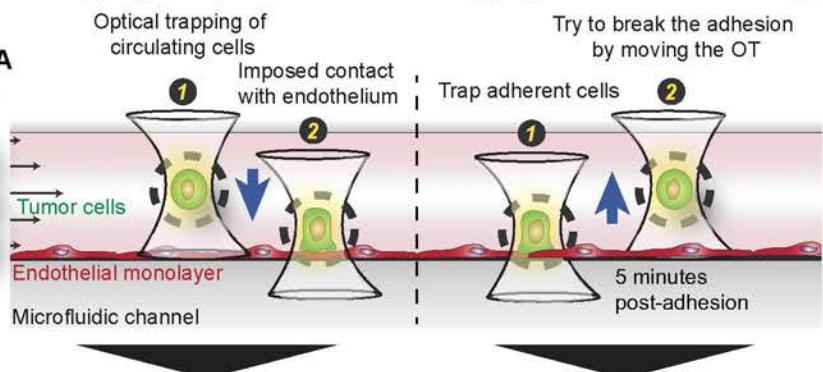% of detachment

siCTL   silTGB1 #1 *   silTGB1 #2 *

Supplemental Figure 3_Follain et al.

Supplemental Figure 4_Follain et al.

A CAO model

ISV8 ISV4 ISV1 Junction

Late CV Early CV

B

Veh. lidocain — Time: 0.065 sec

Lidocain — Time: 0.065 sec

0 — Velocity (µm/sec) — 1400

C

ISV 8 / ISV 4 / ISV 1 — Vehicle / Lidocain

Junction / Early CV / Late CV

Velocity (µm/sec) vs Time (sec)

D

Veh. IBMX — Time: 0.065 sec

IBMX — Time: 0.065 sec

0 — Velocity (µm/sec) — 1400

E

ISV 8 / ISV 4 / ISV 1 — Vehicle / IBMX

Junction / Early CV / Late CV

Velocity (µm/sec) vs Time (sec)

Supplemental Figure 5_Follain et al.

A

IBMX

Dorsal aorta
Caudal veins

Veh. IBMX

Lidocain

Veh. lidocain

B

n=2-3 plexus/condition
- Veh. IBMX
- IBMX
- Veh. lidocain
- Lidocain

Vasculare surface (pxl)

DA   CV

C

n=2-3 plexus/
condition

Number of loops

D

2dpf   3hpi

Dextran
Injection   Imaging

Dextran 500kDa

In
Out

Endothelium
Dextran 500kDa

Veh. IBMX

IBMX

Veh. Lidocain

Lidocain

50 μm

E

	0h	9h	24h
Veh. IBMX			
IBMX			
Veh. Lidocain			
Lidocain			

150 μm

F

Area covered by cells (%)

ns   ns   ns   ns

- DMEM
- DMSO
- IBMX
- EtOH
- Lidocain

Time (h)

G

Crystal violet
staining

DO (590nm)

Veh. IBMX   IBMX   Veh. Lidocain   Lidocain

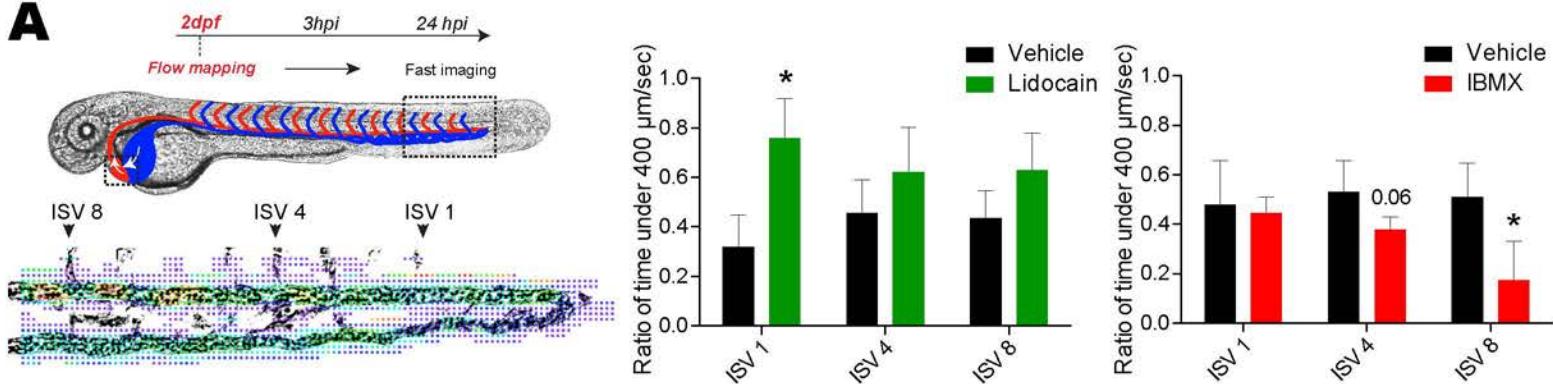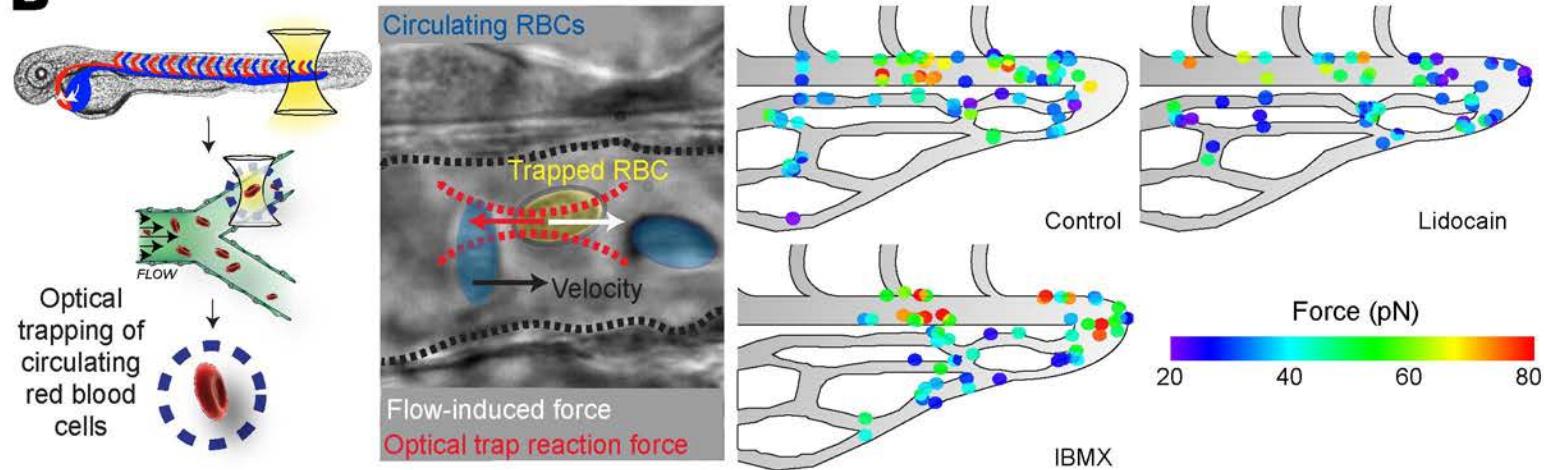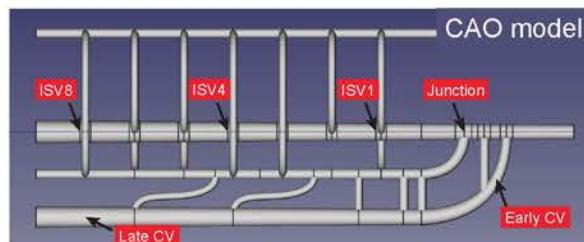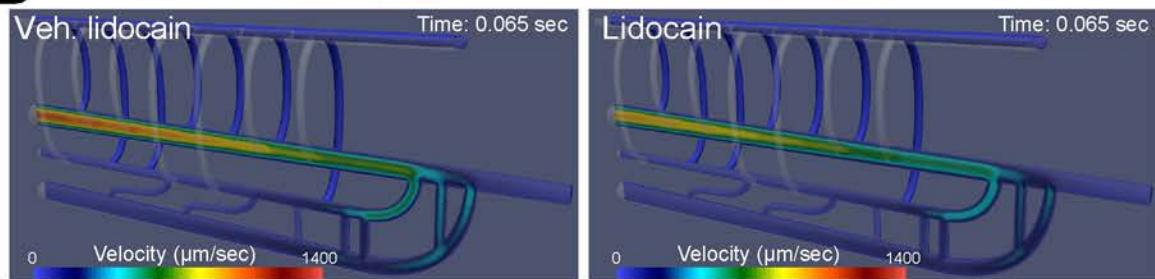*Supplemental Figure 6_Follain et al.*
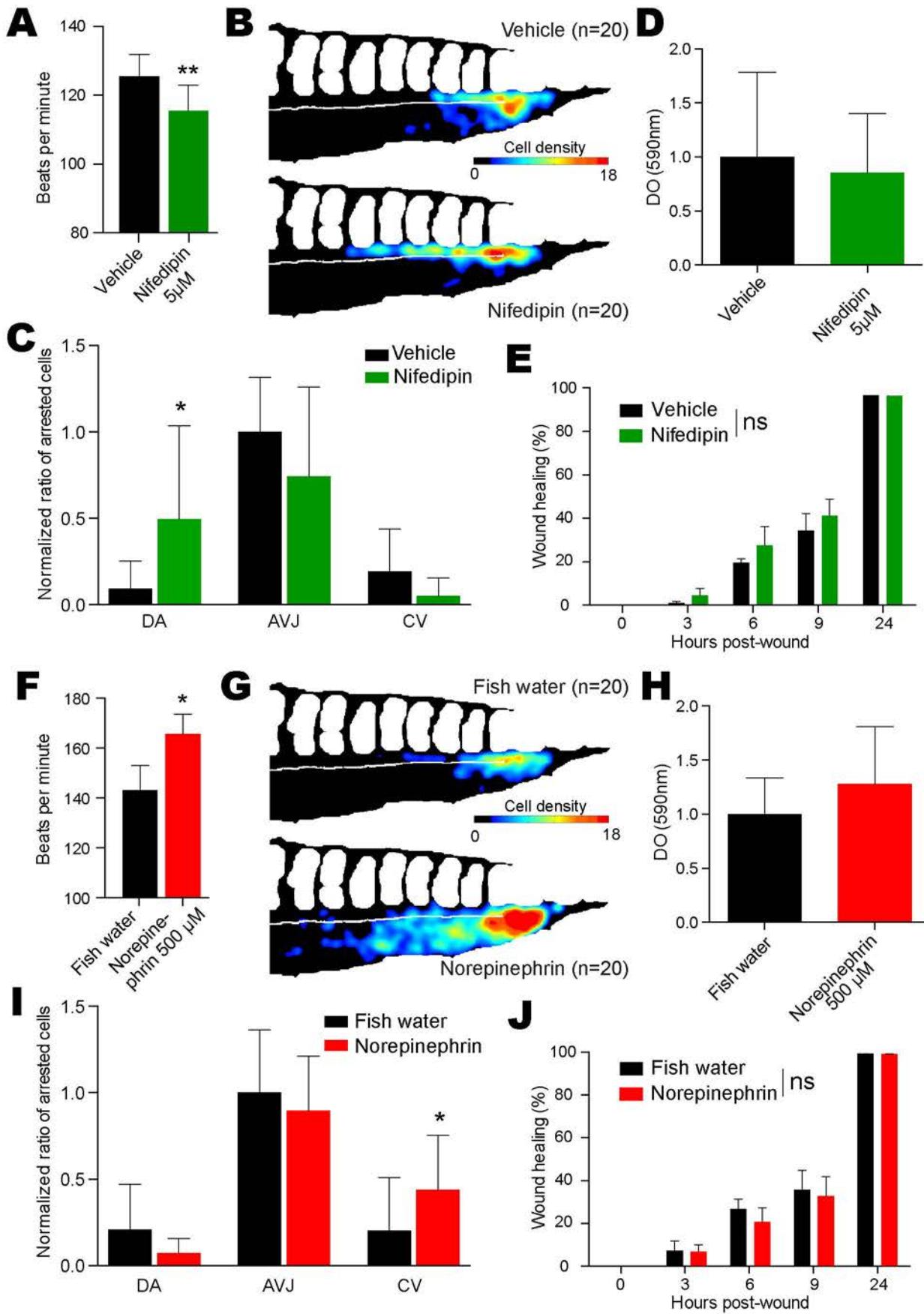
Supplemental Figure 7_Follain et al.

5 Annexe n°3 : Création d'outils « Do it yourself » pour le laboratoire

5.1 L'ascenseur à formvar

Pour éviter que les coupes ultrafines générées par ultramicrotomie passent à travers le maillage des grilles de microscopie électronique il faut au préalable les recouvrir d'une fine pellicule de Formvar. Le Formvar est une résine thermoplastique polymère de polyvinyle.

La méthode entièrement manuelle utilisée au laboratoire consiste à tremper une lame de microscopie dans la solution de formvar, de la laissé sécher puis de tremper la lame dans l'eau pour que le formvar se détache de la lame et flotte à la surface de l'eau. Le formvar est ensuite collecté sur un support, appelé domino, comportant de nombreux trous de la taille d'une grille de microscopie électronique. Les grilles sont ensuite déposées sur la couche de formvar aux niveaux des emplacements prévu sur le domino.

L'étape la plus critique pour obtenir un formvar d'épaisseur régulière est l'immersion et le retrait de la lame de microscopie dans la solution de formvar. Cette étape étant faite manuellement, il est impossible d'obtenir une couche de formvar uniforme et de qualité homogène sur l'ensemble des grilles.

Pour gagner en qualité et aussi du temps, j'ai décidé de remplacer cette étape manuelle par une machine basée sur un microcontrôleur Arduino, un moteur pas à pas et des pièces imprimées en 3D.

Cette machine appelée l'ascenseur à formvar (Figure 44) permet de retirer la lame du formvar à une vitesse prédéfinie par un potentiomètre. Les couches de formvar obtenues sont maintenant reproductibles et constante en épaisseur.

Les cartes Arduino sont des microcontroleurs qui existent depuis une dizaine d'année. Ces cartes exécutent ligne par ligne le code qu'on leur fourni.

Pour la réalisation de cet appareil j'ai eu recours :

- Arduino nano
- Pilote de moteur pas à pas « EasyDriver »
- Un moteur pas à pas (Nema 17)
- Une visse sans fin
- Pièces imprimées en 3D

Code :

// Code permettant la montée et la descente de l'ascenceseur à formvar en prenant en compte la vitesse de déplacement fourni par le potentiomètre

// Code inspiré de http://www.schmalzhaus.com/EasyDriver/EasyDriverExamples.html

```
#include <AccelStepper.h>

// Define the stepper and the pins it will use
AccelStepper stepper1(AccelStepper::DRIVER, 9, 8);

// Define our three input button pins
#define  LEFT_PIN  4
// #define  STOP_PIN  3
#define  RIGHT_PIN 3

// Define our analog pot input pin
#define  SPEED_PIN 0

// Define our maximum and minimum speed in steps per second (scale pot to these)
#define  MAX_SPEED 10000
#define  MIN_SPEED 0.5

void setup() {
  // The only AccelStepper value we have to set here is the max speeed, which is higher than we'll ever go
  stepper1.setMaxSpeed(10000.0);

  pinMode(LEFT_PIN, INPUT_PULLUP);
  pinMode(RIGHT_PIN, INPUT_PULLUP);
}

void loop() {
  static float current_speed = 0.0;      // Holds current motor speed in steps/second
  static int analog_read_counter = 1000;   // Counts down to 0 to fire analog read
  static char sign = 0;               // Holds -1, 1 or 0 to turn the motor on/off and control direction
  static int analog_value = 0;         // Holds raw analog value.

if (digitalRead(LEFT_PIN) == LOW) {
    sign = 1;
  }

 else if (digitalRead(RIGHT_PIN) == LOW) {
    sign = -1;
  }

  else  { sign = 0;}

  // We only want to read the pot every so often (because it takes a long time we don't
  // want to do it every time through the main loop).
  if (analog_read_counter > 0) {
```

```
  analog_read_counter--;
}
else {
  analog_read_counter = 3000;
  // Now read the pot (from 0 to 1023)
  analog_value = analogRead(SPEED_PIN);
  // Give the stepper a chance to step if it needs to
  stepper1.runSpeed();
  //  And scale the pot's value from min to max speeds
  current_speed = sign * ((analog_value/1023.0) * (MAX_SPEED - MIN_SPEED)) + MIN_SPEED;
  // Update the stepper to run at this new speed
  stepper1.setSpeed(current_speed);
}

// This will run the stepper at a constant speed
stepper1.runSpeed();
```
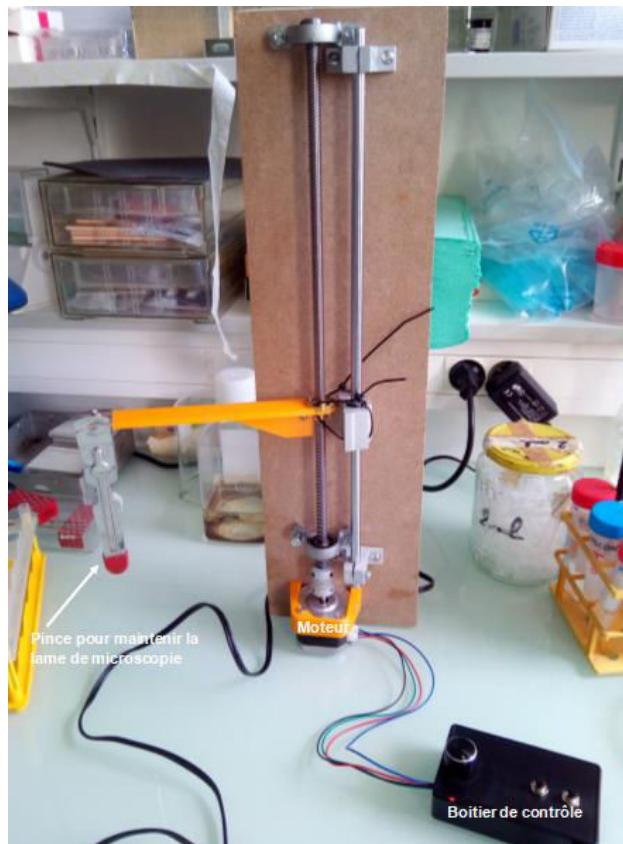

Figure 44 : ***L'ascenseur à formvar***

Un autre outil développé au laboratoire était un thermomètre connecté à internet nous permettant de suivre sur internet la température de deux aquariums. Ce thermomètre faisait aussi appel à une carte arduino couplée à un module ethernet ainsi que deux sondes de températures.

Ce type de microcontrôleur fait de plus en plus son apparition dans le monde de la recherche. Un article y a été même consacré dans la revue Nature (The DIY electronics transforming research, 2017). Des groupes se sont aussi créé notamment au CNRS proposant des ateliers de formation plusieurs fois dans l'année mais aussi lors de conférence comme MiFoBio.

De nombreux projets ont recours à ce type de carte pour par exemple synchroniser la respiration de la souris avec l'imagerie intravitale évitant ainsi l'impact du mouvement respiratoire sur l'imagerie.

6   Conclusion et perspectives

Au début de ce manuscrit nous avons décrit les différentes étapes de la cascade métastatique ainsi que les techniques d'imagerie qui permettent d'étudier ce phénomène *in vivo.* Bien que l'imagerie intravitale soit très informative pour l'étude de la dynamique de l'invasion tumorale, son manque de résolution empêche la description de la machinerie cellulaire mise en jeu par la cellule tumorale pour infiltrer et se disséminer dans tout l'organisme. La CLEM se révèle alors la seule solution pour combiner le meilleur des deux méthodes d'imagerie : l'imagerie dynamique du processus métastatique et la très haute résolution fournie par la microscopie électronique.

Dans ce contexte, j'ai validé au début de ma thèse la technique d'imagerie intravitale de xénogreffes de cellules tumorales dans l'oreille de souris. Ensuite, j'ai participé à la construction de deux protocoles différents de CLEM intravitale en collaboration avec des équipes de recherches allemandes, l'équipe de Y. Schwab (EMBL, Heidelberg) et celle de F. Winkler (DKFZ, Heidelberg). Ces protocoles sont utilisés en routine et ouvrent la voie à l'étude de l'ensemble des étapes de la cascade métastatique à l'échelle ultrastructurale chez la souris.

Le protocole basé sur la corrélation à l'aide du microCT est actuellement appliqué à l'étude de l'extravasation dans le cerveau de souris. En effet, on ne sait pas à l'heure actuelle quels sont les mécanismes qui permettent à la cellule tumorale de sortir d'un vaisseau sanguin et de former une métastase cérébrale. Les invadopodes seraient impliqués dans ce processus actif d'extravasation comme nous l'avons vu dans l'introduction. Une autre possibilité repose sur la capacité des cellules endothéliales à remodeler la paroi du vaisseau sanguin afin d'extraire le corps étranger de la circulation sanguine et de reformer un vaisseau vascularisé. Cela a déjà été mis en évidence dans le cas d'embolie cérébrale chez la souris (Lam et al., 2010).

Ce protocole est aussi appliqué à l'étude d'autres étapes de la cascade métastique. Nous avons ainsi réalisé avec succès une première expérience menée sur l'étude de la dégradation de la membrane basale dans la glande mammaire de souris, en collaboration avec l'équipe de P. Chavrier (Curie, Paris). Lors de cette collaboration nous avons montré que l'imagerie par microCT fournissait suffisamment d'informations pour corréler microscopie intravitale et microscopie électronique. Des améliorations peuvent être apportées par l'imagerie des adipocytes par THG afin de rendre plus précise la corrélation et ainsi la relocalisation des structures d'intérêt par microscopie électronique.

La CLEM intravitale pourrait aussi contribuer à la compréhension de la formation de métastases en étudiant la formation de la niche pré-métastatique. En effet, la niche pré-métastatique peut être induite par le relargage dans la circulation sanguine d'exosomes. Actuellement on ne sait pas comment ces vésicules nanométriques interagissent et sont internalisées par les cellules endothéliales entrainant la déstabilisation des jonctions entre ces cellules.

Nous souhaitons actuellement augmenter le nombre de techniques d'imagerie *in vivo*. Dans cette optique, j'ai été formé par les membres de la plateforme d'imagerie de l'Institut Gustave Roussy à la pose de fenêtres dorsales chez la souris. Cette technique permettrait de pouvoir étudier par exemple, la migration des cellules tumorales le long de fibres de collagène ainsi que la formation d'invadopodes. D'autres membres de l'équipe ont également été formés à la pose de fenêtres abdominales, ce qui nous permettrait d'étudier la formation de métastases au niveau d'autres organes.

Enfin, ce protocole étant disponible sous forme d'article de méthodologie, il peut aussi être appliqué à d'autres thématiques de recherche comme la neuroscience ou la biologie du développement.

Pour améliorer la technique de CLEM, on pourrait imaginer sur le même principe que les microscopes électroniques à balayage couplés à un ultramicrotome, avoir cette fois ci l'ultramicrotome couplé au tomogramme à rayons X. L'appareil pourrait ainsi fournir un bloc où toute la partie ne contenant pas l'échantillon aurait déjà été supprimée, améliorant encore davantage l'efficacité du protocole. D'autres améliorations peuvent aussi être apportées en utilisant des marqueurs bimodalités comme les nanoparticules pouvant à la fois contenir un agent fluorescent et un agent de contraste aux rayons X. L'utilisation de telles sondes dans la circulation sanguine pourrait faciliter la corrélation entre tomographie aux rayons X et imagerie intravitale. Toutefois, la difficulté dans l'utilisation de ces sondes dans la circulation sanguine reste de les conserver liées à l'endothélium au moment de la fixation intracardiaque de la souris pour éviter leur lavage.

L'étude de l'ultrastructure des invadopodes *in vivo* et *in vitro* en collaboration avec l'équipe de F. Saltel (INSERM, Bordeaux) m'a permis de mettre en place au laboratoire une méthode de CLEM *in vitro* grâce à laquelle j'ai pu traiter l'échantillon de la microscopie confocale jusqu'aux coupes sériées ultrafines et l'imagerie par microscopie électronique. La difficulté de préparation de l'échantillon pour la microscopie électronique m'a convaincu de la nécessité de pouvoir créer rapidement ses propres outils. C'est le cas notamment de « l'ascenseur à Formvar » qui nous permet maintenant à la fois un gain de temps et un gain en qualité du revêtement des grilles de microscopie électronique non négligeable. Les lignées cellulaires exprimant à la fois un marqueur des invadopodes (Tks5) ainsi qu'un marqueur de l'actine ont depuis été générées au laboratoire. Elles nous permettront d'observer la formation et la dynamique des invadopodes *in vivo* chez la souris que ce soit dans l'oreille ou dans d'autres organes grâce à la pose de fenêtres implantables. L'observation des invadopodes dans différents organes nous permettrait de valider l'existence des invadopodes *in vivo* ainsi que la théorie de plasticité de ces structures par CLEM.

« Progress in science depends on new techniques, new discoveries ans new ideas, probably in that order » — Sydney Brenner

7 Bibliographie

Abbe. 1873. Beiträge zur Theorie des Mikroskops und der mikroskopischen Wahrnehmung. Archiv für Mikroskopische Anatomie. doi:10.1007/BF02956173. 9:413–418.

Abtin, Jain, Mitchell, Roediger, Brzoska, Tikoo, Cheng, Ng, Cavanagh, A. UHV, Hickey, Firth, and Weninger. 2014. Perivascular macrophages mediate neutrophil recruitment during bacterial skin infection. Nature immunology. doi:10.1038/ni.2769. 15:45–53.

Agronskaia, Valentijn, D. LFV, Schneijdenberg, Humbel, H. PMVBE, Verkleij, Koster, and Gerritsen. 2008. Integrated fluorescence and transmission electron microscopy. Journal of structural biology. doi:10.1016/j.jsb.2008.07.003. 164:183–9.

Alexander, Koehl, Hirschberg, Geissler, and Friedl. 2008. Dynamic imaging of cancer growth and invasion: a modified skin-fold chamber model. Histochemistry and cell biology. doi:10.1007/s00418-008-0529-1. 130:1147–54.

Armer, Mariggi, Png, Genoud, Monteith, Bushby, Gerhardt, and Collinson. 2009. Imaging Transient Blood Vessel Fusion Events in Zebrafish by Correlative Volume Electron Microscopy. PLoS ONE. doi:10.1371/journal.pone.0007716. 4:e7716.

Attia, Anton, Chiper, Akasov, Anton, Messaddeq, Fournel, Klymchenko, Mély, and Vandamme. 2014. Biodistribution of X-Ray Iodinated Contrast Agent in Nano-Emulsions Is Controlled by the Chemical Nature of the Oily Core. ACS Nano. doi:10.1021/nn503973z. 8:10537–10550.

Auguste, Fallavollita, Wang, Burnier, Bikfalvi, and Brodt. 2007. The host inflammatory response promotes liver metastasis by increasing tumor cell arrest and extravasation. The American journal of pathology. doi:10.2353/ajpath.2007.060886. 170:1781–92.

Badowski, Pawlak, and Grichine. 2008. Paxillin phosphorylation controls invadopodia/podosomes spatiotemporal organization. doi:10.1091/mbc.E06-01-0088.

Baluk, Morikawa, Haskell, Mancuso, and nald. 2003. Abnormalities of basement membrane on blood vessels and endothelial sprouts in tumors. The American journal of pathology. doi:10.1016/S0002-9440(10)63540-7. 163:1801–15.

Beerling, Ritsma, Vrisekoop, Derksen, and Rheenen. 2011. Intravital microscopy: new insights into metastasis of tumors. Journal of cell science. doi:10.1242/jcs.072728. 124:299–310.

Berning, Willig, Steffens, Dibaj, and Hell. 2012. Nanoscopy in a living mouse brain. Science (New York, N.Y.). doi:10.1126/science.1215369. 335:551.

Bishop, Nikić, Brinkoetter, Knecht, Potz, Kerschensteiner, and Misgeld. 2011. Near-infrared branding efficiently correlates light and electron microscopy. Nature methods. doi:10.1038/nmeth.1622. 8:568–70.

Briggman, and Bock. 2012. Volume electron microscopy for neuronal circuit reconstruction. Current Opinion in Neurobiology. doi:10.1016/j.conb.2011.10.022. 22:154–161.

Calin, and Croce. 2006. MicroRNA signatures in human cancers.

Campagnola, Wei, Lewis, and Loew. 1999. High-Resolution Nonlinear Optical Imaging of Live Cells by Second Harmonic Generation. Biophysical Journal. doi:10.1016/s0006-3495(99)77165-1. 77:3341–3349.

Cardona, Saalfeld, Schindelin, Arganda-Carreras, Preibisch, Longair, Tomancak, Hartenstein, and Douglas. 2012. TrakEM2 software for neural circuit reconstruction. PloS one. doi:10.1371/journal.pone.0038011. 7:e38011.

Chambers, Groom, and MacDonald. 2002. Dissemination and growth of cancer cells in metastatic sites. Nature reviews. Cancer. doi:10.1038/nrc865. 2:563–72.

Chen. 1989. Proteolytic activity of specialized surface protrusions formed at rosette contact sites of transformed cells. Journal of Experimental Zoology. doi:10.1002/jez.1402510206. 251:167–185.

Chen, Ba, Ma, Cai, Yin, and Wang. 2008a. Characterization of microRNAs in serum: a novel class of biomarkers for diagnosis of cancer and other diseases.

Chen, Winters, and Reese. 2008b. Life Inside a Thin Section: Tomography. The Journal of Neuroscience. doi:10.1523/jneurosci.2992-08.2008. 28:9321–9327.

Chiang, Cabrera, and Segall. 2016. Tumor cell intravasation. American Journal of Physiology - Cell Physiology. doi:10.1152/ajpcell.00238.2015. 311:C1–C14.

Condeelis, and Pollard. 2006. Macrophages: obligate partners for tumor cell migration, invasion, and metastasis. Cell. doi:10.1016/j.cell.2006.01.007. 124:263–6.

Courtneidge, Azucena, Pass, Seals, and Tesfay. 2005. The SRC substrate Tks5, podosomes (invadopodia), and cancer cell invasion. Cold Spring Harbor symposia on quantitative biology. doi:10.1101/sqb.2005.70.014. 70:167–71.

Cox, G., and E. Kable. 2006. Second-Harmonic Imaging of Collagen. 319.

Deerinck, Martone, Lev-Ram, Green, Tsien, Spector, Huang, and Ellisman. 1994. Fluorescence photooxidation with eosin: a method for high resolution immunolocalization and in situ hybridization detection for light and electron microscopy. The Journal of cell biology. 126:901–10.

Denk, and Horstmann. 2004. Serial Block-Face Scanning Electron Microscopy to Reconstruct Three-Dimensional Tissue Nanostructure. PLoS Biology. doi:10.1371/journal.pbio.0020329. 2:e329.

Destaing, Planus, Bouvard, Oddou, Badowski, Bossy, Raducanu, Fourcade, Albiges-Rizo, and Block. 2010. 1A integrin is a master regulator of invadosome organization and function. Molecular biology of the cell. doi:10.1091/mbc.E10-07-0580. 21:4108–4119.

Durdu, Iskar, Revenu, Schieber, Kunze, Bork, Schwab, and Gilmour. 2014. Luminal signalling links cell communication to tissue architecture during organogenesis. Nature. doi:10.1038/nature13852. 0.

Eddy, Weidmann, Sharma, and Condeelis. 2017. Tumor Cell Invadopodia: Invasive Protrusions that Orchestrate Metastasis. Trends in Cell Biology. doi:10.1016/j.tcb.2017.03.003.

Engelenburg, Shtengel, Sengupta, Waki, Jarnik, Ablan, Freed, Hess, and Lippincott-Schwartz. 2014. Distribution of ESCRT Machinery at HIV Assembly Sites Reveals Virus Scaffolding of ESCRT Subunits. Science. doi:10.1126/science.1247786. 343:653–656.

Farina, K. 1998. Cell Motility of Tumor Cells Visualized in Living Intact Primary Tumors Using Green Fluorescent Protein.

Fine, and Hansen. 1971. Optical second harmonic generation in biological systems.

Franco- Barraza, Beacham, Amatangelo, and Cukierman. 2016. Current Protocols in Cell Biology. doi:10.1002/cpcb.2. 10.9.1-10.9.34.

Franken, Hill, Peters, and Weinreich. 1961. Generation of optical harmonics. Physical Review Letters. 7:118.

Friedl, and Alexander. 2011. Cancer invasion and the microenvironment: plasticity and reciprocity. Cell. doi:10.1016/j.cell.2011.11.016. 147:992–1009.

Friedl, and Gilmour. 2009. Collective cell migration in morphogenesis, regeneration and cancer. Nature reviews. Molecular cell biology. doi:10.1038/nrm2720. 10:445–57.

Friedl, and Wolf. 2003. Tumour-cell invasion and migration: diversity and escape mechanisms. Nature reviews. Cancer. doi:10.1038/nrc1075. 3:362–74.

Friedl, and Wolf. 2008. Tube travel: the role of proteases in individual and collective cancer cell invasion. Cancer research. doi:10.1158/0008-5472.CAN-08-0784. 68:7247–9.

Friedl, and Wolf. 2009. Proteolytic interstitial cell migration: a five-step process. Cancer metastasis reviews. doi:10.1007/s10555-008-9174-3. 28:129–35.

Gabor, Kim, Kim, and Hess. 2015. Nanoscale imaging of caveolin-1 membrane domains in vivo. doi:10.1371/journal.pone.0117225.

Gadea, Toledo, Anguille, and Roux. 2007. Loss of p53 promotes RhoA–ROCK-dependent cell migration and invasion in 3D matrices. The Journal of Cell Biology. doi:10.1083/jcb.200701120. 178:23–30.

Gaggioli, Hooper, Hidalgo-Carcedo, Grosse, Marshall, Harrington, and Sahai. 2007. Fibroblast-led collective invasion of carcinoma cells with differing roles for RhoGTPases in leading and following cells. Nature cell biology. doi:10.1038/ncb1658. 9:1392–400.

Gailhouste, Grand, Odin, Guyader, Turlin, Ezan, Désille, Guilbert, Bessard, Frémin, Theret, and Baffet. 2010. Fibrillar collagen scoring by second harmonic microscopy: A new tool in the assessment of liver fibrosis. Journal of Hepatology. doi:10.1016/j.jhep.2009.12.009. 52:398–406.

Gao, Nolan, Mellick, Bambino, nnell, and Mittal. 2008. Endothelial Progenitor Cells Control the

Angiogenic Switch in Mouse Lung Metastasis. Science. doi:10.1126/science.1150224. 319:195–198.

Glentis, Gurchenkov, and Vignjevic. 2014. Assembly, heterogeneity, and breaching of the basement membranes. Cell Adhesion & Migration. doi:10.4161/cam.28733. 8:236–245.

Gligorijevic, Bergman, and Condeelis. 2014. Multiparametric Classification Links Tumor Microenvironments with Tumor Cell Phenotype. PLoS Biology. doi:10.1371/journal.pbio.1001995. 12:e1001995.

Gligorijevic, Kedrin, Segall, Condeelis, and Rheenen. 2009. Dendra2 photoswitching through the Mammary Imaging Window. Journal of visualized experiments : JoVE. doi:10.3791/1278.

Gligorijevic, Wyckoff, Yamaguchi, Wang, Roussos, and Condeelis. 2012. N-WASP-mediated invadopodium formation is involved in intravasation and lung metastasis of mammary tumors. Journal of cell science. doi:10.1242/jcs.092726. 125:724–34.

Goetz, Minguet, Navarro-Lérida, Lazcano, Samaniego, Calvo, Tello, Osteso-Ibáñez, Pellinen, Echarri, Cerezo, Klein-Szanto, Garcia, Keely, Sánchez-Mateos, Cukierman, and Pozo. 2011. Biomechanical Remodeling of the Microenvironment by Stromal Caveolin-1 Favors Tumor Invasion and Metastasis. Cell. doi:10.1016/j.cell.2011.05.040. 146:148–63.

Goetz, Monduc, Schwab, and Vermot. 2015. Using Correlative Light and Electron Microscopy to Study Zebrafish Vascular Morphogenesis. Methods in molecular biology (Clifton, N.J.). doi:10.1007/978-1-4939-1164-6_3. 1189:31–46.

Goetz, Steed, Ferreira, Roth, Ramspacher, Boselli, Charvin, Liebling, Wyart, Schwab, and Vermot. 2014. Endothelial Cilia Mediate Low Flow Sensing during Zebrafish Vascular Development. Cell Reports. doi:10.1016/j.celrep.2014.01.032. 6:799–808.

Hagedorn, Ziel, Morrissey, Linden, Wang, Chi, Johnson, and Sherwood. 2013. The netrin receptor DCC focuses invadopodia-driven basement membrane transmigration in vivo. The Journal of Cell Biology. doi:10.1083/jcb.201301091. 201:903–913.

Ham, Brady, and Kalicharan. 2014. Intravital correlated microscopy reveals differential macrophage and microglial dynamics during resolution of neuroinflammation.

Handschuh, Baeumler, Schwaha, and Ruthensteiner. 2013. A correlative approach for combining microCT, light and transmission electron microscopy in a single 3D scenario. Frontiers in Zoology. doi:10.1186/1742-9994-10-44. 10:1–16.

Harney, Arwert, Entenberg, Wang, Guo, Qian, Oktay, Pollard, Jones, and Condeelis. 2015. Real-Time Imaging Reveals Local, Transient Vascular Permeability, and Tumor Cell Intravasation Stimulated by TIE2hi Macrophage-Derived VEGFA. Cancer discovery. doi:10.1158/2159-8290.cd-15-0012. 5:932–43.

Hayworth, Kasthuri, Schalek, and Lichtman. 2006. Automating the collection of ultrathin serial sections for large volume TEM reconstructions. Microscopy and Microanalysis. 12:86.

Helmchen, and Denk. 2005. Deep tissue two-photon microscopy. Nature Methods. doi:10.1038/nmeth818. 2:932–940.

Hoshino, Costa-Silva, Shen, Rodrigues, Hashimoto, Mark, Molina, Kohsaka, Giannatale, Ceder, Singh, Williams, Soplop, Uryu, Pharmer, King, Bojmar, Davies, Ararso, Zhang, Zhang, Hernandez, Weiss, Dumont-Cole, Kramer, Wexler, Narendran, Schwartz, Healey, Sandstrom, Labori, Kure, Grandgenett, Hollingsworth, Sousa, Kaur, Jain, Mallya, Batra, Jarnagin, Brady, Fodstad, Muller, Pantel, Minn, Bissell, Garcia, Kang, Rajasekhar, Ghajar, Matei, Peinado, Bromberg, and Lyden. 2015. Tumour exosome integrins determine organotropic metastasis. Nature. doi:10.1038/nature15756. 527:329–335.

Hoshino, Kirkbride, Costello, Clark, Sinha, Grega-Larson, Tyska, and Weaver. 2013. Exosome Secretion Is Enhanced by Invadopodia and Drives Invasive Behavior. Cell Reports. doi:10.1016/j.celrep.2013.10.050. 5:1159–1168.

Hotary, Li, Allen, and Stevens. 2006. A cancer cell metalloprotease triad regulates the basement membrane transmigration program. doi:10.1101/gad.1451806.

Huang, Jones, Brandenburg, and Zhuang. 2008. Whole-cell 3D STORM reveals interactions between cellular structures with nanometer-scale resolution. Nature methods. doi:10.1038/nmeth.1274. 5:1047–52.

Hyenne, Apaydin, Rodriguez, Spiegelhalter, Hoff-Yoessle, Diem, Tak, Lefebvre, Schwab, Goetz, and Labouesse. 2015. RAL-1 controls multivesicular body biogenesis and exosome secretion. The Journal of Cell Biology. doi:10.1083/jcb.201504136. 211:27–37.

Ito, S. 2001. REAL-
TIME OBSERVATION OF MICROMETASTASIS FORMATION IN THE LIVING MOUSE LIVE
R USING A GREEN FLUORESCENT PROTEIN GENE–
TAGGED RAT TONGUE CARCINOMA CELL LINE.

Juin, Billottet, Moreau, Destaing, Albiges-Rizo, Rosenbaum, Génot, and Saltel. 2012. Physiological
type I collagen organization induces the formation of a novel class of linear invadosomes. Molecular
Biology of the Cell. doi:10.1091/mbc.E11-07-0594. 23:297–309.

Juin, Martino, Leitinger, Henriet, Gary, Paysan, Bomo, Baffet, Gauthier-Rouvière, Rosenbaum,
Moreau, and Saltel. 2014. Discoidin domain receptor 1 controls linear invadosome formation via a
Cdc42–Tuba pathway. The Journal of Cell Biology. doi:10.1083/jcb.201404079. 207:517–533.

Juncker-Jensen, Deryugina, Rimann, and Zajac. 2013. Tumor MMP-1 activates endothelial PAR1 to
facilitate vascular intravasation and metastatic dissemination. doi:10.1158/0008-5472.CAN-12-
4495.

Jungbluth, and Gautel. 2014. Pathogenic Mechanisms in Centronuclear Myopathies. Frontiers in
Aging Neuroscience. doi:10.3389/fnagi.2014.00339. 6:339.

Kalluri. 2003. Basement membranes: structure, assembly and role in tumour angiogenesis. Nature
reviews. Cancer. doi:10.1038/nrc1094. 3:422–33.

Kaplan, Riba, Zacharoulis, Bramley, Vincent, Costa, MacDonald, Jin, Shido, Kerns, Zhu, Hicklin,
Wu, Port, Altorki, Port, Ruggero, Shmelkov, Jensen, Rafii, and Lyden. 2005. VEGFR1-positive
haematopoietic bone marrow progenitors initiate the pre-metastatic niche. Nature.
doi:10.1038/nature04186. 438:820–7.

Karreman, Hyenne, Schwab, and Goetz. 2016. Intravital Correlative Microscopy: Imaging Life at the
Nanoscale. Trends in Cell Biology. doi:10.1016/j.tcb.2016.07.003. 26:848–863.

Kedrin, Gligorijevic, Wyckoff, Verkhusha, Condeelis, Segall, and Rheenen. 2008. Intravital imaging
of metastatic behavior through a mammary imaging window. Nature methods.
doi:10.1038/nmeth.1269. 5:1019–21.

Kienast, Baumgarten, Fuhrmann, Klinkert, Goldbrunner, Herms, and Winkler. 2010. Real-time

imaging reveals the single steps of brain metastasis formation. Nature medicine. doi:10.1038/nm.2072. 16:116–22.

Kim, Williams, Gavin, Jardine, Chambers, and Leong. 2016. Quantification of cancer cell extravasation in vivo. Nature Protocols. doi:10.1038/nprot.2016.050. 11:937–948.

Knott, Holtmaat, Trachtenberg, Svoboda, and Welker. 2009. A protocol for preparing GFP-labeled neurons previously imaged in vivo and in slice preparations for light and electron microscopic analysis. Nature Protocols. doi:10.1038/nprot.2009.114. 4:1145–1156.

Kolotuev, Schwab, and Labouesse. 2010. A precise and rapid mapping protocol for correlative light and electron microscopy of small invertebrate organisms. Biology of the Cell. doi:10.1042/bc20090096. 102:121–132.

Kopek, Paez-Segala, Shtengel, Sochacki, Sun, Wang, Xu, E. SBV, Taraska, Looger, and Hess. 2017. Diverse protocols for correlative super-resolution fluorescence imaging and electron microscopy of chemically fixed samples. Nature Protocols. doi:10.1038/nprot.2017.017. 12:916–946.

Korogod, Petersen, and Knott. 2015. Ultrastructural analysis of adult mouse neocortex comparing aldehyde perfusion with cryo fixation. eLife. doi:10.7554/elife.05793. 4.

Kremer, Mastronarde, and McIntosh. 1996. Computer visualization of three-dimensional image data using IMOD. Journal of structural biology. doi:10.1006/jsbi.1996.0013. 116:71–6.

Labernadie, Kato, Brugués, Serra-Picamal, Derzsi, Arwert, Weston, González-Tarragó, Elosegui-Artola, Albertazzi, Alcaraz, Roca-Cusachs, Sahai, and Trepat. 2017. A mechanically active heterotypic E-cadherin/N-cadherin adhesion enables fibroblasts to drive cancer cell invasion. Nature Cell Biology. doi:10.1038/ncb3478.

Lam, Yoo, Hiner, Liu, and Grutzendler. 2010. Embolus extravasation is an alternative mechanism for cerebral microvascular recanalization. Nature. doi:10.1038/nature09001. 465:478–482.

Lämmermann, and Sixt. 2009. Mechanical modes of "amoeboid" cell migration. Current Opinion in Cell Biology. doi:10.1016/j.ceb.2009.05.003. 21:636–644.

Leong, Robertson, Stoletov, Leith, Chin, Chien, Hague, Ablack, Carmine-Simmen, McPherson,

Postenka, Turley, Courtneidge, Chambers, and Lewis. 2014. Invadopodia Are Required for Cancer Cell Extravasation and Are a Therapeutic Target for Metastasis. Cell Reports. doi:10.1016/j.celrep.2014.07.050. 8:1558–1570.

Li, Anton, Zuber, Zhao, Messaddeq, Hallouard, Fessi, and Vandamme. 2013. Iodinated α-tocopherol nano-emulsions as non-toxic contrast agents for preclinical X-ray imaging. Biomaterials. doi:10.1016/j.biomaterials.2012.09.026. 34:481491.

Li, Goh, Keeble, Qin, Roediger, Jain, Wang, Chew, Weninger, and Ng. 2012. Intravital multiphoton imaging of immune responses in the mouse ear skin. Nature protocols. doi:10.1038/nprot.2011.438. 7:221–34.

Linder. 2007. The matrix corroded: podosomes and invadopodia in extracellular matrix degradation. Trends in Cell Biology. doi:10.1016/j.tcb.2007.01.002. 17:107117.

Liv, Zonnevylle, Narvaez, Effting, Voorneveld, Lucas, Hardwick, Wepf, Kruit, and Hoogenboom. 2013. Simultaneous correlative scanning electron and high-NA fluorescence microscopy. PloS one. doi:10.1371/journal.pone.0055707. 8:e55707.

Lodillinsky, Infante, Guichard, Chaligné, Fuhrmann, Cyrta, Irondelle, Lagoutte, Vacher, Bonsang-Kitzis, Glukhova, Reyal, Bièche, Vincent-Salomon, and Chavrier. 2016. p63/MT1-MMP axis is required for in situ to invasive transition in basal-like breast cancer. Oncogene. doi:10.1038/onc.2015.87. 35:344–357.

Lodish, H., A. Berk, and S. Zipursky. 2017. Collagen: The Fibrous Proteins of the Matrix. https://www.ncbi.nlm.nih.gov/books/NBK21582/.

Lorenz, Yamaguchi, Wang, Singer, and Condeelis. 2004. Imaging Sites of N-WASP Activity in Lamellipodia and Invadopodia of Carcinoma Cells. Current Biology. doi:10.1016/j.cub.2004.04.008. 14:697–703.

Lyden, Hattori, Dias, Costa, Blaikie, Butros, Chadburn, Heissig, Marks, Witte, Wu, Hicklin, Zhu, Hackett, Crystal, Moore, Hajjar, Manova, Benezra, and Rafii. 2001. Impaired recruitment of bone-marrow-derived endothelial and hematopoietic precursor cells blocks tumor angiogenesis and growth. Nature medicine. doi:10.1038/nm1101-1194. 7:1194–201.

Martino, Henriet, Ezzoukhry, Goetz, Moreau, and Saltel. 2016. The microenvironment controls

invadosome plasticity. J Cell Sci. doi:10.1242/jcs.182329. 129:1759–1768.

Masedunskas, Milberg, Porat-Shliom, mkova, Wigand, Amornphimoltham, and Weigert. 2012. Intravital microscopy: a practical guide on imaging intracellular structures in live animals. Bioarchitecture. doi:10.4161/bioa.21758. 2:143–57.

Massagué, and Obenauf. 2016. Metastatic colonization by circulating tumour cells. Nature. doi:10.1038/nature17038. 529:298–306.

Mayor, and Etienne-Manneville. 2016. The front and rear of collective cell migration. Nature Reviews Molecular Cell Biology. doi:10.1038/nrm.2015.14. 17:97–109.

Meer, G. van, E. Stelzer, R, and K. Simons. 1987. Sorting of sphingolipids in epithelial (Madin-Darby canine kidney) cells. doi:10.1083/jcb.105.4.1623.

Mercier, Böhm, Fekonja, Allio, Lutz, Koch, Goetz, and Laporte. 2016. In vivoimaging of skeletal muscle in mice highlights muscle defects in a model of myotubular myopathy. IntraVital. doi:10.1080/21659087.2016.1168553. 5:e1168553.

Miesenböck, Angelis, and Rothman. 1998. Visualizing secretion and synaptic transmission with pH-sensitive green fluorescent proteins. Nature. doi:10.1038/28190. 394:192–195.

Millard, Jin, Wei, Wuskell, Lewis, and Loew. 2004. Sensitivity of Second Harmonic Generation from Styryl Dyes to Transmembrane Potential. Biophysical Journal. doi:10.1016/s0006-3495(04)74191-0. 86:1169–1176.

MIRONOV, and BEZNOUSSENKO. 2009. Correlative microscopy: a potent tool for the study of rare or unique cellular and tissue events. Journal of Microscopy. doi:10.1111/j.1365-2818.2009.03222.x. 235:308–321.

Muraoka, Dumont, Ritter, Dugger, Brantley, Chen, Easterly, Roebuck, Ryan, Gotwals, Koteliansky, and Arteaga. 2002. Blockade of TGF-beta inhibits mammary tumor cell viability, migration, and metastases. The Journal of clinical investigation. doi:10.1172/JCI15234. 109:1551–9.

Murphy, and Courtneidge. 2011. The "ins" and "outs" of podosomes and invadopodia: characteristics, formation and function. Nature Reviews Molecular Cell Biology. doi:10.1038/nrm3141. 12:413–426.

Narayan, and Subramaniam. 2015. Focused ion beams in biology. Nature Methods. doi:10.1038/nmeth.3623. 12:1021–1031.

Nguyen, Bos, and Massagué. 2009. Metastasis: from dissemination to organ-specific colonization. Nature Reviews Cancer. doi:10.1038/nrc2622. 9:274–284.

Nieswandt, Hafner, Echtenacher, and Männel. 1999. Lysis of tumor cells by natural killer cells in mice is impeded by platelets. Cancer research. 59:1295–300.

Nixon, Webb, Floetenmeyer, Schieber, Lo, and Parton. 2009. A Single Method for Cryofixation and Correlative Light, Electron Microscopy and Tomography of Zebrafish Embryos. Traffic. doi:10.1111/j.1600-0854.2008.00859.x. 10:131–136.

Ota, Li, Hu, and Weiss. 2009. Induction of a MT1-MMP and MT2-MMP-dependent basement membrane transmigration program in cancer cells by Snail1. Proceedings of the National Academy of Sciences. doi:10.1073/pnas.0910962106. 106:20318–20323.

Pagano, Sepanski, and Martin. 1989. Molecular trapping of a fluorescent ceramide analogue at the Golgi apparatus of fixed cells: interaction with endogenous lipids provides a trans-Golgi marker for both light and electron microscopy. The Journal of cell biology. 109:2067–79.

Palumbo, Talmage, Massari, J. CML, Flick, Kombrinck, Hu, Barney, and Degen. 2007. Tumor cell-associated tissue factor and circulating hemostatic factors cooperate to increase metastatic potential through natural killer cell-dependent and-independent mechanisms. Blood. doi:10.1182/blood-2007-01-065995. 110:133–41.

Palumbo, Talmage, Massari, J. CML, Flick, Kombrinck, Jirousková, and Degen. 2005. Platelets and fibrin(ogen) increase metastatic potential by impeding natural killer cell-mediated elimination of tumor cells. Blood. doi:10.1182/blood-2004-06-2272. 105:178–85.

Paris, and Sesboüé. 2004. Metastasis models: the green fluorescent revolution? Carcinogenesis. doi:10.1093/carcin/bgh219.

Paterson, and Courtneidge. 2017. Invadosomes are coming: new insights into function and disease relevance. The FEBS Journal. doi:10.1111/febs.14123.

Paz, Pathak, and Yang. 2014. Invading one step at a time: the role of invadopodia in tumor metastasis. Oncogene. doi:10.1038/onc.2013.393. 33:4193–202.

Peddie, and Collinson. 2014. Exploring the third dimension: Volume electron microscopy comes of age. Micron. doi:10.1016/j.micron.2014.01.009. 61:9–19.

Peinado, Alečković, Lavotshkin, Matei, Costa-Silva, Moreno-Bueno, Hergueta-Redondo, Williams, García-Santos, Ghajar, Nitadori-Hoshino, Hoffman, Badal, Garcia, Callahan, Yuan, Martins, Skog, Kaplan, Brady, Wolchok, Chapman, Kang, Bromberg, and Lyden. 2012. Melanoma exosomes educate bone marrow progenitor cells toward a pro-metastatic phenotype through MET. Nature medicine. doi:10.1038/nm.2753. 18:883–91.

Plotnikov, Millard, Campagnola, and Mohler. 2006. Characterization of the Myosin-Based Source for Second-Harmonic Generation from Muscle Sarcomeres. Biophysical Journal. doi:10.1529/biophysj.105.071555. 90:693–703.

Poincloux, Lizárraga, and Chavrier. 2009. Matrix invasion by tumour cells: a focus on MT1-MMP trafficking to invadopodia. Journal of Cell Science. doi:10.1242/jcs.034561. 122:3015–3024.

Potente, Gerhardt, and Carmeliet. 2011. Basic and therapeutic aspects of angiogenesis. Cell. doi:10.1016/j.cell.2011.08.039. 146:873–87.

Provenzano, Eliceiri, Campbell, Inman, White, and Keely. 2006. Collagen reorganization at the tumor-stromal interface facilitates local invasion. BMC medicine. doi:10.1186/1741-7015-4-38. 4:38.

Qian, Deng, Im, Muschel, Zou, Li, Lang, and Pollard. 2009. A distinct macrophage population mediates metastatic breast cancer cell extravasation, establishment and growth. PloS one. doi:10.1371/journal.pone.0006562. 4:e6562.

Qian, Li, Zhang, Kitamura, Zhang, Campion, Kaiser, Snyder, and Pollard. 2011. CCL2 recruits inflammatory monocytes to facilitate breast-tumour metastasis. Nature. doi:10.1038/nature10138. 475:222–5.

Quail, and Joyce. 2013. Microenvironmental regulation of tumor progression and metastasis. Nature Medicine. doi:10.1038/nm.3394. 19:1423–1437.

Rammal, Saby, Magnien, Van-Gulick, Garnotel, Buache, Btaouri, Jeannesson, and Morjani. 2016.

Discoidin Domain Receptors: Potential Actors and Targets in Cancer. Frontiers in Pharmacology. doi:10.3389/fphar.2016.00055. 7.

Rankin, Moneron, Wurm, Nelson, Walter, Schwarzer, Schroeder, Colón-Ramos, and Hell. 2011. Nanoscopy in a living multicellular organism expressing GFP. Biophysical journal. 100:L63–L65.

Rehberg, Krombach, Pohl, and Dietzel. 2011. Label-Free 3D Visualization of Cellular and Tissue Structures in Intact Muscle with Second and Third Harmonic Generation Microscopy. PLoS ONE. doi:10.1371/journal.pone.0028237. 6:e28237.

Reymond, d'Água, and Ridley. 2013. Crossing the endothelial barrier during metastasis. Nature Reviews Cancer. doi:10.1038/nrc3628. 13:858–870.

Riedl, Crevenna, Kessenbrock, Yu, Neukirchen, Bista, Bradke, Jenne, Holak, Werb, Sixt, and Wedlich-Soldner. 2008. Lifeact: a versatile marker to visualize F-actin. Nature Methods. doi:10.1038/nmeth.1220. 5:605–607.

Romero. 2010. Centronuclear myopathies: A widening concept. Neuromuscular Disorders. doi:10.1016/j.nmd.2010.01.014. 20:223–228.

Rowe, and Weiss. 2008. Breaching the basement membrane: who, when and how? Trends in Cell Biology. doi:10.1016/j.tcb.2008.08.007. 18:560–574.

Rupp, Langlois, Koczorowska, Radwanska, Sun, Hussenet, Lefebvre, Murdamoothoo, Arnold, Klein, Biniossek, Hyenne, Naudin, Velazquez-Quesada, Schilling, Obberghen-Schilling, and Orend. 2016. Tenascin-C Orchestrates Glioblastoma Angiogenesis by Modulation of Pro- and Anti-angiogenic Signaling. Cell Reports. doi:10.1016/j.celrep.2016.11.012. 17:2607–2619.

Sahai, and Marshall. 2003. Differing modes of tumour cell invasion have distinct requirements for Rho/ROCK signalling and extracellular proteolysis. Nature Cell Biology. doi:10.1038/ncb1019. 5:711–719.

Sahl, Hell, and Jakobs. 2017. Fluorescence nanoscopy in cell biology. Nature Reviews Molecular Cell Biology. doi:10.1038/nrm.2017.71.

Schermelleh, Heintzmann, and Leonhardt. 2010. A guide to super-resolution fluorescence microscopy. The Journal of cell biology. doi:10.1083/jcb.201002018. 190:165–75.

Schindelin, Arganda-Carreras, Frise, Kaynig, Longair, Pietzsch, Preibisch, Rueden, Saalfeld, Schmid, Tinevez, White, Hartenstein, Eliceiri, Tomancak, and Cardona. 2012. Fiji: an open-source platform for biological-image analysis. Nature methods. doi:10.1038/nmeth.2019. 9:676–82.

Schnorrenberg, Grotjohann, Vorbrüggen, Herzig, Hell, and Jakobs. 2016. In vivo super-resolution RESOLFT microscopy of Drosophila melanogaster. eLife. doi:10.7554/eLife.15567. 5.

Schoumacher, Goldman, Louvard, and Vignjevic. 2010. Actin, microtubules, and vimentin intermediate filaments cooperate for elongation of invadopodia. The Journal of Cell Biology. doi:10.1083/jcb.200909113. 189:541–556.

Seals, Azucena, Pass, Tesfay, Gordon, Woodrow, Resau, and Courtneidge. 2005. The adaptor protein Tks5/Fish is required for podosome formation and function, and for the protease-driven invasion of cancer cells. Cancer cell. doi:10.1016/j.ccr.2005.01.006. 7:155–65.

Shibue, and Weinberg. 2009. Integrin beta1-focal adhesion kinase signaling directs the proliferation of metastatic cancer cells disseminated in the lungs. Proceedings of the National Academy of Sciences of the United States of America. doi:10.1073/pnas.0904227106. 106:10290–5.

Shu, Lev-Ram, Deerinck, Qi, Ramko, Davidson, Jin, Ellisman, and Tsien. 2011. A Genetically Encoded Tag for Correlated Light and Electron Microscopy of Intact Cells, Tissues, and Organisms. PLoS Biology. doi:10.1371/journal.pbio.1001041. 9:e1001041.

Spiegelhalter, Laporte, and Schwab. 2014. Correlative light and electron microscopy: from live cell dynamic to 3D ultrastructure. Methods in molecular biology (Clifton, N.J.). doi:10.1007/978-1-62703-776-1_21. 1117:485–501.

Spiegelhalter, Tosch, Hentsch, Koch, Kessler, Schwab, and Laporte. 2010. From dynamic live cell imaging to 3D ultrastructure: novel integrated methods for high pressure freezing and correlative light-electron microscopy. PloS one. doi:10.1371/journal.pone.0009014. 5:e9014.

Staedler, Magouroux, Hadji, Joulaud, Extermann, Schwung, Passemard, Kasparian, Clarke, Gerrmann, Dantec, Mugnier, Rytz, Ciepielewski, Galez, Gerber-Lemaire, Juillerat-Jeanneret, Bonacina, and Wolf. 2012. Harmonic nanocrystals for biolabeling: a survey of optical properties and biocompatibility. ACS nano. doi:10.1021/nn204990n. 6:2542–9.

Stoletov, Kato, Zardouzian, Kelber, Yang, Shattil, and Klemke. 2010. Visualizing extravasation dynamics of metastatic tumor cells. Journal of Cell Science. doi:10.1242/jcs.069443. 123:2332–2341.

Streets, Li, Chen, and Huang. 2014. Imaging without Fluorescence: Nonlinear Optical Microscopy for Quantitative Cellular Imaging. Analytical Chemistry. doi:10.1021/ac5013706. 86:8506–8513.

Tarone, Cirillo, Giancotti, Comoglio, and Marchisio. 1985. Rous sarcoma virus-transformed fibroblasts adhere primarily at discrete protrusions of the ventral membrane called podosomes. Experimental Cell Research. doi:10.1016/S0014-4827(85)80044-6. 159:141–157.

Teitelbaum. 2000. Bone resorption by osteoclasts. doi:10.1126/science.289.5484.1504.

Thomas, Voskuilen, Gerritsen, and Sterenborg. 2014. Advances and challenges in label-free nonlinear optical imaging using two-photon excitation fluorescence and second harmonic generation for cancer research. Journal of Photochemistry and Photobiology B: Biology. doi:10.1016/j.jphotobiol.2014.08.025. 141:128–138.

Tien, Chang, Jeng, Lee, Wu, Lin, and Hsu. 2001. Tumor angiogenesis and its possible role in intravasation of colorectal epithelial cells. Clinical cancer research. 7:1627–1632.

Tinevez, Schulze, Salbreux, Roensch, Joanny, and Paluch. 2009. Role of cortical tension in bleb growth. Proceedings of the National Academy of Sciences. doi:10.1073/pnas.0903353106. 106:18581–18586.

Tokui, Yoneyama, Hatakeyama, Yamamoto, Koie, Saitoh, Yamaya, Funyu, Nakamura, Ohyama, and Tsuboi. 2014. Extravasation during bladder cancer metastasis requires cortactin-mediated invadopodia formation. Molecular Medicine Reports. doi:10.3892/mmr.2014.1965. 9:1142–6.

Van Noorden, R. 2014. Insider view of cells scoops Nobel.

VERKADE. 2008. Moving EM: the Rapid Transfer System as a new tool for correlative light and electron microscopy and high throughput for high- pressure freezing. Journal of Microscopy. doi:10.1111/j.1365-2818.2008.01989.x. 230:317–328.

Vestweber. 2015. How leukocytes cross the vascular endothelium. Nature reviews. Immunology. doi:10.1038/nri3908. 15:692–704.

Wang, Wyckoff, Frohlich, Oleynikov, Hüttelmaier, Zavadil, Cermak, Bottinger, Singer, and White. 2002. Single cell behavior in metastatic primary mammary tumors correlated with gene expression patterns revealed by molecular profiling. Cancer research. 62:6278–6288.

Weijer. 2009. Collective cell migration in development. Journal of cell science. doi:10.1242/jcs.036517. 122:3215–23.

White, J., W. Amos, and M. Fordham. 1987. An evaluation of confocal versus conventional imaging of biological structures by fluorescence light microscopy. doi:10.1083/jcb.105.1.4.

Wu, Hsieh, Tsai, and Liu. 2015. In vivo Quantification of the Structural Changes of Collagens in a Melanoma Microenvironment with Second and Third Harmonic Generation Microscopy. Scientific Reports. doi:10.1038/srep08879. 5:8879.

Wyckoff, Jones, Condeelis, and Segall. 2000. A critical step in metastasis: in vivo analysis of intravasation at the primary tumor. Cancer research. 60:2504–11.

Yang, and Weinberg. 2008. Epithelial-mesenchymal transition: at the crossroads of development and tumor metastasis. Developmental cell. doi:10.1016/j.devcel.2008.05.009. 14:818–29.

York, Parekh, Nogare, Fischer, Temprine, Mione, Chitnis, Combs, and Shroff. 2012. Resolution doubling in live, multicellular organisms via multifocal structured illumination microscopy. Nature Methods. doi:10.1038/nmeth.2025. 9:749–754.

Yuan, Dellian, Fukumura, Leunig, Berk, Torchilin, and Jain. 1995. Vascular permeability in a human tumor xenograft: molecular size dependence and cutoff size. Cancer research. 55:3752–3756.

Zhang, L. 1999. Overexpression of Fibroblast Growth Factor 1 in MCF-7 Breast Cancer Cells Facilitates Tumor Cell Dissemination but Does Not Support the Development of Macrometastases in the Lungs or Lymph Nodes.

Zipfel, Williams, and Webb. 2003. Nonlinear magic: multiphoton microscopy in the biosciences. Nature Biotechnology. doi:10.1038/nbt899. 21:1369–1377.

Luc Mercier

Disséquer la cascade métastatique par des approches innovantes d'imagerie cellulaire
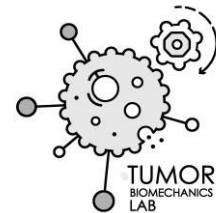
Résumé

La métastase peut être considérée comme le produit final d'un processus à la fois biologique mécanique et chimique où les cellules cancéreuses disséminent dans l'organisme pour envahir un nouvel organe à distance en s'établissant dans un nouvel microenvironnement tissulaire. Bien que les métastases soient la principale cause de décès liée au cancer, les principaux mécanismes impliqués dans ce processus restent à élucider. La communauté scientifique manque de techniques d'imagerie adaptées pour disséquer avec la plus haute résolution possible le comportement des cellules tumorales *in vivo*. Par conséquent, le but principal de ma thèse a été de développer une approche d'imagerie intravitale non-invasive appliquée à la souris. Cette approche a été inclue dans le développement d'un protocole de microscopie corrélative intravitale permettant l'étude de cellules tumorales à différentes échelles dans leur environnement naturel. Ce protocole a été utilisé dans l'étude de cellules invasives tumorales uniques dans l'oreille et le cerveau de la souris. Le but était de décrire les détails des protrusions cellulaires ainsi que les interactions cellule-matrice lors de l'invasion et l'intravasation de cellules cancéreuses.

Mots clés : Cancer, Métastase, Microscopie corrélative intravitale

Résumé en anglais

Metastasis can be considered as the end product of a multistep bio-mechano-chemical process where cancer cells disseminate to anatomically distant organs and home and establish themselves in a new tissue microenvironment. Although metastasis is the leading cause of cancer-related death, the main cellular mechanisms enabling this process remain to be elucidated. Importantly, the scientific community lacks adapted imaging technologies to accurately dissect, at the highest resolution possible, tumor cell behavior *in vivo*. Therefore, the main goal of my PhD thesis was to develop an intravital and non-invasive imaging approach to track tumor progression in the living mouse. This approach was included in the development of an intravital Correlative Light and Electron Microscopy protocol allowing to track tumor cells at different scales in their natural environment. It was used to study single invasive tumor cells in the mouse ear and brain and to describe the details of cell protrusions and cell-matrix interactions during invasion and intravasation of cancer cells.

Key words: Cancer, Metastasis, Intravital correlative microscopy